Apport de l'analyse multi-échelle dans la compréhension des processus géologiques:application aux rifts continentaux et aux volcans boucliers océaniques

Laurent Michon

▶ **To cite this version:**

Laurent Michon. Apport de l'analyse multi-échelle dans la compréhension des processus géologiques:application aux rifts continentaux et aux volcans boucliers océaniques. Géophysique [physics.geo-ph]. Université de la Réunion, 2009. tel-01388225

Mémoire

présenté par

Laurent Michon

Docteur de l'Université Blaise Pascal - Clermont-Ferrand II

pour obtenir

l'Habilitation à Diriger les Recherches

Apport de l'analyse multi-échelle dans la compréhension des processus géologiques:

application aux rifts continentaux et aux volcans boucliers océaniques

Soutenue publiquement le 11 juin 2009 devant le jury composé de:

M. Jacques Déverchère   *(Pr, UMR 6538 Domaines Océaniques, Université de Bretagne Occidentale)*

M. Joan Marti   *(Pr, Institute of Earth Sciences "Jaume Almera", CSIC, Barcelone)*

M. Jacques Malavieille   *(DR, UMR 5243 Géosciences Montpellier)*

M. Olivier Merle   *(Pr, UMR 6524 Laboratoire Magmas et Volcans, Université Blaise Pascal)*

M. Patrick Bachèlery   *(Pr, Laboratoire GéoSciences Réunion, UMR 7154 IPGP, Université de la Réunion)*

Il ne faut pas vendre la peau de l'ours. Non, faut pas la vendre.

Philosophe mésopotamien (IIIème millénaire avant J.C)

Avant Propos

En France, diriger un travail de thèse requiert l'obtention du diplôme ultime: l'Habilitation à Diriger des Recherches. Diriger et orienter ma recherche est pourtant ce que je fais depuis la fin de ma thèse, en 2000. Le présent mémoire est une synthèse de presque 12 années de recherche que j'ai effectuées en tant que doctorant, ATER, post-doctorant puis Maître de Conférences. Durant cette période, j'ai évolué du statut d'étudiant en formation aux métiers de la recherche et de l'enseignement aux statuts d'enseignant-chercheur et formateur. Ce parcours n'a été possible que grâce à des rencontres et des collaborations, fatalement enrichissantes. Les travaux de recherche que j'expose ici ne correspondent donc pas à un travail strictement personnel mais, le plus souvent, à un travail de groupe que j'ai initié et/ou organisé. Par soucis d'exactitude, je rappelle en début de chaque nouvelle section les personnes avec qui j'ai collaboré, et j'utilise la première personne du pluriel pour rédiger les résultats issus de ces collaborations.

Résumé

Ce mémoire synthétise mes travaux de recherche réalisés depuis 1997, date du début de ma thèse. Il présente successivement les deux thématiques que j'ai pu développer en mettant en place une approche multi-disciplinaire, multi-échelle et qui intègre analyse de cas naturels et modélisation des processus géologiques. Comprendre les processus de rifting en domaine continental a été mon premier axe de recherche. Cette thématique repose sur l'analyse du Rift Ouest Européen, formé au Cénozoïque en périphérie de la chaine alpine, et sur la modélisation des processus aux échelles du graben, de la croûte et de la lithosphère. Ces travaux ont permis de proposer un modèle global de formation du Rift Ouest Européen en tenant compte du développement contemporain des Alpes et des Pyrénées. Les modèles analogiques ont mis en lumière le rôle majeur joué par l'héritage structural dans la création des grabens et des dépocentres sédimentaires. Ils ont également montré l'effet de la vitesse d'extension, du nombre de ruptures de la partie fragile de la lithosphère mantellique et des zones de cisaillement ductiles sur la déformation lithosphérique. Le second axe de recherche vise à comprendre les sources et les modalités de déformation des volcans basaltiques. L'étude s'est focalisée sur les volcans de La Réunion, dans l'Océan Indien, et plus particulièrement sur la Piton de la Fournaise, un des volcans les plus actifs au monde. Plusieurs aspects ont été analysés conjointement: la déformation co-éruptive et son impact sur la réactivation des failles pré-existantes; l'origine et la dynamique des calderas en domaine basaltique; le rôle des structures lithosphériques dans l'évolution des édifices volcaniques. Ces différents travaux ont été réalisés en collaboration avec de nombreux chercheurs d'universités et instituts français et étrangers. D'un point de vue quantitatif, ces années de recherche ont conduit à la soutenance de trois Masters 2 recherche et à la publication de 20 articles dans des revues internationales à comités de lecture. Dans le futur, je souhaite organiser ma recherche autour de quatre projets: 1- Dynamique des calderas magmatiques; 2- Rôle du contexte géodynamique dans l'évolution des volcans basaltiques (co-direction de la thèse de Thibault Catry); 3- Distribution et géométrie des injections magmatiques dans les volcans basaltiques: Implications sur la stabilité des édifices; 4- Evolution du Piton de la Fournaise. Les projets 1, 2 et 4 correspondent à un prolongement de la recherche déjà engagée, alors que le projet 3 est un axe nouveau. Ce mémoire présente également un curriculum vitae synthétique dans lequel je résume mon implication au sein du département d'enseignement des Sciences de la Terre de l'Université de La Réunion et les différentes responsabilités administratives que j'ai au sein du département et de l'UFR Sciences et Technologie de l'Université de La Réunion.

Sommaire

Annexes

Annexe 1: Merle, O., L. Michon, G. Camus, A. Goër de (1998) L'extension oligocène sur la transversale septentrionale du rift du Massif Central. Bull. Soc. Géol. Fr., 169, 615-626.

Annexe 2: Michon, L., O. Merle (2001) The evolution of the Massif Central Rift: Spatio-temporal distribution of the volcanism. Bull. Soc. Géol. Fr., 172, 2, 69-80.

Annexe 3: Merle, O., L. Michon (2001) The formation of the West European Rift: A new model as exemplified by the Massif Central area. Bull. Soc. Géol. Fr., 172, 2, 81-89.

Annexe 4: Michon, L., R.T. van Balen (2005) Characterization and quantification of active faulting in the Roer Valley Rift system based on high precision Digital Elevation Models. Quaternary Sci. Rev., 24, 457-474.

Annexe 5: Michon, L., R.T. van Balen, O. Merle, H. Pagnier (2003) The Cenozoic evolution of the Roer Valley rift system integrated at a European scale. Tectonophysics, 367, 101-126.

Annexe 6: Michon, L., O. Merle (2000) Crustal structures of the Rhinegraben and the Massif Central grabens: an experimental approach. Tectonics, 19, 896-904.

Annexe 7: Michon, L., O. Merle (2003) Mode of lithospheric extension: conceptual models from analogue modeling. Tectonics, 22, 4, 1028, doi:10.1029/2002TC001435.

Annexe 8: Michon, L., D. Sokoutis (2005). Interaction between the structural inheritance and the stress field during graben and depocentre formation: new insights from an experimental approach. Tectonophysics, 409, 125-146.

Annexe 9: Michon L., V. Cayol, L. Letourneur, A. Peltier, N. Villeneuve, T. Staudacher (2009), Edifice growth, deformation and rift zone development in basaltic setting: insights from Piton de la Fournaise shield volcano (Réunion Island, Indian Ocean). J. Volcanol. Geotherm. Res., special issue: Piton de La Fournaise, doi: 10.1016/j.jvolgeores.2008.11.002.

Annexe 10: Michon L., N. Villeneuve, Th. Catry, O. Merle (2009), How summit calderas collapse on basaltic volcanoes: new insights from the April 2007 caldera collapse of Piton de la Fournaise volcano. J. Volcanol. Geotherm. Res., special issue: Piton de La Fournaise, doi: 10.1016/j.jvolgeores.2008.11.003.

Annexe 11: Michon, L., T. Staudacher, V. Ferrazzini, P Bachèlery, and J. Marti (2007), April 2007 collapse of Piton de la Fournaise: A new example of caldera formation, Geophys. Res. Lett., 34, L21301, doi:10.1029/2007GL031248.

Annexe 12: Michon, L., F. Saint-Ange (2008), Morphology of Piton de la Fournaise basaltic shield volcano (La Réunion Island): Characterization and implication in the volcano evolution, J. Geophys. Res., 113, B03203, doi:10.1029/2005JB004118.

Annexe 13: Michon, L., F. Saint-Ange, P. Bachèlery, N. Villeneuve, and T. Staudacher (2007), Role of the structural inheritance of the oceanic lithosphere in the magmato-tectonic evolution of Piton de la Fournaise volcano (La Réunion Island), J. Geophys. Res., 112, B04205, doi:10.1029/2006JB004598.

1- Introduction

Au cours de mon cursus universitaire, j'ai quitté l'Université de Nantes après ma licence pour aller me confronter à la volcanologie, à l'Université Blaise Pascal de Clermont-Ferrand. J'y ai réalisé une thèse en Sciences de la Terre, spécialité Tectonique. Ces années de louvoiement thématique ont fait de moi un géologue, i.e. un "*spécialiste de la géologie* (Grand Larousse 2003)". Toujours selon le Grand Larousse, "*la géologie vise à comprendre la nature, la distribution, l'histoire et la genèse des constituants de la Terre. Ses objets d'étude appartiennent à différents niveaux d'organisation: le cristal et le minéral, la roche, le complexe rocheux (…), le complexe structural (…), la plaque lithosphérique, en relation avec les différentes parties de la Terre*". Les aspects multi-disciplinaires et multi-échelles forment donc la pierre angulaire de l'étude géologique.

La recherche que j'ai mise en œuvre s'est successivement focalisée sur les processus de rifting et la déformation des volcans basaltiques. Ces deux thématiques ont été abordées avec la même approche méthodologique qui combine un travail multi-échelle, i.e. de la surface à l'ensemble de la lithosphère, multi-disciplinaire et intégrant étude de cas naturels et modélisation des processus.

J'ai étudié les processus de rifting en menant de front une analyse du Rift Ouest Européen et une modélisation analogique de la formation des grabens et de la déformation interne des niveaux ductiles de la lithosphère. Plusieurs points motivaient un travail sur le Rift Ouest Européen: l'origine de son volcanisme et de la géométrie des grabens, et le lien entre le volcanisme, l'extension et le contexte géodynamique régional, principalement caractérisé par la convergence entre l'Afrique, l'Apulie, l'Ibérie et l'Europe. La modélisation analogique a été initiée pour comprendre l'origine des géométries contrastées entre les grabens du rift du Massif Central et le graben du Rhin; ces variations géométriques n'étant pas expliquées par les modèles existants (e.g. Allemand et Brun, 1991; Buck, 1991). Les expériences ont ensuite été extrapolées à l'échelle lithosphérique afin d'étudier les modalités de l'extension, les processus d'amincissement de la lithosphère et la distribution différente du volcanisme syn-rift dans plusieurs systèmes de rift. Le rôle du contrôle structural et de la direction d'extension dans la formation des grabens et des dépocentres sédimentaires a finalement été le troisième acte de cette d'étude.

Mon recrutement à l'Université de La Réunion m'a conduit a changer d'objet d'étude, mais pas de méthodologie. L'approche multi-échelle m'a permis d'aborder de nombreux aspects ayant attrait aux volcans basaltiques: relation lithosphère - volcans basaltiques, origine et dynamique des rift zones, impact des variations rhéologiques intra-édifices, croissance des édifices volcaniques… Ma recherche a également été influencée par des événements tels que la formation de la caldera du Dolomieu en Avril 2007. Comprendre l'origine des calderas basaltiques et leurs modalités de formations constitue un nouvel axe de ma recherche.

Ce mémoire contient une synthèse de mes travaux de recherche les plus significatifs couvrant les deux thématiques décrites ci-dessus. Les publications utilisées sont jointes en annexe. J'ai volontairement écarté, dans un souci de cohérence, plusieurs articles dont le sujet était trop éloigné des thématiques développées ici. Outre, les résultats de recherche, le mémoire présente mes projets de recherche en cours et à venir, une synthèse de ma production scientifique et un curriculum vitae synthétique dans lequel je décris mon implication dans l'encadrement d'étudiants en Master 2 et en thèse, la répartition de mon enseignement et les responsabilités administratives.

2- Travaux antérieurs

2.1- Processus de rifting en domaine continental

Classiquement, une distinction est faite entre rifts rapides, comme ceux des Basin and Range et de la Mer Égée, et rifts lents du type Rift Est Africain, Rift Baïkal et Rift Ouest Européen (e.g. Buck, 1991). Les premiers sont caractérisés par une largeur importante, une succession de horsts et de grabens, le développement de dômes métamorphiques (metamorphic core complex) et des vitesses d'extension de plusieurs cm/an. L'extension se produit généralement dans des lithosphères préalablement épaissies lors d'épisodes orogéniques. Les seconds correspondent le plus souvent à des structures étroites induites par quelques mm à cm d'extension par an et dont le développement est contemporain d'un volcanisme alcalin plus ou moins abondant. L'origine de la déformation peut soit être liée à la mise en place d'une anomalie mantellique sous la lithosphère continentale (rift actif), soit résulter de contraintes dont la cause est à rechercher aux limites de plaques ou dans les hétérogénéités de densité de la lithosphère (rift passif; e.g. Ruppel, 1995).

Les travaux que j'ai menés se sont focalisés sur les rifts lents pour lesquels l'origine de l'extension et la relation tectonique/magmatisme font fréquemment débat. J'ai étudié dans le détail le Rift du Massif Central et le graben de la Roer, deux segments importants du Rift Ouest Européen, ceci afin de contraindre au mieux l'âge et le type de déformation, les éventuelles relations tectonique/magmatisme et la ou les source(s) du processus de rifting. J'ai entrepris conjointement une étude théorique sur les modalités de l'extension aux échelles du graben, de la croûte et de la lithosphère par une modélisation analogique dimensionnée.

Je présente ci-dessous une synthèse des résultats obtenus pour ces deux thématiques. Pour chaque partie, j'ai intégré les travaux publiés récemment, i.e. depuis la publication des miens.

2.1.1- Le Rift Ouest Européen

Durant l'ère Cénozoïque, la lithosphère européenne a été affectée par des contraintes extensives qui ont mené à la création d'un système de grabens étendu depuis la Mer du Nord, au nord, à la Mer Méditerranée, au sud (Figure 1). Cet ensemble structural s'est développé dans un contexte géodynamique complexe durant lequel contraintes compressives associées aux orogenèses pyrénéenne et alpine, et contraintes extensives ont fréquemment été spatialement et temporellement contigües. Outre l'activité tectonique, un magmatisme alcalin d'ampleur variable s'est mis en place depuis le Massif Bohémien à l'est jusqu'au Golfe du Lion au sud.

Durant les dernières décennies, de nombreux travaux ont porté sur l'origine des grabens et du volcanisme péri-alpins (Tapponnier, 1977; Caire, 1977; Bergerat, 1987; Ziegler, 1992a; Chorowicz et Deffontaines, 1993; Granet et al., 1995; Zeyen et al., 1997a; Stampfli et al., 1998; Merle et Michon, 2001; Michon et al., 2003; Dèzes et al., 2004; Bourgeois et al., 2007). Ces études ont mené à de nombreuses interprétations divergentes qui seront discutées en section 2.1.3. Il est important de noter qu'une part importante des désaccords quant à l'origine du système de grabens réside dans la définition même des limites du système géologique. Selon Ziegler (1992a) et Dèzes et al. (2004), les grabens distribués depuis le Massif Bohémien à l'est jusqu'à la marge languedocienne au sud constituent un unique ensemble structural appelé European Cenozoic Rift System (ECRIS; Figure 1a). Bien que quelques grabens de la marge languedocienne (Alès, Valence, Manosque) aient subi une extension contemporaine de celle des grabens situés plus au nord, il est dorénavant admis que l'ensemble des grabens de la marge languedocienne fait parti du Rift NW Méditerranéen (e.g. Seranne, 1999). Ce rift qui comprend également la fosse de Valence, entre la côte ibérique et l'archipel des Baléares, trouve son origine dans la subduction de la lithosphère africaine à l'est des blocs corso-sarde et baléare (Wortel et Spakman, 1992, 2000;

Marti et al., 1992; Seranne, 1999; Faccenna et al., 2004; Lacombe et Jolivet, 2005). L'ECRIS, tel qu'il est défini par Zielgler (1992a) et Dèzes et al. (2004), englobe donc des grabens issus d'un phénomène de *roll back* d'âge Oligocène moyen - Miocène inférieur pour la terminaison méridionale, et d'une extension éo-oligocène pour la partie septentrionale (Massif Central, Province Rhénane et Massif Bohémien).

En conséquence, nous avons proposé l'existence de deux systèmes de rift contiguës, i.e. le Rift NW Méditerranéen au sud et le Rift Ouest Européen (ROE) au nord (Michon, 2000; Merle et Michon, 2001). L'articulation entre ces deux systèmes se situe au sud du Massif Central où certains fossés ont d'abord enregistré la déformation contemporaine des grabens du ROE, puis, après une période d'inactivité, ont été affectés par l'extension importante liée à la rotation du bloc corso-sarde à partir de l'Oligocène moyen.

Le ROE est constitué de trois provinces situées en périphérie de l'arc alpin: le Massif Central à l'ouest, la Province Rhénane au centre et le Massif Bohémien à l'est (Figure 1b). La province du Massif Central est caractérisée par un large système de grabens parallèles (Limagne, Roanne-Montbrison et Bresse) et d'importants ensembles volcaniques. Les dimensions du système de grabens et le volume de magma émis au cours du Cénozoïque font du Massif Central la province majeure du ROE. La Province Rhénane est composée de deux grabens d'orientation différente: le graben du Rhin au sud et le graben de la Roer au nord (Figure 1a). Le volcanisme cénozoïque est principalement localisé entre ces deux structures, au niveau du Bouclier Rhénan formé d'unités géologiques paléozoïques. La province du Massif Bohémien constitue la partie la plus orientale du ROE. L'extension cénozoïque y a induit la formation du graben de l'Eger qui découpe le socle cadomo-hercynien selon une orientation ENE-WSW. Cette province a également été le siège d'une activité magmatique alcaline principalement centrée sur le graben de l'Eger.
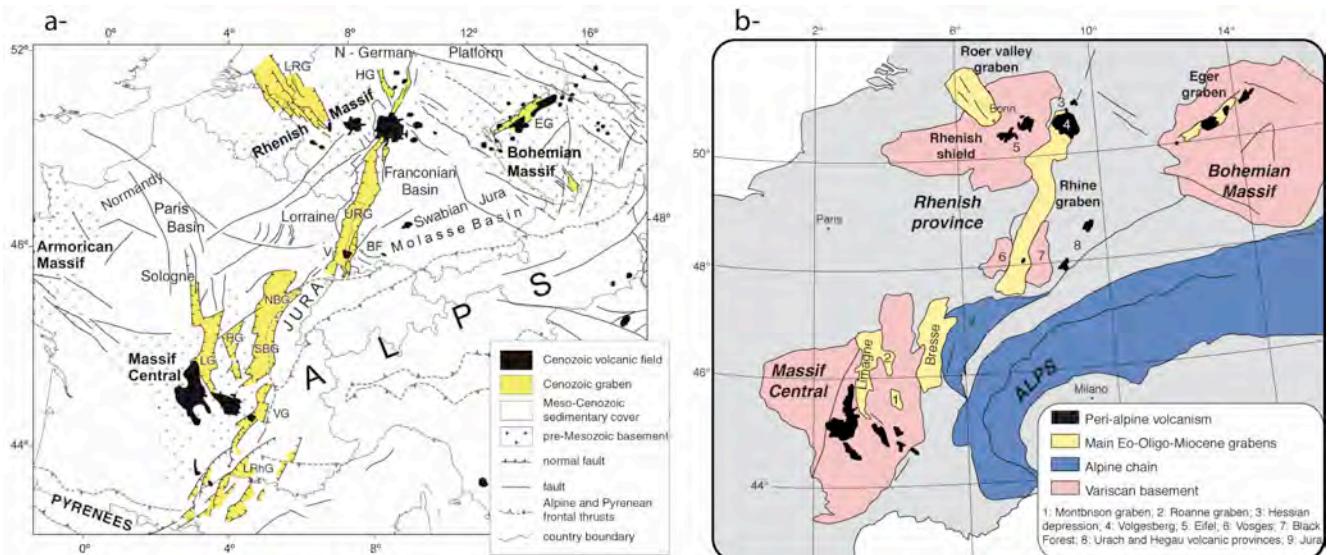

Figure 1 : *a- Carte structurale du système de rift cénozoïque européen (ECRIS). D'après Ziegler (1992a), Dèzes et al. (2004). BF: Black Forest; EG: Eger graben; HG: Hesse graben; LG: Limagne graben; LRG: Lower Rhine graben; LRhG: Lower Rhône grabens; NBG: northern Bresse graben; RG: Roanne graben; SBG: southern Bresse graben; URG: upper Rhine graben; V: Vosges; VG: Valence graben. b- Carte du Rift Ouest Européen (ROE). Les grabens de Valence et de la marge Languedocienne, bien qu'ayant subit en partie l'extension du ROE, ne sont pas représentés. Ces structures résultent principalement de l'extension arrière-arc due à la rotation de la Corse et de la Sardaigne entre l'Oligocène moyen et le Miocène inférieur.*

Etant donné la diversité d'interprétations quant à la formation des grabens du ROE et au développement du volcanisme, dans ce mémoire, j'ai voulu dans un premier temps rappeler les faits géologiques, seules données de base qui ne peuvent être remises en cause et qui doivent inévitablement contraindre les modèles proposés. Le rift du Massif Central et le graben de la Roer ayant été des objets d'étude privilégiés pendant ma thèse de doctorat à l'Université Blaise Pascal de Clermont-Ferrand et mon post-doctorat au TNO-NITG (Utrecht, Pays-Bas), leur description sera particulièrement

détaillée. Elle rappellera les principaux résultats de publications réalisées entre 1998 et 2005, en collaboration avec Olivier Merle, mon directeur de thèse, et Ronald van Balen, *associate professor* à la Vrije Universiteit d'Amsterdam (Merle et al., 1998; Michon et Merle, 2001; Merle et Michon, 2001; Michon et al., 2003; Michon et van Balen, 2005; Annexes 1 à 5). La section sur le graben du Rhin a pour objectif de mettre en lumière les principales données existantes afin de les intégrer dans l'interprétation de l'ensemble du ROE.

2.1.1.1- Le rift du Massif Central

Le rift du Massif Central (RMC) est situé dans la partie est du môle hercynien du Massif Central. Les grabens et le volcanisme sont limités par le Sillon Houiller à l'ouest, les Alpes à l'est et le Bassin Parisien au nord. Au sud, les grabens ayant eu une évolution double, i.e. ROE et Rift NW Méditerranéen, ont quelques points communs avec ceux du RMC. Cependant, leurs caractéristiques (géométrie et sédimentation) ayant été très perturbées par l'ouverture du Rift NW Méditerranéen, ils ne seront pas intégrés à cette étude. Le RMC ainsi défini mesure plus de 200 km d'est en ouest et 300 km du nord au sud. Il est constitué d'un ensemble de grabens principalement répartis dans la moitié nord du Massif Central et spatialement associés à un volcanisme cénozoïque important (Figure 2). Les objectifs de ma thèse de 3ème cycle étaient (1) de caractériser la structure du rift et sa dynamique, (2) de préciser la distribution spatio-temporelle du volcanisme et sa cause, et (3) d'évaluer le lien entre la tectonique extensive à l'origine des grabens et le volcanisme. Atteindre ces objectifs a nécessité une synthèse des différentes données géologiques, géochimiques et géophysiques publiées sur le Massif Central, dont les principaux traits sont résumés ci-dessous.
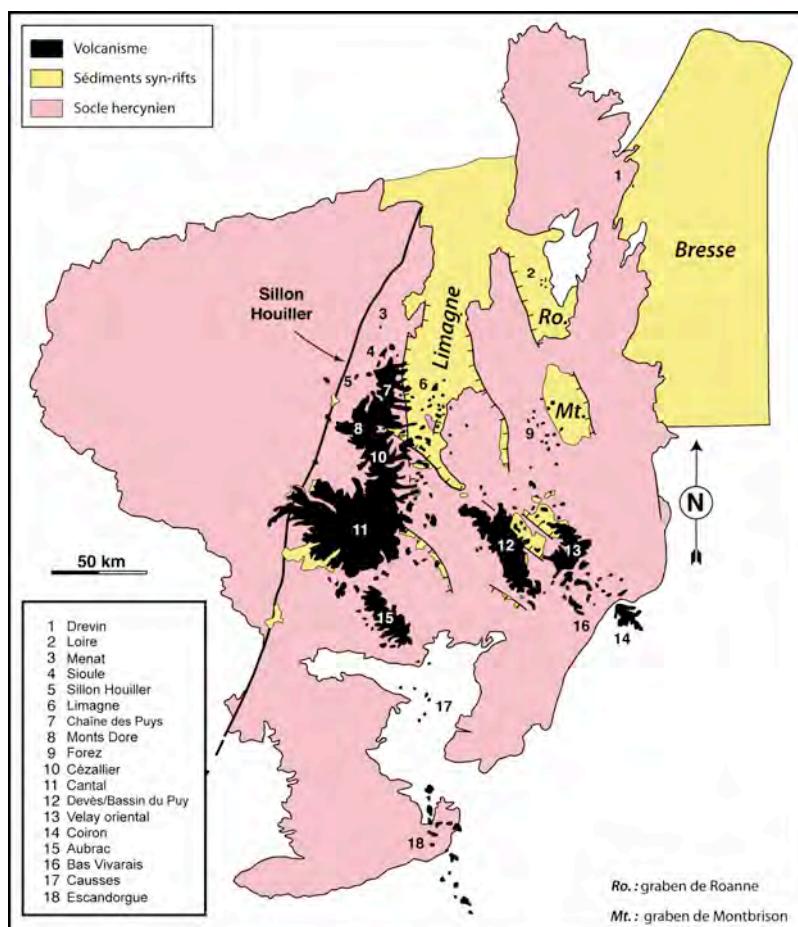

Figure 2 : Carte de localisation des grabens et des provinces volcaniques du Massif Central.

Le volcanisme cénozoïque du Massif Central a fait l'objet de nombreuses études portant sur l'âge, la nature et l'origine des magmas (e.g., Maury et Varet, 1980; Wilson et Downes, 1991; Michon et Merle, 2001; Gautheron et al.,

2005). En tenant compte de l'âge du volcanisme et de sa distribution, 18 provinces volcaniques ont été distinguées. Elles sont réparties à l'est du Sillon Houiller, depuis le Morvan au nord jusqu'à l'Escandorgue au sud (Figure 2). Les datations indiquent que le volcanisme s'est initié à la transition Crétacé-Tertiaire, i.e. depuis 65 Ma. L'activité magmatique s'est principalement poursuivie dans la partie nord du Massif Central jusqu'à l'Oligocène moyen. A partir de l'Oligocène supérieur, le volcanisme est apparu en Limagne et dans le Forez sous forme de volcans monogéniques dispersés. Le Miocène supérieur marque un changement important dans la distribution et la production magmatique. De fait, à partir 13 Ma, un volcanisme intense s'est développé dans la partie centrale du Massif Central, entraînant la construction d'un strato-volcan important (Cantal) et de plateaux basaltiques et phonolitiques (Aubrac, Cézallier, Velay; Figures 2 et 3). A l'inverse, le volcanisme de la partie nord (Limagne et Forez) cessa vers 12 Ma avant de reprendre de manière significative vers 5 Ma, date à partir de laquelle les strato-volcans des Monts Dores et du Sancy se sont formés. L'activité magmatique s'est poursuivie dans le Massif Central jusqu'au Quaternaire, avec des éruptions récentes au niveau du Bas Vivarais, de l'Escandorgue et de la Chaîne des Puys (Berger et al., 1975; Miallier et al., 2004; Guerin et Gillot, 2007). Cette période volcanique initiée vers 13 Ma dans la partie centrale du Massif Central correspond à la phase volcanique majeure de la province (Figure 4).
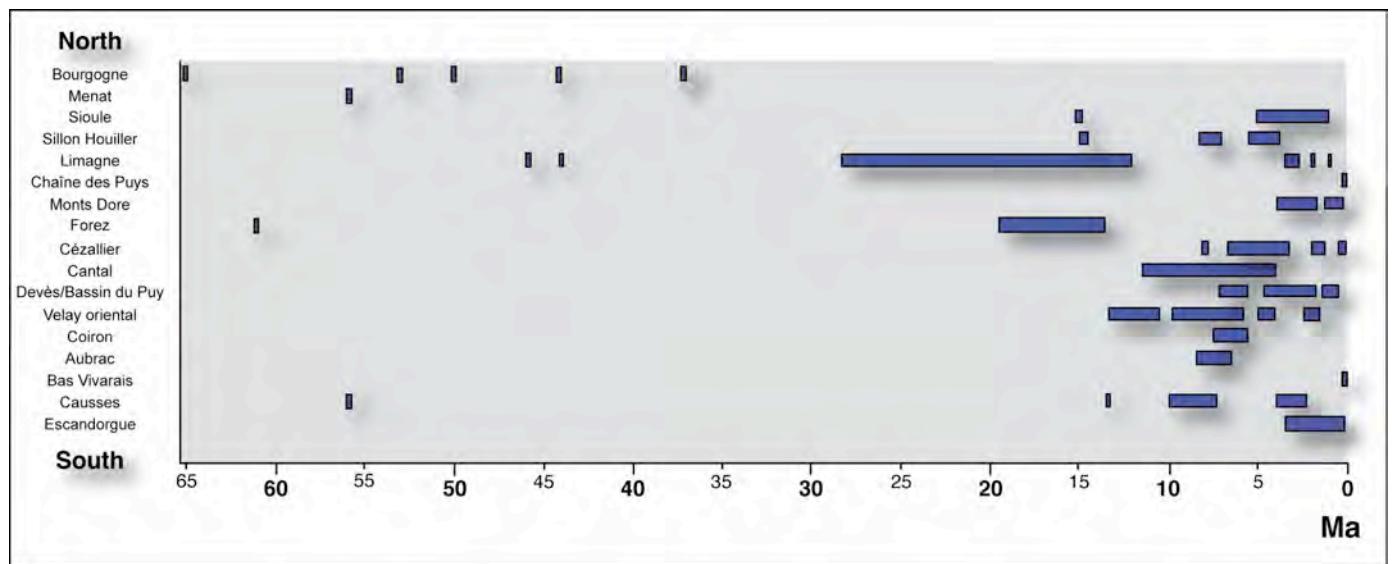

Figure 3 : *Distribution temporelle du volcanisme cénozoïque du Massif Central. Datations : Bellon et al. (1974); Berger et al. (1975); Vincent et al. (1977); Bellon et Hernandez (1979); Baubron et al. (1978); Maury et Varet (1980); Chantepie (1990); Mergoil et Boivin (1993); Cheguer (1996); Chambon (1997); Lenoir et al. (2000a); Guerin et Gillot (2007).*

L'intégration du volume de magma émis au cours du temps permet de distinguer deux pics d'activité magmatique durant la phase volcanique majeure (Figure 4). Le premier pic, daté entre 9,5 et 6 Ma, est limité à la partie centrale du Massif Central, alors que le second pic d'activité, de 6,5 à 0,5 Ma, est généralisé à l'ensemble de la province. Ces deux périodes d'intense activité magmatique ont été spatialement et temporellement superposées à des phases de surrection du socle hercynien.

Les magmas cénozoïques du Massif Central montrent une grande variabilité compositionnelle au sein de la série alcaline (Jung et Brousse, 1962; Wimmenauer, 1974; Cheguer, 1996; Lenoir et al., 2000a). Les laves les plus anciennes, i.e. pré-Oligocène, présentent les plus forts degrés de sous-saturation allant jusqu'au magma mélilitique (Wilson et al., 1995; Lenoir et al., 2000a). Cette faible teneur en silice est interprétée comme le résultat d'un très faible taux de fusion partielle de la limite lithosphère-asthénosphère (Wilson et al., 1995). A partir de l'Oligocène, deux séries saturée et sous-saturée se développent conjointement dans la majorité des provinces volcaniques (Jung et Brousse, 1962; Vatin-Pérignon, 1968). Les signatures géochimiques du Nd, Sr, Pb et de l'O des magmas néogènes suggèrent l'interaction entre deux pôles

mantelliques A et B (Wilson et Downes, 1991; Lenoir et al., 2000a). Le pôle A, d'origine asthénosphérique, serait issu du mélange entre un manteau appauvri et un manteau de type HIMU. Le pôle B représenterait l'apport de la lithosphère hercynienne lors de la remontée de magmas primaires d'origine asthénosphérique. La signature de type HIMU du pôle A peut être interprétée de façons différentes. Selon Wilson et Downes (1991), les affinités du composant asthénosphérique avec une source de type HIMU s'expliqueraient par le recyclage d'une lithosphère océanique de 500-400 Ma lors de l'orogenèse hercynienne. Cette signature isotopique pourrait également s'expliquer par la remontée de matériel mantellique profond (Granet et al., 1995). Les isotopes de l'He, du Ne et de l'Ar plaident en faveur de la première hypothèse, même si la seconde interprétation ne peut être définitivement exclue (Gautheron et al., 2005). En résumé, l'origine des magmas reste assez mal connue malgré l'abondance des données.
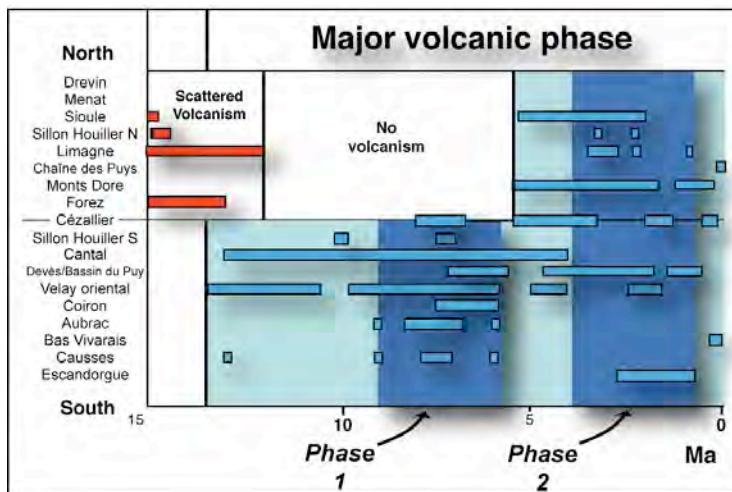

Figure 4: Distribution spatio-temporelle de la phase volcanique majeure au niveau du Massif Central.

Les études isotopiques portant sur la nature des enclaves mantelliques remontées par les magmas basiques révèlent la présence de deux domaines lithosphériques différents sous la partie est du Massif Central (Lenoir et al., 2000b; Downes et al., 2003; Wittig et al., 2007). La lithosphère mantellique au nord de la latitude 45°30' serait ancienne et plus épaisse (>80 km), alors qu'elle serait plus fine (<70 km) et plus récente au sud de cette latitude.

Il est intéressant de noter que la limite entre les deux domaines mantelliques correspond également à la terminaison sud des grands grabens de la partie nord du RMC (grabens de la Limagne, de Montbrison et de la Bresse; Figure 5). Au nord de la latitude 45°30', les fossés d'effondrement sont bien développés et sont orientés selon une direction N-S. En revanche, les grabens de la partie sud sont de taille réduite et présentent une orientation N135 dominante. La puissance des sédiments syn-rifts est très différente entre les parties sud et nord. Au sud, l'épaisseur des sédiments syn-rifts ne dépasse guère 200 m alors qu'elle est d'un ordre de grandeur supérieure dans les grabens de la partie nord (Figure 6). Cette distribution des structures extensives suggère une concentration de l'extension cénozoïque dans la partie nord du Massif Central.

Quelle que soit l'épaisseur des sédiments, il est important de noter que de nombreux grabens du rift du Massif Central montrent des évidences d'incursions marines (e.g., Briot et al., 2001; Sissingh, 2001) qui prouvent que cette province était proche du niveau de la mer et ne subissait pas de surrection au moment du rifting.
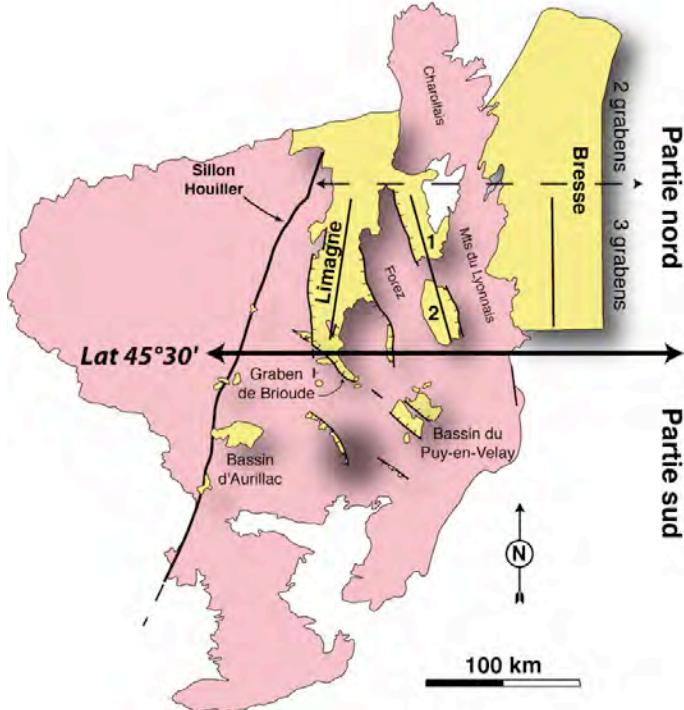
Figure 5: *Carte de répartition des grabens du rift du Massif Central montrant la différence de géométrie des grabens situés au sud et au nord de la latitude 45°30'. 1: graben de Roanne; 2: graben de Montbrison.*

	Limagne	Montbrison	Bresse	
Oligocène sup. à Miocène inf. **Evolution asymétrique**	*Incursions marines*	*Fluvio-lacustre*	*Fluvio-lacustre*	20
	Calcaires à H. *ramondi* Marnes blanche à Cypris **Volcanisme** 1000 m	Détritique fin et grossier **Volcanisme**	Marno-calcaire et détritique Hiatus de sédimentation < 200 m	
				28
Eocène sup. à Oligocène moy. **Evolution Symétrique**	*Incursions marines*	*Fluvio-lacustre*	*Incursions marines*	
	Evaporites Marno-calcaire à Potamides *lamarcki* > 2500 m	Détritique (sables, argiles et conglomérats) + calcaire	Evaporites Marno-calcaire 1400 m	
				37
				Ma
Epaisseur totale des sédiments	**> 3500 m**	**700 m**	**1600 m**	

Figure 6: *Caractéristiques de la sédimentation dans les grabens de la partie nord du Massif Central entre l'Eocène supérieur et le Miocène inférieur. Ce tableau révèle la succession de deux périodes distinctes. De l'Eocène supérieur à l'Oligocène moyen, la sédimentation identique de part et d'autre du graben de Montbrison, i.e. Limagne et Bresse, indique une extension symétrique à l'échelle du RMC. En revanche, de l'Oligocène supérieur au Miocène inférieure, l'extension s'est concentrée dans la partie ouest du RMC induisant une subsidence importante en Limagne et l'apparition d'un volcanisme dispersé.*

Les nombreux forages et les campagnes géophysiques (Morange et al., 1971; Rat, 1974; Bergerat et al., 1990) ont montré que les grabens de la Limagne et de la Bresse sont des demi-grabens limités par une faille majeure de vergence opposée, située à l'ouest pour la Limagne et à l'est pour la Bresse (Figure 7). Au centre du RMC, les grabens de Roanne et de Montbrison présentent une légère asymétrie dont l'inversion au sud et au nord du seuil de la Loire confère une géométrie globalement symétrique à ce système central (Figure 5 et 7). Ainsi, la géométrie d'ensemble du RMC est caractérisée par une symétrie de miroir centrée sur les grabens de Roanne-Montbrison. Au sein de ce système, le graben de la Limagne a enregistré l'extension la plus importante, comme l'atteste l'épaisseur des sédiments éo-oligocènes (Figure

6) et les valeurs d'amincissement crustal (25% en Limagne et 10-13% en Bresse), déduites de la carte de profondeur du Moho de Zeyen et al. (2007b). Ces données montrent sans ambiguïté que le graben de la Limagne est la structure tectonique majeure du RMC, contrairement à ce qui est fréquemment proposé (Caire, 1977; Chorowicz et Deffontaines, 1993; Bourgeois et al., 2007). De plus, l'apparition du volcanisme dispersé en Limagne et dans le Forez au cours de l'Oligocène supérieur suggère un amincissement lithosphérique maximum concentré sous la partie occidentale du RMC (Figure 7).

Au vu des différentes caractéristiques de la période Eocène supérieur - Miocène inférieur, i.e. extension et sédimentation au niveau de la mer, et volcanisme tardif dans les zones amincies, nous interprétons la dynamique extensive du Massif Central comme le résultat d'un rifting passif dont les forces originelles sont à trouver en périphérie du système.
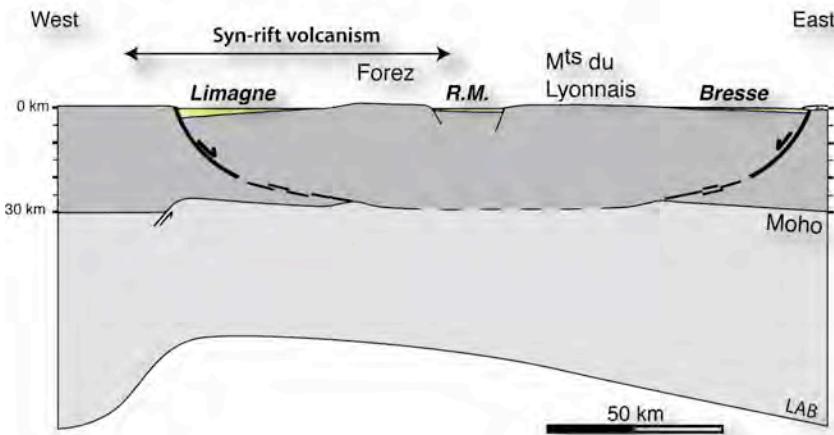

Figure 7: Coupe interprétative à l'échelle lithosphérique de la partie nord du RMC. La distribution symétrique de la sédimentation dans les grabens de la Limagne, de Roanne-Montbrison et de la Bresse suggère que les caractères de symétrie de part et d'autre du graben central résultent de la période d'extension éocène supérieur - oligocène moyen. L'apparition du volcanisme syn-rift et la continuité de la subsidence en Limagne indiquent une seconde période d'extension durant laquelle la déformation s'est concentrée dans la moitié occidentale du RMC.

Concernant la partie centrale du RMC, les données de sismique réfraction montre un Moho à une profondeur relativement constante (Zeyen et al., 2007b) suggérant une absence d'amincissement crustal lors de la période de rifting. En revanche, cette région présente un important amincissement de la lithosphère mantellique lié à une anomalie mantellique imagée par tomographie sismique (Granet et al., 1995; Sobolev et al., 1996; Figure 8a). La superposition de l'anomalie mantellique avec les provinces magmatiques construites durant le premier pic d'activité volcanique (Figure 8b) suggère un lien étroit entre ces deux phénomènes. Nous avons proposé que la mise en place de l'anomalie mantellique sous la partie centrale du RMC avait entraîné le développement de la phase volcanique majeure vers 15 Ma (Michon et Merle, 2001). La répartition conjointe des pics d'activité volcanique et des périodes de surrection présente des similitudes avec le stade initial d'un rifting actif (Sengör et Burke, 1978; Ruppel, 1995).

Nous avons conclu de ce travail de synthèse que le Massif Central a été marqué par:

1- Le développement d'un volcanisme timide entre la transition Crétacé-Tertiaire et l'Eocène moyen, contemporain d'une surrection généralisée de la province (Lefort et Agarwal, 1996, 2002; Barbarand et al., 2001).

2- Une extension éo-oligocène E-W limitée à la partie nord du RMC qui a entrainé la formation d'un large système de grabens et une activité volcanique syn-rift. Cette évolution est caractéristique d'un processus de rifting passif.

3- Une phase volcanique majeure initiée vers 15 Ma dans une zone exempte de toute extension éo-oligocène préalable. Le magmatisme et la surrection conjointe résultent vraisemblablement de la remontée d'une anomalie mantellique à partir du Miocène supérieur. Cette évolution présente de fortes similitudes avec le stade initial d'un rift actif, i.e., avant la formation des grabens.
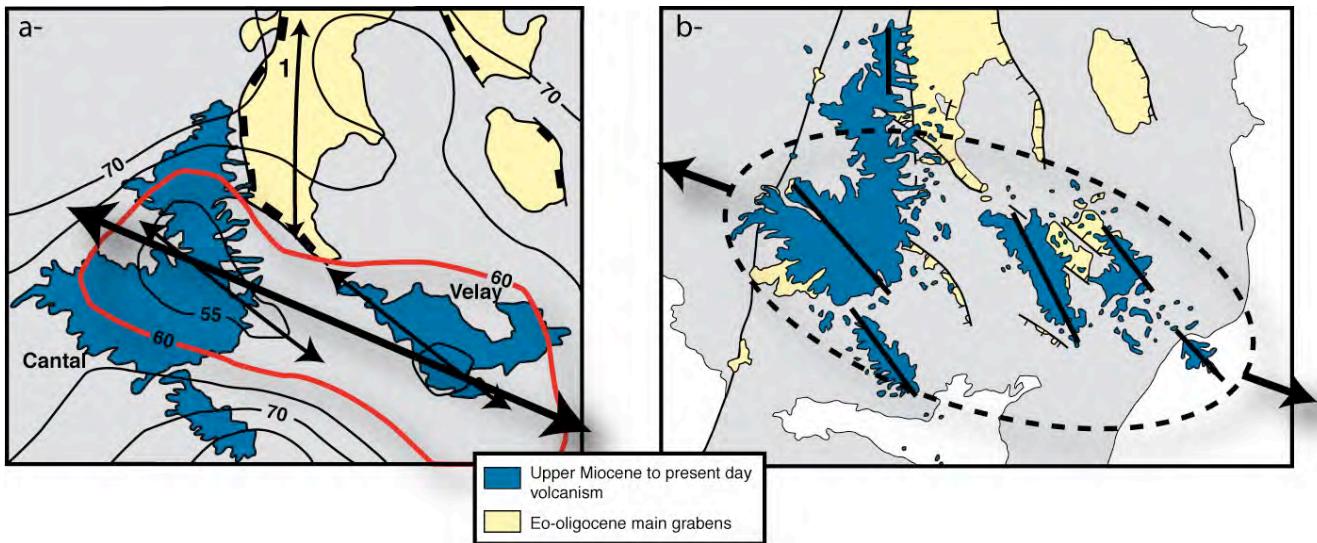

Figure 8 *: a- Carte d'amincissement de la lithosphère mantellique (d'après* Sobolev et al., 1996*); 1 : Localisation de l'amincissement crustal (d'après* Zeyen et al., 1997b*). b- Localisation de la zone couverte par le premier pic d'activité volcanique (9,5-6 Ma).*

2.1.1.2- *Le graben de la Roer*

J'ai poursuivi l'étude du ROE lors de mon post-doctorat au TNO-NITG (Utrecht, Pays-Bas), dans le cadre du projet européen ENTEC (ENvironmental TECtonics). L'objectif initial fixé par Henk Pagnier, mon superviseur, était d'étudier la tectonique actuelle et récente du graben de la Roer. L'intérêt était double: (1) mettre en relation la déformation active avec la sismicité récurrente du graben et (2) d'intégrer cette dynamique à l'échelle de la Province Rhénane. Il m'est apparu que le préalable indispensable à ce travail était de déterminer la structure d'ensemble du graben et son évolution au cours du Cénozoïque. L'intérêt était d'estimer l'âge d'initiation de la tectonique actuelle et de mettre en relation les déformations de surface avec les failles majeures du graben. Pour ce travail, j'ai bénéficié de données abondantes et de qualité, et de collaborations très enrichissantes (Ronald van Balen et Geza Worum; Vrije Universiteit Amsterdam).

Situé au nord du Bouclier Rhénan, le graben de la Roer est la structure majeure d'un ensemble structural subsidant: le système de rift de la Roer (*Roer Valley Rift System*, RVRS; Figure 9a). Son orientation NW-SE diffère sensiblement de celle des autres grabens du ROE, qui montrent une rotation progressive depuis une direction N-S à l'ouest à une orientation ENE-WSW à l'est. Cette typicité du RVRS s'explique par le contrôle d'un fort héritage structural développé avant l'épisode de rifting cénozoïque. L'enregistrement sédimentaire au sein du graben montre en effet qu'il s'est formé pendant le carbonifère et qu'il a ensuite été réactivé lors de l'ouverture de la Mer du Nord (Jurassique supérieur - Crétacé inférieur; Zijerveld et al., 1992; Geluk et al., 1994). Le graben de la Roer est limité respectivement par le Peel Block et le Campine Block à l'est et à l'ouest. Depuis le Paléozoïque, la déformation a été accommodée le long de failles bordières importantes: la faille bordière de Peel (*Peel Boundary fault*, PBF) à l'est et trois segments de faille correspondant aux failles de Feldbiss, de Veldhoven et de Rijen, à l'est (Figure 9c).

Dynamique cénozoïque

L'enregistrement sédimentaire au sein et en périphérie du graben de la Roer révèle une succession de périodes compressives et extensives au cours du Cénozoïque. L'absence ou la faible épaisseur de sédiments d'âge Crétacé supérieur

au niveau du graben, alors que les bordures sont recouvertes par une sédimentation de plusieurs centaines de mètres, indique une forte inversion du graben à la fin du Crétacé et au début du Cénozoïque (Figure 10a). Les contraintes compressives responsables de l'inversion ont provoqué la réactivation en faille inverse des accidents tectoniques bordiers selon deux directions NW-SE et NNW-SSE. L'activité simultanée de ces deux réseaux de failles s'expliquant mal par des contraintes compressives perpendiculaires au graben, nous avons interprété l'inversion comme le résultat d'un jeu transpressif lié à une contrainte principale maximale σ_1 NNE-SSW; identique à celle déduite pour l'inversion d'âge Crétacé terminal du West Netherlands Basin (van Balen et al., 2000).
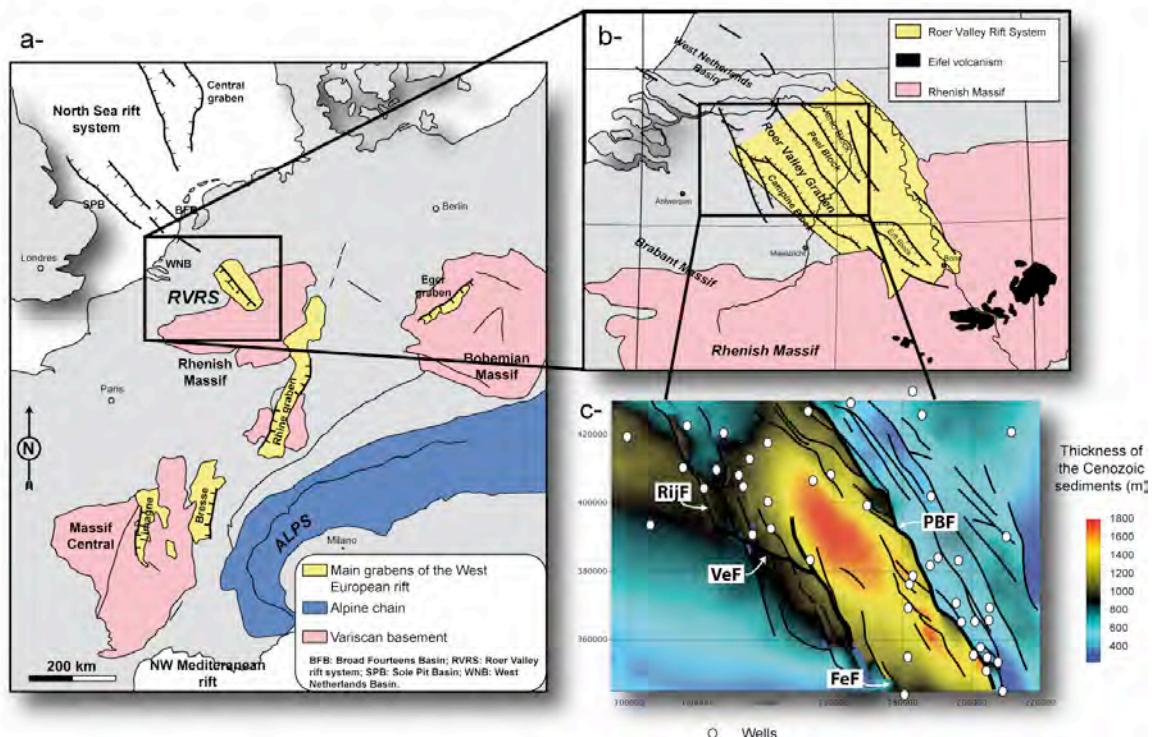

Figure 9 : a- Localisation du graben de la Roer et du Roer Valley Rift System (RVRS), au sein du Rift Ouest-Européen. b- Le RVRS est principalement composé du graben de la Roer, du Venlo Block et du Peel Block, horst faiblement subsidant durant le Cénozoïque. c- Carte d'épaisseur des sédiments cénozoïques indiquant les principales failles et les forages utilisés dans cette étude. FeF: Feldbiss fault; PBF: Peel Boundary fault; RijF: Rijen fault; VeF: Veldhoven fault.

Au Paléocène supérieur, l'ensemble du *Roer Valley Rift System* a subi une faible subsidence sans activité tectonique notable. Une subsidence similaire s'est produite au niveau des grabens de la Mer du Nord où elle a été interprétée comme étant liée soit à une relaxation lithosphérique après l'inversion du début du Paléocène (de Lugt et al., 2003), soit à une extension tardive associée à l'ouverture de l'Atlantique Nord (Ziegler, 1992b). L'Eocène supérieur a été marqué par une seconde période compressive qui a entraîné un bombement du RVRS, sans réactivation importante des failles bordières du graben de la Roer. Les grabens situés dans la partie sud de la Mer du Nord et dans la Manche présentent une évolution identique qui a été mise en relation avec la phase de compression pyrénéenne (Ziegler., 1990). A partir du début de l'Oligocène, le RVRS a été affecté par une nouvelle phase de subsidence, centrée tout d'abord sur le Peel Block, puis concentrée au niveau du graben de la Roer dès l'Oligocène supérieur (Figure 10b). La localisation des dépocentres oligocènes supérieurs principalement dans la moitié sud du graben (Figure 11), au pied de la *Peel Boundary fault*, et leur géométrie allongée, parallèle aux failles bordières, suggèrent une extension oblique WNW-ESE.

Le champ de contrainte oligocène changea drastiquement à la transition oligocène-miocène. De fait, après un bref arrêt de la sédimentation à l'Aquitanien, i.e. Miocène inférieur, l'ensemble du graben de la Roer a subsidé et un dépocentre principal s'est développé dans la partie nord du graben (Figures 10c et 11). La subsidence miocène a été contrôlée par deux réseaux de failles obliques orientés N145–160 et N110–120. Nous avons interprété l'activité simultanée

de ces réseaux de failles et la formation des dépocentres à l'intersection des failles obliques comme le résultat d'une extension NE-SW. Cette interprétation diffère de celle avancée par Kooi et al., 1991 et van den Berg, 1994 pour qui le graben correspondait à un bassin en pull-apart limité par des failles bordières décrochantes.
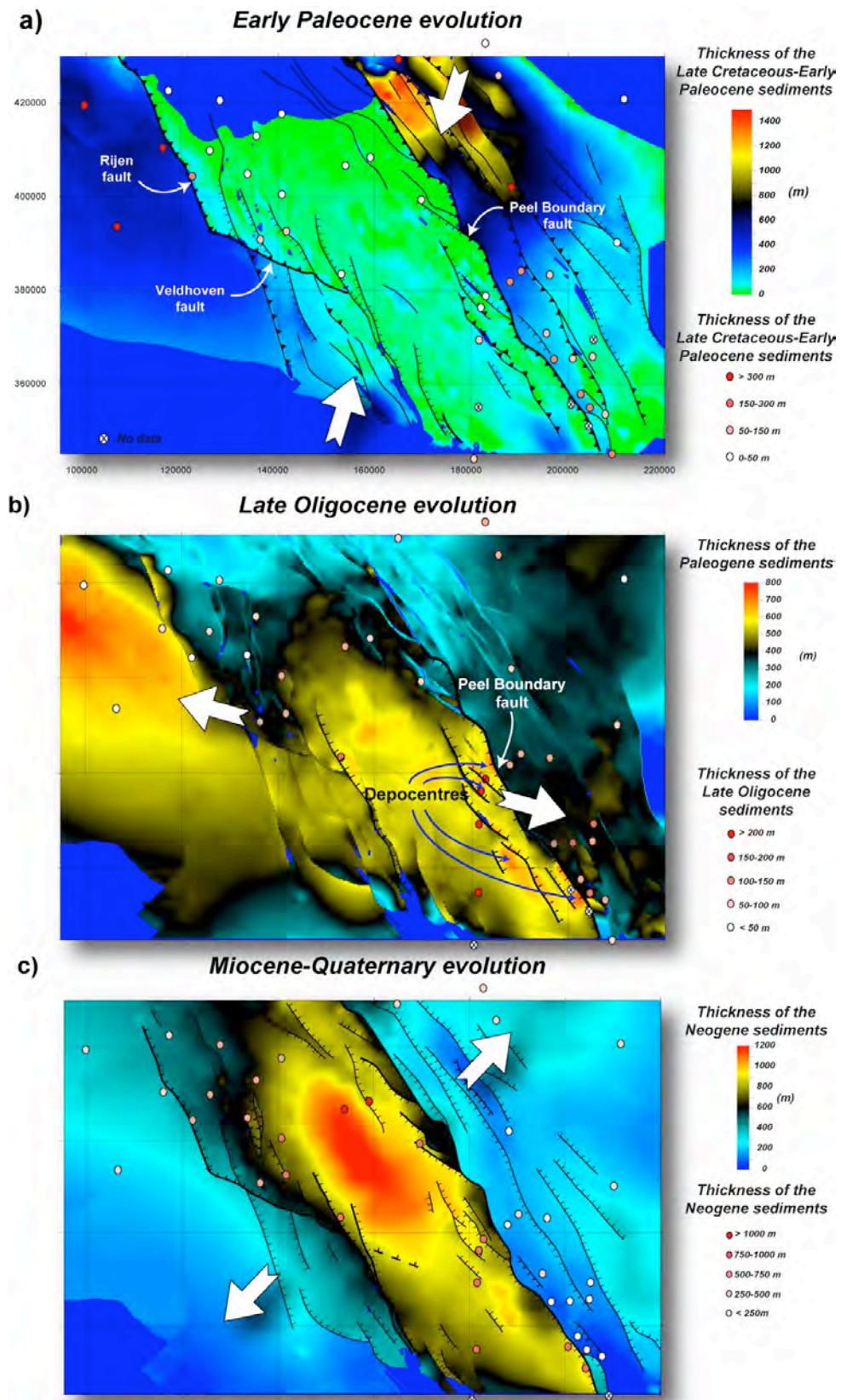

Figure 10: *Evolution cénozoïque du RVRS. a) Inversion paléocène inférieure. b) Subsidence oligocène supérieure due à une extension WNW–ESE. c) Déformation miocène–quaternaire rifting résultat d'une extension NE-SW. Pour l'Oligocène supérieur, l'image correspond à l'épaisseur des sédiments paléogènes. L'épaisseur des sédiments pour chaque période est donnée par les forages.*
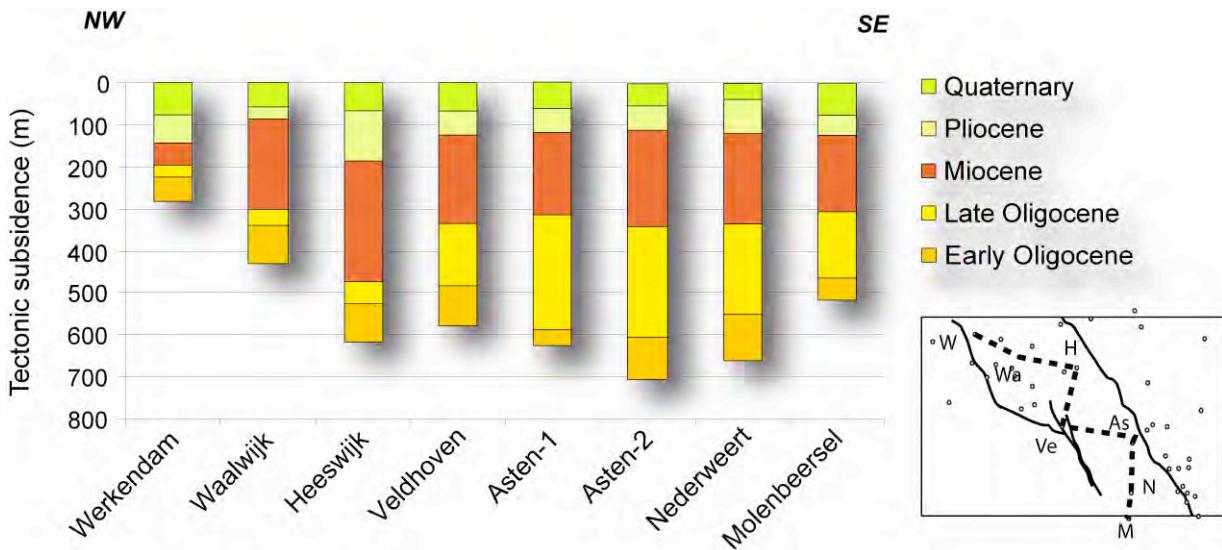
Figure 11: *Epaisseur des sédiments post-éocènes le long d'un profil NW-SE situé au sein du graben de la Roer. Noter une concentration de la sédimentation d'âge Oligocène supérieur dans la partie SE du graben puis une généralisation de la subsidence à partir du Miocène. As.: Asten-1 et Asten-2; H.: Heeswijk; M.: Molenbeersel; N.: Nederweert; V.: Veldhoven; Wa.: Waalwijk; W.: Werkendam.*

Tectonique actuelle

Nous avons utilisé un Modèle Numérique d'Elevation (MNE) de haute résolution (5m) réalisé par altimétrie radar (Rijkswaterstaat, 2000) afin de caractériser et de quantifier la déformation actuelle le long des segments de la Peel Boundary fault et de la Feldbiss fault les plus sismiquement actifs (Michon et van Balen, 2005).
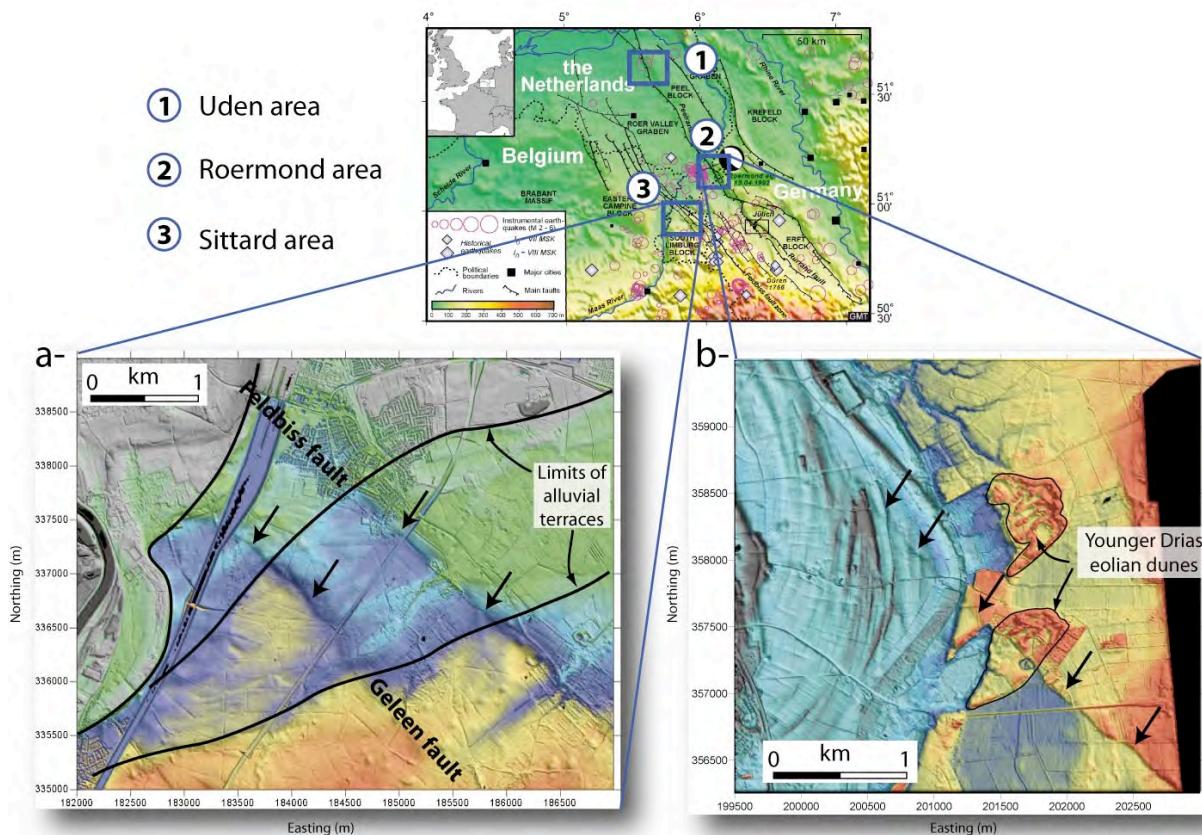
Figure 12: *Modèles numériques de terrain (pas de 5m) illustrant la déformation active le long des failles bordières du graben de la Roer. a) Région de Sittard: partie sud de la faille bordière occidentale du graben de la Roer, subdivisée ici en deux segments de failles. b) Région de Roermond: topographie le long de la faille bordière orientale, la Peel Boundary Fault. Les flèches indiquent les décalages induits par l'activité actuelle du graben de la Roer.*

Les MNE révèlent de manière frappante les escarpements métriques à pluri-métriques liés à l'activité des failles bordières (Figure 12). La cartographie de ces escarpements indique que les limites du graben de la Roer correspondent rarement à des accidents tectoniques uniques mais plutôt à des zones de failles. Dans la région de Sittard, la limite occidentale du graben est composée par plusieurs failles parallèles espacées d'un à plusieurs kilomètres: la *Feldbiss fault*, la *Geleen fault* et l'*Heerlhereide fault zone* (Figure 12a). La superposition des escarpements et d'accidents tectoniques d'âge Carbonifère met en lumière le rôle majeur joué par l'héritage structural dans la localisation de la déformation actuelle du graben de la Roer. Dans la région de Roermond, zone frappée par un séisme de magnitude 5,8 en 1992, la déformation est concentrée sur un accident unique qui se subdivise en deux segments parallèles dans la partie nord du graben (Figure 12b). A l'échelle du graben, l'absence apparente de décalage latéral des terrasses alluviales de la paléo-Meuse et des dunes éoliennes suggère un jeu essentiellement vertical des failles bordières du graben de la Roer. Cette déformation résulte une extension actuelle NE-SW, similaire à celle qui prévalait au Miocène comme le montre la superposition des dépocentres miocènes et pléistocènes (Figure 11; Houtgast et van Balen, 2000).
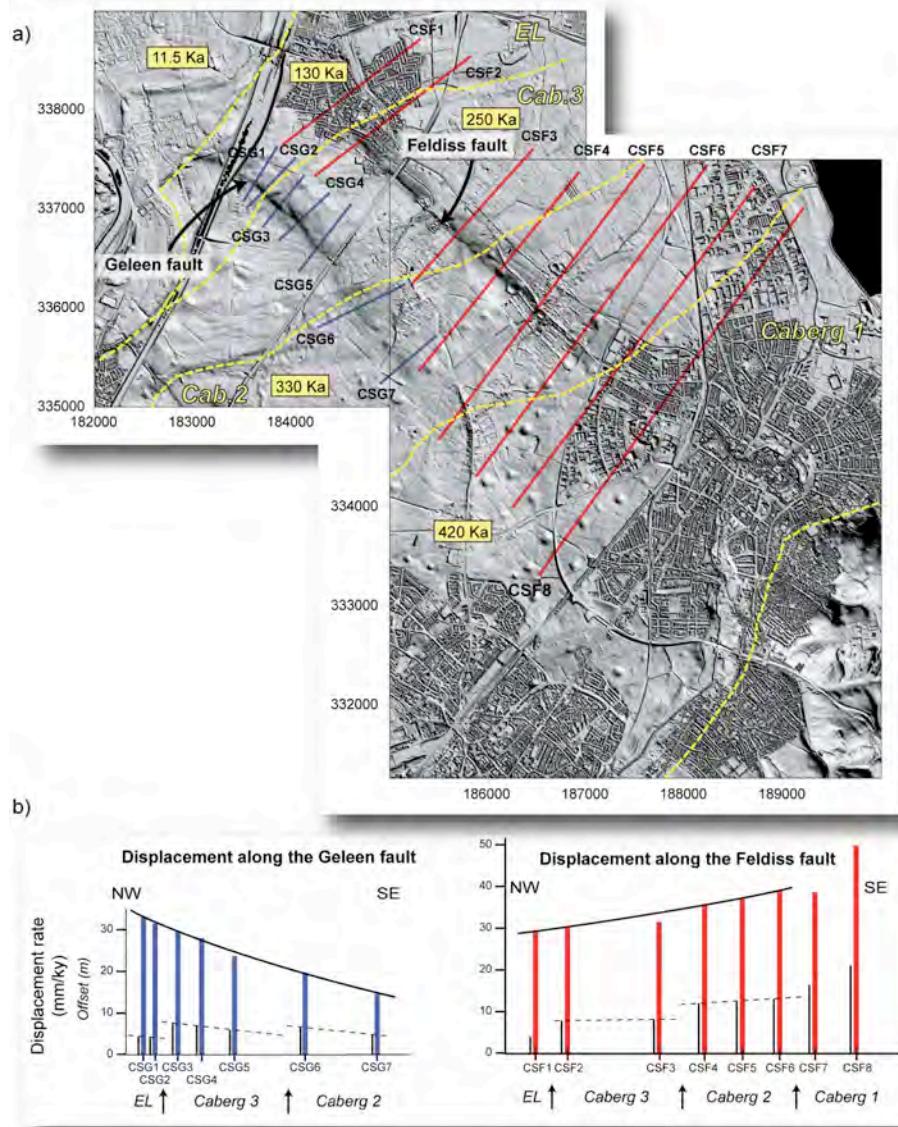
Figure 13*: a) Localisation et âge des terrasses de la Meuse au niveau de la partie sud de la faille bordière occidentale du graben de la Roer (d'après Houlgate et al., 2002). Les lignes pointillées représentent les limites des terrasses. Les profils topographiques utilisés dans cette études correspondent aux lignes bleues et rouges appelées CSG pour la Geleen fault et CSF pour la Feldbiss fault. b) Evolution de l'escarpement (lignes noires) et des taux de déplacement (lignes bleues et rouges) le long des Geleen et Feldbiss faults. Les profils CSF7 et CSF8 ne sont pas intégrés dans cette étude car les escarpements sont perturbés par le développement de vallées et par un important dépôt de lœss.*

15

Les formations géologiques affectées par l'activité des failles bordières du graben de la Roer sont datées entre 11,5 ka pour les dunes éoliennes du Drias inférieur à plusieurs centaines de milliers d'années pour les terrasses anciennes de la Paléo-Meuse. Connaissant l'âge des formations, la quantification des décalages verticaux à partir des MNE nous a permis de déterminer les taux de déformation le long des failles. Dans la région de Sittard, la somme des taux de déformation le long de chaque segment de faille suggère un taux de déformation global entre 55 et 65 mm/ka (Figure 13). Des valeurs similaires ont été déterminées pour la région de Roermond. En revanche, les taux de déformation sont significativement supérieurs dans la partie nord du graben de la Roer (région d'Uden) où ils atteignent 200 mm/ka. Deux paramètres distincts peuvent expliquer de telles différences entre les parties sud et nord. 1- L'extension est accommodée par deux failles bordières de vergence opposée au sud (la *Peel Boundary fault* et la *Feldbiss fault*) et un seul accident tectonique au nord (la *Peel Boundary fault*). 2- La présence du dépocentre majeur dans la partie nord du graben de la Roer indique une quantité d'extension supérieure à celle de la partie sud. Quelle que soit la géométrie symétrique ou asymétrique du graben, la somme des taux de déplacement le long des failles bordières est donc plus importante au nord.

En conclusion, depuis le Crétacé supérieur, le graben de la Roer a été marqué par une succession de phases compressives et extensives liées à la dynamique des systèmes géologique périphériques, i.e., le rift de la Mer du Nord et le ROE. De part son évolution en partie différente de celle du RMC, le graben de la Roer apporte des contraintes fortes pour interpréter l'ensemble du ROE.

2.1.1.3- Le graben du Rhin

Situé dans la partie sud de la Province Rhénane, le graben du Rhin est une structure majeure du ROE. A ce titre, il a fait l'objet des très nombreuses études portant sur sa structure, sa sédimentation et sa dynamique cénozoïque (e.g. Illies, 1972; Sittler, 1974; Villemin et Bergerat, 1987; Brun et al., 1992; Sissingh, 1998; Schumacher, 2002; Behrmann et al., 2003; Dèzes et al., 2004; Rotstein et al., 2006; Bourgeois et al., 2007; Edel et al., 2007; Hinsken et al., 2007).

Le graben du Rhin est un fossé linéaire de 30 à 40 km de large et 300 km de long, d'orientation moyenne N20. Sa partie nord est bordée en majeure partie par des sédiments d'âge Mésozoïque. Vers le sud, le socle hercynien affleure au niveau des massifs cristallins des Vosges et de la Forêt Noire (Figure 14). Enfin, au sud, la zone de transfert Rhin-Bresse, qui correspond à une zone de faille tardi-hercynienne (Ustaszewski et al., 2005) met en relation les grabens du Rhin et de la Bresse. Les données géophysiques révèlent une structuration globale du graben fortement asymétrique avec une faille majeure située à l'est et à l'ouest dans les parties nord et sud, respectivement (Brun et al., 1992). L'inversion de l'asymétrie se produit au niveau de la faille de Lalaye-Lubine-Baden-Baden (LBF), accident tectonique majeur d'âge Hercynien réactivé en faille de transfert lors de la formation du graben (Brun et al., 1992; Chorowicz et Deffontaines, 1993). Outre la LBF, de nombreuses structures hercyniennes ont contrôlé le développement et la structuration du graben. A cet égard, l'orientation globale du graben N20 et sa localisation correspondent à celles de la zone de cisaillement du Rhin (Edel et al., 2007).

La distribution des sédiments tertiaires confirme la géométrie asymétrique du graben du Rhin (Figure 14). Dans la partie nord du graben, l'épaisseur maximum des sédiments atteint 3500 m au pied de la faille majeure, i.e., à l'est, et diminue graduellement vers l'ouest. Au sud, la pile sédimentaire est moins épaisse et organisée en sous-bassins de taille réduite, principalement concentrés dans la partie occidentale du fossé. A noter que cette moitié sud a subi à partir du Miocène supérieur une surrection de 1000-1500 m qui a tronqué une partie de la sédimentation initiale (Villemin et Bergerat, 1987; Ziegler, 1992a).

L'analyse des sédiments cénozoïques du graben du Rhin montre une première phase de sédimentation d'âge Lutétien (Sissingh, 1998; Schumacher, 2002), contemporaine de celle qui s'est produite dans le Massif Central à l'est et à l'ouest du

Sillon Houiller. L'arrêt de la sédimentation pendant quelques millions d'années et la distribution des dépôts, hors des zones affectées ensuite par l'extension, rendent cette sédimentation initiale énigmatique. Il est possible qu'elle traduise l'existence d'une phase d'extension préliminaire de très faible intensité (Dèzes et al., 2004). La sédimentation syn-rift apparaît au Priabonien avec une influence marine prononcée dans la partie sud du graben (Figure 15; Sissingh, 1998; Schumacher, 2002). La subsidence se poursuit de manière continue dans les parties nord et sud durant le Rupélien et le Chattien inférieur. L'Oligocène supérieur marque une transition dans l'évolution du graben. La subsidence se poursuit dans la moitié nord jusqu'au Miocène moyen alors qu'elle cesse au sud (Figure 15). Du Priabonien au Chattien, la sédimentation du graben du Rhin a enregistré de nombreuses incursions depuis la mer molassique et la Mer du Nord située au sud et au nord, respectivement (Sissingh, 1998). Hormis le dépôt de formations détritiques associés au plissement du Jura dans l'extrémité sud du graben, le Miocène inférieur et le Pliocène sont caractérisés par une longue lacune de sédimentation. En revanche le Quaternaire marque une reprise de la subsidence dans l'ensemble du graben et un dépôt maximum de 380 m de sédiments dans le bassin d'Heidelberg (cf Figure 14 pour la localisation; Schumacher, 2002).

L'extension éo-oligocène du graben du Rhin est interprétée comme le résultat d'un rifting passif dont les contraintes sont a rechercher aux limites des plaques (Bergerat , 1987; Ziegler, 1992a).
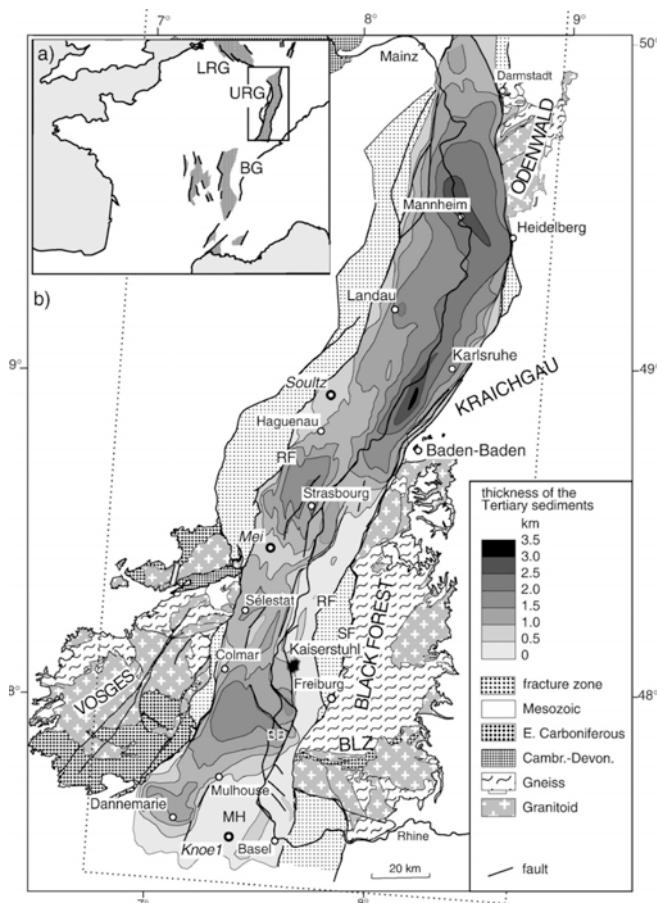

Figure 14: Carte d'épaisseur des sédiments tertiaires du graben du Rhin. URG: Upper Rhine graben; LRG: Lower Rhine graben; BG: Bresse graben (d'après Rotstein et al., 2006).
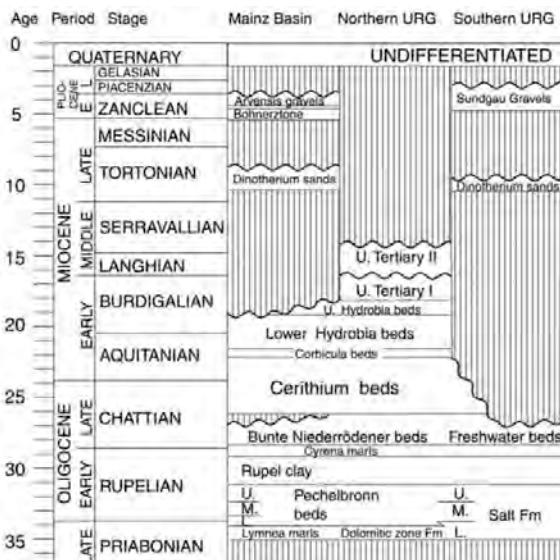
Figure 15: Stratigraphie des sédiments cénozoïques du graben du Rhin (d'après Schumacher, 2002).

Contrairement au RMC, le graben du Rhin est caractérisé par une faible activité volcanique dont l'essentiel s'est déroulé en périphérie du graben avant et après l'extension. Le volcanisme pré-extension a débuté au Crétacé supérieur et s'est poursuivi jusqu'à l'Eocène. Ce volcanisme est caractérisé par des édifices monogéniques très dispersés mettant en jeu des magmas basiques à différenciés, saturés à très sous-saturés en silice (Wimmenauer, 1974; Wilson et al., 1995, Keller et al., 2002; Schmitt et al., 2007). Daté initialement à 100-108 Ma, l'âge d'initiation du volcanisme est actuellement remis en cause par des datations récentes (U-Pb, ^{40}Ar-^{39}Ar) qui tendent à rajeunir le début de cette phase à la fin du Crétacé et au début du Tertiaire (Keller et al., 2002; Schmitt et al., 2007). Le graben du Rhin a également été affecté par un volcanisme post-oligocène, daté entre 18 et 15 Ma (Schleider et al., 1990), et qui s'est mis en place au sein de la partie sud du graben. Les magmas émis sont uniques dans le rift et varient depuis les téphrites, essexites, phonolites jusqu'aux carbonatites (Wimmenauer, 1974). Deux provinces magmatiques se sont développées à l'est du graben du Rhin: l'Hegau et de l'Urach (Figure 1b). Situés dans des régions indemnes de l'épisode d'extension, ces deux ensembles magmatiques résultent d'une activité miocène. La province de l'Hegau s'est construite entre 7-15 Ma et celle de l'Urach s'est édifiée entre 11 et 17 Ma. La composition des laves révèle un magmatisme alcalin sous-saturé à très sous-saturé (Wilson et al., 1995).

Enfin, il est important de noter que l'essentiel de l'activité volcanique de la Province Rhénane a été centrée sur le Bouclier Rhénan. Les premières manifestations datant de la fin du Crétacé ont été contemporaines de l'activité pré-rift autour du graben du Rhin (Lippolt, 1983). Après un arrêt de plusieurs dizaines de millions d'années, le volcanisme est réapparu de façon dispersée à l'Eocène et s'est poursuivi durant l'Oligocène (Huckenholz, 1983; Haase et al., 2004). L'activité magmatique s'est significativement intensifiée entre 6 et 18 Ma, période pendant laquelle les principales provinces volcaniques se sont édifiées (Lippolt, 1983; Haase et al., 2004). L'activité éruptive a de nouveau cessé puis repris au Quaternaire avec la mise en place du volcanisme de l'Eiffel, daté et 0,7-1 Ma et 10000 ans (Schminke et al., 1983). Les récentes investigations géophysiques (tomographie sismique et fonctions récepteurs) ont mis en évidence une anomalie mantellique enracinée à 400 km de profondeur et centrée sur la province quaternaire de l'Eifel (Ritter et al., 2001; Budweg et al., 2006).

2.1.1.4- Evolution globale et origine du rift Ouest Européen

L'origine du ROE et de la dynamique des régions péri-alpines fait l'objet d'un débat intense qui perdure depuis plusieurs décennies (Tapponnier, 1977; Caire, 1977; Bergerat, 1987; Ziegler, 1992a; Chorowicz et Deffontaines, 1993;

Granet et al., 1995; Zeyen et al., 1997a; Stampfli et al., 1998; Merle et Michon, 2001; Michon et al., 2003; Dèzes et al., 2004; Michon et Merle, 2005; Lopes Cardoso et Behrmann, 2006; Schwarz et Henk, 2006; Bourgeois et al., 2007).

La différence de définition du système de grabens (ECRIS ou ROE) mise à part, les principales divergences portent sur (1) les contraintes à l'origine de la formation des grabens, (2) la(les) cause(s) du volcanisme péri-alpin.

1- L'analyse des paléo-contraintes à partir de mesures d'indicateurs cinématiques est une approche qui a été largement mise en œuvre dans les années 1970 et 1980 au niveau des régions péri-alpines (Arthaud et Choukroune, 1972; Illies, 1974; Bergerat, 1977, 1985, 1987; Burg et Etchecopar, 1980; Buchner, 1981; Villemin et Bergerat, 1985, 1987; Larroque et Laurent, 1988). Ces différents travaux ont suggéré la succession de champs de contraintes distincts durant le Cénozoïque. Bien que des différences existent entre les interprétations, il a été classiquement admis que l'Europe occidentale avait subi (i) une compression N-S à l'Eocène en relation avec la phase de compression pyrénéenne; (ii) une extension globalement E-W à l'Oligocène et (iii) une compression NW-SE à partir du Miocène liée à la collision alpine. Une phase de compression NE-SW avait également été proposée par Bergerat (1987). Ces résultats ont été abondamment utilisés pour interpréter la formation du système de grabens cénozoïques (Ziegler, 1992a, 1994; Chorowicz et Deffontaines, 1993; Scumacher, 2002; Dèzes et al., 2004; Bourgeois et al., 2007). La compression N-S aurait réactivé en jeu senestre de grands accidents tectoniques hercyniens orientés NE-SW et consécutivement induit la formation des grabens du ROE ou de l'ECRIS à l'Eocène supérieur et l'Oligocène (Figures 16 et 17).

Les récents travaux d'analyse de paléo-contraintes (Michon, 2001; Ustaszewski et al., 2005; Lopes Cardoso et Behrmann, 2006), de modélisations numérique (Schwarz et Henk, 2006) et analogique (Michon et Sokoutis, 2005), et de rétrodéformation des structures (Behrmann et al., 2003; Bertrand et al., 2005) tendent à remettre en cause la succession de contraintes telle qu'elle a été décrite initialement.

Premièrement, l'absence de faille décrochante dans les sédiments syn-rifts (Villemin et Bergerat, 1987; Michon 2001; Rocher et al., 2003; Ustaszewski et al., 2005), s'explique difficilement dans un contexte global supposé en décrochement. L'origine de ce désaccord se trouve vraisemblablement dans l'âge de la compression N-S. Les mesures microtectoniques indiquant cette compression N-S ont toutes été réalisées dans des formations anté-crétacées. Ceci signifie donc que le développement de cette population de failles date du Crétacé ou du Cénozoïque. Durant cette période, la principale inversion des grabens dans la partie sud de la Mer du Nord et le bombement majeur des massifs hercyniens d'Europe occidentale et centrale se sont produits à la fin du Crétacé et au début du Paléocène, et non à l'Eocène supérieur (Malkovsky, 1987; Barbarand et al., 2002; De Lugt et al., 2003; Worum and Michon, 2005). Bien qu'il soit indiscutable que les Pyrénées aient subi une phase de compression à l'Eocène supérieur, il est fort probable que son impact sur la lithosphère européenne ait été surestimé.

Deuxièmement, différents types de modélisation ont été entrepris pour déterminer les contraintes à l'origine de la sédimentation éo-oligocène du graben du Rhin (Michon et Sokoutis, 2005; Schwarz et Henk, 2006). Les modèles suggèrent une direction d'extension continue WNW-ESE du Priabonien à la fin de l'Oligocène. Ces résultats sont en accord avec la direction d'extension globalement E-W déterminée par rétrodéformation de la structure du graben du Rhin (Bertrand et al., 2005).
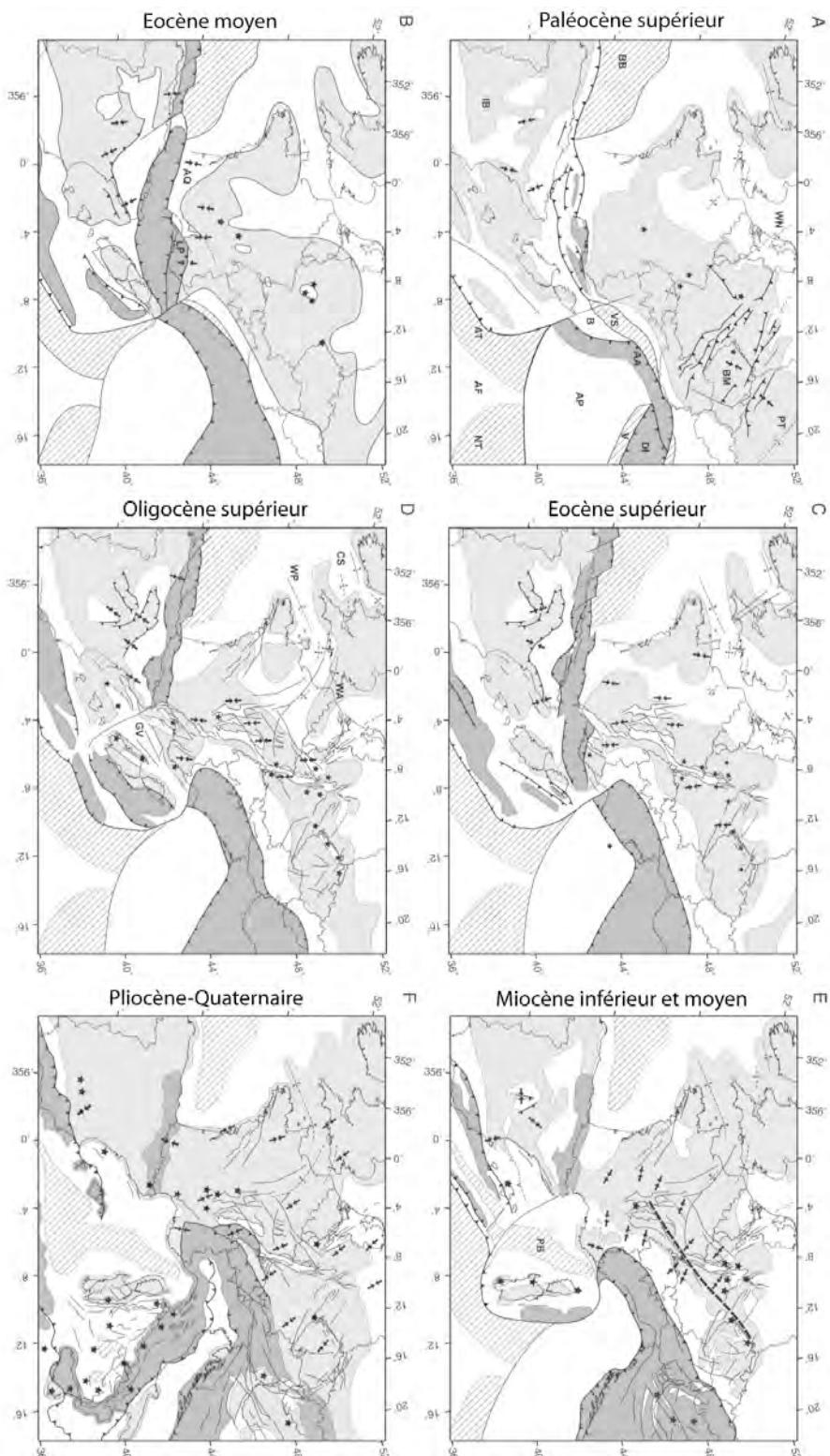
Figure 16: Cartes schématique de la paléo-tectonique de l'Europe occidentale (d'après Dèzes et al., 2004). Légendé: gris foncé: orogènes, gris clair: zone émergée, blanc: bassins sédimentaires, hachures: bassins océaniques, étoiles: volcanisme, flèches: direction de la contrainte compressive horizontal maximum (d'après Bergerat, 1987; Blès and Gros, 1991; Schumacher, 2002), ligne pointillée épaisse: axe de plissement lithosphérique. Abréviations: AA: orogène Austro–Alpine, AF: Afrique, AP: Apulie, AT: Tethys alpine (océan Liguro-Maghrebain), AQ: Bassin aquitain, B: Briançonnais, BB: Golfe de Gascogne, BM: Massif Bohémien, CS: Mer Celtique, DI: Dinarides, GV: Golfe du Lion-rift de Valence, IB: Ibérie, LP: ceinture de plissement Provenço-languedocienne, PB: Bassin provençal, PT: fosse polonaise, V: océan vardar, VS: océan valaisan, WA: axe Weald-Artois, WN: bassin ouest-néérlandais, WP: Approches occidentales.
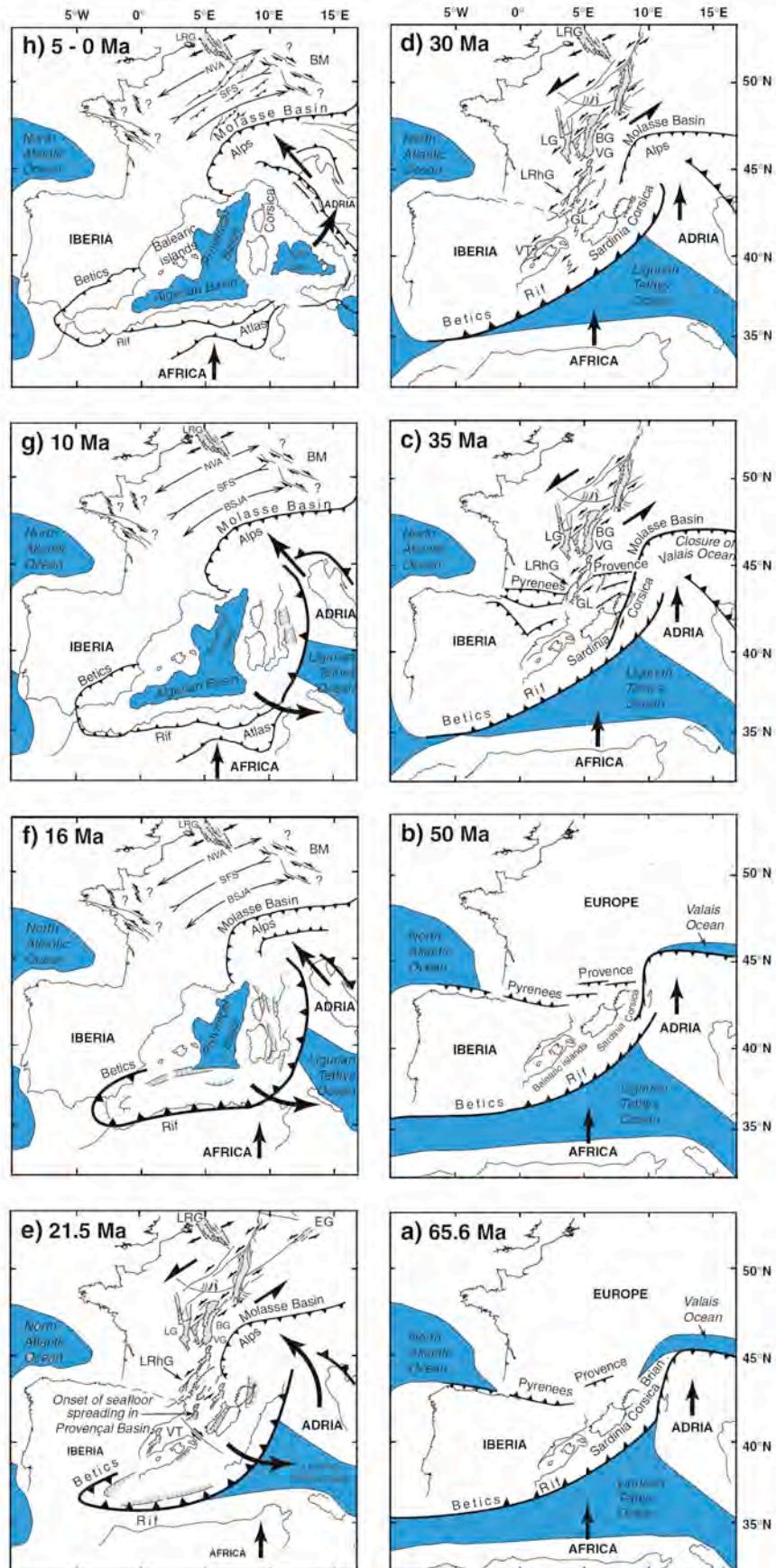
Figure 17: Cartes structurales illustrant l'évolution de l'orogenèse alpine et de son avant-pays pendant le Cénozoïque. D'après Bourgeois et al. (2007). NVA : anticlinal Normandie–Vogelsberg, BSJA : anticlinal Bourgogne – Jura Souabe, BG : graben de la Bresse, BM : Massif Bohémien, EG : graben de l'Eger, GL : Golfe du Lion, LG : graben de la Limagne, LRG : graben de la Roer, LRhG : grabens de la marge languedocienne, SFS : synclinal Sologne – bassin franconien, VT : fosse de Valence.

La Figure 18 synthétise les directions d'extension et de compression ayant affecté les régions péri-alpines entre l'Eocène supérieur et l'Actuel. Deux faits majeurs apparaissent. 1- A certaines périodes, plusieurs champs de contraintes ,i.e. compression et extension, ont coexisté au niveau de la plate-forme européenne. 2- En considérant les grabens de la marge provençale comme essentiellement liés à l'ouverture du Rift NW Méditerranéen (Seranne, 1999; Faccenna et al., 2004), l'extension qu'a subi la plate-forme européenne est concentrée autour de l'arc alpin.
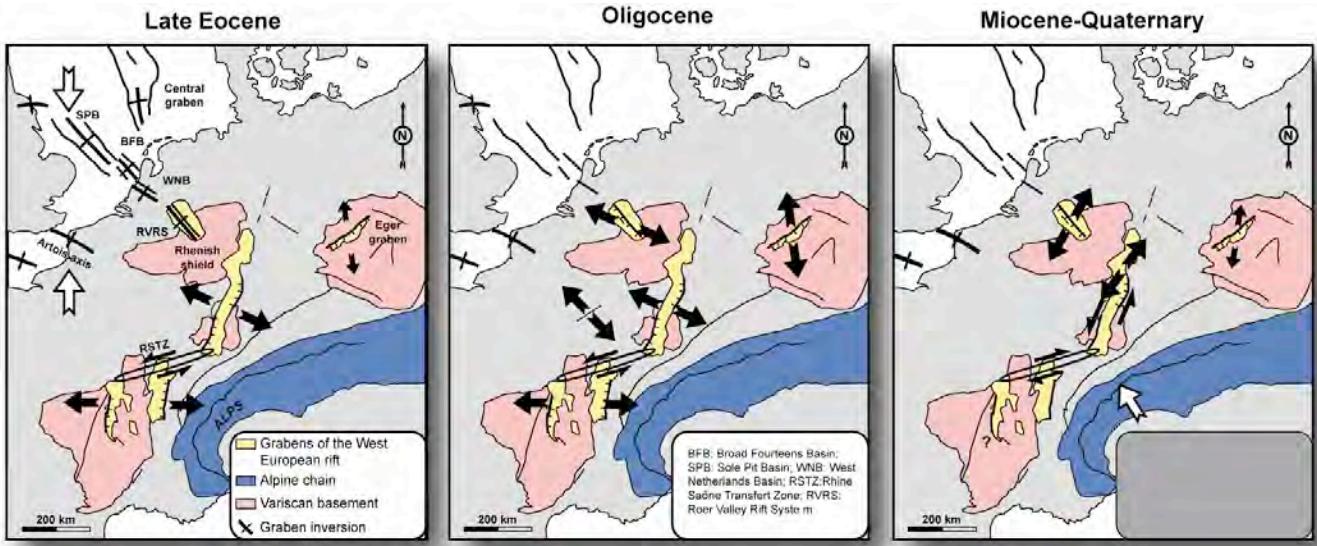
Figure 18: Déformation de la lithosphère en avant de la chaîne alpine durant l'Eocène supérieur et l'Oligocène, et du Miocène au Quaternaire.

2- Actuellement, l'interprétation la plus communément proposée pour expliquer le développement du volcanisme cénozoïque péri-alpin met en jeu la remontée de panaches mantelliques sous la lithosphère européenne depuis la transition Crétacé-Tertiaire (e.g., Hoernle et al., 1995; Granet et al., 1995; Dèzes et al., 2004; Cloetingh et al., 2005; Ziegler et Dèzes, 2007). Cette interprétation s'appuie essentiellement sur les données de tomographie sismique qui ont révélé la présence d'anomalies mantelliques sous le Massif Central et le Bouclier Rhénan (Granet et al., 1995; Ritter et al., 2001) et dans le manteau inférieur (Goes et al., 1999). Cependant, l'absence de structure anomalique claire à l'aplomb du Bouclier Rhénan sous 410 km (Budweg et al., 2006) fragilisent l'interprétation d'un point chaud commun nourrissant des anomalies de petites tailles. Par ailleurs, les provinces volcaniques miocènes du sud du graben du Rhin et le Massif Bohémien ne se situent pas à l'aplomb d'anomalies mantelliques (Achauer et Masson, 2002; Plomerova et al., 2007). Il s'avère, en outre, qu'avant les résultats de tomographie sismique, l'évolution du rift était considérée comme incompatible avec le modèle de point chaud (Ziegler, 1992a). Depuis, des points chauds "pas très énergétiques" (*not-very-energetic mantle plumes* p14 in Dèzes, Schmid et Ziegler, 2004; Ziegler et Dèzes, 2007) seraient responsables de l'apparition du volcanisme à la transition K/T et de l'extension à l'origine des grabens malgré un contexte global en compression. Nous avons remis en cause cette interprétation lors d'un commentaire à publication en rappelant les incompatibilités géologiques et mécaniques auxquelles elle était confrontée (Michon et Merle, 2005).

Récemment, Bourgeois et al. (2007) ont interprété la dynamique cénozoïque de la plate-forme européenne comme étant le résultat d'une compression N-S au Paléogène tournant NW-SE au Néogène. La compression N-S serait responsable de la formation des grabens de l'ECRIS alors que la compression NW-SE aurait entrainé un flambage lithosphérique (Figure 17). Dans ce schéma géodynamique global, le volcanisme Miocène à actuel résulterait de la combinaison du flambage lithosphérique et de l'amincissement lithosphérique dû au rifting. De fait, Bourgeois et al. (2007) indiquent que les régions les plus productives sont situées à l'intersection des anticlinaux lithosphériques et des grabens et que le maximum d'intensité s'est produit dans les zones préalablement les plus amincies. Cette

interprétation est confrontée à plusieurs problèmes: 1- Le volcanisme syn-rift du Massif Bohémien, du Massif Central et du Bouclier Rhénan n'est pas pris en compte. 2- Dans le Massif Central et sur le Bouclier Rhénan, le volcanisme néogène supérieur s'est mis en place dans des zones non amincies par le processus de rifting (cf la conclusion de la section 2.1.1 sur le Massif Central). 3- Une fusion locale due au flambage lithosphérique n'expliquerait pas les anomalies mantelliques sous ces deux provinces magmatiques.

Lors de ma thèse et de mon post-doctorat, j'ai souhaité tenir compte de toutes les données géologiques, géophysiques et géochimiques disponibles au niveau du ROE pour proposer un modèle géodynamique dans lequel volcanisme et tectonique seraient intégrés (Merle, et al., 1998; Michon et Merle, 2000; Michon et Merle, 2001; Merle et Michon, 2001; Michon et al., 2003; Michon et Merle 2005; Michon et Sokoutis, 2005). Nous sommes partis d'un constat géométrique simple: le système de grabens et le volcanisme sont répartis autour de l'arc alpin uniquement. Quel pouvait donc être le lien entre un orogène et un système de rift?

Le modèle que nous avons développé dans plusieurs publications met en avant le rôle moteur joué par la racine lithosphérique alpine dans l'apparition de l'extension dans la lithosphère européenne (Figure 19a). L'enfoncement de cette racine dans l'asthénosphère serait à l'origine d'un fluage asthénosphérique en retour et, en conséquence, de la remontée de matériel mantellique sous la forme d'anomalies mantelliques de tailles réduites (Figure 19b).

L'évolution du Rift Ouest Européen telle que nous l'avons proposée (Michon et al., 2003) peut se résumer de la manière suivante:

1- A la fin du Crétacé et au début du Paléocène, la fermeture de l'océan Piémontais (Ziegler et Roure, 1996) est à l'origine de contraintes compressives dans la lithosphère européenne. Il se produit alors un flambage de grande longueur d'onde, une importante inversion des grabens de la Mer du Nord et un timide volcanisme par faible décompression adiabatique à l'aplomb des anticlinaux lithosphériques.
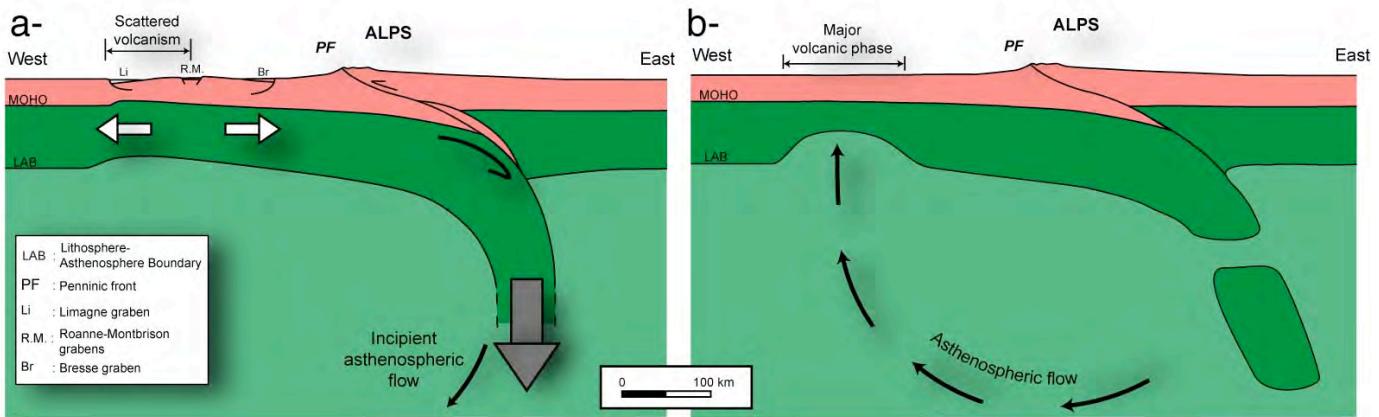
Figure 19: Coupe à l'échelle lithosphérique illustrant (a) l'effet de la racine lithosphérique alpine dans la lithosphère européenne adjacente et (b) le fluage asthénosphérique en retour. La force gravitaire (flèche grise) liée au plongement de la racine initie une extension perpendiculaire au front alpin. L'enfoncement de la racine provoque également un fluage asthénosphérique et une remontée de matériel mantellique chaud sous la lithosphère européenne.

2- La seconde partie de l'Eocène marque le début d'une importante phase de déformation dans la chaine alpine avec un métamorphisme de haute pression (Monié et Philippot, 1989; Tilton et al., 1991; Duchêne et al., 1997) qui traduit le développement d'une profonde racine crustale. Les directions de compression, respectivement N-S et E-W dans les Alpes orientales et occidentales (Lickorish et al., 2002), suggèrent une subduction continentale parallèle aux directions d'extension dans les grabens éo-oligocènes. Cette extension lithosphérique périphérique à la chaine de collision serait induite par la force gravitaire liée au plongement de la racine lithosphérique dans

l'asthénosphère (Figure 19a). Une telle dynamique "locale" n'est pas incompatible avec la compression régionale N-S avérée par l'inversion des grabens en Mer du Nord et en Manche.

3- Le fluage asthénosphérique dû à l'enfoncement de la racine lithosphérique alpine entraine la remontée d'anomalies mantelliques sous la lithosphère européenne et par conséquent le volcanisme miocène péri-alpin. Dans les Alpes, le détachement de la racine lithosphérique à la transition oligo-miocène provoque l'arrêt des contraintes extensives et l'apparition d'une compression NW-SE. Ce changement de contraintes est responsable de la surrection de la région sud du graben du Rhin (Vosges et Forêt Noire), de la réactivation en décrochement senestre du graben du Rhin et de l'extension NE-SW au niveau du graben de la Roer (Figure 19b).

Cette interprétation à fait l'objet de critiques portant sur l'évolution de la chaine alpine et donc sur l'impossibilité de faire jouer à la racine lithosphérique le rôle de moteur de l'extension (Dèzes et al., 2005). Il s'avère que l'évolution des Alpes fait débat et que l'âge du détachement de la racine est encore mal connu. Il est tout de même intéressant de noter que l'existence d'une évolution polyphasée du rift déduite des données géologiques n'est quant à elle pas remise en cause.

2.1.2- Modélisation analogique des rifts lents

Parallèlement à l'étude de rifts naturels, j'ai mené une analyse du développement des grabens par une approche expérimentale. La modélisation analogique a été entreprise au Laboratoire Magmas et Volcans de Clermont-Ferrand et à l'ISES TecLab de l'Université d'Amsterdam, en collaboration avec Olivier Merle et Dimitrios Sokoutis. Nous nous sommes focalisés sur l'étude des rifts lents *via* deux thématiques distinctes: 1- Les modalités d'extension aux échelles crustales et lithosphériques; 2- Le rôle de l'héritage structural crustal et lithosphérique dans la formation des grabens et des dépocentres.

Les résultats de la modélisation analogique peuvent être appliqués à la nature si les contraintes, les géométries, les densités et les rhéologies sont équivalentes dans les modèles et la nature (Hubbert, 1937; Ramberg, 1981). Les expériences que j'ai réalisées avaient pour but de simuler le processus de rifting en domaine continental. Dans un tel contexte, la structure de la lithosphère était considérée comme quadri-couche avec une alternance de niveaux fragiles et ductiles lorsque le gradient géothermique est normal (Ranalli et Murphy, 1987; Davy et Cobbold, 1991). Je discuterai de la pertinence de cette stratification rhéologique ultérieurement dans ce mémoire. Les niveaux fragiles, i.e. croûte supérieure et partie fragile de la lithosphère mantellique, et les niveaux ductiles, i.e. croûte inférieure et partie ductile de la lithosphère mantellique, sont simulés dans les expériences par des couches de sable et de silicone, respectivement. La rupture de la partie fragile de la lithosphère mantellique, qui est en grande partie responsable de la déformation crustale (Davy et Cobbold, 1991; Brun et Beslier, 1996), est reproduite dans les modèles par une discontinuité de vitesse basale ou latérale.

Nous avons utilisé deux approches indépendantes pour satisfaire aux règles du dimensionnement. La première méthode est basée sur le rôle important joué par le couplage mécanique entre les parties fragiles et ductiles de la croûte (Benes et Davy, 1996; Brun, 1999). Ce couplage fragile/ductile peut être estimé par le rapport de résistance entre la croûte supérieure (S_B) et la croûte inférieure (S_D). Nous avons utilisé ce rapport pour dimensionner les modèles. Il correspond à un nombre sans dimension qui doit être du même ordre de grandeur dans les modèles et la nature (Eq. 1). Le détail de la procédure est expliqué dans Michon et Merle (2000) et Michon et Sokoutis (2005), annexes 6 et 8.

$$\left(\frac{S_B}{S_D}\right)_{Modèle} = \left(\frac{S_B}{S_D}\right)_{Nature} . \qquad \text{Eq. 1}$$

Nous avons mis en œuvre une seconde approche de dimensionnement pour comparer les résultats des modèles analogiques à l'échelle crustale que j'ai réalisés en thèse (Michon et Merle, 2000) et des modèles à l'échelle lithosphérique développés par Brun et Beslier (1996). Selon le théorème Π de Buckingham (Buckingham, 1915), un système physique défini par *n* variables et caractérisé par *p* dimensions indépendantes peut être défini pas *m=n-p* nombres sans dimension. Ces *m* nombres sans dimension, appelés Π_1, Π_2,…Π_m, doivent être du même ordre de grandeur dans la nature et les modèles pour satisfaire aux conditions de similitude. Nous avons défini 10 variables communes à la nature et aux modèles à l'échelle crustale et lithosphérique. L'ensemble de ces variables est caractérisé par trois dimensions indépendantes: M (masse), L (longueur) et t (temps). Le dimensionnement des modèles a donc nécessité la définition de 7 nombres sans dimension (Π_1 à Π_7). Le détail de la procédure est expliqué dans Michon et Merle (2003), annexe 7.

2.1.2.1- Modalités de l'extension

Les mécanismes de formation des grabens dans un contexte de rift continental et leur évolution vers la formation de marges passives ont intensément été étudiés durant les dernières décennies. Les débats ont principalement porté sur la géométrie des grabens en surface, sur la déformation à l'échelle lithosphérique et sur l'évolution de cette déformation au cours du processus de rifting (e.g. McKenzie, 1978; Wernicke, 1981, 1985; Buck, 1991; Lister et al., 1991; Reston, 1993; Boillot et al., 1995; Brun et Beslier, 1996; Brun, 1999; Huismans et Beaumont, 2002, 2003; Manatschal, 2004; Lavier et Manatschal, 2006). Les premiers modèles, bien qu'opposés mécaniquement, ont considéré des modes de déformation identiques à l'échelle de la lithosphère. L'extension engendrerait un amincissement homogène de la lithosphère par cisaillement pur (McKenzie, 1978) ou serait accommodée par le développement d'un détachement lithosphérique continu depuis la croûte supérieure jusqu'à la limite lithosphère-asthénosphère (Wernicke, 1981). Cependant, les nombreuses données géologiques collectées sur les marges émergées et immergées ont révélé que cisaillements pur et simple agissaient lors du processus de rifting (e.g., Boillot et al., 1987, 1995; Froitzheim et Eberli, 1990; Manatschal et Bernoulli, 1999). Cochran et Martinez (1988), Lister et al. (1991) et Kusznir et Ziegler (1992) ont donc proposé des modèles intermédiaires dans lesquels la déformation crustale serait contrôlée par une faille de détachement et l'amincissement de la lithosphère mantellique résulterait d'un cisaillement pur. Le développement des modélisations analogiques et numériques a permis de préciser ces modèles et de mettre en relief le rôle des cisaillements crustaux et lithosphériques, des contrastes rhéologiques fragile-ductile et des structures initiales de la lithosphère (e.g., Beslier, 1991; Buck, 1991; Brun et Beslier, 1996; Chemenda et al., 2002; Huismans et Beaumont; 2002, 2003). Récemment, Lavier et Manatschal (2006) ont mis en avant un modèle qui explique les différentes observations faites au niveau des marges passives par la succession de trois modes d'extension affectant tout d'abord la croûte puis l'ensemble de la lithosphère. Bien que cette interprétation soit sans conteste pertinente pour des stades avancés d'extension, elle explique mal la géométrie étroite de la majorité des rifts lents. De fait, les rifts actuels ou récents sont caractérisés (i) en grande partie par un graben unique (graben du Rhin, graben de l'Eger, Mer Rouge, rift Est-Africain), ou (ii) dans une moindre mesure (rift du Massif Central) par plusieurs grabens parallèles contemporains.

Notre étude portant sur les modalités d'extension des rifts lents s'est principalement appuyée sur des modèles analogiques que j'ai réalisés en thèse (Michon et Merle, 2000). Dans un second temps, ces expériences ont été comparées aux modèles à l'échelle lithosphérique de Beslier (1991; Michon et Merle, 2003). Ce travail avait un triple objectif: 1- Déterminer le rôle de la vitesse d'extension dans la géométrie des grabens; 2- Comprendre l'impact d'une ou plusieurs ruptures dans la partie fragile de la lithosphère mantellique sur le nombre de grabens; 3- Caractériser la déformation interne des niveaux ductiles de la lithosphère et son rôle dans l'amincissement lithosphérique global.

Dans les expériences à l'échelle crustale, la structure fragile-ductile de la croûte continentale a été simulée par un assemblage bicouche sable-silicone reposant sur une plaque fixe (Figure 20a). L'extension a été réalisée dans le modèle par l'introduction d'une feuille plastique à la base du dispositif dont le déplacement induisait une discontinuité de vitesse (VD) qui mimait la rupture de la partie fragile de la lithosphère mantellique. L'ajout d'une seconde feuille plastique a permis de reproduire une double rupture de lithosphère mantellique (Figure 20a). Dans les expériences à l'échelle lithosphérique, la structure quadri-couche de la lithosphère a été modélisée par la superposition de couches fragiles et ductiles reposant sur une solution de glucose (Figure 20b). La déformation y a été initiée par deux discontinuités de vitesse latérales simulant une seule rupture de la partie fragile de la lithosphère mantellique. Les expériences ont été réalisées avec des vitesses d'extension correspondant dans la nature à des vitesses entre 1,5 et 7,5 mm/an.

1- Rôle de la vitesse d'extension.

Les expériences avec une VD montrent deux types de déformation, communs aux modèles crustaux et lithosphériques. Lorsque les vitesses d'extension sont faibles, i.e. équivalentes à moins de 2mm/an dans la nature, la VD induit la formation d'un seul graben asymétrique sur la partie mobile (Figure 21a). Pour les fortes vitesses d'extension, entre 2 et 10 mm/an dans la nature, un couple de grabens se met en place de part et d'autre de la VD. Outre le graben asymétrique sur la parte mobile, commun aux expériences à faible vitesse d'extension, l'extension induit le développement d'un graben globalement symétrique sur la partie fixe (Figure 21b). Les deux grabens sont séparés par un horst central qui montre de fortes similitudes avec le bloc H dans le modèles numériques de Lavier et Manatschal (2006). La transition entre les deux domaines de déformation, i.e. un graben asymétrique ou deux grabens, se produit pour des valeurs du rapport de résistance fragile-ductile crustal (S_B/S_D) de 65-70 (Figure 22).
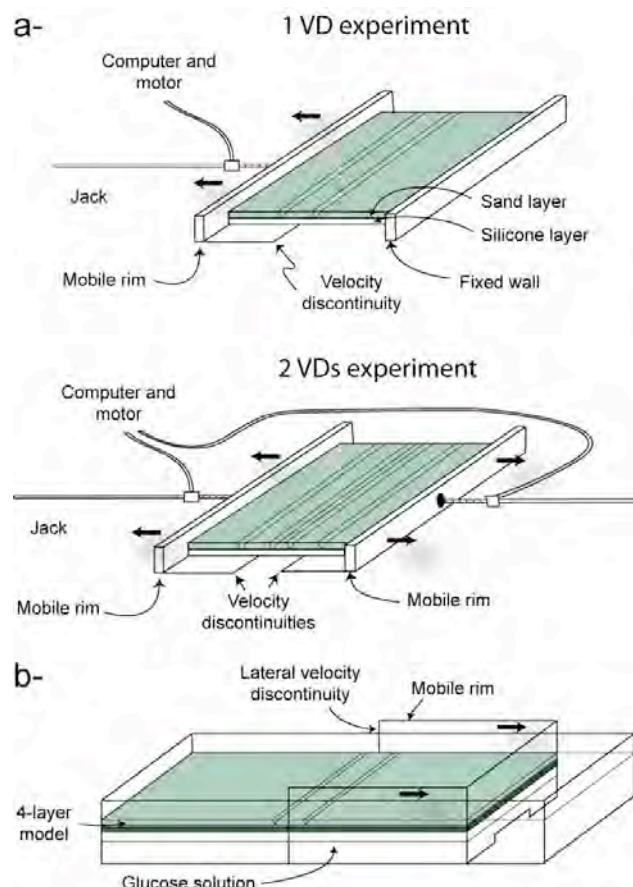
Figure 20: Dispositifs expérimentaux mis en place lors des expériences aux échelles crustales (a-) et lithosphériques (b-). Dans le cadre des expériences à l'échelle crustale, le rôle du nombre de rupture de la partie fragile de la lithosphère mantellique a été investigué en incluant une ou deux VD à la base des modèles. Les modèles à l'échelle lithosphérique ont été par Beslier (1991).
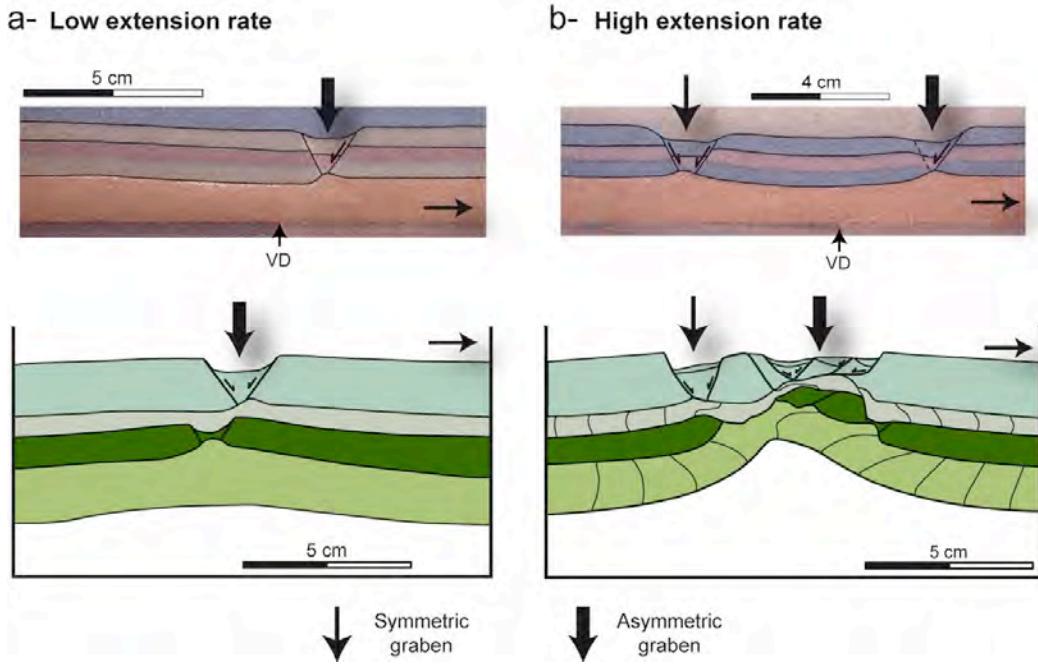
Figure 21: Comparaison entre les expériences réalisées aux échelles crustale et lithosphérique. a- Une faible vitesse d'extension induit la formation d'un graben unique asymétrique sur la partie mobile. b- En revanche, deux grabens se développent pour des fortes vitesses d'extension: un graben globalement symétrique sur la partie fixe et un graben asymétrique sur la partie mobile. VD: Discontinuité de vitesse. Les modèles à l'échelle lithosphérique sont d'après Beslier (1991).
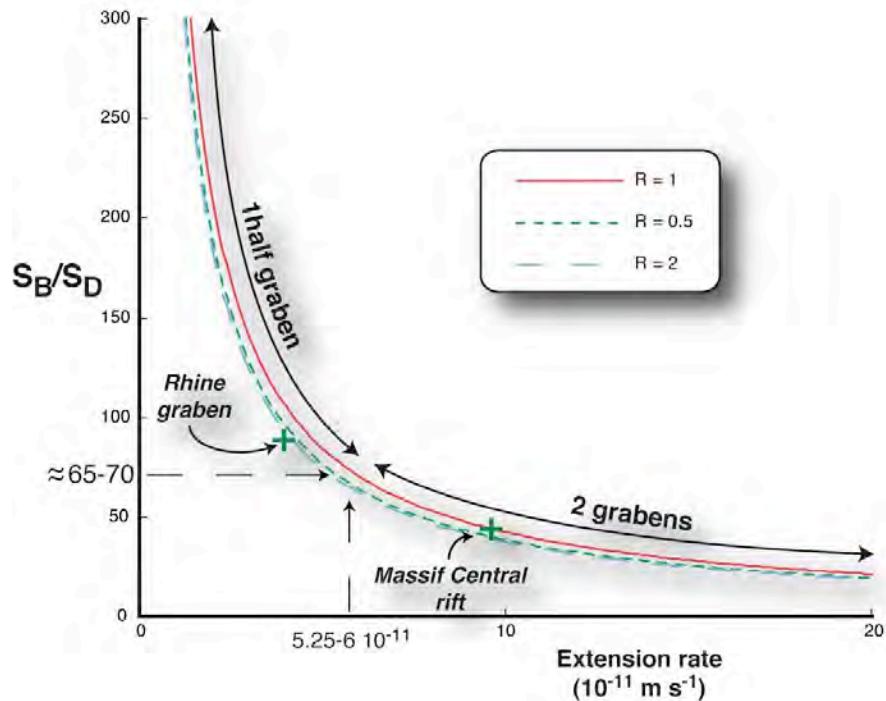
Figure 22: Rapport de résistance fragile-ductile (SB/SD)en fonction de la vitesse d'extension pour trois rapports d'épaisseur fragile-ductile (0,5 à 2).

2- Rôle du nombre de discontinuités de vitesse.

Pour des raisons techniques, ce paramètre a été testé uniquement dans les expériences à l'échelle crustale dans lesquelles le nombre de VD a été limité à deux. La déformation des modèles à faible vitesse d'extension est caractérisée par deux grabens asymétriques quelle que soit la distance initiale entre les VD. En revanche, les expériences à forte vitesse d'extension révèlent une déformation finale qui varie en fonction de la distance initiale entre les VD (Figure 23).
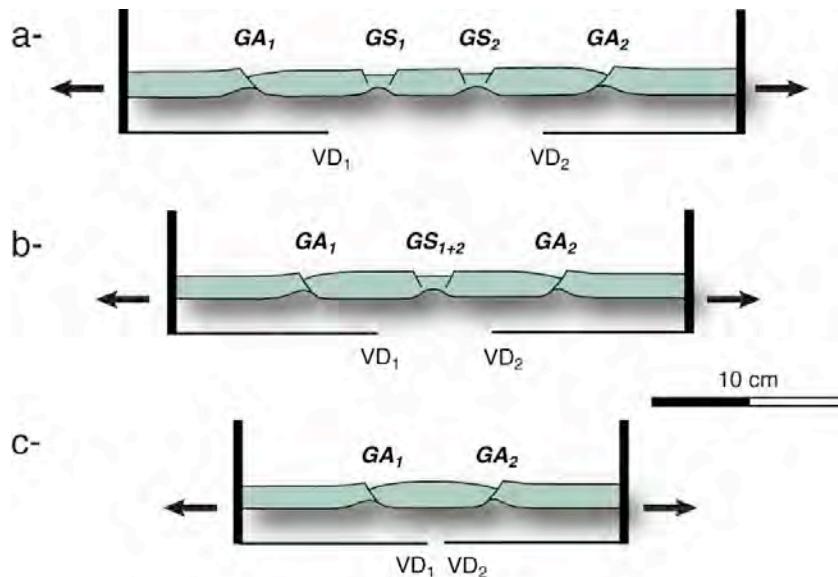
Figure 23: Déformation dans les expériences à l'échelle crustale avec deux VD pour des fortes vitesses d'extension. Distance initiale entre les VD supérieure à 6 cm (a-), entre 4 et 6 cm (b-) et inférieure à 4 cm (c-). GA_1 et GS_1 sont les grabens asymétrique et symétrique associés à la VD_1. GA_2 et GS_2 sont les grabens asymétrique et symétrique associés à la VD_2.

Pour une distance initiale entre les VD supérieure à 6 cm, l'extension induit le développement de deux couples de grabens symétrique/asymétrique; chaque couple étant associé à une VD. Lorsque la distance initiale est de 4 à 6 cm, trois grabens se mettent en place. Les deux grabens latéraux sont asymétriques et le graben central est symétrique. Ce graben est interprété comme le résultat de la superposition des deux grabens symétriques liés aux VD 1 et 2. Enfin, seuls deux grabens asymétriques se forment si la distance entre les VD est inférieure à 4 cm. Dans ce cas, l'apparition des deux grabens symétriques est inhibée par le développement des deux demi-grabens.

Ces résultats sur le rôle de la vitesse d'extension et du nombre de VD, ainsi que l'utilisation du rapport de résistance (S_B/S_D) pour dimensionner nos expériences, nous ont permis d'expliquer les différences de géométrie entre le graben du Rhin et la partie nord du rift du Massif Central (Michon et Merle, 2000). En effet, avec un rapport de résistance de 88 et une vitesse d'extension de 1,2 mm/an ($3,8 \times 10^{-11}$ m.s^{-1}) déduits des données géologiques, la géométrie du graben du Rhin s'explique par une seule rupture de la partie fragile de la lithosphère mantellique (Figures 22 et 24a). La structure de la partie nord du rift du Massif Central, avec deux grabens latéraux asymétriques et un graben central globalement symétrique, résulterait de deux ruptures simultanées de la lithosphère mantellique espacées d'environ 50 km et d'une vitesse d'extension de 3 mm/an ($9,6 \times 10^{-11}$ m.s^{-1}; Figure 22 et 24b).

3- Déformation interne des niveaux ductiles.

Le développement de grabens dans les modèles suggère que la silicone transfert la déformation depuis la discontinuité de vitesse vers la partie fragile sus-jacente. En suivant le protocole expérimental décrit par Brun et Merle (1985), nous avons analysé la déformation interne de la partie ductile des modèles crustaux.

L'expérience avec une forte vitesse d'extension et une discontinuité de vitesse révèle la présence de zones de cisaillement conjuguées, pentées de 25-30° et reliant la VD et la base des grabens (Figure 25a). La déviation des marqueurs verticaux de la silicone montre clairement que l'intensité du cisaillement est maximum au niveau de la zone de cisaillement associée au graben asymétrique. Dans les expériences à faible vitesse d'extension, la géométrie de l'amincissement de la silicone, semblable à celle d'expériences à forte vitesse d'extension, suggère également le développement de deux zones de cisaillement conjuguées (Figure 9 dans Michon et Merle, 2003; Annexe 7). Nous avons considéré l'absence du graben

symétrique dans ces expériences comme le fait d'une intensité du cisaillement trop faible pour provoquer la rupture de la couche fragile.
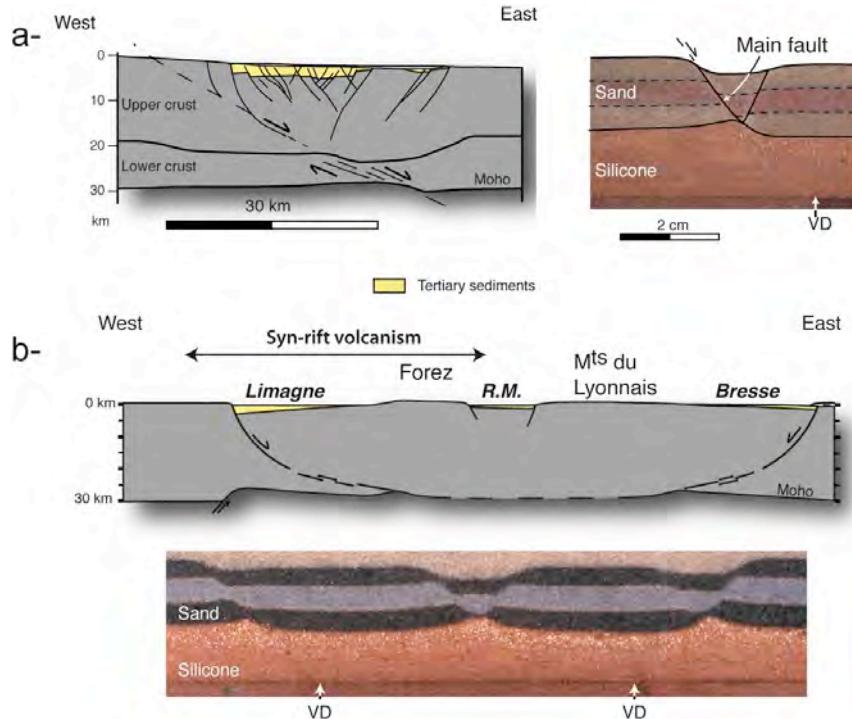

Figure 24: Comparaisons modèle-nature pour (a-) le graben du Rhin et (b-) le rift du Massif Central. La géométrie de la partie sud du graben du Rhin est déduite du profil sismique ECORS (Brun et al., 1992).

Les modèles réalisés à l'échelle crustale permettent de mieux comprendre la déformation interne des niveaux ductiles dans les expériences à l'échelle lithosphérique. De prime abord, la Figure 25b montre l'existence d'une zone de cisaillement affectant l'ensemble du modèle et contrôlant l'amincissement global du modèle. Cette zone de cisaillement qui est associée au graben asymétrique peut être comparée au détachement lithosphérique du modèle de *simple shear* de Wernicke (1981). Cependant, le modèle analogique présente des différences notables avec ce modèle conceptuel. De fait, pris indépendamment, chaque niveau ductile est caractérisé par deux cisaillements conjugués semblables à ceux des modèles crustaux. Ces différentes zones de cisaillement contribuent à l'amincissement du modèle; particulièrement les deux zones situées à l'aplomb du graben asymétrique (Ccp et Cmp dans la Figure 25b) au sein desquelles l'intensité du cisaillement est maximale. Il est intéressant de noter le décalage latéral entre amincissements crustal et lithosphérique. En effet, comme dans les modèles numériques de Lavier et Manatschal (2006), l'amincissement de la lithosphère mantellique est maximum à l'aplomb du horst central, là où l'amincissement de la partie fragile de la croûte est nul. Il existe donc un réel découplage entre l'amincissement de la lithosphère et celui de la croûte fragile. Dans les deux types de modélisation, analogique et numérique, ce découplage est réalisé par un niveau ductile sous la partie fragile de la croûte. Il correspond à la croûte moyenne dans les modèles numériques (Nagel et Buck, 2004; Lavier et Manatschal, 2006) et à la croûte inférieure dans les modèles analogiques.

Une autre expérience de Beslier (1991) montre que l'amincissement du modèle peut également être contrôlé par le Cmp. En intégrant les informations fournies par les différentes expériences, nous avons proposé un nouveau mode d'extension lithosphérique caractérisé par un stade initial unique à l'origine de deux évolutions différentes: *simple shear* ou *necking* (Michon et Merle, 2003). Ces modes d'extension, combinés à l'effet de la vitesse d'extension, sont à même d'expliquer les variations de géométrie et d'évolution de nombreux rifts continentaux.
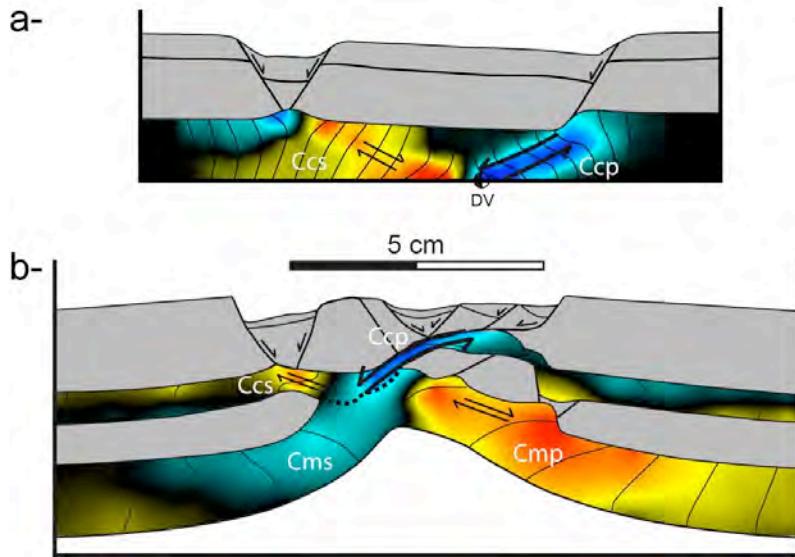
Figure 25: Déformation interne des niveaux ductiles pour les expériences à forte vitesse d'extension aux échelles crustale (a-) et lithosphérique (b-). Les lignes noires dans les niveaux ductiles sont des marqueurs initialement disposés verticalement. Les variations de couleur de bleu clair à bleu foncé indiquent une augmentation de la déformation pour les cisaillements dont le compartiment supérieur se déplace vers la gauche. Les variations de jaune à rouge indiquent une augmentation de la déformation pour les cisaillements dont le compartiment supérieur se déplace vers la droite. Ccp: Cisaillement crustal principal; Ccs: Cisaillement crustal secondaire; Cmp: Cisaillement mantellique principal; Cms: Cisaillement mantellique secondaire.

J'ai précisé en introduction de la section 2.1.2, "Modélisation analogique des rifts lents", que les expériences analogiques avaient pour but de simuler le processus de rifting en domaine continental. Nos modèles reproduisant bien les structures des rifts récents, on peut dire que la modélisation analogique est adaptée pour comprendre les mécanismes de déformation lors de stades initiaux d'extension. En revanche, il est très clair que les modèles discutés ci-dessus ne peuvent être utilisés pour expliquer les structures visibles au niveau des marges passives. Certains processus clés tels que les changements de rhéologie lors de l'amincissement de la lithosphère ne peuvent être pris en compte. Ces effets sont en revanche bien contraints dans les modélisations numériques récentes où des phénomènes tels que la serpentinitisation du manteau lithosphérique sont considérés (Lavier et Manatschal, 2006). Les approches numériques et analogiques sont donc parfaitement complémentaires.

2.1.2.2- Rôle de l'héritage structurale dans la formation des grabens

Les lithosphères continentales sont des ensembles structuraux complexes composés de domaines géologiques d'âge, de géométrie et de nature différentes. Cette structuration générale résulte principalement de la coalescence de blocs lithosphériques durant chaque orogène. Le rôle fondamental de ces structures héritées dans le développement des rifts continentaux a été largement reconnu (e.g., Illies, 1982; Ring, 1994; Bonini et al., 1997; Scumacher, 2002" Corti et al., 2007). Les grabens sont ainsi fréquemment superposés à des failles crustales pré-existantes réactivées selon deux orientations différentes présentant un angle d'environ 40° (Figure 26). La localisation des dépocentres à l'intersection des deux réseaux de faille suggère une activité contemporaine des failles, et non une succession de directions d'extension différentes. Il apparaît donc que lors d'un événement de rifting, un système de grabens subit simultanément une extension orthogonale et oblique selon l'orientation des segments de faille réactivés.

Différents types de modèles analogiques ont été réalisés pour comprendre le rôle de la direction d'extension dans la géométrie des grabens (Tron et Brun, 1991; McClay et White, 1995; Clifton et al., 2000; McClay et al., 2002). Ces modèles dans lesquels une seule direction pré-existante est simulée montrent qu'une extension orthogonale entraine la formation de grabens linéaires parallèles à l'orientation héritée, alors qu'une extension oblique induit le développement de grabens en échelon obliques à la structure héritée. Récemment, le rôle de l'héritage structural a été étudié par l'intégration

d'anisotropies simulant des failles héritées obliques à la direction d'extension et situées uniquement dans la croûte supérieure (Bellahsen et Daniel, 2005). Ces expériences révèlent que les discontinuités pré-existantes sont réactivées et qu'elles interagissent avec les grabens en cours de développement. L'interaction entre l'héritage lithosphérique de grande échelle et l'héritage crustal a également été analysée grâce à la présence d'une discontinuité basale, censée représenter une limite lithosphérique, et de structures pré-existantes dans la partie fragile simulant l'existence de failles crustales (Corti et al., 2007). Les résultats suggèrent que les limites lithosphériques et crustales contrôlent respectivement la géométrie d'ensemble du système de graben et l'orientation des failles bordières des grabens.
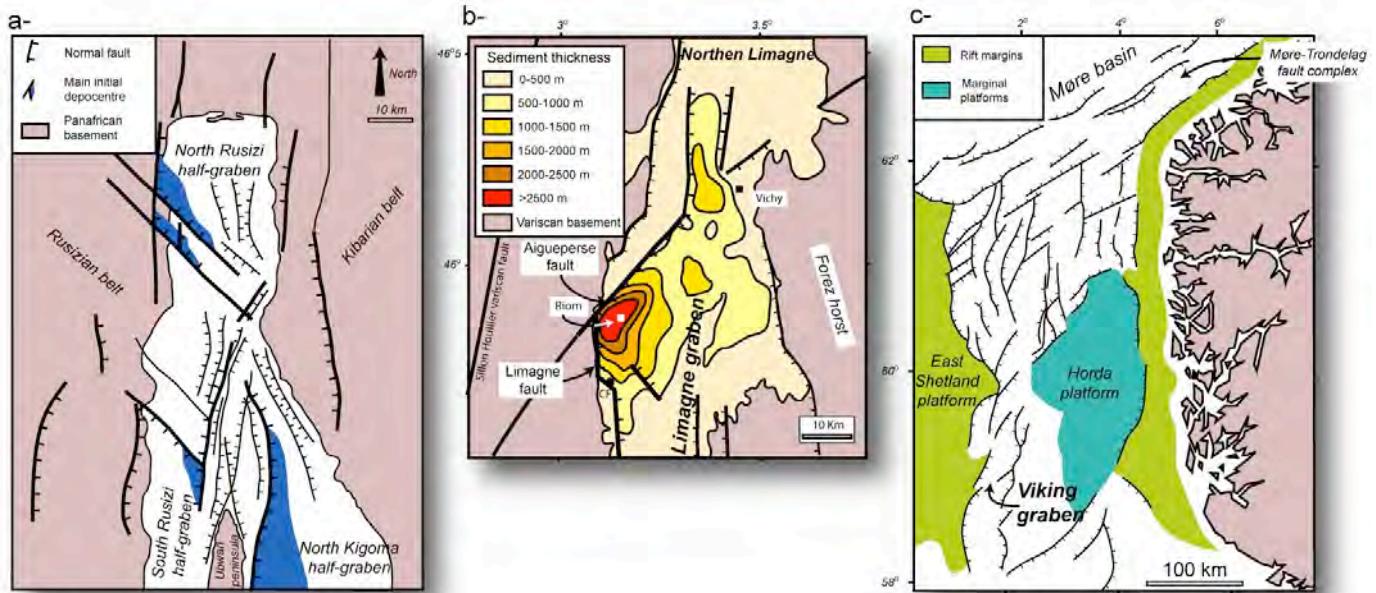
Figure 26: a- Carte géologique simplifiée de la partie nord du Lac Tanganyika montrant la localisation des dépocentres à l'intersection de deux réseaux de failles (d'après Lezzar et al., 2002). b- Carte isopaque des sédiments éocène supérieur - oligocène dans le graben de la Limagne (modifié d'après Morange et al., 1971). c- Carte structurale du Viking graben et des régions adjacentes illustrant les deux réseaux de failles pré-existantes réactivées (d'après Færseth et al., 1997).

Partant du constat que les failles pré-existantes réactivées par un épisode de rifting présentent communément un angle de 40° et que les accidents lithosphériques contrôlent le développement des structures crustales (e.g. Davy et Cobbold, 1991), nous avons réalisé une série de modèles à l'échelle crustale pour déterminer (i) le rôle de fabriques lithosphériques obliques dans le développement des grabens et des dépocentres, (ii) l'effet des directions d'extension sur la géométrie de ces structures et (iii) l'interaction entre grabens linéaires et en échelon.

Le comportement fragile-ductile de la croûte a été simulé par la superposition d'une couche de silicone et de sable de Fontainebleau; l'ensemble reposant sur une plaque qui représente la limite entre la croûte et la lithosphère mantellique (Figure 27a). Dans chaque expérience, la VD est caractérisée par deux segments faisant un angle de 140° (Figure 27b). Cet angle est subdivisé en deux de part et d'autre de l'intersection entre les segments de VD. Chaque segment est donc défini par une valeur α qui correspond à l'angle entre l'intersection et la VD mesuré à partir de l'intersection. De plus, chaque expérience est caractérisée par une valeur α-VAD qui représente la différence entre les deux valeurs d'α. Cette valeur α-VAD permet de déterminer l'angle entre la direction d'extension et la bissectrice des deux segments de VD. L'extension est parallèle à la bissectrice pour α-VAD=0 et s'en éloigne pour des valeurs d' α-VAD croissantes (Figure 26b).
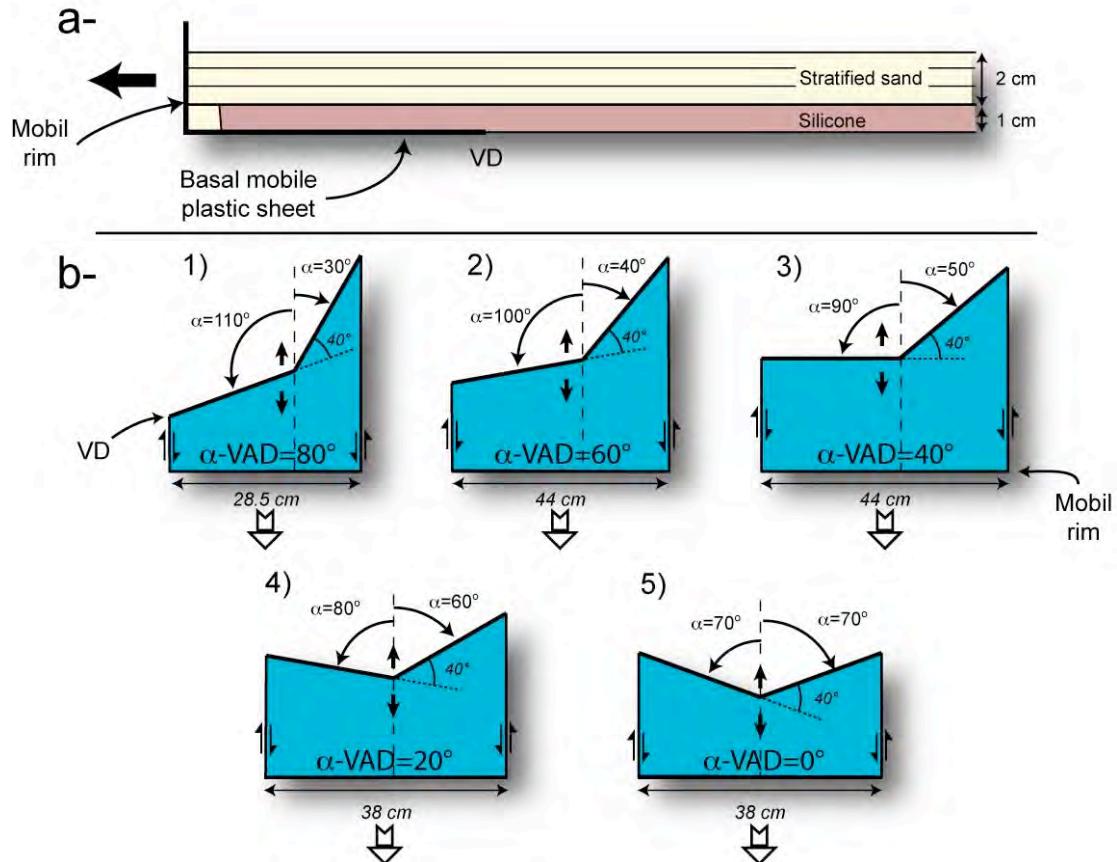
Figure 27: a- Coupe d'un modèle bicouche sable-silicone avant extension. L'extension est initiée par le déplacement d'une feuille plastique dont la limite sépare un domaine se déplaçant et un domaine fixe. Il se produit alors une discontinuité de vitesse (VD) qui simule la rupture de la partie fragile de la lithosphère mantellique. b- Géométrie en carte des différentes feuilles plastiques utilisées dans les expériences. La VD présente dans chaque modèle deux orientations différentes. La valeur α correspond à l'angle mesuré à partir de l'intersection entre la VD et la direction d'extension.
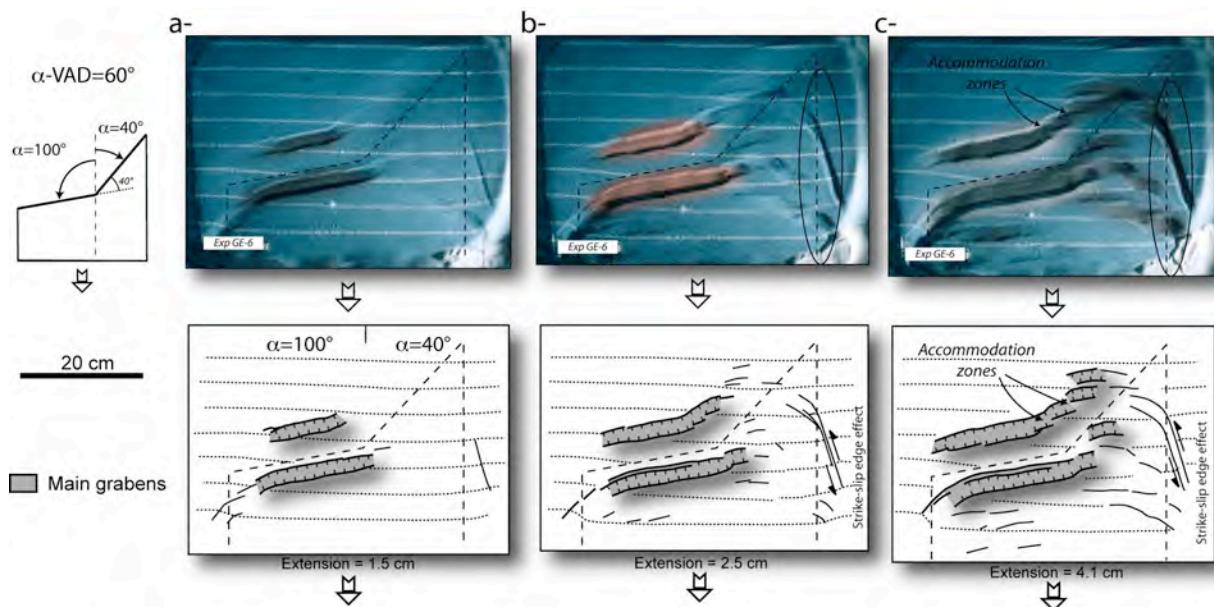
Figure 28: Evolution de la déformation dans le modèle avec α-VAD=60°. Un graben linéaire se développe au niveau du segment suborthogonal à l'extension alors que des grabens en échelon se forment le long du segment de VD très oblique à la direction d'extension.

Dans chaque expérience, les premiers incréments d'extension entrainent la formation de deux grabens parallèles. Ceux-ci apparaissent le long du segment de VD le moins oblique dans les expériences à α-VAD≥60° (Figure 28a) et à l'intersection entre les VD dans les modèles à α-VAD≤40°. Ces deux grabens correspondent au couple de grabens

symétrique/asymétrique des expériences à forte vitesse d'extension décrites dans la section précédente (Figure 29a). L'amincissement de la silicone est concentré entre ces deux structures (Figure 29b). Un système de grabens en échelon apparaît ensuite de part et d'autre des segments de VD dont l'obliquité par rapport à la direction d'extension est ≥ 20° (Figure 28b et c). Entre chaque graben se développe une zone d'accommodation caractérisée par des rampes relais et l'absence de faille décrochante.
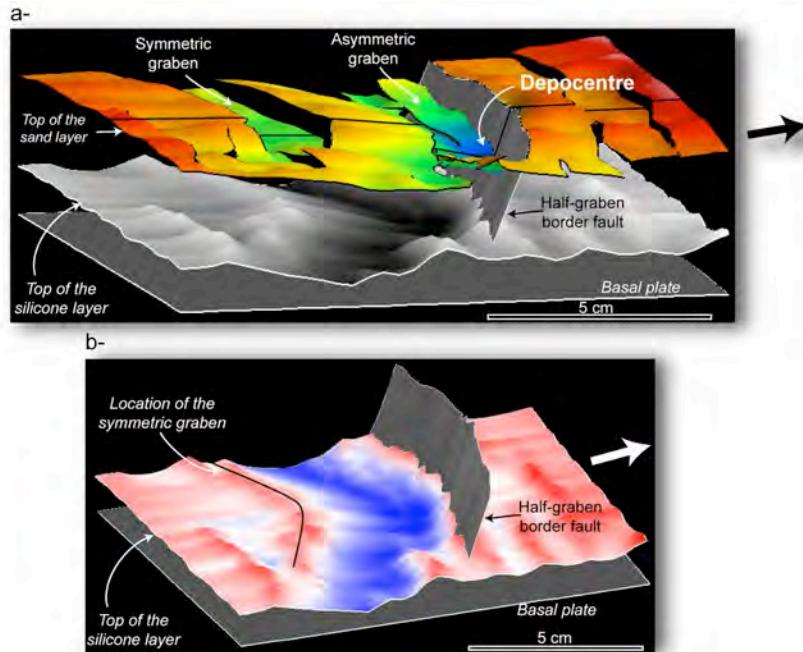
Figure 29: Reconstruction 3D de l'expérience α-VAD=0. a- Géométrie 3D révélant la localisation des dépocentres. Echelle de couleur pour le toit de la couche de sable: du bleu au rouge pour une subsidence croissante. La ligne noire représente la localisation de l'intersection entre les deux orientations des discontinuités de vitesse. b- Amincissement de la couche de silicone. Rouge, blanc et bleu correspondent à des quantités d'amincissement faibles, moyennes et fortes. Le plan gris représente le plan de faille majeur du graben asymétrique.

La subsidence du graben asymétrique, seul graben a se former quelle que soit la vitesse d'extension, a été quantifiée à partir de coupes sériées effectuées dans chaque modèle. Lorsque α-VAD>40°, la subsidence est globalement homogène le long de chaque segment de VD et maximum dans le graben formé par la VD la moins oblique (Figures 30a). En revanche, dans les expériences caractérisées par une α-VAD≤40°, un dépocentre se développe à l'aplomb de l'intersection entre les deux VD (Figure 29a). Sa géométrie devient de plus en plus symétrique pour des valeurs α-VAD décroissantes (Figure 30). L'amincissement de la couche ductile présente une évolution similaire à celle de la subsidence. Il est homogène le long de chaque segment de VD si α-VAD=60° et devient maximum au niveau de l'intersection entre les VD pour des valeurs α-VAD inférieures.

Le rôle de la direction d'extension dans la formation des grabens a fait l'objet de nombreuses études (Tron et Brun, 1991; McClay et White, 1995; Clifton et al., 2000; McClay et al., 2002). L'approche menée ici se distingue de ces travaux par l'utilisation simultanée de deux VD obliques qui simule la réactivation de deux fabriques lithosphériques obliques. Nos résultats expérimentaux suggèrent que l'activation conjointe d'accidents lithosphériques joue un rôle majeur dans le développement des grabens et des dépocentres. L'intersection entre ces failles localise la déformation initiale et consécutivement la formation de dépocentres. Nos modèles révèlent également que la géométrie des dépocentres varie en fonction de la direction d'extension. Appliqué à la nature, ce résultat nous a permis d'interpréter la subsidence continue au niveau du dépocentre principal du graben du Rhin comme la conséquence d'une direction d'extension WNW-ESE à NW-SE, constante entre l'Eocène supérieur et la fin de l'Oligocène (Figure 31). Nous avons également comparé la déformation du modèle α-VAD=40° avec la géométrie des grabens de la partie sud du rift Est Africain, i.e. rifts Tanganyika et Malawi. Le

début de la subsidence dans la partie centrale du rift Tanganyika, à l'intersection entre deux fabriques précambriennes, et le développement du rift Malawi sont interprétés comme le résultat d'une extension E-W entrainant la réactivation de deux fabriques lithosphériques obliques (Michon et Sokoutis, 2005).
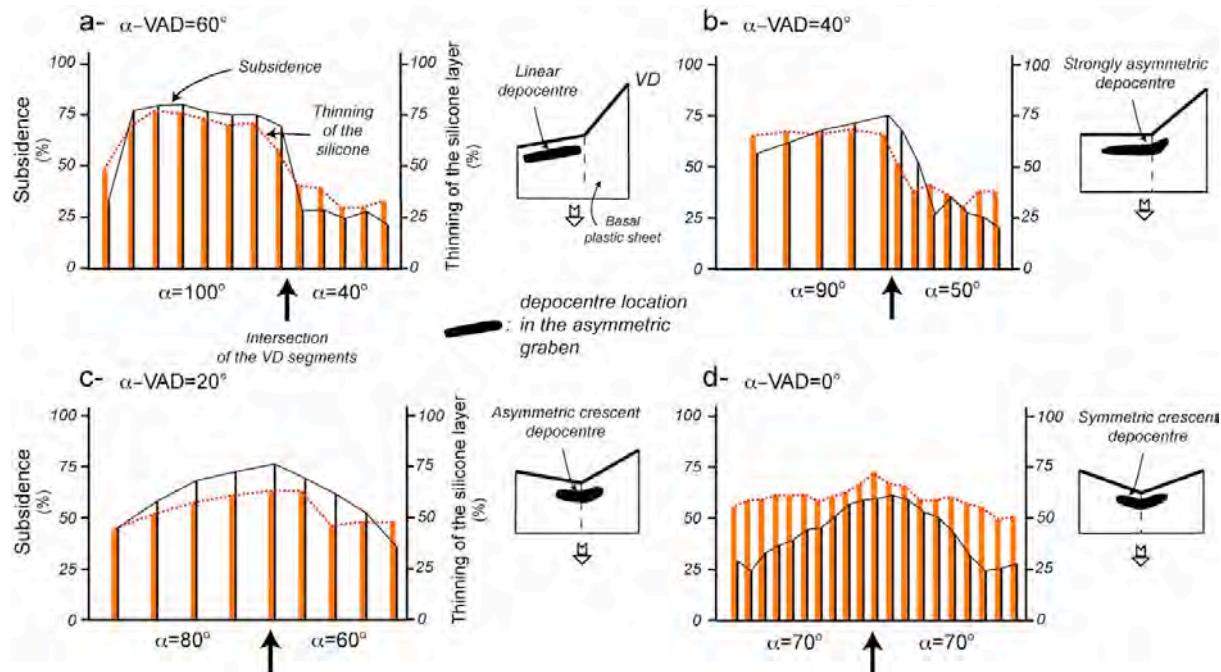
Figure 30: Subsidence (lignes fines et noires) et amincissement de la couche de silicone (lignes épaisses et rouges) mesurés en pourcentage de l'épaisseur initiale, i.e., 1 cm et 2 cm pour les couches de silicone et de sable respectivement. a- Modèle avec α= 40° et 100°. b- Modèle avec α= 50° et 90°. c- Modèle avec α= 60° et 80°. d- Modèle avec α= 70°. Pour chaque expérience, un schéma illustre la localisation et la forme du dépocentre par rapport à la feuille plastique basale..
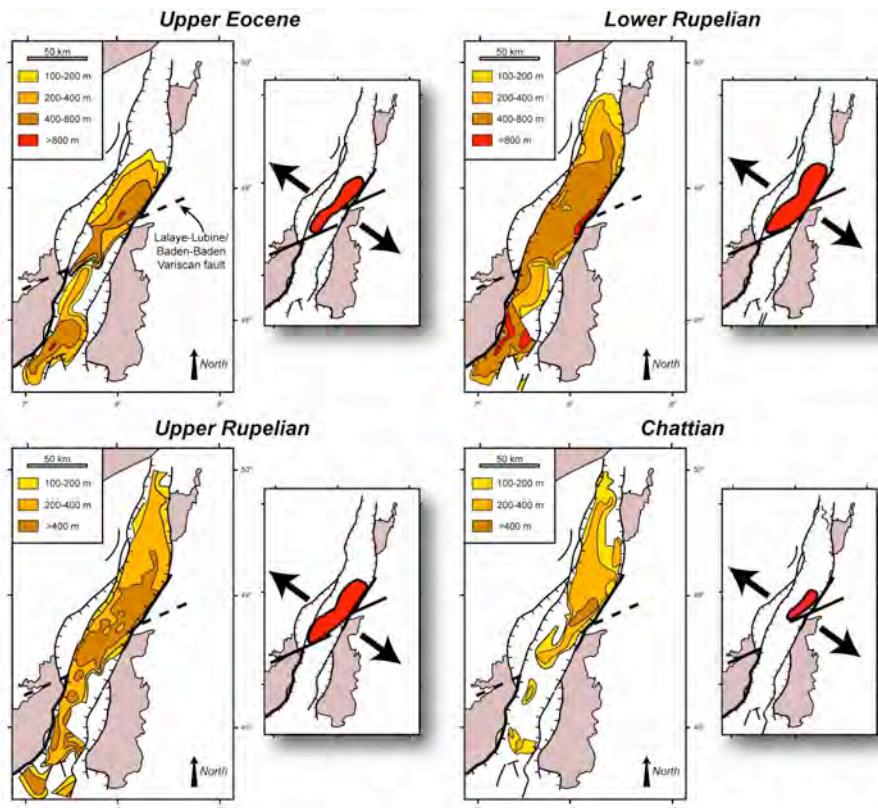
Figure 31: Cartes isopaques des sédiments d'âge Eocène supérieur, Rupélien inférieur, Rupélien supérieur et Chattien au niveau du graben du Rhin (d'après Schumacher, 2002) Pour chaque période, les dépocentres et les directions d'extension déduites de nos modèles sont représentés.

2.2- Dynamique et évolution des volcans boucliers basaltiques: exemple du Piton de la Fournaise et du Piton des Neiges

J'ai commencé à étudier les édifices volcaniques en Septembre 2003, lors de mon recrutement en tant que Maître de Conférences au sein du laboratoire GéoSciences Réunion de l'Université de la Réunion. Pour aborder au mieux ce virage thématique, j'ai souhaité appliquer l'approche multi-disciplinaire / multi-échelle que j'avais développée pour l'étude des rifts. Mon travail s'est focalisé, durant ces premières années, sur certains aspects des volcans réunionnais et de leur évolution. Les résultats les plus significatifs, résumés dans les sections suivantes, ont fait l'objet de 5 publications (Michon et al., 2007a, 2007b, 2009a, 2009b; Michon et Saint-Ange, 2008; Annexes 9 à 13).
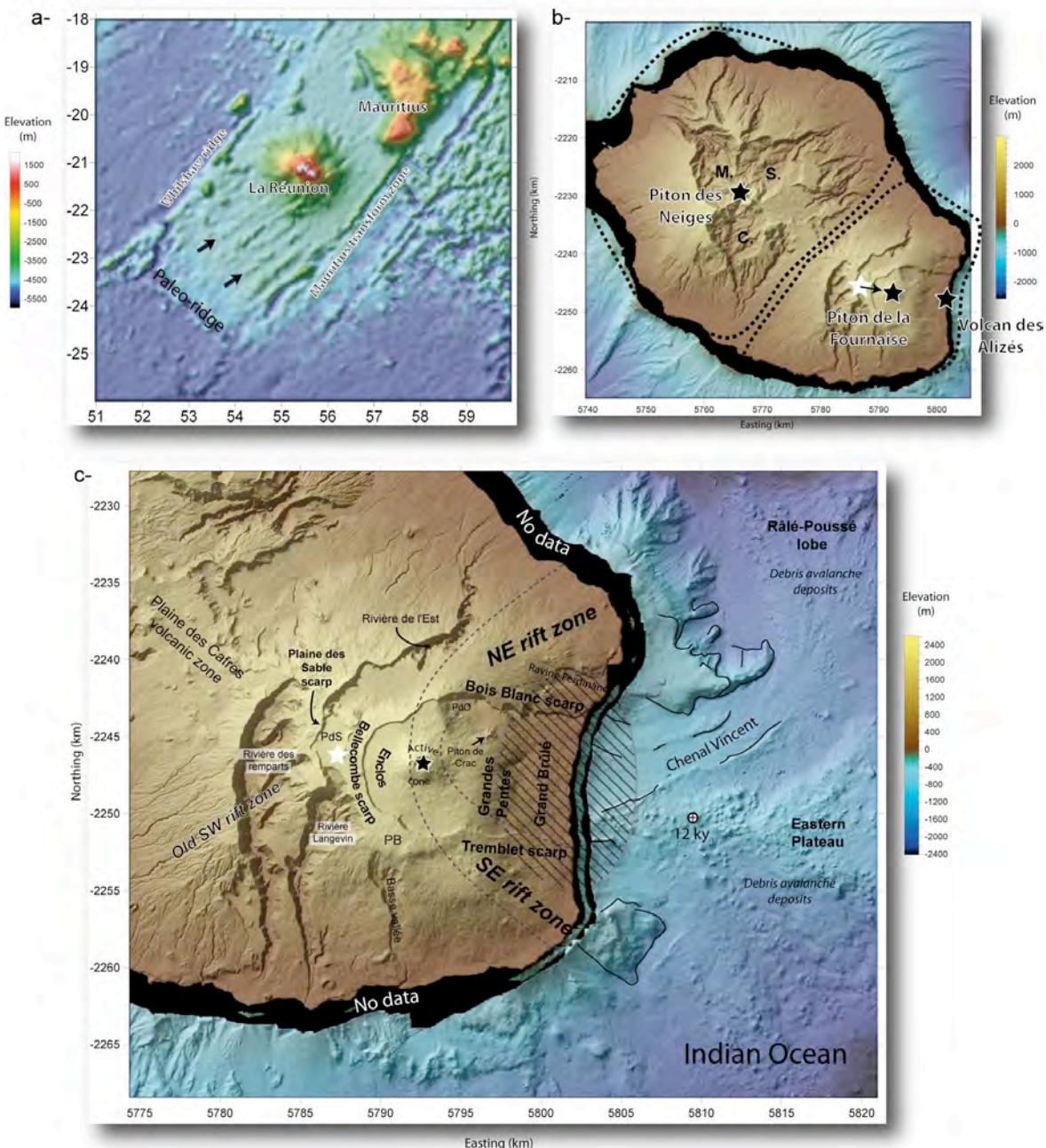
Figure 32: a- Carte de la bathymétrie prédite d'après Smith et Sandwell (1997). Coordonnées en degrés. b- Localisation des massifs volcaniques du Piton des Neiges et du Piton de la Fournaise, et du centre magmatique du volcan des Alizés. C., M. et S. pour les cirques de Cilaos, Mafate et Salazie. L'étoile blanche indique la position du centre magmatique du Piton de la Fournaise avant sa migration à l'est vers 60 ka. Coordonnées dans le référentiel Mercator. c- Parties sous-marines et aériennes du Piton de la Fournaise. La bathymétrie a été acquise lors de la campagne océanographique ERODER. LPB: Planèze du Baril; PdO: Plaine des Osmondes; PdS: Plaine des Sables. La localisation de l'anomalie gravimétrique liée au corps intrusif du volcan des Alizés est indiquée par la zone hachurée.

L'île de La Réunion est la partie émergée d'un volcan bouclier basaltique de 7 km de haut et 220-240 km de diamètre situé sur la bordure sud-est du bassin des Mascareignes. Le magmatisme réunionnais est la manifestation actuelle du point chaud qui a généré les Trapps du Deccan à la transition Crétacé-Tertiaire (Courtillot et al., 1986) et un chapelet d'îles orienté N-S dans l'Océan Indien (O'Neill et al., 2003). L'édifice s'est construit sur un bloc de lithosphère océanique limité à l'est et à l'ouest par des failles transformantes orientées N30-40 et par une paléo-dorsale orientée N120 au sud (Figure 32a). Le plancher océanique au sud de l'île est également marqué par plusieurs rides volcaniques parallèles orientées N55-N65.

En considérant les taux de production magmatique actuels et les âges les plus anciens de la partie émergée (2,08 Ma; McDougall, 1971), le début du magmatisme réunionnais a été estimé entre 5 et 8 Ma (Gillot et al., 1994; Bonneville, 1990). L'évolution initiale était concentrée au niveau de deux édifices adjacents (le Piton des Neiges et le volcan des Alizés; Figure 32b; Lénat et al., 2001a). Leur édification s'est accompagnée de déstabilisations de flancs récurrentes qui ont contribué au démantèlement total et à l'extinction du volcan des Alizés (Lénat et al., 2001a; Bachèlery et al., 2003; Oehler et al., 2004, 2008). Vers 0,53 Ma, le Piton de la Fournaise apparu entre les Piton des Neiges et la position ancienne du volcan des Alizés (Figure 32b). L'édification de ce nouveau volcan, centrée initialement au niveau de l'actuelle Plaine des Sables, a été contemporaine de l'activité tardive du Piton des Neiges. Vers 60 ka, le centre éruptif du Piton de la Fournaise a migré vers l'est, i.e. vers sa position actuelle. Il est fort probable que ce déplacement du centre du volcan résulte de bouleversements volcano-tectoniques majeurs de type glissement de flanc. Depuis 12 ka, date de la dernière éruption du Piton des Neiges (Deniel et al., 1992), seul le Piton de la Fournaise est actif. Cette activité est concentrée dans la caldera de l'Enclos Fouqué ou Enclos, effondrée vers 4,5 ka BP (Bachèlery, 1981; Abchir et al., 1998), au sein de laquelle elle a entrainé la construction d'un cône de 400 m de haut (Figures 32c, 33a).

2.2.1- Croissance, déformation co-éruptive et développement des rift zones

Le premier volet de ma recherche sur les édifices volcaniques a porté sur (i) l'origine de la géométrie fortement pentée du cône actif du Piton de la Fournaise, atypique pour un édifice basaltique effusif, (ii) sa déformation co-éruptive, i.e. lors des intrusions magmatiques associées aux éruptions et (iii) le développement de rift zones de géométrie différente. Cette étude a bénéficié de collaborations avec des membres du laboratoire GéoSciences Réunion (Nicolas Villeneuve, Ludovic Letourneur), du Laboratoire Magmas et Volcans (Valérie Cayol) et de l'Observatoire Volcanologique du Piton de la Fournaise (Aline Peltier, Thomas Staudacher).

La croissance d'un édifice volcanique résulte de processus endogènes, liés à l'intrusion répétée de filons magmatiques, et/ou exogènes, par accumulation de produits volcaniques en surface (e.g. Annen et al., 2001). Les modèles numériques d'Annen et al. (2001) suggèrent que la géométrie pentée du cône sommital du Piton de la Fournaise ne peut résulter de l'accumulation de coulées de lave. En revanche, elle serait issue d'une forte croissance endogène liée à l'intrusion de 10000 dykes épais depuis 4,5 ka et dont seulement 7% aurait induit une éruption. Bien que la géométrie simulée montre de réelles ressemblances à celle du cône sommital, les paramètres d'entrée des modèles sont très différents des données naturelles. Les dykes simulés mesurent 3 m d'épaisseur en moyenne, alors que l'épaisseur des filons du Piton de la Fournaise varie entre 0,3 et 1 m (Fukushima et al., 2005; Peltier et al., 2007). De même, un faible pourcentage d'intrusions mène à des éruptions dans les modèles alors que la période actuelle, i.e. depuis 1972, montre que 92% des intrusions engendrent une éruption.

Nous avons donc mené une étude couplant un travail de terrain, une analyse morpho-structurale, des données GPS et de la modélisation numérique, pour caractériser au mieux la morphologie du cône, sa nature, sa déformation et sa dynamique de croissance.

Le cône actif du Piton de la Fournaise est une structure sub-circulaire d'environ 3,2 km de diamètre. Ses flancs montrent des valeurs de pente différentes entre les parties est et ouest. La moitié occidentale est caractérisée par des flancs pentés de 15-20°, alors que les valeurs de pente de la moitié orientale varient entre 25 et 35° (Figure 33b). Ces fortes pentes s'organisent en deux zones linéaires orientées N55 au sud-est et N150 au nord-est (Figure 33c). Il est intéressant de noter que la zone de pente orientée N55 est alignée avec de nombreux linéaments parallèles qui ne correspondent pas à des limites géologiques (Figure 33d). Au sommet, le cône est découpé par deux structures d'effondrement historiquement appelées *cratères*, alignées selon un axe E-W (Figure 33a). A l'ouest, le *cratère* Bory est une structure de 100-200 m de diamètre dont l'activité a cessé après la mise en place du champ de lave de l'Enclos au XVIIIème siècle (Lénat et al., 2001b). A l'est, le *cratère* Dolomieu est actuellement une caldera de plus de 300 m de profondeur formée lors de l'éruption d'avril 2007 et au sein de laquelle se concentre activités fumerolienne et magmatique. La zone sommitale du cône présente enfin deux parties relativement planes qui correspondent à d'anciennes structures d'effondrement de type pit crater entièrement comblées et recouvertes par de fines coulées de lave (Figure 33c).
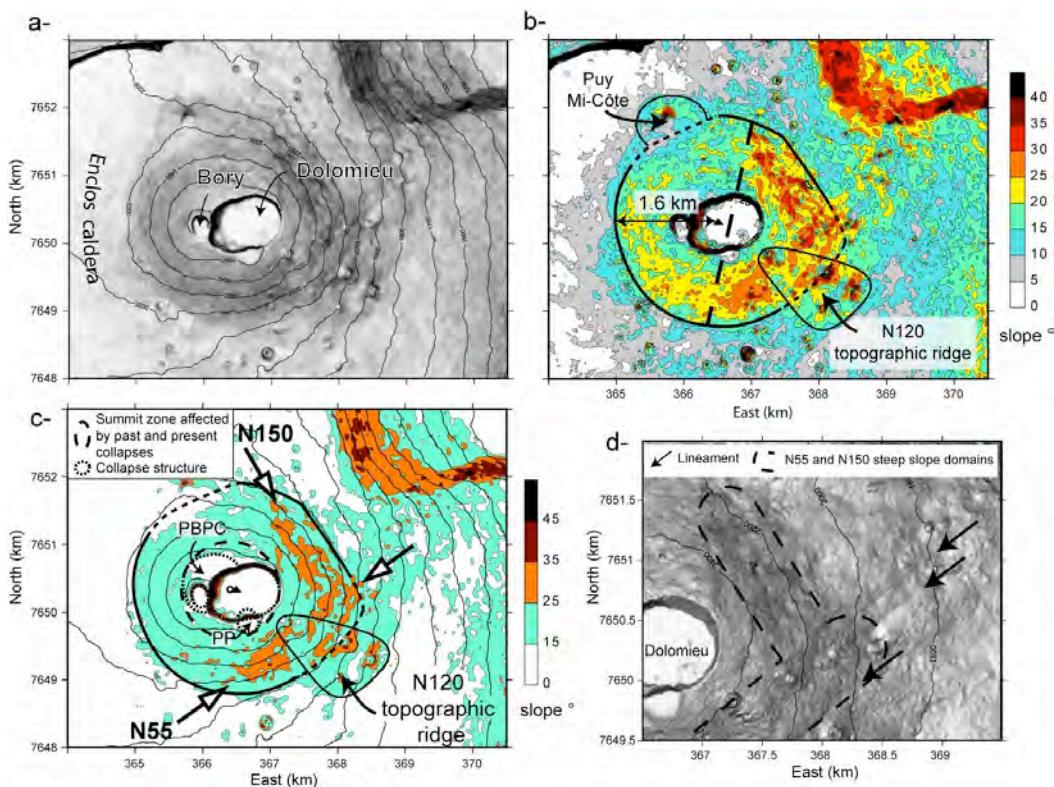
Figure 33: a- Modèle Numérique d'Elevation (MNE) du cône actif du Piton de la Fournaise (résolution du MNE: 25m). b- Carte de pente montrant la géométrie des flancs des parties est et ouest. La ride topographique N120 sur le flanc SE est formée par une succession de cônes volcaniques adventifs. c- Carte de pente calculée à partir du MNE auquel un filtre passe-bas a été appliqué. Les fortes pentes de la partie orientale s'organisent en deux segments orientés N55 et N150. PP: Pit crater de Petit Plateau; PBPC: Pit crater pré-Bory. d- Représentation en relief ombré d'un MNE de haute précision (résolution de 7 m) calculé par stéréophotogrammétrie à partir de photos aériennes acquises en 1989. Coordonnées UTM WGS84 (zone 40S).

Les parois de la caldera formée en avril 2007 montrent que la structure interne du cône sommital est composée de trois types d'unités géologiques. Au nord-ouest et au sud, les parois sont entièrement ou en partie constituées d'une superposition de laves massives, épaisses et horizontales. Ces successions laviques étant spatialement corrélées aux limites des zones morphologiquement planes (Figure 33c), elles sont interprétées comme le remplissage des pit craters. Ces structures mises à part, le cône présente une structuration homogène avec un cœur, formé de scories rouges, recouvert par une pile de fines coulées de laves.

L'analyse des fractures tectoniques de la surface du cône et de la partie adjacente de l'Enclos révèle une corrélation spatiale entre la fracturation, d'une part, et les zones à forte pente et la zone des linéaments N55, d'autre part (Figure 34 a). Ces fractures s'organisent en trois directions principales N20-30, N55-65 et N150-160 (Figure 34b). Contrairement au faisceau N20-30, les fractures N55-65 et N150-160 dessinent des bandes de déformation situées respectivement au niveau des linéaments N55 et à l'est immédiat du Dolomieu (Figure 34c).
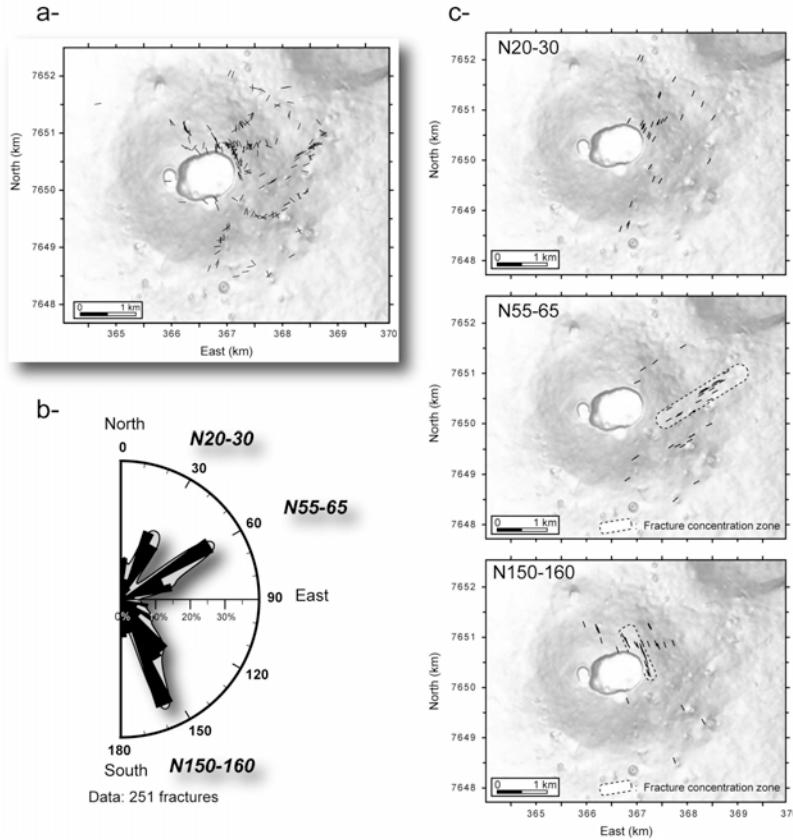
Figure 34: a- Distribution spatiale des fractures tectoniques au niveau du cône et de la zone adjacente de l'Enclos. b- Diagramme en rose représentant l'orientation des fractures. c- Répartition des principaux faisceaux de fractures.

L'étude de la déformation co-éruptive nécessite au préalable de définir les zones d'intrusion préférentielles des filons magmatiques, i.e. les rift zones. Trois types d'éruptions sont reconnus (Peltier et al., 2008): 1- les éruptions sommitales localisées dans le cratère Dolomieu; 2- les éruptions proximales débutant au sommet ou sur les flancs du cône, et se propageant ensuite latéralement; 3- les éruptions distales se développant sur le plancher de l'Enclos. Parmi ces trois types, seules les intrusions associées aux éruptions sommitales et proximales s'injectent dans le cône central.

Il était classiquement admis que ces intrusions magmatiques se propageaient le long de deux rift zones orientées N10 et N170, au nord et au sud du cône respectivement (e.g. Bachèlery, 1981). Les deux orientations avaient été déduites de l'analyse de la direction des fissures éruptives visibles sur le cône et la partie adjacente de l'Enclos en 1981. Nous avons déterminé des orientations identiques à partir de l'analyse de photos aériennes acquises en 2003 (Figure 35; Michon et al., 2009a). Cependant, nous considérons que la distribution des fissures éruptives ne reflète pas l'orientation des zones d'intrusion préférentielles du magma. De fait, l'analyse détaillée des fissures éruptives formées lors d'éruptions entre 1998 et 2004 montre clairement que l'orientation des fissures éruptives évolue pour une même intrusion (Figure 36). Partant du constat que les fissures associées à une même intrusion se développent parallèlement à la ligne de plus grande pente, nous avons proposé que l'orientation des fissures était contrôlée par le champ de contrainte existant en sub-surface. Dans un cône, ce dernier est caractérisé par une contrainte principale maximum σ_1 radiale, parallèle à la ligne de plus grande pente, et par une contrainte principale minimum σ_3 concentrique. L'analyse des éruptions proximales pour la période

1981-2008 montre alors une répartition des intrusions magmatiques organisée en deux rift zones orientées N25-30 et N120 (Figure 37). Contrairement à la rift zone N25-30 qui s'étend de part et d'autre du cône actif, la rift zone N120 est limitée à la partie est du cône uniquement.
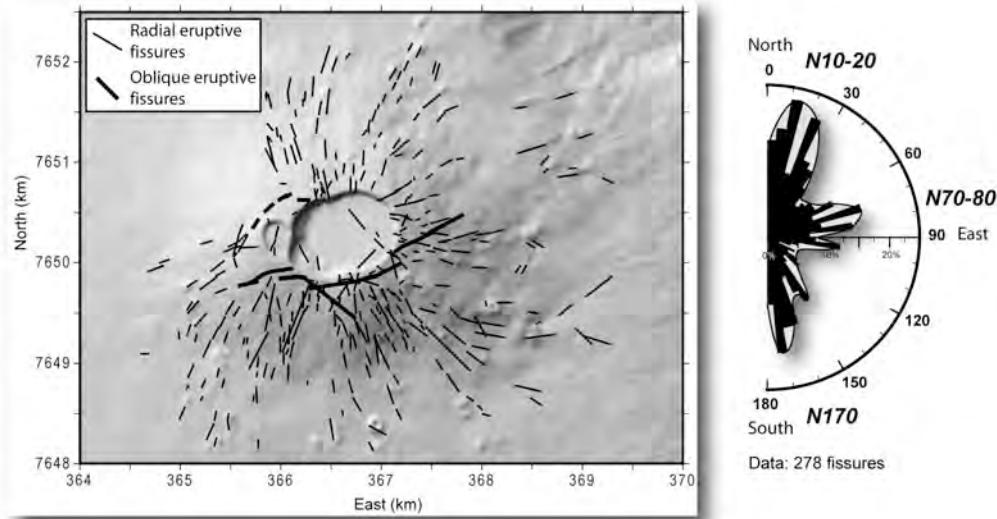
Figure 35: Cartographie et orientation des fissures éruptives sur le cône sommital et sur le plancher de l'Enclos. Les faisceaux N10-20 et N170 représentent la direction supposée des rift zones. L'orientation N70-80 résulte de l'abondance de fissures éruptives parallèlement aux limites du cratère Dolomieu.
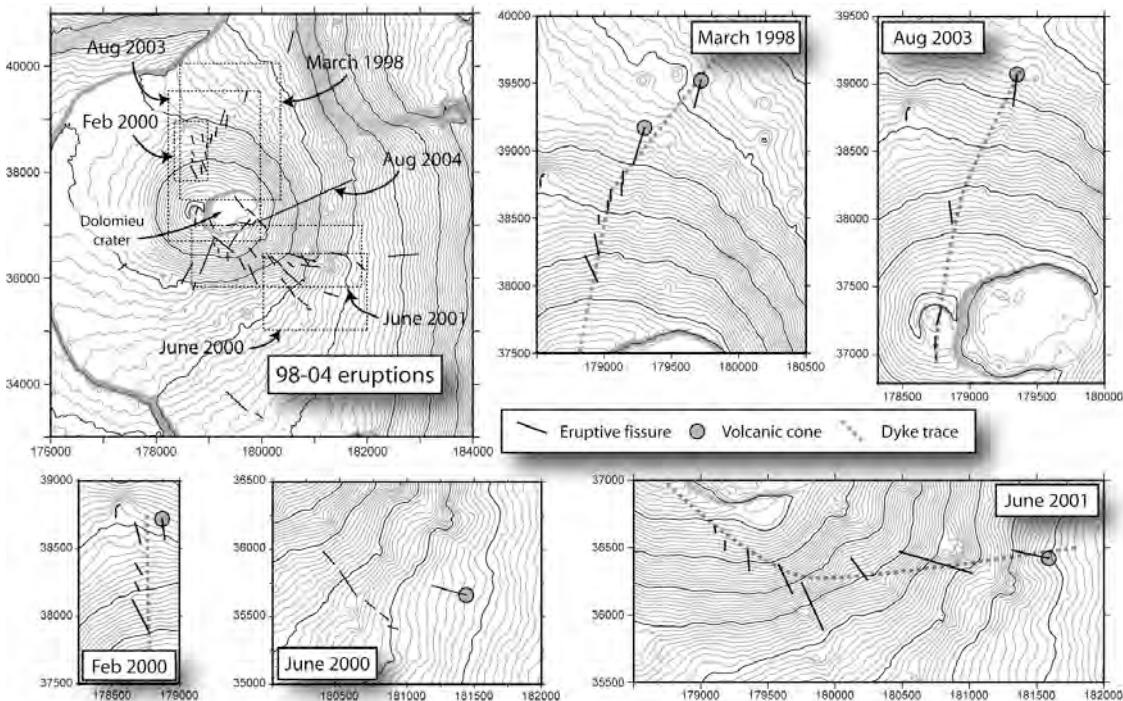
Figure 36: Distribution des fissures éruptives et des injections magmatiques pour les éruptions de 1998 à 2004. La trace des dyke pour les éruptions de Mars 1998 et Août 2003 correspond à celle modélisée à partir des données de déformation par Battaglia et Bachèlery (2003) et Froger et al. (2004), respectivement. Les autres traces sont déduites à partir de la distribution des fissures éruptives.

Nous avons utilisé la méthode 3D des éléments frontières (Cayol et Cornet, 1997) pour modéliser (1) l'impact des injections magmatiques le long des rift zones N25-30 et N120 sur la géométrie du cône, (2) l'interaction entre l'injection des dykes et la fracturation et (3) les changements de contraintes associés aux intrusions le long des segments nord et sud de la rift zone N25-30. La procédure utilisée est détaillée dans l'annexe 9 (Michon et al., 2009a).
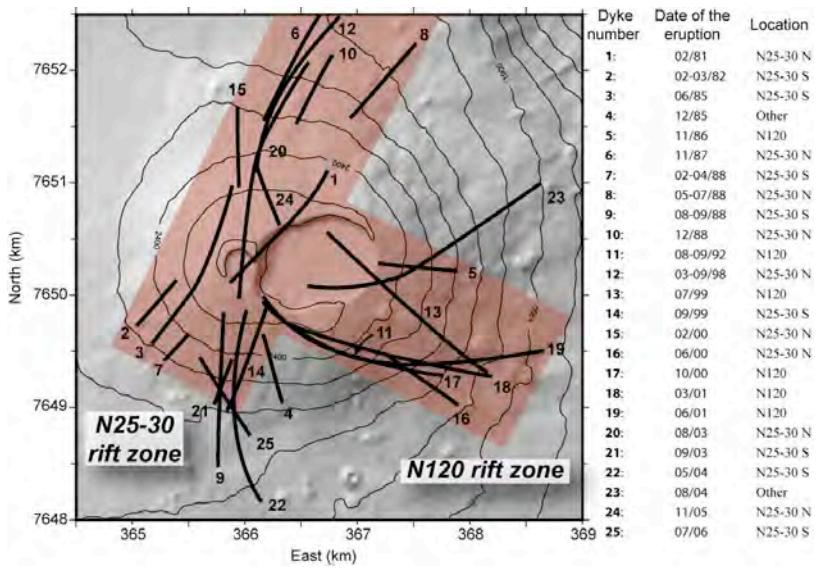
Figure 37: Distribution des intrusions magmatiques associées aux éruptions initiées au sommet ou sur les flancs du cône central du Piton de la Fournaise.
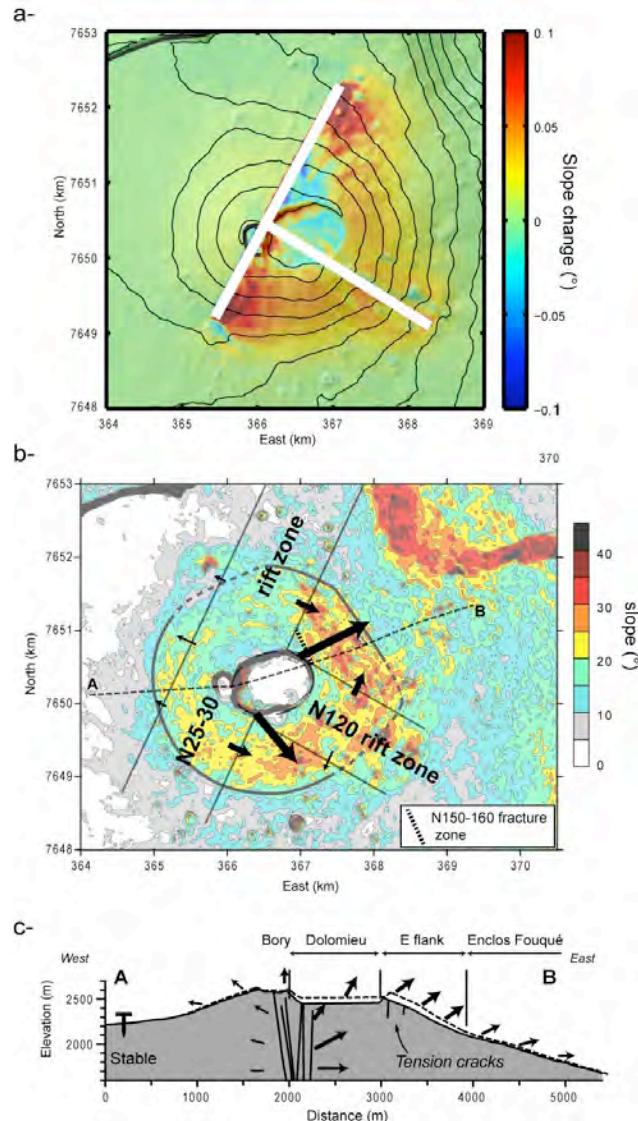
Figure 38: a- Changements de pente associés à l'injection répétée de filons magmatiques le long des rift zones N25-30 et N120. b- Carte de pente du cône central suggérant une origine intrusive aux pentes fortes situées sur les flancs est et sud-est du cône. c- Coupe synthétique illustrant la croissance endogène du cône lors des injections magmatiques le long des rift zones N25-30 et N120.

La modélisation révèle que l'intrusion répétée de dykes le long des rift zones décrites ci-dessus entraine une croissance asymétrique du cône. La pente des flancs est et sud-est augmente, alors qu'elle reste presque inchangée à l'ouest de la rift zone N25-30 (Figure 38a). Seule la zone sommitale située entre le segment nord de la rift zone N25-30 et la rift zone N120 montre un décroissance de la pente. Il est frappant de constater que la limite entre décroissance de pente au sommet et augmentation de pente sur le flanc est est spatialement corrélée à la zone de fracture N150 (Figure 38b). Nous interprétons donc l'apparition de ces fractures comme le résultat d'une croissance hétérogène entre le flanc est et le sommet (Figure 38c).
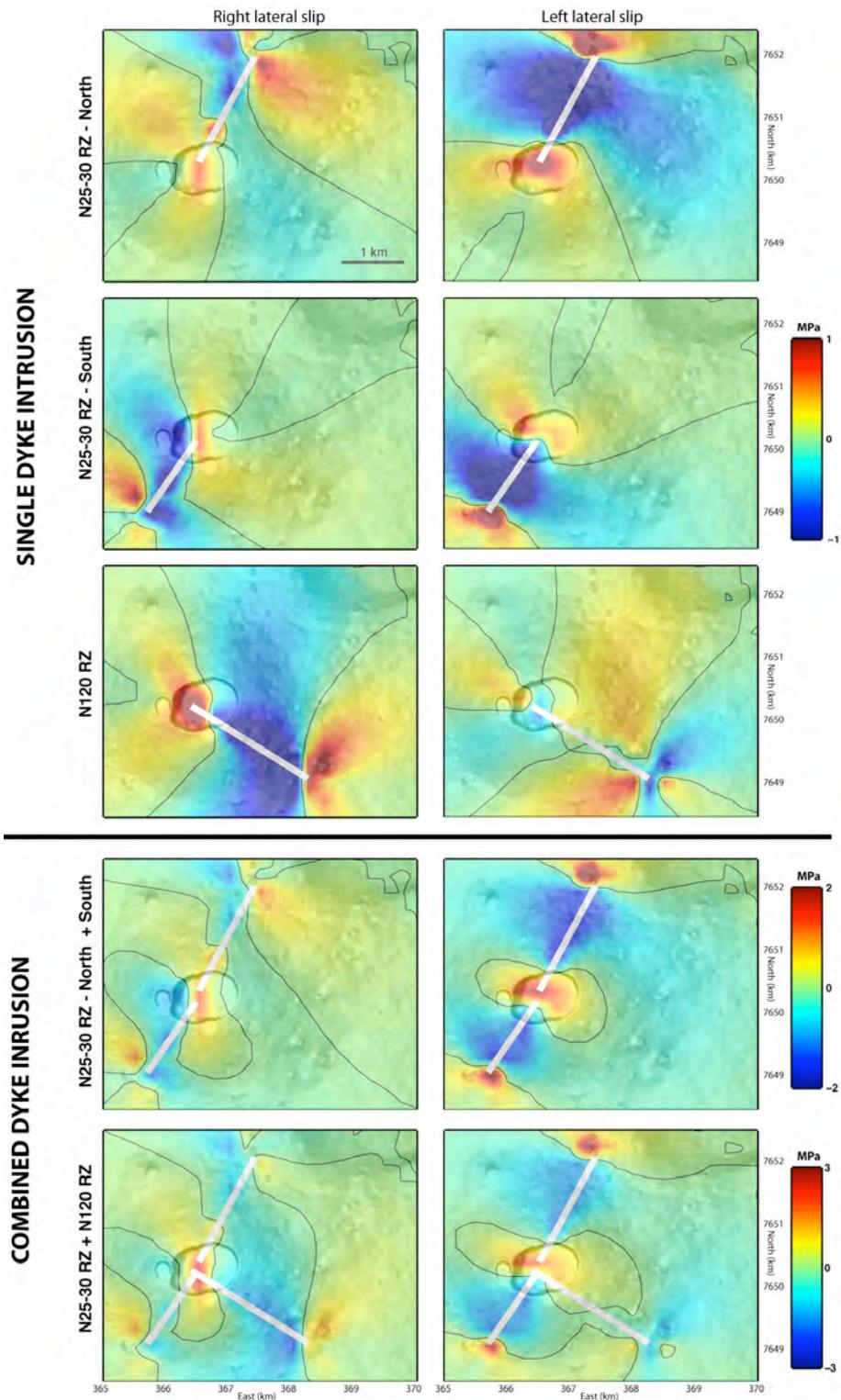
Figure 39: Changements des critères de Coulomb à 1500 m d'altitude lors d'intrusions magmatiques (traits blancs) le long des rift zones sur des fractures orientées N55.

Nous avons également étudié l'interaction entre les injections magmatiques répétées et la fracturation N55 par une analyse des changements des contraintes de Coulomb (ΔS). Ces derniers sont défini par $\Delta S = \Delta\tau - \mu'\Delta\sigma$ (King et al., 1994), où $\Delta\tau$ et $\Delta\sigma$ sont les variations des contraintes cisaillante et normale sur un plan de rupture donné, et μ', est le coefficient de friction apparent incluant l'effet des changements de pression de pores (ici $\mu'=0.4$). La rupture le long des plans est favorisée ou inhibée pour des valeurs de ΔS positives et négatives, respectivement. Les modèles montrent que l'injection de dykes le long des différents segments de la rift zone N25-30 et le long de la rift zone N120 favorisent la rupture le long des plans N55-65 situés à 1 km à l'est du Dolomieu (Figure 39). Si la distribution spatiale des valeurs positives des critères de Coulomb plaide en faveur d'une réactivation fréquente de la zone de fracture N55-65 lors des intrusions magmatiques, l'amplitude des variations semble trop faible pour avoir créer ce réseau de fractures. Nous avons donc proposé que les fractures préexistaient à l'aplomb du système magmatique actuel et qu'elles ont été réactivées par le développement des rift zones N25-30 et N120 (Michon et al., 2009a; annexe 9).

Finalement, nous avons modélisé la variation des contraintes principales induites par l'injection répétée de dykes le long des segments nord et sud de la rift zone N25-30. La propagation des dykes est contrôlée par la distribution du champ de contraintes total σ^t, correspondant à $\sigma^t = \Delta\sigma + \sigma^r$, où $\Delta\sigma$ est le changement de la contrainte dû à l'intrusion et σ^r est la contrainte régionale pré-existante. La valeur exacte de la contrainte régionale ne pouvant être déterminée, nous avons modélisé uniquement les variations de contraintes liées aux injections. La figure 40a révèle que les variations de la contrainte principale minimum, $\Delta\sigma_3$, présentent un orientation sub-verticale et parallèle à la rift zone, alors que les variations de la contrainte principale intermédiaire, $\Delta\sigma_2$, sont sub-horizontales et parallèles à la rift zone. Letourneur et al. (2008) ayant montré que la contrainte principale maximum régionale était verticale, la contrainte principale minimum totale σ^t_3 est en toute vraisemblance horizontale et parallèle à la rift zone N25-30. Ainsi, l'injection récurrente de dykes le long de la rift zone N25-30 encourage les intrusions de dykes N120 et le développement d'une petite rift zone (Figure 40b). L'absence d'injection à l'est de la rift zone N25-30 s'explique alors par le pendage vers l'est des intrusions le long de cette rift zone.
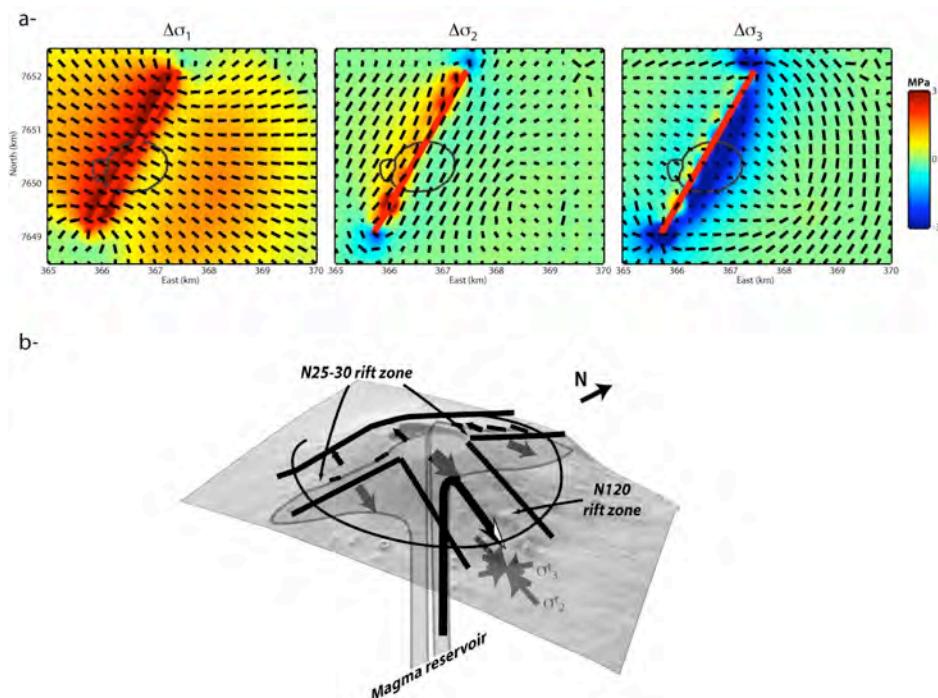
Figure 40: a- Variations de contraintes $\Delta\sigma$ liée aux injections magmatiques successives le long des segments nord et sud de la rift zone N25-30. $\Delta\sigma_1$, $\Delta\sigma_2$ et $\Delta\sigma_3$ correspondent aux contraintes principales maximum, intermédiaire et minimum, respectivement. b- Schéma interprétatif expliquant le développement de la petite rift zone N120 par accumulation de contraintes lors des intrusions le long de la rift zone N25-30.

2.2.2- Modalités de formation des calderas en contexte basaltique

La zone sommitale de l'immense majorité des volcans basaltiques est marquée par une ou plusieurs calderas. Contrairement aux calderas siliceuses dont le développement est clairement lié à la vidange d'une chambre magmatique sous-jacente, les calderas basaltiques semblent présenter trois modes de formation principaux. Elles seraient induites soit par la vidange d'une chambre magmatique (McDonald, 1965; Geshi et al., 2002), soit par la déformation lente du système hydrothermal (Cecchi et al., 2005; Merle et al., 2006), soit par subsidence du système intrusif dense (Walker, 1988). Les deux dernières interprétations se fondent principalement sur la différence, fréquente, entre le volume des calderas et celui des produits volcaniques associés à l'effondrement (e.g., Walker, 1988; Munro et Rowland, 1996).

J'ai entrepris une étude des calderas les mieux préservées du Piton de la Fournaise afin de déterminer leur origine et les différents processus mis en jeu. Ce travail a été mené en collaboration avec des membres du laboratoire GéoSciences Réunion (Francky Saint-Ange, Nicolas Villeneuve, Thibault Catry, Patrick Bachèlery), de l'Observatoire Volcanologique du Piton de la Fournaise (Valérie Ferrazzini, Thomas Staudacher), du Laboratoire Magmas et Volcans (Olivier Merle) et de l'Institut des Sciences de la Terre *"Jaume Almera"* (Joan Marti). Les résultats suggèrent l'existence de deux types d'effondrement: (1) des calderas indubitablement liées à la vidange d'un réservoir magmatique sous-jacent lors d'éruptions importantes et (2) des calderas potentiellement induites par la déformation lente de l'ensemble de l'édifice volcaniques.

2.2.2.1- Les calderas magmatiques

Durant les dernières décennies, trois volcans basaltiques ont subi un effondrement de leur zone sommitale. En 1968, 7 km^2 du plancher de la caldera pré-existante du volcan Fernandina (Galapagos) s'effondrent de près de 300 m après une éruption de très faible ampleur (Simkin et Howard, 1970). En 2000, une intrusion magmatique latérale de grand volume au sein de la croûte entraîne l'effondrement de la zone sommitale du volcan Miyakejima (Japon; Geshi et al., 2002). Enfin, en avril 2007, le sommet du Piton de la Fournaise s'effondre de plus de 300 m lors de l'éruption la plus importante de sa période historique (Michon et al., 2007a).

L'étude détaillée de l'éruption d'avril 2007 et de la caldera associée, puis la comparaison avec la sismicité et la déformation enregistrées lors des effondrements de Fernandina et de Miyakejima, nous a permis de déterminer (1) une dynamique d'effondrement commune aux calderas basaltiques, (2 les mécanismes régissant la dynamique d'effondrement et (3) le style d'effondrement, i.e. cohérent ou non-cohérent, de la colonne de roche au-dessus du réservoir magmatique.

J'ai décidé de ne pas rappeler dans ce mémoire le déroulement précis de l'éruption d'avril 2007, mais de me focaliser sur les événements importants, la géométrie de la caldera et la déformation mesurée par GPS différentiel. Le lecteur pourra se référer aux annexes 10 et 11 et aux différentes références citées dans ces articles pour avoir de plus amples détails quant à l'évolution récente du Piton de la Fournaise.

Avant l'éruption d'avril 2007, le *cratère* Dolomieu était rempli de coulées de lave accumulées lors des éruptions sommitales successives (Figure 41a). L'éruption d'avril 2007 débute le 2, soit 3 jours après une courte phase volcanique initiale. Le magma est émis de manière intense dans les parties basses du volcan où il nourrit de nombreuses coulées de laves. A partir du 5 avril 11:00 UTM, la zone sommitale montre une déflation exponentielle jusqu'à 20:48, heure du premier effondrement de la colonne de roche. Cet événement est contemporain d'un brusque mouvement centrifuge de la bordure du Dolomieu interprété comme la réponse élastique de l'édifice. La déformation de la zone sommitale est ensuite caractérisée par la succession de 38 cycles d'effondrement durant lesquels le sommet subi une déflation croissante jusqu'à l'effondrement de la caldera et au rebond élastique de l'édifice. Les premières observations de la caldera

effectuées l'après-midi du 6 avril, après 16 cycles d'effondrement, indiquent un effondrement du Dolomieu principalement concentré dans la partie nord et la présence de plateaux au sud et à l'est (Figure 41b). La caldera s'est ensuite élargie jusqu'au 10 avril pour atteindre les limites pré-existantes du Dolomieu par effondrement des plateaux (Figure 41c).
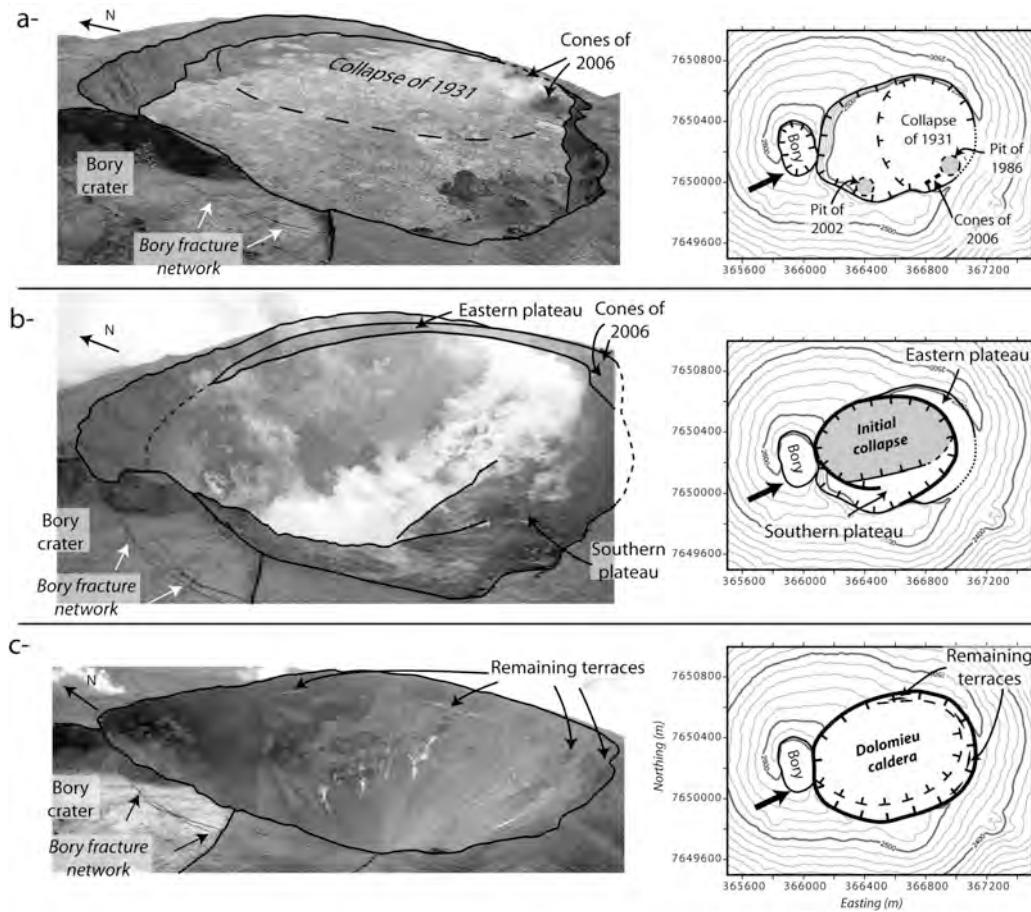
Figure 41: Le *cratère* Dolomieu le 31 octobre 2006 (a), l'après-midi du 6 avril 2007 (b) et le 10 avril 2007 (c).

La géométrie finale de la caldera suggère un effondrement vertical maximum d'environ 340 m situé dans sa moitié nord (Figure 42a). Au NW, la caldera est limitée par un mur sub-vertical au pied duquel des surfaces polies correspondant au plan de faille bordier étaient visibles jusqu'à leur destruction par des éboulements successifs (Figure 42b). Au sud et à l'est, les parois de la caldera sont en revanche plus faiblement pentées et formées par le sommet déformé des plateaux sud et est, basculés et glissés lors des effondrements tardifs (Figure 42a).

La bordure extérieure de la caldera a été affectée par une fracturation concentrique en tension dont la densité varie latéralement. Qu'elle qu'en soit la concentration, les fractures sont limitées à une zone de quelques dizaines de mètres de large en périphérie immédiate de la caldera. Les observations de terrain révèlent une densité importante des fractures néo-formées le long de la moitié sud et, dans une moindre mesure, le long des parois ouest et nord-ouest. L'effondrement caldérique a également réactivé des fractures concentriques pré-existantes. La mesure de l'ouverture de ces fractures en février et mai 2007, i.e. avant et après l'effondrement, le long de profils radiaux confirme l'étroitesse de la zone affectée par les contraintes extensives.

Grâce à l'installation en novembre 2005 d'un dense réseau de mesure GPS réparti autour des *cratères* Bory et Dolomieu, nous avons pu caractériser avec précision la déformation de la sommitale associée à l'effondrement. Ce réseau est constitué de 46 repères d'arpentage distribués en 24 radiales et de deux stations GPS références situées en dehors de l'influence du système magmatique (hors de la caldera de l'Enclos) et au sommet.
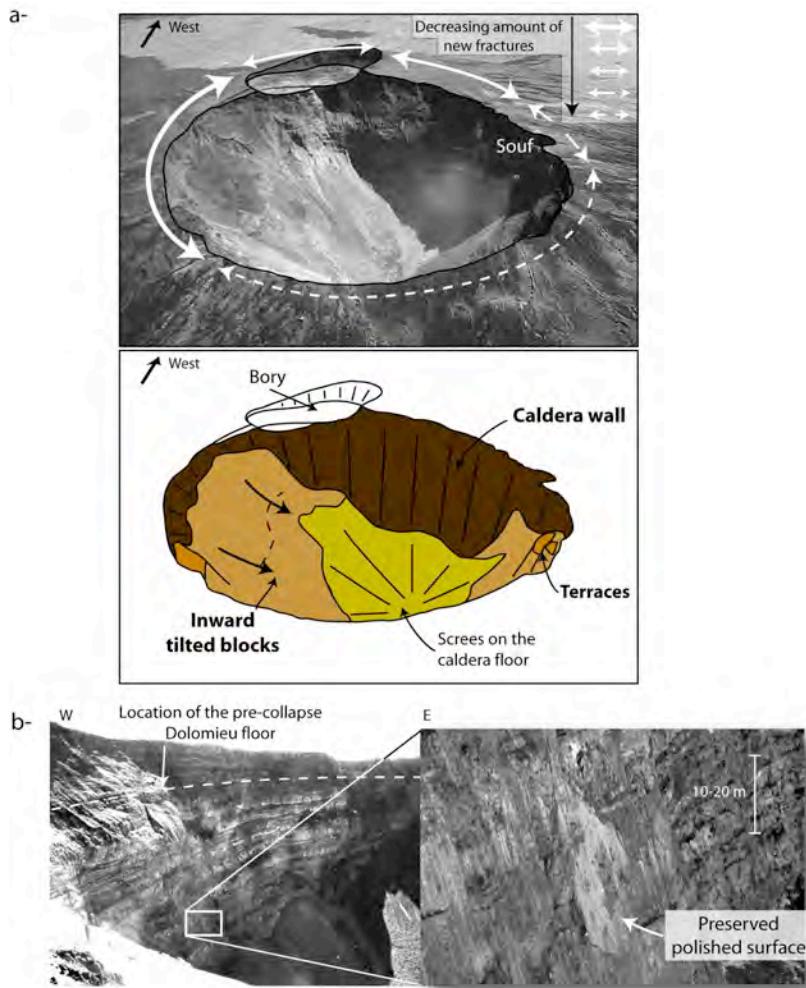
Figure 42: a- Géométrie de la caldera d'avril 2007. Notez la variation de géométrie des murs de la caldera. La densité des fractures concentriques néoformées lors de l'effondrement est représentée par des flèches. Souf: pit crater de Soufrière. b- Vue du mur NW de la caldera sur lequel des surfaces polies étaient visibles jusqu'à leur destruction totale en mai suite aux éboulements de la partie haute de la falaise.

Par chance, le réseau avait été mesuré en mars 2007, soit quelques jours avant le début de l'éruption ayant mené à la formation de la caldera. Deux nouvelles campagnes de mesure, réalisées en mai et novembre 2007, nous ont permis de déterminer le déplacement des repères causé par le développement de la caldera et postérieur à l'effondrement. Pour la période mars-mai 2007, les données GPS indiquent une grande disparité des déplacements de la zone sommitale aussi bien en magnitude (entre 10 et 253 cm) que spatialement (Figure 43a). Les valeurs de déplacement sont maximum le long de la bordure sud de la caldera et diminuent rapidement vers l'est et l'ouest. Le long de chaque radiale, les valeurs de déplacement décroissent rapidement, indiquant une déformation extensive radiale localisée au niveau de la bordure de la caldera. Cette déformation déduite des données GPS est en parfait accord avec l'apparition des fractures concentriques en périphérie immédiate de la bordure caldérique. Les vecteurs déplacement de la composante horizontale montrent tous une déformation centripète liée à une source de déflation probablement située à l'aplomb de la zone affectée par les effondrements initiaux du 5-6 avril (Figure 43b). Déterminer pour chaque repère le rapport entre les composantes horizontale et verticale du déplacement (H/V) permet de contraindre la géométrie de la source de déformation et sa profondeur (Dieterich et Decker, 1975). Les rapports H/V calculés pour les déplacements liés à l'effondrement d'avril 2007 sont tous supérieurs à 1 (Figure 43c). Ceci indique une déformation moyenne caractérisée par des déplacements horizontaux supérieurs aux déplacements verticaux, et par conséquent une contraction horizontale de la zone sommitale. Ce type de déformation peut s'expliquer par une source de déflation axisymétrique allongée verticalement (Dieterich et

Decker, 1975) ou par une source de déflation superficielle. Postérieurement à l'effondrement, la bordure de la caldera a continué un mouvement de déflation centripète d'ampleur limitée (47 cm maximum) interprété par Augier et al. (2008) comme la signature d'une décompression progressive du système hydrothermal.
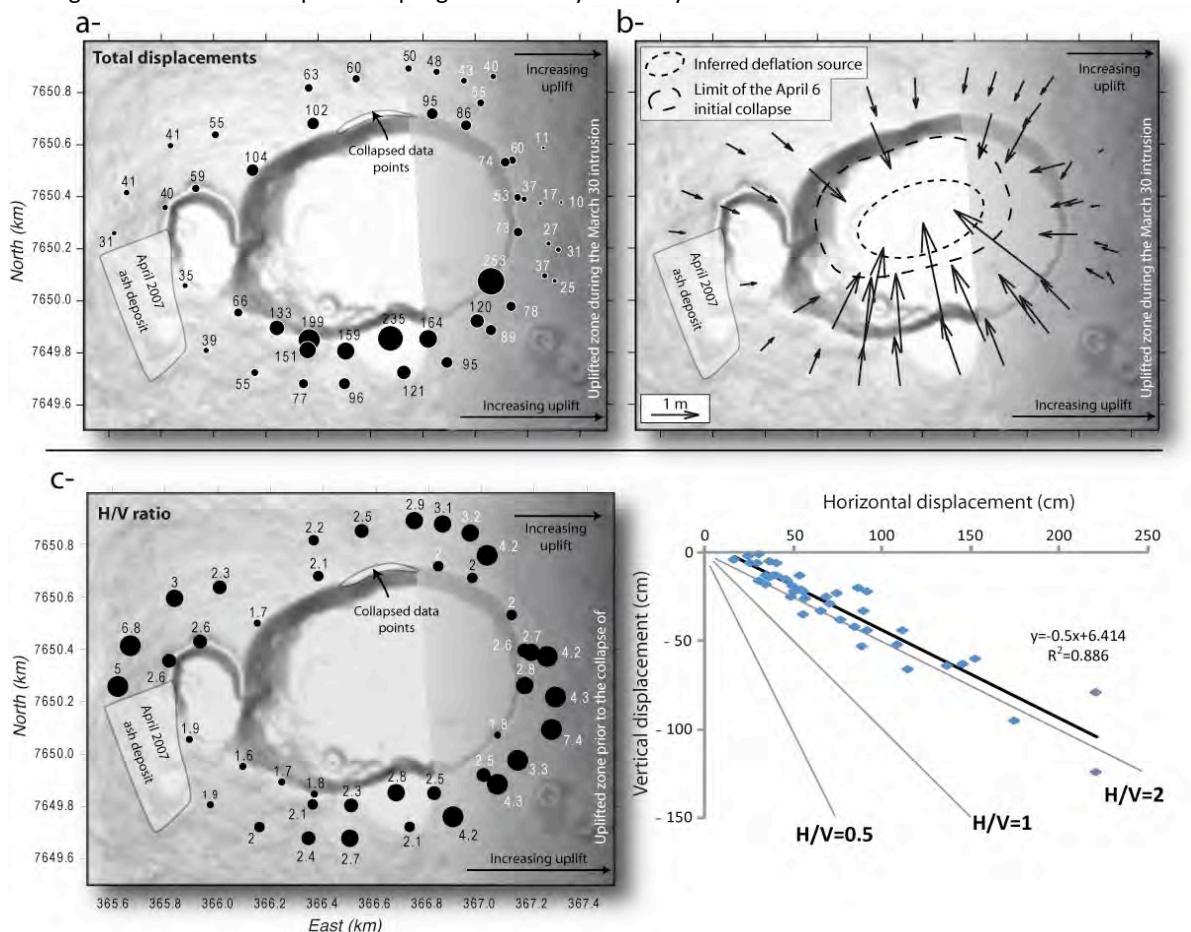
Figure 43: Déplacements (cm) de la bordure du Dolomieu liés à la formation de la caldera d'avril 2007 et mesurés par GPS différentiel. a- Déplacements totaux. b- Vecteurs du déplacement pour la composante horizontale. c- Rapport des déplacements horizontaux et verticaux pour chaque repère. La partie est, en grisée, a également subie une déformation d'ampleur réduite (quelques centimètres) lors de l'intrusion magmatique du 30 mars 2007.

La comparaison de la déformation et/ou de la sismicité enregistrées lors des effondrements caldériques des volcans basaltiques Fernandina, Miyakejima et Piton de la Fournaise met en évidence une dynamique d'effondrement similaire. Les données inclinométriques montrent que les calderas du Miyakejima et du Piton de la Fournaise résultent de cycles d'effondrement successifs; chaque cycle étant caractérisé par une déflation progressive de l'édifice suivie d'un abrupt mouvement centrifuge lors de l'effondrement de la colonne de roche dans la chambre magmatique (Figure 44a). Les signaux sismiques enregistrés au Piton de la Fournaise et à Fernandina, bien que de nature différente, présentent également une cyclicité bien marquée, contemporaine dans le cas du Piton de la Fournaise des cycles d'effondrement (Figure 44b).

Différentes interprétations ont été proposées pour expliquer le caractère répétitif des effondrements menant à la formation des calderas basaltiques de Fernandina et Miyakejima. D'après Simkin et Howard (1970), l'effondrement par à-coup résulterait d'une augmentation constante de la contrainte le long de failles bordières qui serait sporadiquement dissipée par l'effondrement de la colonne de roche. Filson et al. (1973) considèrent qu'une géométrie irrégulière de la base de la colonne de roche couplée à une vidange magmatique à taux constant est à même de produire un effondrement incrémental. Enfin, Kumagai et al. (2001) ont avancé que la colonne de roche au Miyakejima était aspirée épisodiquement par une vidange magmatique à taux constant.
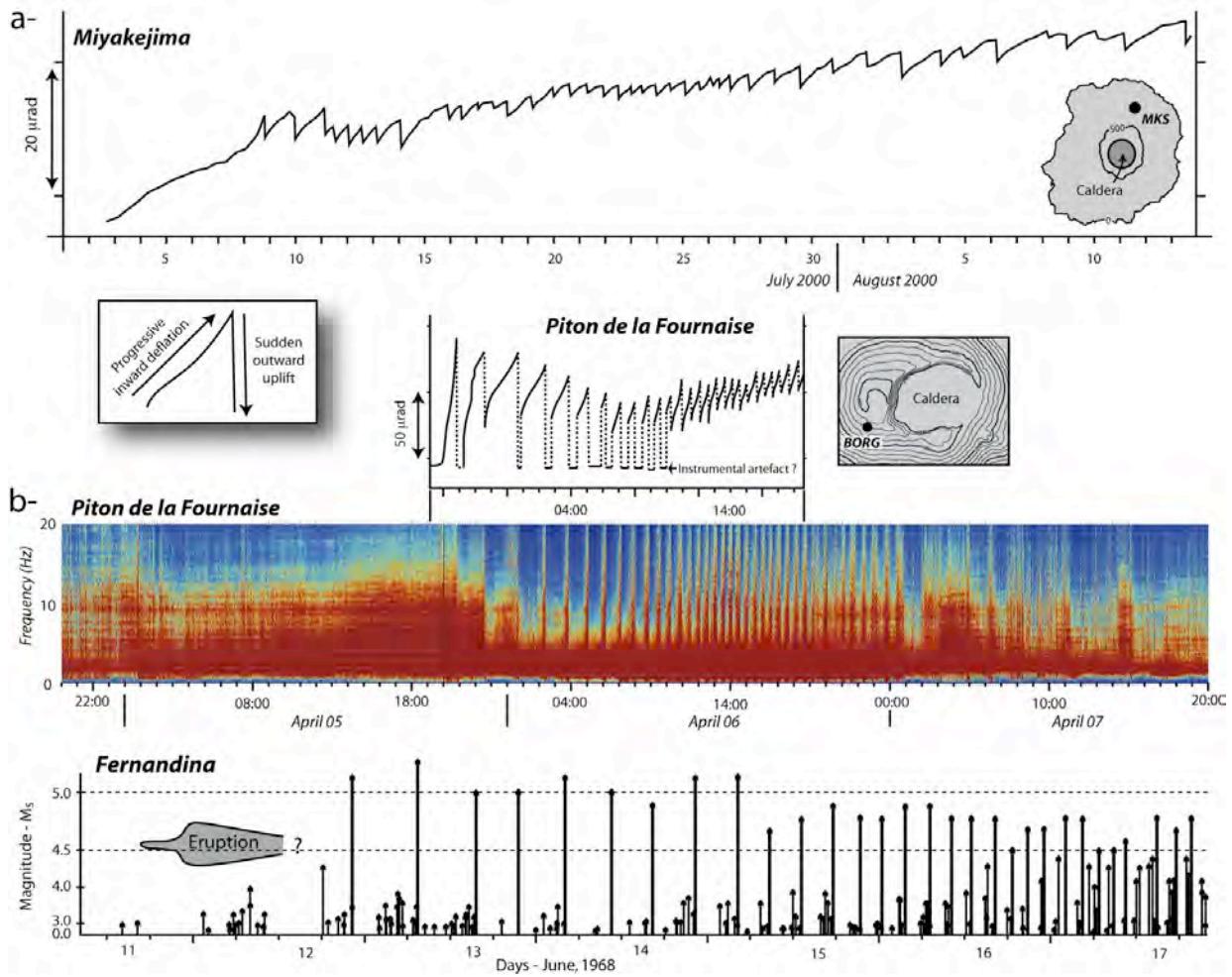
Figure 44: a- Données inclinométriques acquises pendant les effondrements caldériques du Miyakejima en 2000 (d'après Ukawa et al., 2000) et du Piton de la Fournaise en avril 2007 (d'après Staudacher et al., 2009). b- Sismicité enregistrée lors de la formation des calderas du Piton de la Fournaise (spectrogramme; Michon et al., 2007a) et de Fernandina en 1968 (magnitude des événements volcano-tectoniques; Filson et al., 1973). Les données de déformation et de sismicité révèlent un processus d'effondrement commun aux trois volcans, i.e. effondrement incrémental ou par à-coup.

Le comportement similaire des édifices basaltiques lors d'un effondrement caldérique, et ce malgré des différences évidentes en terme de dynamique d'éruption et de géométrie des structures, indique que la dynamique d'effondrement est régie par des processus clés, communs aux trois volcans. Nous avons proposé que la présence de failles annulaires pré-existantes, formées lors d'effondrements sommitaux antérieurs, était un des éléments structural fondamental (Figure 45a). Les modalités de réactivation de ces failles s'effectueraient de la manière suivante.

Premièrement, les calderas basaltiques se forment lors d'injections magmatiques latérales de grand volume depuis une chambre magmatique située sous le sommet (e.g. McDonald, 1965). La baisse de pression dans cette chambre, liée à la vidange magmatique, provoque une subsidence centripète de l'édifice (Figure 45b). Théoriquement, l'effondrement caldérique se produit lorsque

$$\Delta p \geq 4R\tau_c \qquad \text{eq. 2}$$

où Δp correspond à la différence de pression entre la pression descendante $\rho g h$ exercée par la colonne de roche au-dessus de la chambre (ρ, g et h sont respectivement la masse volumique des roches, la gravité et la hauteur de la colonne) et la pression ascendante liée à la pression magmatique, R est le rapport de forme entre la profondeur de la chambre et son diamètre et τ_c est la valeur critique de la contrainte cisaillante le long de la faille annulaire à partir de laquelle la

colonne s'effondre (Roche et Druitt, 2001). La contrainte cisaillante critique est, dans ce cas, une valeur constante liée à la cohésion des matériaux τ_0, leur coefficient de friction interne μ et la contrainte normale au plan de faille σ_n

$$\tau_c = \tau_0 + \mu\sigma_n \qquad \text{eq. 3}$$

Cependant, la déflation induit sur le plan de faille une augmentation de la contrainte normale σ_n et l'apparition d'une contrainte cisaillante τ opposée au mouvement descendant de la colonne de roche (Figure 45b). La conséquence directe est l'augmentation de la résistance au cisaillement le long de la faille bordière. La colonne de roche ne s'effondre donc que lorsque Δp excède cette valeur croissante de la résistance au cisaillement. La relaxation des contraintes liée à l'effondrement entraine alors un rebond élastique de l'édifice. L'enfoncement de la colonne de roche dans la chambre magmatique augmentant la pression de cette dernière, l'effondrement s'arrête lorsque Δp devient inférieure à la résistance au cisaillement du plan de faille (Figure 45c). La vidange constante ou croissante de la chambre magmatique entretient la déflation de l'édifice et augmente à nouveau la résistance au cisaillement des plans de faille. Un nouvel effondrement se produira quand Δp aura surpassé la résistance au cisaillement. Ainsi, chaque cycle d'effondrement est caractérisé par une phase de déflation centripète que inhibe l'effondrement de la colonne de roche, suivie de l'effondrement soudain de la colonne. La variation de la durée de chaque cycle au cours d'une même éruption indique que d'autres paramètres tels que l'affaiblissement de la résistance au cisaillement interviennent durant la formation d'une caldera (Michon et al., 2009a).
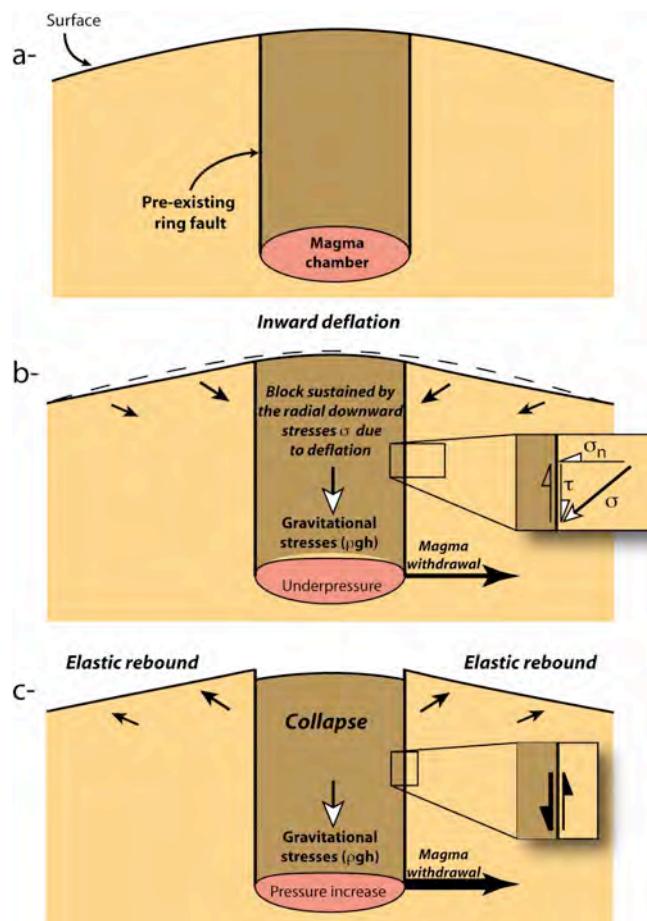
Figure 45: Représentation schématique du mécanisme d'effondrement des calderas magmatiques en contexte basaltique. a- Stade initial. L'édifice est affecté par des failles pré-existantes liées à des effondrements précédents. b- Déflation centripète lors de la décompression de la chambre magmatique associée à une intrusion magmatique latérale. Malgré la force gravitaire exercée au toit de la chambre par la colonne de roche sus-jacente, l'effondrement est bloqué par l'augmentation des contraintes normales σ_n et cisaillante τ le long des plans de faille pré-existants. c- L'effondrement se produit lorsque la différence de pression entre la chambre et la colonne de roche sus-jacente est supérieure à la résistance au cisaillement le long de la faille. Cet effondrement entraine un rebond élastique de l'édifice par relaxation des contraintes. Chaque incrément d'effondrement est ensuite caractérisé par la succession des stades b et c.

La dynamique d'effondrement est donc essentiellement contrainte par la déflation centripète, la mécanique le long des plans de faille et la différence de pression Δp. Une dynamique d'effondrement incrémental a également été proposée pour expliquer la présence d'ignimbrites stratifiées associées à certaines calderas siliceuses (Rosi et al., 1996; Reubi et Nicholls, 2004). Ceci soulève deux interrogations: Le mécanisme décrit ci-dessus pour le contexte basaltique est-il extrapolable à l'ensemble des calderas? Si oui, comment expliquer la présence de dépôts ignimbritiques continus qui suggèrent un effondrement régulier du toit de la chambre?

Je pense que tant qu'un édifice volcanique est caractérisé par un réservoir magmatique et des failles annulaires pré-existantes, le mécanisme décrit ci-dessus peut être appliqué; et ce malgré des différences essentielles en termes de composition du magma, de dynamique éruptive et de localisation de l'évent, i.e. à l'aplomb de la chambre pour les éruptions siliceuses et latéral en contexte basaltique. Le comportement incrémental ou continu de l'effondrement pourrait alors être principalement lié au taux de vidange magmatique et à la fréquente remontée du magma siliceux le long des failles annulaires. Un débit magmatique important serait favorable à un effondrement continu car il entretiendrait une forte différence de pression Δp qui excèderait toujours la résistance au cisaillement le long des failles bordières. L'intrusion magmatique le long des failles annulaires aurait pour effet de diminuer la résistance au cisaillement des failles et par conséquent favoriser l'effondrement continu du toit de la chambre, même pour un taux de vidange magmatique relativement faible. Il est donc possible que les comportements incrémentaux et continus se succèdent au cours d'une même éruption.

La modélisation analogique des calderas a permis d'améliorer très significativement notre connaissance sur la déformation du toit de la chambre au cours des effondrements (e.g., Marti et al., 1994; Roche et al., 2000, 2001; Acocella, 2007). Les principaux enseignements sont que (1) la géométrie des failles bordières dépend du rapport de forme R entre la profondeur de la chambre et son diamètre et que (2) la colonne de roche s'effondre de manière cohérente (comme un piston) pour $R<1$ et de manière non-cohérente (par effondrement successif de panneaux) pour $R>1$ (Roche et al., 2000). Stix et Kobayashi (2008) ont déterminé des valeurs R d'environ 0,3 pour la caldera de Fernandina et entre 1,9 et 3,8 pour celle de Miyakejima. Au Piton de la Fournaise, la profondeur de la chambre magmatique étant estimée à environ 2 km sous le sommet pour un diamètre proche de 1 km (Peltier et al., 2008), R est proche de 2. D'après les résultats de modélisation analogique, l'effondrement aurait du être cohérent à Fernandina et non-cohérent au Miyakejima et au Piton de la Fournaise. Cependant, l'existence d'une dynamique d'effondrement identique aux trois volcans suggère un effondrement du même type. Filson et al. (1973) et Kumagai et al. (2001) ont interprété la cyclicité des effondrements de Fernandina et Miyakejima comme le résultat de la subsidence intermittente d'une colonne homogène de type piston. Nous avons adopté la même conclusion pour l'effondrement du Dolomieu en avril 2007. La différence entre les modèles analogiques et les cas naturels réside principalement dans l'existence de failles annulaires pré-existantes qui ne sont pas prises en compte dans les modèles. Il me semble donc que la distinction entre effondrements cohérent et non-cohérent à partir du rapport de forme est caduque pour les volcans ayant déjà subi des effondrements caldériques.

2.2.2.2- Déformation lente et effondrements verticaux

Les volcans basaltiques sont découpés par de grandes structures caldériques dont l'origine magmatique ne peut être démontrée avec certitude, faute de dépôt associé. A cet égard, la structure en U du Piton de la Fournaise, composée d'ouest en est de l'Enclos, des Grandes Pentes et du Grand Brûlé (Figure 32c), fait l'objet d'un intense débat depuis le début des années 1980. Elle résulterait d'un glissement de flanc unique (Duffield et al., 1982; Labazuy, 1991, 1996; Gillot et al., 1994; Lénat et al., 2001a), de la coalescence d'au moins trois calderas magmatiques à l'origine de l'Enclos et d'un glissement de flanc dont la tête serait la zone des Grandes Pentes (Bachèlery, 1981) ou d'un glissement de flanc lent qui

aurait permis un effondrement sommital par déformation du système hydrothermal (Merle et Lénat, 2003). Son âge oscillerait entre 4,5 et 10 ka (Bachèlery, 1981; Merle et Lénat, 2003).

Plutôt que de se focaliser uniquement sur la structure en U, nous avons mené une étude morpho-structurale à l'échelle de l'édifice afin de déterminer l'évolution du Piton de la Fournaise depuis la formation de la caldera de la Plaine des Sables, i.e. environ 60 ka, jusqu'à l'Actuel. Nous avons utilisé des Modèles Numériques d'Elevation (MNE) au pas de 12,5 m, 25 m et 50 m calculés à partir du fichier originel à 25 m du MNE de l'Institut Géographique National. Morphologiquement, les flancs du Piton de la Fournaise sont caractérisés par des pentes de 8-15° à basses altitudes, de 20-35° aux altitudes intermédiaires et de 2-8° au sommet (Figure 46a). Cette distribution d'ensemble ne tient pas compte des remparts caldériques et de la géométrie du cône sommitale dont l'origine a été discutée en section 2.2.1. Exception faite des structures sus-nommées, le Piton de la Fournaise présente donc une morphologie très similaire à celles des volcans basaltiques Fernandina, Wolf et Cerro Azul (Galapagos; Rowland et Garbeil, 2000).
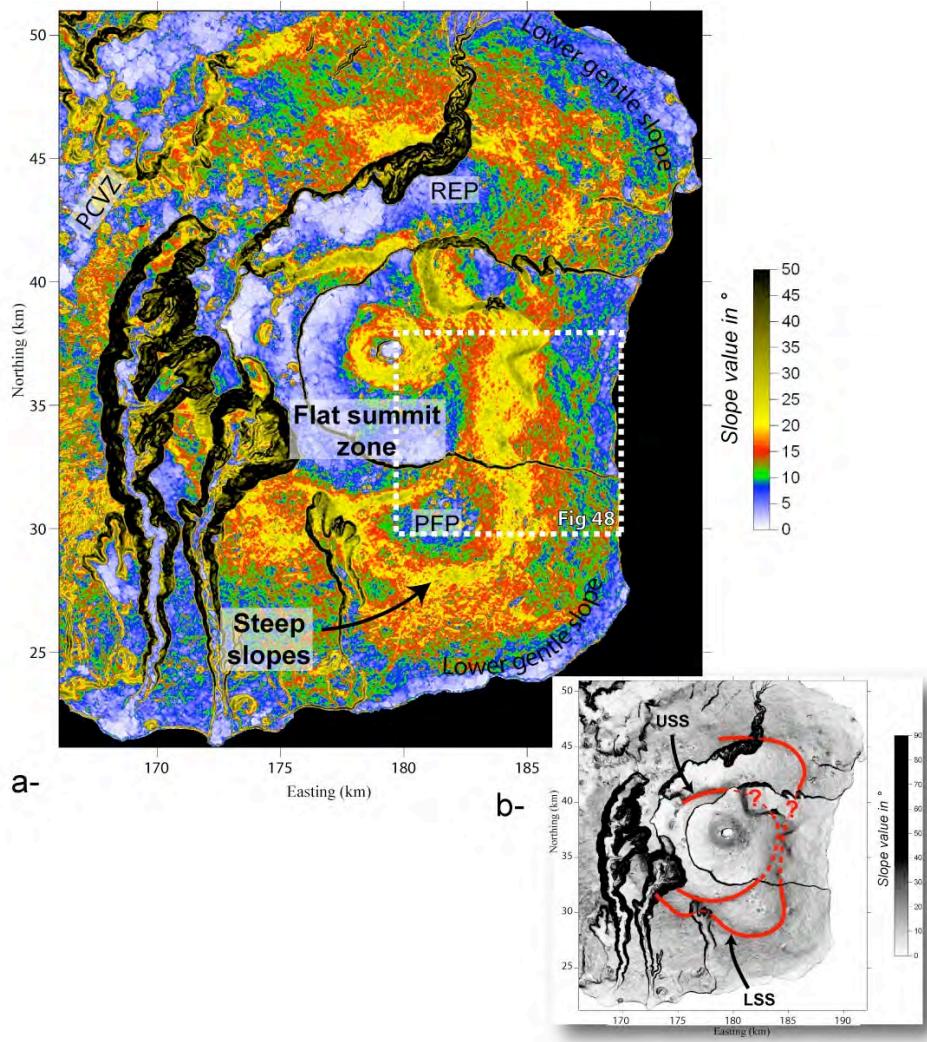
Figure 46: a- Carte de pente du Piton de la Fournaise montrant les variations de pente importantes le long des flancs du volcan. PFP: plateau du Piton de Fourche; REP: plateau de la Rivière de l'Est; PCVZ: zone volcanique de la Plaine des Cafres. b- Carte de pente avec la localisation des zones à forte pente supérieure (USS) et inférieure (LSS) caractérisées par des valeurs de pente de 20-30°. Coordonnées en Gauss Laborde Réunion.

Radialement, les flancs sud et nord du Piton de la Fournaise montrent une géométrie en escalier basculée vers la mer avec deux zones à forte pente, supérieure et inférieure, séparant des plateaux à pente faible et régulière (Figure 47a). Les variations d'altitude de deux plateaux successifs sont toujours inférieures au niveau de la zone supérieure à forte pente (USS) qu'au passage de la zone inférieure à forte pente (LSS). Le long de chaque profil, l'USS et la LSS sont respectivement à

des altitudes de près de 2000m et entre 1000-1200m (Figure 47b). Ainsi, pour chaque flanc, nord et sud, la continuité cartographique et les similitudes morphologiques suggèrent la présence de deux niveaux de pentes continus (Figure 46b). A l'est, le flanc n'est caractérisé que par une seule zone à forte pente correspondant aux Grandes Pentes. Le changement d'altitude entre les plateaux situés à l'amont et l'aval de cette zone est très supérieur à chaque changement d'altitude le long de l'USS et de la LSS. Cependant, il est proche de la valeur T correspondant à la somme des changements d'altitude (USS+LSS), qui augmente régulièrement d'ouest en est (Figure 47a). Il est donc fort légitime de s'interroger sur une continuité éventuelle entre les zones à forte pente situées sur les flancs sud et nord, et la zone des Grandes Pentes qui est définie au sein de la structure en U comme le résultat d'un glissement de flanc.
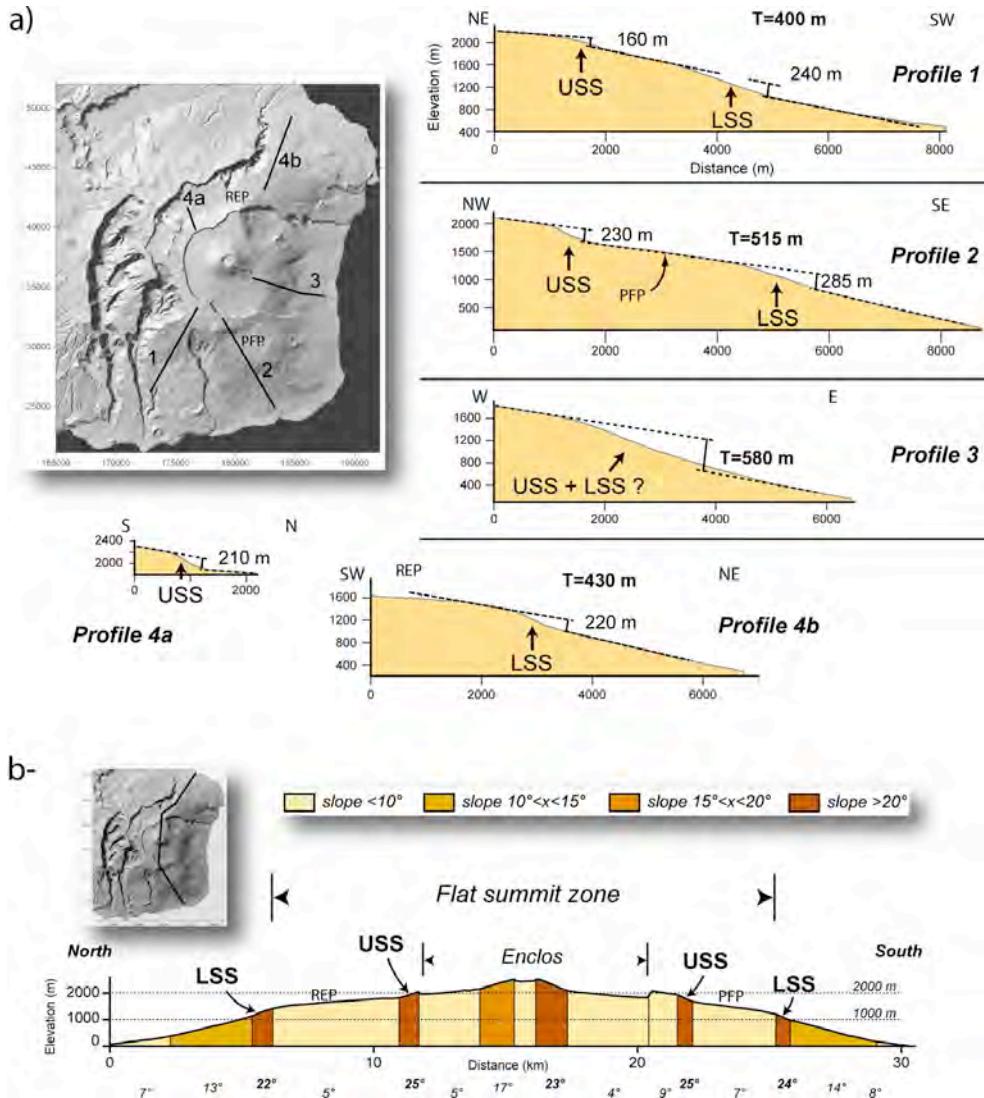
Figure 47: a- Profils topographique radiaux présentant la succession de domaines de pente faible et de forte pente. Le changement d'altitude entre chaque niveau en pente douce est déterminé. Pas d'exagération verticale. T correspond à la somme des changements d'altitude pour chaque profil. LSS: zone à forte pente inférieure; USS: zone à forte pente supérieure; REP: plateau de la Rivière de l'Est; PFP: plateau du Piton de Fourche. b- Profil topographique N-S illustrant la géométrie en bouclier du Piton de la Fournaise et les différents domaines de pente. Notez l'altitude similaire des zones de pente supérieure et inférieure sur les flancs nord et sud du volcan.

L'analyse morpho-structurale de détail au niveau du rempart sud (Tremblet) de la structure en U permet d'évaluer la continuité éventuelle des zones à forte pente. Cette partie du flanc est est caractérisée par des structures linéaires orientées ENE-WSW et NNW-SSE, dont certaines limitent une dépression en V située dans la partie basse des Grandes Pentes (Figures 48a et 48b). Cette structure était classiquement interprétée comme la niche d'arrachement d'un glissement secondaire (Bachèlery, 1981). Cependant, la continuité latérale des structures bordières et la sismicité récurrente à l'aplomb de ces limites (Frédéric Massin, comm pers) suggèrent une origine tectonique à cette dépression

(Michon et Saint-Ange, 2008).
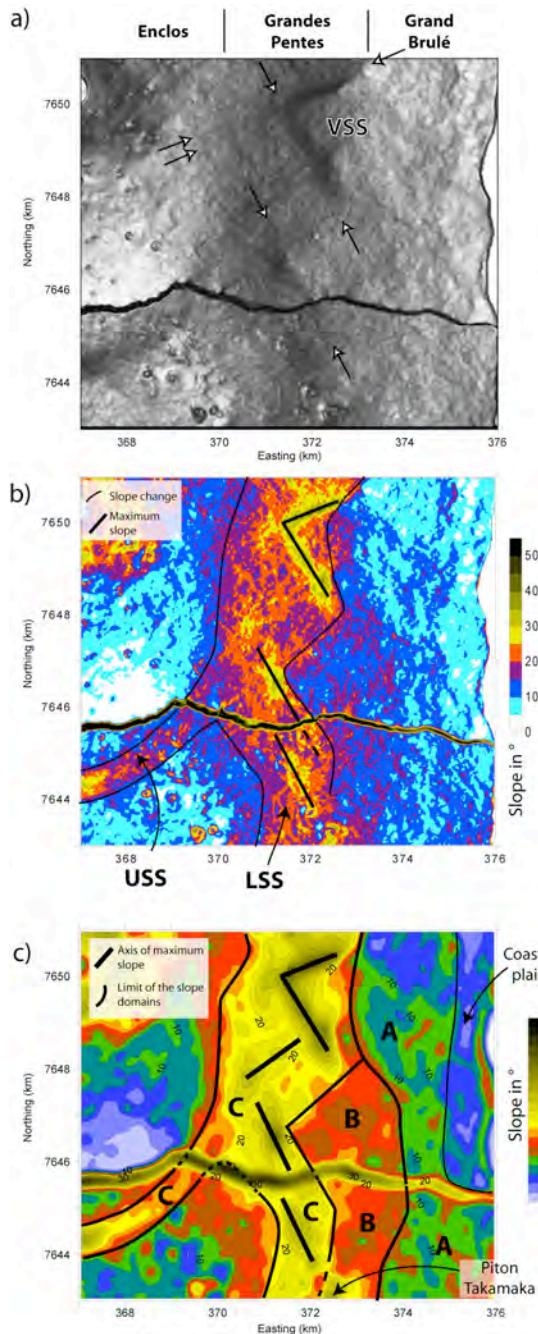
Figure 48: a) Carte de pente en niveau de gris calculée à partir d'un Modèle Numérique d'Elevation (MNE) au pas de 12,5 m illustrant la morphologie des Grandes Pentes (cf figure 46a pour la localisation). Plusieurs linéaments soulignés par des flèches y sont observés. Certains limitent une structure en V (VSS) qui est classiquement interprétée comme un glissement de flanc secondaire. b) Carte de pente montrant les axes de pente forte et les changements de pente importants. c) Carte de pente filtrée (MNE au pas de 50 m avec filtre passe-bas) révélant les caractères morphologiques de grande longueur d'onde. Trois domaines de pente A, B et C apparaissent en continuité de par et d'autre du rempart du Tremblet. Les pentes faibles du Grand Brûlé à proximité de la côte résultent de l'accumulation de deltas de lave. Coordonnées en UTM WGS84.

La carte de pente révèle des variations franches des valeurs de pente dans chacun des domaines situés de part et d'autre du rempart du Tremblet (Figure 48b). Cependant, les irrégularités de la topographie et de la végétation perturbant le signal topographique, nous avons calculé une nouvel MNE au pas de 50 m qui a ensuite été filtré afin de visualiser les informations topographiques de grande longueur d'onde. Ce traitement met en lumière l'existence de trois domaines de pente (A, B et C) dont les limites sont en réelle continuité de part et d'autre du rempart (Figure 48c). Ainsi, l'USS et la LSS se prolongent dans la structure en U où elles coalescent pour former les Grandes Pentes. Cette simple observation remet

en cause les différentes interprétations dans lesquelles les Grandes Pentes sont limitées à la structure en U et liées à sa formation (Bachèlery, 1981; Duffield et al., 1982; Lénat et al., 1989, 2001; Labazuy, 1991, 1996; Gillot et al., 1994; Merle et Lénat, 2003; Oehler et al., 2004, 2008). Elle soulève également plusieurs problèmes: 1- Quelles est l'origine des USS et LSS? 2- Quelle est la relation entre la structure en U et les zones à fortes pentes?

1- Nous avons décrit en détail dans un article publié à Journal of Geophysical Research (Michon et Saint-Ange, 2008; annexe 12) les différents processus menant à la formation de zones à forte pente dans un volcan basaltique. Trois grandes familles de processus ont été recensées: les processus constructifs (endogène et/ou exogène), les processus destructifs et les processus liés à la déformation de l'édifice.

Parmi les zones à forte pente du Piton de la Fournaise, deux ont fait l'objet d'un consensus général (Bachèlery, 1981; Merle et Lénat, 2003; Oehler et al., 2004, 2008): les Grandes Pentes et la zone à forte pente correspondant à l'USS du flanc sud (cf Figure 32c pour la localisation). Cette dernière est considérée comme la trace du prolongement vers l'est de la caldera de la Plaine des Sables, entièrement comblée par des coulées de lave (e.g. Bachèlery, 1981). Ce segment de l'USS ayant une morphologie très régulière, les coulées de laves émises depuis la zone centrale, effondrée depuis, devaient être de même longueur et réparties radialement de manière uniforme pour construire un relief concentrique homogène. Ce type d'hypothèses est très peu probable pour le Piton de la Fournaise où la longueur des coulées varie beaucoup d'une éruption à l'autre et où la présence de rift zones concentre la croissance de l'édifice. Nous avons donc proposé une hypothèse alternative pour expliquer le développement de zones concentriques à forte pente. Cette interprétation est basée sur le résultat de modèles analogiques qui montrent qu'un édifice volcanique peut se déformer lentement sur un système hydrothermal dont le comportement rhéologique s'apparenterait à celui d'un fluide visqueux (Cecchi et al., 2005). Deux types de structures peuvent se développer conjointement: des zones concentriques à forte pente et des effondrements sommitaux. Nous interprétons donc la formation de l'USS et de la LSS comme le résultat d'un étalement gravitaire du Piton de la Fournaise sur son système hydrothermal (Figure 49).
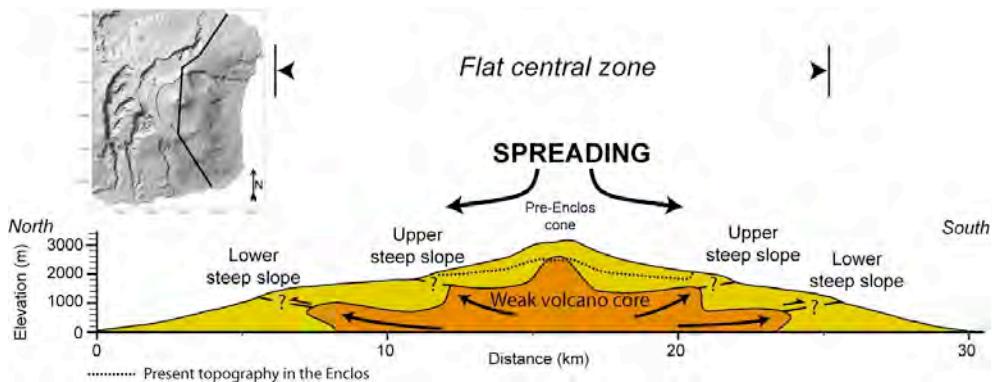
Figure 49: Schéma interprétatif N-S illustrant l'origine des zones supérieures et inférieures à forte pente, USS et LSS, par étalement gravitaire de l'édifice sur le système hydrothermal.

2- Déterminer la relation entre les zones à forte pente et la structure en U impose de déterminer l'âge relatif des structures. L'absence de décalage latéral significatif des domaines de pente situés de part et d'autre du rempart du Tremblet peut s'expliquer soit par un effondrement vertical de l'ensemble de la structure en U postérieurement au développement des fortes pentes, soit par la formation des fortes pentes depuis 4,5 à 10 ka, i.e. après l'effondrement de la structure en U. La seconde hypothèse est peu probable car elle impliquerait des taux de déformation de plusieurs centimètres par an, i.e. du même ordre de grandeur que la déformation associée au glissement de flanc d'Hilina à Hawaii où les déplacements induisent une sismicité importante (e.g. Delaney et al., 1998). Ni la sismicité, ni les déplacements de l'ensemble du sommet sont enregistrés actuellement. Ainsi, la structure en U se serait formée par effondrement(s) vertical(aux) dont l'origine est actuellement très mal contrainte. Plusieurs hypothèses peuvent cependant être avancées.

Tout d'abord, un effondrement vertical unique de l'ensemble de la structure en U causé par une même source me semble invraisemblable. Ceci nécessiterait, selon les différents modèles de caldera, une chambre magmatique de gros volume, un corps hydrothermal ou un corps intrusif très étirés vers l'est. L'existence de telles structures n'est pas supportée par les données géologiques et géophysiques disponibles. Il est donc probable que le développement de la structure en U résulte d'une combinaison de processus, comme l'ont déjà proposé Bachèlery (1981) et Merle et Michon (2003). Contrairement à ces auteurs, et en tenant compte des données morpho-structurales et géologiques, nous considérons que le Grand Brûlé résulte d'un effondrement vertical. Nous avons envisagé plusieurs sources potentielles à cet effondrement: (i) caldera par vidange magmatique, (ii) glissement de type slump profondément enraciné, (iii) fluage de corps intrusif du volcan des Alizés (cf Figure 32c pour sa localisation) par déformation des olivines et (iv) subsidence du corps intrusif du volcan des Alizés (Michon et Saint-Ange, 2008). Il apparaît que l'hypothèse de la subsidence du corps intrusif du volcan des Alizés est la plus compatible avec les données géologiques. Outre la formation progressive du Grand Brûlé, la subsidence du corps intrusif expliquerait la sismicité récurrente entre 3 et 7 km de profondeur sous le flanc est de l'édifice (Lénat et al., 1989). Elle expliquerait également, par une déformation continue, la présence de coulées de lave d'origine aériennes jusqu'à 440 m de profondeur comme l'a montré le forage d'exploration géothermique du Grand Brûlé (Rançon et al., 1989). Enfin, elle induirait des contraintes extensives radiales dans sa périphérie, ce qui favoriserait la propagation latérale des injections magmatiques le long des rift zones NE et SE (Figure 32c).

La formation de la caldera poly-lobée de l'Enclos est actuellement expliquée par la coalescence de trois calderas magmatiques (Bachèlery, 1981) ou par le fluage du système hydrothermal (Merle et Lénat, 2003). Le développement de trois calderas adjacentes nécessite la migration latérale de la chambre magmatique après chaque événement. Un tel processus a déjà été invoqué à Tenerife pour expliquer la formation de trois calderas contigües (Marti et Gudmundsson, 2000). Cependant, le temps nécessaire à la croissance d'une chambre magmatique est estimé à 200 ka, ce qui est bien supérieur à ce qui peut être déterminé pour le Piton de la Fournaise. De fait, étant donné la géométrie du plancher de la caldera, l'effondrement le plus ancien serait celui à l'origine du lobe ouest qui est daté à 4,5 ka (Bachèlery, 1981). Il est très peu probable que trois effondrements de grande ampleur se succèdent en un laps de temps aussi court. L'hypothèse d'un effondrement de l'ensemble de l'Enclos par fluage du système hydrothermal sous-jacent permet d'expliquer l'absence de produits magmatiques associés. Cependant, le modèle proposé par Merle et Lénat (2003) est confronté à certaines données géologiques et morpho-structurales. Le Grand Brûlé ne résulte pas d'un glissement de flanc. Le Piton de Crac, qui correspond à un relief isolé en place à l'ENE du cône central (Figure 32c), limite la possibilité de fluage du système hydrothermal sommital vers l'est.

Malgré les commentaires effectués ci-dessus, je pense que chacun des phénomènes, i.e. magmatique et fluage, peut avoir contribué à la formation ou la réactivation de la caldera. Tout d'abord, nous avons proposé que les zones concentriques à forte pente (LSS et USS) résulteraient de l'étalement gravitaire de l'édifice sur le système hydrothermal (Figure 49). Les modèles analogiques montrent que ce processus s'accompagne d'un effondrement sommital (Cecchi et al., 2005). La caldera de l'Enclos pourrait donc, au même titre que les zones à forte pente, correspondre à une structure tectonique qui s'intègre dans un processus global de déformation de l'édifice. Par ailleurs, les données interférométriques montrent que la vidange magmatique durant l'éruption d'avril 2007 a entraîné une déformation de l'ensemble de l'Enclos (Augier et al., 2008). Cette éruption, bien que la plus importante de la période historique ($0,12$ km^3), reste modeste par rapport à certaines éruptions/intrusions s'étant produites récemment sur d'autres volcans basaltiques (e.g. 1.1 km^3 au Miyakejima; Ito et Yoshioka, 2002; 1 km^3 à Sierra Negra en 1979; Reynolds et al., 1995). Les hypothèses magmatiques et hydrothermales telles qu'elles sont présentées ici ne pouvant être exclues, il me semble essentiel de considérer les deux processus comme ayant participé ensemble à la formation de l'Enclos plutôt que de considérer l'un ou l'autre comme la solution exclusive. Quelles que soient les causes, l'effondrement de l'Enclos s'est produit par une subsidence différentielle

des trois lobes. Le mouvement différentiel a été accommodé par des failles linéaires pluri-kilométriques tel que l'accident N65 qui sépare les lobes ouest et sud de l'Enclos (cf Fig 7 dans Michon et Saint-Ange, 2008; annexe 12).

2.2.3- Contrôle de la structure lithosphérique sur l'évolution magmato-tectonique

J'ai décrit dans les sections précédentes des processus de croissance et de déformation liés à la dynamique des systèmes magmatiques et hydrothermaux. Par exemple, l'injection récurrente de filons magmatiques le long de la rift zone N25-30 du Piton de la Fournaise entraîne à la fois une croissance endogène asymétrique du cône central et le développement d'une seconde rift zone orthogonale à la principale. Ces phénomènes semblent être propres à cet édifice et isolés de toute interaction avec le contexte extérieur. Cependant, l'influence des structures crustales dans l'évolution des volcans basaltiques a été mis en avant au niveau de nombreux volcans basaltiques océaniques tels ceux d'Hawaii, des îles Australes, de la Société et de Tenerife (e.g., McDonald et Abbott, 1970; Binard et al., 1991; Marinoni et Gudmundsson, 2000). A La Réunion, l'allongement de l'île selon un axe N120, causé par l'alignement du Piton des Neiges et du Piton de la Fournaise, et la fracturation N30 du Piton des Neiges sont depuis longtemps considérés comme le résultat d'un contrôle crustal (e.g. Chevallier, 1979). L'étude volcano-structurale entreprise par Chevallier (1979) au niveau du Piton des Neiges n'avait pas d'équivalence au Piton de la Fournaise. Nous avons donc analysé les structures volcaniques, tectoniques et géophysiques affectant ce volcan pour ensuite les intégrer aux échelles de l'île et de la croûte. Ce travail a été particulièrement motivé par la présence d'une sismicité diffuse distribuée sous l'ensemble de l'édifice réunionnais qui suggère une déformation active dans des zones exemptes d'activité magmatiques récentes (Figure 50).
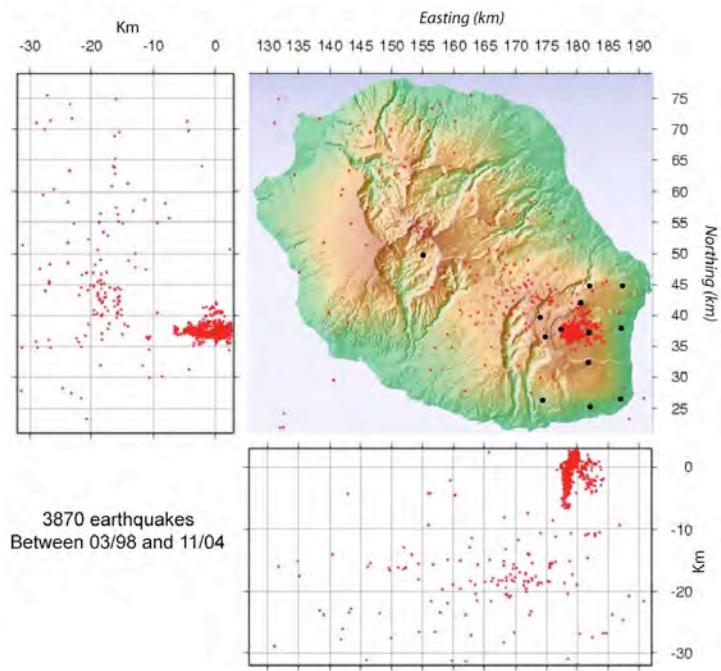
Figure 50: Carte de la sismicité entre Mars 1998 - Novembre 2004. Les points noirs représentent les stations sismiques de l'OVPF ayant permis à la localisation des séismes.

Les structures magmatiques actives du Piton de la Fournaise, décrites dans le détail dans la section 2.2.1., s'organisent autour de deux rift zones N25-30 et N120. L'orientation similaire de ces rift zones et des dykes affleurants dans le rempart de l'Enclos (Figure 51a), dont l'âge est antérieur à 4,5 ka, indique une préservation des structures malgré l'effondrement caldérique. La caldera de l'Enclos est également caractérisée par une zone de failles N55-65 à l'est du cône central (Figure 33c) et un accident tectonique pluri-kilométrique orienté N65 entre les lobes ouest et sud (cf Figure 7 dans Michon et Saint-Ange, 2008; Annexe 12). En complément de ces données volcano-structurales, les données géophysiques

révèlent l'existence de zones à fortes vitesses orientées N30 et N120, limitées aux parties internes de l'édifice, i.e. sous le niveau de la mer, et interprétées comme la trace des rift zones en profondeur (Brenguier et al., 2007).

Hors de l'Enclos, l'identification de structures tectoniques est rendue très difficile par une dense végétation tropicale qui recouvre les flancs du volcan et la majeure partie des flancs de vallée. Néanmoins, en combinant l'analyse morpho-structurale et les données géophysiques disponibles, nous avons proposé l'existence de structures tectoniques pluri-kilométriques orientées N70-75 (Michon et al., 2007b). Au nord de l'Enclos, cet accident est parallèle et en continuité avec une structure rémanente du volcan des Alizés sous-jacent (cf Figures 9 et 10 dans Michon et al., 2007b).

Nous avons mené, dans le cadre du travail de thèse de Ludovic Letourneur, une campagne de mesure systématique des intrusions du Piton des Neiges. Les données mettent en évidence trois principales directions d'intrusion (N10-30, N120 et N160); les deux premières orientations étant identiques à celles mesurées au Piton de la Fournaise (Figure 51a). Il est intéressant de constater les variations importantes de répartition spatiale des intrusions associées à chaque faisceau. Les intrusions N10-30 sont fortement concentrées dans le cirque de Cilaos, celles orientées N120 présentent une assez grande densité dans la partie occidentale du cirque de Mafate, tandis que les intrusions N160 sont distribuées de manière relativement uniforme dans les trois cirques (Figure 51b). A noter tout de même, une concentration des intrusions N160 dans le Bras de Sainte-Suzanne et la Rivière Saint-Denis (zones difficiles d'accès non échantillonnées durant ce travail; Figure 51b)
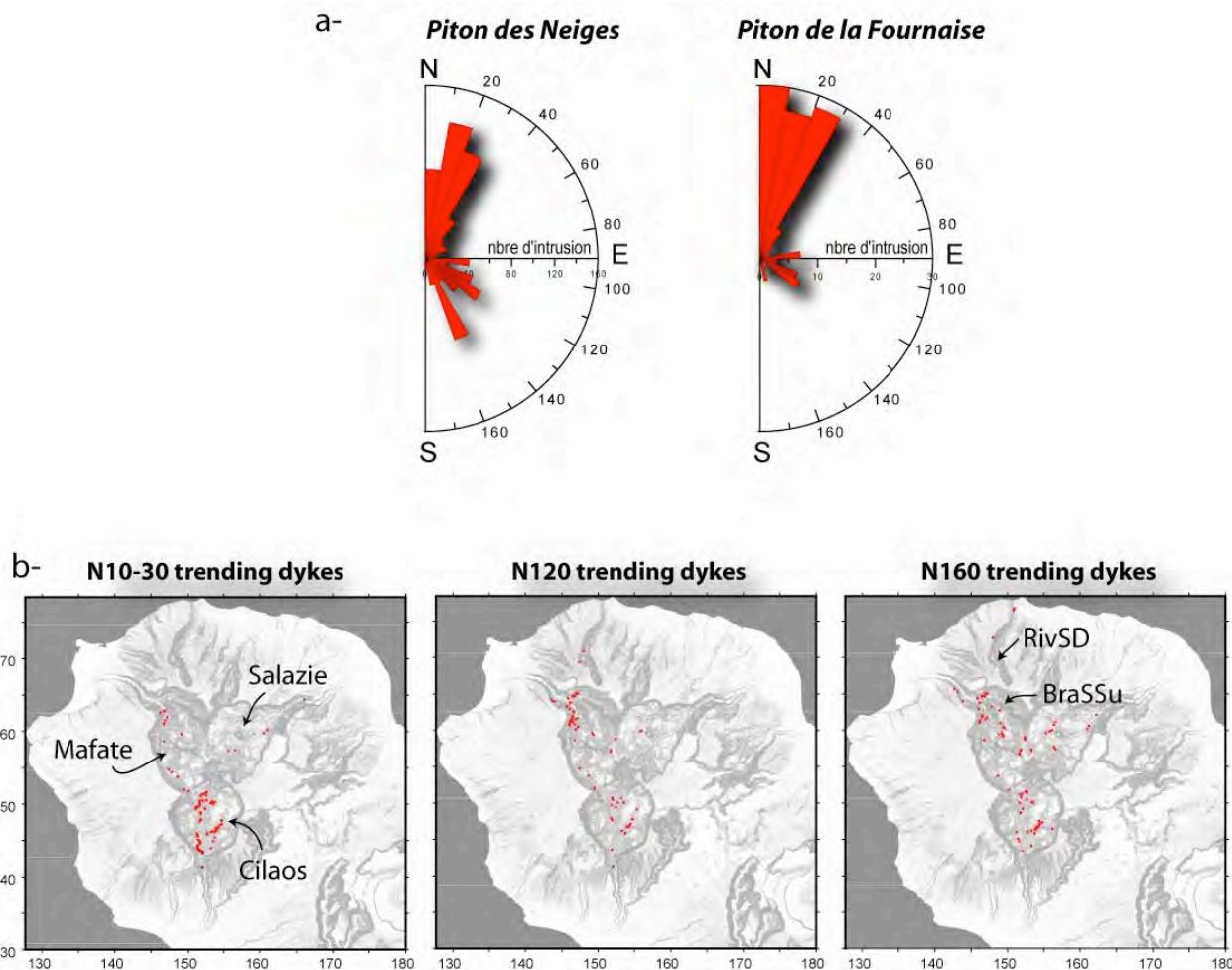
Figure 51: a- Orientation des intrusions dans le Piton des Neiges et du Piton de la Fournaise. b- Localisation des dykes orientés N20, N120 et N160. BraSSu: Bras de Sainte-Suzanne; RivSD: Rivière Saint-Denis. Coordonnées en km dans le référentiel Gauss Laborde Réunion.

La concentration des intrusions N10-30, l'alignement de cônes volcaniques sur la bordure ouest du cirque de Cilaos et la ride topographique située sur le flanc sous-marin au large de la ville de l'Etang Salé sont autant de strutures qui confirment l'existence d'une rift zone longue et étroite au sud-ouest du Piton de Neiges (Figure 52a; Lénat et al., 2001a). L'anomalie magnétique inverse au niveau de la ride sous-marine indique une édification antérieure à 700 ka, durant la phase de construction basaltique du Piton des Neiges (Lénat et al., 2001a). L'activité de la rift zone a ensuite perduré pendant plusieurs centaines de milliers d'année jusqu'à la phase différenciée du volcan, i.e. post 350 ka.
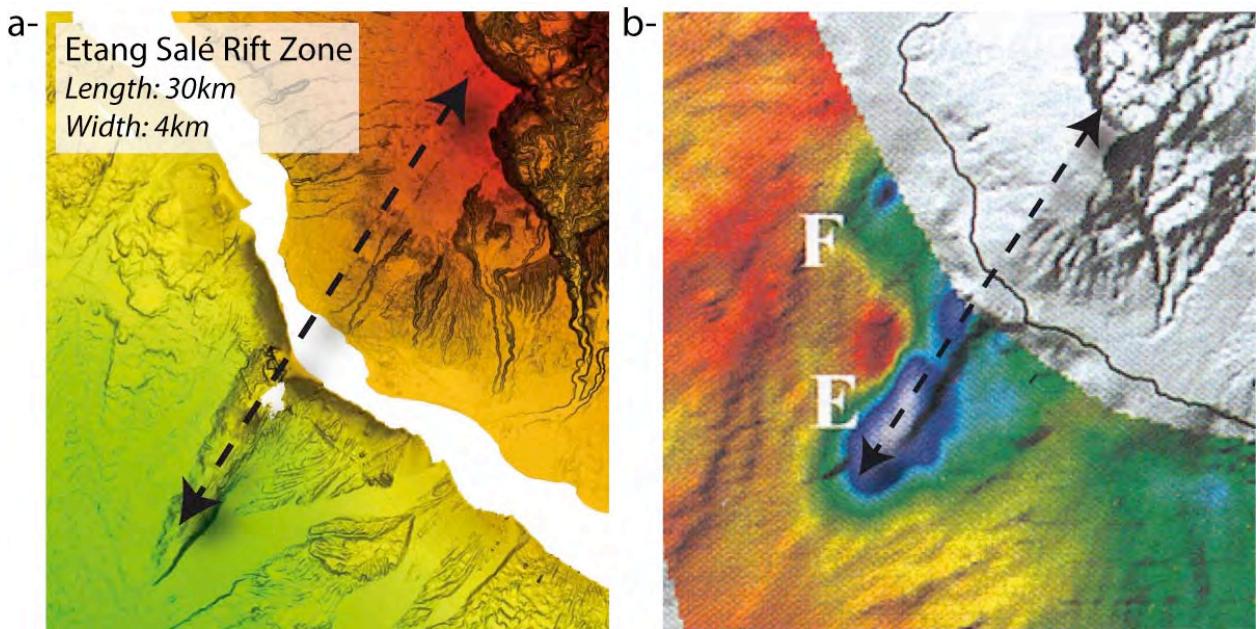
Figure 52: a- Modèle Numérique d'Elevation montrant le relief construit par la rift zone de l'Etang Salé en domaine sous-marin et sa partie aérienne, ponctuée de cônes volcaniques. Ces structures définissent la rift zone de l'Etang Salé orientée N30. b- Carte d'anomalie magnétique en domaine sous-marin au sud-ouest du Piton des Neiges (d'après Lénat et al., 2001a). L'anomalie E indique que la ride de l'Etang Salé date au minimum de 0,7 Ma.

La répartition globale des intrusions associées aux faisceaux N120 et N160 diffère clairement de celle du faisceau N10-30. Bien que la partie ouest du cirque de Mafate et la zone nord-nord-ouest du Piton des Neiges puissent être le siège de rift zones N120 et N160, la dispersion des intrusions dans l'ensemble des cirques suggère un contrôle structural diffus à l'échelle du massif. Concernant le faisceau d'intrusions N120, le rôle d'un tel contrôle structural est renforcé par le développement d'une zone volcanique large de 8-10 km, entre le Piton des Neiges et la Piton de la Fournaise (Figure 32c). A l'échelle de l'île, le magmatisme N120 dessine donc un axe volcanique au sein duquel la concentration des intrusions est relativement faible (Figure 53). L'activité de cet axe a perduré de manière continu entre 2 Ma, âge des laves les plus anciennes au niveau du massif de La Montagne (voir Figure 51b pour la localisation), et 29 ka au niveau de la Plaine des Cafres (MacDougall, 1971), i.e. durant l'édification des volcans réunionnais.

L'âge des intrusions N160 reste quant à lui mal contraint. La présence de nombreuses intrusions au sein du massif de La Montagne suggère un développement précoce de cette rift zone dans l'histoire du Piton des Neiges. Cependant, la détermination de sa longévité et de son extension latérale nécessite l'acquisition d'un plus grand nombre de données.
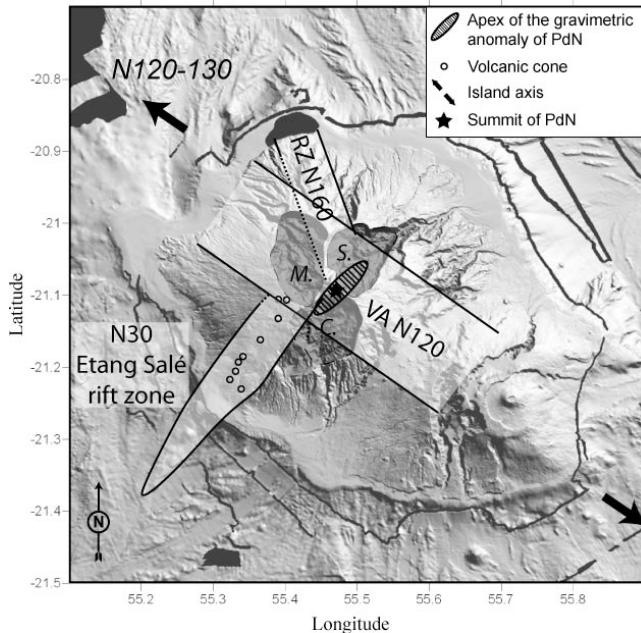
***Figure 53**: Distribution des principaux axes intrusifs du Piton des Neiges. M, S et C: Cirques de Mafate, Salazie et Cilaos, respectivement. VA N120: axe volcanique N120.

Les édifices volcaniques réunionnais reposent sur une croûte océanique d'âge fini-Crétacé dont les principales structures correspondent aux failles transformantes et au grain crustal acquis lors de l'accrétion. A l'échelle régionale, ces structures tectoniques sont respectivement orientées N120 et N30-40 (e.g. Fretzdorff et al., 1998). Cette géométrie se complexifie significativement autour de La Réunion: seul le domaine situé entre La Réunion, l'île Maurice et la faille transformante de Maurice présente une structuration organisée selon une direction N80 (Figure 54).
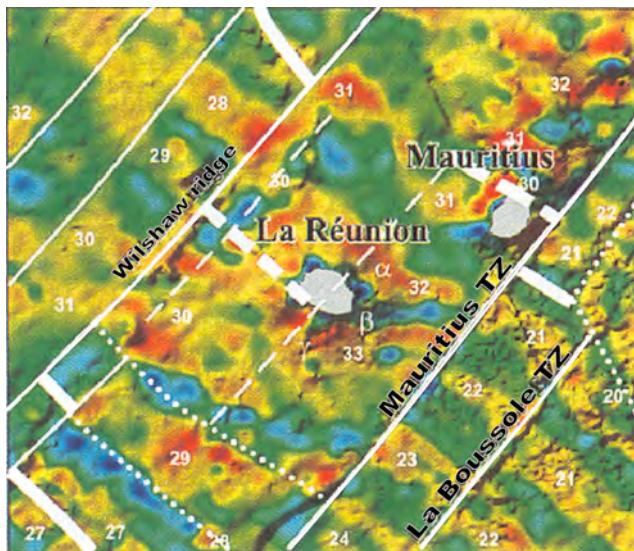
***Figure 54:** Anomalies magnétiques crustales autour des îles de la Réunion et de Maurice (d'après Lénat et al., 2001a). Les failles transformantes sont orientées N30-40 et la croûte est caractérisée par un grain crustal N120. La zone entre Maurice, la Réunion et la faille transformante de Maurice présente une orientation particulière, N80.

J'ai montré ci-dessus que chaque niveau structural, i.e. (i) le système magmatique actif du Piton de la Fournaise, les massifs (ii) du Piton des Neiges et (iii) du Piton de la Fournaise et (iv) la croûte océanique, était caractérisé par des directions dominantes. Il est généralement difficile de déterminer pour un niveau structural donné si les différentes structures sont liées à des effets locaux ou à des processus régionaux. Les processus locaux tels que la déformation intra-édifice, les variations de champ de contraintes induites par les glissements de flanc ou la surpression magmatique occasionnent le développement de structures limitées à l'édifice volcanique. En revanche, la déformation de grande

échelle est à même d'influencer la formation de structures multi-échelles. Dans le cas de La Réunion, l'intégration de plusieurs échelles révèle un parallélisme évident des principaux faisceaux N30-40, N70-80 et N120-130 (Figure 55). Les faisceaux N30-40 et N120-130 correspondent (1) aux directions d'injection préférentielle au Piton des Neiges et Piton de la Fournaise, (2) à l'allongement des corps intrusifs dense au Piton des Neiges et entre les deux massifs (Malengreau et al., 1999), (3) à deux des principaux faisceaux de failles du Piton des Neiges (Chevallier, 1979) et (4) aux orientations régionales de la croûte. Le faisceau N70-80 est représenté par (1) la troisième direction principale des failles du Piton des Neiges (Chevallier, 1979), (2) les structures reconnues sur les flancs nord et sud du Piton de la Fournaise, (3) une forte anomalie magnétique inverse sous le flanc sous-marin est du Piton de la Fournaise (Lénat et al., 2001a), (4) un horst allongé (de Voogd et al., 1999) et (5) la fabrique crustale entre La Réunion et la zone transformante de Maurice. Nous avons donc interprété le parallélisme entre ces différentes structures comme le résultat d'un fort contrôle structural joué par la croûte océanique dans l'évolution des volcans réunionnais (Michon et al., 2007b). Dans ce cadre, les orientations secondaires ou celles observées à un seul niveau structural résulteraient de phénomènes locaux.
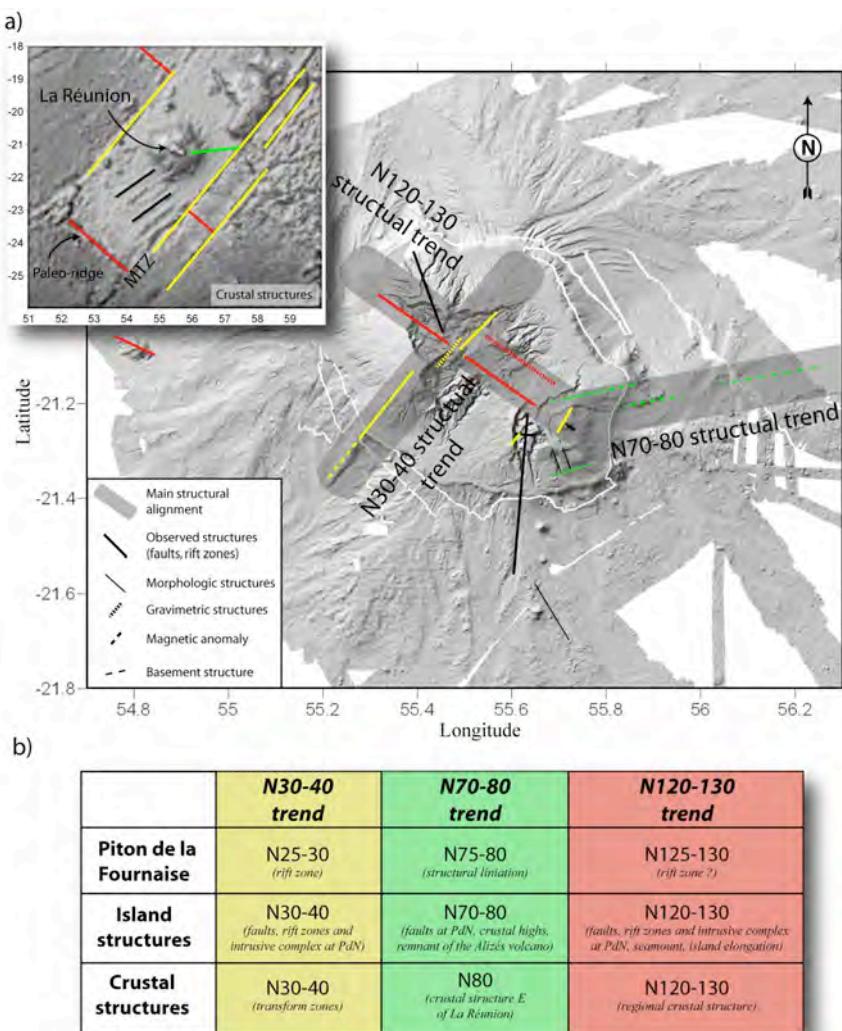
Figure 55: a- Distribution des principales structures du Piton de la Fournaise, du Piton des Neiges et de croûte océanique. Les traits jaunes, rouges et verts correspondent respectivement aux structures orientées N30-40, N120-130 et N70-80. b- Résumé des orientations principales.

La construction d'un volcan basaltique sur le plancher océanique s'accompagne fréquemment d'une flexure de la lithosphère, comme celles observées au niveau des édifices d'Hawaii, de Tenerife, du Cap Vert et des Marquises (Watts et Cochran, 1974; Watts et al., 1980, 1985, 1997; Bodine et al., 1981; Minshull et Charvis, 2001; Ali et al., 2003). Les données géophysiques acquises autour de La Réunion suggèrent une absence de flexure et révèlent l'accrétion d'un important sous-

plaquage en base de croûte sous la partie SW de l'édifice (Charvis et al., 1999; Gallart et al., 1999; de Voogd et al., 1999). La déformation de la lithosphère lors de la mise en place d'un volcanisme de type point chaud dépend (1) de la taille, i.e. la charge, de l'édifice, (2) de l'épaisseur élastique de la lithosphère et (3) de l'ampleur du sous-plaquage magmatique et de l'amincissement de la lithosphère mantellique. La hauteur de l'édifice réunionnais étant du même ordre de grandeur qu'à Hawaii, au Cap Vert et à Tenerife, une différence de charge ne peut expliquer l'absence de flexure sous La Réunion par rapport aux autres édifices. Bien que des erreurs significatives puissent être faites sur l'épaisseur élastique de la lithosphère (Minshull et Charvis, 2001), la proximité des valeurs déterminées pour La Réunion (28 km; Bonneville, 1990), Cap Vert (29 km; Ali et al., 2003), Tenerife (26 km; Watts et al., 1997) et Hawaii (30-35 km; Wessel et Keating, 1994) ne permet également pas d'expliquer de telles différences de géométrie de la lithosphère. Enfin, les données sismiques suggèrent de réelles différences de volume de sous-plaquage magmatique (Watts et al., 1997). Cependant, l'absence de corrélation entre l'ampleur de la flexure et du sous-plaquage invalide l'hypothèse d'une force ascendante significative liée au sous-plaquage qui contre-balancerait la subsidence due à la charge.

Nous avons vu lors de l'étude du rift du Massif Central (section 2.1.1.1.) que l'érosion thermique de la base de la lithosphère est un processus capable de produire une force ascendante importante. La quantité de lithosphère érodée et de surrection dépendent de la durée de résidence de la lithosphère à l'aplomb de l'anomalie thermique et de la température de l'anomalie. Il est donc attendu que les déséquilibres isostatiques soient favorisés au niveau des plaques à faibles vitesses de déplacement, et soient quasiment inexistants pour les plaques se déplaçant rapidement (Figure 56). Le déplacement de l'île de La Réunion par rapport au point chaud, depuis 2 Ma, a été estimé à moins de 40 km (Charvis et al., 1999). Dans un tel contexte, nous pensons que l'amincissement thermique de la lithosphère mantellique a pu être efficace. Nous avons donc interprété l'absence de flexure lithosphérique au niveau de La Réunion comme le résultat d'une érosion thermique importante de la base de la lithosphère (Michon et al., 2007b). La flexure importante au niveau des Marquises et d'Hawaii serait à l'inverse liée à la vitesse de déplacement importante de la plaque Pacifique, qui ne permettrait pas de développer une érosion thermique suffisante pour contre-balancer la charge de l'édifice. Enfin, la présence d'une flexure importante sous Tenerife, où la vitesse de déplacement de la plaque est lente, peut s'expliquer par une anomalie thermique moins active que dans les cas classiques de point chaud.

En domaine continental, le mouvement ascendant de la lithosphère entraîne la réactivation de failles crustales qui contrôlent le développement du volcanisme (Michon et Merle, 2001; Le Gall et al., 2004). D'une manière similaire, nous avons interprété la surrection de la lithosphère sous La Réunion comme le moteur de la réactivation des failles crustales qui ont ensuite contrôlé le développement des principales structures volcano-tectoniques.
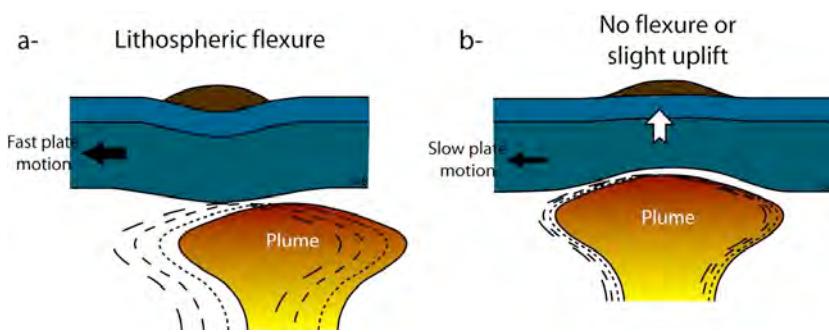
Figure 56: Impacts de la mise en place d'un panache mantellique sous une lithosphère se déplaçant rapidement (a-) ou lentement (b-). a- Le mouvement rapide de la lithosphère ne permet pas au panache mantellique d'éroder thermiquement la base de la lithosphère. La charge de l'édifice volcanique entraine alors une flexure de la lithosphère, identique à celle observée à Hawaii. b- A l'inverse, un déplacement lent de la plaque favorise une érosion thermique efficace de la base de la lithosphère. Ceci induit un déséquilibre isostatique et un mouvement ascendant de la lithosphère qui est a même de contrecarrer la subsidence liée à la charge de l'édifice. Cette évolution peut être appliquée à La Réunion.

2.3- Synthèse sur les approches multi-échelle et multi-disciplinaire

J'ai, depuis le début de ma thèse, développé successivement deux axes de recherche: (1) processus de rifting en domaine continental puis (2) dynamique des édifices volcaniques. La recherche que j'ai mise en œuvre n'est donc pas caractérisée par une constance thématique mais par une constance méthodologique articulée autour de trois principes illustrés par les figures 57, 58, 59 et 60.

1- Etudier les processus géologiques à différentes échelles et intégrer les résultats afin d'élaborer des modèles géologiques globaux.

2- Combiner les approches et les outils pour contraindre au mieux chaque système géologique.

3- Confronter les données naturelles aux résultats de la modélisation (analogique ou numérique) dans le but de valider les interprétations.
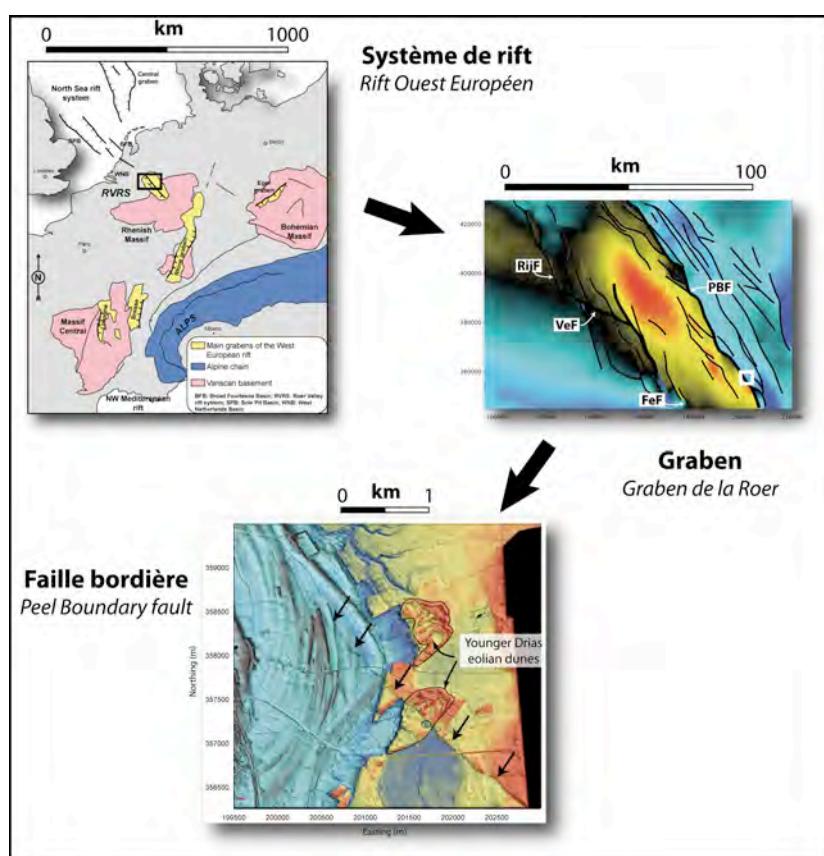
Figure 57: Représentation synthétique des approches multi-échelle et multi-disciplinaire mises en œuvre pour l'étude du Rift Ouest Européen.

L'intérêt premier d'une telle démarche est son applicabilité à n'importe quel contexte géologique. Elle permet en outre d'élaborer des interprétations robustes basées sur les faits géologiques, puis corroborées par des modèles physiques ou expérimentaux. Je compte donc l'appliquer dans l'avenir à d'autres systèmes volcaniques (Galapagos, Karthala, Hawaii) afin d'expliquer les différences majeures en terme de croissance et de déformation des édifices.
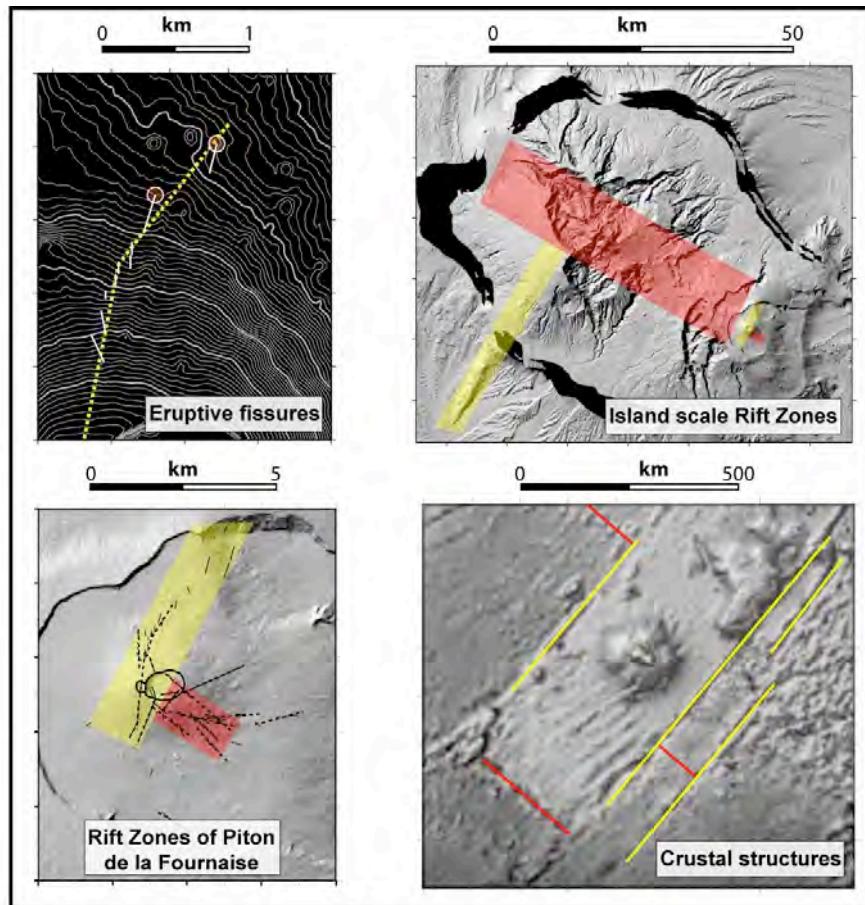
Figure 58: Echelles étudiées au cours de ce travail sur les relations volcano-structurales des volcans basaltiques réunionnais. En jaune et rouges sont représentées les structures N30-40 et N120.
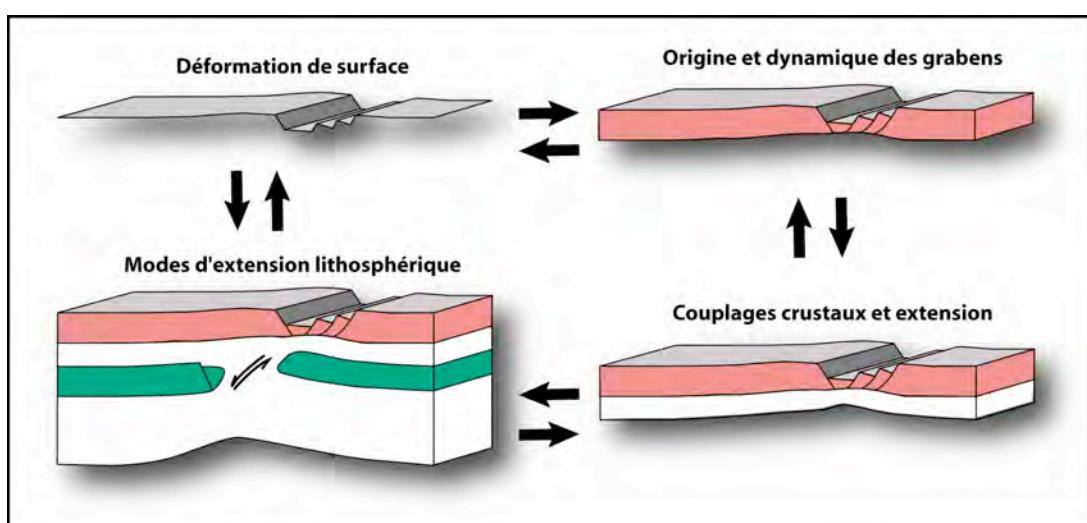
Figure 59: Représentation schématique des différents niveaux structuraux étudiés lors de ma recherche sur les processus de rifting.
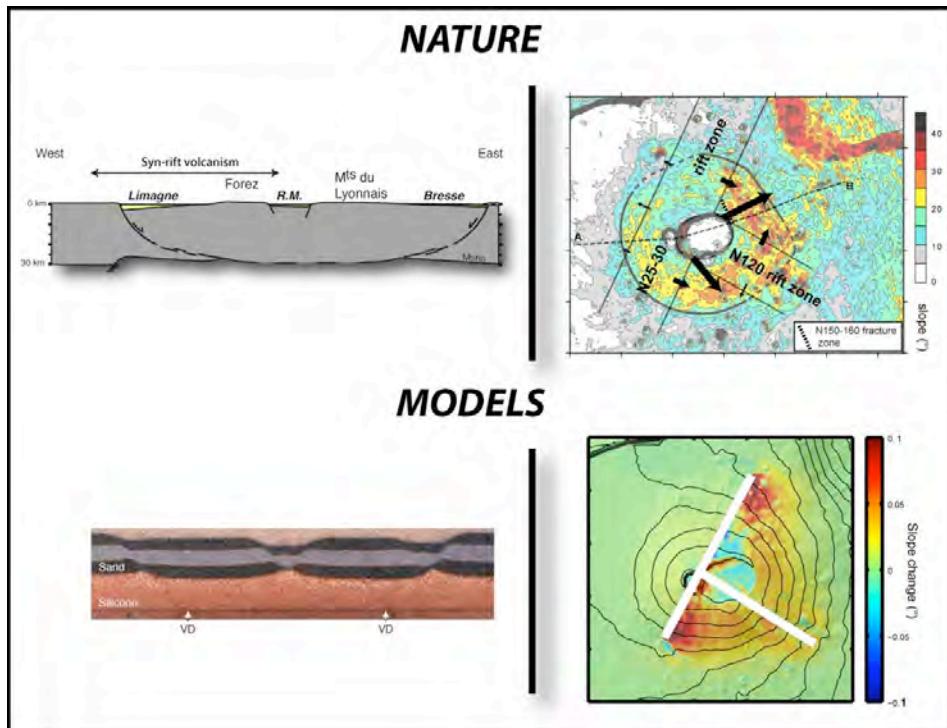
Figure 60: Comparaison modèle / nature illustrant (1) la géométrie de la partie nord du Rift du Massif Central à l'échelle crustale et celle d'une expérience analogique avec deux discontinuités de vitesse basales (extrait de la Figure 24) et (2) la morphologie du cône central du Piton de la Fournaise et un modèle numérique d'injection de dykes le long des rift zones N25-30 et N120 (extrait de la Figure 38).

3- Projets en cours et futurs

Durant les prochaines années, je veux organiser ma recherche autour de quatre axes principaux qui me permettront de poursuivre des travaux déjà initiés et d'en engager de nouveaux. Ces projets sont bâtis sur un réseau de collaboration solide que je souhaite développer.

1- Dynamique des calderas magmatiques.

Cette thématique est une continuité de ce que j'ai déjà entrepris sur la dynamique des calderas (Michon et al., 2007a; 2009b). Nous avons décrit la cyclicité de l'effondrement et proposé une origine mécanique pour l'ensemble des calderas basaltiques. Cependant, les données de déformation, couplées aux données sismiques, doivent permettre de comprendre avec plus de finesse le comportement de l'édifice volcanique lors de l'effondrement caldérique. Par exemple, la figure 61 révèle que les premiers cycles d'effondrement, qui sont les plus longs, sont associés à un gonflement de la zone sommitale. A l'inverse, la seconde phase de l'effondrement est caractérisée par une déflation d'ensemble et une succession de cycles courts. Les données inclinométriques enregistrées lors de l'effondrement caldérique de Miyakejima suggèrent également une première phase d'inflation suivie d'une déflation continue (Ukawa et al., 2000). A Miyakejima, une troisième phase caractérisée par une augmentation de la durée des cycles peut être individualisée. Il m'apparaît donc nécessaire de poursuivre une recherche sur les effondrements caldériques qui se déclinera en quatre points:

1 - Etablir une comparaison de détail des données acquises au Piton de la Fournaise et à Miyakejima. Je souhaite pour cela développée une collaboration avec Nubuo Geshi du Geological Survey of Japan qui travaille sur l'effondrement de la caldera de Miyakejima.
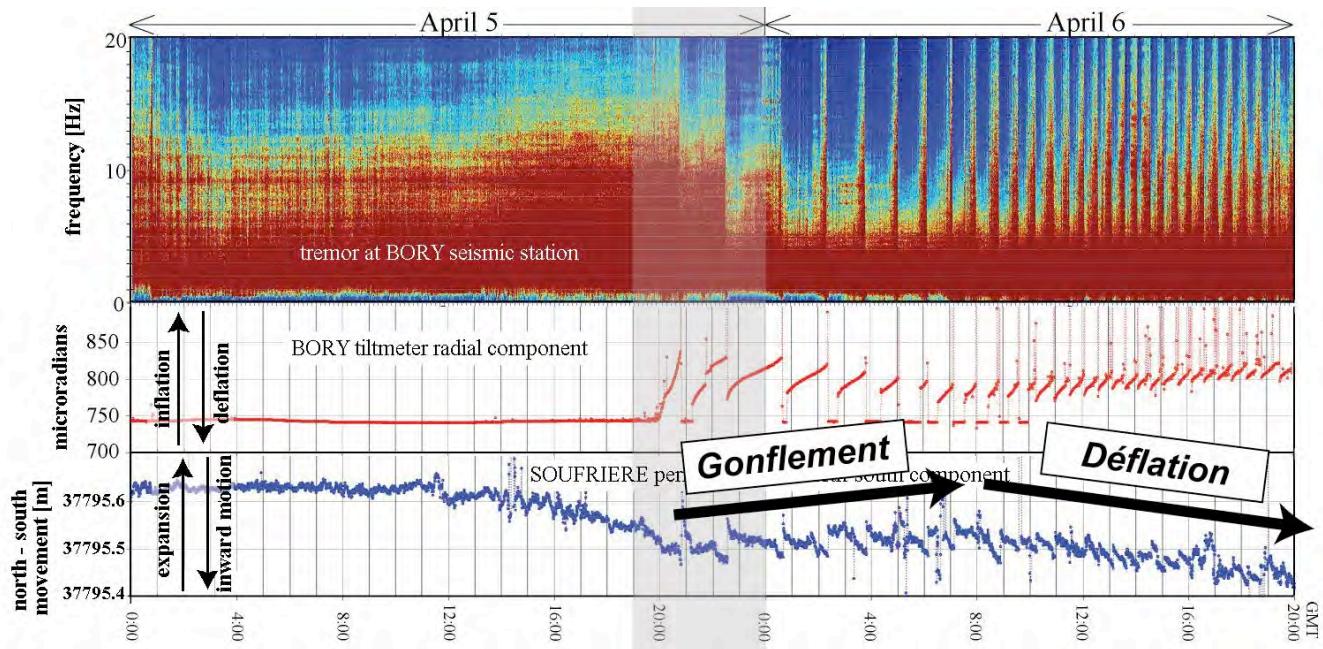
Figure 61: Signal sismique (en haut) et déformation (inclinomètre au milieu et GPS en bas) enregistrés lors de l'effondrement de la caldera du Dolomieu en Avril 2007 (modifié d'après Staudacher et al., 2009).

2- Comprendre la relation entre l'effondrement de la colonne de roche, la dynamique de la chambre magmatique et le flux magmatique. Cette thématique a été abondamment étudiée dans le cadre des calderas siliceuse (e.g Marti et al., 2000), mais peu ou pas en contexte basaltique.

3- Caractériser et quantifier les paramètres physiques (e.g. géométrie des failles bordières, pression magmatique, géométrie du filon "d'évacuation", géométrie de l'édifice, amplitude de la déflation …) contrôlant la dynamique des effondrements en domaine basaltique.

4- Comparer le comportement des calderas basaltiques et des calderas siliceuses.

2- Rôle du contexte géodynamique dans l'évolution des volcans basaltiques.

Ce second axe de recherche s'appuie sur deux projets différents qui permettront d'étudier l'évolution des édifices volcaniques en domaine intra-plaque (La Réunion), en contexte convergent (Stromboli et Vulcano) et domaine extensif (Kerguelen).

- Je co-dirige avec Claudia Romagnoli (Université de Bologne) la thèse de Thibault Catry financée par le programme VINCI dont l'objectif est de déterminer le rôle du contexte géodynamique dans l'évolution des volcans Stromboli, Vulcano et de La Réunion. Ce travail vise à caractériser les paramètres externes et internes influant la construction et la déformation des édifices volcaniques. Le projet s'appuie sur un important jeu de données bathymétriques, d'imagerie et de sismique acquises récemment autour de La Réunion, de Stromboli et de Vulcano lors de plusieurs campagnes océanographiques.

- L'évolution du volcanisme et l'interaction volcanisme - tectonique à Kerguelen sont les deux objectifs principaux du projet DyLiOKer coordonné par Bertrand Moine (Laboratoire Magmas et Volcans, Université Jean Monnet; financement Institut Paul Emile Victor). Dans le cadre de ce projet, je vais participer en Décembre 2009 - Février 2010 à une mission de terrain à Kerguelen afin de caractériser la déformation que j'aurai été étudiée au préalable par télédétection (imagerie SPOT et Modèles Numériques d'Elevation). Ce travail s'effectuera en collaboration avec Nicolas Villeneuve (IRD, La Réunion) et Benjamin van Wyk de Vries (Laboratoire Magmas et Volcans, Université Blaise Pascal).

3- Distribution et géométrie des injections magmatiques dans les volcans basaltiques: Implications sur la stabilité des édifices.

Les volcans basaltiques sont caractérisés par des rift zones le long desquelles se propagent les injections magmatiques latérales (e.g. Walker, 1999). Ces intrusions et l'augmentation de pression de pores associée ont fréquemment été proposées comme moteur des déstabilisations de flanc de grands volumes (MacGuire et al., 1990; Elsworth et Voight, 1995; Iverson, 1995; Hürlimann et al., 2000). Dans ces différents travaux, la déstabilisation du flanc nécessite un plan de glissement pré-existant à pendage externe.

Au Piton des Neiges, l'intense érosion a incisé le volcan sur plusieurs milliers de mètres, laissant à l'affleurement de manière exceptionnelle, le système intrusif interne du volcan. Structuralement, deux types d'intrusions peuvent être distinguées: 1- des filons sub-verticaux répartis de manière plus ou moins homogène dans l'édifice (cf Figure 51), 2- des niveaux sub-horizontaux à très forte concentration d'intrusions situés à des interfaces lithologiques (Figure 62). Ce second groupe est mal connu dans les volcans actif car situé en profondeur.

Nous avons initié, avec Vincent Famin (Maître de Conférences au Laboratoire GéoSciences Réunion), une étude structurale au niveau du cirque de Salazie où la pile de sills s'est injectée entre un massif de gabbro et un dépôt d'avalanche de débris, dans un plan de détachement qui a enregistré une intense déformation ductile puis cassante (Figure 62c). Les différents critères de déformation suggèrent une déformation initiale continue, suivie d'une déstabilisation de flanc de grande ampleur à l'origine des dépôts d'avalanche de débris. Les données montrent que les sills qui se sont ensuite injectés dans le plan de glissement ont favorisé une déformation continue de l'édifice. Ce travail révèle le rôle fondamental que peuvent jouer les intrusions sub-horizontales dans la stabilité des édifices volcaniques (Famin et Michon, in prep).

Il est nécessaire de poursuivre nos investigations de détail dans les autres cirques du Piton des Neiges où affleurent des piles de sills similaires (Figure 63a). Cette étude structurale se fait conjointement à une analyse pétrologique et géochimique afin de déterminer l'impact des grandes déstabilisations dans la dynamique du système éruptif. Pour cela nous souhaitons travailler en collaboration avec Benoît Villemant de l'Institut de Physique du Globe de Paris.

Appliqués aux autres volcans basaltiques, ce mécanisme permettrait de comprendre l'abondance des déstabilisations de flancs qui sont souvent mal expliquées par les modèles mécaniques actuels. L'injection répétée de sills pourrait être à l'origine d'une partie de la déformation du flanc sud du Kilauea qui enregistre un glissement dont les vitesses varient en relation avec l'activité magmatique (Delaney et Denlinger, 1999).
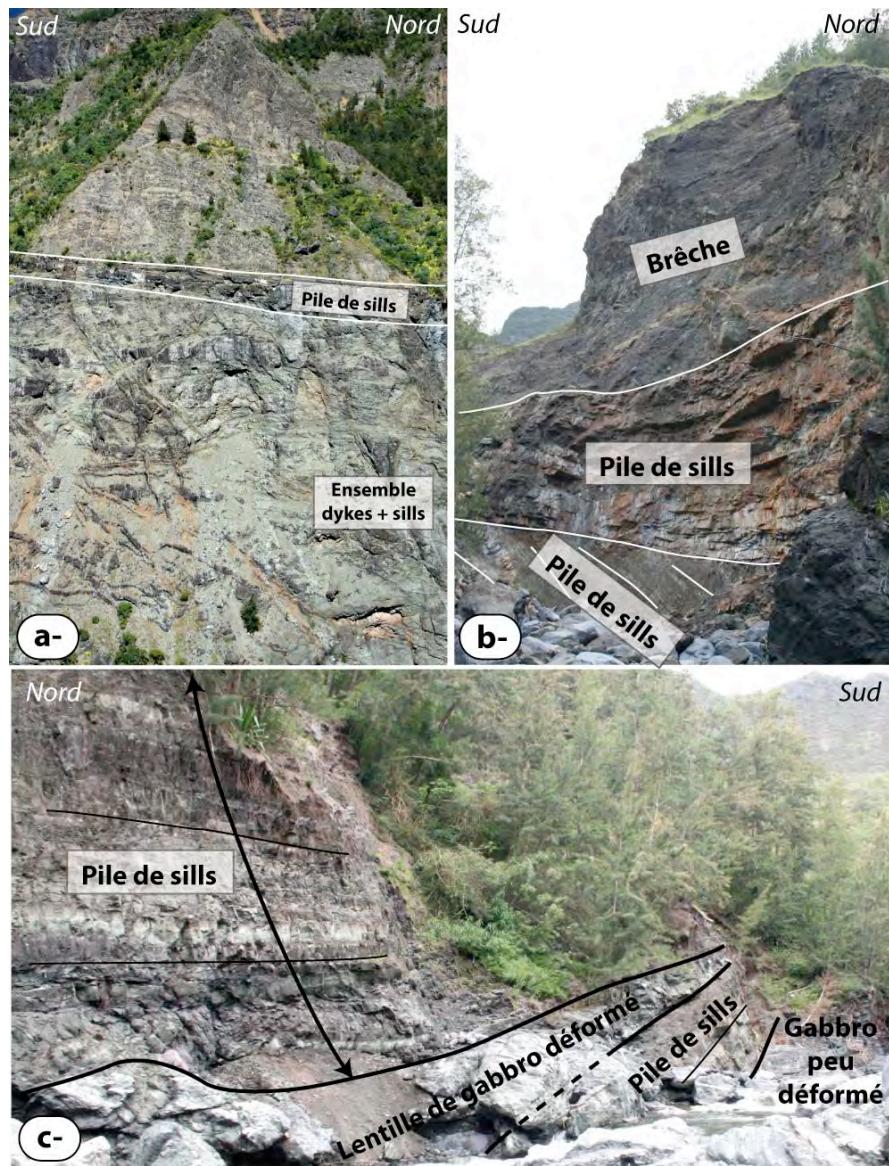
Figure 63: Agencement des injections magmatiques au Piton des Neiges. Ce volcan basaltique présente une abondance de sills principalement organisés en pile sub-horizontales. a- Affleurement d'environ 150 m de haut dans la partie ouest du cirque de Cilaos. b- Falaise de 100-120 m dans la zone amont du cirque de Salazie montrant deux générations d'intrusions. La pile de sills inclinée est recoupée par des sills horizontaux. c- Pile de sills dans une zone d'intense déformation située au toit d'une chambre magmatique dans le cirque de Salazie.

4- Evolution du Piton de la Fournaise.

J'ai commencé à étudier l'évolution du Piton de la Fournaise immédiatement après mon recrutement à l'Université de La Réunion. J'ai pour cela bénéficié d'un soutien financier en 2004 via le BQR de l'Université de La Réunion. Nous avons

également obtenus plusieurs financements annuels et pluri-annuels de la part du Conseil Régional de La Réunion (cf liste des projets dans le curriculum vitae synthétique - section 5). Ce travail a abouti à plusieurs publications sur l'histoire récente du Piton de la Fournaise, i.e. de 60 ka à l'Actuel (Michon et al., 2007b; Michon et Saint-Ange, 2008; Michon et al., 2009b).

La délégation CNRS d'Olivier Merle au Laboratoire GéoSciences Réunion du 1er septembre 2007 et 31 août 2008 a permis d'initier une réévaluation de l'histoire ancienne du Piton de la Fournaise. Cette étude qui s'inscrit dans le projet ANR Volcarisk s'est faite en collaboration avec Patrick Bachèlery et Philippe Mairine (chercheur associé au Laboratoire GéoSciences Réunion). Plusieurs problématiques ont été abordées: 1- La reconnaissance des calderas anciennes; 2- Les événements ou périodes de démantèlement du volcan; 3- La migration des centres éruptifs.

Parallèlement à ce travail, nous avons entrepris au niveau de la Plaine des Sables et de l'Enclos une étude de terrain couplée à une campagne de tomographie de résistivité électrique (collaboration avec Eric Delcher, Laboratoire GéoSciences Réunion). Nous avons confirmé l'hypothèse d'une caldera intermédiaire enfouie sous la Plaine des Sables (Bachèlery, 1981; Lénat et al., 2000) et précisé son tracé dans la partie centrale (Figure 64). Les continuités nord et sud de cette caldera étant encore mal contraintes, nous projetons une seconde campagne géophysique pour l'année 2009.
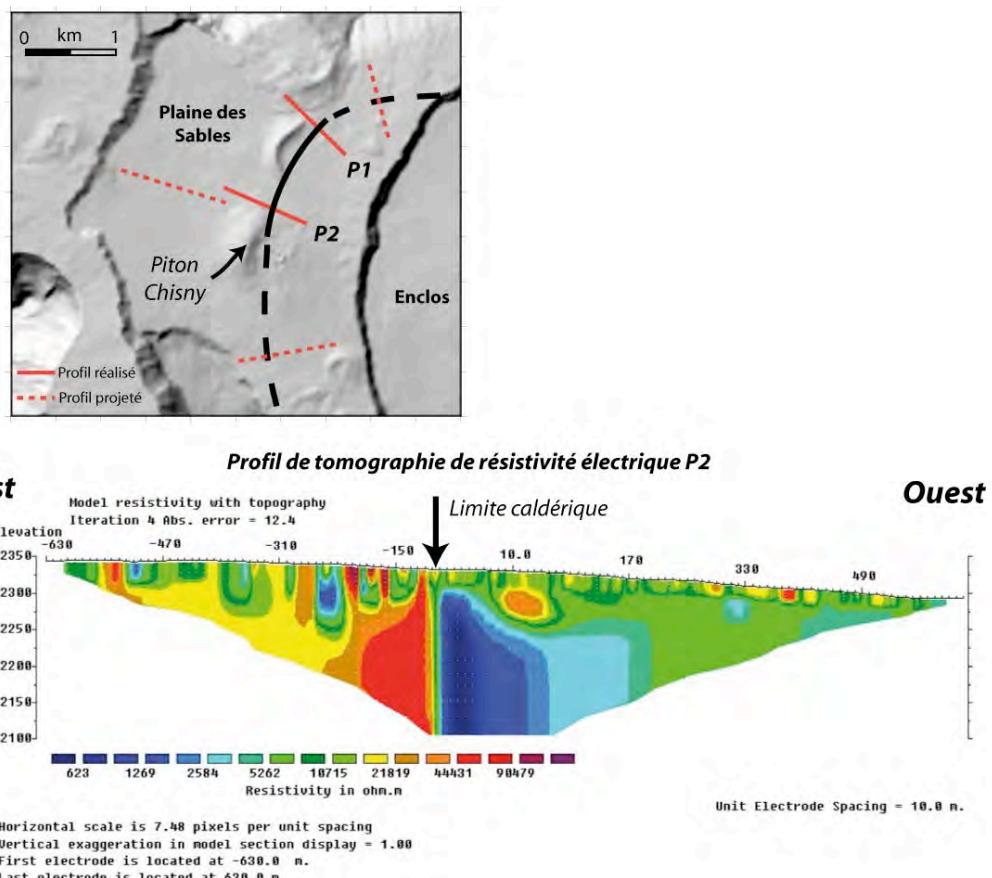
Figure 64: Tracé de la caldera intermédiaire dont la limite est imagée par tomographie de résistivité électrique.

Notre connaissance du Piton de la Fournaise bénéficiera prochainement de forages carottés situés à l'est du Piton Chisny. Cette opération est menée par le Conseil Régional de La Réunion qui souhaite explorer le potentiel géothermique de cette partie du volcan. L'Agence Nationale de la Recherche finance un projet coordonné par Jean-François Lénat (Laboratoire Magmas et Volcans) dont les objectifs sont de fédérer une recherche multi-disciplinaire autour du forage et de valoriser les données. J'ai proposé dans ce cadre un échantillonnage des formations affleurant dans les remparts situés

à proximité de la Plaine des Sables. Intégrés aux données de forage, les logs permettront de déterminer la continuité latérale des ensembles géologiques et d'établir une géométrie 3D de cette partie ancienne du Piton de la Fournaise.

4- Production scientifique

4.1- Revues nationales et internationales à comités de lecture

(1) Merle, O., **L. Michon**, G. Camus, A. Goër de (**1998**) L'extension oligocène sur la transversale septentrionale du rift du Massif Central. Bull. Soc. Géol. Fr., 169, 615-626.

(2) **Michon, L**., O. Merle (**2000**) Crustal structures of the Rhinegraben and the Massif Central grabens: an experimental approach. Tectonics, 19, 896-904.

(3) **Michon, L**., O. Merle (**2001**) The evolution of the Massif Central Rift: Spatio-temporal distribution of the volcanism. Bull. Soc. Géol. Fr., 172, 2, 69-80.

(4) Merle, O., **L. Michon** (**2001**) The formation of the West European Rift: A new model as exemplified by the Massif Central area. Bull. Soc. Géol. Fr., 172, 2, 81-89.

(5) **Michon, L.** (**2003**) Role of the Alpine belt in the Cenozoic lithospheric deformation of Europe: sedimentologic/stratigraphic/tectonic synthesis, Géologie de la France, 1, 115-119.

(6) **Michon, L**., O. Merle (**2003**) Mode of lithospheric extension: conceptual models from analogue modeling. Tectonics, 22, 4, 1028, doi:10.1029/2002TC001435.

(7) **Michon, L**., R.T. van Balen, O. Merle, H. Pagnier (**2003**) The Cenozoic evolution of the Roer Valley rift system integrated at a European scale. Tectonophysics, 367, 101-126.

(8) Miallier, D., **L. Michon**, J. Evin, T. Pilleyre, S. Sanzelle, G. Vernet (**2004**) Volcans de la Chaîne des Puys (Massif Central, France) : point sur la chronologie Vasset-Kilian-Pariou-Chopine. C. R. Géosciences, 336,13345-1353.

(9) **Michon, L**., D. Sokoutis (**2005**). Interaction between the structural inheritance and the stress field during graben and depocentre formation: new insights from an experimental approach. Tectonophysics, 409, 125-146.

(10) **Michon, L**., O. Merle (**2005**) Discussion on "Evolution of the European Cenozoic Rift System: interaction of the Alpine and Pyrenean orogens with their foreland lithosphere, Tectonophysics, 401, 251-256.

(11) **Michon, L**., R.T. van Balen (**2005**) Characterization and quantification of active faulting in the Roer Valley Rift system based on high precision Digital Elevation Models. Quaternary Sci. Rev., 24, 457-474.

(12) Worum, G., **L. Michon** (**2005**) Continuous, syn-sedimentary basin inversion induced by the alpine compression: The Paleogene inversion of the West Netherlands Basin integrated into a NW European scale. J. Geol. Soc., London, 162, 73-85.

(13) Worum, G., **L. Michon**, R.T. van Balen, J.D. van Wees, S. Cloetingh, H. Pagnier (**2005**) Comparison and modelling of the present-day fault activity in the West Netherlands Basin and Roer Valley Rift System (southern Netherlands) in light of their pre-Neogene evolution. Quaternary Sci. Rev., 24, 475-490.

(14) Cloetingh, S., T. Cornu, P.A. Ziegler, F. Beekman and Environmental Tectonics (ENTEC) Working Group (K. Ustaszewski, S.M. Schmid, P. Dèzes, R, Hinsch, K, Decker, G. Lopes Gardozo, M. Granet, G. Bertrand, J. Behrmann, R. van Balen, **L. Michon**, H. Pagnier, S. Rozsa, B. Heck, M. Tesauro, H.G. Kahle, T. Dewez, S. Carretier, T. Winter, N. Hardebol, G. Bada, B. Dost, T. van Eck) (**2006**). Neotectonics and intraplate continental topography of the northern Alpine Foreland. Earth-Science Rev., 74, 127-196.

**(15)** **Michon, L.,** T. Staudacher, V. Ferrazzini, P Bachèlery, and J. Marti (**2007**), April 2007 collapse of Piton de la Fournaise: A new example of caldera formation, Geophys. Res. Lett., 34, L21301, doi:10.1029/2007GL031248.

(16) **Michon, L.,** F. Saint-Ange, P. Bachèlery, N. Villeneuve**,** and T. Staudacher (**2007**), Role of the structural inheritance of the oceanic lithosphere in the magmato-tectonic evolution of Piton de la Fournaise volcano (La Réunion Island), J. Geophys. Res., 112, B04205, doi:10.1029/2006JB004598.

(17) **Michon, L.,** F. Saint-Ange (**2008**), Morphology of Piton de la Fournaise basaltic shield volcano (La Réunion Island): Characterization and implication in the volcano evolution, J. Geophys. Res., 113, B03203, doi:10.1029/2005JB004118.

(18) Merle, O., **L. Michon,** P. Bachèlery. (**2008**), Caldera rim collapse: a hidden volcanic hazard, J. Volcanol. Geotherm. Res., 177, 525-530. doi:10.1016/j.jvolgeores.2008.06.011

(19) **Michon** L., N. Villeneuve, Th. Catry, O. Merle (**2009**), How summit calderas collapse on basaltic volcanoes: new insights from the April 2007 caldera collapse of Piton de la Fournaise volcano. J. Volcanol. Geotherm. Res., special

issue: Piton de La Fournaise, doi: 10.1016/j.jvolgeores.2008.11.003.

(20) **Michon L.,** V. Cayol, L. Letourneur, A. Peltier, N. Villeneuve, T. Staudacher (**2009**), Edifice growth, deformation and rift zone development in basaltic setting: insights from Piton de la Fournaise shield volcano (Réunion Island, Indian Ocean). J. Volcanol. Geotherm. Res., special issue: Piton de La Fournaise, doi: 10.1016/j.jvolgeores.2008.11.002.

(21) Letourneur L., **L. Michon, A.** Gudmundsson. The origin of sill level at Piton des Neiges Volcano (Réunion Island): Field evidence and numerical modelling. J. Volcanol. Geotherm. Res., accepté avec révisions majeures.

Bilan des publications entre 1998 et 2009:

Revue	Nombre d'articles	Nombre d'articles en 1er auteur
Bulletin de la Société Géologique de France (IF=0,75)	3	1
Comptes Rendus Géoscience (IF=0,880)	1	0
Earth-Science Reviews (IF=4,310)	1	0
Géologie de la France	1	1
Geophysical Research Letters (IF=2,744)	1	1
Journal of Geophysical Research (IF=2,953)	2	2
Journal of the Geological Society of London (IF=2,304)	1	0
Journal of Volcanology and Geothermal Research (IF=1,742)	4	2
Quaternary Science Review (IF=4,11)	2	1
Tectonics (IF=2,398)	2	2
Tectonophysics (IF=1,729)	3	3
Total (Impact Factor moyen=2,392)	**21**	**13**
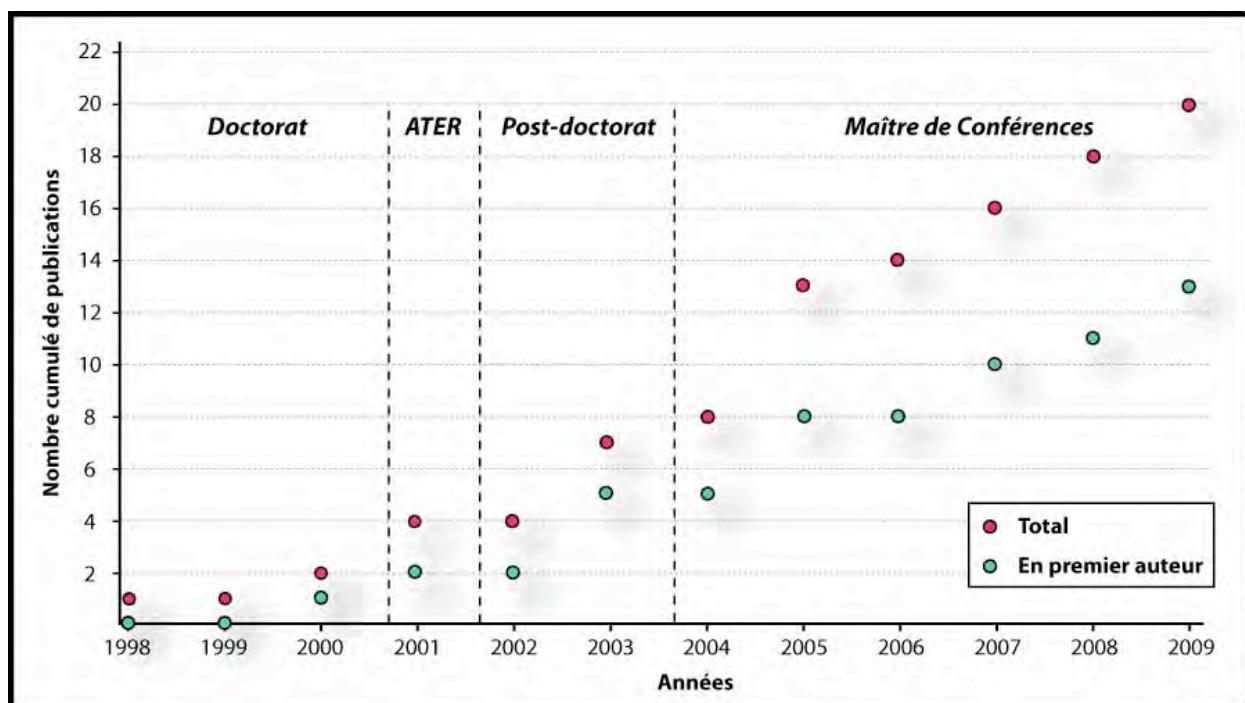
4.2- Congrès nationaux et internationaux

18 présentations orales et 5 posters depuis 1998.

4.3- Diffusion grand public

Michon, L., O. Merle (**1999**) Le rift de la Limagne. *Doc. BRGM., 291,* 115-130.

Merle, O., **L. Michon** (**2001**) Interprétation tectonique du rift du Massif Central. Géologues, 130/131, 92-94.

Cloetingh, S., P. Ziegler, T. Cornu, K. Ustaszewski, S. Schmid, P. Dèzes, R. Hinsch, K. Decker, G. Lopes-Cardoso, M. Graner, G. Bertrand, J. Behrmann, **L. Michon**, H. Pagnier, J.D. van Wees, S. Rozsa, B. Heck, M. Mayer, J. Verdun, H.G. Kahle, U. Fracassi, T. Winter, E. Burov (**2003**) Investigating Environmental Tectonics in the Northern Alpine Foreland of Europe. EOS, 84(36), 356-357.

Merle, O., **L. Michon** (**2006**) Massif Central: une volcanisme venu des Alpes? Eruption, 11, 31-37.

5- Curriculum Vitae synthétique

Laurent MICHON
Célibataire, 3 enfants
Né le 27 Février 1974
Nationalité française

Maître de Conférences
Université de la Réunion
Section CNU 36
Classe normale

Expériences professionnelles

❖ Depuis 2005: Membre de l'Institut de Physique du Globe de Paris, UMR 7154, Equipe Géologie des systèmes volcaniques.

❖ Depuis 2003: Maître de conférences au sein du Laboratoire GéoSciences Réunion de l'Université de la Réunion

❖ 2001-2003: Post-doctorat au TNO-NITG dans le cadre du projet européen ENTEC (ENvironmental TECtonics) coordonné par Sierd Cloetingh (VU Amsterdam).

❖ 2000-2001: Attaché Temporaire d'Enseignement et de Recherche à l'Université Blaise Pascal (Clermont-Ferrand) au sein du Laboratoire Magmas et Volcans

❖ 1997-2000: Moniteur à l'Université Blaise Pascal (Clermont-Ferrand) au sein du Laboratoire Magmas et Volcans

Cursus universitaire

❖ 2000: **Doctorat d'Université** (Sciences de la Terre: spécialité tectonique) soutenue à l'Université Blaise Pascal (Clermont-Ferrand) le 6 Octobre 2000, Mention Très Honorable avec Félicitations.

❖ 1997: **Diplôme d'Etudes Approfondies**: Processus magmatiques et métamorphiques, Volcanologie. Université Blaise Pascal. Mention Bien.

❖ 1996: **Maîtrise** de Sciences de la Terre. Université Blaise Pascal. Mention Assez Bien.

❖ 1995: **Licence** de Sciences de la Terre. Université Sciences et Technique de Nantes.

❖ 1994: **DEUG** de Sciences de la Terre. Université Sciences et Technique de Nantes.

Direction et participation à projets scientifiques

❖ Partenaire du projet ANR "Volcarisk" dédié à la reconnaissance des risques volcaniques associés au Piton de la Fournaise. Coordination Olivier Merle (Laboratoire Magmas et Volcans, Université Blaise Pascal)

❖ Partenaire du projet ANR "Forage Piton de la Fournaise" pour la valorisation du forage d'exploration géothermique du Piton de la Fournaise. Coordination Jean-François Lénat (Laboratoire Magmas et Volcans, Université Blaise Pascal)

❖ Partenaire du projet IPEV "DyLioKer" ayant pour but de comprendre les relations volcano-tectoniques dans un contexte de plateau basaltique. Coordination Bertrand Moin (Laboratoire Magmas et Volcans, Université Jean Monnet)

❖ Partenaire du projet 3F dédié à l'étude de la circulation et au rôle des fluides au sein d'une faille active: la faille de Nojima (Japon). Financement INSU. Coordination Vincent Famin (Laboratoire GéoSciences Réunion).

❖ Responsable du projet "Le risque volcanique au Piton de la Fournaise: source et profondeur des éruptions hors-Enclos" financé par le conseil régional de La Réunion.

❖ Partenaire du projet "Retrouver les grandes déstabilisations du Piton des Neiges pour comprendre celles du Piton de la Fournaise" financé par le conseil régional de La Réunion.

❖ Partenaire du projet pluri-annuel "Reavolc: Recherche autour du volcan de La Réunion" financé par le conseil régional de la Réunion. Coordination Patrick Bachèlery et Gilles Lajoie (Université de La Réunion).

❖ Partenaire du projet PPF "SURVOLtOI 1" qui fédère la recherche en télédétection et analyse spatiale à l'Université de la Réunion, en partenariat avec l'IRD. Coordination Anthony Finizola (Laboratoire GéoSciences Réunion)

❖ Responsable du projet PPF "SURVOLtOI 2" qui fédère la recherche en télédétection et analyse spatiale à l'Université de la Réunion, en partenariat avec l'IRD.

Encadrement et co-direction d'étudiant (M2 et thèse)

Depuis mon recrutement en Septembre 2003, j'ai encadré 3 étudiants de M2 Recherche et je suis actuellement co-directeur d'une thèse en co-tutelle Université de La Réunion - Université de Bologne (Italie).

❖ **Ludovic Letourneur** (2005; M2 Recherche Magmas et Volcans, Clermont-Ferrand): *Etude des relations tectonique-volcanisme dans la dynamique du Piton de la Fournaise, Il de la Réunion.*

Pourcentage d'encadrement: 100%

❖ **Thibault Catry** (2007; M2 Recherche Magmas et Volcans, La Réunion): *Dynamique et impact des événements de type pit-craters au Piton de la Fournaise*

Pourcentage d'encadrement: 50%

Depuis Février 2008: Thèse en co-tutelle financée par le programme VINCI de l'Université Franco-Italienne.

Pourcentage d'encadrement: 50%

❖ **Julia Eychenne** (2008; M2 Recherche Géosciences et Ressources, INPL Nancy): *Origine et conséquences de la déformation interne du Piton des Neiges, Ile de La Réunion*

Pourcentage d'encadrement: 50%

Ludovic Letourneur a ensuite continué en thèse à Göttingen sous la direction d'Agus Gundmundsson (soutenance en juillet 2008). Julia Eychenne commence une thèse au Laboratoire Magmas et Volcans sous la direction d'Alain Gourgaud et Jean-Luc Le Pennec.

Participation à jury de M2 et thèse

❖ Etant donné la co-habilitation du M2 Recherche Magmas et Volcans entre l'Université Blaise Pascal, l'Université Jean Monnet et l'Université de La Réunion, j'ai été membre permanent du jury de M2 Recherche Magmas et Volcans en juin 2007.

❖ Membre du jury de thèse de Delphine Debeuf (Université de La Réunion) en qualité d'examinateur en 2004.

Animation de réseaux et autres responsabilités collectives

❖ Membre élu du Conseil de la Faculté des Sciences et Technologie de l'Université de La Réunion depuis le 1er septembre 2007.

❖ Membre de la commission disciplinaire des Sciences de la Terre de l'Université de La Réunion.

❖ Président de jury de concours interne pour un poste d'Adjoint-Technique en 2007.

❖ Co-éditeur, avec Thomas Staudacher, d'un volume spécial de Journal of Volcanological and Geothermal Research sur le Piton de la Fournaise. Publication prévue en 2009.

Enseignement et responsabilités associées

❖ Le Département d'enseignement des Sciences de la Terre gère sa formation Sciences de la Terre et de l'Atmosphère (STA) et participe activement à la formation Sciences de la Vie et de la Terre dont l'objectif principal est de préparer aux métiers de l'enseignement. Une part importante de mon enseignement est mutualisé entre ces deux formations afin de limiter notre charge horaire, qui est déjà excédentaire (cf les volumes horaires réalisés ces trois dernières années). Je suis responsable des Unités d'Enseignement de Tectonique - Géodynamique, de Magmas et Métamorphisme, de Géologie Régionale, de Géologie de terrain. J'enseigne également dans des Unités d'Enseignement spécifiques à notre parcours LMD (Licence STA et Master Géosphère): Modélisation des processus géologiques, stage de terrain et Volcanologie - édifices et risques volcaniques.

2005-2006: 219 h eq. TD (CM: 41%; TD: 13%; TP: 46%)

2006-2007: 216 h eq. TD (CM: 51%; TD: 24%; TP: 25%)

2007-2008: 234 h eq. TD (CM: 43%; TD: 37%; TP: 20%)

La répartition Cours Magistraux, Travaux Dirigés et Travaux Pratiques évolue peut d'une année à l'autre. J'attache une grande importance à réaliser les cours théoriques, les TD et les TP. Pédagogiquement, ceci permet d'établir une progression régulière au cours du semestre et d'illustrer concrètement en TP et TD les concepts abordés en cours.

❖ Coordination et co-rédaction, avec Thierry Portafaix (Département d'enseignement de Physique), de la maquette de la licence Sciences de la Terre et de l'Atmosphère.

❖ Responsable pédagogique des 2ème et 3ème années de Licence Sciences de la Terre et de l'Atmosphère.

❖ Directeur-adjoint du Département d'enseignement des Sciences de la Terre de l'Université de La Réunion depuis 2004.

6- Références citées

ABCHIR, M. A., SEMET M., BOUDON G., ILDEFONSE P., BACHELERY P., CLOCCHIATI R. (1998) Huge hydrothermal explosive activity on Piton de la Fournaise, Réunion Island: The Bellecombe ash member, 2700 BC, in Volcanic Risk—The European Laboratory Volcanoes, Publ. EUR 18161 EN, edited by R. Casal et al., pp. 447–455, Eur. Comm., Brussels.

ACHAUER U., MASSON F. (2002) Seismic tomography of continental rifts revisited: from relative to absolute heterogeneities. Tectonophysics, 358, 17–37.

ACOCELLA V. (2007) Understanding caldera structure and development: Anoverview of analogue models compared to natural calderas. Earth- Sci. Rev., 85, 125-160.

ALI M.Y., WATTS A.B., HILL I. (2003) A seismic reflection profile study of lithospheric flexure in the vicinity of the Cape Verde Islands. J. Geophys. Res., 108, 2239, doi:10.1029/2002JB002155.

ALLEMAND P., BRUN J.P. (1991) Width of continental rifts and rheological layering of the lithosphere. Tectonophysics, 188, 63-69.

ANNEN C., LENAT J.-F., PROVOST A. (2001) The long-term growth of volcanic edifices: numerical modelling of the role of dyke intrusion and lava-flow emplacement. J. Volcanol. Geotherm. Res., 105, 263-289.

ARTHAUD F., CHOUKROUNE P. (1972) Méthode d'analyse des la tectonique cassante à l'aide des microstructures dans les zones peu déformées: exemple de la plate-forme nord-aquitaine. Rev. Inst. Fr. Pétrole, 27, 715-732.

AUGIER A., FROGER J.L., CAYOL V., FUKUSHIMA Y., TINARD P., SOURIOT T., MORA O., STAUDACHER T., DURAND P., FRUNEAU B., VILLENEUVE N. (2008) The April 2007 eruption at Piton de la Fournaise, Réunion Island, imaged with ENVISAT-ASAR and ALOS-PALSAR data. USEReST workshop, Napoli, Italy.

BACHELERY P. (1981) Le Piton de la Fournaise (Ile de la Réunion): Etude volcanologique, structurale et pétrologique, Ph.D. thesis, Univ. Clermont-Ferrand II, Clermont-Ferrand, France.

BACHELERY P., ROBINEAU B., COURTEAUD M., SAVIN C. (2003) Avalanches de débris sur le flanc occidental du volcan-bouclier Piton des Neiges (Réunion). Bull. Soc. Geol. Fr., 174, 125–140.

BARBARAND J., LUCAZEAU F., PAGEL M., SERANNE M. (2001) Burial and exhumation history of the South Eastern Massif Central (France) constrained by apatite fission tracks thermochronology. Tectonophysics, 335, 275–290.

BARBARAND J., CARTER A., PAGEL M. (2002) Histoire thermotectonique mésocénozoïque du Massif Central— Conséquences sur la déformation de la lithosphère de l'Europe de l'Ouest. 19ème RST. Nantes, 55–56.

BATTAGLIA J., BACHELERY P. (2003) Dynamic dyke propagation deduced from tilt variations preceding the March 9, 1998, eruption of Piton de la Fournaise volcano. J. Volcanol. Geotherm. Res., 120, 289–310.

BAUBRON J.C., DEFAUT B., DEMANGE J. & MAURY R. (1978) Existence d'un volcanisme anté-néogène dans les Causses (Massif Central français). B.R.G.M., Rés. Sci. Techn. SGN pour 1978, p29.

BEHRMANN J., HERMAN O., HORSTMANN M., TANNER D.C., BERTRAND G. (2003) Anatomy and kinematics of oblique continental rifting revealed: a three-dimensional case study of the southeast Upper Rhine Graben (Germany). Am. Assoc. Petrol. Geol. Bull., 87, 1105–1121.

BELLAHSEN N., DANIEL J.-M. (2005) Fault reactivation control on normal fault growth: an experimental study. J. Struct. Geol., 27, 769–780.

BELLON H., HERNANDEZ J. (1979) Chronologie du volcanisme dans le Forez (Massif central français). Place dans l'activité magmatique tertiaire de France. C. R. somm. Soc. Géol. Fr., 4, 175-179.

BELLON H., GILLOT P.Y., NATIVEL P. (1974) Eocene volcanic activity in Bourgogne, Charolais, Massif Central (France). Earth Plan. Sci. Lett., 23, 53-58.

BENES V., DAVY P. (1996) Modes of continental lithospheric extension: experimental verification of strain localization processes. Tectonophysics, 254, 69-87.

BERGER E., BROUSSE R., MAURY R.C. (1975) Recent age (11770 +/- 270 years BP) of last eruptions in Vivarais. C. R. Hebd. Acad. Sci., 280, 4,
419-422.

BERGERAT F. (1977) Le rôle des décrochements dans les liaisons tectoniques entre le fossé de la Saône et du Rhin. Analyse et essai d'interprétation dynamique. C. R. somm. Soc. Géol. Fr., 4, 195-198.

BERGERAT F. (1985) Déformations cassantes et champs de contraintes tertiaires dans la plate-forme européenne. Thèse d'état, univ. P. et M. Curie, 315pp.

BERGERAT F. (1987) Stress fields in the European Platform at the time of Africa-Eurasia collision. Tectonics, 6, 99-132.

BERGERAT F., MUGNIER J.L., GUELLEC S., TRUFFERT C., CAZES M., DAMOTTE B., ROURE F. (1990) Extensional tectonics and subsidence of the Bresse basin: an interpretation from ECORS data. Mém. Soc. Géol. Fr., 156, 145-156.

BERTRAND G., HORSTMANN M., HERMANN O., BEHRMANN J., (2005) Retrodeformation of the southern Upper Rhine Graben: new insights on continental oblique rifting. Quatern. Sci. Rev., 24, 345-352.

BESLIER M.O. (1991) Formation des marges passives et remontée du manteau: modélisation expérimentale et exemple de la marge de la Galice. Mém. et Doc. Géosciences Rennes, 45, 199pp.

BINARD N., HEKINIAN R., CHEMINEE J.L., SEARLE R.C., STOFFERS P. (1991), Morphological and structural studies of the Society and Austral hotspot regions in the South Pacific, Tectonophysics, 186, 293–312.

BODINE J.H., STECKLER M.S., WATTS A.B. (1981) Observations of flexure and rheology of the oceanic lithosphere. J. Geophys. Res., 86, 3695-3707.

BOILLOT G., et al. (1987) Tectonic dénudation of the upper mantle along passive margins: a model based on drilling results (ODP Leg 103, western Galicia margin, Spain). Tectonophysics, 132, 335-342.

BOILLOT G., BESLIER M.O., KRAWCZYK C.M., RAPPIN D., RESTON T.J. (1995) The formation of passive margins: Constraints from the crustal structure and segmentation of the deep Galicia margin (Spain), in: M. S. STOCKER, G. B. SHIMMLIED, A. W. TUDHOPE (Eds) The Tectonic, Sedimentation and Palaeoceanography of the North Atlantic Region, Geol. Soc. Spec. Publ., 90, 71–91.

BONINI M., SOURIOT T., BOCCALETTI M., BRUN J.P. (1997) Successive orthogonal and oblique extension episodes in a rift zone: laboratory experiments with application to the Ethiopian Rift. Tectonics, 16, 347–362.

BONNEVILLE A. (1990) Structure de la lithosphere, in: J-.F. Lénat (eds) Le volcanisme de la Réunion, Cent. de Rech. Volcanol., Clermont-Ferrand, France, 1–18.

BOURGEOIS O., FORD M., DIRAISON M., LE CARLIER DE VESLUD C., GERBAULT M., PIK R., RUBY N., BONNET S. (2007) Separation of rifting and lithospheric folding signatures in the NW-Alpine foreland. Int. J. Earth Sci., 96, 1003-1031.

BRENGUIER F., SHAPIRO N.M., CAMPILLO M., NERCESSIAN A., FERRAZZINI V. (2007) 3-D surface wave tomography of the Piton de la Fournaise volcano using seismic noise correlations. Geophys. Res. Lett., 34, L02305, doi:10.1029/2006GL028586.

BRIOT D., POIDEVIN J.-L., HUGUENEY M. (2001) Apports de l'étude isotopique Sr et Nd des sédiments cénozoïques de Limagne à la compréhension du fonctionnement du rift du Massif central français. Bull. Soc. géol. Fr., 172, 17-24.

BRUN J.P. (1999) Narrow rifts versus wide rifts: inferences for the mechanics of rifting from laboratory experiments. Phil. Trans. R. Soc. Lond., 357, 695-712.

BRUN J.P., MERLE O. (1985) Strain patterns in models of spreading-gliding nappes. Tectonics. 4, 7, 705-719.

BRUN J.P., BESLIER M.O. (1996) Mantle exhumation at passive margin. Earth Planet. Sci. Lett., 142, 161-173.

BRUN J.P., GUTSCHER M.A., DEKORP-ECORS Teams (1992) Deep crustal structure of the Rhine Graben from DEKORP-ECORS seismic reflexion data : a summary. In: ZIEGLER P.A. (Eds) Geodynamics of Rifting, Volume I. Case History Studies on Rifts: Europe and Asia. Tectonophysics, 208, 139-147.

BUCHNER F. (1981) Rhinegraben: horizontal stylolites indicating stress regimes of earlier stages of rifting. Tectonophysics, 73, 113-118.

BUCK W.R. (1991) Modes of continental lithosphere extension. J. Geophys. Res., 96, 20161-20178.

BUCKINGHAM E. (1915) The principle of similitude. Nature, 96, 396–397.

BUDWEG M., BOCK G., WEBER M. (2006) The Eifel Plume—imaged with converted seismic waves, Geophys. J. Int., 166, 579–589

BURG J.P., ETCHECOPAR A. (1980) Détermination des systèmes de contraintes liés à la tectonique cassantes au cœur du Massif Central français: la Région de Brioude (Haut-Allier). C. R. Acad. Sci. Paris, 290, 397-400.

CAIRE A. (1977) Interprétation unitaire des fossés des Limagnes, de la Bresse et du Rhin. C. R. Acad. Sci. Paris, 285, 1279-1281.

CAYOL V., CORNET F.H. (1997) 3D mixed boundary elements for elastostatic deformation field analysis, Int. J. Rock Mech. Min. Sci., 34, 275-287.

CECCHI E., VAN WYK DE VRIES B., LAVEST J.M. (2005) Flank spreading and collapse of weak-cored volcanoes. Bull. Volcanol., 67, 72–91, doi:10.1007/s00445-004-0369-3.

CHAMBON S. (1997) Géochronologie 39Ar/40Ar de quelques amphiboles de Limagne. Mém. Maîtrise, Univ. Clermont-Ferrand, 16p.

CHANTEPIE M. (1990) Le volcanisme basaltique miocène et pliocène dispersé dans la région de Clermont Ferrand et sur le plateau des Dômes. Etude pétrologique et géochronologique. Implications volcanologiques et morphotectoniques. Mém. D.E.A., Univ. Clermont-Ferrand, 40pp.

CHARVIS P., LAESANPURA A., GALLART J., HIRN A., LEPINE J.-C, DE VOOGD B., MINSHULL T.A., HELLO Y., PONTOISE B. (1999) Spatial distribution of hotspot material added to the lithosphere under la Réunion, from wideangle seismic data. J. Geophys. Res., 104, 2875–2893.

CHEGUER L. (1996) Les laves miocènes de la Limagne d'Allier et des plateaux bordiers (Massif Central français). Caractérisation d'une série magmatique alcaline sous-saturée (basanite-phonolite) associée à un rifting continental. Thèse 3ème cycle, Univ. Clermont-Ferrand, 201p.

CHEMENDA A., DEVERCHERE J., CALAIS E. (2002) Threedimensional laboratory modelling of rifting: Application to the Baikal rift, Russia. Tectonophysics, 356, 253–273.

CHEVALLIER L. (1979) Structures et évolution du volcan Piton des Neiges, île de la Réunion: Leurs relations avec les structures du Bassin des Mascareignes, Océan Indien occidental, Ph.D. thesis, Grenoble Univ., Grenoble, France, 187 pp.

CHEVALLIER L., VATIN-PERIGNON N. (1982) Volcano-structural evolution of Piton des Neiges, Reunion Island, Indian Ocean. Bull. Volcanol., 45, 285-298.

CHOROWICZ J., DEFFONTAINES B. (1993) Transfer faults and pull-apart model in the Rhinegraben from analysis of multisource data. J. Geophys. Res., 98, 14339-14351.

CLIFTON A.E., SCHLISCHE R.W., WITHJACK M.O., ACKERMANN R.V. (2000) Influence of rift obliquity on fault population systematics: results of experimental clay models. J. Struct. Geol., 22, 1491–1509.

CLOETINGH S., ZIEGLER P.A., BEEKMAN F., ANDRIESSEN P.A.M., HARDENBOL N., DEZES P. (2005) Intraplate deformation and 3D rheological structure of the Rhine Rift System and adjacent areas of the northern Alpine foreland. Int. J. Earth Sci., 94, 758–778.

COCHRAN J.R., MARTINEZ F. (1988) Evidence from the northern Red Sea on the transition from continental to oceanic rifting. Tectonophysics, 153, 25–53, 1988.

CORTI G., VAN WIJK J., CLOETINGH S., MORLEY C.K. (2007) Tectonic inheritance and continental rift architecture: Numerical and analogue models of the East African Rift system. Tectonics, 26, TC6006, doi:10.1029/2006TC002086.

COURTILLOT, V., BESSE D., VANDAMME D., MONTIGNY R., JAEGGER J. J., CAPETTA H. (1986) Deccan flood basalts at the Cretaceous/Tertiary boundary?. Earth Planet. Sci. Lett., 80, 361–374.

CULLEN A.B., MacBIRNEY A.R., ROGERS R.D. (1987) Structural controls on the morphology of galapagos shields. J. Volcanol. Geotherm. Res., 34, 143-151.

DAVY P., COBBOLD P.R. (1991) Experiments on shortening of a 4-layer model of the continental lithosphere. Tectonophysics, 188, 1–25.

DELANEY P.T., DENLINGER R.P. (1999) Stabilization of volcanic flanks by dike intrusion: an example from Kilauea. Bull. Volcanol., 61, 356-362.

DELANEY P.T., DENLINGER R.P., LISOWSKI M., MIKLIUS A., OKUBO P.G., OKAMURA A.T., SAKO M.K. (1998) Volcanic spreading at Kilauea. 1976– 1996, J. Geophys. Res., 103, 18003–18023.

DE LUGT I.R., VAN WEES J.D., WONG Th.E. (2003) The tectonic evolution of the southern Dutch North Sea during the Paleogene: a case study for basin inversion in pulses. Tectonophysics, 373, 141-159

DE VOOGD B., POU PALOME S., HIRN A., CHARVIS P., GALLART J., ROUSSET D., DANOBEITIA J., PERROUD H. (1999) Vertical movements and material transport during hotspot activity: Seismic reflection profiling offshore la Réunion. J. Geophys. Res., 104, 2855–2874.

DEZES P., SCHMID S.M., ZIEGLER P.A. (2004) Evolution of the european cenozoic rift system; interaction of the Pyrenean and Alpine orogens with the foreland lithosphere. Tectonophysics, 389, 1–33.

DIETERICH J.H., DECKER R.W. (1975) Finite element modeling of surface deformation associated with volcanism. J. Geophys. Res., 80, 4094- 4102.

DOWNES H., REICHOW M.K., MASON P.R.D., BEARD A.D., THIRLWALL M.F. (2003) Mantle domains in the lithosphère beneath the French Massif Central: trace élément and isotopic évidence from mantle clinopyroxenes. Chem. Geol., 200, 71-87.

DUCHENE S., BLICHERT-TOFT J., LUAIS B., TELOUK P., LARDEAUX J.M., ALBAREDE F., (1997) The Lu–Hf dating of garnets and the ages of the alpine high-pressure metamorphism. Nature, 387, 586–589.

DUFFIELD W.A., STIELJES L., VARET J. (1982) Huge landslide blocks in the growth of Piton de la Fournaise, La Réunion, and Kilauea Volcano, Hawaii. J. Volcanol. Geotherm. Res., 12, 147–160.

EDEL J.-B., SCHULMANN K., ROTSTEIN Y. (2007) The Variscan tectonic inheritance of the Upper Rhine Graben: evidence of reactivations in the Lias, Late Eocene–Oligocene up to the recent. Int. J. Earth Sci. (Geol Rundsch), 96, 305–325.

ELSWORTH D., VOIGHT B. (1995) Dike intrusion as a trigger for large earthquake and the failure of volcano flanks. J. Geophys. Res., 100, 6005-6024.

FACCENNA C., PIROMALLO C., CRESPO-BLANC A., JOLIVET L., ROSSETTI F. (2004) Lateral slab deformation and the origin of the western Mediterranean arcs. Tectonics, 23, TC1012, doi:10.1029/2002TC001488.

FÆRSETH R.B., KNUDSEN B.E., LILJEDAHL T., MIDBØE P.S, SØDERSTRØM B. (1997) Oblique rifting and sequential faulting in the Jurassic development of the northern North Sea. J. Struct. Geol., 19, 1285–1302.

FILSON J., SIMKIN T., LEU L.-K. (1973) Seimicity of a caldera collapse: Galapagos Islands 1968. J. Geophys. Res., 78, 8591-8622.

FRETZDORFF S., STOFFERS P., DEVEY C.W., MUNSCHY M. (1998) Structure and morphology of submarine volcanism in the hotspot region around Réunion Island, western Indian Ocean. Mar. Geol., 148, 39–53.

FROGER J.-L., FUKUSHIMA Y., BRIOLE P., STAUDACHER T., SOURIOT T., VILLENEUVE N. (2004) The deformation field of the August 2003 eruption at Piton de la Fournaise, Reunion Island, mapped by ASAR interferometry. Geophys. Res. Lett., 31, L14601, doi:10.1029/2004GL020479.

FROITZHEIM N., EBERLI G.P. (1990) Extensional detachment faulting in the évolution of a Tethys passive continental margin, eastern Alps, Switzerland. Geol. Soc. Am. Bull., 102, 1297-1308.

FUKUSHIMA Y., CAYOL V., DURAND P. (2005) Finding realistic dike models from interferometric synthetic aperture radar data: The February 2000 eruption at Piton de la Fournaise. J. Geophys. Res., 110, B03206, doi: 10.1029/2004JB003268.

GALLART J., DRIARD L., CHARVIS P., HIRN A., LEPINE J.-C., DIAZ J., DE VOOGD B. (1999) Perturbation of the lithosphere along the hotspot track of La Réunion from an onshore-offshore seismic transect. J. Geophys. Res., 104, 2895-2908.

GAUTHERON C., MOREIRA M., ALLEGRE C. (2005) He, Ne and Ar composition of the European lithospheric mantle. Chem. Geol., 217, 97-112.

GELUK M.C., DUIN E.J., DUSAR M., RIJKERS R.H, VAN DEN BERG M.W., VAN ROOIJEN P. (1994) Stratigraphy and tectonics of the Roer Valley Graben. Geol. Mijnb., 73, 129–141.

GESHI N., SHIMANO T., CHIBA T., NAKADA S. (2002) Caldera collapse during the 2000 eruption of Miyakejima Volcano, Japan. Bull. Volcanol., 64, 55–68.

GILLOT P.-Y., LEFEVRE J.-C., NATIVEL P.E. (1994) Model for the structural evolution of the volcanoes of Reunion Island. Earth Planet. Sci. Lett., 122, 291–302.

GOES S., SPAKMAN W., BIJWAARD H., (1999) A lower mantle source for

Central European Volcanism. Science 286, 191–193.

GRANET M., WILSON M., ACHAUER U. (1995) Imaging a mantle plume beneath the French Massif Central. Earth Planet. Sci. Lett., 136, 281-296.

GUERIN G., GILLOT P.Y. (2007) New elements of chronology of "Bas Vivarais" Pleistocene volcanism (Ardeche, France) by thermoluminescence dating. C.R. Geosciences, 339, 40-49.

HAASE K.M., GOLDSCHMIDT B., GARBE-SCHOENBERG C.D. (2004) Petrogenesis of Tertiary continental intra-plate lavas from the Westerwald region, Germany. J. Petrol., 45, 883-905

HINSKEN S. USTASZEWSKI K., WETZEL A. (2007) Graben width controlling syn-rift sedimentation: the Palaeogene southern Upper Rhine Graben as an example. Int. J. Earth Sci. (Geol Rundsch), 96, 979–1002.

HOERNLE K., ZHANG Y.S., GRAHAM D. (1995) Seismic and geochemical evidence for large-scale mantle upwelling beneath the eastern Atlantic and western and central Europe. Nature, 374, 34-39.

HOUTGAST R.F., VAN BALEN R.T. (2000) Neotectonics of the Roer Valley Rift System, the Netherlands. Global Planet. Change, 27, 131–146.

HOUTGAST R.F., VAN BALEN R.T., BOUWER L.M., BRAND G.B.M., BRIJKER J.M. (2002) Late Quaternary activity of the Feldbiss Fault Zone, Roer Valley Rift System, the Netherlands, based on displaced fluvial terrace fragments. Tectonophysics, 352, 295–315.

HUBBERT K.M. (1937) Theory of scale models as applied to the study of geologic structures. Geol. Soc. Amer. Bull., 48, 1459–1520.

HUCKENHOLZ H.G. (1983) Tertiary volcanism of the Hocheifel area. In: K. FUCHS, VON GEHLEN K., MALZER H., MURAWSKI H., SEMMEL A. (Eds) Plateau uplift, the Rhenish Shield – A case history. Springer-Verlag, Berlin, 121-128.

HUISMANS R.S., BEAUMONT C.H. (2002) Asymmetric lithospheric extension: The role of frictional plastic strain softening inferred from numerical experiments. Geology, 30, 211–214.

HUISMANS R.S., BEAUMONT C.H. (2003) Symmetric and asymmetric lithospheric extension; relative effects of frictional-plastic and viscous strain softening. J. Geophys. Res., 108, doi:10.1029/2002JB002026.

HÜRLIMANN M. GARCIA-PIERA J.O., LEDESMA A. (2000) Cause and mobility of large volcanic landslides: application to Tenerife, Canary Islands, J. Volcanol. Geotherm. Res., 103, 121-134.

ILLIES J.H. (1972) The Rhine graben rift system — plate tectonics and transform faulting. Geophys. Surv., 1, 27–60.

ILLIES J.H. (1974) Taphrogenesis and plate tectonics. In: FUCHS K., ILLIES J.H. (Eds) Approaches to taphrogenesis, Stuttgart, Schweizerbart, 433-460.

ILLIES J.H. (1981) Mechanism of graben formation. Tectonophysics, 73, 249–266.

ITO T., YOSHIOKA S. (2002) A dike intrusion model in and around Miyakejima, Niijima and Kozushima in 2000. Tectonophysics, 359, 171–187.

IVERSON R.M. (1995) Can magma-injection and groundwater forces cause massive landslides on Hawaiian volcanoes? J. Volcanol. Geotherm. Res., 66, 295-308.

JUNG J., BROUSSE R. (1962) Les provinces néogènes et quaternaires de la France. Bull. Serv. Carte géol. France, 58, 1-61.

KELLER J., KRAML M., HENJES-KUNST F. (2002) 40Ar/39Ar single crystal laser dating of early volcanism in the Upper Rhine Graben and tectonic implications. SCHWEIZ. MINERAL. PETROGR. MITT., 82, 121–130

KING G.C.P., STEIN R.S., LIN J. (1994) Static stress changes and the triggering of earthquake. Bull. Seism. Soc. Am., 84, 935-953.

KOOI H., CLOETINGH S., REMMELTS G. (1991) Lithospheric dynamics and the rapid Pliocene-Quaternary subsidence phase in the Southern North Sea Basin. Tectonophysics, 192, 245–259.

KUMAGAI H., OHMINATO T., NAKANO M., OOI M., KUBO A., INOUE H., OIKAWA J. (2001) Very-long-period seismic signals and the caldera formation at Miyake Island, Japan. Science, 293, 687-690.

KUSZNIR N.J., ZIEGLER P.A. (1992) The mechanics of continental extension and sedimentary basin formation: A simple-shear/pure-shear flexural cantilever model. Tectonophysics, 215, 117–131.

LABAZUY P. (1991) Instabilités au cours de l'évolution d'un édifice volcanique en domaine intraplaque océanique: Le Piton de la Fournaise (Ile de la Reunion). Ph.D. thesis, University of Clermont-Ferrand, France, 260 pp

LABAZUY P. (1996) Recurrent landslides events on the submarine flank of Piton de la Fournaise volcano (Reunion Island). In: McGUIRE W.J., JONES A.P., NEUBERG J. (eds) Volcano instability on the Earth and other planets. J. Geol. Soc. London. Spec. Pub., 110, 295–306.

LACOMBE O., JOLIVET L. (2005) Structural and kinematic relationships between Corsica and the Pyrenees-Provence domain at the time of the Pyrenean orogeny. Tectonics, 24, TC1003, doi:10.1029/2004TC001673.

LARROQUE J., LAURENT P. (1988) Evolution of the stress field pattern in the south of the Rhine Graben from the Eocene to the present. Tectonophysics, 148, 41–58.

LAVIER L.L., MANATSCHAL G. (2006) A mechanism to thin the continental lithosphere at magma-poor margins. Nature, 440, doi:10.1038/nature04608.

LEFORT J.P., AGARWAL B.N.P. (1996) Gravity evidence for Alpine buckling of the crust beneath the Paris Basin. Tectonophysics, 258, 1-14.

LEFORT J.P., AGARWAL B.N.P. (2002) Topography of the Moho undulations in France from gravity data: their age and origin. Tectonophysics, 350, 193-213.

LE GALL B., GERNIGON L., ROLET J., EBINGER C., GLOAGUEN R., NILSEN O., DYPVIK H., DEFFONTAINES B., MRUMA A. (2004) Neogene-Holocene rift propagation in central Tanzania: Morphostructural and aeromagnetic evidence from the Kilombero area. Geol. Soc. Am. Bull., 116, 490–510.

LENAT J.-F. BACHELERY P., BONNEVILLE A., HIRN A. (1989) The beginning of the 1985-1987 eruptive cycle at Piton de la Fournaise (La Reunion); New insights in the magmatic and volcano-tectonic systems. J. Volcanol. Geotherm. Res., 36, 209-232.

LENAT J.-F., FITTERMAN D., JACKSON D.B., LABAZUY P. (2000) Geoelectrical structure of the central zone of Piton de la Fournaise volcano (Réunion). Bull. Volcanol., 62, 75–89.

LENAT J.-F., GIBERT-MALENGREAU B., GALDEANO A. (2001a) A new model for the evolution of the volcanic island of Réunion (Indian Ocean), J. Geophys. Res., 106, 8646– 8663.

LENAT J.-F., BACHELERY P., DESMULIER F. (2001b) Genèse du champs de lave de l'Enclos Fouqué: une éruption d'envergure exceptionnelle au Piton de la Fournaise (Réunion) au 18ème siècle. Bull. Soc. géol. Fr., 172, 177-188.

LENOIR X., DAUTRIAT J.M., BRIQUEU L., CANTAGREL J.M., MICHARD A. (2000a) Nouvelles données géochronologiques, géochimiques et isotopiques sur le volcanisme du Forez: relation avec l'évolution cénozoïque du manteau du Massif Central. C. R. Acad. Sci. Paris, 330, 201-207.

LENOIR X., GARRIDO C.J., BODINIER J.-L., DAUTRIA J.M (2000b) Contrasting lithospheric mantle domains beneath the Massif Central (France) revealed by geochemistry of peridotite xenoliths. Earth Planet. Sci. Lett., 181, 359-375.

LETOURNEUR L., PELTIER A., STAUDACHER TH., GUDMUNDSSON A. (2008) The effects of rock heterogeneities on dyke paths and asymmetric ground deformation: The example of Piton de la Fournaise (Réunion Island). J. Volcanol. Geotherm. Res., 173, 289-302.

LEZZAR K.E., TIERCELIN J.J., LE TURDU C., COHEN A.S., REYNOLDS D.J., LE GALL B., SCHOLZ C.A. (2002) Control of normal fault interaction on the distribution of major Neogene sedimentary depocenters, Lake Tanganyika, East African rift. Bull. Am. Assoc. Pet. Geol., 86, 1027–1059.

LICKORISH W.H., FORD M., BURGISSER J., COBBOLD P.R. (2002) Arcuate thrust systems in sandbox experiments: a comparison to the external arcs of the Western Alps. Geol. Soc. Am. Bull., 114, 1089–1107.

LIPPOLT H.J. (1983) Distribution of the volcanism in space and time. In: K. FUCHS, VON GEHLEN K., MALZER H., MURAWSKI H., SEMMEL A. (Eds) Plateau uplift, the Rhenish Shield – A case history. Springer-Verlag, Berlin, 112-120.

LISTER G.S., ETHERIDGE M.A., SYMONDS P.A. (1991) Detachment models for the formation of passive continentale margins. Tectonics, 10, 1038-1064.

LOPES CARDOSO G.G.O., BEHRMANN J.H. (2006) Kinematic analysis of the Upper Rhine Graben boundary fault system. J. Struct. Geol., 28, 1028-1039.

MacBIRNEY A.R., WILLIAMS H. (1969) Geology and petrology of the Galapagos Islands. Mem. Geol. Soc. Am., 118,

MacCLAY K.R., WHITE M.J. (1995) Analogue modelling of orthogonal

and oblique rifting. Mar. Pet. Geol., 12, 137–151.

MacCLAY K.R., DOOLEY T., WHITEHOUSE P., MILLS M. (2002) 4-D evolution of rift systems: insights from scaled physical models. Am. Assoc. Pet. Geol., 86, 935–959.

MacDONALD G.A. (1965) Hawaiian calderas. Pac. Sci., 19, 320–334.

MacDONALD G.A. (1972) Volcanoes, Prentice-Hall, Englewood Cliffs, N. J., 510 pp.

MacDONALD G.A., ABBOTT A.T. (1970) Volcanoes in the Sea: The Geology of Hawaii, Univ. Press of Hawaii, Honolulu, 441 pp.

MacDOUGALL I. (1971) The geochronology and evolution of the Young island of Réunion, Indian Ocean. Geochim. Cosmochim. Acta, 35, 261–270.

MacGUIRE W.J., PULLEN A.D., SAUNDERS S.J. (1990) Recent dyke-induced large-scale block movement at Mount Etna and potential slope failure. Nature, 343, 357–359.

MacKENZIE D. (1978) Some remarks on the development of sedimentary basins. Earth Planet. Sci. Lett., 40, 25-42.

MALENGREAU B., J.-F. LENAT, J.-L. FROGER (1999) Structure of the Réunion Island (Indian Ocean) inferred from the interpretation of gravity anomalies. J. Volcanol. Geotherm. Res., 88, 131–146.

MALKOVSKY M. (1987) The Mesozoic and Tertiary basins of the Bohemian Massif and their evolution. Tectonophysics, 137, 31-42.

MANATSCHAL G. (2004) New models for evolution of magma-poor rifted margins based on a review of data and concepts from West Iberia and the Alps. I. J. Earth Sci., 93, 432-466.

MANATSCHAL G., BERNOULLI D. (1999) Architecture and tectonic evolution of nonvolcanic margins: present-day Galicia and ancient Adria. Tectonics, 18, 1099-1119.

MARINONI L.B., GUDMUNDSSON A. (2000) Dykes, faults and palaeostresses in the Teno and Anaga massifs of Tenerife (Canary Islands). J. Volcanol. Geotherm. Res., 103, 83–103.

MARTI J., GUDMUNDSSON A. (2000) The Las Cañadas caldera (Tenerife, Canary Islands): an overlapping collapse caldera generated by magma-chamber migration. J. Volcanol. Geotherm. Res., 103, 161-173.

MARTI J., MITJAVILA J., ROCA E., APARICIO A. (1992), Cenozoic magmatism of the Valencia trough (western Mediterranean): Relationship between structural evolution and volcanism. Tectonophysics, 203, 145–165.

MARTI J., ABLAY G.J., REDSHAW L.T., SPARKS R.S.J. (1994) Experimental studies of collapse calderas. J. Geol. Soc., London, 151, 919-929, doi:10.1144/gsjgs.151.6.0919.

MARTI J., FOLCH A., NERI A., MACEDONIO G. (2000) Pressure evolution during explosive caldera-forming eruptions. Earth Planet. Sci. Lett., 175, 275-287.

MAURY R.C., VARET J. (1980) Le volcanisme tertiaire et quaternaire en France. In: A. AUTRAN et J. DERCOURT (Eds) Evolutions géologiques de la France. Mém. B.R.G.M., 107, 137-159.

MERGOIL J., BOIVIN P. (1993) Le Velay. Son volcanisme et les formations associées. Notice de la carte au 1/10000. Géol.Fr., 3, 3-96.

MERLE O., MICHON L. (2001) The formation of the West European rift: a new model as exemplified by the Massif Central area. Bull. Soc. Géol Fr., 172, 213–221.

MERLE O., LENAT J.-F. (2003) Hybrid collapse mechanism at Piton de la Fournaise volcano, Reunion Island, Indian Ocean. J. Geophys. Res., 108(B3), 2166, doi:10.1029/2002JB002014.

MERLE O., MICHON L., CAMUS G., GOER A. de (1998) L'extension oligocène sur la transversale septentrionale du rift du Massif Central. Bull. Soc. Géol. Fr., 169, 615-626.

MERLE O., BARDE-CABUSSON S., MAURY R.C., LEGENDRE C., GUILLE G., BLAIS S., (2006) Volcano core collapse triggered by regional faulting. J. Volcanol. Geotherm. Res., 158, 269-280.

MIALLIER D., MICHON L., EVIN J., PILLEYRE T., SANZELLE S., VERNET G. (2004) Volcans de la Chaîne des Puys (Massif Central, France) : point sur la chronologie Vasset-Kilian-Pariou-Chopine. C. R. Géosciences, 336,13345-1353.

MICHON L. (2001) Dynamique de l'extension continentale—Application au Rift Ouest-Européen par l'étude de la Province du Massif Central. Thèse 3ème cycle, Université Blaise Pascal, Clermont-Ferrand (France), Mém. Géosciences Rennes, 99, 266pp.

MICHON L., MERLE O. (2000) Crustal structures of the Rhinegraben and the Massif Central grabens: an experimental approach. Tectonics, 19, 896-904.

MICHON L., MERLE O. (2001) The evolution of the Massif Central rift: spatio-temporal distribution of the volcanism. Bull. Soc. géol. Fr., 172, 201-211.

MICHON L, MERLE O (2005) Discussion on ''Evolution of the European Cenozoic Rift System: interaction of the Alpine and Pyrenean orogens with their foreland lithosphere'' by P. DEZES, S. M. SCHMID AND P. A. ZIEGLER. Tectonophysics, 401, 251–256.

MICHON L., SOKOUTIS D. (2005) Interaction between structural inheritance and extension direction during graben and depocentre formation: An experimental approach. Tectonophysics, 409, 125-146.

MICHON L., VAN BALEN R.T. (2005) Characterization and quantification of active faulting in the Roer valley rift system based on high precision digital elevation models. Quatern. Sci. Rev., 24, 457–474.

MICHON L., SAINT-ANGE F. (2008) Morphology of Piton de la Fournaise basaltic shield volcano (La Réunion Island): characterization and implication in the volcano evolution. J. Geophys. Res., 113, B03203, doi: 10.1029/2005JB004118.

MICHON L., VAN BALEN R.T., MERLE O., PAGNIER H. (2003) The cenozoic evolution of the Roer Valley rift system integrated at a European scale. Tectonophysics, 367, 101–126.

MICHON L., STAUDACHER T., FERRAZZINI V., BACHELERY P., MARTI J. (2007a) April 2007 collapse of Piton de la Fournaise: A new example of caldera formation. Geophys. Res. Lett., 34, L21301, doi:10.1029/2007GL031248.

MICHON L., SAINT-ANGE F., BACHELERY P., VILLENEUVE N., STAUDACHER T. (2007b) Role of the structural inheritance of the oceanic lithosphere in the magmato-tectonic evolution of Piton de la Fournaise volcano (La Réunion Island). J. Geophys. Res., 112, B04205, doi:10.1029/2006JB004598.

MICHON L., CAYOL V., LETOURNEUR L., PELTIER A., VILLENEUVE N., STAUDACHER T. (2009a) Edifice growth, deformation and rift zone development in basaltic setting: insights from Piton de la Fournaise shield volcano (Réunion Island). J. Volcanol. Geortherm. Res., doi: 10.1016/j.jvolgeores.2008.11.002.

MICHON L., VILLENEUVE N., CATRY TH, MERLE O. (2009b) How summit calderas collapse on basaltic volcanoes: new insights from the April 2007 caldera collapse of Piton de la Fournaise volcano. J. Volcanol. Geortherm. Res., doi: 10.1016/j.jvolgeores.2008.11.003

MINSHULL T.A., CHARVIS PH. (2001) Ocean island densities and models of lithospheric flexure. Geophys. J. Int., 145, 731-739.

MONIE P., PHILIPPOT P. (1989) Mise en évidence de l'âge Eocène moyen du métamorphisme de haute-pression dans la nappe ophiolitique du Monviso (Alpes occidentales) par la méthode 39Ar–40Ar. C. R. Acad. Sci. Paris, 309, 245–251.

MORANGE A., HERITIER F., VILLEMIN J. (1971) Contribution de l'exploration pétrolière à la connaissance structurale et sédimentaire de la Limagne, dans le Massif Central. Symposium J. Jung. Plein Air Service , Clermont Ferrand, 295-308.

MUNRO D. C., ROWLAND S. K. (1996) Caldera morphology in the western Galapagos and implications for volcano eruptive behavior and mechanisms of caldera formation. J. Volcanol. Geotherm. Res., 72, 85– 100.

NAGEL T., BUCK W.R. (2004) Symmetric alternative to asymmetric rifting model. Geology, 32, 937-940.

NAUMANN T., GEIST D. (2000) Physical volcanology and structural development of Cerro Azul Volcano, Isabela Island, Galapagos: Implications for the development of Galapagos-type shield volcanoes. Bull. Volcanol., 61, 497–514.

OEHLER J.-F., LABAZUY P., LENAT J.-F. (2004) Recurrence of major flank landslides during the last 2 Ma-history of Réunion Island. Bull. Volcanol., 66, 585–598.

OEHLER J.-F., LENAT J.-F., LABAZUY P. (2008) Growth and collapse of the Reunion Island volcanoes. Bull Volcanol, 70, 717–742, doi: 10.1007/s00445-007-0163-0.

O'NEILL C., MULLER D., STEINBERGER B. (2003) Geodynamic implications of moving Indian Ocean hotspots. Earth Planet. Sci. Lett., 215, 151–168.

PELTIER A., STAUDACHER TH, BACHELERY P. (2007) Constraints on magma transfers and structures involved in the 2003 activity at Piton de La Fournaise from displacement data. J. Geophys. Res., 112, B03207, doi: 10.1029/2006JB004379.

PELTIER A., FAMIN V., BACHELERY P., CAYOL V., FUKUSHIMA Y., STAUDACHER TH. (2008) Cyclic magma storages and transfers at

Piton de La Fournaise volcano (La Réunion Island) inferred from deformation and geochemical data. Earth. Planet. Sci. Lett., 270, 180-188, doi:10.1016/j.epsl.2008.02.042.

PLOMEROVA J., ACHAUER U., BABUSKA V., VECSEY L., BOHEMA WORKING GROUP (2007) Upper mantle beneath the Eger Rift (Central Europe): plume or asthenosphere upwelling? Geophys. J. Int., 169, 675–682.

RAMBERG H. (1981) Gravity, Deformation and the Earth's Crust. Academic Press, London. 452 pp.

RANALLI G., MURPHY D.C. (1987) Rheological stratification of the lithosphere. Tectonophysics, 132, 281–296.

RANÇON J.-P., LEREBOUR P., AUGE T. (1989) The Grand Bruˆleˊ exploration drilling: New data on the deep framework of the Piton de la Fournaise volcano. part 1: Lithostratigraphic units and volcanostructural implications. J. Volcanol. Geotherm. Res., 36, 113–127.

RAT P. (1974) Le système Bougogne-Morvan-Bresse (articulation entre le bassin parisien et le domaine péri-alpin). In: J. DEBELMAS (Eds) Géologie de la France; les chaînes plissées du cycle alpin et leur avant-pays. Doin, 480-500.

RESTON T.J. (1993) Evidence for extensional shear zones in the mantle, offshore Britain, and their implications for the extension of the continental lithosphere, Tectonics, 12, 492 –506.

REUBI O., NICHOLLS I.A. (2004) Variability in eruptive dynamics associated with caldera collapse: an example from two successive eruptions at Batur volcanic field, Bali, Indonesia. Bull. Volcanol., 66, 134-148, doi:10.1007/s00445-003-0298-6.

REYNOLDS R.W., GEIST D., KURZ M.D. (1995) Physical volcanology and structural development of Sierra Negra volcano, Isabela Island, Galapagos Archipelago. Geol. Soc. Am. Bull., 107, 1398–1410.

RING U. (1994) The influence of preexisting structure on the évolution of the Cenozoic Malawi rift (East African rift system). Tectonics, 13, 313–326.

RITTER J.R.R., JORDAN M., CHRISTENSEN U.R., ACHAUER U. (2001) A mantle plume below the Eifel volcanic fields, Germany. Earth Planet. Sci. Lett., 186, 7-14.

ROCHE O., DRUITT T.H. (2001) Onset of caldera collapse during ignimbrite eruptions. Earth Planet. Sci. Lett., 191, 191-202.

ROCHE O., DRUITT T.H., MERLE O. (2000) Experimental study of caldera formation. J. Geophys. Res., 105, 395-416.

ROCHE O., VAN WYK DE VRIES B., DRUITT T.H. (2001) Sub-surface structures and collapse mechanisms of summit pit craters. J. Volcanol. Geotherm. Res., 105, 1-18.

ROCHER M., CHEVALIER F., PETIT CH., GUIRAUD M. (2003). Tectonics of the Northern Bresse region (France) during the alpine cycle. Geodin. Acta. 16, 131–147.

ROSI M., VEZZOLI L., ALEOTTI P., DE CENSI M. (1996) Interaction between caldera collapse and eruptive dynamics during the Campanian Ignimbrite eruption, Phlegraean Fields, Italy. Bull. Volcanol., 57, 541-554.

ROTSTEIN Y., EDEL J.B., GABRIEL G., BOULANGER D., SCHAMING M., MUNSCHY M. (2006) Insight into the structure of the Upper Rhine Graben and its basement from a new compilation of Bouguer Gravity. Tectonophysics, 425, 55-70.

ROWLAND S.K., GARBEIL H. (2000) Slopes of oceanic basalt volcanoes, in Remote Sensing of Active Volcanism, Geophys. Monogr. Ser., vol. 116, edited by P. J. Mouginis-Mark, J. A. Crisp, and J. H. Fink, pp. 223–247, AGU, Washington, D. C.

RIJKSWATERSTAAT (2000) Productspecificatie AHN 2000. Report of the Survey Department of the Ministry of Transport, Public Works and Water Management of the Netherlands.

RUPPEL C. (1995) Extensional processes in continental lithosphere. J. Geophys. Res., 100, 24187-24215.

SCHLEIDER H., KELLER J., KRAMM U. (1990) Isotope studies on alkaline volcanics and carbonatites from the Kaiserstuhl, Federal Republic of Germany. Lithos, 26, 21-35.

SCHMINKE H.U., LORENZ V., SECK H.A. (1983) The quaternary Eifel volcanic field. In: K. FUCHS, K. VON GELHEN, H. MALZER, H. MURAWSKI, A. SEMMEL (Eds). Plateau uplift. The Renish Shield – A case history. Springer-Verlag, Berlin, 139-151.

SCHMITT A.K., MARKS M.A., NESBOR H.D., MARKL G. (2007) The onset and origin of differentiated Rhine Graben volcanism based on U-Pb ages and oxygen isotopic composition of zircon. Eur. J. Mineral., 19, 849-857.

SCHUMACHER M. E. (2002) Upper Rhine Graben: Role of preexisting structures during rift évolution. Tectonics, 21, 1006, doi:10.1029/2001TC900022.

SCHWARZ M., HENK A. (2006). Evolution and structure of the Upper Rhine Graben: insights from three-dimensional thermomechanical modelling. Int J Earth Sci (Geol Rundsch), 94, 732–750.

SENGOR A.M.C., BURKE K. (1978) Relative timing of rifting and volcanism on Earth and its tectonic implications. Geophys. Res. Lett., 5, 419-421.

SERANNE M. (1999) The Gulf of Lion continental margin (NW Mediterranean) revisited by IBS: An overview, in The Mediterranean Basins: Tertiary Extension Within the Alpine Orogen, edited by B. Durand et al., Geol. Soc. Spec. Publ., 156, 21 –53.

SIMKIN T., HOWARD K.A. (1970) Caldera collapse in Galapagos Islands, 1968. Science, 169, 429-437.

SISSINGH W. (1998) Comparative Tertiary stratigraphy of the Rhine Graben, Bresse Graben and Molasse Basin: correlation of Alpine foreland events. Tectonophysics, 300, 249-284.

SISSINGH W. (2001) Tectonostratigraphy of the West Alpine Foreland: corrélation of Tertiary sedimentary sequences, changes in eustatic sea-level and stress regimes. Tectonophysics, 333, 361-400.

SITTLER C. (1974) Le fossé Rhénan ou la plaine d'Alsace. In: Debelmas, J. (Ed.),Géologie de la France, vol. 1.Doin Editeurs, Paris, 78–104.

SMITH W.H.F., SANDWELL D.T. (1997) Global sea floor topography from satellite altimetry and ship depth soundings. Science, 277, doi: 10.1126/science.277.5334.1956.

SOBOLEV S.V., ZEYEN H., STOLL G., WERLING F., ALTHERR R., FUCHS K. (1996). Upper mantle temperatures from teleseismic tomography of French Massif Central including effects of composition, mineral reactions, anharmonicity, anelasticity and partial melt. Earth. Planet. Sci. Lett., 139, 147-163.

STAMPFLI G., MOSAR M.J., MARQUER D., MARCHANT R., BAUDIN T., BOREL G. (1998) Subduction and obduction processes in the Swiss Alps, Tectonophysics, 296, 159-204.

STAUDACHER TH., FERRAZZINI V., PELTIER A., KOWALSKI PH., BOISSIER P., CATHERINE PH., LAURET F., MASSIN F. (2009) The April 2007 eruption and the Dolomieu crater collapse, two major events at Piton de la Fournaise (La Réunion Island, Indian Ocean). J. Volcanol. Geotherm. Res., doi:10.1016/j.jvolgeores.2008.11.005.

STIX J., KOBAYASHI T. (2008) Magma dynamics and collapse mechanisms during four historic caldera-forming events. J. Geophys. Res., 113, B09205, doi:10.1029/2007JB005073.

TAPPONNIER P. (1977) Evolution tectonique du système alpin en Méditerranée: poinçonnement et écrasement rigide-plastique. Bull. Soc. Géol. Fr., 19, 437-460.

TILTON G.R., SCHREYER W., SCHERTL H.P. (1991) Pb–Sr –Nd isotopic behavior of deeply subducted crustal rocks from the Dora Maira Massif, Western Alps, Italy: II. What is the age of the ultrahigh-pressure metamorphism? Contrib. Mineral. Petrol., 108, 22–33.

TRON V., BRUN J.P. (1991) Experiments on oblique rifting in brittle–ductile systems. Tectonophysics, 188, 71– 84.

UKAWA M., FUJITA E., YAMAMOTO E., OKADA Y., KIKUCHI M. (2000) The 2000 Miyakejima eruption: crustal deformation and earthquake observed by the NIED Miyakejima observation network. Earth Planets Space, 52, xix-xxvi.

USTASZEWSKI K., SCHUMACHER M.E., SCHMID S.M. (2005) Simultaneous normal faulting and extensional flexuring during rifting—an example from the southernmost Upper Rhine Graben. Int. J. Earth Sci., 95, 680–696.

VAN BALEN R.T., VAN BERGEN F., DE LEEUW C., PAGNIER H., SIMMELINK H., VAN WEES J.D., VERWEIJ J.M. (2000) Modelling the hydrocarbon generation and migration in the West Netherlands Basin, the Netherlands. Geol. Mijnb., Neth. J. Geosci., 79, 29–44.

VAN DEN BERG M.W. (1994) Neotectonics of the Roer Valley rift system. Style and rate of crustal deformation inferred from syntectonic sedimentation. Geol. Mijnb. 73, 143–156.

VATIN-PERIGNON N. (1968) Les formations éruptives et la structure de l'édifice volcanique au centre du Cantal (Massif Central Français). Bull. Volcanol., 32, 207-251.

VILLEMIN T., BERGERAT F., (1985) Tectonique cassante et paléocontraintes tertiaires de la bordure NE du Fossé Rhénan (RFA). Oberrhein. Geol. Abh. 34, 63– 87

VILLEMIN T., BERGERAT F. (1987) L'évolution structurale du fossé rhénan au cours du Cénozoïque: un bilan de la déformation et des

effets thermiques de l'extension. Bull. Geol. Fr., 8, 245–255.

VINCENT P.M., AUBERT M., BOIVIN P, CANTAGREL J.M., LENAT J.F. (1977) Découverte d'un volcanisme paléocène en Auvergne: les maars de Menat et leurs annexes; études géologique et géodésique. Bull. Soc. géol. Fr., 5, 1057-1070.

WALKER G.P.L. (1988) Three Hawaiian calderas: An origin through loading by shallow intrusions. J. Geophys. Res., 93, 14773–14784.

WALKER G.P.L. (1999) Volcanic rift zones and their intrusion swarms. J. Volcanol. Geotherm. Res., 94, 21-34.

WATTS A.B., COCHRAN J.R. (1974) Gravity anomalies and flexure of the lithosphere along the Hawaiian-Emperor Seamount Chain. Geophys. J. Roy. Astron. Soc., 38, 119-141.

WATTS A.B., BODINE J.H., STECKLER M.S. (1980) Observations of flexure and the state of stress in the oceanic lithosphere. J. Geophys. Res., 85, 6369–6376.

WATTS A.B., TEN BRINK U.S., BUHL P., BROCHER T.M. (1985) A multichannel seismic study of lithospheric flexure across the Hawaiian-Emperor seamount chain. Nature, 315, 105–111.

WATTS A.B., PIERCE C., COLLIER J., DALWOOD R., CANALES J.P., HENSTOCK T.J. (1997), A seismic study of lithospheric flexure in the vicinity of Tenerife, Canary Islands, Earth Planet. Sci. Lett., 146, 431–447.

WERNICKE B. (1981) Low-angle normal faults in the Basin and Range Province – nappe tectonics in an extending orogen. Nature, 291, 645-648.

WERNICKE B. (1985) Uniform-sense normal simple shear of the continental lithosphere. Can. J. Earth Sci., 22, 108-125.

WESSEL P., KEATING B. (1994) Temporal variations of flexural deformation in Hawaii. J. Geophys. Res., 99, 2747–2756.

WILSON M., DOWNES H. (1991) Tertiary-Quaternary Extension-Related Alkaline Magmatism in Western and Central Europe. J. Petrol., 32, 811-849.

WILSON M., ROSENBAUM J.M., DUNWORTH E.A. (1995) Melilitites: partial melts of the thermal boundary layer? Contrib. Mineral. Petrol., 119, 181-196.

WIMMENAUER W. (1974) The alkaline province of the Central Europe and France. In: SØRENSEN (Eds) The alkaline rocks. John Wiley & Sons, 238-271.

WITTIG N., BAKER J.A., DOWNES H. (2007) U-Th-Pb and Lu-Hf isotopic constraints on the evolution of sub-continental lithospheric mantle, French Massif Central. Geochim. Cosmochim. Acta. 71, 1290-1311.

WORTEL M. J. R., SPAKMAN W. (1992) Structure and dynamic of subducted lithosphere in the Mediterranean. Proc. K. Ned. Akad. Wet., 95, 325 – 347.

WORTEL M. J. R., SPAKMAN W. (2000) Subduction and slab detachment in the Mediterranean-Carpathian Region, Science, 290, 1910 – 1917.

WORUM G., MICHON L. (2005) Continuous, syn-sedimentary basin inversion induced by the alpine compression: The Paleogene inversion of the West Netherlands Basin integrated into a NW European scale. J. Geol. Soc., London, 162, 73-85.

WORUM G., MICHON L., VAN BALEN R.T., VAN WEES J.D., CLOETINGH S., PAGNIER H., (2005). Comparison and modelling of the present-day fault activity in the West Netherlands Basin and Roer Valley Rift System (southern Netherlands) in light of their pre-Neogene evolution. Quaternary Sci. Rev., 24, 475-490.

ZEYEN H., VOLKER F., WEHRLE V., FUCHS K., SOBOLEV S., ALTHERR R. (1997a) Styles of continental rifting: crust-mantle detachment and mantle plumes. Tectonophysics, 278, 329-352.

ZEYEN H., NOVAK O., LANDES M., PRODEHL C., DRIAD L., HIRN A. (1997b) Refraction-seismic investigations of the northern Massif Central (France). Tectonophysics, 275, 99-117.

ZIEGLER P.A. (1990) Geological atlas of western and central Europe, 2nd ed. Shell Internationale Petroleum Mij., distributed by Geol. Soc., London, Publ. House, Bath. 238 pp., 56 encl.

ZIEGLER P.A. (1992a) European Cenozoic rift system. In: P.A. ZIEGLER (Eds) Geodynamics of Rifting, Volume I. Case History Studies on Rifts: Europe and Asia. Tectonophysics, 208, 91-111.

ZIEGLER P.A., (1992b) North Sea rift system. In: Ziegler, P.A. (Ed.), Geodynamics of Rifting, Volume I. Case History Studies on Rifts: Europe and Asia. Tectonophysics, 208, 55–75.

ZIEGLER P.A. (1994) Cenozoic rift system of western and central Europe: an overview. Geol. Mijnbouw, 73, 99-127.

ZIEGLER P.A., ROURE F. (1996) Architecture and petroleum systems of the Alpine orogen and associated basins. In: ZIEGLER, P.A., HORVATH, F. (Eds.), Peri-Tethys Memoir 2: Structure and Prospects of Alpine Basins and Forelands. Mém. Mus. Natn. Hist. Nat., vol. 170, pp. 15– 45.

ZIEGLER P.A., DEZES P. (2007) Cenozoic uplift of Variscan Massifs in the Alpine foreland: Timing and controlling mechanisms. Global. Planet. Changes, 58, 237-269.

ZIJERVELD L., STEPHENSON R., CLOETINGH S., DUIN E., VAN DEN BERG M.W., (1992) Subsidence analysis and modelling of the Roer Valley Graben (SE Netherland). Tectonophysics, 208, 159–171.

Annexes

Annexe 1 :

Merle, O., L. Michon, G. Camus, A. Goër de (1998) L'extension oligocène sur la transversale septentrionale du rift du Massif Central. *Bull. Soc. Géol. Fr.*, 169, 615-626.

L'extension oligocène sur la transversale septentrionale du rift du Massif central

par Olivier MERLE*, Laurent MICHON*, Guy CAMUS* et Alain DE GOER*

Mots clés. – Tectonique, Rift, Massif central, Modélisation analogique.

Résumé. – L'évolution oligocène du rift du Massif central (MCR) est abordée par la synthèse et l'interprétation des données géologiques existantes. L'apport respectif de ces différentes données est discuté pour retenir les éléments de premier ordre, qui permettent de proposer une évolution cohérente de l'extension oligocène. L'un des enseignements principaux de cette évolution oligocène est que l'on doit considérer les trois fossés parallèles de la Limagne, de Roanne-Montbrison et de la Bresse comme un ensemble indissociable, dont la géométrie globale reflète les modalités de l'étirement lithosphérique sur cette transversale. Une modélisation analogique de l'extension à l'échelle crustale, dans le cadre de l'hypothèse d'un rifting passif, permet de mieux comprendre la disposition des fossés d'effondrement et la symétrie générale du système.

Oligocene extensional processes along the northern transect of the Massif central rift (France)

Key words. – Tectonic, Rift, Massif Central, Analogue modelling.

Abstract. – The process of extension in the Massif Central Rift (MCR) is discussed through the synthesis of available geological data. The MCR is 200 km wide and its overall geometry is best described as two opposite half-grabens arranged on both sides of a smaller symmetrical graben. This striking mirror symmetry is thought to result from the Oligocene extension during which sedimentation took place. Volcanism occurred later during the Miocene and is restricted to the west of the whole extensional province. Analogue modelling reveals that the geometry of the sedimentary basins may be interpreted in term of failure of the brittle upper-part of the lithospheric mantle during passive rifting. The most significant data strongly suggest that the initiation of the rift is due to farfield stresses acting on the lithosphere (i.e. stress-generated or passive rift) and does not result from an ascending mantle plume (i.e. plume-generated or active rift).

ABRIDGED ENGLISH VERSION

Introduction

The Massif Central Rift (MCR) is part of the west-European rift system that formed during the Tertiary. It corresponds to an extensional province composed of three principal sedimentary basins from the Sillon Houiller in the west to the Jura mountains in the east. These three sedimentary basins display an overall north-south trend and the sedimentation area is 200 km wide along an east-west transect (fig. 1). Two of these north-south basins are themselves as wide as the Rhine graben, which is located northward of the MCR beyond the Rhine-Saone transform zone (fig. 1). Its width far exceeding the 35-40 km wide Rhine graben, the MCR appears to be a diffuse rift whose genesis needs to be explained. The goal of this paper is to propose a tectonic history of the MCR explaining the formation of sedimentary basins at crustal scale during the Oligocene.

Geological constraints

The MCR is best described by three main grabens oriented north-south (fig. 1). Seismic data [Morange *et al.*, 1971; Bergerat *et al.*, 1990; Truffert *et al.*, 1990] reveal a remarkable symmetry on either side of the centre of the central graben. Both eastern and western basins are two half-grabens resulting from two listric faults facing in opposite directions, whereas the central graben is roughly symmetric (fig. 2 and 3). This overall symmetry is reinforced by the distribution of Lower and Middle Oligocene marine sediment occurences. These are found in both the eastern and western basins but not in the central graben (table I). Likewise, only 500 m of sediments accumulated in the central grabens during this period, inferior to thicknesses in the western (2 000 m) and eastern (1 200 m) half-grabens. This symetrical pattern came to a halt in the upper Oligocene during which the sedimentation remained very active in the western half-graben while there was a lull in central and eastern basins (table I).

Oligocene sedimentation lacked accompanying volcanism. Volcanism started in the Miocene and was restricted to the west of the MCR, from the central graben in the east to the Sillon Houiller in the west. It was associated with uplift, together with the end of the period of sedimentation, along the western part of this northern transect of the MCR.

Wilson and Downes [1991] have shown that primary magmas can be modelled by two component mixing : (i) an asthenospheric component resulting from a mixture of DM and HIMU endmembers for which there is no need to invoke the existence of a deep mantle plume and (ii) a lithospheric component created by the interaction of the ascending magma with the old Variscan lithosphere. The depth at which partial melting occurred would be in the range 80-110 km [Mergoil et Boivin, 1993; Granet *et al.*, 1995b].

Seismic data reveal that the Moho (fig. 4) is at 26 km depth in the west and 29 km in the east [Truffert *et al.*, 1990; Zeyen *et al.*, 1997], indicating a thinning of the crust to 23.3 km and 27.5 km below the western and eastern half-grabens,

* Département des Sciences de la Terre, Univ. B. Pascal, 5 rue Kessler, 63038 Clermont-Ferrand.

respectively (table II). This yields 25 % crustal thinning beneath the western half-graben and 11 % below the eastern half-graben. Crustal thickness between the two half-grabens is around 29 km. Given the fact that the Variscan basement visible on both sides of the central graben displays elevations above 1 000 m and has probably suffered erosion since the Oligocene, it can be questioned whether the crust bordering the central graben has been thinned at all. Geophysical data [e.g. Perrier et Ruegg, 1973; Souriau, 1976; Lucazeau et Bayer, 1982; Babuska et Plomevora, 1992; Granet *et al.*, 1995a et b; Sobolev *et al.*, 1996, 1997] show that the lithosphere-asthenosphere boundary (LAB) is located at about 60-70 km and 90-100 km below the western and eastern half-grabens, respectively. This shows that the thinning of the lithosphere is much more pronounced in the west of the rift, which is consistent with the western location of volcanism and uplift.

Discussion

The linear relationship between the crustal thinning calculated from present-day cross sections and the thickness of Oligocene sediments (fig. 4) indicates that crustal thinning occurred during the Oligocene and terminated at the end of the sedimentation period. Thinning of the lithospheric mantle, which is greater than crustal thinning, is unlikely to have occurred before the Miocene as it cannot be coeval with sedimentation at sea level during the Oligocene for purely isostatic reasons. Furthermore, iso-depth curves of the LAB are clearly centered in the south of the MCR around big Mio-Pliocene volcanic provinces (Cantal/Mont-Dore and Veley/Deves) again suggesting that significant thinning of the lithospheric mantle postdated the Oligocene crustal extension. Given the fact that significant Miocene extension of the lithospheric mantle could not have taken place without further crustal extension in the crust, we consider Miocene thinning to be due to the thermo-mechanical erosion of the lithospheric mantle, without extension of the whole lithosphere. This Miocene and Pliocene event, well visible from tomographic studies [Granet *et al.*, 1995a and b], might result from asthenospheric movements during the formation of the deep lithospheric root of the Alpine chain.

The present-day lithospheric cross-section (fig. 5) is then the result of a two-fold process : relatively weak Oligocene extension leading to the formation of three sedimentary basins followed by considerable thermal thinning of the lithospheric mantle in the Miocene. This explains why the asymmetric model of Wernicke [1985] is not consistent with the localisation and amount of crustal and lithospheric thinning (fig. 6).

Active or passive rifting ?

It has been long acknowledged that plume-generated rifts (i.e. active rifts) start with doming and exhibit abundant vulcanicity from the earliest stages. Extension may lag behind volcanism by several tens of millions of years. In contrast, stress-generated rifts (i.e. passive rifts) commence with graben formation and develop vulcanicity and doming at a later stage [e.g. Park, 1988, p. 85; Ruppel, 1995]. In the MCR, a thick sedimentary sequence (up to 3 000 m in the west and up to 1 500 m in the east) has been deposited during the Oligocene. Marine Oligocene deposits have been clearly identified from stratigraphic [Giraud, 1902; Chauve *et al.*, 1980; Rat, 1984] and geochemical [Poidevin et Briot, 1996] studies. This demonstrates that sedimentation took place at sea level and that no doming developed during the first rifting stage. Furthermore, this period of sedimentation lacks volcanism, which occurred later in the Miocene. This chronology is well consistent with a stress-generated or passive rifting scenario. Thus, to understand the geometry of sedimentary basins along the northern transect of the MCR, we have conducted experiments of extension during passive rifting process at crustal scale.

Analogue modelling

The basins' geometry and sedimentary records indicate a tectonic evolution during the Lower and Middle Oligocene that is roughly similar on both sides of a symmetric central graben. During this period, thinning of the crust, subsidence and sedimentation with marine incursions principally occurred in the western and eastern edge of the MCR through the formation of two half-grabens. This symmetric pattern was lost at the end of the Oligocene as shown by the sedimentary history (table I) and the western localisation of volcanism. The longer activity of the western listric fault towards the end of the Oligocene is consistent with greater crustal thinning in the west. What we model now are the extensional mechanisms that led to the formation of this conspicuous basin geometry during the Lower and Upper Oligocene along the northern MCR transect.

Extension of a four-layer strength profile lithosphere [Buck, 1991] is mainly controled by the rupture of the brittle mantle layer [e.g. Brun and Beslier, 1996]. A series of experiments was conducted in order to simulate mantle rupture. Two velocity discontinuities represented boundaries between the crust and the mantle (fig. 7 and 8). The goal of these scaled experiments (see Appendix) was to understand the rôle that the localisation of the brittle mantle rupture exerts on the geometry of extensional crustal structures. Results show that each velocity discontinuity initiates above it the formation of a half graben associated with a symmetrical graben (fig. 9). The half-graben reveals striking similarities with the crustal structure of the Rhine graben (fig. 10).

When two DV were active simultaneously, the association half graben/symmetrical graben above each DV developed only if the distance between them was large enough (fig. 11, top). For small distances between the two DV at the beginning of the experiments, a space problem prevented the two symmetrical grabens from forming and only one central graben developed, shared by the two half-grabens (fig. 11, middle). When two DV were adjacent or very close to each other, there was no space for the central graben to form and the two half grabens were separated by a central horst (fig. 11, bottom).

According to model ratios, a single symmetrical graben is expected where the distance between the two border faults of the half-grabens is about 180 km, and two symmetric grabens for a greater distance. Symmetric grabens would be

about 20 km wide for a 30 km thick crust and a brittle/ductile ratio close to 1. This is consistent with the width of the central graben (20 km) and the distance between the western and eastern half-graben (185 km) along the northern transect of the MCR.

Conclusion

Analogue modelling shows that main field data of the MCR can be interpreted in terms of passive rifting during the Oligocene. The striking mirror symmetry of the sedimentary basins may result from two major ruptures localized in the brittle mantle layer, the distance between these two zones of rupture being the key parameter controlling the basins' surface geometry. The later evolution of the MCR during the upper Oligocene indicates that extension was only active in the western half-graben. This may be due to the Alpine deformation whose westward migration may have inhibited extension in the eastern half-graben of the MCR. Then, thermal thinning of the lithospheric mantle along the western part of the rift system ultimately led to Miocene volcanism and uplift of the rift.

INTRODUCTION

Le rift ouest-européen est constitué de trois segments majeurs disposés globalement autour de l'arc alpin. D'est en ouest, on distingue le graben de l'Eger orienté NE-SW, le graben du Rhin orienté NNE-SSW et les fossés d'effondrement du Massif central orientés N-S. La sédimentation est pour l'essentiel d'âge oligocène dans ces trois segments, ce qui montre le synchronisme de cette période d'extension tertiaire. Dans la partie occidentale de ce système, la comparaison des cartes structurales montre une différence marquée de structure entre le graben du Rhin au nord et les fossés d'effondrement du Massif central au sud (fig. 1). Dans le graben du Rhin, la sédimentation oligocène se localise le long d'un fossé étroit et linéaire de 35 km de large sur 300 km de long. La sédimentation oligocène dans le Massif central est diffuse, soulignée par trois grands fossés parallèles (le fossé de la Limagne, le fossé de Roanne-Montbrison et le fossé de la Bresse) et plusieurs bassins de moindre importance (e.g. les bassins d'Olby, d'Ambert, etc). Au total, la sédimentation liée au rifting s'étend du Sillon houiller à l'ouest jusqu'à la faille bordière de la Bresse à l'est, soit sur plus de 200 km de large. Ces deux segments majeurs du rift ouest-européen sont séparés par la zone transformante Rhin-Saône [Bergerat, 1977] (fig. 1).

La structure crustale du graben du Rhin a été récemment élucidée grâce aux campagnes sismiques DEKORP-ECORS [Brun et al., 1992]. L'extension à l'échelle de la croûte est clairement asymétrique, associée à la formation d'une faille bordière majeure qui entraîne une forte dissymétrie du remplissage sédimentaire. Moins connue, la structure du rift du Massif central (MCR) doit, pour être comprise, être étudiée dans sa totalité. Proposer un modèle mécanique de l'évolution de ce rift nécessite de comprendre comment se sont formés ces trois fossés parallèles et synchrones, dont deux ont une largeur équivalente au seul graben du Rhin, et de voir si la géométrie d'ensemble du système peut être interprétée par une évolution tectonique cohérente. En synthétisant, sur la transversale septentrionale du MCR, les données actuellement disponibles sur la structure en surface et en profondeur, cet article montre que les données géologiques de premier ordre de ce rift peuvent être intégrées dans un modèle simple d'extension de la lithosphère ouest-européenne.

SYNTHÈSE GÉOLOGIQUE

La géométrie des fossés

Si on s'affranchit des bassins de moindre importance, la disposition et la géométrie des trois fossés principaux révèlent une symétrie frappante (fig. 2). Le graben central de
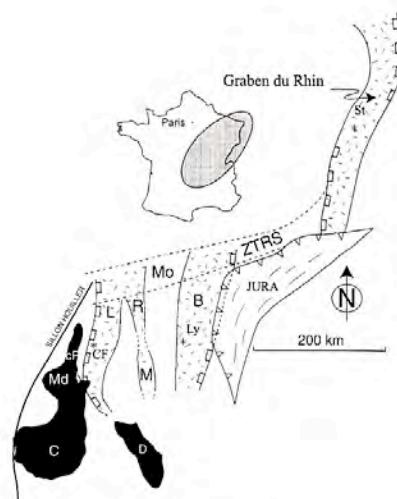
FIG. 1. – Localisation géographique du graben du Rhin et du rift du Massif central (ZTRS : zone transformante Rhin-Saône, B : fossé de la Bresse, R et M : fossé de Roanne-Montbrison, L : fossé de la Limagne, St : Strasbourg, Ly : Lyon, CF : Clermont-Ferrand, cP : chaîne des Puys, Md : Monts Dore, C : Cantal, D : Devez).

FIG. 1. – *Simplified geological map of the Rhine Graben and the Massif Central Rift (MCR) (ZTRS : Rhin-Saone transform zone, B : Bresse basin, R and M : Roanne-Montbrison basin, L : Limagne basin, St : Strasbourg, Ly : Lyon, CF : Clermont-Ferrand, cP : chaîne des Puys, Md : Monts Dore, C : Cantal, D : Devez).*

Roanne-Montbrison, de géométrie relativement symétrique [Le Griel, 1991], est encadré par deux barrières nord-sud où le socle varisque est porté à des altitudes supérieures à 1 000 m (les monts du Forez et les monts du Lyonnais). Ce socle varisque s'abaisse à l'ouest vers le fossé de la Limagne et à l'est vers le fossé de la Bresse, pour disparaître sous les sédiments tertiaires. Les données sismiques montrent que ces deux fossés latéraux sont des demi-grabens, caractérisés par le fonctionnement de deux failles bordières majeures et un remplissage dissymétrique des dépôts sédimentaires (fig. 3) [Morange et al., 1971 ; Bergerat et al., 1990 ; Truffert et al., 1990]. En coupe, l'image complète de la structure des trois fossés principaux est celle d'une symétrie de miroir passant au centre du graben central, qui apparaît encadré par deux demi-grabens majeurs dont les failles bordières à regards opposés sont distantes d'environ 185 km (fig. 2).

Vers le nord, au niveau de la transformante Rhin-Saône, le fossé de Roanne-Montbrison rejoint celui de la Limagne (fig. 1) et la structure globale est celle de deux fossés (Limagne et Bresse) séparés par un horst central (le Morvan). Là encore, une symétrie de miroir est observable de part et d'autre du horst central du Morvan [Allemand, 1990, p. 15]. Cet article s'attache plus particulièrement à l'interprétation de l'extension oligocène sur la transversale où trois fossés sont individualisés, transversale qui recoupe les aires de sédimentation maximale et qui se trouve en dehors de la zone transformante Rhin-Saône. Cependant, nous verrons que notre interprétation est compatible avec celle déjà proposée pour la bordure nord du MCR [Allemand, 1990].
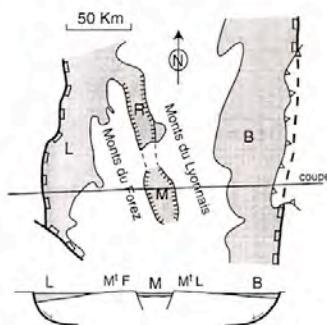

FIG. 2. – Carte et coupe géologiques simplifiées du rift du Massif central montrant la symétrie globale du système, soulignée par les deux demi-grabens latéraux de la Limagne (L) et de la Bresse (B), disposés de part et d'autre du graben symétrique de Roanne-Montbrison (R). En grisé : sédiments tertiaires. Coupe synthétique d'après les données de sismique ou de forage de Lienhardt [1962], Morange *et al.* [1971], Debeglia [1984], Bergerat *et al.* [1990], Blanc *et al.* [1991].

FIG. 2. – *Geological map and cross-section of the MCR showing the overall symmetry of the structures revealed by the two eastern and western half-grabens (Bresse and Limagne) arranged on both sides of the central symmetric graben (Roanne-Montbrison). Dotted area : Tertiary sediments. Synthetic cross-section from seismic or drill-hole data [Lienhardt, 1962 ; Morange et al., 1971 ; Debeglia, 1984 ; Bergerat et al., 1990 ; Blanc et al., 1991].*

Le remplissage sédimentaire des fossés

Cette disposition symétrique se trouve également enregistrée dans l'histoire sédimentaire de ces trois fossés pendant l'Oligocène inférieur et moyen (table I). Si le remplissage du graben central est essentiellement fluvio-lacustre [Ech-Cherif El Kettani, 1996], la sédimentation des deux demi-grabens latéraux est marquée par de nombreuses incursions marines, comme l'attestent certains faciès à gypse et évaporites, les faunes [e.g. Giraud, 1902 ; Chauve *et al.*, 1980 ; Rat, 1984] ou les rapports isotopiques du strontium [Poidevin et Briot, 1996]. De même, la sédimentation à l'Oligocène inférieur et moyen est sensiblement moins épaisse dans le graben central (200 m) que dans le demi-graben occidental (2 000 m) et oriental (1 200 m) (table I).

Cependant, l'histoire sédimentaire cesse d'être symétrique à l'Oligocène supérieur. Cette période est marquée par une évolution très contrastée entre les grabens central et oriental d'une part et le demi-graben occidental d'autre part. On enregistre en particulier une sédimentation détritique fluvio-lacustre peu épaisse (< 100 m) dans le demi-graben oriental, tandis que la sédimentation se poursuit dans le demi-graben occidental par des marnes et des calcaires, sur plus de 1 000 m d'épaisseur (sondage de Mirabel dans la fosse de Riom), avec persistance des influences marines [Gorin, 1974]. Cette évolution différente vers la fin de l'Oligocène montre que le rejet supérieur de la faille bordière du demi-graben de la Limagne (jeu minimal proche de

TABL. I. – Tableau indiquant l'évolution stratigraphique à l'Oligocène inférieur et moyen et à l'Oligocène supérieur dans les trois grands fossés de la transversale nord du MCR.

TABLE I. – *Tab showing sedimentation records during the Lower and Middle Oligocene and the Upper Oligocene in the northern MCR transect.*

	Limagne	Montbrison	Bresse
Oligocène sup.	Incursions marines	Fluvio-lacustre	Fluvio-lacustre
	Calcaires à Helix ramondi Marnes blanches à Cypris	Détritiques fins et grossiers + calcaires lacustres	Détritiques fins et grossiers
	> 1000 m	300 m	< 100 m
Oligocène inf. et moy.	Incursions marines	Fluvio-lacustre	Incursions marines
	Marno-calcaires à Potamides lamarcki et Cypris Calcaires à Striatelles	Détritique (sables, argiles et conglomérats)	Dépôts lagunaires à évaporites Formations marines à smectites
	< 2000 m	200 m	> 1200 m
Epaisseur totale maximum	3000 m	500 m	1300 m
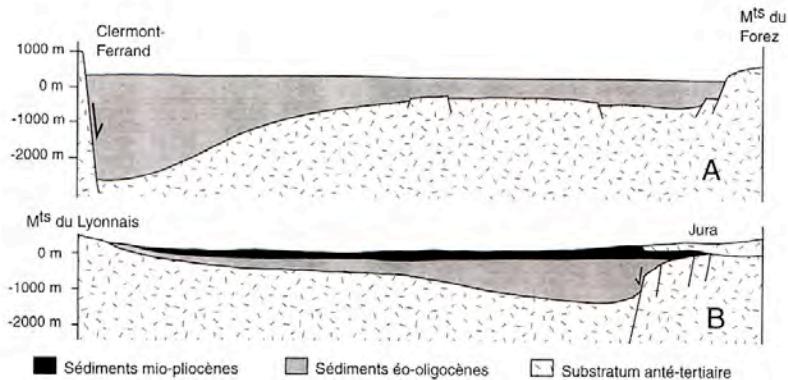
FIG. 3. – Coupe des demi-grabens de Limagne (haut) et de la Bresse (bas) d'après les données sismiques (Morange *et al.* [1971] pour la Limagne, Bergerat *et al.* [1990] et Blanc *et al.* [1991] pour la Bresse).

FIG. 3. – *Geological cross-sections of the western (top) and eastern (bottom) half-grabens from seismic data (after Morange et al. [1971] for the top cross-section, after Bergerat et al. [1990] and Blanc et al. [1991] for the bottom cross-section).*

4 km) par rapport à celui de la faille bordière du demi-graben de la Bresse est à mettre directement en relation avec la sédimentation nettement plus épaisse en Limagne qu'en Bresse (table I).

De même, il est important de signaler que l'épisode de sédimentation dans le demi-graben de la Limagne est définitivement terminé au Miocène alors qu'il se poursuit au Miocène inférieur dans le demi-graben de la Bresse, et pratiquement jusqu'à l'actuel [cf. la synthèse de Ech-Cherif El Kettani, 1996]. L'évolution ultime du demi-graben de la Bresse n'est sans doute plus à relier au rifting du Massif central mais plutôt à la propagation vers l'ouest du bassin flexural de la chaîne alpine au cours du Miocène.

Le volcanisme

Sur cette transversale nord du MCR, en dehors du volcanisme quaternaire tardif de la chaîne des Puys, le volcanisme est caractérisé par des édifices ponctuels de laves peu différenciées déchaussés par l'érosion, et divers diatrèmes pépéritiques, disséminés dans la partie occidentale du rift, du Sillon houiller jusqu'au milieu du graben central de Roanne-Montbrison. La partie orientale du rift, monts du Lyonnais et fossé de la Bresse, est indemne de toute activité magmatique, ce qui montre un décentrage complet du volcanisme vers l'ouest du système. La limite occidentale du volcanisme, au niveau du Sillon houiller, confirme que cet accident d'âge varisque est une discontinuité mécanique à l'échelle de la lithosphère toute entière, et que cette discontinuité a canalisé l'ascension des magmas les plus occidentaux.

Plus de 300 datations géochronologiques par K/Ar et Ar/Ar sur des sites différents montrent sans ambiguïté que le volcanisme du MCR est d'âge Miocène et Pliocène [e.g. Cantagrel et Thonat, 1976; Maury et Varet, 1980; Chantepie, 1990; Mergoil et Boivin, 1993; Cheguer, 1996], clairement postérieur à la sédimentation. Les âges les plus anciens obtenus par la méthode Ar/Ar datent de la limite Oligo-Miocène à 24 Ma [Chambon, 1997], tandis que quelques rares dépôts pépéritiques interstratifiés dans le Chattien supérieur montrent que le volcanisme a probablement démarré à la limite supérieur de l'Oligocène [Hourière et al., 1998].

Cependant, quelques rares âges éocènes, antérieurs à la sédimentation oligocène, ont été établis par la méthode K/Ar. Ils concernent 9 points d'émission : 7 dans les monts du Charollais [Bellon et al., 1974], 1 dans le nord du Puy-de-Dôme [Vincent et al., 1977] et 1 à la bordure occidentale du fossé de Montbrison [Bellon et Hernandez, 1979]. La rareté et l'antériorité de ce volcanisme par rapport à la sédimentation rend sa signification énigmatique. Quoi qu'il en soit, il convient d'insister sur l'absence de volcanisme pendant la sédimentation oligocène et sur son apparition généralisée à la fin de la période de sédimentation.

Le volcanisme du Massif central s'est exacerbé localement plus au sud avec l'édification tardive des strato-volcans du Cantal et des Monts-Dores, ou des plateaux basaltiques du Velay, de l'Aubrac et du Cézallier. Cette évolution spectaculaire de la fin du Miocène jusqu'à l'actuel, contemporaine d'un soulèvement important réalisé par le rejeu des failles hercyniennes antérieures, a occulté la géométrie initiale des grabens oligocènes, qui est très difficile à reconstituer (Michon et Merle, en prép.). Il apparaît clairement que seule la partie septentrionale du MCR, objet de cet article, se prête à l'étude de l'extension oligocène puisque la surrection et le volcanisme ultérieurs n'y ont pas détruit les témoins de cet épisode initial.

Par ailleurs, les études géochimiques montrent que les roches volcaniques ont des caractéristiques isotopiques (Nd-Sr-Pb) mixtes pouvant être séparées en deux composantes distinctes. La première, issue de l'asthénosphère, correspond à un mélange de manteau appauvri (DM) et de manteau type Saint Hélène (HIMU), pour lequel il n'est pas nécessaire d'invoquer l'existence d'un point chaud [Wilson et Downes, 1991]. La seconde est une composante de manteau enrichi (EM) que Wilson et Downes [1991] interprètent en terme de contamination lithosphérique pendant l'ascension des magmas vers la surface. La profondeur à laquelle la fusion s'est produite peut être déduite du champ de stabilité du magma initial (péridotites à grenat) ou calculée à partir des données expérimentales de Hirose et Kushiro [1993]. Elle serait comprise entre 80 et 110 km de profondeur [Mergoil et Boivin, 1993; Granet et al., 1995b].

Le Moho

La profondeur du Moho sur cette transversale peut être appréciée à partir des résultats de plusieurs campagnes sismiques en Limagne ou en Bresse [e.g. Perrier et Rueg, 1973; Hirn et Perrier, 1974; Truffert et al., 1990; Bergerat et al., 1990; Zeyen et al., 1997]. Pour rendre compte de l'amincissement crustal au Tertiaire, la profondeur du Moho donnée par rapport au niveau de la mer doit être corrigée, soit en retranchant l'épaisseur des sédiments tertiaires situés sous ce niveau de base, soit en ajoutant l'altitude du socle situé au dessus de ce niveau de base.

La compilation des données sismiques montre que l'amincissement crustal est sensible à l'aplomb de la faille bordière du demi-graben de la Limagne où l'épaisseur de la croûte sans la couverture tertiaire est de 23,5 km (Moho à 26 km, table II). Le Moho subit une inflexion marquée vers l'ouest où il s'enfonce brutalement jusqu'à 30 km sous la chaîne des Puys [Zeyen et al., 1997], ce qui correspond à la profondeur moyenne dans le domaine occidental du Massif central non affecté par l'extension oligocène. Vers l'est, le Moho s'enfonce progressivement de 26 km sous la faille bordière de la Limagne, à 28 km sous les monts du Forez et sous les monts du Lyonnais [Zeyen et al., 1997], jusqu'à 29 km sous la faille bordière de la Bresse [Bergerat et al., 1990]. Ces données, corrigées de l'épaisseur des sédiments tertiaires ou de l'altitude du socle, indique une croûte épaisse d'environ 29,5 km sous les monts du Forez et sous les monts du Lyonnais, et épaisse de 27,5 km sous

TABL. II. – Tableau indiquant la profondeur du Moho et l'altitude des formations anté-tertiaires (socle ou sédiments mésozoïques) par rapport au niveau de la mer, l'épaisseur de la croûte amincie et le taux de l'amincissement crustal pour les différents domaines de la Limagne, des monts du Forez et du Lyonnais et de la Bresse. Le taux d'amincissement crustal est calculé à partir d'une épaisseur de départ de 31 km, égale à celle observée au niveau de la chaîne des Puys immédiatement à l'ouest de la faille bordière de la Limagne. L'altitude maximale du socle est de 1 634 m à Pierre sur Haute pour les monts du Forez et de 1 432 au mont Pilat pour les monts du Lyonnais.

TABLE II. – *Tab showing the Moho depth and the basement altitude with respect to sea level, the thickness of the crust and the stretching amount in Limagne, Monts du Forez, Monts du Lyonnais and Bresse areas.*

	Profondeur du MOHO (km)	Position des formations anté-tertiaires par rapport au niveau de la mer (m)	Epaisseur de la croûte (km)	Amincissement crustal maximal
Limagne	26	-2700	**23,3**	25%
Monts du Forez	28	+1500	**29,5**	5%
Monts du Lyonnais	28	+1500	**29,5**	5%
Bresse	29	-1500	**27,5**	11%

la faille bordière du demi-graben de la Bresse (table II). Au niveau des monts du Forez et du Lyonnais, on ne connaît pas la quantité d'érosion subie par le socle dont l'altitude actuelle avoisine 1 500 m (table II), si bien qu'il est tout à fait envisageable que ces deux domaines des monts du Forez et du Lyonnais n'aient pas subi d'amincissement crustal. Ces données montrent que l'amincissement crustal est principalement localisé au niveau des demi-grabens occidental et oriental et qu'il n'est véritablement important qu'au niveau du demi-graben de la Limagne (table II).

Les deux réflecteurs sismiques repérés à l'intérieur de la croûte sous le demi-graben de la Limagne vers 11-12 km et 20 km sont pratiquement horizontaux et ne présentent aucune inflexion, en particulier au niveau du ressaut brutal subi par le Moho entre la chaîne des Puys et la faille bordière de la Limagne [Zeyen *et al.*, 1997]. En Bresse, la croûte inférieure litée plonge comme le Moho, des monts du Lyonnais jusqu'à la faille bordière de la Bresse, et ne paraît pas affectée par l'extension dans la croûte fragile [Truffert *et al.*, 1990].

La limite lithosphère-asthénosphère

Les nombreux travaux géophysiques montrent tous que la limite lithosphère-asthénosphère (LAB) remonte nettement au sud du Massif central jusqu'à des profondeurs de l'ordre de 50 km [e.g. Perrier et Ruegg, 1973 ; Souriau, 1976 ; Lucazeau et Bayer, 1982 ; Babuska et Plomevora, 1992 ; Granet *et al.*, 1995a et b ; Sobolev *et al.*, 1996, 1997], en liaison avec le développement considérable du volcanisme dans cette partie méridionale du MCR.

Il est plus difficile d'apprécier la profondeur du LAB sur la transversale nord orientée est-ouest, d'autant plus que les courbes d'isoprofondeur du LAB sont clairement centrées sur les provinces volcaniques du sud, d'âge miocène et pliocène, et ne montrent pas de relation directe avec les fossés d'effondrement de direction sub-méridienne. Cependant, les cartes les plus récentes du LAB [e.g. Fig. 5 in Sobolev *et al.*, 1996 ou Fig. 6 in Sobolev *et al.*, 1997] indiquent que cette limite, sur la transversale nord objet de cette étude, est située plus haut à l'ouest (65-70 km sous la Limagne et les monts du Forez) qu'à l'est (90-100 km sous les monts du Lyonnais et la Bresse). On notera qu'un amincissement de la lithosphère mantelique plus marqué à l'ouest qu'à l'est est bien en accord avec le décentrage observé du volcanisme miocène vers l'ouest du rift.

DISCUSSION

La formation des fossés à l'Oligocène

La symétrie de miroir des fossés d'effondrement relève d'une histoire oligocène inférieur et moyen. En effet, cette période s'accompagne d'un amincissement crustal et d'une sédimentation plus importante dans les deux demi-grabens latéraux avec une sédimentation épaisse et une récurrence des influences marines, tandis que le graben central avec un amincissement crustal et une sédimentation moindre reste constamment au dessus du niveau de base (table I).

L'extension crustale à l'Oligocène inférieur et moyen est marqué par le fonctionnement synchrone des deux failles bordières des demi-grabens occidental et oriental, qui se traduit par un remplissage sédimentaire important extrêmement localisé. Le basculement du socle associé à ces failles bordières correspond à deux « roll over » montrant que les deux failles limitant les demi-grabens sont des failles listriques (fig. 2). L'enracinement horizontal de ces deux failles bordières se produit à la base de la croûte fragile, en tout état de cause avant 11-12 km en Limagne puisque le réflecteur sismique observé à cette profondeur dans le demi-graben de la Limagne n'est pas affecté par la faille [Fig. 9 in Zeyen *et al.*, 1997], et avant 18 km en Bresse comme le montrent également les données sismiques sur les réflecteurs de la croûte profonde [Truffert *et al.*, 1990]. L'extension ainsi réalisée dans la croûte fragile doit s'accompagner d'une extension synchrone dans la croûte ductile, et c'est logiquement que l'amincissement crustal est maximal à l'aplomb de ces deux failles bordières.

La rupture dans cette évolution symétrique paraît se réaliser à l'Oligocène supérieur. A cette époque, la dessalure des dépôts du demi-graben oriental est contemporaine d'apports détritiques en provenance des monts du Lyonnais qui s'individualisent [Chauve *et al.*, 1980 ; Rat, 1984]. La même évolution se retrouve dans le graben central où des conglomérats à blocs métriques d'origine ouest signalent la surrection des monts du Forez [Ech-Cherif El Kettani, 1996]. Rien de tel n'est observé à l'Oligocène supérieur dans le demi-graben occidental où la sédimentation est de type marno-calcaire (1 000 m) avec incursions marines et où les sondages pétroliers indiquent au contraire une diminution des apports détritiques de provenance ouest [Morange *et al.*, 1971]. La poursuite de la sédimentation dans le demi-graben occidental pendant l'Oligocène supérieur est à mettre directement en relation avec l'amincissement crustal plus prononcé sous la Limagne que sous la Bresse.

Modèle d'extension asymétrique ?

Les différents éléments structuraux discutés jusqu'à présent, tels que la géométrie des fossés ou l'allure du Moho et du LAB, sont reportés sur une coupe à l'échelle lithosphérique de la transversale nord du MCR (fig. 4). La remontée du LAB décentrée vers l'ouest du système évoque un modèle d'extension asymétrique, où une faille de détachement recoupe obliquement toute la lithosphère, d'une faille bordière majeure en surface jusqu'à l'interface lithosphère-asthénosphère [e.g. Wernicke, 1985 ; Ruppel, 1995]. Dans ce modèle théorique, on observe un décalage entre l'amincissement crustal et l'amincissement de la lithosphère mantellique (fig. 5). La transposition de ce modèle à la transversale nord du MCR reviendrait à relier la faille bordière de la Bresse à la remontée de l'asthénosphère à l'ouest, ce qui impliquerait que le fort amincissement du manteau lithosphérique sous la partie occidentale du système s'accompagne d'un fort amincissement crustal sous la Bresse. Ceci n'est à l'évidence pas observé. La faille bordière de la Bresse a un rejet notoirement insuffisant pour jouer un tel rôle, et l'amincissement crustal maximal est localisé au niveau du demi-graben de la Limagne. On peut également remarquer que les données de géophysique profonde, telles que l'allure du Moho ou les réflecteurs horizontaux dans la croûte, ne montrent pas la trace d'une faille de détachement recoupant obliquement la croûte continentale [Bergerat *et al.*, 1990 ; Truffert *et al.*, 1990].

Une variante à ce modèle asymétrique serait de le restreindre à la croûte seule et de relier la faille bordière de la Bresse au décalage du Moho à l'aplomb du demi-graben de la Limagne, avec une extension globalement symétrique du manteau sous-jacent, selon un modèle observé dans le fossé rhénan [Brun *et al.*, 1992] (fig. 10). Outre qu'un tel modèle nécessiterait une faille de détachement traversant la croûte ductile obliquement sur 200 km de distance, la faille maîtresse du système en surface serait de nouveau la faille bordière de la Bresse ; et la formation du demi-graben de la Limagne avec le fort rejet de sa faille bordière, son taux d'amincissement crustal important et son épaisse sédimentation resterait inexpliquée. De même, ce modèle ne serait pas en mesure d'expliquer la remontée décentrée de l'asthénosphère à l'ouest du système.
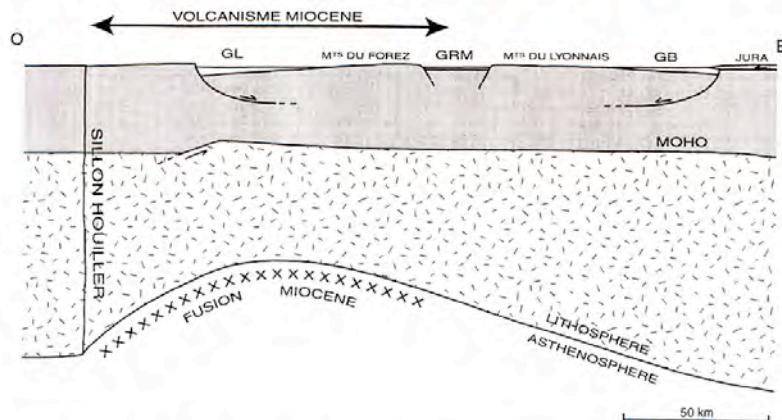
FIG. 4. – La coupe lithosphérique actuelle de la transversale nord du rift du Massif central résulte d'une extension crustale avec formation de fossés d'effondrement à l'Oligocène suivie d'un amincissement du manteau lithosphérique par érosion thermo-mécanique au Miocène (discussion dans le texte). Même échelle verticale et horizontale.

FIG. 4. – *The lithospheric cross-section of the northern MCR transect reveals Oligocene crustal extension followed by Miocene thermal thinning of the lithospheric mantle (explanation in the text). Same vertical and horizontal scale.*

Extension crustale oligocène/amincissement miocène du manteau lithosphérique

Le taux d'amincissement crustal maximal observé sur la coupe sismique actuelle (table II) peut être relié directement à l'épaisseur maximale des sédiments oligocènes dans les trois fossés d'effondrement (fig. 6). Cette relation linéaire entre épaisseur des sédiments oligocènes et taux d'amincissement montre que l'amincissement crustal observé actuellement a été réalisé pendant l'extension oligocène et n'a pas été modifié pendant l'évolution miocène et pliocène du rift.

Les courbes d'isoprofondeur du LAB, clairement centrées sur les deux grands centres volcaniques d'âge miopliocène du sud du Massif central (Cantal et Velay-Deves), suggèrent que l'amincissement du manteau lithosphérique est en grande partie postérieur à l'extension oligocène. Cette hypothèse est confortée par le taux d'amincissement maximal du manteau lithophérique sur la transversale septentrionale du rift. Nettement supérieur à celui de la croûte puisqu'il dépasse 50 %, il est difficilement compatible, pour des raisons purement isostatiques, avec une sédimentation au niveau de la mer pendant la période oligocène. En revanche, l'amincissement du manteau lithosphérique au Miocène s'accorde avec le soulèvement de la partie occidentale de cette transversale à cette époque, et l'apparition quasi-synchrone du volcanisme, lui aussi limité à la partie occidentale du système.

La coupe lithosphérique (fig. 4) résulte d'une évolution en deux temps puisqu'elle intègre des éléments structuraux qui ne sont pas synchrones : la formation des fossés et l'amincissement crustal relève d'une histoire oligocène tandis que l'amincissement prononcé du manteau lithosphérique relève principalement d'une évolution ultérieure miocène. Le diachronisme entre l'amincissement oligocène de la croûte et l'amincissement miocène du manteau lithosphérique n'est viable cinématiquement que si l'on considère que seul l'Oligocène correspond à une période d'extension, d'ailleurs d'ampleur assez modeste. Il n'est en effet pas envisageable de réaliser une extension aussi importante dans le manteau lithosphérique au Miocène sans affecter la croûte elle-même, si bien que le Miocène correspond à une période d'amincissement du manteau lithosphérique, sans extension de la lithosphère. Nous
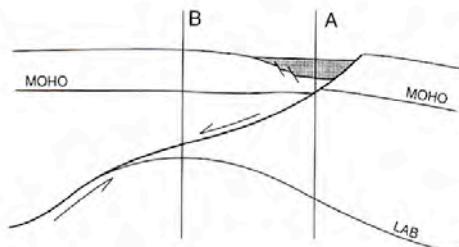
FIG. 5. – Le modèle d'extension asymétrique de Wernicke [1985] implique un décalage entre l'amincissement crustal (A) et l'amincissement du manteau lithosphérique (B). Ce modèle ne peut s'appliquer à la transversale nord du MCR (discussion dans le texte). Même échelle verticale et horizontale.

FIG. 5. – *The asymmetric model of Wernicke [1985] shows maximum thinning of the crust at (A) and maximum thinning of the lithospheric mantle at (B). This model is not consistent with structural characteristics along the northern transect of the MCR (details in text). Same vertical and horizontal scale.*
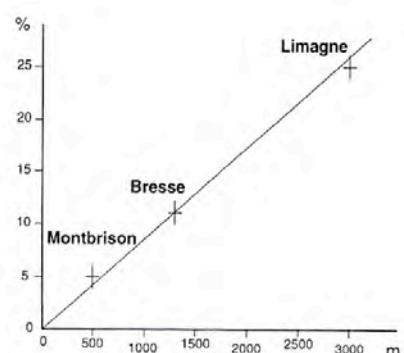
FIG. 6. – L'amincissement crustal (%) observé actuellement en fonction de l'épaisseur (m) des sédiments oligocènes dans les trois fossés de la transversale nord du MCR.

FIG. 6. – *Crustal thinning (%) calculated from the present-day crustal cross-section as a function of the thickness of Oligocene sediments in the three main grabens of the northern transect of the MCR.*

interprétons cet épisode miocène (et pliocène), bien révélé par les études de tomographie sismique [Granet, 1995a et b ; Sobolev *et al.*, 1996 et 1997], comme le résultat d'une importante érosion thermo-mécanique de la lithosphère alors que l'extension proprement dite de la lithosphère est déjà achevée. C'est cette évolution post-oligocène qui a jusqu'à présent focalisée l'attention de la plupart des chercheurs [e.g. Coisy et Nicolas, 1978 ; Lucazeau *et al.*, 1984 ; Nicolas *et al.*, 1987 ; Granet *et al.*, 1995a et b ; Sobolev *et al.*, 1996 et 1997].

Le basculement du Moho au Miocène

La profondeur actuelle du Moho sur cette transversale (fig. 4) ne peut s'expliquer seulement par l'évolution oligocène. A cet égard, il faut en effet expliquer pourquoi le Moho est moins profond sous les monts du Forez et du Lyonnais (environ 28 km) que sous la Bresse (29 km), alors que ces deux premiers domaines ont subi un amincissement crustal nul, ou moindre que le demi-graben oriental. Nous proposons, à la suite de Lucazeau et Bayer [1982], que le soulèvement isostatique consécutif à l'érosion thermo-mécanique de la lithosphère mantellique sous le demi-graben de la Limagne ait induit au Miocène (et sans doute jusqu'à l'actuel) une flexure de la lithosphère. Les régions adjacentes des monts du Forez et du Lyonnais situées sur les flancs de cette flexure ont également été soulevées, ce qui a porté le socle à des altitudes non négligeables, relevant le Moho vers la surface. Il est clair également que la formation progressive des Alpes à la limite orientale du système se marque par un enfoncement du Moho vers l'est, susceptible de conjuguer ses effets avec le basculement lié à la remontée isostatique plus à l'ouest.

RIFTING ACTIF OU PASSIF ?

Il n'est pas dans le but de cet article de discuter les causes du rifting ouest européen. Il est cependant important, ne serait-ce que pour justifier le dispositif expérimental choisi dans la section suivante, de choisir entre les deux grands modèles de rifting : actif ou passif. A cet égard, il est utile de rappeler que l'évolution tectonique d'un rift est fortement dépendante du moteur de l'extension. L'ascension d'un point chaud (i.e. rift actif) provoque dans un premier temps un bombement topographique marqué, dont les causes essentiellement thermiques ont été modélisées numériquement [Fleitout *et al.*, 1986]. Si le volcanisme peut être synchrone de ce bombement en liaison avec la décompression de l'asthénosphère, l'extension de la lithosphère n'apparaît qu'ensuite, comme une conséquence de ce soulèvement. Il en résulte que la sédimentation est tardive dans l'évolution générale du système. L'évolution tectonique classique associée à ce mode de rifting correspond à la suite chronologique : bombement topographique et volcanisme puis extension et sédimentation [e.g. Park, 1988, p. 85]. A l'inverse, le rifting d'une lithosphère dû à des forces trouvant leur origine aux limites des plaques (i.e. rift passif) provoque d'abord un bassin de sédimentation où le volcanisme peut être rare ou absent. Ce n'est que dans un second temps qu'un soulèvement d'origine thermique et un volcanisme concomitant se produit. L'évolution tectonique classique associée à ce mode de rifting correspond alors à la suite chronologique : extension et sédimentation puis soulèvement et volcanisme [e.g. Park, 1988, p. 85].

Dans le cas du Massif central, le volcanisme demeure absent ou très timide durant l'Eocène supérieur et l'Oligocène, au cours desquels une sédimentation épaisse signe la phase majeure du rifting. L'absence d'un réseau hydrographique organisé, et de multiples et brèves incursions marines durant cette période, impliquent qu'aucun soulèvement

notable ne s'est encore réalisé. Ce n'est qu'à partir du Miocène, et jusqu'au Pléistocène, que le volcanisme s'intensifie et se généralise, concurremment à la surrection d'ensemble du Massif central. Cette chronologie bien établie plaide en faveur d'un rifting passif [Bois, 1993].

Il a été récemment proposé que l'anomalie thermique observée sous la partie sud du MCR corresponde à un diapir mantellique de taille réduite, issu d'un gigantesque point chaud (de type hawaiien) sous-jacent et commun à toute l'Europe occidentale et centrale [Granet *et al.*, 1995b]. Avorté en profondeur, ce point chaud serait le parent d'un essaim de diapirs mantellique, dont celui du Cantal. Cette hypothèse séduisante se heurte à la géométrie de l'anomalie thermique déduite des études tomographiques qui ne ressemble en rien à celle d'un diapir mantellique (cf. à titre de comparaison l'allure des points chauds d'Hawaii ou de l'Islande, ou ceux obtenus par modélisation numérique [e.g. Fleitout *et al.*, 1986] ou analogique [e.g. Ramberg, 1981 ; Mulugeta, 1985 ; Griffiths and Campbell, 1991] des rifts actifs). La présence d'un point chaud sous-jacent, qui ne serait pas en lui-même la cause du rifting, mais qui serait spatialement localisé au niveau du rift ouest européen, relève d'une coïncidence trop forte pour que les deux phénomènes ne soient pas liés. Plutôt qu'issu d'un point chaud dont on ne retrouve pas vraiment les caractéristiques pétrologiques [Berger, 1998], le volcanisme Cantal-Monts Dore et Velay-Devès, plusieurs (dizaines de) millions d'années après l'extension et la sédimentation, pourrait être la conséquence de déplacement de matériel asthénosphérique pendant la formation de la profonde racine lithosphérique des Alpes. Cette remontée de matériel asthénosphérique chaud serait accompagnée d'une érosion thermo-mécanique de la lithosphère mantellique à l'origine d'un soulèvement généralisé (i.e. lorsque l'amincissement de la lithosphère mantellique devient supérieur à celui de la croûte). Ces mouvements seraient localisés dans le manteau supérieur et ne relèveraient pas de l'activité d'un point chaud proprement dit. Il resterait de cette évolution post-extension et post-oligocène sous le MCR une anomalie thermique prononcée, observée par les études tomographiques.

MODÉLISATION DE L'EXTENSION OLIGOCÈNE

L'extension crustale à l'Oligocène inférieur et moyen ne peut se comprendre sans tenir compte de la déformation de l'ensemble de la lithosphère continentale. A cette échelle, le litage rhéologique de la lithosphère exerce un contrôle majeur sur le mécanisme d'extension. L'hypothèse de base de la modélisation est de considérer une structure thermique froide, héritée du rééquilibrage thermique après l'orogenèse varisque 300 Ma auparavant. La stratification rhéologique serait alors constituée d'une couche fragile pour la partie supérieure de la croûte, une couche ductile pour la partie inférieure de la croûte, de nouveau une couche fragile pour la partie supérieure du manteau lithosphérique et une couche ductile pour la partie inférieure du manteau lithosphérique [e.g. Buck, 1991]. Ce modèle quadricouche est caractérisé par le fort contrôle que les parties fragiles résistantes, en particulier celle du manteau, exerce sur la localisation des déformations.

La géométrie des fossés sur la transversale septentrionale du MCR est suffisamment caractéristique pour tenter de la relier à un mode d'étirement simple de la lithosphère. Cette géométrie correspond en surface à une symétrie globale de part et d'autre du graben central de Roanne-Montbrison. Cette symétrie de la déformation globale en surface implique sans doute que la déformation en profondeur, à l'échelle de la lithosphère tout entière, est elle aussi globalement symétrique, comme l'ont montré des expériences

sur le degré de symétrie des rifts lors de l'amincissement de la lithosphère [Allemand *et al.*, 1989].

Par ailleurs, d'autres expériences sur l'exhumation du manteau lithosphérique [Brun et Beslier, 1996] ont montré que la localisation de l'amincissement dans la partie supérieure fragile de la lithosphère mantellique produisait une asymétrie dans le système. Il n'y a pas forcément une correspondance étroite entre la localisation de la rupture dans le manteau fragile et la croûte fragile, parce que la couche ductile de la croûte inférieure joue le rôle d'une zone de décollement entre les deux parties fragiles de la lithosphère [Brun and Beslier, 1996], et/ou également parce que les failles majeures dans la croûte fragile peuvent correspondre à la réactivation de failles préexistantes. La géométrie des déformations en surface peut être induite par un certain nombre de paramètres, tels que la distance entre les zones de rupture dans le manteau lithosphérique fragile, le couplage mécanique entre les couches fragiles et ductiles du système ou le rapport fragile/ductile de la croûte.

Ces paramètres ont été étudiés par une approche expérimentale dont les résultats détaillés seront publiés ultérieurement, mais dont il est utile de montrer ici un des enseignements principaux. Le dispositif expérimental correspond à un bi-couche sable-silicone de 50 cm de longueur et 3 cm d'épaisseur, étiré transversalement aux limites du système grâce à deux vérins pilotés par ordinateur (fig. 7). La localisation de la déformation asymétrique est obtenue par des discontinuités de vitesse (DV) situées à la base du modèle (fig. 7 et 8), selon une procédure expérimentale déjà utilisée pour étudier la formation des bassins sédimentaires asymétriques [Faugère *et al.*, 1986]. Les expériences sont conduites à l'échelle de la croûte (1 cm dans le modèle représente 10 km dans la nature) et les matériaux utilisés permettent de modéliser un profil de résistance proche de celui supposé dans la nature (fig. 8), à savoir une partie supérieure fragile (15 km) régie par le critère de rupture Mohr-Coulomb et une partie inférieure ductile de comportement visqueux (15 km). Le choix du sable pour la partie fragile et d'une silicone pour la partie ductile permet de dimensionner correctement les expériences [e.g. Faugère et Brun, 1984] (cf. Annexe). Dans ce type d'expériences, les discontinuités de vitesse (DV) localisées à la base de la couche ductile représentent les zones de rupture dans la partie fragile de la lithosphère mantellique [Allemand *et al.*, 1989] (fig. 8). Toutes les expériences ont été effectuées avec un rapport fragile/ductile de 1.

La première série d'expériences a testé la géométrie des structures lorsque le modèle ne possède qu'une seule DV à la base de la couche ductile. Le fonctionnement de cette DV unique entraîne la formation de deux fossés parallèles. En coupe, ces deux fossés correspondent à l'association d'un demi-graben asymétrique et d'un graben symétrique (fig. 9). La reproductibilité de ces expériences permet de mettre en évidence deux constantes, d'une part la largeur du graben symétrique (Ca ≈ 2 cm) et d'autre part la distance entre la faille bordière du demi-graben et le centre du graben symétrique (Cb ≈ 8 cm) (fig. 9). La géométrie du demi-graben est contrôlée par le fonctionnement de la faille bordière dont l'enracinement dans la couche ductile assure localement le basculement des couches de sable initialement horizontales, selon une évolution de type roll-over. La géométrie du demi-graben asymétrique présente des analogies frappantes avec l'un des segments du fossé rhénan déduit des études géophysiques [Brun *et al.*, 1992] (fig. 10).

La seconde série d'expériences a consisté à faire fonctionner simultanément deux DV à la base de la couche ductile. Lorsque les deux DV sont initialement éloignées d'une distance suffisante (> 6 cm), deux grabens symétriques se
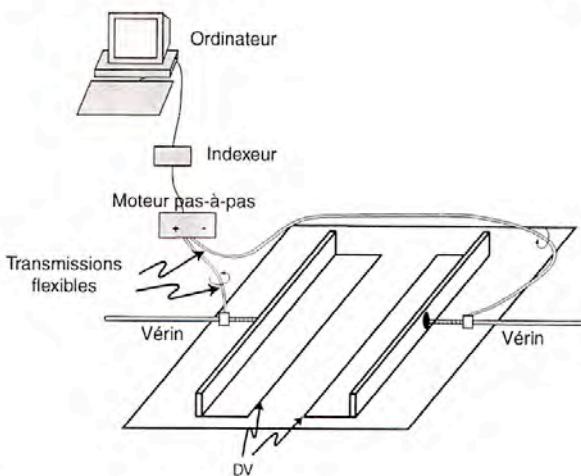

FIG. 7. – Dispositif expérimental. Le bi-couche sable-silicone est placé entre les deux parois latérales qui s'écartent sous l'action des deux vérins. A la base du modèle, deux films plastiques, solidaires des parois latérales, induisent deux discontinuités de vitesse (DV) où se localise la déformation extensive.

FIG. 7. – *Experimental device. The two-layer model (sand-silicone) is emplaced between two lateral walls that move aside when pulled out by two screw-jacks. At the base of the model, plastic films attached to the walls induce two velocity discontinuities (DV) which initiate the deformation.*
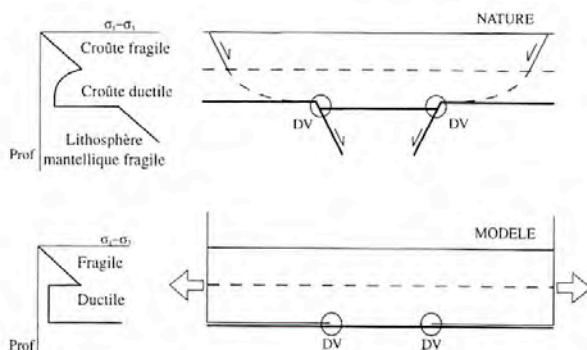

FIG. 8. – Profils de résistance dans la nature et dans les modèles. Interprétation des discontinuités de vitesse dans les expériences en terme de rupture de la partie fragile de la lithosphère mantellique (explication dans le texte).

FIG. 8. – *Strength profiles in nature and models. Rupture in the brittle layer of the lithosphere is simulated by the two DV at the base of the models (further explanation in text).*

forment en association avec chacun des deux demi-grabens (fig. 11, sommet). Une distance initiale plus importante entre les deux DV se solde toujours par une augmentation de la distance entre les deux grabens symétriques sans apparition de nouveau graben. L'association demi-graben/graben symétrique est clairement liée au fonctionnement de chacune des deux DV, comme dans les expériences témoins avec une seule DV, et les deux constantes Ca et Cb sont égales à celles mesurées dans ces expériences témoins.

En revanche, lorsque la distance initiale entre les deux DV est comprise entre 4 et 6 cm, il ne se forme qu'un seul graben symétrique, qui est en quelque sorte partagé par les deux demi-grabens (fig. 11, milieu). Une certaine fluctuation dans la valeur de la constante Cb s'observe alors pour

ajuster le système en trois fossés, mais cette fluctuation reste toujours inférieure au centimètre.

D'après les rapports de longueur entre modèle et nature, on en déduit que pour une distance voisine de 180 km entre

les deux failles bordières, pour une croûte de 30 km d'épaisseur et un rapport fragile/ductile de 1, il ne se forme qu'un seul graben symétrique entre deux demi-grabens à vergence opposée. Le graben symétrique est alors d'une vingtaine de kilomètres de largeur. Sur une transversale passant par le graben de Montbrison, la largeur de celui-ci est proche de la constante Ca, et la distance entre les deux failles bordières de la Limagne et de la Bresse est d'environ 185 km. Les expériences présentées ci-dessus suggèrent fortement

FIG. 9. – Expérience réalisée avec une seule DV à la base du modèle (rapport fragile/ductile de 1 et épaisseur du modèle de 3 cm). Le fonctionnement de la DV est à l'origine de la formation d'un demi-graben et d'un graben symétrique. La largeur du graben symétrique (Ca) ainsi que la distance entre la faille bordière du demi-graben et le centre du graben symétrique (Cb) sont constantes dans toutes ces expériences à une seule DV.

FIG. 9. – *Experiment with a single DV at the base of the model (brittle/ductile ratio equal to 1 and thickness of the model equal to 3 cm). A half-graben and a symmetric graben formed above the DV. The width of the symmetric graben (Ca) and the distance between the border fault of the half-graben and the centre of the symmetric graben (Cb) are constant in this type of experiments.*

FIG. 10. – Le demi-graben obtenu dans les expériences à une seule DV (sommet) montre des analogies frappantes avec la structure crustale du graben du Rhin telle qu'elle a été déduite des études sismiques [bas : Brun *et al.*, 1992].

FIG. 10. – *The half-graben formed in experiments with a single DV (top) shows striking similarities to the crustal structure of the Rhine graben as deduced from seismic studies [bottom after Brun et al., 1992].*

FIG. 11. – Représentation synthétique des structures extensives obtenues dans les expériences en fonction de la distance initiale entre les deux DV basales. Sommet : lorsque les deux DV sont au départ suffisamment éloignées, chaque DV forme une association demi-graben/graben symétrique comme dans les expériences à une seule DV. Une distance initiale supérieure entre les deux DV augmente seulement le horst central séparant les deux groupes de structures associés à chaque DV. Milieu : lorsque la distance initiale entre les deux DV est réduite, un seul graben symétrique est partagé par les deux demi-grabens latéraux car la distance séparant ces derniers est insuffisante pour créer deux grabens symétriques. Bas : lorsque les deux DV sont initialement contiguës ou très proches, la distance séparant les deux failles bordières devient même insuffisante pour créer un graben symétrique et les deux demi-grabens sont séparés par un horst central.

FIG. 11. – *Schematic representation (drawn from photo) of extensional structures in experiments with two basal DV. Top : when the starting distance between the two DV is large, each DV initiates a pair of half-graben/symmetric graben as in single DV experiments. A larger starting distance between the two DV simply increases the width of the central horst between the two groups of structures linked to each DV. Middle : when the starting distance between the two DV is reduced, a single symmetrical graben is shared by the two half-grabens as the distance between those two is not enough to create two symmetrical grabens. Bottom : when the two DV are touching or are very close, the distance between the two border faults becomes too short for creating a symmetrical graben and the two half-grabens are separated by a central horst.*
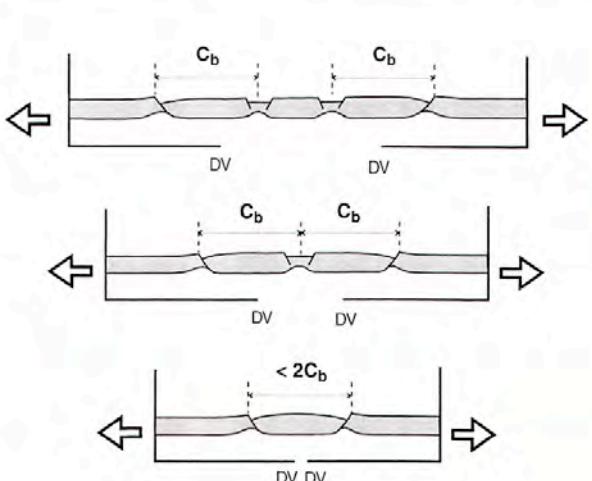
que la structure générale des fossés sur la transversale septentrionale du MCR résulte de deux ruptures mantelliques distantes d'une cinquantaine de kilomètres.

Un cas limite correspond aux expériences où les deux discontinuités de vitesse sont contiguës ou très proches au début de l'extension. La diminution de la distance entre les deux failles bordières (< 2Cb) ne permet plus la formation du graben central et les deux demi-grabens sont séparés par une zone haute assimilable à un horst (fig. 11, bas). Des résultats similaires ont été obtenus avec un dispositif expérimental sensiblement identique [Allemand, 1990]. Dans ces expériences, les deux DV sont liées au fonctionnement de deux tapis roulants qui s'écartent à la même vitesse de part et d'autre d'un point central [fig. III.6 in Allemand, 1990, p. 84]. Les résultats ont servi à l'interprétation de l'extrémité nord du MCR où les fossés de Limagne et de Bresse encadrent le horst central du Morvan [fig. V.8b in Allemand, 1990, p. 152]. Cette géométrie de la bordure nord a été interprétée comme résultant d'une seule rupture mantellique sous le Morvan [Allemand, 1990, p. 153]. Il est tentant de considérer la réunion progressive vers le nord des deux fossés de Roanne et de la Limagne à l'ouest du Morvan (fig. 1) comme l'expression en surface de la jonction de deux ruptures mantelliques filant sous l'axe du Morvan.

CONCLUSION

Les conclusions principales de ce travail sur la transversale nord du MCR sont les suivantes :

1) la structure lithosphérique actuelle résulte de deux épisodes distincts : (i) une extension oligocène avec formation de fossés d'effondrement proches du niveau de la mer et (ii) un amincissement du manteau lithosphérique au Miocène, sans extension, probablement par érosion thermo-mécanique. Ce deuxième épisode est responsable de la surrection et du volcanisme observé du Miocène à l'actuel ;

2) la période d'extension oligocène s'accompagne de la formation de trois grands fossés d'effondrement, dont la géométrie est celle d'une symétrie de miroir de part et d'autre d'un graben central symétrique encadré par deux demi-grabens à vergence opposée. Cette symétrie se retrouve pendant l'Oligocène inférieur et moyen dans l'évolution stratigraphique, l'épaisseur des sédiments et la quantité d'amincissement crustal ;

3) la modélisation analogique montre que la géométrie en surface des fossés d'effondrement peut s'expliquer par deux ruptures peu éloignées dans la partie fragile du manteau lithosphérique ;

4) l'évolution du rift à l'Oligocène supérieur montre que l'étirement s'est ensuite localisé au niveau du demi-graben occidental. Les causes de cette évolution ne peuvent être définies avec certitude, même si on peut supposer que la progression du bassin flexural des Alpes vers le domaine de la Bresse est à même de perturber le régime extensif apparu dans ce domaine à la fin de l'Eocène.

Annexe

Le rapport des longueurs L* modèle-nature (m/n) est de 10^{-6} (1 cm dans le modèle représente 10 km dans la nature). Le rapport des masses volumiques entre matériaux analogues et roches naturelles est de 0,5. Les expériences s'effectuant dans le champ gravitationnel terrestre (g* = 1), le rapport des contraintes entre le modèle et la nature est de :

$$\sigma^* = \rho^* g^* L^* = 5 \times 10^{-7} \qquad (1)$$

Les matériaux utilisés dans les expériences doivent être 2×10^6 fois moins résistants que ceux du prototype expérimental. Pour simuler la partie fragile de la croûte, dont le comportement est indépendant de la vitesse de déformation, le sable est un matériau analogue particulièrement bien adapté. Son angle de friction interne, qui est un nombre sans dimension, est identique à celui de la plupart des roches ($\Phi = 30°$) et sa cohésion négligeable. La cohésion des roches étant estimé à 10^7 Pa, la cohésion du matériau

analogue τ_0 déduite du rapport des contrainte σ^* doit être de l'ordre de 5 Pa, ce qui est effectivement négligeable.

Le matériel analogue utilisé dans les expériences pour simuler la partie inférieure ductile de la croûte est une silicone, matériel newtonien de viscosité égale à 3×10^4 Pas. En considérant que la viscosité de la croûte ductile est de l'ordre de 5×10^{20} Pas, le rapport des viscosités modèle-nature est de 0,6 10^{-16}. Le rapport des vitesses est alors donné par la relation :

$$V^* = \frac{\sigma^* L^*}{\mu^*} = \frac{\rho^* g^* L^{*2}}{\mu^*} = 8,3 \times 10^3 \qquad (2)$$

Si la vitesse d'extension dans la nature est de l'ordre de 1 cm/a, la vitesse d'extension imposée dans les modèles doit être de l'ordre de 1 cm/h. La vitesse de déplacement aux deux limites latérales de la boîte expérimentale, obtenue par deux vérins reliés à un moteur pas à pas (fig. 5), est alors de 0,5 cm/h.

Références

ALLEMAND P. (1990). – Approche expérimentale de la mécanique du rifting continental. – *Mém. Doc. Géosci. Rennes*, **38**, 175 p.

ALLEMAND P., BRUN J.P., DAVY Ph. & Van DEN DRIESSCHE J. (1989). – Symétrie et asymétrie des rifts et mécanismes d'amincissement de la lithosphère. – *Bull. Soc. géol. Fr.*, (8), **V**, 445-451.

BABUSKA V. & PLOMEROVA J. (1992). – The lithosphere in Central Europe : seismological and petrological aspects. – *Tectonophysics*, **207**, 141-163.

BELLON H., GILLOT P.Y. & NATIVEL P. (1974). – Eocene volcanic activity in Bourgogne, Charollais, Massif central (France). – *Earth Planet. Sci. Lett.*, **23**, 53-58.

BELLON H. & HERNANDEZ J. (1979). – Chronologie du volcanisme dans le Forez (Massif central français) : place dans l'activité tertiaire de France. – *C. R. somm. Soc. géol. Fr.*, **4**, 175-179.

BERGER E. (1998). – 25 ans de modèles expliquant le volcanisme du Massif central : fausses certitudes et vraies hypothèses. – *17e RST*, Brest, p. 72.

BERGERAT F. (1977). – La fracturation de l'avant-pays jurassien entre les fossés de la Saône et du Rhin. Analyse et essai d'interprétation dynamique. – *Rev. Géogr. Phys. Géol. Dyn.*, **2**, 19, 325-338.

BERGERAT F., MUGNIER J.L., GUELLEC S., TRUFFERT C., CAZES M., DAMOTTE B. & ROURE F. (1990). – Extensional tectonics and subsidence of the Bresse basin : an interpretation from ECORS data. – *Mém. Soc. géol. Fr.*, **156**, 145-156.

BLANC G., DOLIGEZ B., LAJAT D. & MASCLE A. (1991). – Evaluation du potentiel pétrolier des formations paléozoïques de la Bresse et de sa bordure jurassienne. – *Bull. Soc. géol. Fr.*, **162**, 409-422.

BOIS C. (1993). – Initiation and evolution of the Oligo-Miocene rift basins of southwestern Europe : contribution of deep seismic reflection profiling. – *Tectonophysics*, **226**, 227-252.

BRUN J.P. & BESLIER M.O. (1996). – Mantle exhumation at passive margin. – *Earth Planet. Sci. Lett.*, **142**, 161-173.

BRUN J.P., GUTSCHER M.A. & DEKORP-ECORS teams (1992). – Deep crustal structure of the Rhine Graben from DEKORP-ECORS seismic reflection data : a summary. – *Tectonophysics*, **208**, 139-147.

BUCK W.R. (1991). – Modes of continental lithospheric extension. – *J. Geophys. Res.*, **96**, 20161-20178.

CANTAGREL J.M. & THONAT A. (1976). – Age du volcanisme dans le Cézallier (MCF) et migration de l'activité volcanique. – *C. R. Acad. Sci.*, Paris, **282**, 1837-1840.

CHAMBON S. (1997). – Géochronologie $^{39}/^{40}$Ar de quelques amphiboles de pépérites de Limagne. – TER (inédit), Clermont-Ferrand, 37 p.

CHANTEPIE M. (1990). – Le volcanisme basaltique miocène et pliocène dispersé dans la région de Clermont-Ferrand et sur le plateau des Domes : étude pétrographique et géochronologique. – Diplôme d'Etudes Approfondies, Clermont-Ferrand, 40 p.

CHAUVE P., ENAY R., FLUCK P. & SITTLER C. (1980). – L'Est de la France (Vosges, fossé rhénan, Bresse, Jura). – *2ᵉ Cong. Géol. Intern.*, Paris, 3-81.

CHEGUER L. (1996). – Les laves miocènes de la Limagne d'Allier et des plateaux bordiers (Massif central français). Caractérisation d'une série magmatique alcaline sous-saturée (basanite-phonolites) associée à un rift intracontinental. – Thèse d'Université, Clermont-Ferrand.

COISY P. & NICOLAS A. (1978). – Regional structure and geodynamics of the upper mantle beneath the Massif Central. – *Nature*, **274**, 429-336.

DEBEGLIA N. (1984). – Interprétation des profils gravimétriques de la Bresse. In : S. DEBRAND-PASSARD Ed. – *Mém. BRGM*, **125**, 52-57.

ECH-CHERIF EL KETTANI D. (1996). – Géologie du fossé du Forez : essai de synthèse et comparaison avec les autres bassins tertaires du Massif central Français. – Thèse d'Université, St-Etienne, 372 p.

FAUGERE E. & BRUN J.P. (1984). – Modélisation expérimentale de la distension continentale. – *C. R. Acad. Sci.*, Paris, **299**, 365-370.

FAUGERE E., BRUN J.P. & VAN DEN DRIESSCHE J. (1986). – Bassins asymétriques en extension pure et en décrochement : modèles expérimentaux. – *Bull. Centre Rech. Explor. Prod. Elf Aquitaine*, **10**, 2, 13-21.

FLEITOUT L., FROIDEVAUX C. & YUEN D. (1986). – Active lithosphere thinning. – *Tectonophysics*, **132**, 271-278.

GIRAUD J. (1902). – Etudes géologiques sur la Limagne (Auvergne). – Thèse d'Etat. – Ed. Ch. Béranger, Paris, 410 p.

GORIN G. (1974). – Etude palynostratigraphique de sédiments paléogènes de la Grande Limagne (Massif central, France). – Thèse d'Université, Genève, 314 p.

GRANET M., STOLL G., DOREL J., ACHAUER U., POUPINET G. & FUCHS K. (1995a). – Massif central (France) : new constraints on the geodynamical evolution from teleseismic tomography. – *Geophys. J. Internat.*, **121**, 1, 33-48.

GRANET M., WILSON M. & ACHAUER U. (1995b). – Imaging a mantle plume beneath the French Massif Central. – *Earth Planet. Sci. Lett.*, **136**, 281-296.

GRIFFITHS R. & CAMPBELL I. (1991). – Interaction of mantle plume heads with the Earth's surface and onset of small-scale convection. – *J. Geophys. Res.*, **96**, 18295-18310.

HIRN A. & PERRIER G. (1974). – Deep seismic sounding in the Limagne graben. In : J.H. ILLIES & K. FUCH Eds., Approaches to taphrogenesis. – Springer, Stuggart, 329-340.

HIROSE K. & KUSHIRO I. (1993). – Partial melting of dry peridotites at high pressures : determination of compositions of melts segregated from peridotites using aggregates of diamond. – *Earth Planet. Sci. lett.*, **114**, 477-489.

HOURRIERE F., LEYRIT H., BESSONNEAU D., BULTEAU J.F. & DERVIN T. (1998). – Age, genèse et évolution des diatrèmes pépéritiques de Limagne (Massif central). – *17ᵉ RST*, Brest, p. 131.

LE GRIEL A. (1991). – L'évolution géomorphologique du Massif central français. – Thèse d'Etat, Lyon, 3 tomes (imprimé à compte d'auteur).

LIENHARDT G. (1962). – Géologie du bassin houiller stéphanien du Jura et de ses morts-terrain. – *Mém. BRGM*, **9**.

LUCAZEAU F. & BAYER R. (1982). – Evolution géothermique et géodynamique du Massif central français depuis l'Oligocène. – *Ann. Geophys.*, **38**, 405-429.

LUCAZEAU F., VASSEUR G. & BAYER R. (1984). – Interpretation of heat flow data in the French Massif central. – *Tectonophysics*, **103**, 99-119.

MAURY R.C. & VARET J. (1980). – Le volcanisme tertiaire et quaternaire en France. – *Mém. BRGM*, **107**, 138-159.

MERGOIL J. & BOIVIN P. (1993). – Le Velay, son volcanisme et les formations associées. – *Géol. France*, **3**, 3-96.

MORANGE A., HERITIER F. & VILLEMIN J. (1971). – Contribution de l'exploration pétrolière à la connaissance structurale et sédimentaire de la Limagne dans le Massif central. In : Symposium J. Jung : Géologie, géomorphologie et structure profonde du Massif central Français. – Plein Air Service, Clermont-Ferrand, 295-308.

MULUGETA G. (1985). – Dynamic models of continental rift valley systems. – *Tectonophysics*, **113**, 49-73.

NICOLAS A., LUCAZEAU F. & BAYER R. (1987). – Peridotite xenoliths in Massif Central basalts, France : textural and geophysical evidence for asthenospheric diapirism. In : P.H. NIXON Ed., Mantle xenolith. – John Wiley, Chichester, 563-574.

PARK R.G. (1988). – Geological structures and moving plates. – Blackie & Son Ltd, Bishopbriggs, Glasgow, 337 p.

PERRIER G. & RUEGG J.C. (1973). – Structure profonde du Massif central français. – *Ann. Geophys.*, **29**, 435-502.

POIDEVIN J.L. & BRIOT D. (1996). – Les invasions marines dans le Rupélien supérieur de Limagne (MCF) : Apports des isotopes du strontium. – *16ᵉ RST*, 10-12 avril, p. 13.

RAMBERG H. (1981). – Gravity, deformation and the Earth's crust. – Academic Press (second edition), New York, 452 p.

RAT P. (1984). – Une approche de l'environnement structural et morphologique du Pliocène et du Quaternaire bressan. – *Géol. France*, **3**, 185-196.

RUPPEL C. (1995). – Extensional processes in continental lithophere. – *J. Geophys. Res.*, **100**, B12, 24187-24215.

SOBOLEV S.V., ZEYEN H., STOLL G., WERLING F., ALTHERR R. & FUCHS K. (1996). – Upper mantle temperature from teleseismic tomography of French Massif central including effects of composition, mineral reactions, anharmonicity, anelasticity and partial melt. – *Earth Planet. Sci. Lett.*, **139**, 147-163.

SOBOLEV S.V., ZEYEN H., GRANET M., ACHAUER U., BAUER C., WERLING F., ALTHERR R. & FUCHS K. (1997). – Upper mantle temperatures and lithosphere-asthenosphere system beneath the French Massif Central constrained by seismic, gravity, petrologic and thermal observation. – *Tectonophysics*, **275**, 143-164.

SOURIAU A. (1976). – Structure profonde sous la France obtenue à partir des ondes de surface. – *Bull. Soc. géol. Fr.*, **18**, 1035-1093.

TRUFFERT C., BURG JP., CAZES M., BAYER R., DAMOTTE B. & REY D. (1990). – Structures crustales sous le Jura et la Bresse : contraintes sismiques et gravimétriques le long des profils ECORS Bresse-Jura et Alpes II. – *Mém. Soc. géol. Fr.*, **156**, 157-164.

VINCENT P., AUBERT M., BOIVIN P., CANTAGREL J.M. & LENAT J.F. (1977). – Découverte d'un volcanisme paléocène en Auvergne : les maars de Menat et leurs annexes : étude géologique et géophysique. – *Bull. Soc. géol. Fr.*, **14**, 1057-1070.

WERNICKE B. (1985). – Uniform-sense normal simple shear of the continental lithosphere. – *Can. J. Earth Sci.*, **22**, 108-125.

WILSON M. & DOWNES H. (1991). – Tertiary Quaternary extension related alkaline magmatism in western and central Europe. – *J. Petrol.*, **32**, 811-849.

ZEYEN H., NOVAK O., LANDES M., PRODEHL C., DRIAD L. & HIRN A. (1997). – Refraction-seismic investigations of the northern Massif Central (France). – *Tectonophysics*, **275**, 99-118.

Annexe 2 :

Michon, L., O. Merle (2001) The evolution of the Massif Central Rift: Spatio-temporal distribution of the volcanism. *Bull. Soc. Géol. Fr.,* 172, 2, 69-80.

The evolution of the Massif Central rift :
spatio-temporal distribution of the volcanism

LAURENT MICHON[1] and OLIVIER MERLE[1]

Key words. – Massif Central, Cenozoic, Rifting, DEM, Volcanism, Tectonic

Abstract. – The Massif Central area is the largest magmatic province of the West-European Rift system. The spatial-temporal distribution of Tertiary-Quaternary volcanism in the Massif Central, France, shows that three magmatic phases can be defined, each of them characterized by different volumes and different locations. The first event, termed the *pre-rift magmatic event*, is very scarce and restricted to the north of the Massif Central. It is suggested that this could result from lithospheric bending of the European lithosphere ahead of the incipient Alpine chain during the Paleocene. The second event, termed the *rift-related magmatic event*, is located in the north of the Massif Central only and is spatially connected with zones of high crustal thinning (i.e. the Limagne graben). It immediately follows Oligocene graben formation and associated sedimentation, and is represented by more than 200 scattered monogenic edifices. This second event can be attributed to partial melting as a consequence of lithospheric thinning that affected the north of the Massif Central during the rifting event. The lack of volcanism in the south during the same period of time is probably related to the very slight lithospheric thinning during the Oligocene. The third event, termed the *major magmatic event*, started first in the south in the upper Miocene at about 15 Ma, well after the end of the sedimentation. It is unrelated to any extensional event. This major magmatic event reached the north of the Massif Central at about 3.5 Ma, following a pause in volcanism of about 6 Ma after the rift-related magmatic event. These two episodes of the major magmatic event are spatially and temporally associated with the two main periods of uplift, suggesting a common origin for volcanism and uplift processes. The major magmatic event can be attributed to late thermal erosion of the base of the lithosphere above a mantle diapir, as suggested by seismic tomography data. This general magmatic evolution drawn from data at the Massif Central scale may apply to the Eger graben as well, as the three magmatic events described in this study (pre-rift magmatic event, rifting event and post-Miocene volcanic event) are also reported in the literature. This suggests that a single cause should explain the formation of the entire western European rift surrounding the Alpine mountain belt.

Evolution du rift du Massif central :
distribution spatio-temporelle du volcanisme

Mots clés. – Massif Central, Cénozoïque, Rifting, MNT, Volcanisme, Tectonique.

Résumé. – Le rift Ouest-européen correspond à un épisode d'extension lithosphérique qui s'est produit de l'Eocène supérieur jusqu'au Miocène inférieur. La direction d'extension est globalement perpendiculaire au front de la chaîne alpine et s'exprime, d'est en ouest, par la formation du graben de l'Eger, du graben du Rhin et des fossés d'effondrement du Massif central. Le Massif central est la plus importante province magmatique liée à cet épisode de rifting. Le volcanisme de cette province peut être séparé en trois épisodes successifs. 1. *Episode de magmatisme pré-rift.* Cet épisode correspond à 15 localités répertoriées presque exclusivement dans le nord du Massif central et datées du Paléocène à la fin de l'Eocène. 2. *Episode de magmatisme syn-rift.* La sédimentation oligocène s'est effectuée à un niveau proche de celui de la mer et pratiquement sans manifestation volcanique. A l'échelle du rift (i.e. de la Bresse à la Limagne), l'extension symétrique de l'Eocène supérieur à l'Oligocène moyen est devenue asymétrique à partir de l'Oligocène supérieur. L'épisode de magmatisme a débuté à l'Oligocène supérieur et s'est principalement développé au Miocène inférieur, pendant une quinzaine de millions d'années. Il est spatialement lié aux zones d'amincissement crustal maximal (fossé de la Limagne) et est absent de la partie sud du Massif central où les récentes données géophysiques montrent que l'amincissement crustal est négligeable. 3. *Episode de magmatisme majeur.* Cet épisode a démarré au sud du Massif central près de 15 Ma d'années après la fin de la sédimentation oligocène. C'est l'épisode majeur avec le développement des grandes provinces magmatiques du Cantal, du Velay ou de l'Aubrac. Une reprise plus tardive du volcanisme se produit dans la partie nord du Massif central, près de 6 Ma après la fin de l'épisode précédent dit syn-rift. Dans son ensemble, cet épisode majeur est caractérisé par deux pics d'activité : de 9 à 6,5 Ma uniquement au sud du Massif central, puis de 3,5 à 0,5 Ma tant au nord qu'au sud du Massif central.

L'analyse du MNT permet de montrer que le nord du Massif central présente un champ de structures dominé par des failles nord-sud. Il s'agit de failles d'âge varisque réactivées en faille normale pendant l'extension et la création des fossés d'effondrement. L'étude des profils d'équilibre des rivières au passage de certaines failles ainsi que l'âge des coulées de lave actuellement en position de reliefs inversés montrent que le soulèvement dans cette partie nord a débu-

té il y a environ 3 Ma et se poursuit actuellement. Au sud, le MNT révèle un champ de failles dominant orienté N135°E, souligné en particulier par des alignements volcaniques tels l'Aubrac, le Velay ou le Deves. Cette direction majeure a été acquise pendant le soulèvement de la partie sud qui a débuté il y a environ 10 Ma, bien avant le soulèvement plus récent de la partie nord. Ce soulèvement s'est ralenti entre 5,5 Ma et 3-3,5 Ma pour redevenir très actif depuis cette période jusqu'à l'actuel, comme dans la partie nord.

L'épisode magmatique pré-rift, extrêmement limité en volume, est attribué à une flexure de la lithosphère européenne au moment des premières compressions alpines pendant le Paléocène. Cette flexure de la lithosphère est encore apparente à l'échelle de la France grâce aux données de géophysique ou de géomorphologie dans le Massif central et le Morvan. L'épisode magmatique syn-rift, restreint au nord du Massif central, est clairement associé aux zones d'amincissement crustal maximal résultant principalement de l'extension asymétrique E-W oligocène supérieur à miocène inférieur. Cet amincissement lithosphérique permet d'expliquer, par décompression du manteau, le faible taux de fusion partielle nécessaire pour rendre compte du volcanisme, localisé au nord, de l'Oligocène supérieur au Miocène inférieur. L'orientation N-S dominante observée sur le MNT est un héritage de cette période d'extension E-W où les failles sub-méridiennes d'âge varisque ont été réactivées. L'épisode magmatique majeur est caractérisé par deux pics d'activité qui sont synchrones des deux périodes de soulèvement maximal : au sud vers 10-5,5 Ma, puis au nord et au sud à partir de 3-3,5 Ma. Au sud, la radiographie de la croûte et de la limite lithosphère-asthénosphère obtenue par sismique classique et tomographie sismique montre que le manteau lithosphérique a subi un très fort amincissement tandis que l'épaisseur de la croûte est quasi-normale. L'anomalie thermique définie sous la lithosphère dans cette partie sud témoigne alors d'une érosion thermique de la base de la lithosphère, responsable du soulèvement isostatique et du premier pic d'activité magmatique. Un second épisode d'érosion thermique à la base de la lithosphère, plus diffus mais réparti du nord au sud, expliquerait la seconde période de soulèvement isostatique ainsi que le second pic d'activité magmatique enregistrés au nord et au sud à partir de 3,5 Ma.

INTRODUCTION

The West-European plate was affected by a rifting episode from the upper Eocene to the early Miocene (Priabonian to Burdigalian) [Ziegler, 1992; Bois, 1993]. Extension is roughly perpendicular to the Alpine front and generated a graben system, which includes, from east to west, three main segments : the Eger graben of the Czech Republic, the Rhinegraben of Germany and the French Massif Central grabens. These three segments are characterised by the occurrence of a typical intraplate alkaline volcanism either within the grabens or along their margins [Wilson and Downes, 1991].

The Massif Central area is the largest magmatic province of the West-European Rift system. The origin of the magmatism is still a matter of debate [Wilson and Downes, 1991]. The presence of a hot spot below the Massif Central has long been advocated [Brousse, 1974]. Different hypotheses such as the upwelling of numerous associated mantle diapirs [Nicolas et al., 1987] or a large aborted mantle plume located at depth and common to the entire western part of the European plate [Hoernle et al., 1995; Granet et al., 1995] have been proposed. It has also been suggested that the magmatism could result from a mantle destabilization induced by the Alpine collision [Sobolev et al., 1997].

In these previous studies, the link between extension and magmatism was not clearly established. The aim of this paper is to provide an interpretation of the spatio-temporal distribution of the volcanism by integrating recent geological, geophysical and geochemical data from the Massif Central. This makes it possible to unravel the different kinematic history between the northern and the southern part of the Massif Central during the Tertiary.

DISTRIBUTION OF THE VOLCANISM

The Massif Central Cenozoic volcanism is spread out from the Drevin in the north to the Escandorgue area in the south

(fig. 1 and 2). Volcanism started 65 Ma ago in the Paleocene and the most recent eruptions can be dated from the Holocene [Bellon et al., 1974; Brousse, 1974; Vincent et al., 1977; Maury and Varet, 1980; Mergoil et Boivin, 1993; Nehlig et al., 1999]. The classification into different magmatic provinces has been attempted [Goër de Herve and Mergoil, 1971; Brousse, 1974 ; Maury and Varet, 1980 ; Mergoil and Boivin, 1993]. These studies clearly show that each magmatic province is characterised by some well defined periods of activity and that two main volcanic phases can be distinguished during the Cenozoic : the pre-rift and the post-rift volcanic phases.

This distinction in two periods can be significantly improved and refined by compiling the different ages of the volcanic provinces, which are geographically listed from north to south (fig. 1). Such a classification allows the distinction of three main volcanic phases.

Pre-rift magmatic event

From the early Paleocene up to the end of the Eocene, a scarce and scattered volcanism, consisting of less than 15 necks and volcanoes, occurred in the northern part of the Massif Central. Only one magmatic manifestation is reported from the southern part (fig 2a). In the Charollais area, 7 volcanoes have been recognised dated from 64.5 to 36.7 Ma with K/Ar method [Bellon et al., 1974]. Near Menat, several outcrops of basalt around a maar have been dated from the Paleocene at around 60 Ma with the K/Ar method [Vincent et al., 1977], a result consistent with paleontological data [Kedves, 1967; Russel, 1967]. In the Forez, the pre-rift magmatic activity is restricted to a single volcano, which erupted 62 Ma ago [Lenoir et al., 2000]. Here, the lava has a melilitite composition and corresponds to the most under-saturated magma type recorded in the Massif Central [Hernandez, 1976]. Along the borders of the Limagne graben, near Vichy and Servant, two volcanoes (45.8 and 44 Ma) display inverted reliefs (Mont Péroux and the Champonier dyke) [Brousse and Lefevre, 1990]. The only pre-rift volcanic manifestation described in the south-
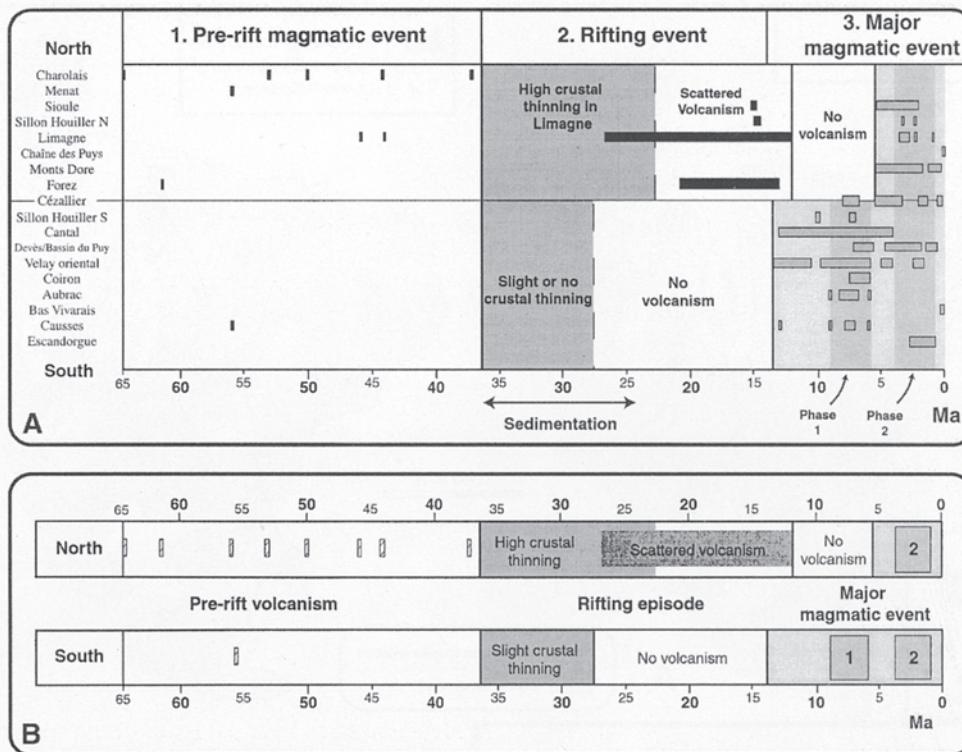
FIG. 1. – A) Spatio-temporal distribution of the volcanism in the Massif Central area : the rifting event include both the sedimentation/extensional period and the scattered volcanism recorded in the north. Note the lack of volcanism after the sedimentation period in the south. For explanation see the text Established from radiometric data [Bellon *et al.*, 1974; Vincent *et al.*, 1977; Baubron *et al.*, 1978; Cantagrel and Boivin, 1978; Bellon and Hernandez, 1979; Maury and Varet, 1980; Baubron and Demange, 1982; Cantagrel and Baubron, 1983; Gastaud *et al.*, 1983; Chantepie, 1990; Goër *et al.*, 1991b; Mergoil and Boivin, 1993; Rochette *et al.*, 1993; Cheguer, 1996; Nehlig *et al.*, 1999]. B) Synthetic representation of volcanism in the Massif Central. Boxes 1 and 2 represent the two peaks of activity during the major magmatic event.

FIG. 1. – A) *Répartition spatio-temporelle du volcanisme : l'épisode de rifting inclut les périodes d'extension et de sédimentation, et la phase de volcanisme dispersé dans la partie nord. Noter l'absence de volcanisme après la période de sédimentation dans la moitié sud. [D'après les travaux de Bellon* et al., *1974; Vincent* et al., *1977; Baubron* et al., *1978; Cantagrel and Boivin, 1978; Bellon and Hernandez, 1979; Maury and Varet, 1980; Baubron and Demange, 1982; Cantagrel and Baubron, 1983; Gastaud* et al., *1983; Chantepie, 1990; Goër* et al., *1991a; Mergoil and Boivin, 1993; Rochette* et al., *1993; Cheguer, 1996; Nehlig* et al., *1999]. B) Représentation synthétique du volcanisme du Massif central. Les caissons 1 et 2 représentent les deux pics d'activité durant la phase majeure de volcanisme.*

ern part of the Massif Central is a basanitic neck in the Tassières hamlet near Séverac le Château (57 Ma) [Baubron *et al.*, 1978].

The above ages were obtained in the 1970s and the 1980s by the K/Ar method. New datings using the $^{40}Ar/^{39}Ar$ method, carried out in the Massif Central, clearly shows that previously published ages based on the K/Ar method must be interpreted with care. For example, the Marcoux melilitite, which has been previously dated at 49.8 Ma with the K/Ar method [Bellon and Hernandez, 1979], has given an age of about 62 Ma using the $^{40}Ar/^{39}Ar$ method [Lenoir *et al.*, 2000]. However, these data confirm the time span of the pre-rift magmatism from Paleocene to Upper Eocene. The lavas of the pre-rift volcanism are highly under-saturated (alkali basalt to melilitite), which strongly suggests small degrees of partial melting (< 5%) of a CO_2- and H_2O-rich mantle source [Edgar, 1987; Wilson *et al.*, 1995].

Rifting magmatic event

From the upper Eocene to the end of the lower Miocene, the Massif Central was affected by east-west extension, which led to the formation of numerous grabens [Bergerat, 1985;

Blès *et al.*, 1989; Lacombe *et al.*, 1993; Merle *et al.*, 1998]. In the northern part of the Massif Central, the three most important grabens are N-S oriented. From east to west, they are the Bresse graben, the Roanne-Montbrison graben and the Limagne graben [fig. 1 in Merle *et al.*, 1998]. As shown from an experimental study, the geometry of the system can be explained as resulting from symmetric extension during the upper Eocene and middle Oligocene [Merle *et al.*, 1998; Michon and Merle, 2000]. In the upper Oligocene and to a lesser extent in the lower Miocene, subsidence remained very active as indicated by the sedimentation rate in the western Limagne graben while there was a lull in Roanne-Montbrison and Bresse grabens [Merle *et al.*, 1998; Hugueney *et al.*, 1999]. In the south, the main sedimentary basins are Le Puy, Saint Flour and Aurillac basins but these are much less developed than in the northern part. The distinction between well defined N-S grabens in the north and small and non-oriented basins in the south is reinforced by recent geophysical data [Zeyen *et al.*, 1997].

The Moho depth, together with thick sequences of Oligocene syn-rift sediments (up to 3000 m in the Limagne graben) [Morange *et al.*, 1971], clearly reveal high crustal
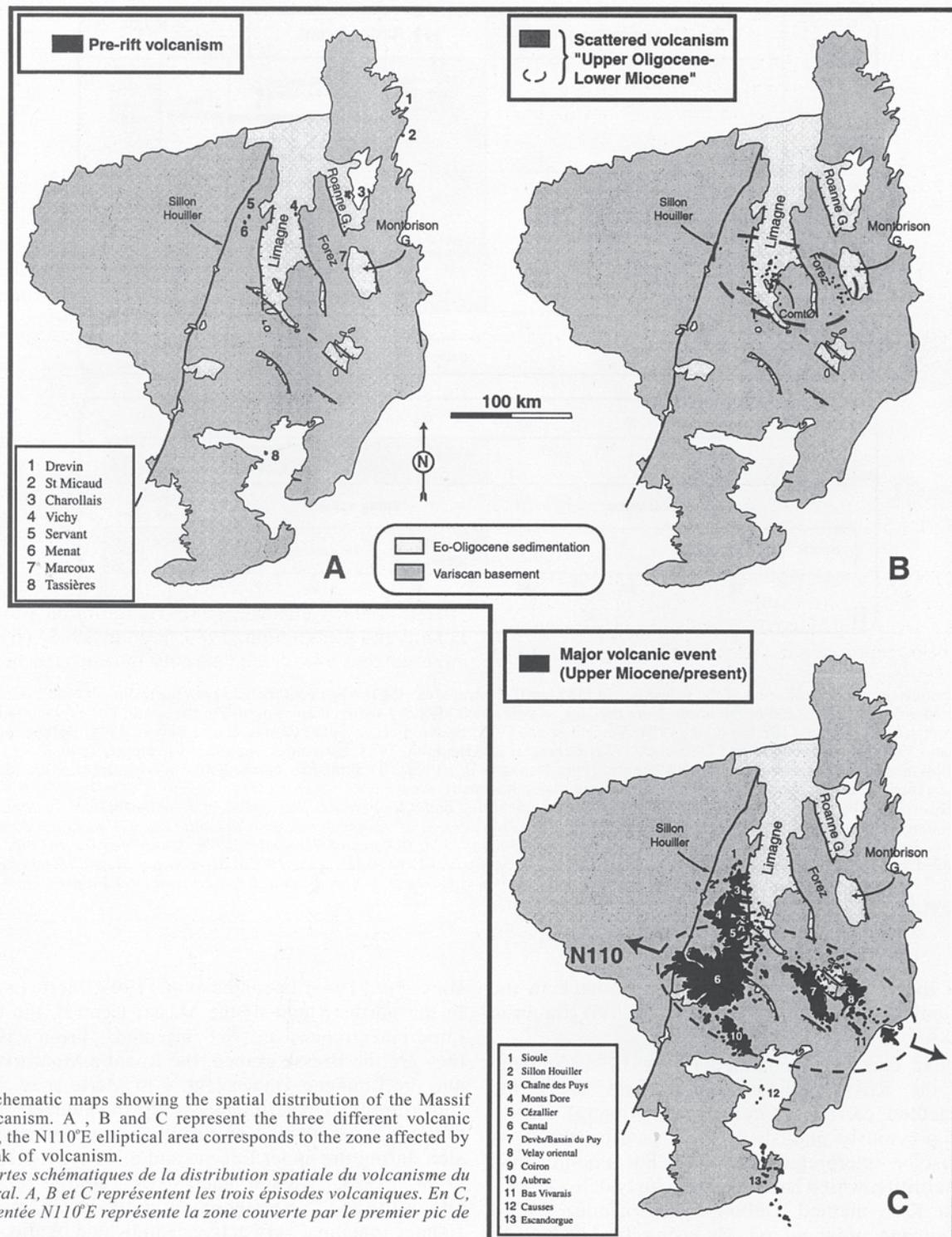
FIG. 2. – Schematic maps showing the spatial distribution of the Massif Central volcanism. A , B and C represent the three different volcanic events. In C, the N110°E elliptical area corresponds to the zone affected by the first peak of volcanism.

FIG. 2. – *Cartes schématiques de la distribution spatiale du volcanisme du Massif central. A, B et C représentent les trois épisodes volcaniques. En C, l'ellipse orientée N110°E représente la zone couverte par le premier pic de volcanisme.*

thinning in the northern part of the Massif Central [fig 11 in Zeyen *et al.*, 1997]. The Moho is at 26 km depth in the west [Zeyen *et al.*, 1997] and 29.5 km in the east [Bergerat *et al.*, 1990], indicating a thinning of the crust to 23.3 km and 28 km below the Limagne and Bresse grabens, respectively. This yields 25 % crustal thinning beneath the Limagne graben and 10 % below the Bresse [Merle *et al.*, 1998]. According to the sedimentation history, most of the 25 %

crustal thinning in the Limagne graben can be considered to have occurred in the upper Oligocene and to a lesser extent in the lower Miocene.

In the southern part of the Massif Central, the Moho is flat-lying at a depth of about 28 km. The average topographic elevation of the Variscan basement is about 1000 m. This suggests slight crustal thinning during the

rifting event. This is correlated with the low thickness of the Eo-Oligocene sediments, which never exceeds a few hundred meters.

These data reveal a strikingly different tectonic evolution between a northern part of the Massif Central where significant crustal thinning has occurred and the southern part where the rifting was limited. Despite the occurrence of a few volcanic minerals in some upper Rupelian sediments [Devineau, 1996], the rifting event is mainly characterised by the lack of volcanic activity during sedimentation both in the north and the south of the Massif Central.

The *"rift-related magmatic event"* started in the late Oligocene at a time when sedimentation was on the decline. It lasted about 15 Ma up to the end of the lower Miocene. Peperitic deposits interbedded in the upper Oligocene sediments [Hourrière et al., 1998] prove that this scattered magmatic event is coeval with the asymmetric phase of rifting. The volcanism is located in the northern part of the Massif Central only and is totally unknown in the southern part (fig. 1). Moreover, it is restricted to the western area of the northern part, which indicates that it is spatially connected with the area of high crustal thinning, that is the Limagne graben.

More than 200 monogenic scattered volcanoes erupted during this period mainly within the Limagne graben (*s.l.*) or the Forez areas (fig. 2b). Two volcanic manifestations only have been reported far away from the graben areas near the Variscan Sillon Houiller fault (fig 2b). The magmatism is mainly characterised by alkaline basaltic to nephelinitic lavas (85% of the total volume) and the only magmas exhibiting a differentiation trend are located in the Comté area, in the heart of the Limagne graben [Tricot, 1975] (fig. 2b). Recent $^{40}Ar/^{39}Ar$ dating from this area indi-cate volcanic activity between 20 and 22 Ma with a climax at about 21 Ma [Cheguer, 1996].

Major magmatic event

The beginning of the major magmatic event is not coeval in the southern and northern parts of the Massif Central. It started in the south, in areas that lack any volcanism before that period, except the Paleocene Tassières neck (fig 1 and 2a). Eruptions took place from the upper Miocene, at least 15 Ma after the end of the sedimentation. In the north, the major magmatic event started after a gap of about 6 Ma in the upper Miocene. The volume of erupted magma during this period is much larger than during any previous magmatic events, and is estimated from 1000 to 1500 km³.

As revealed by the estimation of volumes erupted during this period, the major magmatic event was characterised by two peaks of activity (fig. 1b). The first peak can be dated from 9 to 6 Ma and is associated with the building of the largest magmatic provinces of the Massif Central (Cantal, Aubrac, Velay, Causses and Coirons), following a N120°E/N140°E average trend (Cantal (85% of the trachy-andesitic stratovolcano ages between 9-6 Ma), Aubrac (8,7-6 Ma), South Velay (83% of the ages between 9-6 Ma), Causses (9.2-5.8 Ma) and Coirons (7.9-6.2 Ma)) [Baubron and Demange, 1982; Mergoil and Boivin, 1993; Féraud and Campredon, 1983; Fréour, 1998] (fig 2c). This huge volume of volcanic activity is restricted to a N110°E oriented elliptical area in the south (fig. 2c) where the Oligocene crustal thinning was negligible (<< 5 %). There is a very good correlation between the location and orientation of these large magmatic provinces in the field and the mantle thermal anomaly beneath as deduced by seismic
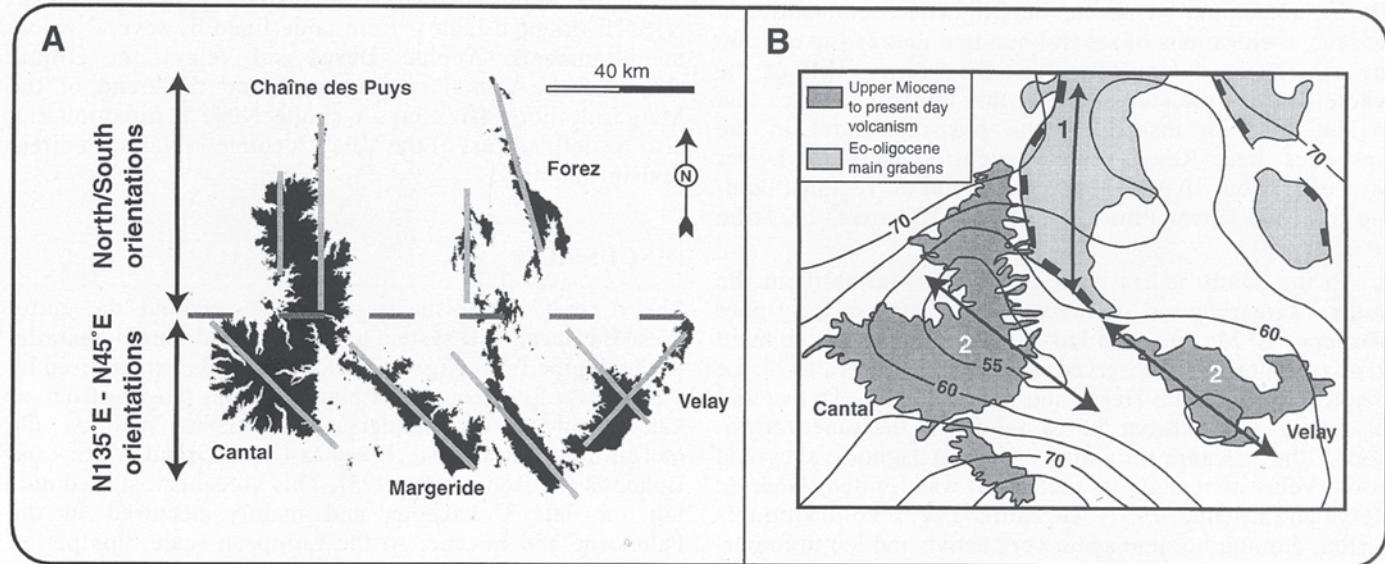
FIG. 3. – A) Structural setting of the northern and the southern parts of the Massif Central. In black, elevation higher than 1000 m. Prominent orientations are N135°E in the south and N-S in the north. B) Schematic map presenting the orientation of the Eo-Oligocene crustal thinning in the north (1) and the thermal anomaly orientation in the south (2). Lithosphere asthenosphere boundary (LAB) topography given in kilometres [from Sobolev et al., 1997].

FIG. 3. – A) *Cadre structural des parties nord et sud du Massif Central. En noir sont représentées les altitudes supérieures à 1000 m. Les orientations dominantes de la moitié sud sont N135°E et la partie nord est marquée par des directions N-S. B) Carte schématique présentant l'orientation de l'amincissement crustal éo-oligocène dans le nord (1) et l'orientation de l'anomalie thermique dans le sud (2) Limite lithosphère-asthénosphère (LAB) en kilomètres [d'après Sobolev* et al., *1997].*

tomographic studies [Granet *et al.*, 1995; Sobolev *et al.*, 1997] (fig. 3).

In contrast to the first peak, the second peak of volcanism occurred both in the north and the south of the Massif Central. From 3.5 Ma to 0.5 Ma, it led both to the building of new provinces such as Escandorgue, Monts Dore and Devès, and the reactivation of old magmatic provinces (Limagne, Causses, Velay and Sioule). The spatial distribution of this second peak is more elongated in the north-south direction (from the Chaîne des Puys to the Escandorgue) than the first peak but has a quite similar east-west width. The main volcanic provinces formed during this period are the Monts Dore and Sancy stratovolcanoes and the Devès basaltic shield. The other provinces are characterised by limited monogenic activity (Escandorgue, Velay) during which relatively small volumes of lava were erupted. Following this second peak, the last eruptions in the Massif Central occurred from the upper Pleistocene to the present-day in the Chaîne des Puys, the Cézallier and in the Ardèche area (Bas Vivarais) [Goer *et al.*, 1991a; Rochette *et al.*, 1993].

Erupted magmas are sub-alkaline (basalt to rhyolite) or alkaline (basanite to phonolite) intraplate lavas. The geochemical and Sr-Nd-Pb isotopic compositions of the most primitive mafic magmas from the Cantal stratovolcano can be modelled by mixing partial melts of: (i) an asthenospheric component with isotopic composition between depleted mantle and high µ (HIMU) endmembers for which there is no need to invoke the existence of a deep mantle plume and (ii) a lithospheric component derived from the old Variscan lithosphere [Wilson and Downes, 1991].

TIMING OF UPLIFT

Marine to laguno-lacustrine Eo-Oligocene sediments can be seen at elevations of several hundred metres (up to 1000 m), which clearly indicates post-Oligocene uplift of the whole area. In the studied zone, this uplift post-dates that of the southern margin of the Massif Central in the Cévennes area [Rey, 1973]. It occurred from the Upper Miocene (about 10 Ma) with a maximum of regional doming from the Upper Pliocene (3.5 Ma) [Derruau, 1971; Le Griel, 1988].

In the south, it has been shown that the uplift in the Velay, Margeride and southern Forez started in the Upper Miocene, 10 Ma ago, and led to the formation of the main trend of topography observed nowadays [Etienne, 1970; Le Griel, 1988; Goër de Herve and Etienne, 1991; Defive and Cantagrel, 1998]. From 5.5 to 3-3.5 Ma, the superimposition of the volcanic formations in the Allagnon valley and in the Velay area suggests that uplift was limited [Goër de Herve and Etienne, 1991; Augendre, 1997]. Following this period, doming became again very active and led to important inverted relief of volcanic formations (e.g. the Cézallier eastern border, the Allagnon and Allier valley and the Escandorgue).

In the north, some very clear fault traces and the study of river entrenchment, together with the cross-cutting relationships with well-dated Cenozoic volcanic formations, demonstrates that the main uplift of the northern part of the Massif Central postdates 3-3.5 Ma. Firstly, departures from equilibrium profiles, as in the Forez area (fig. 4), at the

crossing of fault traces along streams running in the same lithology cannot be ascribed to the Oligocene sedimentation period but demonstrates very recent differential uplift. Secondly, from the Lower Miocene to the Upper Pliocene, this uplift was slight or even inactive as lava flows from that period of time are now found superposed, which indicates that they flowed out within the same paleo-valleys. The occurrence of several Pliocene volcanic formations several hundred metres above the present day watercourses clearly shows a strong excavation of the rivers since 3-3.5 Ma.

PRESENT-DAY STRUCTURAL TRENDS

Using a Digital Elevation Model (DEM with a 50 m resolution step), it can be shown that the northern Massif Central displays a N-S oriented fault pattern whereas the southern part displays a N135°E oriented fault pattern (fig. 3a). Both directions result from older Variscan tectonics, as shown by structural studies in other areas of the Massif Central that lack any imprint of the rifting episode [Feybesse, 1981].

Although the prominant directions of the major faults in the north are commonly N-S or near N-S, some oblique orientations are reported either in the Limagne graben or within the Hercynian basement area on the edge of the graben. In the Combrailles area (NW of Clermont-Ferrand), uplift is indicated by a downthrow of more than one hundred metres of Variscan basement through reactivation of well defined Variscan faults such as the Sillon Houiller or through the reactivation of some previously undescribed oblique networks such as the Morge faulted zone (N55°E) (fig 5). The Morge faulted zone is one of the most seismic areas of the Massif Central [Dorel *et al.*, 1995] possibly resulting from residual or continuing activity of the uplift process.

In the south, the DEM analysis reveals a prominant N135°E oriented fault pattern underlined by several volcanic alignments (Aubrac, Devès and Velay), the elliptic shape of the Cantal stratovolcano and the trend of the Margeride horst (fig. 3a). A single N045°E direction can also be defined east of the Velay, a common Variscan direction in this area.

DISCUSSION

The pre-rift volcanism is present throughout the entire West-European Rift system and is arranged roughly parallel to the Alpine front (fig. 6). It is scarce and characterised by a few tens of outcrops of primary magmas ranging from alkali basalt to very undersaturated lavas such as the melilitites of Marcoux, Essey-la-Côte, Grand Valtin and Bohemia [Wilson *et al.*, 1995]. This volcanism started during the late Cretaceous and mainly occurred in the Paleocene and Eocene. At the European scale, this period (i.e. around the Cretaceous-Tertiary transition) corresponds to the early Alpine compression and to the peak of the high-pressure metamorphism in the Sesia zone [see Merle and Michon, 2001].

The buckling of the lithosphere as a response to compression was recently studied by numerical modelling [Cloetingh *et al.*, 1999]. For a 300 Ma lithosphere, that is the inferred age of the European Variscan lithosphere, results show that the buckling can be preserved during several
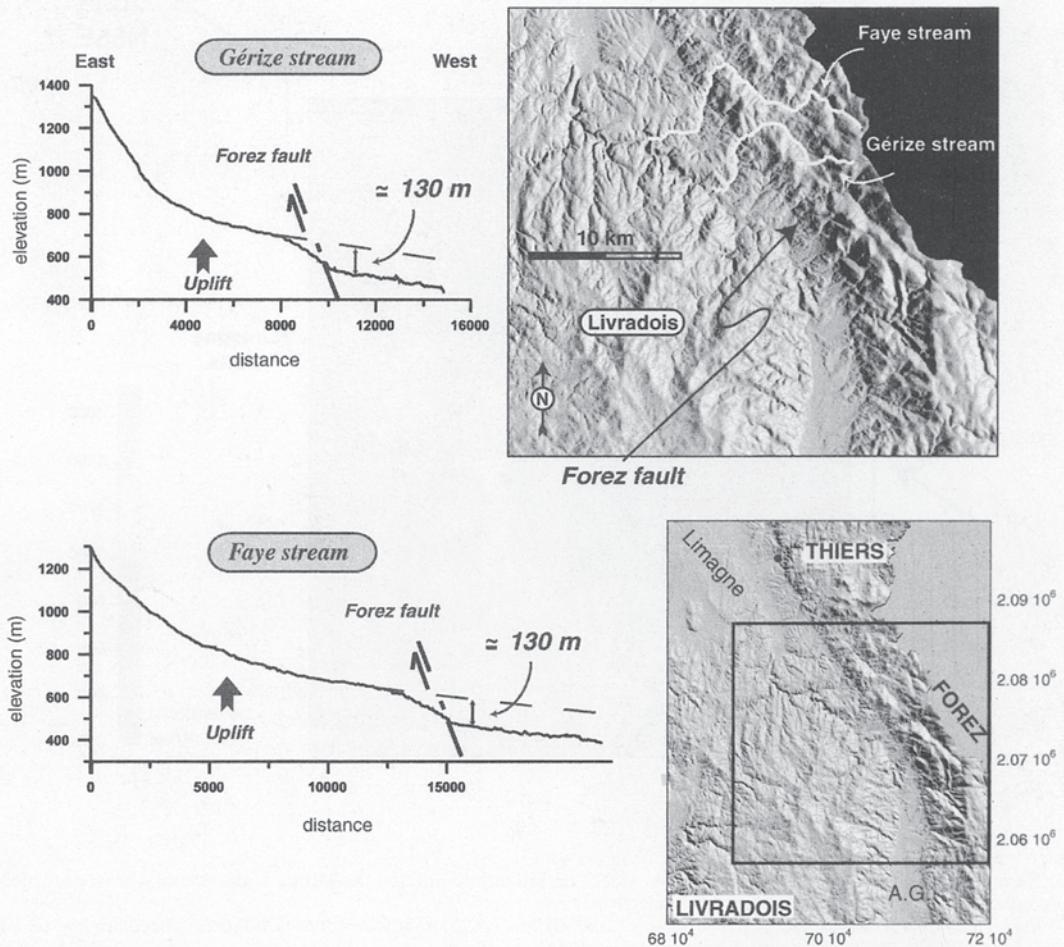
FIG. 4. – Topographic profiles of two streams running across the Forez fault. Departures from the equilibrium profiles of the streams when crossing the fault indicate recent vertical movements, as already suggested by the very clear fault trace of the fault on the DEM. A.G.: Ambert graben.
FIG. 4. – *Profils topographiques de deux ruisseaux recoupant la faille du Forez. Les ruptures de pentes des profils aux passages de la faille du Forez indiquent des mouvements verticaux récents. Cette tectonique est également suggérée par le tracé très net de la faille du Forez sur le MNT. A.G. : Fossé d'Ambert.*

tens of million years. They are also in good agreement with geological studies at the scale of the Massif Central. Gravity data show the existence of crustal ridges which have been attributed to lithospheric buckling at about 60 Ma as a result of early Alpine compression [Lefort and Argawal, 1996]. Southeast of the Paris Basin, the doming is concentric around the Alpine belt and reveals a curved uplifted zone, which goes from the north of the Massif Central to the south of the Rhine graben [Lefort and Agarwal, 1996, Fig 10]. We believe significant that this concentric ridge around the Alpine belt corresponds to the location of the pre-rift volcanism. As an attempt to interpret this pre-rift volcanism, whose spatial distribution is not related to the main Limagne and Rhine grabens but with a large-scale crustal undulation, we propose that it may result from a low to very low degrees of mantle melting induced by lithospheric doming and adiabatic decompression during the early Alpine compressive event. The activity of the pre-rift volcanism up to the Eocene could be explained by the preservation of the lithospheric buckling. This hypothesis is reinforced by geomorphological studies which show a general uplift of the Massif Central and Morvan area at the same period [Le Griel, 1988; Wyns, 1999].

The rifting volcanic event, which is contemporaneous with the upper Oligocene-lower Miocene rift sedimentation, occurred in the west of the northern part of the Massif Central. This magmatic phase is clearly related in space and time to the asymmetric rifting episode, which induced significant crustal thinning in the west, mostly below the Limagne graben [Merle *et al.*, 1998]. Assuming that high crustal thinning results from the stretching of the whole lithosphere, the scattered volcanic activity recorded from the upper Oligocene to lower Miocene may be induced by low degrees of mantle melting (< 10 %) due to mantle decompression during extension. This interpretation is reinforced by the lack of volcanism in the southern part where very slight crustal thinning occurred during the Oligocene. The scattered volcanic event is then interpreted as a consequence of the rifting episode in the northern part of the
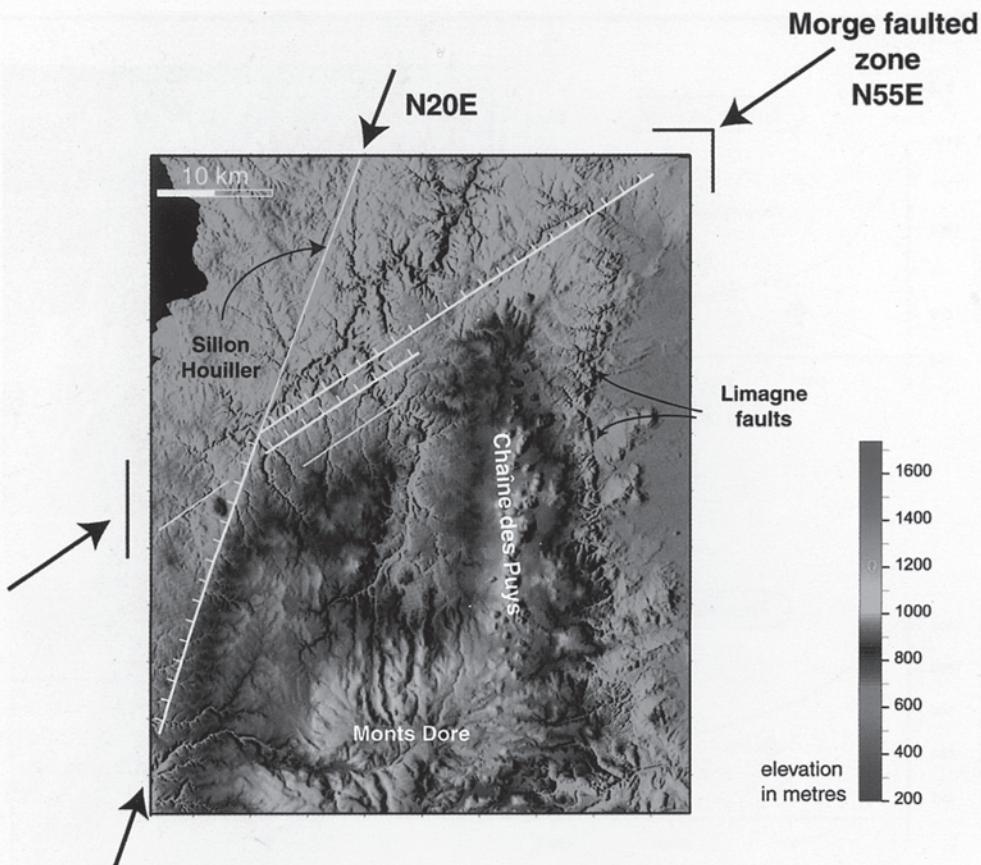
FIG. 5. – Digital Elevation Model (DEM) of the Combrailles area. The Sillon houiller and the Morge faults bound a horst on which the Monts Dore and Chaîne des Puys volcanic provinces were built up.
FIG. 5. – *Modèle numérique de terrain* (MNT) *de la région des Combrailles. Le Sillon houiller et la faille de la Morge bordent un horst sur lequel se sont construites les provinces volcaniques des monts Dores et de la chaîne des Puys.*
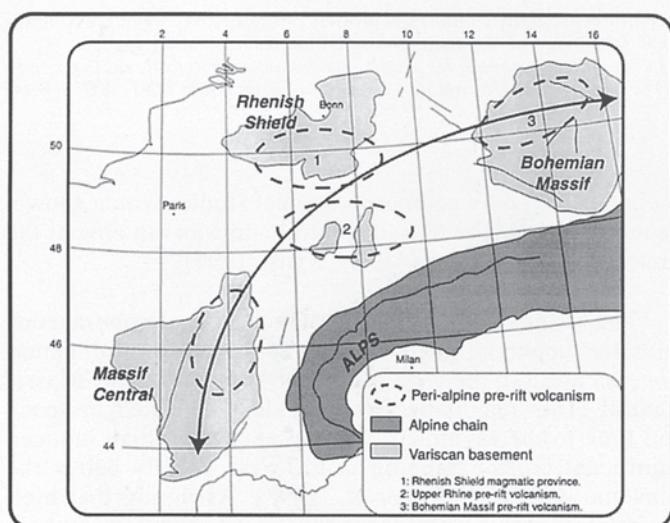

FIG. 6. – Distribution of the pre-rift volcanism in western Europe showing a concentric trend around the Alpine belt.
FIG. 6. – *Distribution du volcanisme pré-rift en Europe de l'Ouest montrant l'arrangement concentrique autour de la chaîne alpine.*

Massif Central. In this area, the main structures which formed during this rifting event are N-S oriented, mostly perpendicular to the extension direction [Bergerat, 1985], and the present structure is probably inherited from that period.

After a lack of volcanism both in the northern and southern parts, voluminous magmatic activity started at 14 Ma and 5.5 Ma ago in the southern and northern parts, respectively. This major volcanic event is characterised by a more or less continuous activity up to the present-day and can be divided into two volcanic peaks. These two peaks are spatially and temporally associated with the two main periods of uplift, suggesting a common origin for volcanism and uplift processes.

In the south, it is probably significant to consider the parallelism between the trend of major faults, the long axis of the two principal magmatic provinces (Cantal and Devès-Velay) and the thermal anomaly orientation (fig 3). The elongated thermal anomaly just below the Cantal and Devès-Velay volcanic provinces suggests that the major volcanic event was induced by this significant asthenospheric upwelling south of the main rifting area. In contrast with lithospheric mantle thinning deduced from the seismic tomography, slight crustal thinning in the same area indicates that upwelling of the lithosphere/ asthenosphere boundary does not result from Eo-Oligocene extension but is probably due to a late process of thermo-mechanical ero-

sion along the lithosphere base. Such a thermal erosion at the lithosphere base would have caused (i) the major magmatic event and (ii) the uplift of the volcanic area as a result of isostatic adjustment.

The occurrence of two peaks of magmatism and uplift could be attributed to two episodes of thermal erosion at the base of the lithosphere spaced by about 5 Ma. The first episode, from 9 Ma to 6 Ma, was restricted to the southern part of the Massif Central whereas the second one, from 3.5 to 0.5 Ma, was less pronounced, but more widespread : from the Chaîne des Puys in the north to the Escandorgue in the south.

This general magmatic evolution drawn from data at the Massif Central scale may apply to the Eger graben as well, as the three magmatic events described in this study (pre-rift magmatic event, rifting event and post-Miocene volcanic event) are also reported in the literature [Bellon and Kopecky, 1977; Dudek and Elias, 1984] (fig 7). This suggests that a single cause should explain the formation of the entire western European rift surrounding the Alpine mountain belt.

CONCLUSIONS

This study on the spatio-temporal distribution of volcanism in the Massif Central makes it possible to propose three successive magmatic events during the Tertiary evolution of the Massif Central.

1. Pre-rift magmatic event. – This volcanic phase is extremely small, but common to the entire West-European Rift system [Bellon and Kopecky, 1977; Vincent *et al.*, 1977; Lippolt, 1983; Brousse and Lefèvre, 1990]. The parallelism between the pre-rift volcanic belt and the Alpine

front could be explained by a flexure of the lithosphere during early Alpine late Cretaceous-Paleocene compression.

2. Rifting magmatic event. – From the Priabonian up to the end of the early Miocene, three main N-S grabens were initiated in the northern part of the Massif Central. In the upper Oligocene, extension remained active in the west only, leading to a significant crustal thinning below the western Limagne graben (up to 25%). This lithospheric stretching induced a scattered late Oligocene-lower Miocene volcanic phase located from the Roanne-Montbrison graben in the east to the Sillon Houiller in the west. In the south, a very slight crustal thinning occurred during the Oligocene rifting period. It is considered that this thinning was not large enough to trigger volcanism, as it occurred in the north during the lower Miocene.

3. Major magmatic event. – This volcanic episode, which started 14 Ma ago in the south and 5.5 Ma ago in the North, is characterised by two peaks of volcanism (9-6 and 3.5-0.5 Ma). Timing and structural features of the major magmatic event indicate that it is unrelated to Eo-Oligocene extensional processes. The first peak of this major magmatic event, which occurred in the south of the Massif Central only, is coeval with an episode of uplift and is attributed to a thermal erosion along the base of the lithosphere. The second peak, which is also coeval with an episode of uplift, would be induced by a similar process, but below a larger area, from north to south, than for the first peak.
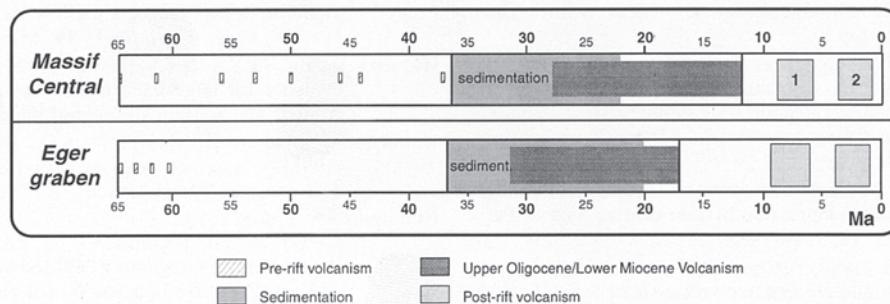
FIG. 7. – Comparative Tertiary evolution of the Massif Central and of the Eger graben. In the Massif Central, data from the northern and southern part are gathered in the same diagram and the major magmatic event is schematically represented by the two peaks of activity (1 and 2). Note the strong similarities between these two segments of the West-European rift, separated by several hundred kilometres. The similarity indicates an evolution linked to common regional factors.
FIG. 7. – *Comparaison de l'évolution tertiaire du Massif central et du graben de l'Eger. Dans le Massif central, les données des parties sud et nord sont rassemblées en un tableau unique et la phase majeure de volcanisme est représentée par les deux pics de magmatisme (1 et 2). Noter les fortes similitudes d'évolution entre ces deux segments du rift Ouest-européen, séparés par plusieurs centaines de kilomètres.*

References

AUGENDRE M. (1997). – Les enseignements des marqueurs en paléogéographie dans une aire volcanisée : l'exemple de la vallée de l'Allagnon en aval de Joursac. – Mém. Maîtrise, Univ. Lyon II, 144p.

BAUBRON J.C., DEFAUT B., DEMANGE J. & MAURY R. (1978). – Existence d'un volcanisme anté-néogène dans les Causses (Massif central français). – BRGM, Rés. Sci. Techn. SGN pour 1978, p.29.

BAUBRON J.C. & DEMANGE J. (1982). – First geochronological study of the volcanic plateau of Aubrac (French Massif Central) – Tectonic and regional implication. – J. Volc. Geotherm. Res., 14, 67-75.

BELLON H., GILLOT P.Y. & NATIVEL P. (1974). – Eocene volcanic activity in Bourgogne, Charollais, Massif Central (France). – Earth Planet. Sc. Lett., 23, 53-58.

BELLON H. & HERNANDEZ J. (1979). – Chronologie du volcanisme dans le Forez (Massif central français). Place dans l'activité magmatique tertiaire de France. – C. R. somm. Soc. Géol. Fr., 4, 175-179.

BELLON H. & KOPECKY L. (1977). – Spectres d'âges radiométriques du volcanisme de rift du Massif bohémien. – 5ème Réun. Ann. Sci. Terre, Rennes, p.57.

BERGERAT F. (1985). – Déformations cassantes et champs de contraintes tertiaires dans la plate-forme européenne. – Thèse d'état, univ. P. et M. Curie, 315 p.

BERGERAT F., MUGNIER J.L., GUELLEC S., TRUFFERT C., CAZES M., DAMOTTE B. & ROURE F. (1990). – Extensional tectonics and subsidence of the Bresse basin : an interpretation from ECORS data. – Mém. Soc. géol. Fr., 156, 145-156.

BLES J.L., BONIJOLY D., CASTAING C. & GROS Y. (1989). – Successive post-Variscan stress fields in the French Massif Central and its borders (western European plate) : comparison with geodynamic data. – Tectonophysics, 169, 79-111.

BOIS C. (1993). – Initiation and evolution of the Oligo-Miocene rift basins of southwestern Europe : contribution of deep seismic reflection profiling. – Tectonophysics, 226, 227-252.

BROUSSE R. (1974). – Le volcanisme en France. – Revue Haute-Auvergne, 44, 221-242.

BROUSSE R. & LEFEVRE C. (1990). – Le volcanisme en France et en Europe limitrophe. – Guides géologiques régionaux. – Masson, Paris, 263p.

CANTAGREL J.M. & BAUBRON J.C. (1983). – Chronologie des éruptions dans le massif volcanique des Monts Dore (méthode potassium-argon). Implications volcanologiques. – Géol. Fr., 1-2, 123-142.

CANTAGREL J.M. & BOIVIN P. (1978). – Datation K-Ar de quelques basaltes du socle du Massif central au Nord-Est de Clermont-Ferrand. – 6e RAST, Paris, p.89.

CHANTEPIE M. (1990). – Le volcanisme basaltique miocène et pliocène dispersé dans la région de Clermont Ferrand et sur le plateau des Dômes. Etude pétrologique et géochronologique. Implications volcanologiques et morphotectoniques. – Mém. D.E.A., Univ. Clermont-Ferrand, 40p.

CHEGUER L. (1996). – Les laves miocènes de la Limagne d'Allier et des plateaux bordiers (Massif central français). Caractérisation d'une série magmatique alcaline sous-saturée (basanite-phonolite) associée à un rifting continental. – Thèse 3e cycle, Univ. Clermont-Ferrand, 201p.

CLOETINGH S., BUROV E. & POLIAKOV A. (1999). – Lithosphere folding : Primary response to compression ? (from central Asia to Paris basin). – Tectonics, 18, 1064-1083.

DEFIVE E. & CANTAGREL J.M. (1998). – Chronologie de l'encaissement du réseau hydrographique en domaine volcanisé : l'exemple de la haute vallée de la Loire. – INQUA COT/UISPP 31 Inter-congress Symposium, Brives-Charensac, 12-17.

DERRUAU M. (1971). – Sur la morphologie du Massif central. In : Géologie, géomorphologie et structure profonde du Massif central français. Symp. J. Jung. – Plein Air Service, Clermont Ferrand, 33-44.

DEVINEAU K. (1996). – Dynamique d'un rift intracontinental : enregistrement par les variations isotopiques Sr-Nd dans la fraction détritique des sédiments. – Mém. D.E.A., Univ. Clermont II, 29p.

DOREL J., FOURVEL D. & DONNADIEU G. (1995). – Etude de la sismicité de l'Auvergne et des régions limitrophes (Massif central français). – Bull. Soc. géol. France, 166, 271-284.

DUDEK A. & ELIAS M. (1984). – Magmatic history. In : M. SUK et al., (Eds) Geological history of the territory of the Czech Socialist Republic. – Geol. Surv., Prague, 231-262.

EDGAR A.D. (1987). – The genesis of alkaline magmas with emphasis on their source regions : inferences from experimental studies. In : J.G. FITTON and B.G. UPTON, Eds., Alkaline igneous rocks. – Geol. Soc. Lond. Spec. Publ., 30, 29-52.

ETIENNE R. (1970). – Les monts du Forez. Le rôle de l'érosion différentielle et de la tectonique dans l'édification du relief. – Thèse 3e cycle, Univ. Clermont Ferrand, 183p.

FEYBESSE J.L. (1981). – Tectonique et microtectonique de la région de Laroquebrou (Cantal, Massif central français) – Rôle de la déformation ductile et évolution du Sillon houiller. – Thèse d'Etat, Univ. Clermont Ferrand II, 227p.

FÉRAUD G. & CAMPREDON R. (1983). – Geochronological and structural study of Tertiairy and Quaternary dykes in southern France and Sardinia : an example of the utilization of dykes swarms as paleostress indicator. – Tectonophysics, 98, 297-325.

FRÉOUR G. (1998). – Modèle d'évolution volcano-structural du Cantal : Rôle et répartition des déstabilisations de flancs en zone proximale (Cantal – France). – M.G., nE 89, IGAL, Cergy, 2 tomes, 101 et 73p.

GASTAUD J., CAMPREDON R. et FERAUD G. (1983). – Les systèmes filoniens des Causses et du Bas Languedoc (Sud de la France) : géochronologie, relations avec les paléocontraintes. – Bull. Soc. géol. Fr., (7), XXV, 737-746.

GOER DE HERVE A. & MERGOIL J. (1971). – Structure et dynamique des édifices volcaniques tertiaires et quaternaires. Symp. J. Jung. – Plein Air Service, Clermont Ferrand, 345-375.

GOER DE HERVE A. de, BAUBRON J.C., CANTAGREL J.M. & MAKHOUL J. (1991b). – Le volcanisme de l'Aubrac (Massif central) : un bref épisode basaltique (250 000 ans) au Miocène supérieur (7,5 Ma). – Géol. Fr., 4, 3-14.

GOËR DE HERVE A. de, CAMUS G., BOIVIN P., GOURGAUD A., KIEFFER G., MERGOIL J. & VINCENT P.M. (1991a). – Volcanologie de la chaîne des Puys (Massif Central français) – Carte au 25000e. – Ed Parc Naturel Régional des Volcans d'Auvergne, (Notice explicative : 127p).

GOËR de HERVE A. de & ETIENNE R. (1991). – Le contact Margeride Cézallier Cantal, les incidences de la tectonique et du volcanisme sur la sédimentation et l'hydrographie. – Bull. Labo. Rhod. Géom., 27-28, 3-21.

GRANET M., STOLL G., DOREL J., ACHAUER U., POUPINET G. & FUCHS K. (1995). – Massif central (France) : new constraints on the geodynamical evolution from teleseismic tomography. – Geophys. J. Int., 121, 33-48.

HERNANDEZ J. (1976). – Données nouvelles sur la composition minéralogique de la néphélinite à mélilite de Marcoux (Forez). – Bull. Soc. Fr. Minér. Cristallogr., 99, 61-66.

HOERNLE K., ZHANG Y.S. & GRAHAM D. (1995). – Seismic and chemical evidence for large-scale mantle upwelling beneath the eastern Atlantic and western and central Europe. – Nature, 374, 34-39.

HOURRIERE F., LEYRIT H., BESSONNEAU D., BULTEAU J.F. & DERVIN T. (1998). – Age, genèse et évolution des diatrèmes pépéritiques de Limagne (Massif central). – 17e RST, Brest, 131.

HUGUENEY M., POIDEVIN J.L., BODERGAT A.M., CARON J.B. & GUERIN C. (1999). – Des mammifères de l'Aquitanien inférieur à La Roche-Banche-Gergovie (Puy-de-Dôme, France), révélateurs de l'activité post-oligocène du rift en Limagne de Clermont. – C. R. Acad. Sci., Paris, 328, 847-852.

KEDVES M. (1967). – Quelques types sporomorphes du bassin lignitifère de Menat. – Acta Univ. Szeged. Acta. Biol., 13, 11-23.

LACOMBE O., ANGELIER J., BYRNE D. & DUPIN J.M. (1993). – Eocene-Oligocene tectonics and kinematics of the Rhine-Saone continental transform zone (eastern France). – Tectonics, 12, 874-888.

LEFORT J.P. & AGARWAL B.N.P. (1996). – Gravity evidence for Alpine buckling of the crust beneath the Paris Basin. – Tectonophysics, 258, 1-14.

Le Griel A. (1988). – L'évolution géomorphologique du Massif central français. Essai sur la genèse d'un relief. – Thèse d'état, Univ. Lyon II, 768p.

Lenoir X., Dautriat J.M., Briqueu L., Cantagrel J.M. & Michard A. (2000). – Nouvelles données géochronologiques, géochimiques et isotopiques sur le volcanisme du Forez : relation avec l'évolution cénozoïque du manteau du Massif central. – C. R. Acad. Sci., Paris, 330, 201-207.

Lippolt H.J. (1983). – Distribution of the volcanism in space and time. In : K. Fuchs, K. Von Gehlen, H. Malzer, Murawski & A. Semmel (Eds) Plateau uplift, the Rhenish shield. – A case history. – Springer-Verlag, Berlin, 112-120.

Maury R.C. & Varet J. (1980). – Le volcanisme tertiaire et quaternaire en France. In : A. Autran & J. Dercourt, Eds., Evolutions géologiques de la France. – Mém. BRGM, 107, 137-159.

Mergoil J. & Boivin P. (1993). – Le Velay, son volcanisme et les formations associées. – Géol. France, 3, 3-96.

Merle O., Michon L., Camus G. & Goër A. de (1998). – L'extension oligocène sur la transversale septentrionale du rift du Massif central. – Bull. Soc. géol. Fr., 169, 5, 615-626.

Merle O. & Michon L. (2001). – The formation of the West-European Rift : a new model exemplified by the Massif central area. – Bull. Soc. géol. Fr., 172, n° 2, 213-221.

Michon L. & Merle O. (2000). – Crustal structures of the Rhinegraben and the Massif Central rift: An experimental approach. – Tectonics, 19, 5, 896-904.

Morange A., Heritier F. & Villemin J. (1971). – Contribution de l'exploration pétrolière à la connaissance structurale et sédimentaire de la Limagne, dans le Massif central. – Symposium J. Jung. – Plein Air Service, Clermont Ferrand, 295-308.

Nehlig P., Freour G., Huguet D., Leyrit H., Roger J., Roig J.Y., Trieblemont D. & Vidal N. (1999). – Histoire géologique simplifiée du volcan du Cantal. – Doc. BRGM, 291, 49-78.

Nicolas A., Lucazeau F. & Bayer R. (1987).– Peridotite xenoliths in Massif Central basalts, France. Textural and geophysical evidence for asthenospheric diapirism. In : P.H. Nixon, Eds., Mantle xenoliths. – John Wiley and Sons, Chichester, 563-574.

Rey R. (1973). – Biostratigraphie des formations sédimentaires du Cantal. – Rev. Scient. Bourbonnais, Moulins, 77-128.

Rochette P., Bertrand H., Braun C. & Berger E.T. (1993). – La province volcanique Pléistocène supérieur du Bas Vivarais (Ardèche, France) : propagation de fentes crustales en échelons ? – C. R. Acad. Sci., Paris, 316, 913-920.

Russel D.E. (1967). – Sur Menathotherium et l'âge paléocène du gisement de Menat (Puy de Dôme). In : Problèmes actuels de paléontologie (évolution des vertébrés). – Coll. Int. CNRS., 163, 483-489.

Sobolev S.V., Zeyen H., Granet M., Achauer U., Bauer C., Werling F., Altherr R. & Fuchs K. (1997). – Upper mantle temperatures and lithosphere-asthenosphere system beneath the French Massif Central constrained by seismic, gravity, petrologic and thermal observations. – Tectonophysics, 275, 143-164.

Tricot B. (1975). – Le volcanisme du Comté d'Auvergne (MCF). – Thèse 3e cycle, Univ. Clermont-Ferrand, 117p.

Vincent P.M., Aubert M., Boivin P, Cantagrel J.M. & Lénat J.F. (1977). – Découverte d'un volcanisme paléocène en Auvergne : les maars de Menat et leurs annexes; études géologique et géodésique. – Bull. Soc. géol. Fr., (7), V, 1057-1070.

Wilson M. & Downes H. (1991). – Tertiary-Quaternary extension-related alkaline magmatism in western and central Europe. – J. Petrol., 32, 4, 811-849.

Wilson M., Rosenbaum J.M. & Dunworth E.A. (1995). – Melilitites : partial melts of the thermal boundary layer ? – Contrib. Mineral. Petrol., 119, 181-196.

Wyns R. (1999). – Contraintes géologiques et géomorphologiques à l'histoire de la mobilité verticale de la lithosphère continentale en Europe de l'ouest depuis le Crétacé; relation avec la genèse des grabens et du volcanisme tertiaires. – Doc. BRGM, 291, 46-47.

Zeyen H., Novak O., Landes M., Prodehl C., Driad L. & Hirn A. (1997). – Refraction-seismic investigations of the nothern Massif Central (France). – Tectonophysics, 275, 99-117.

Ziegler P.A. (1992). – European Cenozoic rift system. – Tectonophysics, 208, 91-111.

Annexe 3 :

Merle, O., L. Michon (2001) The formation of the West European Rift: A new model as exemplified by the Massif Central area. *Bull. Soc. Géol. Fr.,* 172, 2, 81-89.

Séance spécialisée : SGF-BRGM
Volcanisme, tectonique et
sédimentation péri-alpins
Aurillac, 7-10 septembre 1999

The formation of the West European rift :
A new model as exemplified by the Massif Central area

OLIVIER MERLE[1] and LAURENT MICHON[1]

Key words. - Massif Central, Alps, West European Rift, Tectonic, Volcanism, Cenozoic.

Abstract. - In this paper, we use mainly field data from the Massif Central area, which have been presented in a companion paper [Michon and Merle, 2001], to discuss the origin and the evolution of the West European Rift system. It is shown that the tectonic event in the Tertiary is two-stage. The overall geological evolution reveal a tectonic paradoxe as the first stage strongly suggests passive rifting, whereas the second stage displays the first stage of active rifting. In the north, crustal thinning, graben formation and sedimentation at sea level without volcanism during the Lower Oligocene, followed by scattered volcanism in a thinned area during Upper Oligocene and Lower Miocene, represent the classical evolution of a rift resulting from extensional stresses within the lithosphere (i.e. passive rifting). In the south, thinning of the lithospheric mantle associated with doming and volcanism in the Upper Miocene, together with the lack of crustal thinning, may be easily interpreted in terms of the first stage of active rifting due to the ascent of a mantle plume. This active rifting process would have been inhibited before stretching of the crust, as asthenospheric rise associated with uplift and volcanism are the only tectonic events observed. The diachronism of these two events is emphasized by two clearly distinct orientations of crustal thinning in the north and mantle lithospheric thinning in the south. To understand this tectonic paradox, a new model is discussed taking into account the Tertiary evolution of the Alpine chain. It is shown that the formation of a deep lithospheric root may have important mechanical consequences on the adjacent lithosphere. The downward gravitational force acting on the descending slab may induce coeval extension in the surrounding lithosphere. This could trigger graben formation and laguno-marine sedimentation at sea level followed by volcanism as expected for passive rifting. Concurrently, the descending lithospheric flow induces a flow pattern in the asthenosphere which can bring up hot mantle to the base of the adjacent lithosphere. Slow thermal erosion of the base of the lithosphere may lead to a late-stage volcanism and uplift as expected for active rifting.

La formation du rift Ouest-européen : un nouveau modèle tectonique

Mots-clés. - Massif Central, Alpes, Rift Ouest-européen, Tectonique, Volcanisme, Cénozoïque.

Résumé. - La synthèse des données géologique montre une évolution tout à fait différente entre le nord et le sud du Massif central. Le nord du Massif central est principalement caractérisé à l'Oligocène par un fort amincissement crustal, la formation de fossé d'effondrement au niveau de la mer avec une sédimentation épaisse (jusqu'à 3000 m) sans volcanisme, suivie de la fin de l'Oligocène supérieur au Miocène inférieur d'un volcanisme localisé dans les zones de plus fort amincissement crustal. Cette évolution est typique d'un rift de type passif. Au sud, l'évolution tectonique est caractérisée au Miocène supérieur par un très fort amincissement de la lithosphère mantellique sans amincissement crustal, un soulèvement et une importante phase magmatique. Cette évolution est cohérente avec celle attendue lors des premiers stades d'un rift de type actif. Le diachronisme de ces deux événements est souligné par l'orientation N-S de l'amincissement crustal au nord et l'orientation N135°E de l'amincissement de la lithosphère mantellique au sud. Le modèle proposé pour expliquer ce paradoxe part de l'hypothèse que cette évolution procède d'une cause unique, qui se trouve dans la formation de la chaîne alpine immédiatement plus à l'est. La chaîne alpine est spatialement et temporellement connectée au Rift Ouest-européen. Celui-ci comprend, d'est en ouest, le graben de l'Eger, le graben du Rhin et les fossés d'effondrement du Massif central, l'ensemble du système de grabens étant disposés concentriquement autour du front alpin. La déformation dans les Alpes démarre à l'Eocène comme en témoigne les données géochronologiques récentes sur le métamorphisme de haute pression dans les zones les plus internes de la chaîne. La progression vers l'ouest des déformations est attestée par les données stratigraphiques qui montrent que le chevauchement du Briançonnais sur la zone dauphinoise date du début de l'Oligocène. La formation de ce chevauchement crustal majeur de la chaîne alpine est ainsi contemporaine de la formation des grabens et de la sédimentation dans le Massif central. Deux questions se posent : la formation d'une chaîne de montagne peut-elle générer dans la lithosphère adjacente un épisode d'extension ? les modalités de cette extension peuvent-elles se dérouler en deux étapes successives, la première ayant les caractéristiques d'un rift passif et la seconde les caractéristiques d'un rift actif? Pendant la collision continentale, le découplage de la croûte et du manteau lithosphérique entraîne la formation d'une profonde racine constituée de manteau lithosphérique. Des simulations numériques ont montré que la force gravitaire de cette racine lourde, plus dense que l'asthénosphère environnante, engendrait une compression dans la croûte sus-jacente et de l'extension dans la croûte adjacente. Un tel système est à même de dépasser la résistance en extension de la lithosphère adjacente et de provoquer un épisode de rifting qui présentera les caractéristiques d'un rift de type passif. La création de la racine li-

thosphérique s'accompagne également d'un autre processus. Lorsque la racine lithosphérique se forme, elle prend la place de l'asthénosphère et provoque son déplacement latéral. Ceci induit un flux asthénosphérique, ascendant au niveau de la lithosphère adjacente, qui contrebalance le mouvement descendant lié à la racine. La cellule ainsi créée amène de l'asthénosphère chaude à la base de la lithosphère adjacente. Si le processus connaît une ampleur suffisante, pendant une durée de temps de plusieurs millions d'années, une érosion thermique de la base de la lithosphère adjacente se produit, conduisant à un soulèvement isostatique et une phase de volcanisme, d'une manière tout à fait semblable à ce qui est observé dans le cas d'un rift actif. La création de la racine lithosphérique d'une chaîne de montagne peut produire ainsi deux effets dans la lithosphère adjacente : une extension lithosphérique et une érosion thermique à la base de la lithosphère. Ces deux effets ne sont pas synchrones et le second est différé dans le temps. Dès que la racine lithosphérique commence à se former, la force verticale agissant sur cette racine peut engendrer l'extension dans la lithosphère adjacente. En revanche, l'érosion thermique est un phénomène tardif qui nécessite (i) que la racine atteigne une certaine profondeur pour engendrer un flux asthénosphérique conséquent et (ii) un temps relativement long pour réaliser une érosion thermique significative. Le paradoxe tectonique enregistré dans le Massif central peut être résolu en considérant la formation de la profonde racine alpine. D'une façon tout à fait semblable à l'évolution en deux temps découlant du modèle proposé, le Massif central est d'abord affecté par un rifting de type passif suivi quelques millions d'années plus tard par les premiers stades d'un rift de type actif.

INTRODUCTION

The formation of the West European rift remains a subject of great debate. As a continental rift, its origin may be attributed to two different tectonic processes. The first hypothesis involves continental rifting, which would be entirely governed by lithosphere extension. Such rifts, which are termed passive rifts, result from extensional failure of the continental lithosphere, where the main cause is to be found in far-field stresses generated at plate boundaries. The second hypothesis refers to a continental rift initiated above a mantle plume or diapir. This second type, usually termed active rifting, is associated with thermal thinning of the base of the lithosphere due to heat advection at the lithosphere-asthenosphere boundary (LAB).

The initial stages of these two different types of rift are thought to be significantly different, which allows distinction in the field [Park, 1988]. Plume-generated rifts are associated with crustal doming and abundant volcanism in their initial stages. Graben formation and sedimentation occurs later, when the doming reaches a critical level to initiate extensional faulting within the crust. In contrast, far-field stress-generated rifts start with graben formation and sedimentation close to sea level and develop doming and volcanism at a later stage.

In this paper, we use mainly field data from the Massif central area, which have been presented in a companion paper [Michon and Merle, 2001], to discuss the origin and the evolution of the West European Rift system. As exemplified by the evolution of the Massif Central rift, we show that this extension is closely related to the formation of the Alps. A new tectonic model is proposed which takes into account the role of the deep lithospheric root created during mountain building processes in the deformation of the surrounding lithosphere.

THE TECTONIC PARADOX OF THE MASSIF CENTRAL

In this study, we do not deal with the very sparse volcanic manifestations which occurred in the Paleocene at around 60-65 Ma [Vincent et al., 1977]. We believe that this rare pre-rift volcanism may be attributed to the flexure of the lithosphere associated with the first compressions recorded in the Alps [see the discussion in Michon and Merle, 2001],

as testified by the oldest radiometric data at about 65 Ma in the Sesia Austro-Alpine unit [Froitzheim et al., 1996; Rubatto et al., 1999] and geophysical data about the buckling of the French lithosphere during the Paleocene [i.e. Lefort and Agarwal, 1996].

Synthesis of the main geological data reveals a strikingly different structural evolution between the northern and the southern parts of the Massif Central. It is useful to summarize these differences as they reveal the fundamental constraints that must be taken into account before proposing a general tectonic model.

The northern part of the Massif Central is characterized by the following structural features :

1) grabens are well developed and display a clear north-south orientation. Sedimentation rates have been high with up to 3500 m in the Limagne graben;

2) upper Eocene and Oligocene sedimentation occurred close to sea level, as demonstrated by repeated marine incursions [Giraud, 1902; Gorin, 1974; Chauve et al., 1980; Rat, 1984; Briot and Poidevin, 1998; Bodergat et al., 1999];

3) crustal thinning is locally important, up to 25% in the Limagne graben [Merle et al., 1998]. It is spatially connected with the main grabens, and is especially visible below the Limagne and the Bresse grabens [e.g. Bergerat et al., 1990; Truffert et al., 1990; Zeyen et al., 1997];

4) there is a linear relationship between the thickness of Oligocene sediments in the grabens and the amount of crustal thinning, showing that crustal thinning took place in the Oligocene and was achieved when the sedimentation stopped [Fig. 6 in Merle et al., 1998];

5) the sedimentation period lacked accompanying volcanism. Volcanism started by the end of the sedimentation and was mainly developed in the lower Miocene;

6) this scattered volcanism occurred in the west, especially in the Limagne graben, that is in the zone of highest crustal thinning [Fig. 2 in Michon and Merle, 2001];

7) a second magmatic event started after a gap of about 6 Ma in the upper Miocene. This second magmatic event is also restricted to the west, but mainly occurred in an area where geophysical data have revealed no crustal thinning [Zeyen et al., 1997] (e.g. The Chaîne des Puys, The Mont Dore, The Sioule, etc). It is coeval with regional doming [Michon and Merle, 2001].

The southern part of the Massif Central is characterized by the following structural features :

1) basins are not preferentially oriented or bounded by a N135°E oriented horst zone. Upper Eocene-Oligocene sedimentation is never as thick as in the north, with a maximum thickness of a few hundred meters;

2) sedimentation mainly occurred at sea level [Dangeard, 1933; Rey, 1973; Turland *et al.*, 1994].

3) the Moho is flat-lying at a depth of about 28 km [Zeyen *et al.*, 1997]. According to the average elevation at about 1000 m of the Variscan basement, the crust is about 29 km thick and crustal thinning is considered to be negligible;

4) the lithospheric mantle is strongly thinned, up to 65%, along a direction which is nearly perpendicular to the orientation of crustal thinning recorded in the north [Granet *et al.*, 1995 a and b; Sobolev *et al.*, 1996] [Fig. 3 in Michon and Merle, 2001];

5) volcanism started in the upper Miocene more than 10 Ma after the end of the main phase of sedimentation [Michon and Merle, 2001]. It is associated with huge volumes of magma and is undisputably the major volcanic phase in the Massif Central;

6) doming of the area is shown to be coeval with this major magmatic event [e.g. Le Griel, 1988; Goër de Herve and Etienne, 1991; Defive and Cantagrel, 1998].

When comparing the north and the south of the Massif Central, these data reveal a tectonic paradox. The Oligocene and lower Miocene history in the north of the Massif Central presents all the characteristics of passive rifting whereas the upper Miocene to present-day history in the south strongly suggests active rifting (fig.1).

In the north, crustal thinning, graben formation and sedimentation at sea level without volcanism during the Lower Oligocene, followed by scattered volcanism in a thinned area during Upper Oligocene and Lower Miocene, represent the classical evolution of a rift resulting from extensional stresses within the lithosphere.

In the south, thinning of the lithospheric mantle associated with doming and volcanism in the Upper Miocene, together with the lack of crustal thinning, may be easily interpreted in terms of the first stage of active rifting due to the ascent of a mantle plume. This active rifting process would have been inhibited before stretching of the crust, as asthenospheric rise associated with uplift and volcanism are the only tectonic events observed. The diachronism of these two events is emphasized by two clearly distinct orientations of crustal thinning in the north and mantle lithospheric thinning in the south.

The negligible crustal thinning in the south explains well the lack of volcanism following the Upper Eocene-Oligocene sedimentation period. This merely indicates that the Oligocene passive rifting event recorded in the north has weakly affected the south, and that the lithospheric stretching was not strong enough at that time to induce partial melting in the mantle. In the same way, the late second magmatic event is recorded in the north in a non-thinned crustal area, after an interruption of volcanism for several millions years. This suggests that the southern active rifting phase has propagated to the north in the very late Tertiary.

According to this interpretation, we face the following dilemna. It could be considered that these two rifting events result from two different processes which are completely unrelated. However, two superimposed unrelated rifting events in the Tertiary would be a surprising coincidence, all the more because the same tectonic evolution is recorded far away from the Massif Central area in the Eger graben of the Czech Republic [Michon and Merle, 2001]. Another alternative would be to consider that the whole Tertiary history of the Massif Central area and the Eger graben result from a single cause at the scale of western Europe. We discuss this hypothesis in the following section.

THE ALPS AS A SINGLE CAUSE

Several models have been proposed to explain the formation of the West European rift [e.g. Bergerat, 1985; Bles *et al.*, 1989; Ziegler, 1992; Lacombe *et al.*, 1993]. Among them, the compression associated with the late stages of the Pyrenean orogeny has been advocated as a source for far-field stresses capable of reactivating the Permo-Carboniferous fracture systems. In such an hypothesis, the formation of the Eger graben in the Bohemian Massif (fig. 2), far away from the Pyrenees, which reveals a tectonic evolution surprisingly similar to that of the Massif Central [Michon and Merle, 2001], is poorly understood.
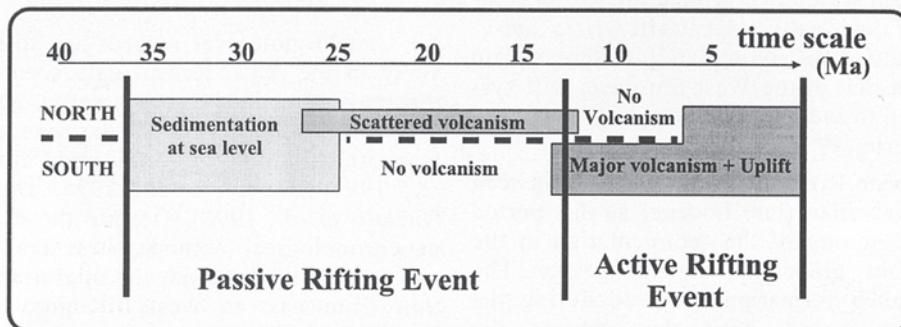

FIG. 1. – Summary of main geological data that allow us to propose a two-fold evolution of the rifting process during the Tertiary. Sedimentation at sea level followed by scattered volcanism fits with a passive rifting event, whereas the major phase of volcanism associated with uplift fits with an active rifting event (explanation in the text).

FIG. 1. – *Résumé des principales données géologiques permettant de proposer une double évolution du processus de rifting au cours du Tertiaire. Au nord, la sédimentation au niveau de la mer, suivie d'un volcanisme dispersé s'accorde avec un modèle de rift passif. En revanche, au sud, la phase majeure de volcanisme associée à une surrection s'accorde avec une évolution de type rift actif (c.f. explication dans le texte).*
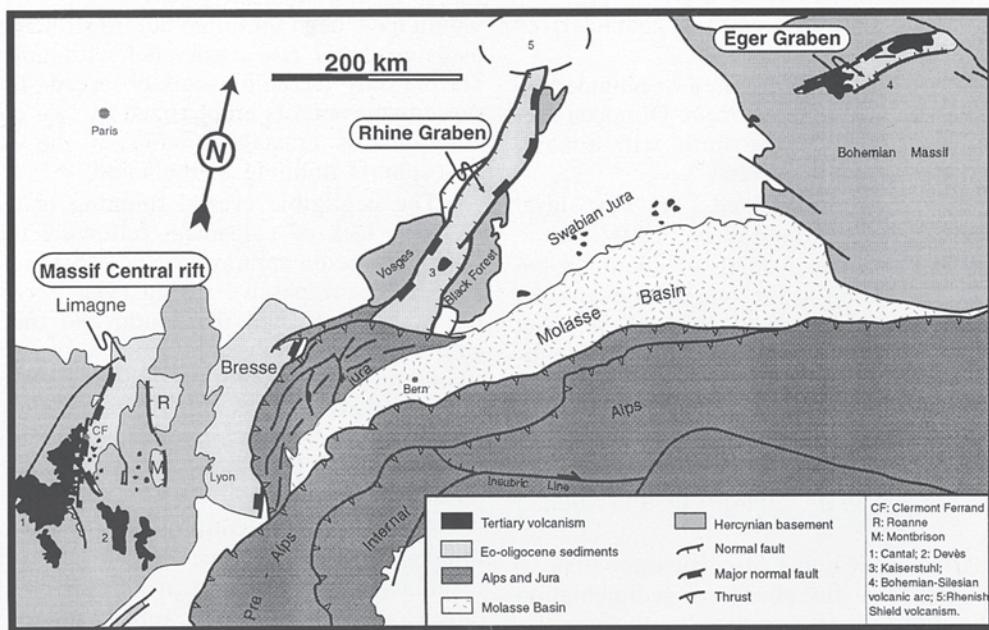
FIG. 2. – Simplified geological map showing the close spatial relationship between the Alps and the West European Rift system. Most structural features of the rifts, including the Massif Central area, the Rhinegraben, the Swabian Jura and the Eger Graben are concentric around the Alpine chain.
FIG. 2. – *Carte géologique simplifiée montrant l'étroite relation spatiale entre les Alpes et le rift Ouest-européen. Les principaux segments du rift (le Massif central, le graben du Rhin, le Jura souabe et le graben de l'Eger) sont disposés concentriquement autour de la chaîne alpine.*

In a search of a single cause at the scale of plate tecto-nics which can explain not only the Oligocene rifting but also the following asthenospheric rise and related magmatism, it is clear that the Alps should be considered as the best candidate because this mountain chain is tempo-rally and spatially connected with the entire West European Rift system (fig. 2).

The West European Rift system displays a series of grabens or volcanic manifestations which roughly surround the Alpine chain. From east to west, these include the Eger graben, the Swabian Jura, the Rhine graben and the Massif Central (fig. 2). To the south of the Massif Central, the present-day structure of grabens and the volcanism are re-lated to the opening of a marginal basin during the counter-clockwise rotation of the Corso-Sardinia micro-plate [Channell and Mareschal, 1989; Carminati et al., 1998; Seranne, 1999], an event which overprinted the earlier sedi-mentary basins due to the West European rift *stricto sensu*. This rifting event results from a completely different plate kinematic history than that of the West European Rift sys-tem and is best referred to as the North-West Mediterranean Rift [Seranne and Merle, 1999].

In the West European Rift system, incipient basins can be dated from the Priabonian (late Eocene) as this period corresponds to the beginning of the sedimentation in the Massif Central, the Rhine graben and the Eger graben. The major episode of graben formation occurred during the Oligocene. Deposition lasted until the end of the Oligocene. In a few areas, some residual basins of small ex-tent reveal ongoing sedimentation during the Aquitanian [Gerbe et al., 1998; Hugueney et al., 1999].

The beginning of the major phase of deformation in the Alps can be dated from stratigraphic records. During the Eocene, a large paleogeographical domain including the

Briançonnais and the sub-Briançonnais zones of the Alps corresponded to a zone of widespread deep marine sedi-mentation [e.g. Kerchove, 1980]. This so-called Nummulit-ic sedimentation ended in the late Eocene with olistostrome formations, immediately followed by nappe emplacement. Most olistostromes in the sub-Briançonnais and Briançonnais zones can be dated from the Priabonian [e.g. Kerckhove, 1969; Bravard et al., 1981; Kerckhove and Pairis, 1986; Barféty et al., 1992].

The formation of the Frontal Penninic thrust is usually considered to occur at the beginning of the Oligocene [Tricart, 1986]. According to this major event, a sedimenta-tion of «Red Molasse» took place in the Dauphinois zone during the Oligocene [Kerckhove, 1980]. These molassic sediments result from the erosion of the high relief formed at that time in the internal domain.

Geochronological records are still a matter of contro-versy in the Alps. Recent data seem to indicate that HP metamorphism in the most internal zones, with the excep-tion of the Austro-Alpine Sezia zone, occurred in the range from 50 to 30 Ma [e.g. Monié and Philippot, 1989; Tilton et al., 1991; Bowtel et al., 1994; Duchêne et al., 1997, Rubatto et al., 1998]. Despite the uncertainties linked to geochronological methods, these ages from the most inter-nal zones, together with the migration of crustal deforma-tion from east to west, fit quite well with the late-Eocene/early Oligocene deformation recorded at the bound-ary between the internal and the external domain (i.e. Fron-tal Penninic thrust). From these data, it can be concluded that the major deformation in the Alps started in the middle Eocene in the most internal units and reached the boundary with the external domain in the end of the Priabonian or the beginning of the Rupelian.

The beginning of crustal thinning and graben formation recorded in the north of the Massif Central and the Rhine graben appears to be coeval with crustal thickening and major crustal wedge overthrusting in the western Alps. What must be explained is the juxtaposition of two lithospheric domains, which exhibit at the same time extension and compression. The questions are the following : can the formation of a mountain chain generate extension in the surrounding lithosphere? Can the deformation in the surrounding lithosphere be two-phase and mimic first a passive rifting and then an active rifting?

THE ROLE OF THE LITHOSPHERIC ROOT

To answer these questions, the deformation associated with the collision of two lithospheric plates must be considered in its entirety. In most mountain chains, the deformation in the crust and the mantle lithosphere is decoupled along a major shear zone located at the interface between the lower crust and the mantle. Such a process, which was first proposed for the Himalayan chain [Mattauer, 1986], leads to the formation of both an upper stack of crustal wedges and a lower mantle lithospheric root. The depth of this lithospheric root is linked to the amount of shortening following the continental collision.

The formation of a mantle lithospheric root has important mechanical consequences. It has been known for a long time that the mantle lithosphere is denser that the asthenosphere. This difference in densities is the key parameter which explains the sinking of oceanic lithosphere in subduction zones. It is responsible for the downward body force usually referred to as the trench pull [e.g. Turcotte and Schubert, 1982].

In the same way, the mantle root in continental collision is denser than the surrounding asthenosphere. It follows that this slab exerts on the whole collisional system a downward gravitational body force. This downward body force is usually considered as sufficient to maintain the convergent belt in a state of compression even after convergence has ceased [Fleitout and Froidevaux, 1982].

Numerical simulations have been conducted to study the effect and the deformation associated with this major vertical body force [e.g. Fleitout, 1984; Channell and Mareschal, 1989]. It has been shown that a mantle lithospheric root is pulled down into the asthenosphere generating a zone of crustal compression flanked by zones of crustal extension. These numerical models explain the compression in the collision zone and contemporaneous extension in adjacent areas [Mc Kenzie, 1978; Fleitout and Froidevaux, 1982; Channell and Mareschal, 1989]. Significant extensional deformation may be expected as the extensional strength of the lithosphere as a whole is considerably less than its compressive strength [Kusznir and Park, 1986]. The extension should occurr in a way similar to that expected for passive rifting.

As an interesting result of the numerical simulation, the deformation in the adjacent lithosphere is dependant of the asymmetry of the lithospheric thickening [Channell and Mareschal, 1989]. Asymmetric lithospheric thickening leads to enhanced extension in the adjacent lithosphere but on one flank only of the collision zone, the other flank beeing almost devoided of extensional stresses (fig. 3).
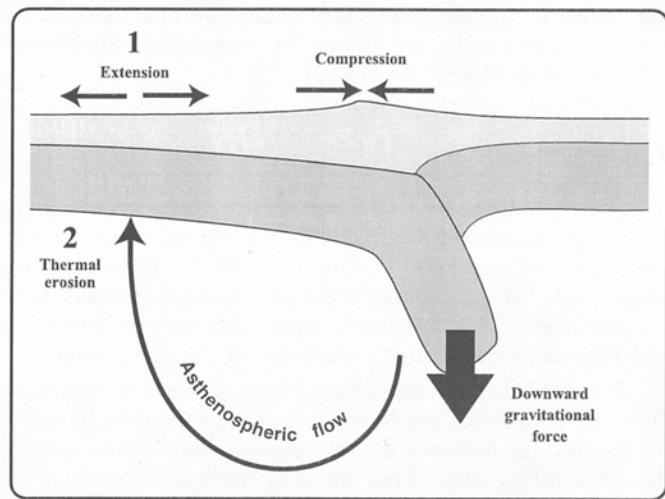

FIG. 3. – Schematic representation of the role of the lithospheric root in triggering rifting in the adjacent lithosphere [after Channel and Mareschal, 1989]. The downward gravitational force of the dense root induces extension (1) in the adjacent lithosphere and is responsible for a deformation event which resembles passive rifting. The mantle flow due to the sinking of the root brings hot asthenosphere to the base of the adjacent lithosphere. This induces thermal erosion (2) leading to a deformation event which resembles active rifting (2).

FIG. 3. – *Représentation schématique du rôle de la racine lithosphérique dans la création d'un épisode de rifting dans la lithosphère adjacente [d'après Channel and Mareschal, 1989]. La force gravitaire de la racine lithosphérique dense induit de l'extension (1) dans la lithosphère adjacente et est responsable de l'épisode de déformation de type rift passif. Le flux asthénosphérique dû à l'enfoncement de la racine lithosphérique entraîne du matériel mantellique chaud à la base de la lithosphère adjacente. Ceci induit une érosion thermique (2) et un épisode de déformation de type rift actif (2).*

THE ASTHENOSPHERIC FLOW

Another process follows from the formation of the mantle lithospheric root. Its consequence on adjacent lithosphere has not been fully studied yet but is clearly apparent in numerical simulations. When sinking into the asthenosphere, the mantle lithospheric root replaces the asthenosphere and expells it away from the root. This induces an asthenospheric flow.

The general flow pattern from numerical modelling clearly shows that downward movement of the mantle lithospheric root is counterbalanced by upward motion of the asthenosphere below the adjacent lithosphere [Channell and Mareschal, 1989] (fig. 3). Considering that the lithosphere is sufficiently cool to behave rigidly, the flow pattern is restricted within the asthenosphere, which exhibits a fluid-like behavior on geologic time scales.

This process brings upward to the base of the lithosphere some asthenospheric mantle, which is hotter than the temperature usually considered to define the lower boundary of the lithosphere, that is about 1300°C. If such a process takes place over a sufficient time span, thinning of the lithospheric mantle by thermal erosion may occur, leading to volcanism and uplift by isostatic adjustment, in a way similar to active rifting (fig. 3).

Again, when the lithospheric thickening is asymmetric, the resulting flow pattern is also strongly asymmetric and

the ascent of the asthenosphere occurs on one flank of the collision zone only, as shown by numerical simulations [Channel and Mareschal, 1989] (fig. 3).

THE MODEL

It has been shown that the formation of a mountain chain may have important mechanical consequences in the surrounding lithosphere [Fleitout, 1984; Channel and Mareschal, 1989]. Two different processes may result from the creation of a lithospheric root : lithospheric extension and thermal erosion along the base of the lithosphere.

It is doubtful that these two processes are simultaneous. Once the process of the formation of the lithospheric root is on the way, a downward gravitational body force acts on the descending slab. This induces immediate extensional stresses in the adjacent lithosphere, which may eventually overcome its strength and produce whole-lithosphere failure.

By contrast, thermal erosion of the adjacent lithosphere should be a late process for two different reasons. Firstly, the lithospheric root must reach a certain depth to induce significant asthenospheric flow. As shown from numerical modelling [Channell and Mareschal, 1989], the amplitude of this flow is directly proportional to the volume of the asthenosphere replaced by mantle lithosphere. Secondly, as a thermal effect, it needs time for the hot asthenosphere brought up to the base of the lithosphere to induce thermal erosion. As a result, the passive rifting recorded in the adjacent lithosphere should predate the active rifting due to the asthenospheric flow.

We propose to solve the tectonic paradox described in the Massif Central area by taking into account the mechanical decoupling between the crust and the mantle during the formation of the Alpine chain. In the Alps, such a process certainly occurred as demonstrated by geophysical data which reveal a deep mantle lithospheric root over 220 km thick [e.g. Panza and Mueller, 1979; Spakman, 1986; Mueller and Panza, 1986; Babuska et al., 1990]. This corresponds to the Alpine "verschluckungszone" defined by Laubscher in 1971. The root is in marked contrast with the LAB depth of about 90-100 km to the west of the Sillon Houiller, a stable domain since the Hercynian orogeny which was not-affected by the rifting event [Lucazeau et al., 1984; Sobolev et al., 1996].

As expected in the process under consideration, the rifting event in the Massif Central resulting from the formation of the Alps is two-fold. It initially resembles passive rifting and is followed a few millions years later by a second stage which mimics the first stage of an active rifting.

According to geochronological data on high pressure terranes in the Alps, crustal thickening started in the middle Eocene. It appears that the lithospheric root could have been deep enough to generate extension at the time when the Frontal Penninic thrust developed (i.e. end of Priabonian or beginning of Rupelian). Then, the time available to create a significant lithospheric root capable of generating extension in the adjacent lithosphere would be about 20 Ma, from the middle Eocene to the end of the Eocene. The resulting effect in the Massif Central area is the formation of grabens at sea level which lack volcanism (fig. 4a). Stretching of the lithosphere took place over

10 Ma until the end of the Oligocene. From the upper Oligocene, decompression partial melting occurred in the zones of greatest lithospheric thinning (i.e. below the Limagne graben). This scattered volcanism lasted about 15 Ma up to the Upper Miocene. We consider that this first event of passive rifting ends in the Upper Miocene with the end of volcanic activity.

The flow pattern in the asthenosphere due to the creation of the lithospheric root in the Alps induces thermal erosion along the base of the adjacent lithosphere in the south of the Massif Central about 15 Ma after the end of the
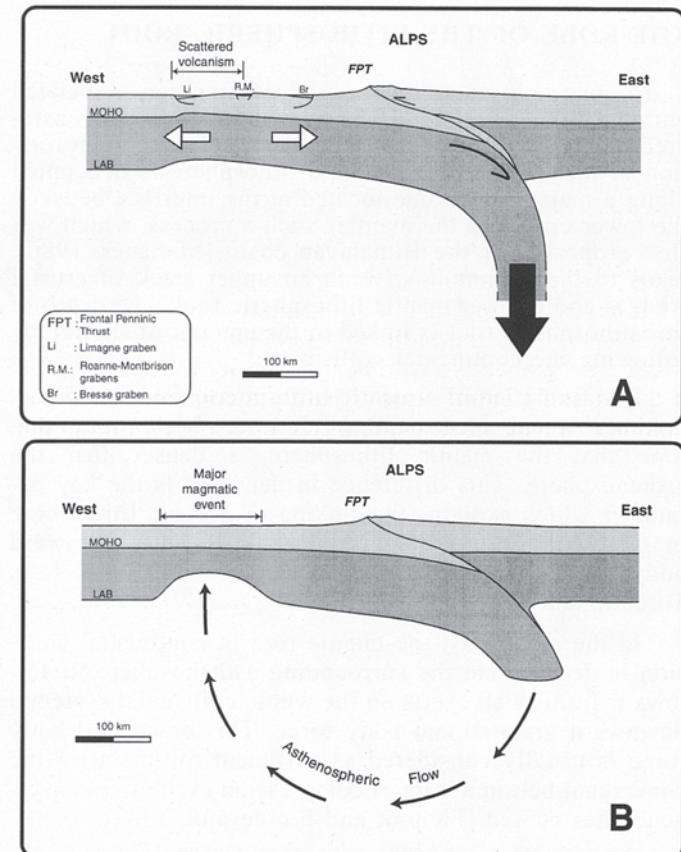

FIG. 4. – The two-fold evolution of the rifting event in the Massif Central area as explained by the deep lithospheric root of the Alps. A) The formation of the lithospheric root in Eocene-Oligocene time has induced extension in the Massif Central, which started by sedimentation at sea level followed by scattered volcanism in the late Oligocene and lower Miocene. At that time, the root is supposed to be deeper and steeper than nowadays as it is coeval with subduction of crustal slices (UHP and HP metamorphism), which were exhumed later and outcrop now at the surface. Thermal erosion of this root may also be assumed since the Oligocene B) The formation of the lithospheric root has induced a mantle flow, which resulted in thermal erosion at the base of the lithosphere trigerring volcanism and uplift of the whole area from the Upper Miocene to the present-day (further explanation in the text).

FIG. 4.– *Double évolution de l'épisode de rifting dans le Massif central liée à la création de la profonde racine lithosphérique des Alpes. A) La formation de la racine lithosphérique à l'Eo-Oligocène a induit de l'extension dans le Massif central, qui s'est d'abord manifestée par une sédimentation au niveau de la mer, puis par une phase de volcanisme dispersé à l'Oligocène supérieur et au Miocène inférieur. A cette époque, la racine était probablement plus profonde qu'actuellement et était associée à une subduction crustale, comme le montre le métamorphisme de ultra-haute pression dans les unités crustales les plus internes de la chaîne. B) La formation de la racine lithosphérique a induit un flux asthénosphérique sous le Massif central qui a pour effet une érosion thermique de la lithosphère et le développement de la phase volcanique majeure contemporaine d'une surrection du Miocène supérieur à l'actuel (cf explications dans le texte).*

sedimentation period. This thermal erosion was accompanied by intense volcanism and uplift of the whole area (fig. 4b). This second event of active rifting propagated to the north of the Massif Central generating a renewal of volcanism after an interruption of about 6 Ma. As expected, this second phase of volcanism in the north is unrelated to previous zones of crustal stretching and mainly occurred in zones of normal crustal thickness (fig. 4b).

The question arises as to why the active rifting event started earlier in the south than in the north of the Massif Central and was significantly less developed in the north. Furthermore, to generate the second stage of magmatism, it is necessary to produce a thermal anomaly in the upper mantle of about 200°C [Granet *et al.*, 1995b; Sobolev *et al.*, 1996]. This requires that the lithospheric root triggers an upwelling from a deep thermal boundary layer in the upper mantle. We feel that the answer to these questions needs further studies of the flow pattern associated with the sinking of a lithospheric root. Such an understanding of the deep processes involved during the creation of a lithospheric root might be achieved by the means of numerical and analogue modelling.

It has been stressed in a companion paper [Michon and Merle, 2001] that the sedimentary and magmatic evolution of the Eger graben is surprisingly similar to that recorded in the Massif Central. This is hardly a coincidence. When looking at a map of the depth of the lithospheric root in the

Alps (fig. 5), it appears that the Alpine root is strongly non-linear. This may explain the three major segments of the West European rift, which are linked by large scale transform zones (i.e. The Rhin-Saône and Franconie transform zones). Likewise, reactivation of Variscan faults may explain the slight deviation of these grabens from perfect parallelism around the Alpine belt.

CONCLUDING REMARKS

From our study of the Massif Central area, we conclude that the West European Rift system may result from the coeval formation of the deep lithospheric root in the Alpine chain. Such a process would induce a two-stage rifting event in the adjacent lithosphere, as shown in the Massif Central area and the Eger graben. The first stage resembles passive rifting whereas the second stage mimics the beginning of an active rifting. This hypothesis explains most data gathered from the north and the south of the Massif Central area. Further studies on the deep structure of the Rhine graben and the Eger graben should show if the similar temporal evolution of graben formation, sedimentation and volcanism recorded in these areas can be attributed to the same overall tectonic process.
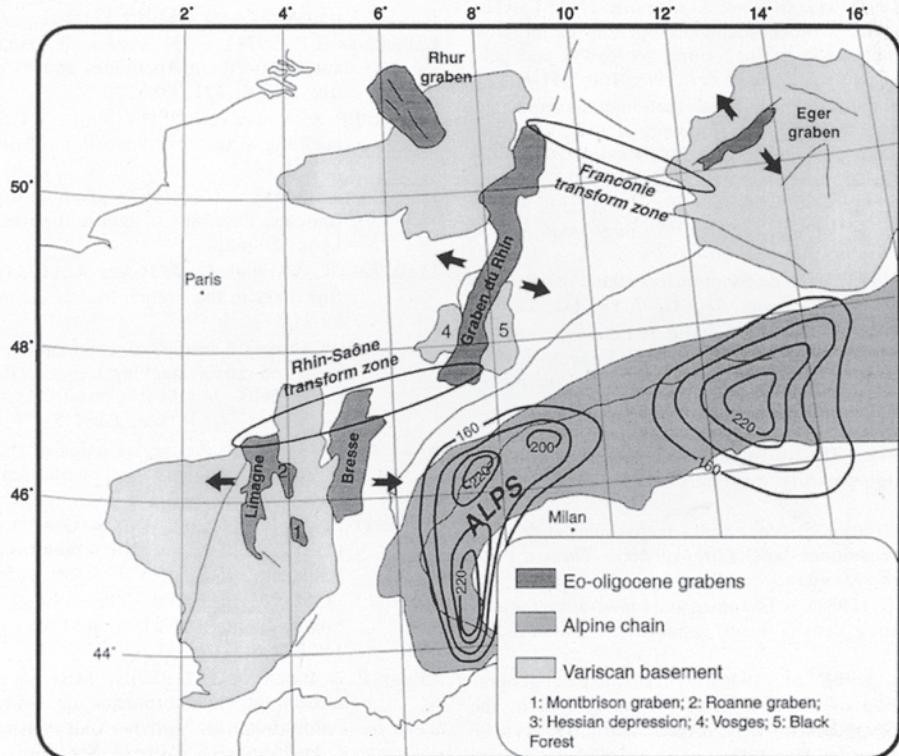
FIG. 5. – Depth to the thermal lithosphere-asthenosphere boundary beneath the Alps showing the localisation of the deep lithospheric root with respect to the three main segments of the West European Rift (depth of the lithosphere-asthenosphere boundary after Babuska *et al.* [1990]).
FIG. 5. – *Carte de la profondeur du LAB dans les Alpes montrant la position de la profonde racine lithosphérique par rapport aux trois segments principaux du Rift Ouest-européen (profondeur de la racine lithosphérique d'après Babuska* et al. *[1990]).*

References

BABUSKA V., PLOMEROVA J. & GRANET M. (1990). – The deep lithosphere in the Alps : a model inferred from P residuals. – *Tectonophysics*, **176**, 137-165.

BARFETY J.C., TRICART P. & JEUDY DE GRISSAC C. (1992). – La quatrième écaille près de Briançon (Alpes françaises) : un olithostrome précurseur de l'orogenèse pennique Eocène. – *C. R. Acad. Sci., Paris*, **314**, 71-76.

BERGERAT F. (1985). – Déformations cassantes et champs de contraintes tertiaires dans la plate-forme européenne. – Thèse d'état, univ. P. et M. Curie, 315 p.

BERGERAT F., MUGNIER JL., GUELLEC S., TRUFFERT C., CAZES M., DAMOTTE B. & ROURE F. (1990). – Extensional tectonics and subsidence of the Bresse basin : an interpretation from ECORS data. – *Mém. Soc. géol. Fr.*, **156**, 145-156.

BLES J.L., BONIJOLY D., CASTAING C. & GROS Y. (1989). – Successive post-Variscan stress fields in the French Massif Central and its borders (Western European plate) : comparison with geodynamic data. – *Tectonophysics*, **169**, 79-111.

BODERGAT A.M., BRIOT D., HUGUENEY M., POIDEVIN J.L., PICOT L., GIRAUD F., BERGER J.P., LEVY A. & POIGNANT A. (1999). – Incursions marines dans l'environnement lacustre du rift oligocène de Limagne (Massif central, France) : apport des organismes halophiles et des isotopes du strontium; datation par les mammifères. – *Bull. Soc. géol. Fr.*, **170**, 499-511.

BOWTEL S.A., CLIFF R.A. & BARNICOAT A.C. (1994). – Sm-Nd isotopic evidence on the age of the eclogitisation in the Zermatt-Saas ophiolites. – *J. Metamorph. Geol.*, **12**, 187-196.

BRAVARD C., KERCKHOVE C. & BARBIER R. (1981). – Réinterprétation du sommet de la série des aiguilles d'Arves et de ses rapports avec la zone subriançonnaise dans la vallée de l'Arc. – *C. R. Acad. Sci., Paris*, **292**, 531-534.

BRIOT D. & POIDEVIN J.L. (1998). – Stratigraphie $^{87}Sr/^{86}Sr$ de quelques laminites carbonatées du Rupélien supérieur du fossé de Limagne : incursions marines dans le rift du Massif central français. – *C. R. Acad. Sci., Paris*, **326**, 479-483.

CARMINATI E., WORTEL M.J.R., SPAKMAN W. & SABADINI R. (1998). – The role of slab detachment processes in the opening of the western-central Mediterranean basins : some geological and geophysical evidence. – *Earth Planet. Sci. Lett.*, **160**, 651-665.

CHANNEL J.E. & MARESCHAL J.C. (1989). – Delamination and asymmetric lithospheric thickening in the development of the Tyrrhenian Rift. *In* : M.P. COWARD, D. DIETRICH & R.G. PARK, Eds., Alpine tectonics. – *Geol. Soc. Lond. Sp. Pub.*, **45**, 285-302.

CHAUVE P., ENAY R., FLUCK P. & SITTLER C. (1980). – L'Est de la France (Vosges, fossé rhénan, Bresse, Jura). – *26e Cong. Géol. Intern. Paris*, 3-81.

DANGEARD L. (1933). – Sur la présence de foraminifères dans l'Oligocène du Massif central. – *C. R. Somm. Soc. Géol. Fr.*, **1-2**, 12-13.

DEFIVE E. & CANTAGREL J.M. (1998). – Chronologie de l'encaissement du réseau hydrographique en domaine volcanisé : l'exemple de la haute vallée de la Loire. – INQUA COT/UISPP *31 Inter-congress Symposium*, Brives-Charensac, 12-17.

DUCHENE S., BLICHERT-TOFT J., LUAIS B., TELOUK P., LARDEAUX J.M. & ALBAREDE F. (1997). – The Lu-Hf dating of garnets and the ages of the Alpine high-pressure metamorphism. – *Nature*, **387**, 586-589.

FLEITOUT L. (1984). – Modélisation des contraintes tectoniques et des instabilités thermomécaniques dans la lithosphère. – *Thèse d'Etat, Univ. Paris-Sud, Paris*, 433p.

FLEITOUT L. & FROIDEVAUX C. (1982). – Tectonics and topography for a lithosphere containing density heterogeneities. – *Tectonics*, **1**, 21-56.

FROITZHEIM N., SCHMID S.M. & FREY M. (1996). – Mesozoic paleogeography and the timing of eclogite-facies metamorphism in the Alps : A working hypothesis. – *Eclogae geol. Helv.*, **89**, 81-110.

GERBE M.C., GONORD H. & ARNAUD N. (1998). – Age miocène des formations de bordure du fossé du Forez (Massif central). – *Géol. Fr.*, **2**, 47-53.

GIRAUD J. (1902). – Etudes géologiques sur la Limagne (Auvergne). – Thèse d'Etat, Ed. Ch. Béranger, Paris, 410p.

GOËR de HERVE A. & ETIENNE R. (1991). – Le contact Margeride Cézallier Cantal, les incidences de la tectonique et du volcanisme sur la sédimentation et l'hydrographie. – *Bull. Labo. Rhod. Géom.*, **27-28**, 3-21.

GORIN G. (1974). – Etude palynostratigraphique de sédiments paléogènes de la grande Limagne (Massif central, France). – Thèse 3e cycle, Genève, 314p.

GRANET M., STOLL G., DOREL J., ACHAUER U., POUPINET G. & FUCHS K. (1995a). – Massif Central (France) : new constraints on the geodynamical evolution from teleseismic tomography. – *Geophys. J. Int.*, **121**, 1, 33-48.

GRANET M., WILSON M. & ACHAUER U. (1995b). – Imaging a mantle plume beneath the French massif Central. – *Earth Planet. Sci. Lett.*, **136**, 281-296.

HUGUENEY M., POIDEVIN J.L., BODERGAT A.M., CARON J.B. & GUERIN C. (1999). – Des mammifères de l'Aquitanien inférieur à la Roche blanche-Gergovie (Puy de Dôme, France), révélateur de l'activité post-oligocène du rift en Limagne de Clermont. – *C. R. Acad. Sci., Paris*, **328**, 847-852.

KERCKHOVE C. (1969). – La zone du flysch dans les nappes de l'Embrunais-Ubaye. – *Géol. Alpine*, **45**, 5-204.

KERCKHOVE C. (1980). – Panorama des séries synorogéniques des Alpes occidentales. *In* : A. AUTRAN & J. DERCOURT, Eds., Evolutions géologiques de la France, *26e congr. géol. int.*, colloque C7. – *Mém. BRGM*, **107**, 241.

KERCKHOVE C. & PAIRIS J.L. (1986). – Dynamique des dépôts nummulitiques marins dans les zones alpines internes : l'exemple du Flysch subbriançonnais de Saint Clément (nappes de l'Embrunais-Ubaye, haut-Embrunais, Alpes occidentales française). – *C. R. Acad. Sci., Paris*, **303**, 1227-1232.

KUSZNIR N.J. & PARK R.G. (1986). – The extensional strength of the continental lithosphere : its dependance on geothermal gradient and crustal composition and thickness. *In* : M.P. COWARD, J.F. DEWEY & P.L. HANCOCK, Eds., Continental extensional tectonics. – *Geol. Soc. Lond. Sp. Publ.*, **28**, 35-52.

LACOMBE O., ANGELIER J., BYRNE D. & DUPIN J.M. (1993). – Eocene-Oligocene tectonics and kinematics of the Rhine-Saone continental transform zone (eastern France). – *Tectonics*, **12**, 874-888.

LAUBSCHER H.P. (1971). – The large scale kinematics of the western Alps and the northern Apennines and its palinspatic implications. – *Am. J. Sci.*, **271**, 193-226.

LEFORT J.P. & AGARWAL B.N.P. (1996). – Gravity evidence for Alpine buckling of the crust beneath the Paris Basin. – *Tectonophysics*, **258**, 1-14.

LE GRIEL A. (1988). – L'évolution géomorphologique du Massif Central français. Essai sur la genèse d'un relief. – Thèse d'état, Univ. Lyon II, 768p.

LUCAZEAU F., VASSEUR G. & BAYER R. (1984). – Interpretation of heat flow data in the French Massif central. – *Tectonophysics*, **103**, 99-119.

MATTAUER M. (1986). – Intracontinental subduction, crust mantle decollement and crustal stacking wedge in the Himalaya and other collision belts. *In* : M.P. COWARD & A.C. RIES, Eds., Collision tectonics. – *Geol. Soc. Lond. Sp. Publ.*, **19**, 37-50.

MCKENZIE D. (1978). – Active tectonics of the Alpine-Himalayan belt : The Aegean sea and surrounding regions. – *Geophys. J. Royal Astr. Soc.*, **55**, 217-254.

MERLE O., MICHON L., CAMUS G. & de GOER A. (1998). – L'extension oligocène sur la transversale septentrionale du rift du Massif Central. – *Bull. Soc. géol. Fr.*, **169**, 615-626.

MICHON L. & MERLE O. (2001). – The evolution of the Massif Central rift : Spatio-temporal distribution of the volcanism. – *Bull. Soc. géol. Fr.*, **172**, 2, 201-211.

MONIE P. & PHILIPPOT P. (1989). – Mise en évidence de l'âge Eocène moyen du métamorphisme de haute-pression dans la nappe ophiolitique du Monviso (Alpes occidentales) par la méthode $^{39}Ar-^{40}Ar$. – *C. R. Acad. Sci., Paris*, **309**, 245-251.

MUELLER S. & PANZA G.F. (1986). – Evidence of a deep reaching lithosphere root under the Alpine arc. – *Terra Cognita*, **6**, p.579.

PANZA G.F. & MUELLER S. (1979). – The plate boundary between Eurasia and Africa in the Alpine area. – *Mem. Sci. Geol.*, **33**, 43-50.

PARK R.G. (1988). – Geological structures and moving plates. – Blackie & Son Ltd, Bishopbriggs, Glasgow, 337p.

RAT P. (1984). – Une approche de l'environnement structural et morphologique du Pliocène et du Quaternaire bressan. – *Géol. Fr.*, **3**, 185-196.

REY R. (1973). – Biostratigraphie des formations sédimentaires du Cantal. – *Rev. Scient. Bourbonnais*, Moulins, 77-128.

RUBATTO D., GEBAUER D. & FANNING M. (1998). – Jurassic formation and Eocene subduction of the Zermatt-Saas-Fee ophiolites : implications for the geodynamics evolution of the Central and Western Alps. – *Contrib. Mineral. Petrol.*, **132**, 269-287.

RUBATTO D., GEBAUER D. & COMPAGNONI R. (1999). – Dating of eclogite-facies zircons : the age of Alpine metamorphism in the Sesia-Lanzo zone (western Alps). – *Earth Planet. Sci. Lett.*, **167**, 141-158.

SERANNE M. (1999). – The Gulf of Lion continental margin (NW Mediterranean) revisited by IBS : an overview. *In* : B. DURAND, L. JOLIVET, F. HORAVAT & M. SERANNE, Eds., The Mediterranean basins : Tertiary extension within the Alpine orogen. – *Geol. Soc. Lond. Sp. Publ.*, **156**, 15-36.

SERANNE M. & MERLE O. (1999). – Cenozoic rift-basins of western Europe. – Colloque GéoFrance 3D : Résultats et Perspectives. 23-24 Novembre 1999. – *Doc. BRGM*, **293**, 112-115.

SOBOLEV S.V., ZEYEN H., STOLL G., WERLING F., ALTHERR R. & FUCHS K. (1996). – Upper mantle temperature from teleseismic tomography of French Massif Central including effects of composition, mineral reactions, anharmonicity, anelasticity and partial melt. – *Earth Planet. Sci. Lett.*, **139**, 147-163.

SPAKMAN W. (1986). – The upper mantle structure in the central European-Mediterranean region. *In* : R. FREEMAN, S. MUELLER & P. GIESE, Eds., *Third EGT Workshop* – The central segment. – European Science Foundation (Strasbourg, France), 215-221.

TILTON G.R., SCHREYER W. & SCHERTL H.P. (1991). – Pb-Sr-Nd istopic behaviour of deeply subducted rocks from the Dora Maira massif, Western Alps, Italy-II : What is the age of the ultrahigh pressure metamorphism ? – *Contrib. Mineral. Petrol.*, **108**, 22-33.

TRICART P. (1986) – Le chevauchement de la zone briançonnaise au sud-est du Pelvoux : clé des rapports zone externe/zone internes dans les Alpes occidentale. – *Bull. Soc. géol. Fr.*, **(8)**, **2**, 233-244.

TRUFFERT C., BURG J.P., CAZES M., BAYER R., DAMOTTE B. & REY D. (1990). – Structures crustales sous le Jura et la Bresse : contraintes sismiques et gravimétriques le long des profils ECORS Bresse-Jura et Alpes II. – *Mém. Soc. géol. Fr.*, **156**, 157-164.

TURCOTTE D.L. & SCHUBERT G. (1982). – Geodynamics. Application of continuum physics to geological problems. – John Wiley, Chichester, 450p.

TURLAND M., MARTEAU P., JOUVAL J. & MONCIARDINI Ch. (1994). – Découverte d'un épisode marin oligocène dans la série paléogène lacustre à fluviatile du bassin du Puy en Velay. – *Géol. Fr.*, **4**, 63-66.

VINCENT P.M., AUBERT M., BOIVIN P, CANTAGREL J.M. & LENAT J.F. (1977). – Découverte d'un volcanisme paléocène en Auvergne : les maars de Menat et leurs annexes; études géologique et géodésique. – *Bull. Soc. géol. Fr.*, **5**, 1057-1070.

ZEYEN H., NOVAK O., LANDES M., PRODEHL C., DRIAD L. & HIRN A. (1997). – Refraction-seismic investigations of the northern Massif Central (France). – *Tectonophysics*, **275**, 99-117.

ZIEGLER P.A. (1992). – European Cenozoic rift system. *In* : P.A. ZIEGLER (Eds) Geodynamics of rifting, Volume I. Case history studies on rifts : Europe and Asia. – *Tectonophysics*, **208**, 91-111.

Annexe 4 :

Michon, L., R.T. van Balen (2005) Characterization and quantification of active faulting in the Roer Valley Rift system based on high precision Digital Elevation Models. *Quaternary Sci. Rev.*, 24, 457-474.

Characterization and quantification of active faulting in the Roer valley rift system based on high precision digital elevation models

Laurent Michon[a,b,*], Ronald T. Van Balen[c]

[a]*TNO-NITG, Department of Geo-Energy, P.O. Box 80015, 3508 TA Utrecht, The Netherlands*
[b]*Geologisches Institut, Freiburg Universität, Albertstr. 23b, 79104 Freiburg i. Br., Germany*
[c]*Department of Quaternary geology and Geomorphology, Vrije Universiteit Amsterdam, De Boelelaan 1085, 1081 HV Amsterdam, The Netherlands*

Abstract

The Roer valley rift system (RVRS) is located in the northern prolongation of the upper Rhine Graben. During the Cenozoic, the evolution of the RVRS was influenced by two different rift systems situated in the North and in the South (the North Sea rift system and the West European rift system, respectively). During the last decades, moderate seismicity revealed the continuous activity of the graben border faults (the Peel Boundary fault zone -PBFZ- and the Feldbiss fault zone-FFZ-). We use a high precision digital elevation model (DEM) to characterize and quantify the present-day deformation along these faults. The fault pattern shows similarity to a strike-slip structure. However, analysis of the DEM reveals that the Recent to Quaternary formations and landforms affected by the fault activity are only vertically offset. This suggests a pure normal faulting mode for the main border faults and a direction of extension perpendicular to the graben (i.e., NE–SW). Quantification of the offset dated markers allows the determination of the displacement rates along the fault segments. In the southeastern part of the RVRS, the vertical displacement rates inferred for the FFZ and the southeastern PBFZ range between 55 and 65 mm/ky and around 65 mm/ky, respectively. In contrast, the displacement rates determined for the northwestern segment of the PBFZ are around 200 mm/ky. We explain these differences between the northwestern and southeastern parts of the RVRS by the large-scale geometry of the graben, the RVRS being symmetric in the south-east and asymmetric (half-graben) in the north-west. The deformation is accommodated by two border faults (FFZ and the south-eastern part of the PBFZ) in the south-east and by only one fault in the north-west (the north-western segment of the PBFZ). In addition, the thickness of the Neogene main depocentre in the northwestern half of the RVRS indicates a larger amount of extension in this part of the graben than in the south-east. The combination of the graben geometry and the amount of extension can explain the differences in the displacement rate.

© 2004 Elsevier Ltd. All rights reserved.

1. Introduction

In the past decades, the occurrence of two major earthquakes in the Roer valley rift system (RVRS) (Roermond in 1992, $M_b = 5,8$ and Aachen in 2002, $M_b = 4,9$) demonstrated that this rift system is one of the most active European rift structures. Studies of the recent deformation associated with the fault activity indicate that this seismicity is part of a deformation process which extends at the graben scale (e.g., Van den Berg, 1994; Camelbeeck and Meghraoui, 1998; Houtgast and Van Balen, 2000). It is generally accepted that the present-day dynamics of the RVRS is induced by the Alpine collision (e.g., Ziegler, 1990). The resulting deformation has mainly been interpreted as dominated by a NW–SE strike slip motion, where the RVRS corresponds to a pull-apart graben (Kooi et al., 1991; Van den Berg, 1994). In such a model, the graben border faults are expected to be strike-slip faults, as proposed by Van den Berg (1994). However, this interpretation is

*Corresponding author. Laboratoire des Sciences de la Terre de l'Université de la Réunion, Université de la Réunion, 15 rue René Cassin, 97715 Saint Denis cedex 9, France. Tel.: +262-262-93-82-04; fax: +262-262-93-82-66.

E-mail address: laurent.michon@univ-reunion.fr (L. Michon).

in disagreement with the present-day local stress field (NE–SW pure extension) inferred from earthquake focal mechanisms (Plenefish and Bonjer, 1997). To clarify this debate, we focus our study on the present-day deformation along the main fault zones of the RVRS. We use a high precision digital elevation models (DEM) in order to characterize the active faults, to quantify the deformation and to determine the origin of the present-day dynamics.

The DEMs are located on the most active faults of the RVRS where the denser and stronger seismic activity was recorded (i.e., the peel boundary fault zone –PBFZ- and the Feldbiss fault zone –FFZ-) (Houtgast and Van Balen, 2000). Two of the DEMs are situated on the northwestern and southeastern segments of the PBFZ; the third area is located on the FFZ.

The goal of this article is (1) to determine precisely the geometry of the active faults, and (2) to quantify the vertical and/or lateral offsets related to the fault activity and the displacement rates along the faults of the RVRS. We integrate our results at a crustal scale in order to understand the strong variations of the displacement rates between the southeastern and northwestern parts of the RVRS.

2. Geological setting

To the north of the upper Rhine graben, the RVRS corresponds with the northern segment of the West European Rift (Ziegler, 1988; Michon et al., 2003) (Fig. 1). The Cenozoic RVRS developed upon the pre-existing basins of Carboniferous (Campine foreland basin) and Mesozoic (rift) age. It is structurally related closely to the Mesozoic basin. During the Mesozoic, the area was characterized by several periods of subsidence and inversion, which have reactivated the Variscan faults (Ziegler, 1990; Zijerveld et al., 1992; Winstanley, 1993; Geluk et al., 1994). During the Cenozoic, the RVRS was affected by two periods of inversion named the Laramide phase (early Paleocene) and the Pyrenean phase (late Eocene-early Oligocene) and by continuous subsidence since the beginning of the Oligocene (Geluk et al., 1994; Michon et al., 2003). The subsidence analysis combined with the study of 2D seismic lines allows the distinction of two successive periods of subsidence. During the Oligocene, an ESE-WNW extension has induced a local subsidence in the southeastern part of the RVG, leading to the development of narrow depocentres (Michon et al., 2003). In contrast, during the Miocene-Quaternary evolution, the subsidence has mainly affected the northwestern part of the graben with the formation of a large depocentre. The shape of the depocentre and the geometry of the Miocene faults were recently interpreted as the result of a NE–SW extension (Michon et al., 2003).

The RVRS is part of the lower Rhine embayment. From south-west to north-east, it consists of the Campine Block, the Roer valley graben (RVG) and the Peel Block (Fig. 1). The graben, which is 20 km wide and 130 km long, was controlled by the multi-stage activity of several major fault zones (PBFZ, Veldhoven fault zone, Rijen fault zone and FFZ) of Mesozoic or probably of older age. The PBFZ is a NW–SE oriented
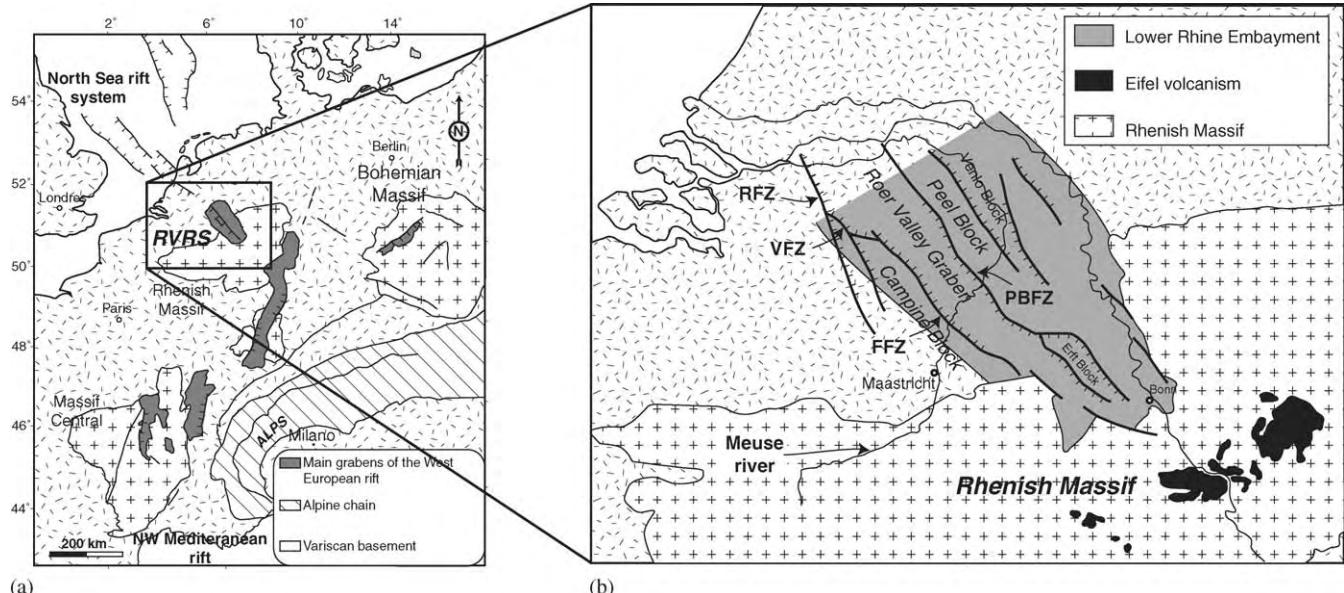

Fig. 1. Location map of the Roer valley rift system (RVRS) within the West European platform. (a) The RVRS corresponds to the northern segment of the West European rift, which was mainly formed during the Oligocene-Early Miocene period. During the Mesozoic and the Early Tertiary, the RVRS was the southern end of the North Sea rift system. (b) Tectonic map of the RVRS and the Lower Rhine Embayment. The Roer Valley graben is bounded in the North by the PBFZ, and in the South by the FFZ, the RFZ and the Veldhoven fault zone (VFZ).
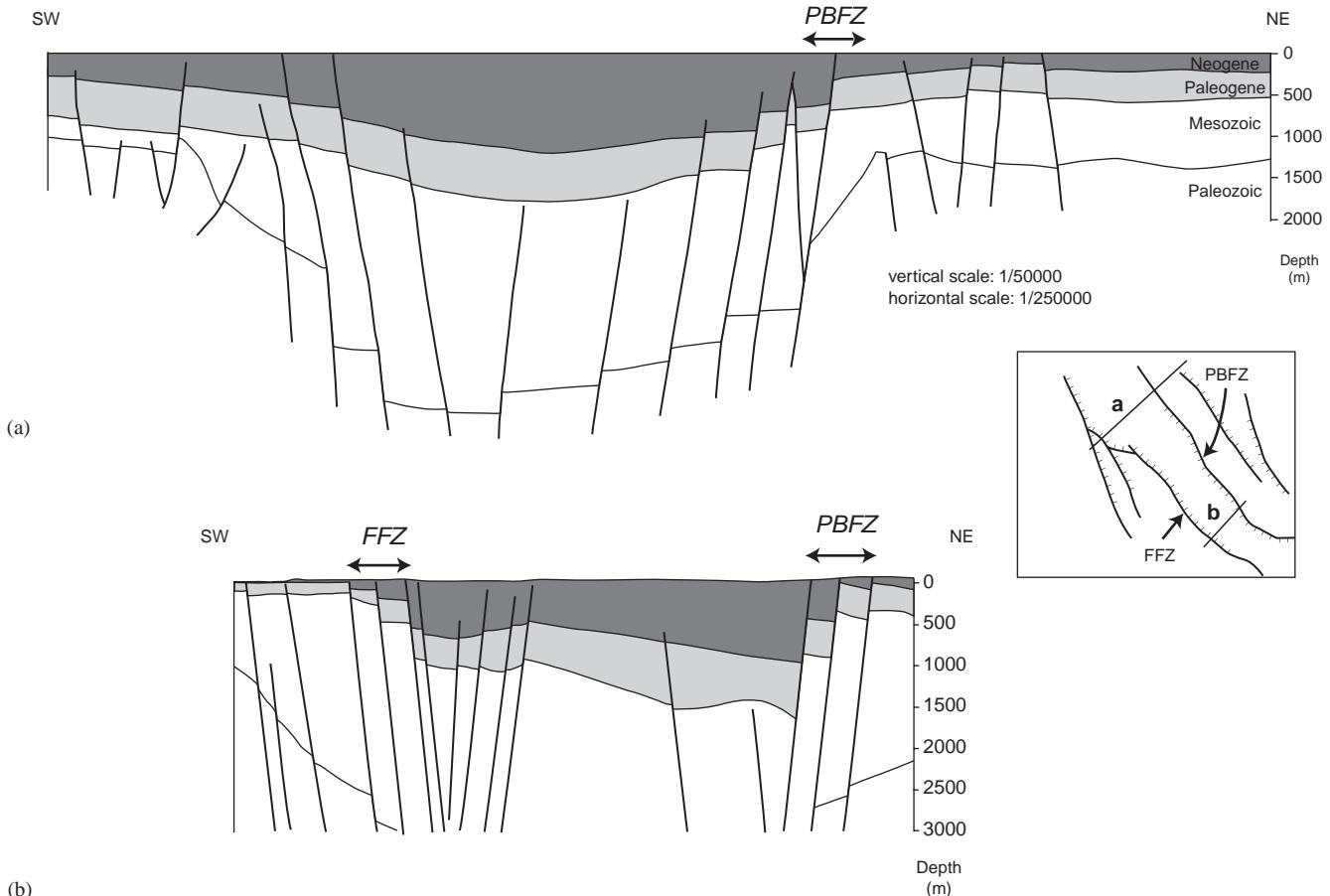
Fig. 2. Synthetic cross sections based on seismic data perpendicular to the RVRS located in the northwestern (a) and the southeastern (b) parts of the graben.

100 km long narrow deformation zone composed of the peel boundary fault and several secondary faults. In the southeastern part of the RVRS, the FFZ corresponds to the southwestern limit of the graben. This fault zone is 80 km long and is mainly composed of the Feldbiss fault, the Geleen fault and the Heerlerheide fault. Synthetic cross sections deduced from 2D seismic lines reveal that the geometry of the graben changes between the northern and southern parts (Fig. 2). In the north, the RVG is an asymmetric graben (half-graben) bounded by a major fault in the northeast (i.e., the PBFZ). The thickness of the tertiary sediments progressively decreases towards the southwest and is slightly affected by small secondary faults (i.e. the Rijen fault). In contrast, in its southern part, the RVG is a symmetric graben (full-graben) limited by two important faults located on each side. In this part, the offsets at the PBFZ (∼1000 m) and the FFZ (∼600 m) are of the same order of magnitude.

Several studies based on geomorphological and DEM analysis allowed the determination of the Quaternary faults in the RVRS (e.g., Van den Berg et al., 1994; Houtgast and Van Balen, 2000). Analysis of gradient maps (i.e., slope maps) inferred from DEMs with a 100 m step highlighted the occurrence of three main fault orientations (NW–SE, NE–SW and N–S). On the peel block and on the southern border of the RVG, the NW–SE lineaments prevail whereas the central part of the RVG is characterized by the predominance of the NE–SW orientation (Van den Berg et al., 1994). Such a fault pattern has been interpreted as the result of a present-day strike-slip motion of the RVRS where the PBZF and the FFZ play the role of the main strike slip faults (Van den Berg, 1994). Nevertheless, Houtgast et al. (2002) have recently shown that the FFZ was characterized by a normal faulting mode during the quaternary. To solve these antagonist interpretations, we analyze a high precision DEM in order to quantify the vertical and lateral displacement along the PBFZ and the FFZ.

3. Methodology

3.1. DEM analysis

Our study aims to analyze the present-day deformation of the surface along the RVG border faults (i.e., the

PBFZ and the FFZ). Three different areas were selected taking into account the importance of the fault trace in the field, the location of several trenches dug during previous studies (Van den Berg et al., 2002; Houtgast et al., 2003) and the seismicity recorded since the beginning of the XXth century (Fig. 3). In Limburg (southern part of the Netherlands), the tectonic activity of the FFZ was intensively studied by shallow well analysis, trenching and mapping of the Meuse terraces (Van den Berg, 1989; Van Balen et al., 2000; Houtgast et al., 2002). We have also studied this zone with the DEM in order to compare our results to those obtained with different approaches. On the PBFZ we have selected the two most seismic active zones, which are the Uden area in the northwestern part of the RVG and the Roermond area in the south-east, as demonstrated by the occurrence of two large earthquakes during the XXth century: the Roermond earthquake ($M_1 = 5.8$) in 1992 and the Uden earthquake ($M_1 = 5.5$) in 1932.

The data on which the DEMs are based were obtained by laser altimetry (Rijkswaterstaat, 2000). The original data density is at least one data point per $16\,m^2$, with the exception of heavily forested areas where the density is half. The original data have been partly corrected for outliers, vegetation and buildings, except for urbanized areas. As the filtering has been made by different private companies, the quality of the data may vary. The DEM is constructed from the filtered data by interpolation to a $5\,m \times 5\,m$ grid by inverse-squared distance weighting, with a footprint of $8\,m$. By comparison of the laser altimetry-derived data to reference points the precision in the horizontal plane is calculated to be less than

$30\,cm$. For the $5\,m \times 5\,m$ DEM the standard error in the estimated heights is $16\,cm$ (68% of the data has an error less than $16\,cm$).

In the different areas, the surface deformation was measured from the DEM. For each fault, we determined several parallel topographic profiles distributed perpendicular to the fault trace. The location of each profile was selected by taking into account the influence of human activity, vegetation and erosion and sedimentation, and the offset values were corrected for these parameters. Because a fault scarp is continuously smoothed by erosion, the length of our profiles taken is large enough (between 600 and 4000 m; average length around 1200 m) to prevent this problem. The offset value is determined from the difference between the average elevations of the footwall and the hangingwall (Fig 4). The comparison of offset values determined from the DEM with those obtained from shallow well analysis (Houtgast et al., 2002) and trenching (Van den Berg et al., 2002; Houtgast et al., this issue) reveals nearly similar results, which allows a validation of our method.

We use two types of stable geological markers to determine the fault motion along the FFZ and the PBFZ: eolian dunes and Paleo-Meuse terrace boundaries. The eolian dunes and the fluvial terraces are mainly composed of sand, which is a material that well records passively vertical and horizontal deformations as shown in analogue experiments (e.g., Davy and Cobbold, 1991). Deformation was studied with young (eolian dunes –11.5 ky-) and old (paleo-Meuse terraces-several 100 ky) formations in order to cover a larger time scale.
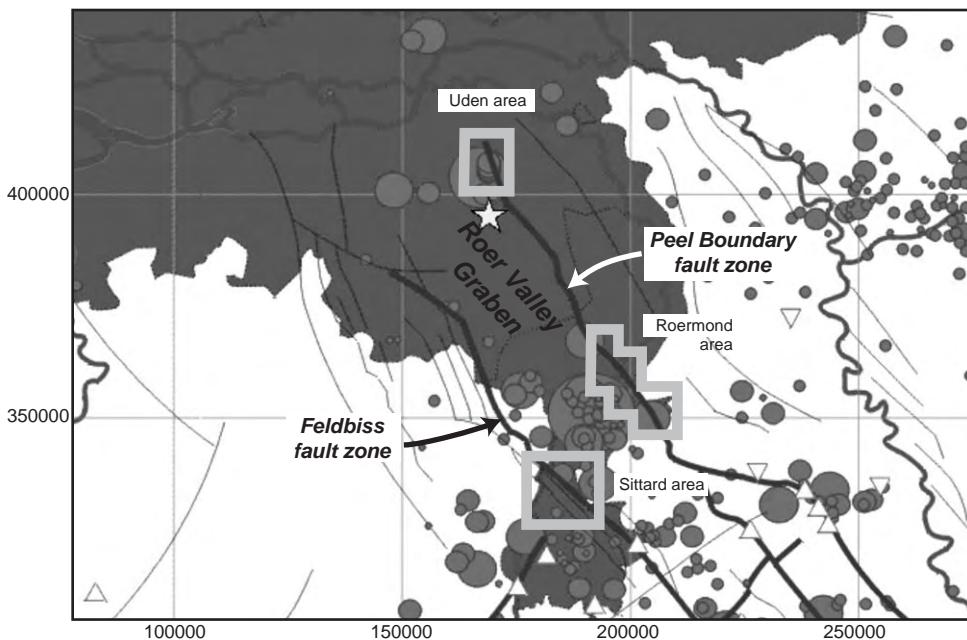

Fig. 3. Location of the three areas covered by the 5 m step digital elevation models. The background map corresponds to the distribution of the recent seismicity recorded by Dutch Seismological Institute (KNMI).
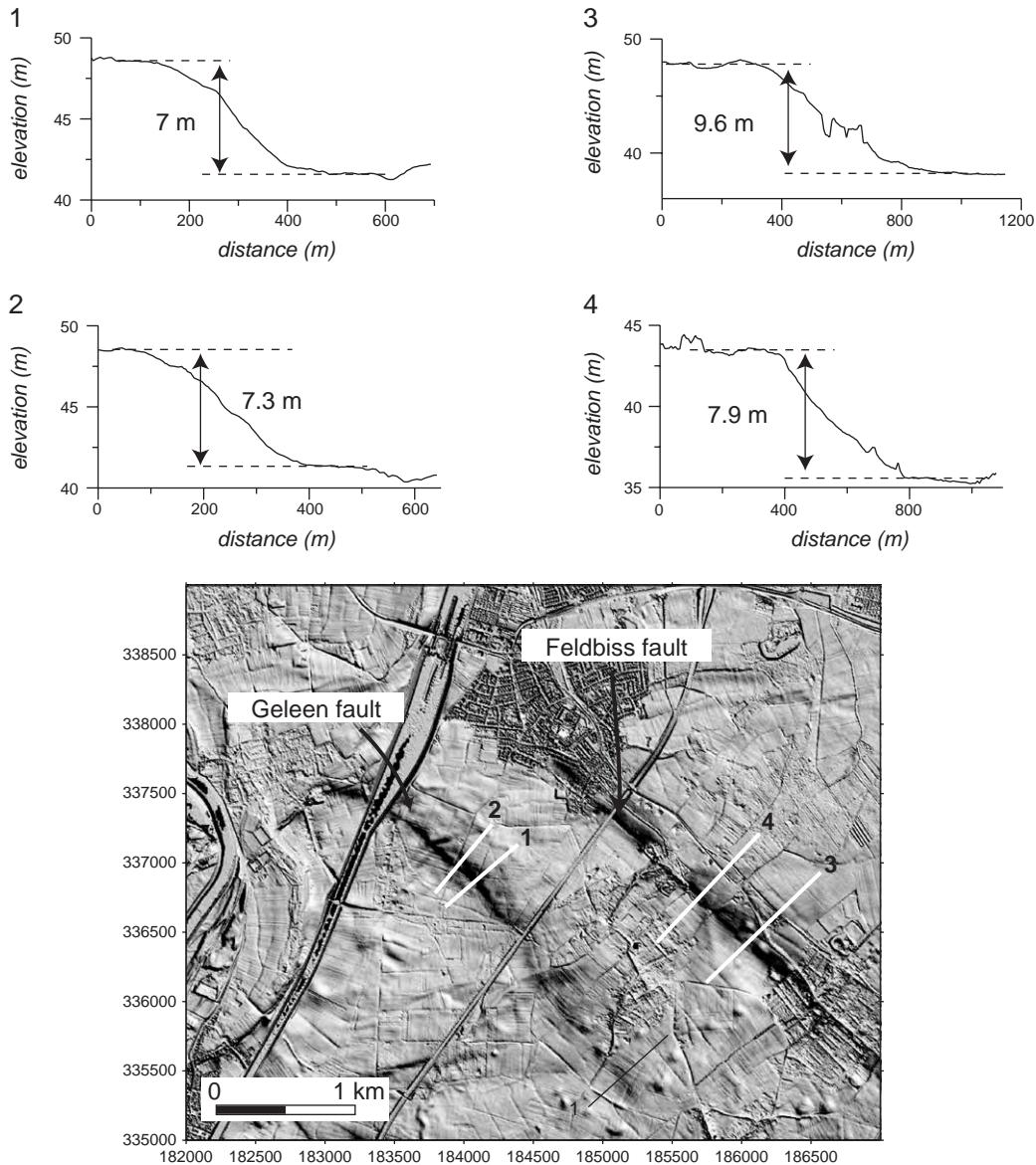
Fig. 4. Example of several SW–NE trending topographic profiles used to determine the offset between the foot-wall and the hanging-wall on both sides of the FFZ. Offsets created by the PBFZ activity were determined with the same methodology.

3.2. Age of the formations

The geomorphological and sedimentological evolution during the most recent geological history (Saalian to Holocene) of the southeastern part of the Netherlands is important to date the fault movements, and, to some extent, to interpret the fault scarps. Terraces formed by the Meuse river characterize the landscapes near Sittard and Roermond. These terraces are well dated, especially the younger ones, which are used in our work. The terrace sequence is a consequence of the long-term uplift of the area (Van den Berg, 1989; Van Balen et al., 2000), but they are also faulted. The displacement of the terraces can be used to determine

fault displacement rates and fault pattern (Houtgast et al., 2002). Periglacial eolian processes have deposited a blanket of fine sand and loess everywhere in the study area during the Weichselian Pleniglacial, except on the Lateglacial to Holocene terraces near the Meuse. This blanket has probably leveled the fault-related morphology of pre-Weichselian age. During the late Pleniglacial and the Lateglacial, dunes were formed in the Uden and Roermond areas. In the Sittard area, the eolian deposits are too fine grained (loess) for dune formation. Near Roermond these dunes are faulted. More detailed information on the geomorphology and sedimentology will be given in the discussion of different areas.

4. Results

4.1. Geometry of the active faults

The DEM analysis reveals surface escarpments along the graben border faults, which are not single faults but correspond to active fault zones composed of parallel faults.

In the Sittard area (Fig. 5), the Geleen and Feldbiss faults were already recognized as forming an overstepping fault system (Houtgast et al., 2002). The shaded relief image indicates that the Geleen fault corresponds to several adjacent and kilometric-long segments of faults whereas the Feldbiss fault is a unique and linear fault (Fig. 5). As indicated by well analysis (Houtgast et al., 2002), the Geleen fault progressively disappears toward the South-East where its displacement is taken over by the Feldbiss fault. The DEM also allows the determination of the surface deformation generated by the Heerlerheide fault zone in the Late Saalian deposits (i.e., 130 ka). This fault zone is bounded in the South and the North by two main normal faults of which the southern limit corresponds to the main fault visible in seismic cross-sections. Between these two faults, the differential deformation is accommodated by a 150–200 m wide micro-graben. It is

worth noting that the complex geometry of the Heerlerheide fault zone is directly controlled by a Carboniferous fault system, which consists in this area of two parallel faults coincident with the limit of the present-day deformed area. In the northwestern part of the study area, the recent activity of the FFZ cannot be recognized in the young Meuse terraces (3 and 11 ka). According to the displacement rates determined by Houtgast et al. (2002) for the Feldbiss and Geleen faults (24 and 28 mm/ky, respectively), the surface displacements associated with the Feldbiss and Geleen faults are about 0.3 m in the Geistingen terrace (11 ka). The anthropogenic activity, the orientation of the Paleo-Meuse meanders and the standard error of the DEM probably not allow the detection of such small surface deformations linked to fault activity. The fault orientation inferred from the DEM indicates a very constant trend around N130–140 for the FFZ (Fig. 6a).

In the Roermond area, the surface deformation generated by the PBFZ activity is visible along a 20 km-long segment (Fig. 7). Contrary to the FFZ in the Sittard area, the PBFZ corresponds here to a unique fault with a clear trace on the DEM except between Neer and Roermond where the Meuse River crosscuts the PBFZ. This trace has different orientations depending on the area. In the southern part, the PBFZ presents
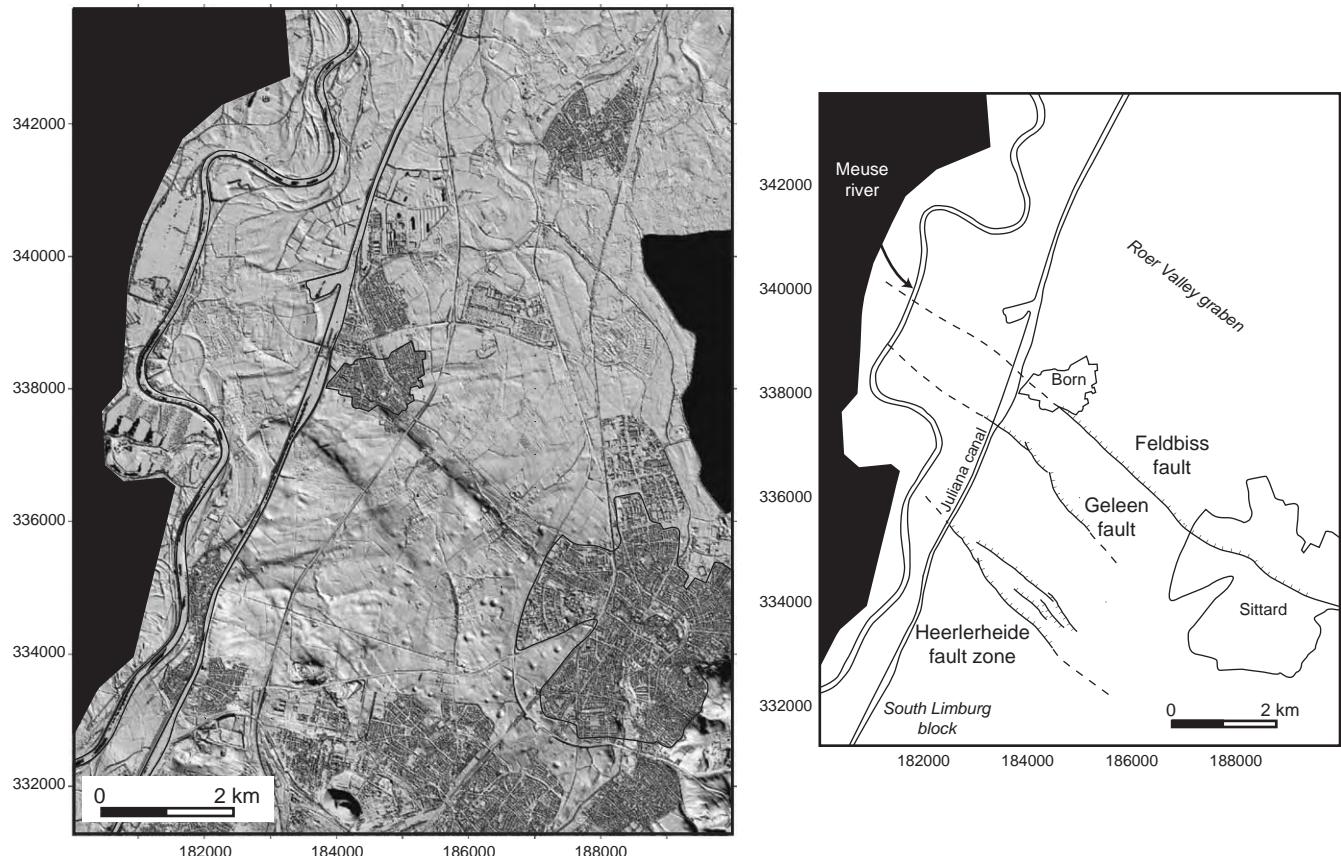

Fig. 5. Geometry of the FFZ in the Sittard area. The shaded relief map is characterized by an artificial illumination from the SW. NW–SE lineaments corresponds to the FFZ trace while SW–NE lineaments results from paleo-Meuse terrace boundaries as revealed by Houtgast et al., 2002.

Sittard area

Roermond area
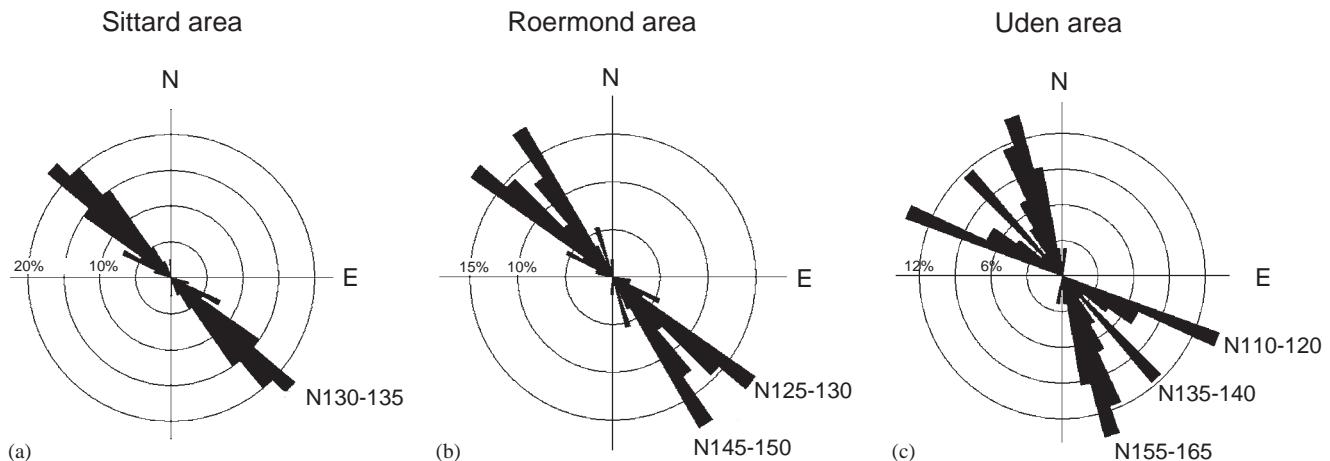
Uden area

Fig. 6. Rose diagrams showing the direction of the active faults in (a) the Sittard area, (b) the Roermond area and (c) the Uden area.
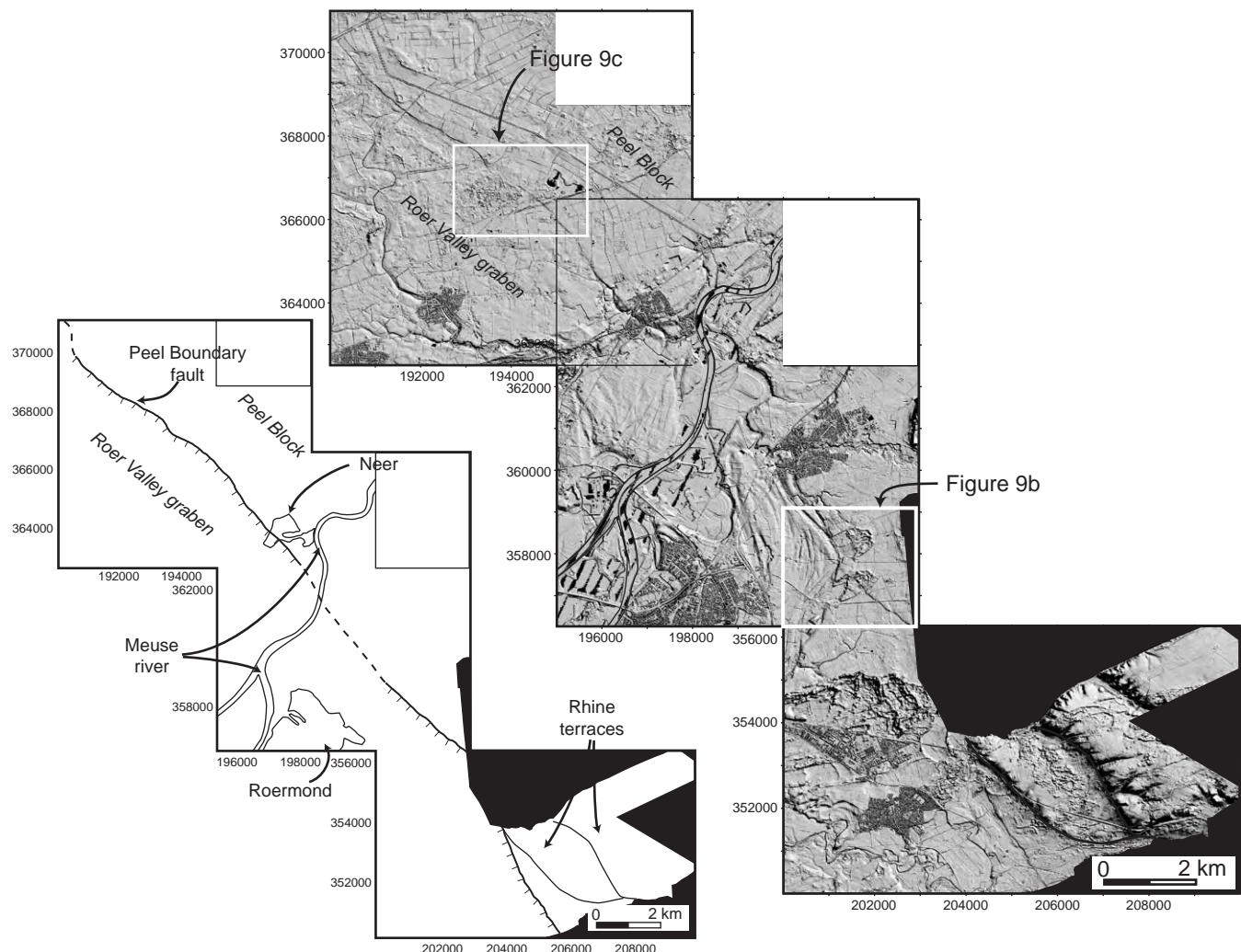

Fig. 7. Geometry of the southern segment of the PBFZ in the Roermond area. The shaded relief map is characterized by an artificial illumination from the NE.

a N145–150 average orientation. The second main orientation (N125–130) is represented east of Roermond and in the northwestern part of the studied area. Thus,

the general NW–SE orientation of the PBFZ results in the Roermond area from the combination of two main fault trends (N125–130 and N145–150) (Fig. 6b).

In the northwestern part of the RVRS, the PBFZ geometry is more complex with the development of two ~14 km-long parallel faults: the peel boundary fault in the West and the 2nd peel boundary fault in the east (Fig. 8). From the south-east, these faults present long and linear traces that are from south to north westward shifted by two N110–120 fault segments of about 2 km. In the north, the scarp of the 2nd peel boundary progressively dies out whereas the deformation due to the peel boundary fault is still visible in the northwestern corner of the study area (Fig. 8). In the southern part of the studied area, the peel boundary fault scarp decreases south of Uden. Nevertheless, combination of the elevation map and the shaded relief image indicates that the fault continues with smaller offsets. Analysis of the fault orientation reveals the occurrence of three directions of faults: N110–120, N135–140 and N155–160 (Fig. 6c). The first trend (i.e., N110–120) corresponds to the direction of the oblique faults, which control the lateral shift of the peel boundary fault and the 2nd peel boundary fault north of Uden. The two other directions represent the local changes of the PBFZ orientations.

4.2. Characterization of fault motion

Using passive geological markers such as stable eolian dunes and Paleo-Meuse terrace boundaries, we determined precisely the fault motion along the FFZ and the
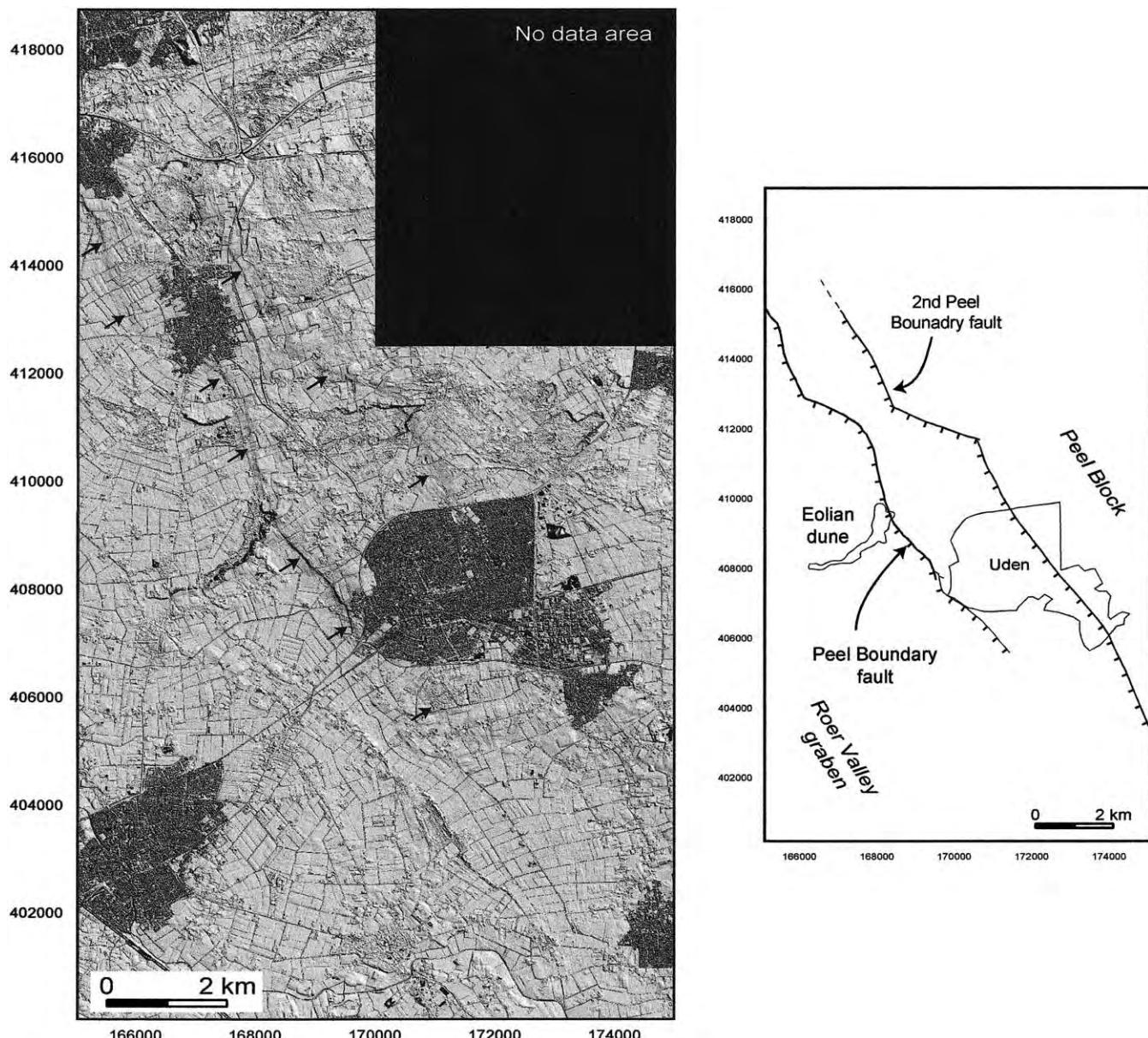

Fig. 8. Geometry of the northern segment of the PBFZ in the Uden area. The shaded relief map is characterized by an artificial illumination from the NE. Small arrows indicate the location of the escarpments associated with the fault activity.

PBFZ. In the Sittard area, the lack of lateral offset and the important vertical deformation (i.e., up to 7.2 m) of the Paleo-Meuse terrace limits where they crosscut the FFZ suggests that the faults representing this trend are pure normal faults since at least 330 ky (i.e., age of the older Meuse terrace boundary in the studied area) (Fig. 9a). East of Roermond, the vertical displacement of recent geological formations, like eolian dunes and meander scroll bars, without any lateral component indicates that the southeastern part of the PBFZ is characterized by pure normal faulting since 12.9 ky (i.e., age of the scroll bars) (Fig. 9b). West of Roermond, a similar fault motion is determined as the limit of the Late Pleniglacial terrace present a vertical offset of about 1 m with no lateral displacement (Fig. 9c). Like in the Roermond area, passive markers of the deformation (i.e., eolian dunes) in the Uden area indicate that the PBFZ is characterized by a normal faulting mode in its northwestern part (Fig. 9d).

4.3. Quantification and age of the deformation

The use of a high precision DEM allows determination of the escarpments associated with the fault
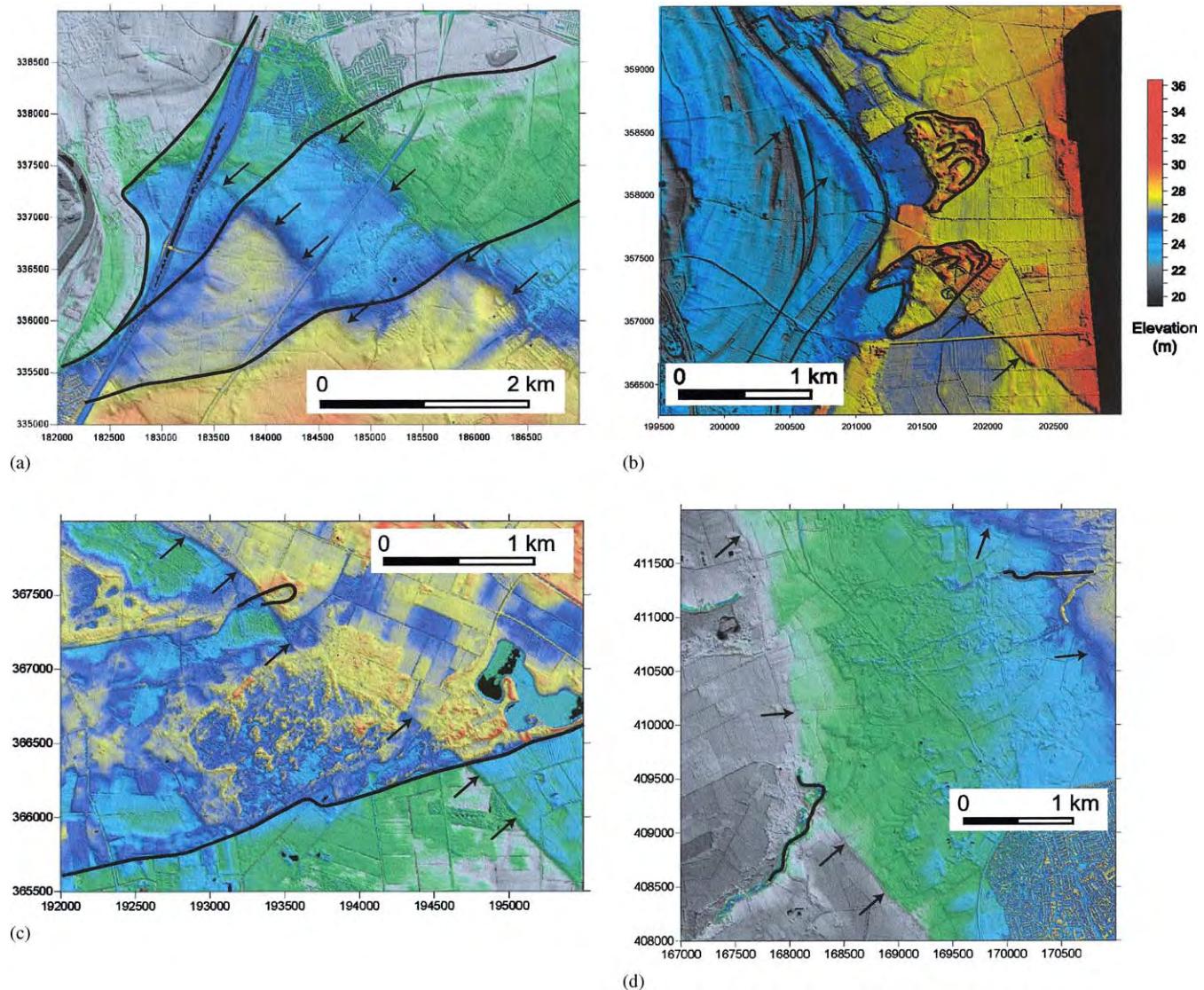

Fig. 9. Deformation of the eolian dunes and paleo-Meuse terraces induced by tectonic activity (see the black arrows for fault location). (a) In the Sittard area, the terrace boundaries (black lines) present a vertical displacement without any lateral offset. Increasing elevations are represented by black, gray, green, blue, yellow and red colors. (b) East of Roermond, the PBFZ activity deforms an eolian dune in the vertical plane only, proving the pure normal mode of deformation of the PBFZ. (c) West of Roermond, the vertical deformation of the Late Pleniglacial terrace limit and the eolian dunes confirms this fault motion for the southeastern part of the PBFZ (same color scale than A). (d) In the Uden area, the PBFZ, which is composed by two parallel faults offsets the eolian dunes only vertically proving that the PBFZ is a pure normal fault (same color scale than A).

activity. Knowing the age of the Paleo-Meuse terraces upper part (i.e., when the river abandoned the terrace) and the age of eolian dune formation, which are affected by the tectonic activity, we have deduced displacement rates along the FFZ and the PBFZ.

4.3.1. Sittard area

In this part of the RVRS, the FFZ is crossed by the Meuse river. Uplift of the area South of the FFZ caused the Meuse river to incise during the Pliocene and the Quaternary, and as a consequence, a flight of terraces was formed (e.g. Van den Berg, 1989; Van Balen et al., 2000; Houtgast et al., 2002). The terrace deposits are often covered by eolian deposits, mainly sandy loess (Mücher, 1986). The terrace deposits are underlain by tertiary Breda or Kiezelöoliet formations, which consist of fine to coarse sands (Felder et al., 1989). Due to northwestward tilting, terrace remnants are preserved mainly on the east bank of the Meuse river valley. The Meuse terraces in South Limburg have been the subject of many studies and have been extensively described (for an overview see Houtgast et al., 2002). Five terrace levels can be discriminated in the study area.

The oldest terrace in the study area is the Caberg-1 terrace (Fig. 10a). By interpolation and by correlation to the δ^{18}O curve of ODP 667 the age of this terrace is estimated at 420 ka (Van den Berg, 1989; Houtgast et al., 2002). Similarly, the next younger terrace, Caberg-2, is estimated at 330 ka. The Caberg-3 terrace is dated by thermoluminescence and paleontological remains at 250 ± 20 ka (Huxtable and Aitken, 1985; Van Kolfscho-ten et al., 1993). By correlation to the δ^{18}O curve of ODP 667, the Eisden–Lanklaar terrace is estimated to be 130 ka (Van den Berg, 1989; Houtgast et al., 2002). An important stratigraphic characteristic of the next younger terrace, the Geistingen terrace, is the complete absence of eolian coversands. Consequently, this terrace was formed during or after the last period of coversand deposition, i.e. during or after the Younger Dryas period (Paulissen, 1973), estimated at 11.5 cal (calibra-ted) ka BP (10 ka ^{14}C).

In the Sittard area, 14 topographic profiles perpendicular to the Geleen and Feldbiss faults are used to determine the offsets related to fault displacements (Fig. 10a). On the Geleen fault, the escarpment reaches a maximum value of 7.4 m in the central part of the fault (i.e., on the Caberg-3 terrace). From this location, the surface deformation decreases progressively toward the south-east and abruptly toward the north-west down to 4.1 m (Fig. 10a). In more detail, the surface deformation created by the fault activity for each terrace is maximum in its northwestern part and decreases progressively toward the south-east. The deformation along the Feldbiss fault has been determined from 7 topographic profiles distributed on terraces dating between 130 and

420 ky. These profiles show (1) a general step-like increase of the offsets from the youngest to oldest terraces and (2) a slight increase of the surface deformation toward the south-east for each terrace (Fig. 10b). Topographic profiles CSF7 and CSF8 show again an increase of the displacement linked to the Feldbiss fault. However, in this part of the Sittard area, the surface of the Caberg-1 terrace is covered by a thick loess deposit, forming a ridge (see Fig. 8 in Houtgast et al., 2002). The surface topography then corresponds to the accumulation of the deformation associated to the Feldbiss fault activity and the preexisting topography of the Caberg-1 terrace.

Considering the offsets determined from the DEM analysis and the age of the Paleo-Meuse terraces, we calculated displacement rates along the Geleen and the Feldbiss faults (Fig. 10b). As previously demonstrated by analyses of borehole data by Houtgast et al. (2002), the displacement rate along the Geleen fault decreases toward the south-east. In the northwestern end of the visible Geleen fault, the displacement rate is around 33 mm/ky and it decreases progressively down to 14.5 mm/ky in its south-eastern extremity. It is important to note that the values obtained from the offset at the base of the terrace (Houtgast et al., 2002) and from the surface deformation are nearly similar. Consequently, the deformation observed at the surface mainly results from tectonic activity and was hardly affected by differential erosion and sedimentation between the footwall and the hangingwall. Contrary to the Geleen fault, the Feldbiss fault presents an increase of the displacement rate toward the south-east. On the Eisden–Lanklaar terrace, the displacement rate inferred from the offset of 3.8 m is 29.2 mm/ky. The rate progressively increases up to 39 mm/ky determined for a displacement of 12.9 m affecting the Caberg-2 terrace. The offset values deduced for topographic profiles CSF7 and CSF8 being partly wrong (see discussion in the previous paragraph), we do not incorporate the displacement rates for these profiles in our study. Although the general tendency observed for the variation of the displacement rate along the Feldbiss fault is similar for the present study and that of Houtgast et al. (2002), the exact values of the displacement rates are different: Eisden-Lanklaar 19 mm/ky, Caberg-3 26 mm/ky and Caberg-2 31 mm/ky. However, results of a recent study of a trench across the Feldbiss fault showed that the offset value at the Caberg-3 terrace obtained by Houtgast et al. (2002) from an analyses of borehole data were underestimated by about 50% (10 m instead of 6 m; Houtgast et al., this issue).

4.3.2. Roermond area

In this study area the Meuse river crosses the PBFZ. During the late Saalian to Holocene time interval the
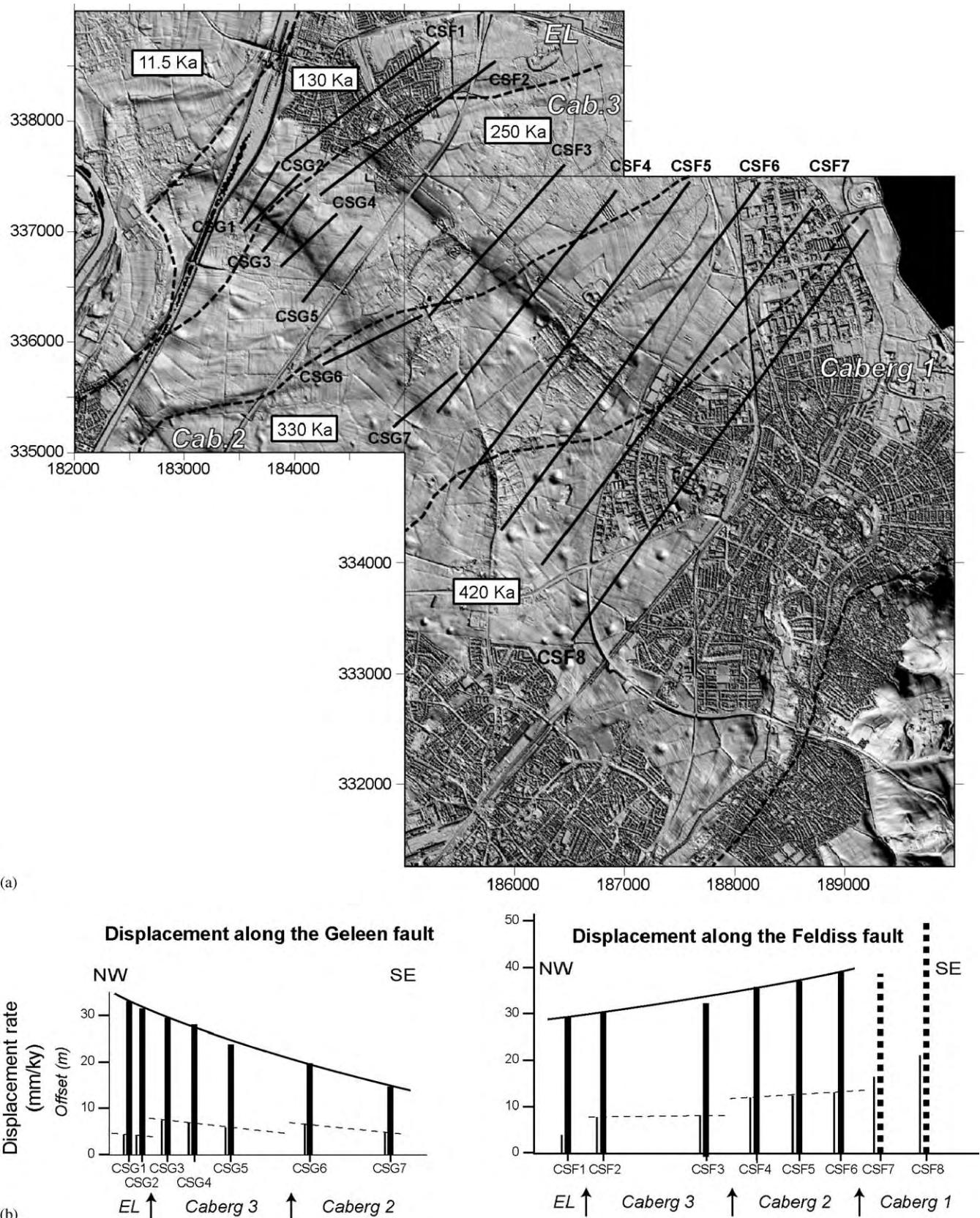
Fig. 10. (a) Location and age of the paleo-Meuse terraces in the Sittard area (after Houtgast et al., 2002). Dashed lines represent the limits of the paleo-Meuse terraces. The topographic profiles used in the present study are represented by black linear segment named CSG for the Geleen fault and CSF for the Feldbiss fault. (b) Evolution of the escarpment (thin lines) and the displacement rate (thick lines) along the Geleen and Feldbiss faults. The same vertical scale and different units are used for the displacement rates and the offset. Profiles CSF7 and CSF8 (thick dashed lines) are not integrated in the study as the escarpment is disturbed by the development of a valley and by an important loess deposit.

Meuse river formed an incised valley in this study area (Zonneveld, 1974; Van den Berg, 1989) with terraces which can be correlated southward to the Sittard area (see above) and northward, across the peel block, to the border of the Rhine–Meuse delta (Zonneveld, 1974; Huisink, 2000). The terraces are covered by eolian sandsheet deposits. The most characteristic terrace in the study area has a ridge and swale morphology, which was formed by a meandering river (Paleo Meuse). Similar river terrace fragments have been documented further downstream (e.g. Huisink, 2000), and dated at an Allerød age (12.9 cal ka BP, 11.0 ^{14}C ka). The next

lower terrace is characterized by a relatively straight, braided river channel pattern. This terrace is also documented further downstream and dated at a Younger Dryas age (11.5 cal ka BP, 10.0 ^{14}C ka). The terrace gradients resulting from the downstream correlation are in line with the present-day river gradient, confirming the correlations. On the south-eastern side of the Meuse valley, the Allerød terrace is cut in to an older terrace of either Pleniglacial (Zuidam, 1980) or late Saalian (Zonneveld, 1974) age (Fig. 11a). A late Saalian interpretation is supported by the vertical position of a river terrace on the other side of the Meuse valley, to the
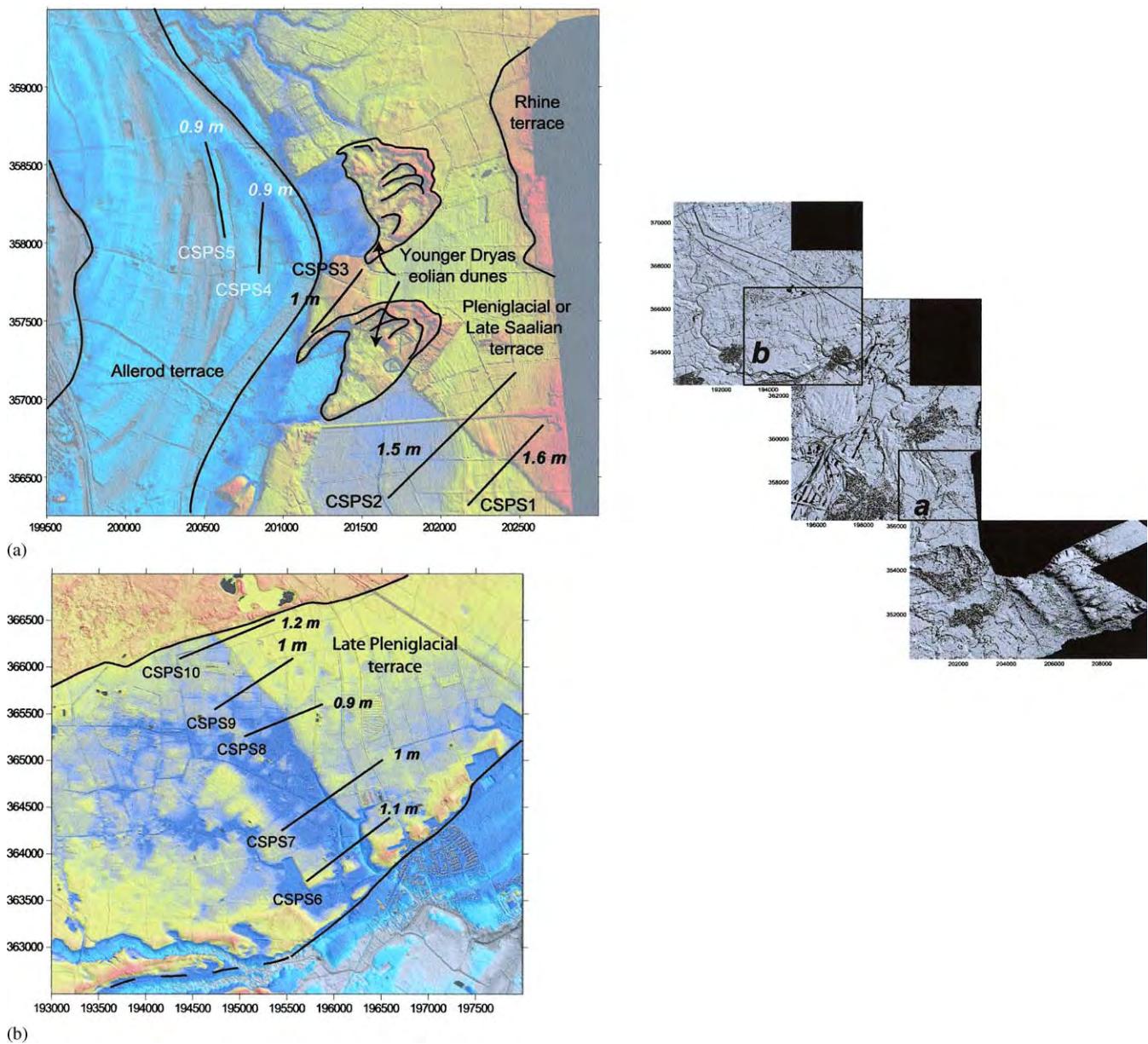

Fig. 11. Age and deformation of the Quaternary formations used in the Roermond area for the determination of the displacement rates on the eastern (a) and western (b) sides of the Meuse river valley. For each topographic profile the name and the offset value are indicated. Gray and blue colors and yellow and red colors correspond to low and high elevation, respectively.

west of Roermond (Fig. 11b), which is of Pleniglacial age according to Van den Berg et al. (2002). This terrace is in a morphological lower position than the terrace level under consideration, but higher than the Allerød level. A Pleniglacial age, on the other hand, is consistent with the local geology. Eolian dunes of Younger Dryas age are located on top of the terrace (Fig. 11a). The dunes are displaced by the PBFZ. Drilling into the dunes revealed that floodplain loam deposits are preserved in between the base of the dune and the eolian top of the underlying terrace, with an equal thickness on both sides of the fault. Given their distance of less than 200 m to the Allerød channel and their stratigraphic position, the most likely age for these loams is Allerød. This interpretation favors a Pleniglacial age of the terrace deposits underlying the loam. In any case, the late Pleniglacial sand sheet deposits on top of the terrace will have partly or completely leveled the fault scarp morphology, which is confirmed by the similar thickness of the loam (post-dating the eolian sand sheets) on both sides of the fault.

Analysis of the fault segment located on both sides of the Meuse river allows determination of the offsets induced by a fault activity (Fig. 11). East of Roermond (i.e., on the eastern side of the Meuse river valley), the offsets determined from the topographic profiles CSPS4, CSPS5 and CSPS6 at the top of the Allerød terrace vary between 0.7 and 1 m (average value of 0.85 m) (Fig. 11a). Considering the age of the terrace, this suggests an average displacement rate of 66 mm/ky. East of the Allerød terrace, the offsets range between 1 m (CSPS3) and 1.6 m (CSPS1) at the top of the Late Saalian or Pleniglacial terrace. The high values deduced South-East of the eolian dune can result either from a larger tectonic activity in the southeastern part of the study area or from a remnant offset which was not completely leveled during the emplacement of the sandsheet. Assuming that the sandsheet, covering the terrace dates from the late Pleniglacial, we obtain displacement rates ranging from 69 to 111 mm/ky. Finally, the Younger Dryas eolian dune affected by the fault activity has an offset of 0.9 m at its base and 0.8 m at the top (offset estimated from the envelope curve), which indicates a displacement rate of 70 mm/ky. On the western side of the Meuse river valley, the offsets inferred from the topographic profiles at the top of the Pleniglacial terrace vary between 0.9 and 1.2 m (Fig. 11b). A similar value (0.9–1 m) was observed in a trench dug at the same location as the topographic profile CSPS7 (Van den Berg et al., 2002). According to our values, the average displacement rate is around 65 mm/ky for this segment of the PBFZ; the high displacement rates obtained from the topographic profiles CSPS1 and CSPS2 do not represent a larger tectonic activity but probably results from a remnant offset before the deposition of the sandsheet.

4.3.3. Uden area

Tectonically, the Uden area is situated at the northeastern rim of the RVRS. The Roer valley graben is situated to the southwest of the fault scarps, the peel block is to the northeast. As a result, the subsurface geological build-up is quite different in terms of the completeness and thickness of the Cenozoic deposits (Van den Toorn, 1967; Bisschops, 1973; Van Balen et al., 2000). During the early Pleistocene the RVG was a depocentre for the Meuse as well as the Rhine river. However, during the early Middle Pleistocene the Rhine took abruptly a more northward directed course, whereas the Meuse changed its course gradually northwards, leaving deposits on the peel block. After the Meuse left the area, local fluvial and eolian deposits were formed. Thus, the shallow geology of this area consists of middle Pleistocene Meuse deposits (Veghel formation; younging in a northeastward direction) overlain by eolian and local fluvial deposits of late Pleistocene age (Elsterian up to Weichselian in age), which in turn is locally overlain by Holocene peat. The largest landform in the Uden area is a wide flat area of late Pleniglacial sand sheet deposits, which formed in response to permafrost degradation (Rijks Geologische Dienst, 1983). The age of these sheet deposits is 16–14.4 cal ka BP (14–12.5 ^{14}C Ka; Kasse, 1999). On this planation surface eolian ridges (ER) and eolian dunes (ED) of late Bølling to Younger Dryas/early Holocene age (14.4–10.5 cal ka BP; 12.5–9.0 ^{14}C ka; Kasse, 1997; 1999) were formed by remobilization of the sand (Fig. 12). The dunes and ridges were reactivated during the middle ages as a result of farming activities. Some of them are still active at present, as evidenced by a lack of soil on top of them. The uplifted peel block is dissected by gullies (Fig. 12). The formation of the gullies is related to permafrost conditions, inducing enhanced surface runoff and, as a result, overdeepened fluvial valleys. They are, in origin, slightly older than the late Pleniglacial sand sheet deposits. Remnants of a small river valley are present West of the city of Uden. The valley has enhanced the size of the escarpment by fluvial incision into the late Pleniglacial eolian planation surface along the fault trace. The former river course was blocked by the formation of the dunes (ED) and ridges (ER); the river now takes a more westward course. Therefore the age of the valley is also late Pleniglacial. In the northeastern corner of the study area a small patch of the late Pleniglacial terrace (LPG) of the Meuse river is indicated (Fig. 12).

The PBFZ is represented by two parallel faults, which have induced the formation of parallel fault scarps (Figs. 8 and 12). Although the offset located at the fault escarpment can be easily determined, the amount of displacement due to tectonic activity is hard to assess. The human activity and the fluvial erosion along the scarp have potentially disturbed the original fault scarp.

Fig. 12. Age and deformation of the Quaternary formations along peel boundary fault and the 2nd peel boundary fault in the Uden area. Blue and yellow colors correspond to low and high elevation, respectively.

these two values, the topographic profiles show a homogeneous deformation along the fault with an average offset of about 4 m. If we assume that this deformation is post late Pleniglacial, the average displacement rate is higher along this fault than along the peel boundary fault. However, it is very likely that the 4 m offset partly corresponds to a remnant offset (i.e. older than late Pleniglacial). The emplacement of the late Pleniglacial sandsheet from the West has induced a differential coverage in the RVG and the peel block, controlled by the morphology. Consequently, we propose that the peel boundary fault scarp was leveled during the late Pleniglacial, whereas the scarp of the 2nd peel boundary fault was only smoothened. The displacement rates inferred from the offset values then correspond to an overestimation, which cannot be quantified.

5. Discussion

From the geometry of the active faults, Van den Berg et al. (1994, 2002) and Camelbeeck and Meghraoui (1998) have proposed a strike slip motion along the border faults of the RVRS. Van den Berg et al. (2002) consider the PBFZ as a left lateral strike slip fault zone and the FFZ as characterized by a right lateral motion. In contrast, Camelbeeck and Meghraoui (1998) interpret the en echelon pattern of the FFZ as the result of left lateral extension. These interpretations are in disagreement and they do not fit with the NE–SW direction of extension deduced from the analysis of earthquake focal mechanisms (Plenefish and Bonjer, 1997).

Although the DEM analysis reveals a fault geometry compatible with a strike slip motion of the major faults, the vertical displacement of passive markers like eolian dunes and the limit of fluvial terraces indicates a pure normal faulting mode for the late Quaternary period, related to a NE–SW extension. This apparent paradox can be solved taking into account the role of the structural inheritance in the location and the geometry of the active faults. It has been recently shown that the orientation of the active faults during the Mesozoic and the Cenozoic periods was identical whatever the paleostress field (i.e., Triassic extension, Late Cretaceous N–S compression, Miocene NE–SW extension) (Michon et al., 2003). The age of the structural inheritance is at least Carboniferous and most likely Caledonian (Thorne and Watts, 1989; Houtgast et al., 2002). As these geological events were characterized by the development of large NW–SE strike slip faults (i.e., the Peel Boundary fault and the Feldbiss fault), the fault pattern, which is reactivated in normal faulting mode during the Quaternary is similar to a strike slip fault pattern.

In the different areas, the orientation of the active fault slightly differs (Fig. 6). In the Sittard area, the

For the peel boundary fault, the topographic offsets range between 1.9 and 7 m, with the lowest values in the northern part of the fault and the highest values West of Uden (Fig. 12). Given the occurrence of fluvial erosion and the development of gullies in the southern segment of the peel boundary fault, we consider that the offset values are not constrained enough to determine displacement rates. In contrast, the northern segment (i.e., North to the last gully) was preserved from important erosion, and the offsets (between 1.9 and 3.3 m) are most likely related to fault activity. In this part, the displacement rates range between 132 and 229 mm/ky with an average value around 184 mm/ky.

The offsets determined along the 2nd peel boundary fault vary between 1.7 and 4.4 m (Fig. 12). Two of the nine topographic profiles give peculiar offset values. In the northern part, the location of the northern topographic profile in a gully can explain the relatively small offset (1.7 m; leveled by erosion). In the central part, the second offset value (2.6 m) may result from the presence of an eolian dune on the hanging-wall (Fig. 12), leading to an underestimation of the real offset. Besides

faults are grouped in a single N130–135 oriented trend, whereas in the Uden area, three distinct directions are distinguished (i.e., N110–120, N135–140 and N155–165). Integration of the geometry of the Miocene faults makes it possible to explain this difference. For the Miocene period, the border faults of the south-eastern part of the RVRS are characterized by a constant NW–SE direction (Fig. 13). In contrast, the PBFZ in the North-West is composed of the peel boundary fault itself and by N110–120 oriented oblique faults, which have partly controlled the graben subsidence during the Miocene (Michon et al., 2003). The coeval activity of the different fault trends during the Miocene and the Quaternary suggests (1) that the Miocene structural inheritance has controlled the development of the Quaternary faults and (2) there was a similar stress field for the Miocene and Quaternary periods. The superposition of the Miocene and Pleistocene depocentres strongly supports this interpretation. Finally, one can note in our study the lack of the NE–SW trend determined by Van den Berg et al. (1994) and Houtgast and Van Balen (2000) from a 100 m step DEM. The lack of such an orientation is confirmed by inspection of seismic lines, which show that the Mesozoic and Cenozoic sedimentation is never affected by NE–SW faults. Apparently, the

NE–SW lineaments represent other geomorphic features, like eolian ridges.

The use of high precision DEM has allowed determination of displacement rates along the PBFZ and the FFZ. In the Sittard area, the global displacement rate for the FFZ (i.e., the Geelen fault and the Feldbiss fault) shows small-scale lateral variations ranging from 50 mm/ky in the SE (the Caberg-2 terrace) up to 62.2 mm/ky in the NW (the Eisden–Lanklaar terrace). Such a variation, which was already recognized by Houtgast et al. (2002), suggests a slightly nonlinear deformation along the FFZ since 330 ka. In the northern prolongation of the FFZ, Camelbeeck and Meghraoui (1998) have determined a displacement rate of the same order of magnitude (80 ± 40 mm/ky), which indicates a large-scale constant deformation of the FFZ. In the Roermond area, our study has shown a similar constant deformation along the PBFZ with an average displacement rate of about 65 mm/ky. This displacement rate drastically increases in the northern segment of the PBFZ (Uden area) where it reaches an average value of 184 mm/ky. We have already shown in a previous section that fluvial erosion in the Uden area could have disturbed the scarp geometry and in consequence the determination of the displacement rate. However, two independent studies based on the reconstructed
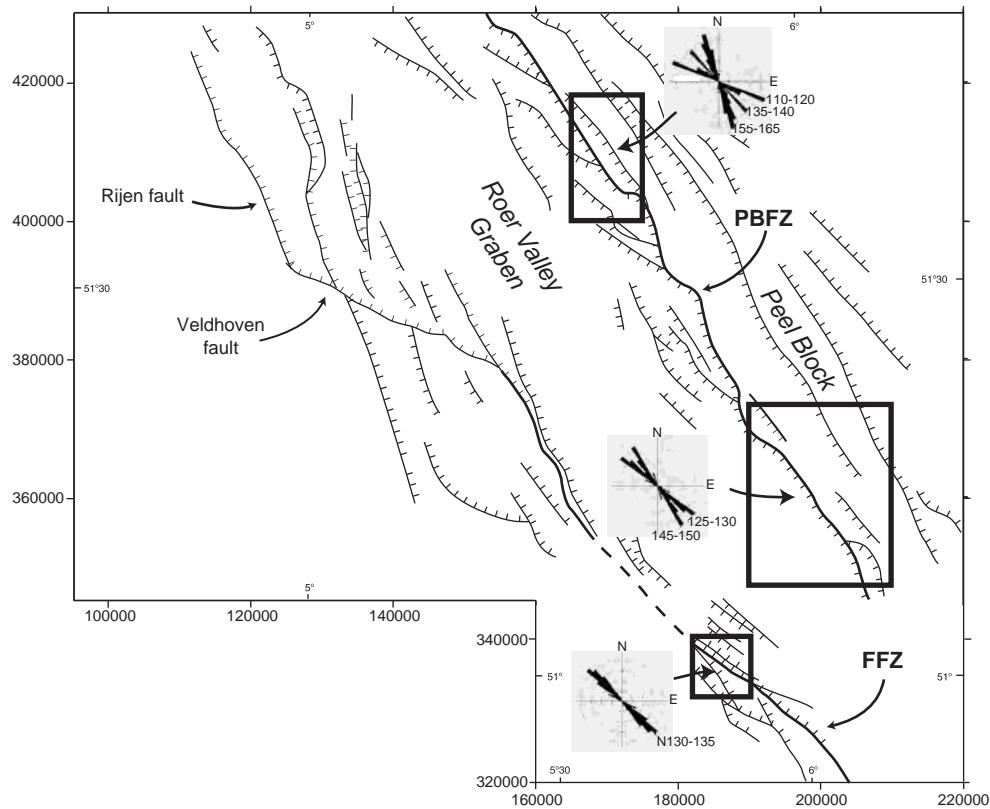

Fig. 13. Comparison of the geometry of the Miocene faults of the RVRS and the orientation of the Quaternary faults determined in the studied areas from the DEM analysis.

Holocene paleogroundwater levels along the Rhine and Meuse rivers (north of the Uden area; Stouthamer and Berendsen, 2000) and the distribution of a fluvial unit containing pumices from the Laacher See eruption (11063 BP; Verbraeck, 1990) have revealed similar displacement rates of the PBFZ (between 130 and 300 mm/ky, and 181 mm/ky, respectively). In addition, a recent study by Cohen et al. (2003) of the deformation of the top of the late Pleniglacial terrace by one of the faults of the PBFZ, probably the 2nd peel boundary fault, gave a time-averaged displacement rate of 60 mm/ky. Consequently, the high displacement rate values obtained from the DEM analysis are real and they represent a strong increase of the deformation along the northern segment of the PBFZ.

We propose to explain these displacement rate differences by taking into account the large-scale geometry of the RVRS. First the RVRS has a different geometry in the northwestern and southeastern parts (Fig. 2). In the south-east, the graben is nearly symmetric and the deformation is accommodated by two main border faults (the PBFZ and the FFZ). The structural profile determined from seismic sections shows that the PBFZ was more active (i.e., larger offset of the base of the Miocene formation) than the FFZ since the beginning of the Miocene. For the Quaternary period, we also demonstrate that the PBFZ is around 20–30% more active than the FFZ. In the north-west, this geometry changes. The RVRS is from a structural point of view an asymmetric graben bounded by only one major fault, the PBFZ, which accommodates the main deformation. With a similar amount of extension, the displacement rate along the northern segment of the PBFZ (around 184 mm/ky) should roughly correspond to the sum of the displacement rates along the PBFZ and the FFZ in the southeastern part (around 120 mm/ky). The difference suggests that another mechanism occurred.

The distribution of the Neogene sediments shows the development of a main Neogene depocentre in the northwestern part of the RVRS with the accumulation of 1200 m of sediments (Fig. 14). During the same period, the subsidence was 33% less active in the southeastern part with the deposition of around 800 m of sediments. During the Quaternary, the evolution continued with the superposition of the Miocene and Quaternary depocentres (Houtgast and Van Balen, 2000). Assuming that the development of the depocentre is linked to a larger amount of extension in the northwestern part than in the southeastern half, the deformation accommodated by border faults should be more important in the north-west than in the south-east. The difference between the displacement rates determined for the northwestern and southeastern parts is around 35% (184 mm/ky in the north-west and 120 mm/ky in the south-east). The nearly similar values for the difference of the subsidence and for the displacement rate difference suggest that the subsidence in the RVRS is mainly fault-controlled. The same conclusion was made by Houtgast and Van Balen (2000) based on analyses of the bore-hole record in the RVRS. Thus, the different displacement rates determined for each studied area can be explained by the contribution of the large scale-geometry and a differential extension between the northwestern and southeastern parts of the RVRS.
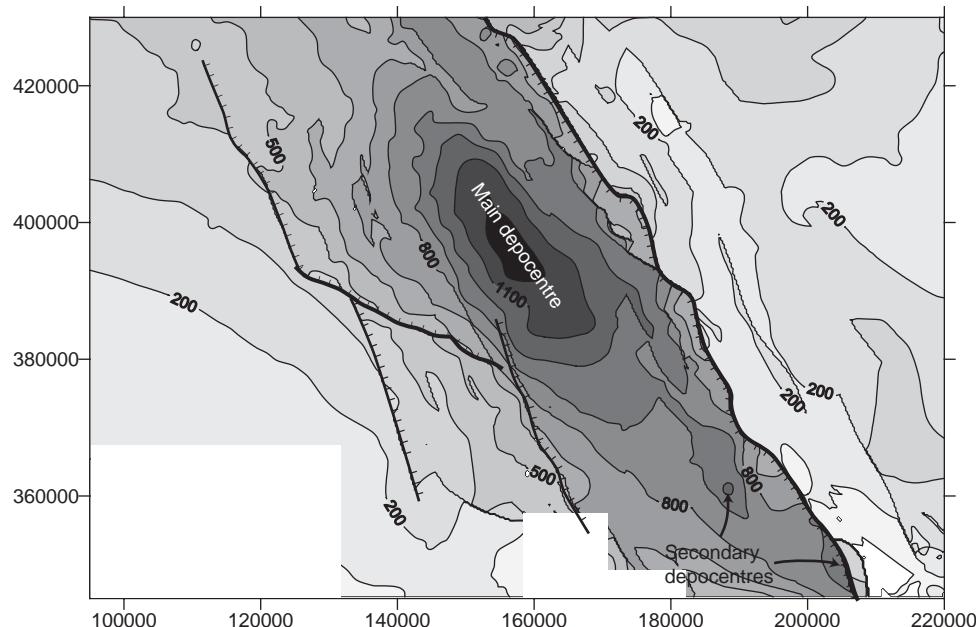

Fig. 14. Thickness map of the Neogene sedimentation showing the location of the main depocentre. The numbers indicate the thickness of Neogene sediments. Only the border faults are represented.

6. Conclusion

The active faulting of the RVRS was studied with a high precision DEM. We show that the use of such a DEM is essential to determine and quantify the neotectonics of the province. The geometry of the active faults, which is compatible with strike-slip motion, results from the interaction between the present-day stress field and the Paleozoic and Mesozoic structural inheritance. The vertical displacement, which affects the Quaternary geological formation along the FFZ and the PBFZ reveals that the border faults of the RVRS are characterized by a pure normal faulting mode without significant lateral motion. In consequence, we claim that the present-day stress field is responsible for a NE–SW extension (perpendicular to the graben). This direction of extension is similar to the one obtained from the analysis of the earthquake focal mechanisms (Plenefisch and Bonjer, 1997). In the graben, the superimposition of the Miocene and Quaternary depocentres suggests that this stress field was constant since the beginning of the Miocene. At a regional scale, the RVRS Miocene to present-day stress field could be explained by the left-lateral motion of the upper Rhine graben induced by a general NW main compression direction associated with the collision between the African and Eurasian plates (Fig. 16 in Michon et al., 2003).

The displacement rate values determined along the FFZ and the PBFZ show that the northwestern part of the RVRS is significantly more active than the southeastern part. The difference may result from the combination of a differential amount of extension between the northwestern and southeastern parts and a different large-scale geometry of the graben in the North-West (half-graben) and the South-East (full-graben).

Acknowledgements

References

Bisschops, J.H., 1973. Toelichtingen bij de geologische kaart van Nederland 1:50.000, blad Eindhoven Oost (51O). Rijks Geologische Dienst, Haarlem.

Camelbeeck, T., Meghraoui, M., 1998. Geological and geophysical evidence for large scale palaeo-earthquakes with surface faulting in the Roer Graben (northwest Europe). Geophysical Journal International 132, 347–362.

Cohen, K., Gouw, M.J.P., Holten, J.P., 2003. Fluvio-deltaic flood-basin deposits recording differential subsidence within a coastal prism (central Rhine-Meuse delta, the Netherlands). In: Blum, M. et al. (Eds.), Fluvial Sedimentology VII, Special Publication 35. International Association of Sedimentologists, Blackwell, pp. xx–xx.

Davy, Ph., Cobbold, P., 1991. Experiments on shortening of 4-layer continental lithosphere. Tectonophysics 228, 255–274.

Felder, W.M., Bosch, P.W., Bisschops, J.H., 1989. Geologische kaart van Zuid-Limburg en omgeving, schaal 1:50.000. Afzettingen van de Maas. Rijks Geologische Dienst, Haarlem.

Geluk, M.C., Duin, E.J., Dusar, M., Rijkers, R.H., van Denberg, M.W., van Rooijen, P., 1994. Stratigraphy and tectonics of the Roer Valley Graben. Geologie en Mijnbouw 73, 129–141.

Houtgast, R.F., Van Balen, R.T., 2000. Neotectonics of the Roer Valley Rift System, the Netherlands. Global Planetary Change 27, 131–146.

Houtgast, R.F., Van Balen, R.T., Bouwer, L.M., Brand, G.B.M., Brijker, J.M., 2002. Late Quaternary activity of the Feldbiss Fault Zone, Roer Valley Rift System, the Netherlands, based on displaced fluvial terrace fragments. Tectonophysics 352, 295–315.

Houtgast, R.F., Van Balen, R.T., Kasse, C., Vandenberghe, J., 2003. Late Quaternary tectonic evolution and aseismic near surface fault displacements along the Geleen Fault (Feldbiss Fault Zone—Roer Valley Rift System, the Netherlands), based on trenching. Netherlands Journal of Geosciences/Geologie en Mijnbouw 82, xx–xx.

Huisink, M., 2000. Changing river styles in response to Weichselian climate changes in the eastern Netherlands. Sedimentary and Geology 133, 115–134.

Huxtable, J., Aitken, J., 1985. Thermolimunescence dating results for the Palaeolithic site Maastricht-Belvédère—Meded. Rijks Geologische Dienst 39, 41–44.

Kasse, C., 1997. Cold-climate aeolian sand-sheet formation in North-Western Europe (c. 14–12.4 Ka); a response to permafrost degradation and increased aridity. Permafrost and Periglacial Processes 8, 295–311.

Kasse, C., 1999. Late Pleniglacial and Late Glacial aeolian phases in The Netherlands. In: Schirmer, W. (Ed.), Dunes and fossil soils; GeoArchaeoRhein 3, 61–82.

Kooi, H., Cloetingh, S., Remmelts, G., 1991. Lithospheric dynamics and the rapid Pliocene-Quaternary subsidence phase in the Southern North Sea Basin. Tectonophysics 192, 245–259.

Michon, L., Van Balen, R.T., Merle, O., Pagnier, H., 2003. The Cenozoic evolution of the Roer Valley Rift System integrated at a European scale. Tectonophysics 367, 101–126.

Műcher, H.J., 1986. Aspects of loess and loess-derived slope deposits: an experimental and micromorphological approach. Fysisch Geografisch en Bodemkundig Laboratorium, Universiteit van Amsterdam, pp. 267.

Paulissen, E., 1973. De morfologie en de Kwartairstratigrafie van de Maas vallei in Belgisch Limburg–Verh. Kon. Acad. Wetensch. Lett. en Schone Kunsten. Klassieke Wetenschappen 35 (127), 1–266.

Plenefish, T., Bonjer, K.P., 1997. The stress field in the Rhine Graben area inferred from earthquake focal mechanisms and estimation of frictional parameters. Tectonophysics 275, 71–97.

Rijks Geologische Dienst, 1983. Geomorfologische kaart van Nederland 1:50.000, blad 45. Rijks Geologische Dienst, Haarlem.

Rijkswaterstaat, 2000. Productspecificatie AHN 2000. Report of the Survey Department of the Ministry of Transport, Public Works and Water Management of the Netherlands.

Stouthamer, E., Berendsen, H.J.A., 2000. Factors controlling the Holocene alvulsion history of the Rhine-Meuse Delta (the Netherlands). Journal of Sedimentary Research 70, 1051–1064.

Thorne, J.A., Watts, A.B., 1989. Quantitative analysis of North Sea subsidence. AAPG Bulletin 73, 88–116.

Van Balen, R.T., Houtgast, R.F., Van der Wateren, F.M., Vandenberghe, J., Bogaart, P.W., 2000. Sediment budget and tectonic evolution of the Meuse catchment in the Ardennes and the Roer Valley Rift System. Global Planetary Change 27, 113–129.

Van den Berg, M.W., 1989. Geomorfologische kaart van Nederland 1:50.000 kaartblad 59 Genk, 60 Sittard, 61 Maastricht, 62 Heerlen, met toelichting en de kaart Maasterrassen en hellingklassen. Staring Centrum, Wageningen en Rijks Geologische Dienst, Haarlem. 32pp.

Van den Berg, M.W., 1994. Neotectonics of the Roer Valley rift system. Style and rate of crustal deformation inferred from syntectonic sedimentation. Geologie en Mijnbouw 73, 143–156.

Van den Berg, M.W., Groenewoud, W., Lorenz, G.K., Lubbers, P.J., Brus, D.J., Kroonenberg, S.B., 1994. Patterns and velocities of recent crustal movements in the Dutch part of the Roer Valley rift system. Geologie en Mijnbow 73, 157–168.

Van den Berg, M.W., Vanneste, K., Dost, B., Lokhorst, A., Van Eijk, M., Verbeeck, K., 2002. Paleoseismic investigations along the peel boundary fault: geological setting, site selection and trenching results. Netherlands Journal of Geosciences/Geologie en Mijnbouw 81, 39–60.

Van den Toorn, J.C., 1967. Toelichtingen bij de geologische kaart van Nederland 1:50.000, blad Venlo West (52W). Rijks Geologische Dienst, Haarlem.

Van Kolfschoten, T., Roebroeks, W., Vandenberghe, J., 1993. The Middle and Late Pleistocene sequence at Maastricht-Belvédère: the type locality of the Belvédère Interglacial. Mededelingen Rijks Geologische Dienst, N.S. 47, 81–91.

Verbraeck, A., 1990. De Rijn aan het einde van de laatste ijstijd: De vorming van de jongere afzettingen van de Formatie van Kreftenheye. Geografisch Tijdschrift Nieuwe Reeks 24, 328–340.

Winstanley, A.M., 1993. A review of the Triassic play in the Roer Valley Graben, SE onshore Netherlands. In: Parker J.R. (Eds.), Petroleum geology of Northwest Europe. Proceedings of the Fourth Conference. Geological Society of London, pp. 595–607.

Ziegler, P.A., 1988. Evolution of the Artic North Atlantic and the western Tethys. American Association Petroleum Geolology Mem. 43, 198pp.

Ziegler, P.A., 1990. Geological atlas of western and central Europe. 2nd ed. Shell Internationale Petroleum Mij., distributed by Geological Society of London, Publishing House, Bath, 238p, 56 encl.

Zijerveld, L., Stephenson, R., Cloetingh, S., Duin, E., Van den Berg, M.W., 1992. Subsidence analysis and modelling of the Roer Valley Graben (SE Netherland). Tectonophysics 208, 159–171.

Zonneveld, J.I.S., 1974. The terraces of the Maas (and Rhine) downstream of Maastricht. In: L'évolution Quartenaire des Bassins Fluviaux de la Mer du Nord Meridionale, Centenaire de la Société Géologique de Belgique, Liège, pp. 133–157.

Zuidam, R.A., 1980. Het Meinweggebied en Roergebied. Een tektonisch en eolisch beïnvloed terrassenlandschap nabij Roermond (Midden Limburg). Geografisch Tijdschrift Nieuwe Reeks 14, 2, 120–133.

Annexe 5 :

Michon, L., R.T. van Balen, O. Merle, H. Pagnier (2003) The Cenozoic evolution of the Roer Valley rift system integrated at a European scale. *Tectonophysics,* 367, 101-126.

ELSEVIER

The Cenozoic evolution of the Roer Valley Rift System integrated at a European scale

Laurent Michon[a],*, Ronald T. Van Balen[b], Olivier Merle[c], Henk Pagnier[a]

[a] *Department of Geo-Energy, TNO-NITG, PO Box 80015, 3508 TA Utrecht, The Netherlands*
[b] *Department of Quaternary Geology, Vrije Universiteit Amsterdam, De Boelelaan 1085, 1081 HV Amsterdam, The Netherlands*
[c] *Laboratoire Magmas et Volcans, OPGC, Université Blaise Pascal, 5 rue Kessler, 63038 Clermont-Ferrand, France*

Abstract

The Roer Valley Rift System (RVRS) is located between the West European rift and the North Sea rift system. During the Cenozoic, the RVRS was characterized by several periods of subsidence and inversion, which are linked to the evolution of the adjacent rift systems. Combination of subsidence analysis and results from the analysis of thickness distributions and fault systems allows the determination of the Cenozoic evolution and quantification of the subsidence. During the Early Paleocene, the RVRS was inverted (Laramide phase). The backstripping method shows that the RVRS was subsequently mainly affected by two periods of subsidence, during the Late Paleocene and the Oligocene–Quaternary time intervals, separated by an inversion phase during the Late Eocene. During the Oligocene and Miocene periods, the thickness of the sediments and the distribution of the active faults reveal a radical rotation of the direction of extension by about 70–80° (counter clockwise). Integration of these results at a European scale indicates that the Late Paleocene subsidence was related to the evolution of the North Sea basins, whereas the Oligocene–Quaternary subsidence is connected to the West European rift evolution. The distribution of the inverted provinces also shows that the Early Paleocene inversion (Laramide phase) has affected the whole European crust, whereas the Late Eocene inversion was restricted to the southern North Sea basins and the Channel area. Finally, comparison of these deformations in the European crust with the evolution of the Alpine chain suggests that the formation of the Alps has controlled the evolution of the European crust since the beginning of the Cenozoic.
© 2003 Elsevier Science B.V. All rights reserved.

Keywords: Roer Valley Rift System; Western Europe; Rift; Cenozoic; Subsidence; Inversion

1. Introduction

North of the Upper Rhine Graben (URG), the Roer Valley Rift System (RVRS) corresponds to the northern segment of the European Cenozoic rift system described by Ziegler (1988) (Fig. 1a). The Cenozoic RVRS developed upon pre-existing basins of Carbon-

iferous (Campine foreland basin) and Mesozoic (rift) age. It is structurally closely related to the Mesozoic basin. During the Mesozoic, the area was characterized by several periods of subsidence and inversion, which have reactivated the Variscan structural trends (Ziegler, 1990; Zijerveld et al., 1992; Winstanley, 1993; Geluk et al., 1994). During the Cenozoic, the RVRS was affected by two periods of inversion named the Laramide phase (Earliest Tertiary) and the Pyrenean phase (Late Eocene–Early Oligocene)
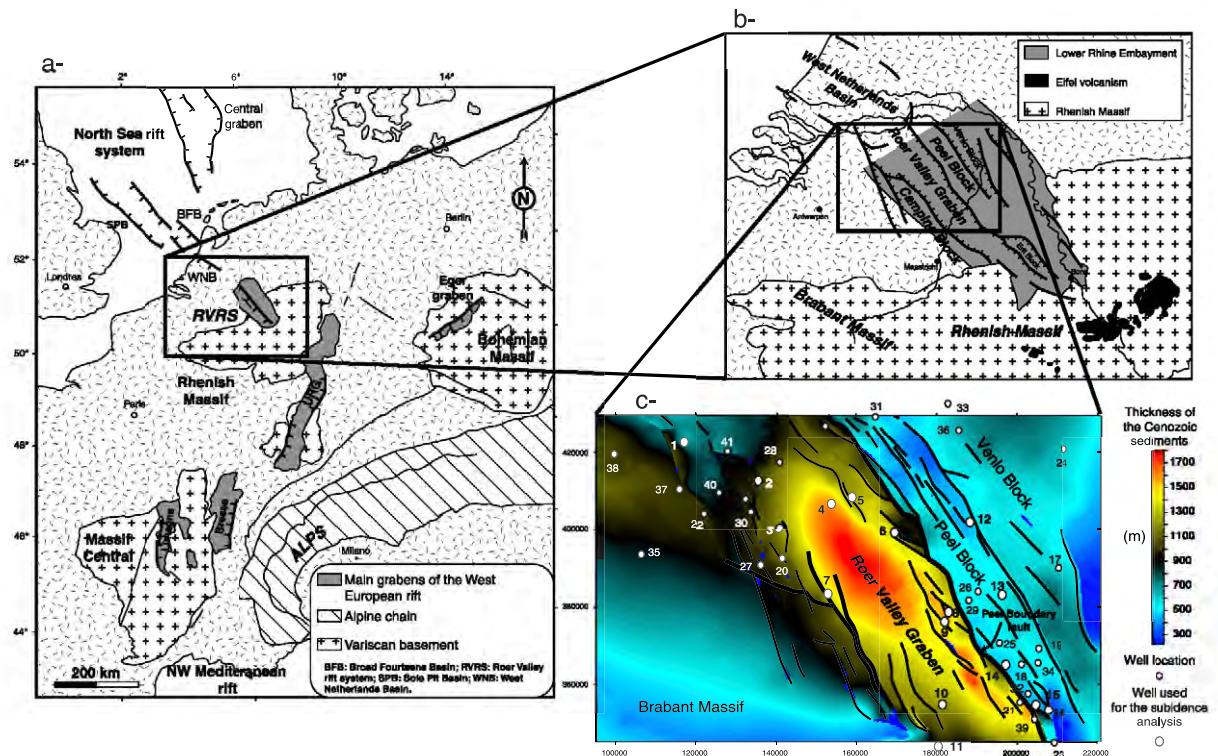
Fig. 1. (a) Location map of the Roer Valley rift system (RVRS) in northwestern Europe. (b) Tectonic features of the Lower Rhine Embayment and the RVRS. The insert corresponds to the studied area covered by the seismic interpretation. (c) Location map of the deep wells used for the subsidence analysis and the additional wells. The background image is a seismic interpretation of the thickness of the Tertiary sediments. See Appendix A for the name of the wells.

and by continuous subsidence since the beginning of the Oligocene (Geluk et al., 1994; Houtgast and Van Balen, 2000). Preserved Late Oligocene–Early Miocene marine sediments on the Rhenish Massif demonstrate that the Roer Valley Graben (RVG) was connected to the URG (Murawski et al., 1983; Sissingh, 1998), indicating a common evolution during at least this period. A close relationship between these two grabens is also suggested by the distribution of the earthquake focal mechanisms in the northern part of the URG and the RVG which indicate a present-day NE–SW extension in both areas (Plenefisch and Bonjer, 1997).

Structurally, the RVRS is part of the Lower Rhine Embayment and consists from southwest to northeast of the Campine Block, the RVG and the Peel Block (Fig. 1b). The graben, which is 20 km wide and 130 km long, has been controlled by the multi-stage activity of several major fault zones (Peel Boundary

fault zone, Veldhoven fault zone, Rijen fault zone and Feldbiss fault zone) of Mesozoic or (probably) older age. The different activity of these fault zones has induced the formation of a present-day asymmetric structure with the main offsets located along the Peel Boundary fault zone.

The aim of this paper is to determine precisely the Cenozoic evolution of the RVG and the paleo-stress fields that have caused the reactivation of this structure. This study is based (1) on subsidence analysis inferred from deep wells situated in the graben and on its shoulders and (2) on inspection of maps (depth of base Late Cretaceous, base Tertiary and base Miocene sedimentation) resulting from mainly 2D and 3D seismic interpretation. The combination of these two approaches allows the quantification of the tectonic subsidence and determination of fault activity during the different Cenozoic time periods. For each period of sedimentation (or erosion), the characteristics of

subsidence and the paleo-stress field can be deduced. Nevertheless, the density of seismic lines is not high enough to allow observation of small-scale tectonic structures (e.g., en echelon folds), which could provide additional information on the paleo-stress field. Comparison with the Cenozoic evolution of the surrounding rift systems (i.e., European Cenozoic rift system and the southern North Sea rift) allows to integrate the RVG evolution at a European scale. Our results are partly in agreement with the paleo-stress field orientations inferred from microtectonic data (e.g., Villemin and Bergerat, 1987). We discuss in a later section the potential origin of the differences found for the Late Eocene and Oligocene periods.

Subsidence analysis determines the tectonic subsidence apart from the total subsidence by applying the backstripping method (e.g., Van Hinte, 1978; Zijerveld et al., 1992). The other components of evolution are, for example, isostasy and compaction. The subsidence analysis is based on the analysis of 16 deep wells distributed in the graben and on its shoulders (Fig. 1c and Appendix A). Six of these wells have already been studied by Zijerveld et al. (1992). However, the large time frame studied in their work (250 Ma) does not provide detailed information concerning the Cenozoic evolution of the RVRS. In this paper, the tectonic subsidence of the Cenozoic time interval is studied in more detail and it is supplemented by the results for 10 additional wells, in order to determine the subsidence distribution and to assess the development of depocentres through time.

Although subsidence analysis provides fundamental information concerning the quantification of tectonic subsidence, the spatial distribution is poorly constrained. To close this gap of information, we have studied 25 additional deep wells for which the stratigraphic data are not detailed enough for backstripping analyses, but can still help to define the dynamics of each block and the tectonic activity for each period (Late Cretaceous–Early Paleocene, Late Paleocene, Early Oligocene, Late Oligocene and Miocene–Quaternary). Thus, altogether 41 wells are used to constrain the spatio-temporal distribution of the subsidence during the Cenozoic.

The Netherlands Institute of Applied Geoscience TNO-National Geological Survey has recently published the map sheets XIII and XIV of the Geological Atlas of the Subsurface of the Netherlands (NITG-TNO, 2001). These maps, which represent the depth and the thickness of several horizons, have been inferred from 2D and 3D seismic interpretation. For the Cenozoic period, maps corresponding to the "base Tertiary" (base Late Paleocene) and base Miocene (Breda Formation) horizons were created, allowing the thicknesses of the Paleogene and Neogene sediments to be determined. An additional map corresponding to the thickness of the Chalk deposits (Late Cretaceous–Early Paleocene) has been used in the present study in order to determine the deformation caused by the Laramide phase in the beginning of the Cenozoic.

2. Geological setting and fault system

The RVRS is the southwestern part of the Lower Rhine Embayment. Located in Belgium, Germany and the Netherlands, it consists of, from southwest to northeast, the Campine Block, the Roer Valley Graben and the Peel Block (the Campine and Peel Blocks corresponding to the RVG shoulders). The southeastern end of the RVRS is formed by the Erft Block, which is not in the prolongation of the RVG but shifted towards the northeast (Fig. 1b). In the northwest, the West Netherlands Basin is the continuation of the Mesozoic RVRS. The transition area between these two Mesozoic structures is characterized by a sedimentation and a fault pattern which has similarities with both grabens.

During the Mesozoic, the RVRS was affected by several periods of subsidence. Between the Late Permian and Early Triassic, the RVRS was characterized by thermal subsidence and minor fault activity as attested by a thick homogeneous sedimentation in the RVG, on the Peel Block and on the Campine Block (Zijerveld et al., 1992; Winstanley, 1993). Contrary to this period, the Late Jurassic–Early Cretaceous evolution corresponds to a major rifting event during which the RVG has strongly subsided, and the Peel and Campine Blocks were uplifted (Zijerveld et al., 1992; Geluk et al., 1994). Subsidence was controlled by the reactivation of the main Variscan faults in a normal faulting mode (the Peel Boundary fault zone, the Rijen fault zone and the Veldhoven fault zone). Most of the sediments deposited during this period have been later eroded during the first Late Creta-

ceous inversion event (Winstanley, 1993). A second phase of inversion, characterized by two pulses, occurred during the latest Late Cretaceous and the earliest Tertiary, contemporaneous with a general transgression. In the RVRS, the erosion or the lack of sedimentation of Chalk (Cenomanian–Danian) deposits renders the distinction between these two pulses of inversion impossible. The resulting sedimentation is characterized by a very thin sediment deposit in the RVG and an important subsidence of the Peel Block (Gras and Geluk, 1999).

At a regional scale, the RVRS is characterized by a NW–SE orientation which is regarded as parallel to the main Variscan inheritance (e.g., Ziegler, 1990; Geluk et al., 1994). This general trend can be specified by the analysis of detailed fault maps for the Triassic, Late

Cretaceous and Miocene periods which provide essential information concerning (1) the role of the inheritance in the RVRS and (2) the distinction of two different structural domains. Fault distribution determined from the Triassic, Late Cretaceous and Miocene active faults reveals that most of the Triassic structures were reactivated during the Late Cretaceous and Miocene evolutions, whatever the type of deformation (inversion, thermal subsidence and rifting) (Fig. 2). Comparison of the rose diagrams of fault strikes inferred for different time periods shows only minor differences. Their similarity can be explained by reactivation of the inherited fault orientations, despite different stress fields responsible for the faulting activity.

The fault orientations also indicate the existence of two distinct structural domains separated by the cen-
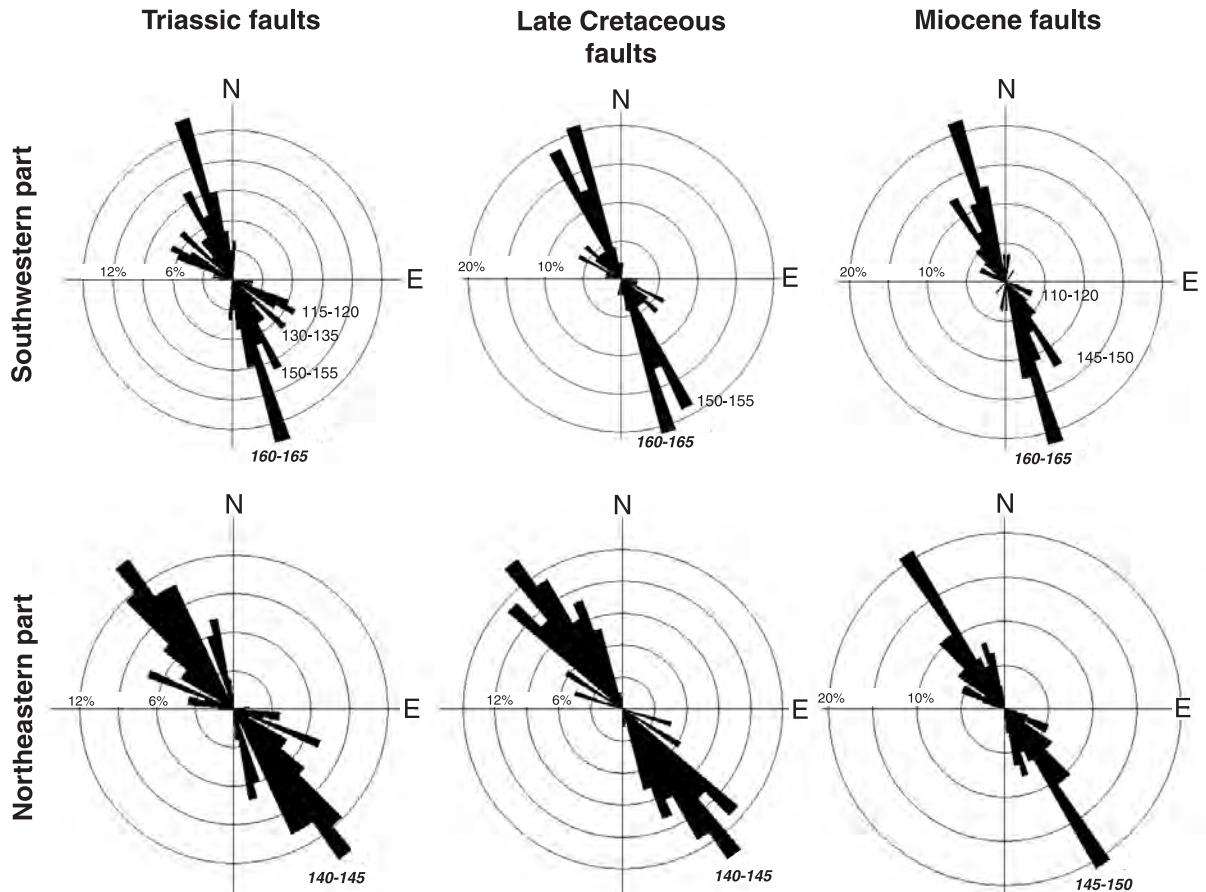

Fig. 2. Distribution of the active faults during the Triassic, Late Cretaceous and Miocene periods. The rose diagram representation is based on fault frequency and allows determination of the most important fault trends. See text for explanation.

tral axis of the RVG. The southwestern border is characterized by a main structural orientation of N160–165, whereas in the northeastern border (i.e., the Peel Boundary fault zone and the Peel Block) the N135–145 orientation widely prevails (Fig. 2). To the west, the West Netherlands Basin (Racero-Baena and Drake, 1996) is characterized by a similar fault orientation style as the southwestern part of the RVRS, and the Noord–Holland Platform has similar fault orientations as the northeastern part of the RVRS (Fig. 3). Thus, the boundary between these two fault orientation domains continues along the Zandvoort Ridge, the IJmuiden High and the Indefatigable Fault Zone into the Southern North Sea basin, and seems to represent a fundamental fault zone separating two crustal domains. At the RVRS scale, the development of the two different fault trends cannot be explained by different stress fields but rather by different structural orientations in the basement, which have been inherited from at least the Variscan evolution (the age of the original orientation being poorly constrained).

From this complex structural framework, the different stress fields related to the Cenozoic periods have induced the reactivation of specific fault orientations according to the direction of compression or extension. The analysis of the active faults and their displacement mode during each Cenozoic period then allows determination of the paleo-stress fields.

3. Subsidence analysis

Subsidence analysis requires specification of the thickness, the age, the lithology, the porosity/depth curve and the depositional water depth for each unit.
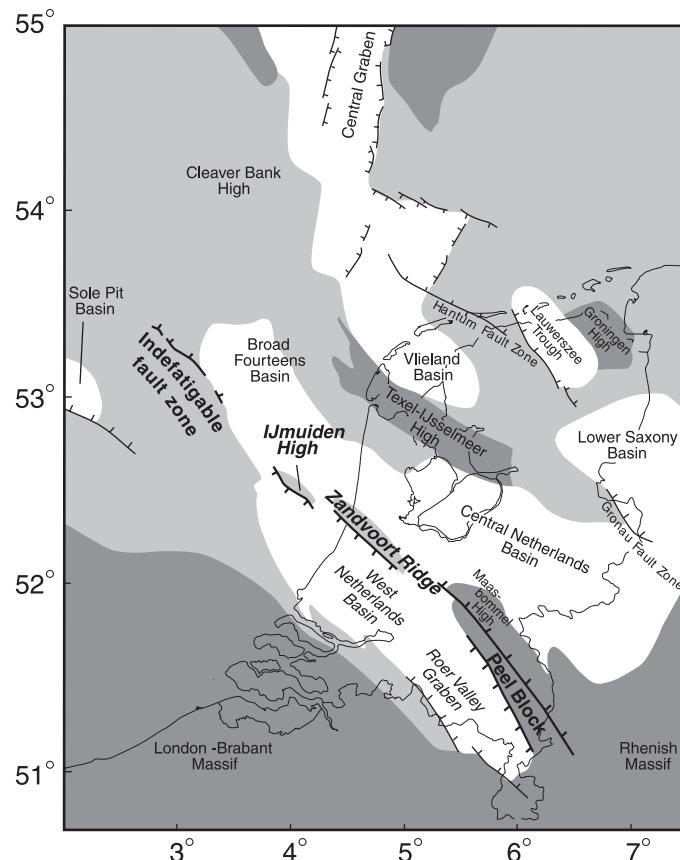

Fig. 3. Simplified structural map of the southern part of the North Sea rift system (after Van Balen et al., 2002).

In the RVRS, the stratigraphy has been derived from the Stratigraphic Nomenclature of the Netherlands (Nederlandse Aardolie Maatschappij BV and Rijks Geologische Dienst, 1980). We have used standard exponential curves for the porosity–depth relationship corrections taking into account the different lithologies for each wells (e.g., Sclater and Christie, 1980). Paleobathymetry may have a strong influence on the backstripping results. Nevertheless, the RVRS was located on the peripheral margin of the North Sea basin and the paleogeographic interpretations suggest that paleobathymetry never exceeded 50–100 m (Zagwijn, 1989). Geohistory evolutions determined for different paleobathymetric values reveal that pale-

obathymetric variations do not significantly influence the calculated tectonic subsidence (<10%). The subsidence analysis thus allows quantification of the tectonic subsidence and the tectonic subsidence rates (TSR) for each period of sedimentation.

Subsidence analysis has been carried out for 16 wells located in the Roer Valley Graben and the Peel Block (Fig. 1c). Calculated tectonic subsidence curves show a Cenozoic evolution marked by two periods of subsidence (Late Paleocene and Oligocene–Quaternary) separated by a hiatus during the Eocene time, resulting from a period of erosion during the Late Eocene (Fig. 4). This Late Eocene event was characterized by an uplift which cannot be quantified with
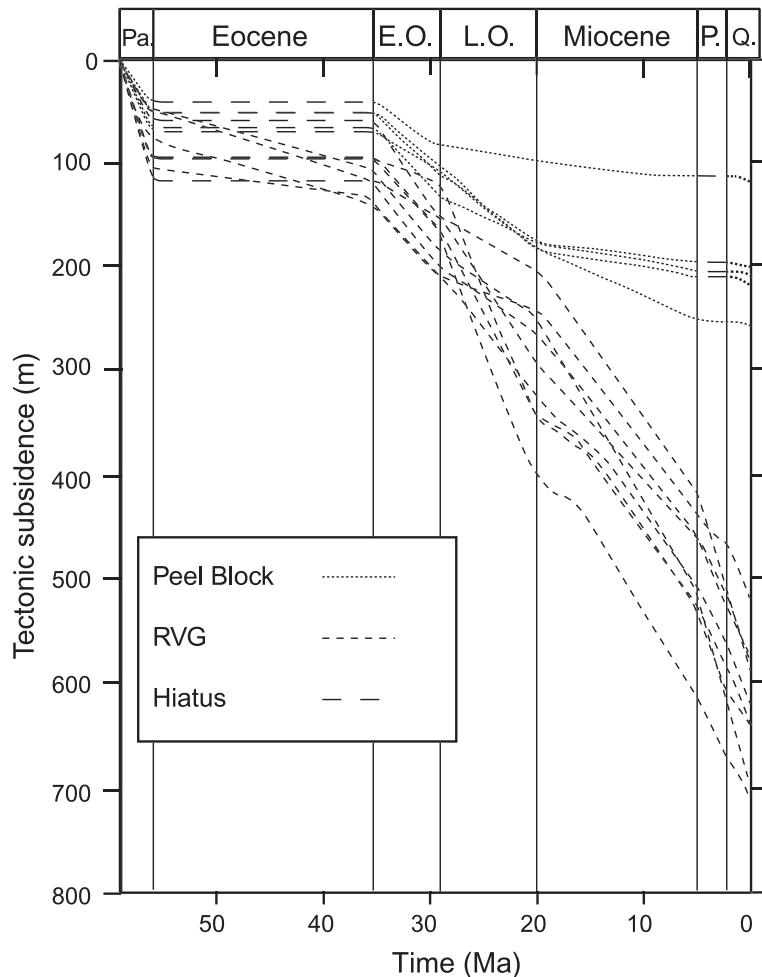

Fig. 4. Calculated tectonic subsidence for wells located in the Roer Valley Graben and the Peel Block. The Late Paleocene and Oligocene–Quaternary periods of subsidence are separated by an inversion phase, which is related to the Pyrenean phase during the Late Eocene.

the available data. Models from apatite-fission track analyses indicate that the uplift in the western part of the RVRS varies between 200 and 600 m. (Van Balen et al., 2002). A second minor hiatus is visible for four wells located on the Peel Block during the start of the Pliocene. Although this hiatus could be interpreted in terms of tectonic inversion (uplift and erosion), it can be considered as the result of a lack of sedimentation related to the Late Miocene marine regression.

The first phase of subsidence (Late Paleocene) was characterized by the widespread sedimentation of the Landen Formation in the RVG and on the Peel Block (see below). For this period, tectonic subsidence rates indicate a different evolution between the southeastern part of the RVG, and the Peel Block and the northwestern part of the RVG. From southeast to northwest, the tectonic subsidence rates in the RVG decrease from 38–47 to 20–22 mm/ky. This feature could suggest a tectonic activity mainly concentrated in the southeastern part of the graben. However, it has been shown that the West Netherlands Basin, which corresponds to the northwest continuation of the RVG, was strongly inverted during the early Tertiary phase creating an important relief (Van Balen et al., 2000). The persistence of this relief during the first stage of the Late Paleocene evolution may explain the weak thickness of the Landen formation in the northwestern part of the RVG. In that case, the TSR low

values in the northwestern part likely represent an underestimation of the real tectonic subsidence. In contrast, the difference between the tectonic subsidence rates inferred from the wells located on the southeastern part of the Peel Block (21–25 mm/ky) and those located in the graben (38–47 mm/ky) clearly suggests a tectonic activity with a fault-controlled tectonic subsidence mainly restricted to the graben.

The second period of subsidence began in the Early Oligocene and is still active during the Quaternary. After the Late Eocene inversion, the RVG and the Peel Block started to subside with similar tectonic subsidence rates (18–19 mm/ky), inducing the deposition of the Rupel formation. This common evolution stopped at the beginning of the Late Oligocene, when the tectonic subsidence decreased in the northwestern part of the RVG and the Peel Block (TSR around 10 mm/ky), whereas it strongly accelerated in the southeastern part of the graben (TSR between 20 and 34 mm/ky). The Late Oligocene period was then characterized by a concentration of the deformation mainly located in the northeastern side of the southeastern part of the RVG, where the maximum TSR values are recorded. After the regressive phase at the Oligocene–Miocene transition, the evolution of the northwestern and the southeastern parts became similar with a constant TSR around 19 mm/ky. This Miocene
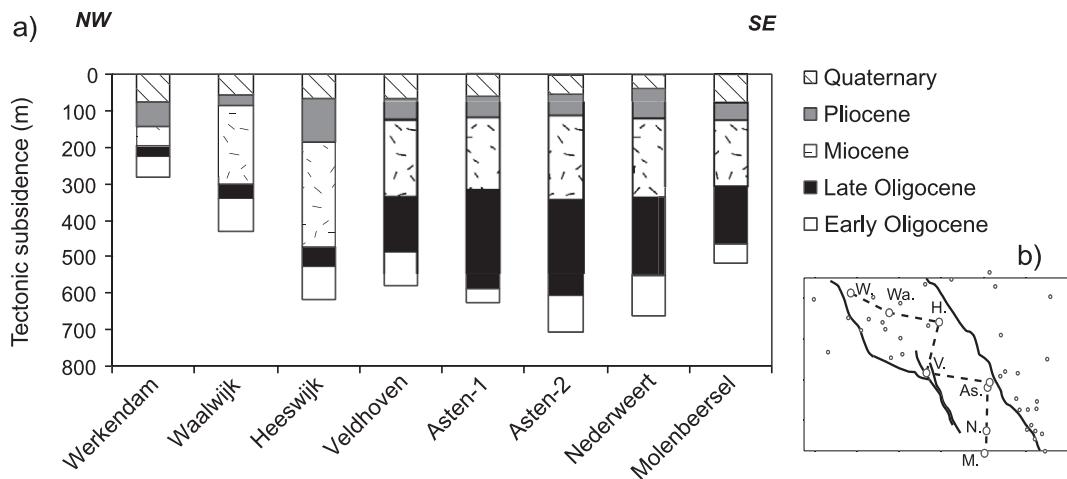
Fig. 5. (a) NW–SE cross section established from eight wells located into the RVG. The development of the Late Oligocene and the Miocene–Quaternary depocentres is suggested by the amount of tectonic subsidence along the cross section. (b) Location of the wells used for the cross section. As.: Asten-1 and Asten-2; H.: Heeswijk; M.: Molenbeersel; N.: Nederweert; V.: Veldhoven; Wa.: Waalwijk; W.: Werkendam.

subsidence was also characterized by the development of a large depocentre in the northwestern part, indicating a northwestward migration of the depocentre between the Late Oligocene and the Miocene (Fig. 5). On the Peel Block, the tectonic subsidence decreases drastically (TSR < 5 mm/ky) suggesting a change in the general evolution of the RVRS with a subsidence restricted to the graben. As it has been already observed (Zijerveld et al., 1992), tectonic subsidence curves reveal an increase of the TSR in the RVG (+40%) at the Miocene–Pliocene transition. Thus, since the Pliocene, the subsidence led to the deposition of a 300–400 m thick Plio-Quaternary sedimentation outside the depocentre and more than 500 m of sediments within the depocentre.

During the Quaternary, the subsidence rate has rapidly changed (Houtgast and Van Balen, 2000) and the subsidence rates determined for this period are between three and four times higher than the TSR deduced for the Plio-Quaternary evolution. One explanation could be that the TSR inferred for geological times (i.e., several m.y.) correspond to an average of the real tectonic subsidence which is probably characterized by short periods of strong subsidence and periods of quiescence. An alternative explanation could be found in the comparison of the amount of tectonic and total subsidence during a rifting event. Assuming that the accommodation space related to the extension was continuously filled by sediments in the RVRS, the comparison of the tectonic subsidence and the thickness of the sediments (i.e., total subsidence) inferred for the northwestern and southeastern parts of the RVG shows a time-dependent increasing difference between the tectonic

and total subsidence (Fig. 6). The resulting total subsidence rates deduced for the Quaternary are between three and four times higher than the TSR. In consequence, the rapid subsidence of the RVG (88 mm/ky) determined by Houtgast and Van Balen (2000) could be explained by 25% of tectonic subsidence and 75% of compaction and isostatic process. For example, delayed compaction of Miocene clays due to slow dewatering could contribute to Quaternary subsidence (Houtgast and Van Balen, 2000). The general trend of tectonic subsidence during Quaternary is characterized by a gradual decrease and a sudden increase during the last 250 ky.

4. Plan view tectonic evolution

In this section, we combine information provided by the thickness maps for the Late Cretaceous–Early Paleocene, Paleogene and Neogene periods, with the thickness of the sediments observed in 41 wells at different periods (Late Cretaceous–Early Paleocene, Late Paleocene, Eocene, Early Oligocene, Late Oligocene and Miocene–Quaternary). This approach allows us to determine for each period the fault activity and to characterize the distribution of the vertical displacements (i.e., uplift or subsidence). Additional inspection of seismic lines crossing the main border faults reveals that the amount of shortening and extension never exceeded 1–2 km for each period.

For the Late Cretaceous–Early Paleocene period, it is generally assumed that the RVG was affected by compression related to the Late Cretaceous and early
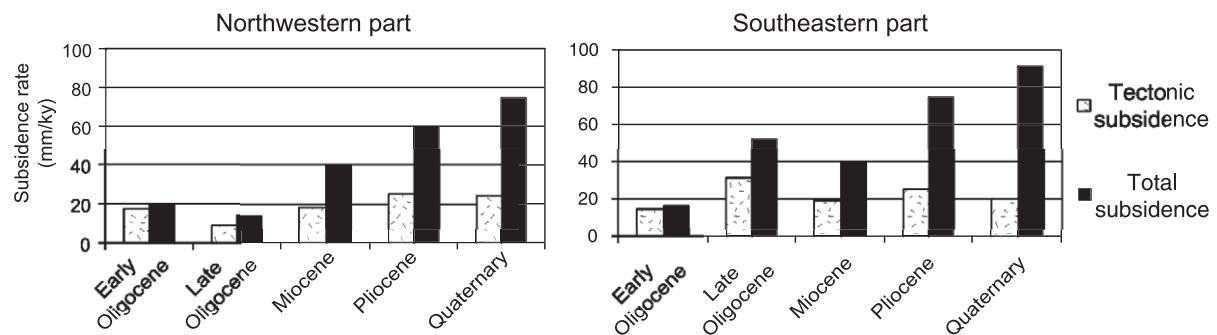

Fig. 6. Comparison of the total subsidence rate and tectonic subsidence rate for the northwestern and southeastern parts of the RVG. See text for explanation.

Tertiary phases which have induced graben inversion and reactivation of Mesozoic normal faults in a reverse faulting mode (e.g., Ziegler, 1988; Geluk et al., 1994). The distribution of the Late Cretaceous Chalk formation confirms this evolution and clearly shows contrasted thicknesses with a minor thickness of sediments in the RVG and a strong subsidence on its shoulders (Figs. 7a and 8). The uplift is restricted to the graben and has been controlled by the main border faults as it is shown by seismic (Fig. 8). It is noteworthy that these faults present two oblique orientations (WNW–ESE and NW–SE) that are hardly consistent with a compression perpendicular to the graben. Despite the lack of evidence for important strike slip displacement along the NW–SE trending faults, we interpret the Late Cretaceous–Early Paleocene final geometry as the result of a transpressional context with the greatest principal horizontal stress (σ_1) between NE–SW and N–S, comparable to the nearby West Netherlands Basin (Racero-Baena and Drake, 1996; Van Balen et al., 2000).

Subsidence analysis for the Late Paleocene period suggests (1) a global subsidence in the studied area (RVG, Peel Block and Venlo Block) (Fig. 7b) and (2) a small fault activity between the Peel Block and the RVG (i.e., the Peel Boundary fault zone). Quantification of the tectonic subsidence provides an estimate for minor vertical displacements along the Peel Boundary fault zone ranging between 50 and 70 m during this period. It is unlikely that the Late Paleocene subsidence of the Lower Rhine Embayment has resulted from a rifting event generated by far field stresses, because during a rifting process subsidence is generally controlled by a substantial fault activity and is restricted to a graben area. In contrast, it has been proposed that the elastic response of the lithosphere after a period of compression is able to induce subsidence of the inverted area (de Lugt et al., 2003). Then, the slight subsidence (< 100 m) developed after a main compressive phase might result from a stress relaxation and a lithospheric sagging.

Most of the information concerning the Eocene evolution has been partially destroyed by a strong erosion event during the Late Eocene. This erosion phase is related to the uplift of the whole area during the Pyrenean phase (Ziegler, 1988; Geluk et al., 1994). Well data indicate a progressive decrease of the thickness of the Dongen formation (Eocene) towards the east (Fig. 7c). This thinning could result from (1) a less active subsidence in the eastern part of the RVRS and/or (2) a doming of the central part of the Lower Rhine Embayment (i.e., eastern part of the RVRS).

The Early Oligocene marked the onset of the rifting phase in the RVRS. The thickness of the sediments combined with subsidence analysis indicates that the Early Oligocene was affected by a general subsidence with a maximum of vertical displacement in the central part of the Lower Rhine Embayment (Fig. 7d). Similar sediment thicknesses on the Peel Block and the RVG suggest a minor or no fault activity of the Peel Boundary fault zone during this period. In consequence, the origin of Lower Rhine Embayment subsidence is uncertain. Similarly to the Late Paleocene evolution, the Early Oligocene subsidence could result form the elastic response of the lithosphere after the Late Eocene doming. An alternative and additional explanation could be that a slight extension phase has affected the Lower Rhine Embayment during this period.

During the Late Oligocene period, the tectonic subsidence increased in the southeastern part of the RVG with the development of narrow depocentres close to the Peel Boundary fault zone, whereas it decreased in the northwestern half of the RVG and the Peel Block. Well data reveal that the Peel Boundary fault zone was active in its southeastern part only, with vertical offsets ranging between 250 and 300 m. Secondary fault activity along the Peel Boundary fault zone antithetic faults has also controlled the development of the depocentres (Fig. 7e). Such an evolution demonstrates a concentration of the deformation with a significant fault activity bounding the graben. The fault orientation, with a maximum trend around N140–145 and a secondary trend at N130, suggests again that the inherited structure were reactivated

---

Fig. 7. Cenozoic evolution of the RVRS. (a) Early Paleocene inversion. (b) Late Paleocene subsidence. (c) Late Eocene doming. (d) Early Oligocene subsidence. (e) Late Oligocene concentrated subsidence due to WNW–ESE rifting. (f) Miocene–Quaternary rifting resulting from a NE–SW extension. For the Late Paleocene, Late Eocene, Early Oligocene and Late Oligocene periods, the background image corresponds to the thickness of the Paleogene sedimentation. The thickness information for each period is provided by the well data.

a) *Early Paleocene evolution*

b) Late Paleocene evolution

c) *Late Eocene evolution*
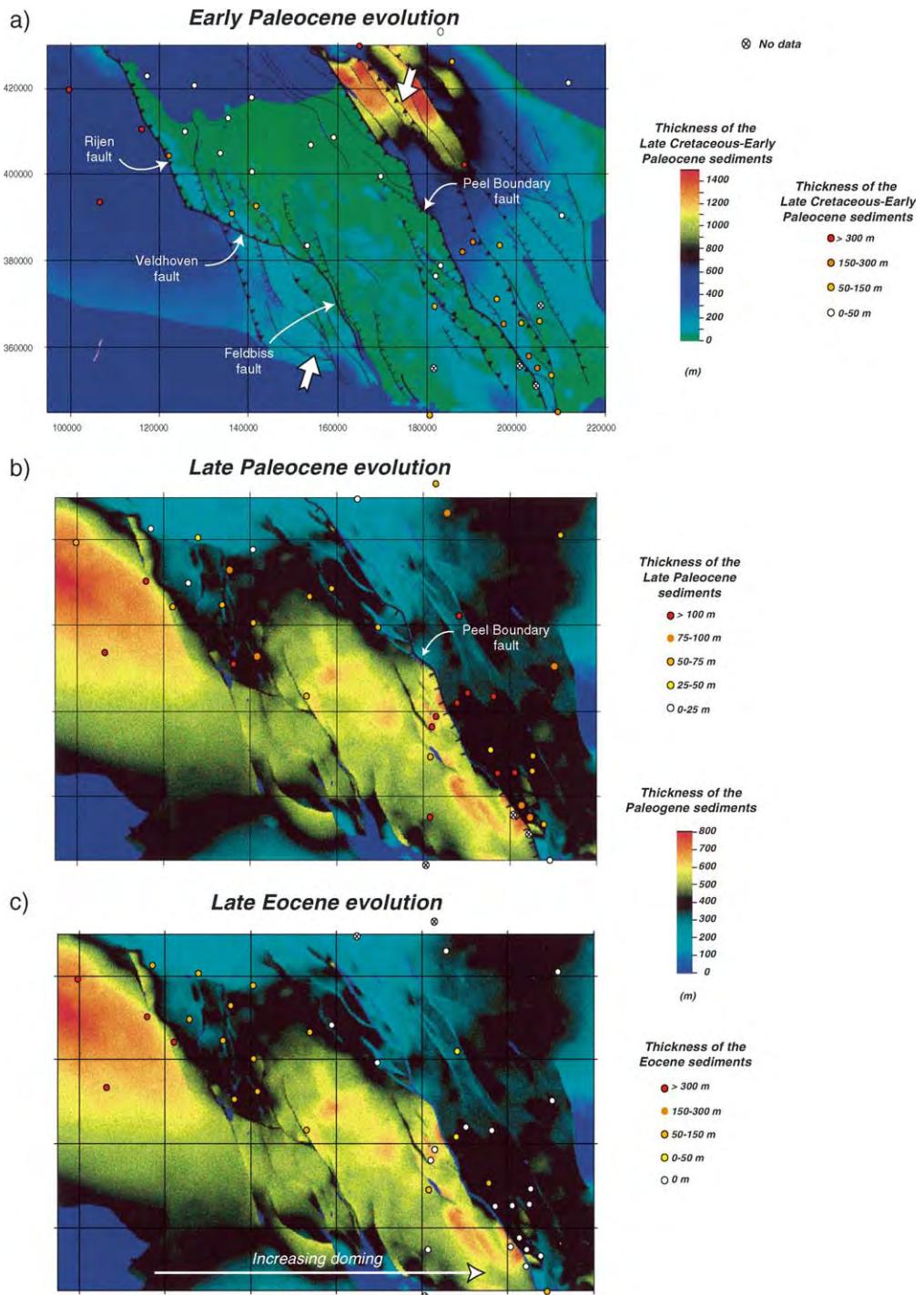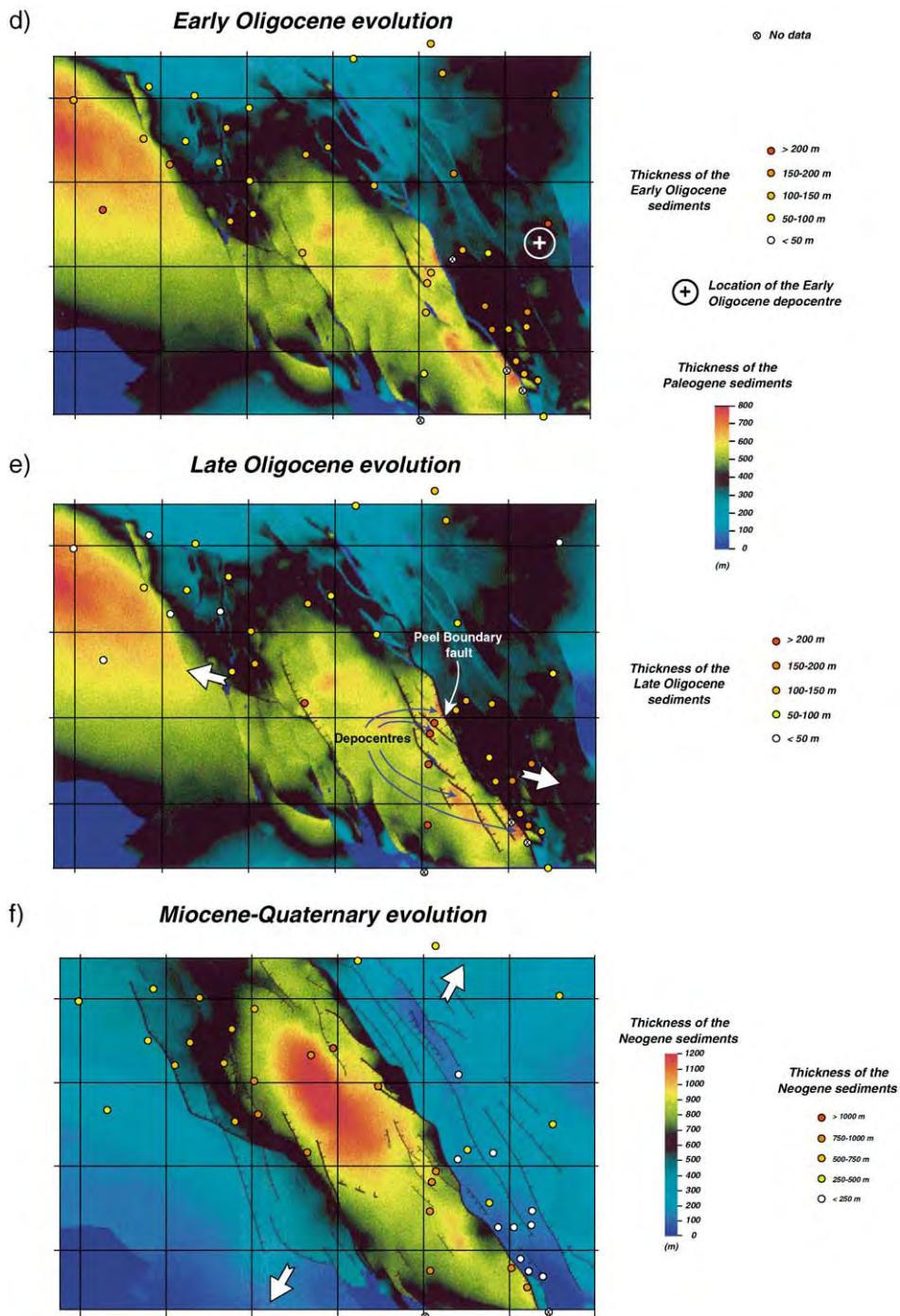
Fig. 7 (*continued*).

during this period. Because the geological inheritance is always reactivated during the evolution of the RVRS, the determination of the paleo-stress field is uncertain. Nevertheless, we interpret the narrow deformation as the result of a WNW–ESE oblique extension which has only affected the southeastern part of the graben.

After the regressive phase at the Oligocene–Miocene boundary and a short stop in the sedimentation during the Aquitanian (Verbeek et al., 2002), deformation was extended to the northwestern part of the RVG where a main depocentre developed (Fig. 7f). Seismic data show the development of onlap and downlap (Fig. 8b), which are interpreted in terms of
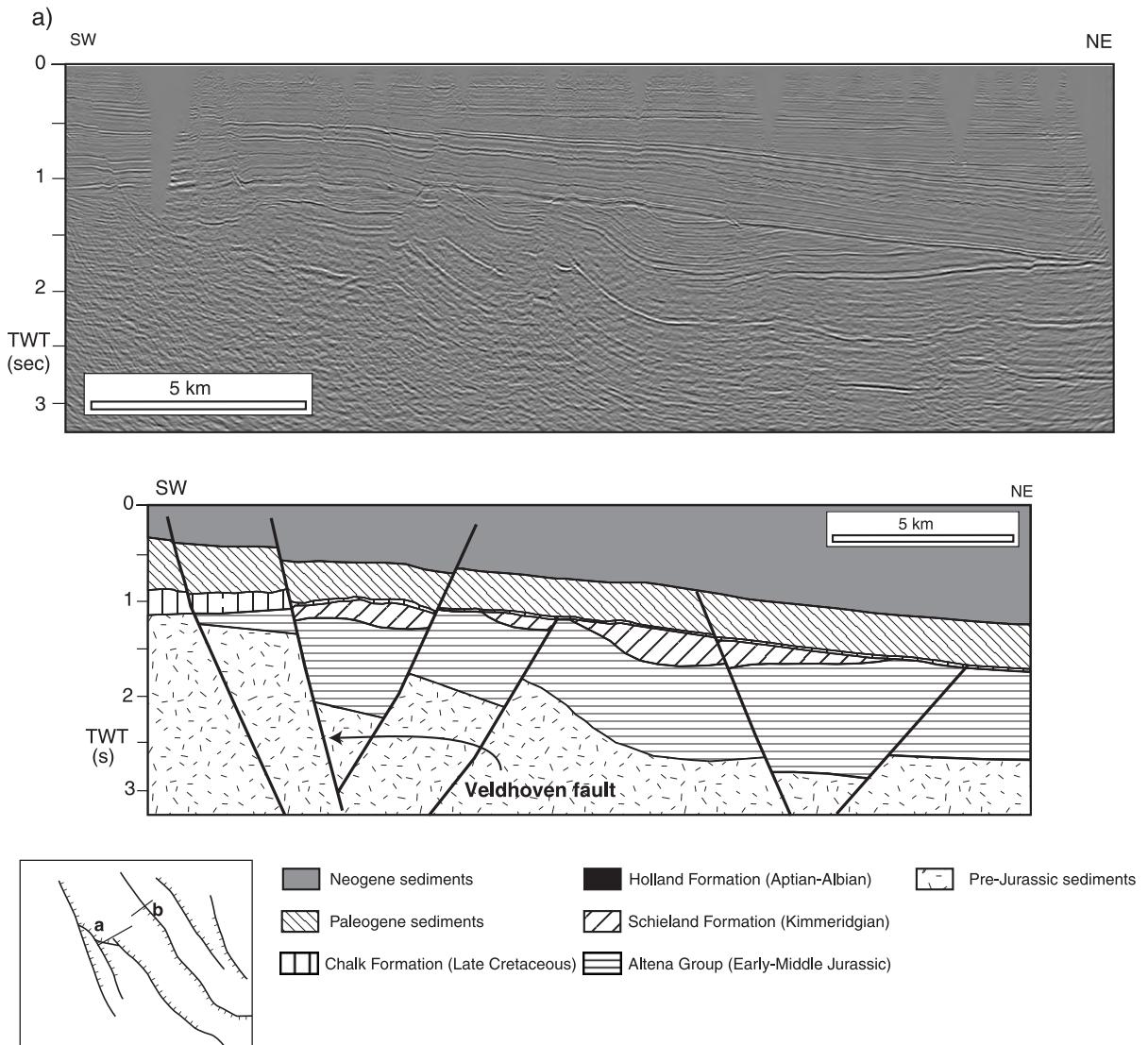

Fig. 8. Seismic lines and structural profiles perpendicular to the Peel Boundary (a) and the Veldhoven (b) faults. The contrasted thickness of the Late Cretaceous and Neogene sediments demonstrate that the graben border faults were active during each in reverse and normal faulting mode, respectively.

Seismic line #8117 provided by Clyde Petroleum

Peel Boundary fault
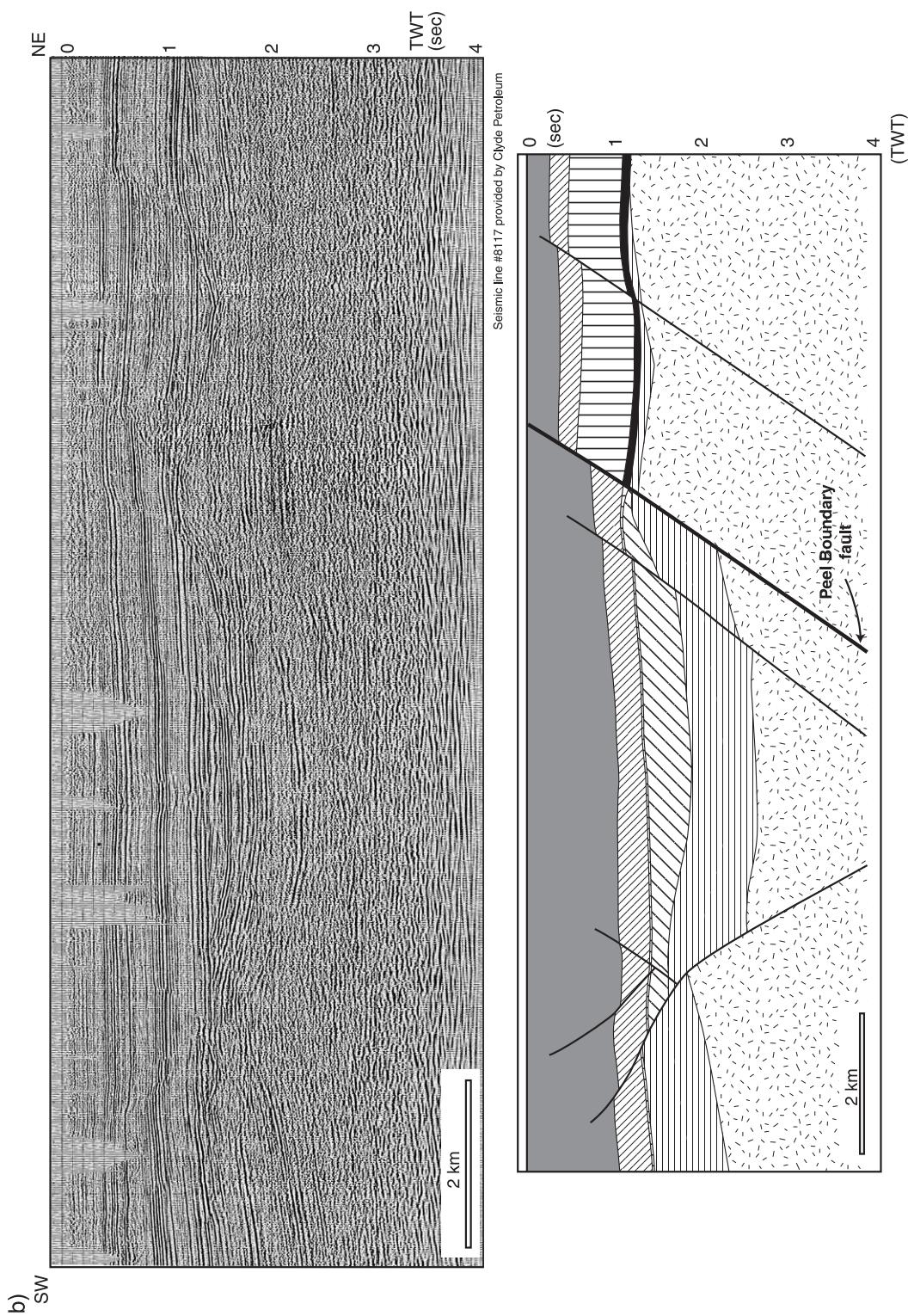
Fig. 8 (*continued*).

sea-level variations and an increase of the subsidence during the Burdigalian (Verbeek et al., 2002). A similar increase of the subsidence occurred contemporaneously in the northern part of the URG (Sissingh, 1998). Contrary to the Late Oligocene evolution, the oblique orientation was strongly reactivated especially along the Veldhoven fault zone. The resulting distribution is characterized by two main trends: the N145–160 trend corresponding to the general orientation of the graben, and the N110–120 oblique orientation. It is noteworthy that the offsets resulting from the N110–120 and N145–160 faults in the northwestern part of the Peel Boundary fault zone are similar. This indicates a direction of extension corresponding to the bissectrix of these two orientations (i.e., NE–SW). Extension has also induced the formation of two depocentres: a main depocentre in the northwestern part of the RVG and a minor one in the southeastern part. The western limit of the main depocentre is parallel to the N150 trend represented by the Feldbiss fault zone. In the south, the depocentre boundary is superimposed on the Jurassic Veldhoven fault zone. Seismic profiles which cross-cut this Mesozoic fault show that the southeastern prolongation of the Miocene Veldhoven fault zone controls the deformation, inducing a flexure of the Miocene sediments. To sum up, the Miocene subsidence of the RVG was controlled by two oblique orientations (N145–160 and N110–120). The orientation of the active faults and the development of the main depocentre at the intersection of two oblique main faults can be interpreted as the result of a NE–SW extension. In addition, the superimposition of the Miocene and Pleistocene depocentres (Houtgast and Van Balen, 2000) suggests a continuous extension with the same stress field. Analysis of the earthquake focal mechanism data also shows that the RVRS is affected by a present-day NE–SW extension related to a nearly vertical greatest principal stress (σ_1) (Plenefisch and Bonjer, 1997).

5. Discussion and conclusions

One aim of our study is to integrate the evolution of the RVRS at the European scale. Nevertheless, it is beyond the scope of this paper to describe in detail the evolution of the different provinces and grabens of the

North Sea and West European rift (WER), which have been extensively studied during the past decades (e.g., Ziegler, 1988, 1992a,b; Merle et al., 1998; Sissingh, 1998; Michon, 2001). The southern limit of the considered area corresponds to the southern part of the Massif Central. South of this province (southeastern France), the extension related to the formation the WER has only induced a very weak subsidence (Hippolyte et al., 1993), whereas the area was mainly affected by the strong extension generated by the rotation of the Corsica–Sardinia block since the Late Oligocene (e.g., Seranne, 1999). In the north, the studied area is limited to the southern part of the North Sea where the deformation was influenced by both the rifting stage linked to the Atlantic rifting and the compressive stress generated by the Europe–Africa collision (Ziegler, 1990). In our restricted area, we distinguish six successive periods during the Cenozoic evolution with analogy with the periods determined in the RVRS (only the distinction for the Eocene and Oligocene periods present minor differences).

5.1. Early Paleocene

The Early Paleocene evolution of the RVRS was characterized by graben inversion and the reactivation of the Mesozoic faults in a reverse faulting mode (Fig. 7a). The southern North Sea basins (the West Netherlands Basin, the Broad Fourteens Basin, the Sole Pit Basin and the southern part of the Central graben) were also affected by an inversion phase regarded as the result of a main N–S compression (Ziegler, 1992a; Oudmayer and De Jager, 1993; Brun and Nalpas, 1996; Van Balen et al., 2000; de Lugt et al., 2003). During this period, a Late Cretaceous–Paleocene late-rifting stage linked to the Faroe–Norwegian–Greenland Sea rift system induced extension in the northern and central North Sea (Ziegler, 1992a) (Fig. 9). South of the RVRS, evidences of doming and graben inversion (Meyer et al., 1983; Malkovsky, 1987; Le Griel, 1988; Lefort and Agarwal, 1996; Roure and Coletta, 1996; Peterek et al., 1997; Barbarand et al., 2002) suggest that the deformation was induced by a N–S compression, like in the southern North Sea. At the European scale, this compression is contemporaneous with the closure of the oceanic Piemont (Ziegler and Roure, 1996) and the Eo-Alpine
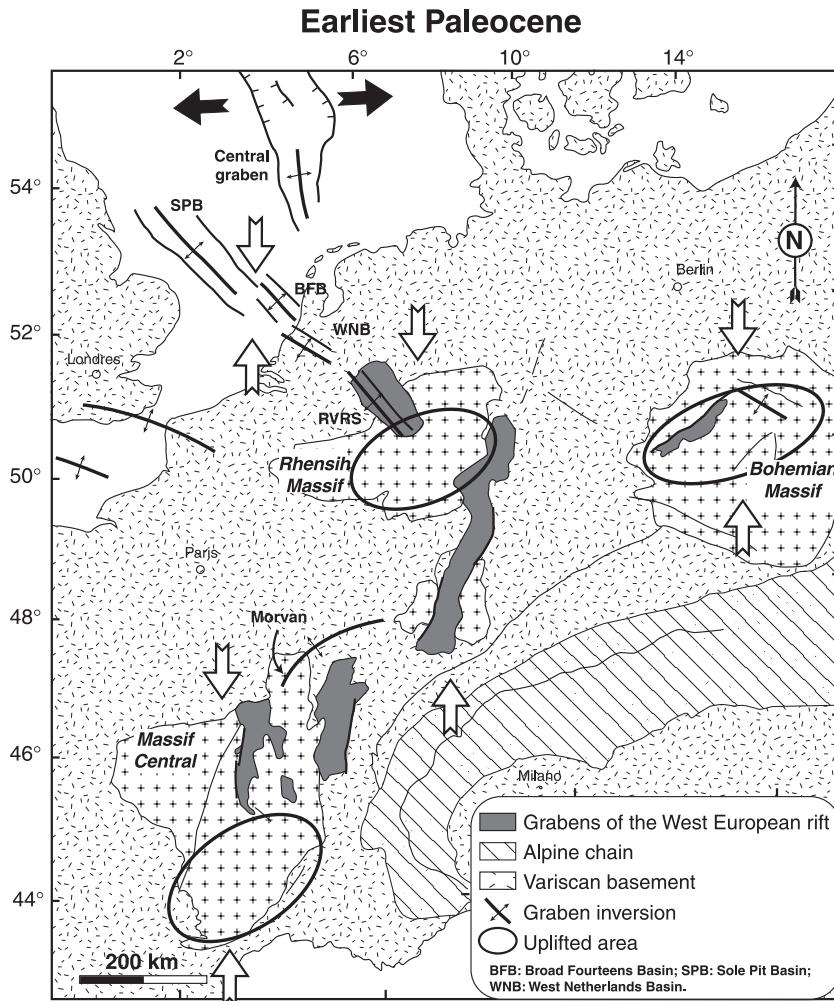
Fig. 9. Early Paleocene inversion associated to the N–S collision between Europe and Africa (Laramide phase). White arrows: direction of compression. Black arrows: direction of extension.

compressive phase (Michon and Merle, 2001). Consequently, the synchronicity of the beginning of the continental collision events and the inversion phases could suggest that during the first step of a continent–continent collision the stress is directly propagated in the adjacent plate.

5.2. Late Paleocene

For the Late Paleocene period, the lack of precise information, mainly due to the continental paleogeography of western Europe, renders a determination of

Late Paleocene deformation south to the RVRS difficult. In the RVRS, our study shows that this period was characterized by subsidence and minor fault activity (Fig. 7b). In the North Sea basins, this evolution is similar (Ziegler, 1992a; Oudmayer and De Jager, 1993; de Lugt et al., 2003) and it has been attributed to the continuous late-rifting process in the northern Atlantic (Ziegler, 1992a) or a lithospheric relaxation after the Early Paleocene inversion (de Lugt et al., 2003). During this period, the RVRS then corresponded to the southern end of the North Sea rift system (Fig. 10).
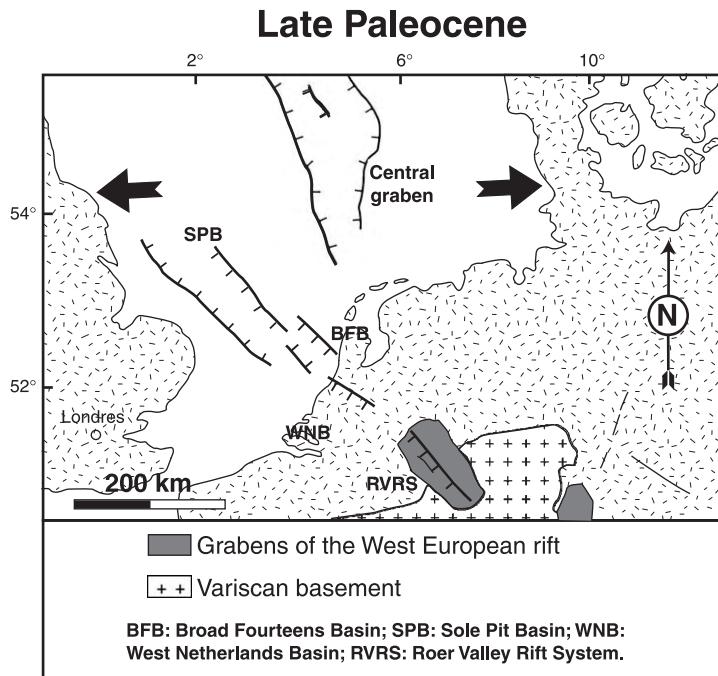
Late Paleocene

Fig. 10. Late Paleocene subsidence of the southern North Sea basins generated by lithosphere relaxation after the Laramide inversion (de Lugt et al., 2003) and/or by a late-rifting stage related to the rifting in North Atlantic between Greenland and the Fareoe Islands (Ziegler, 1992a,b).

5.3. Early Eocene

The Early Eocene sedimentation was probably partly eroded in the RVRS during the Late Eocene doming. In the southern North Sea, subsidence has induced an important sedimentation with minor fault activity (de Lugt et al., 2003), suggesting a thermal subsidence after the late-rifting stage or continued sagging due to stress relaxation, which ended at the end of the Paleocene (Ziegler, 1992a). In southwestern Europe, in the larger WER area, two sediment facies are attributed to the Early Eocene period: the Siderolithic formation and the Lutetian continental sedimentation (e.g., Rat, 1974; Sissingh, 1998). The Siderolithic formation, which results from the in-situ erosion of the outcropping rock has a widespread distribution from the Upper Rhine Graben area up to the Massif Central (Sissingh, 1998; Michon, 2001). The Lutetian continental sedimentation outcrops in the northern Upper Rhine Graben and the Massif Central or outside the grabens (Fig. 11). This spatial distribution suggests that the Lutetian sedimentation did not result from a period of subsidence linked to

the Late Eocene–Oligocene rifting phase but rather from the development of local lakes in a peneplain domain. To sum up, these data suggest that the Early Eocene period corresponds to a tectonically quiet period in the North Sea and the WER.

5.4. Late Eocene

Compared to the Early Eocene evolution, the Late Eocene period was characterized by intensive and opposite deformation in the southern North Sea and the WER. The southern North Sea basins were affected by a second phase of inversion, whereas this period corresponds to the onset of the rifting event in the WER (Fig. 12). In the southern North Sea and the Channel area, reactivation of the Meso-zoic and Cenozoic faults in a reverse faulting mode (Oudmayer and De Jager, 1993; Van Balen et al., 2000; de Lugt et al., 2003) has been interpreted as resulting from a nearly N–S compression related to the Pyrenees formation (Ziegler, 1990). In contrast, the Late Eocene sedimentation in the Massif Central graben (Merle et al., 1998), the central part of the
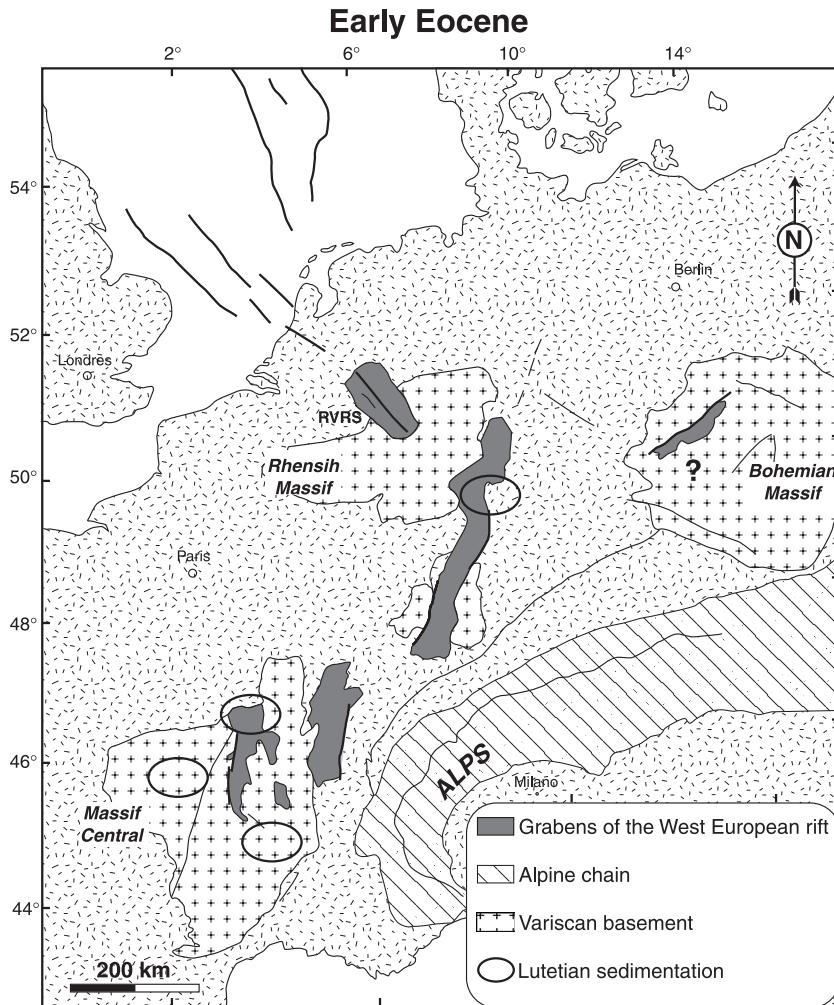
Early Eocene

Fig. 11. Early Eocene evolution characterized by a thermal subsidence in the southern North Sea and a continental sedimentation in the Alpine foreland. ? represents a lack of data concerning this period in the Bohemian Massif.

URG (Sissingh, 1998; Schumacher, 2002) and the Eger graben (Chlupac et al., 1984) proves that the WER was affected by extension during this period. Based only on microtectonic data obtained in the Variscan basement and the Triassic–Jurassic formations, Villemin and Bergerat (1987) proposed that this early period of extension resulted from a N–S compression. Nevertheless, in the main grabens of the WER, the fault orientation and the shape of the depocentres allow precise characterization of the paleo-stress field, which has caused the graben development. In the Limagne graben and the URG where

the subsidence was controlled by the reactivation of oblique Variscan faults (Michon, 2001; Schumacher, 2002), the location of the depocentres at the intersection of the main faults and their crescent shape suggest an E–W extension for the Limagne graben (i.e., the Massif Central rift) and an ESE–WNW/ SE–NW extension in the URG. These directions of extension are confirmed by recent analogue experiments, which show that (1) the shape of the depocentres is directly controlled by the stress-field and (2) crescent shape depocentres are only created with direction of extension corresponding to the bissectrix
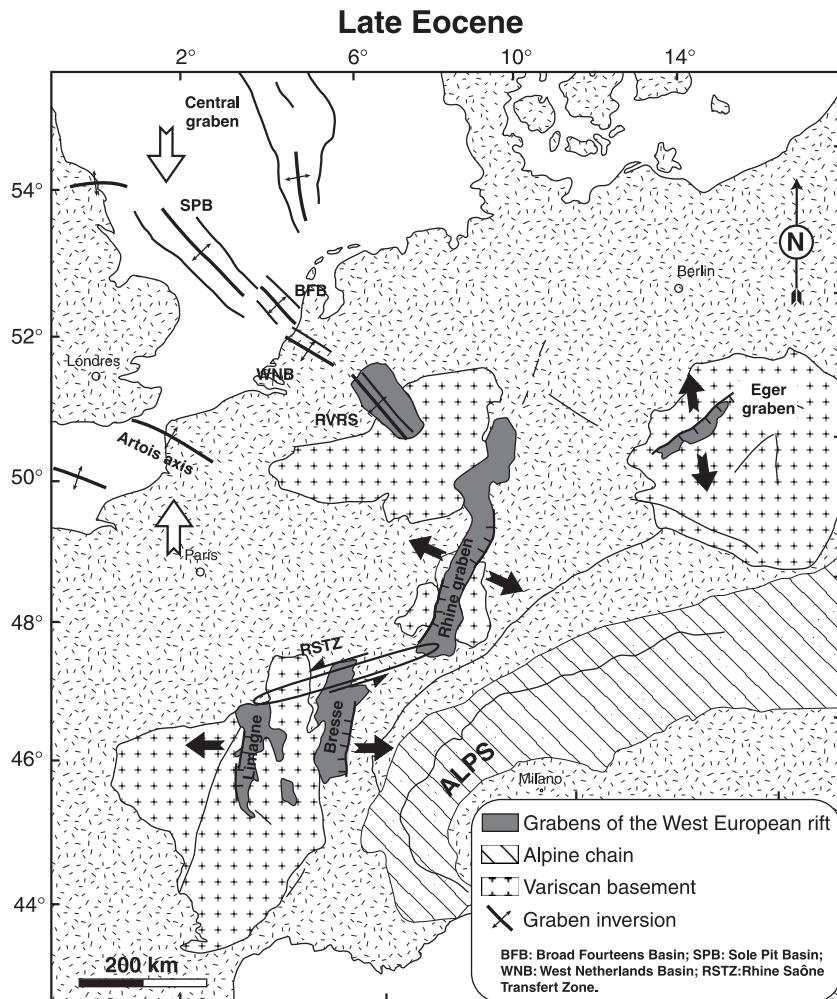
Late Eocene

Fig. 12. Late Eocene inversion phase in the southern North Sea basins and the Channel area (Pyrenean phase) related to the collision between Europe and Africa. This inversion is coeval with the onset of the rifting in the West European rift.

of the oblique faults (Michon and Sokoutis, in prep). As the age of the deformation is poorly constrained by the microtectonic approach, we propose that the N–S compression deduced by Villemin and Bergerat (1987) is more likely related to the Early Paleocene main compression than to the Late Eocene event, which has induced uplift and inversion in the southern North Sea basins and the Channel only.

In the Eger graben, Variscan faults were also reactivated (Malkovsky, 1987). The maximum thickness of the sediments along the main N60E fault (Malkovsky, 1987) suggests that this fault has controlled the subsidence by a normal faulting mode

resulting from a nearly N–S extension. Consequently, in the WER, the direction of extension inferred from strongly constrained data suggest a clockwise rotation of the direction of extension towards the east (Michon, 2001) (Fig. 12).

5.5. Oligocene

According to microtectonic studies (e.g., Villemin and Bergerat, 1987), the Oligocene is marked by changes in the stress field with a general E–W extension during the Rupelian and a NE–SW compression during the Chattian. However, the super-

position and the similar shape of the Late Eocene and Oligocene (Rupelian and Chattian) main depocentres in the Massif Central grabens and the central part of URG suggest a constant direction of extension during the Late Eocene and the Oligocene. At a European scale, the Oligocene evolution corresponds to a propagation of the extension related to the WER towards the north and a stop of the inversion phase in the southern North Sea basins (Fig. 13). North to the URG, the RVRS subsidence resumed in the Early Oligocene and accelerated in the Late Oligocene (Fig. 7d,e). In the northeastern part of the Paris Basin, the deformation linked to the extension was also recog-

nized and the average direction of extension was NW–SE (Coulon, 1992). In the southern North Sea, the Oligocene corresponds to a phase of subsidence due to thermal relaxation of the lithosphere and sedimentary load, without or with minor fault activity (Ziegler, 1990; Oudmayer and De Jager, 1993; de Lugt et al., 2003). Contrary to this quiescent evolution, the Channel area and the northern end of the Paris basin were affected by inversion especially during the Late Oligocene and the Early Miocene (Lake and Karner, 1987; Ziegler, 1990).

Two main mechanisms were proposed to explain the formation of the WER. The development of the
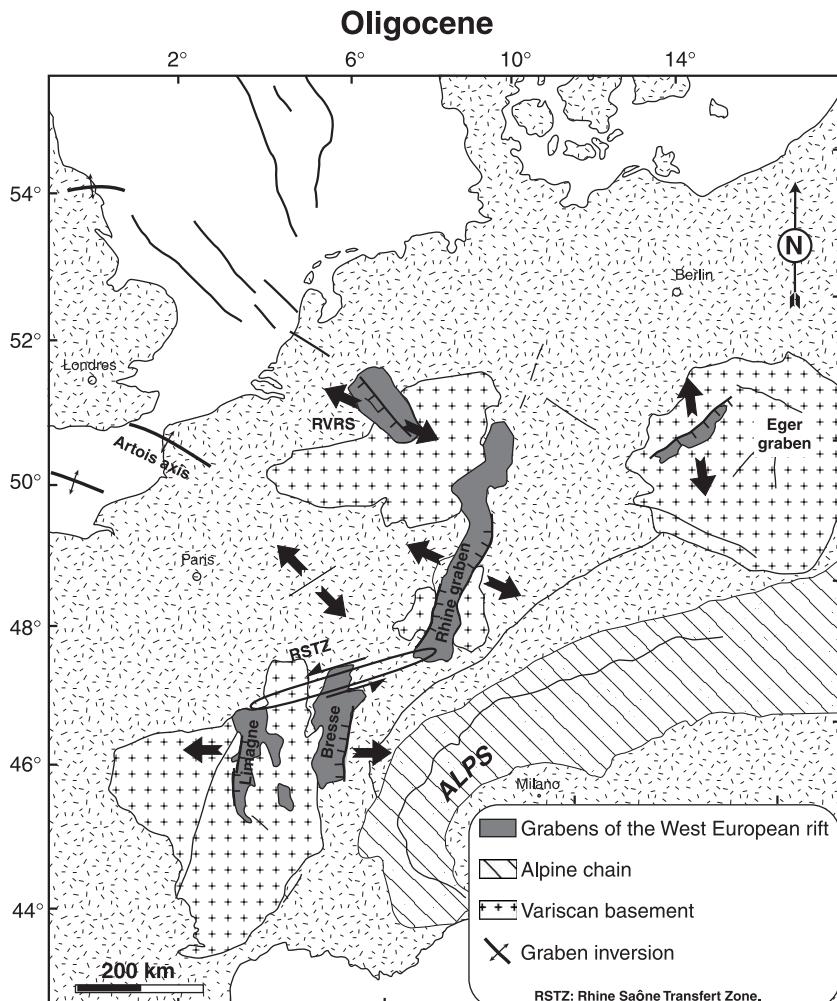

Fig. 13. Oligocene extension in the West European rift and thermal subsidence in the southern North Sea basins.

WER during the Late Eocene–Oligocene could result from the combined effect of the N–S Alpine compression and the opening of the northern Atlantic (e.g., Tapponnier, 1977). In the alternative model, the WER was induced by successive phases of compression and extension initiated by far field stresses (e.g., Bergerat, 1985; Ziegler, 1992b). In both models, only the western part of the WER is considered (i.e., the Massif Central grabens and the Rhine graben) and the Oligocene direction of extension is supposed to be E–W at a European scale. However, geological data indicate that the direction of extension was not E–W at a European scale but perpendicular to the direction of shortening in the Alpine mountain chain (see Fig. 2a in Lickorish et al., 2002) (Fig. 14). Assuming that the global stress field was characterized by a N–S compression caused by the collision between African and European plates, the formation

of the WER with a N–S extension in the Bohemian massif is hard to explain.

We propose herein a working hypothesis in which the role of the stress field generated by the formation of the Alpine mountain chain is taken into account. It is worth to note that the Late Eocene–Oligocene period corresponds to a phase of strong deformation in the Alpine chain with the formation of the eclogitic rocks (i.e., HP metamorphism) (Monié and Philippot, 1989; Tilton et al., 1991; Duchêne et al., 1997). Kinematic data show that the directions of crustal displacement were E–W in the western Alps, NW–SE in western Switzerland and probably N–S in the central Alps during this period (Lickorish et al., 2002). It seems reasonable to assume that the direction of crustal displacement was similar to and mainly controlled by the direction of continental subduction. Then, the Eocene–Oligocene period was likely
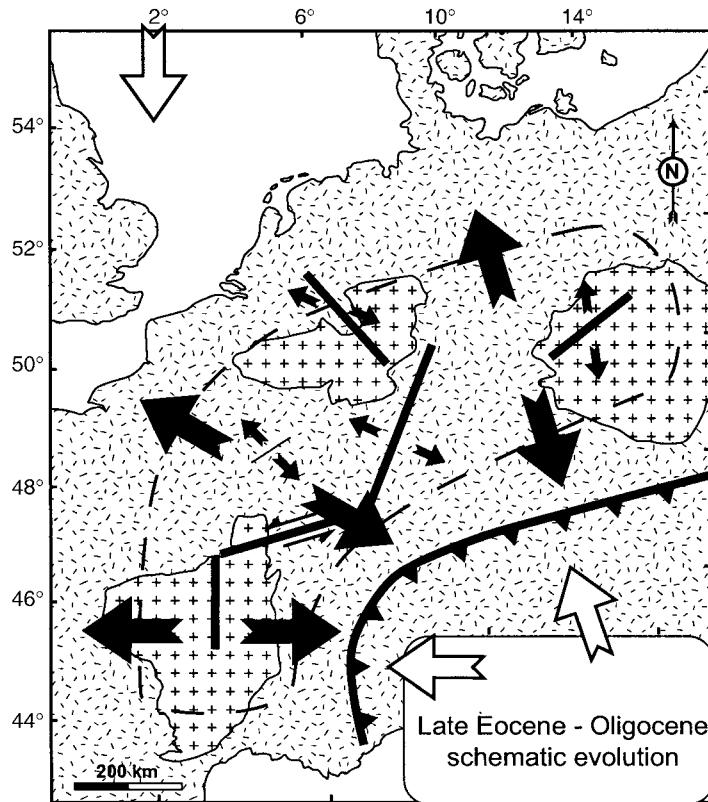

Fig. 14. Schematic representation of the Late Eocene–Oligocene rifting in the WER. Geological data show that the direction of extension is E–W in the Massif Central and presents a clockwise rotation towards the East (nearly N–S in the Eger Graben). See text for explanation.

marked by the development of a N–S deep lithospheric root in the western Alps and a E–W lithospheric root in the central Alps, similar to the present-day geometry of the Alpine lithospheric root (Babuska et al., 1990). It has been shown that the formation of a deep lithospheric root can produce a downward gravitational force, which may induce extension in the adjacent lithosphere (Fleitout, 1984). In such a model, the direction of extension is perpendicular to the lithospheric root. In consequence, we speculate that

the formation of the Alpine lithospheric root during the Eocene–Oligocene period could have induced the formation of the WER, as already proposed by Merle and Michon (2001). This model, where a ''local'' effect (i.e., the downward gravitational stress due to the formation of the lithospheric root) causes the formation of the WER, does not contradict the overall N–S compression, which has induced inversion in the southern North Sea and the Channel. The magnitude of stress generated by each process would have
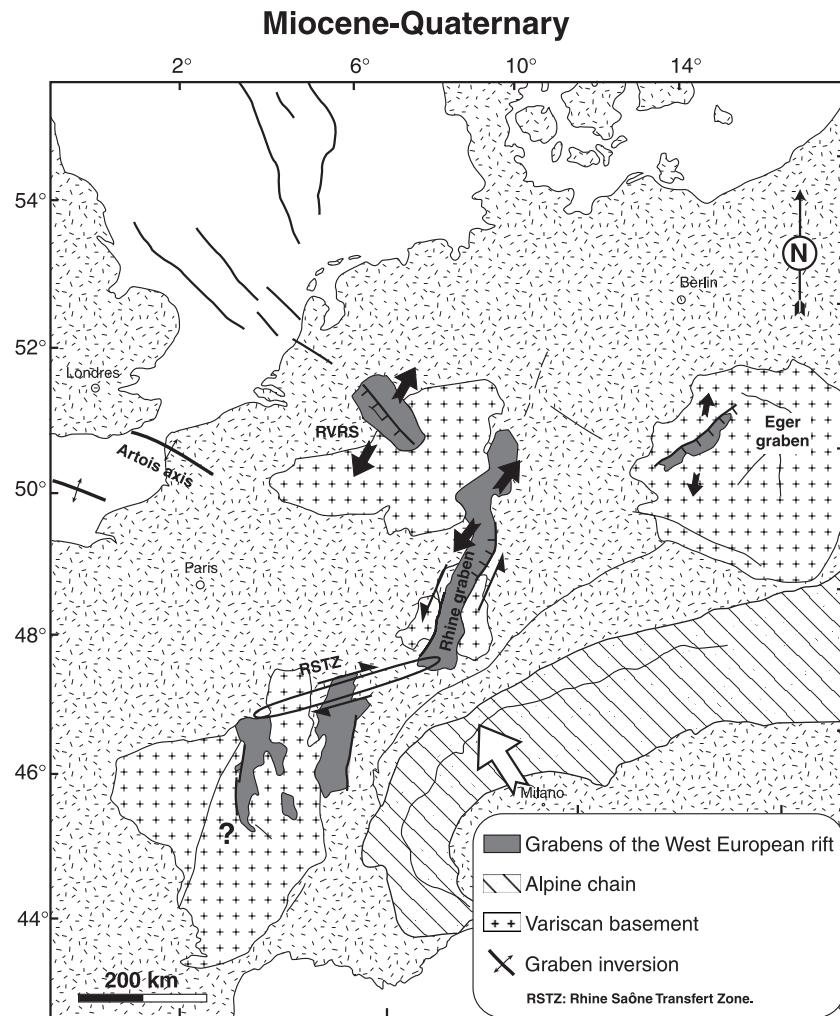

Fig. 15. Miocene–Quaternary evolution of western Europe. In the RVRS, the URG and the Eger graben, the fault orientation and the shape of the depocentres indicate a rotation of the direction of extension at the Oligocene–Miocene transition. A slight inversion and a thermal subsidence characterized the evolution of the Channel area and the North Sea basins, respectively.

controlled the location of the areas affected by compression or extension.

5.6. Miocene–Quaternary

The RVRS, the Eger graben and the URG subsided more or less continuously during the Oligocene–Quaternary evolution. However, the Oligocene–Miocene transition was marked by a radical change in the European geodynamics. In the RVRS, the northwestward migration of the depocentre and the orientation of the most active faults indicate a counter clockwise rotation of 70–80° of the direction of extension (i.e., NE–SW extension) (Fig. 15). A similar rotation has been described for the northern part of the URG where new depocentres developed (Meier and Eisbacher, 1991; Schumacher, 2002). These new depocentres are interpreted in terms of pull-apart basins resulting from sinistral strike slip faulting (Illies, 1981). In the Eger graben, the depocentre shapes in the Cheb sub-basin, which are different for the Late Oligocene–Earliest Miocene and Miocene–Pliocene periods (Spicakova et al., 2000), suggest a change of the stress field around the Oligocene–Miocene transition and an identical stress field for the Middle Miocene and Late Pliocene periods. In the Massif Central, the Miocene–Quaternary evolution was characterized by a strong uplift of the whole area, which makes a determination of the regional stress field in this province difficult. Preservation of Miocene sediments below lava flows shows that the complete Miocene sedimentation was very thin and restricted to elongated narrow lakes parallel to the grabens (Hugueney et al., 1999). In the Bresse graben, although sedimentation developed during the Miocene–Quaternary evolution, a westward propagation of the Alpine flexural basin was proposed to explain this subsidence (Merle et al., 1998). Finally, the displacement along the Rhine–Saône transfer zone, which was a left lateral fault zone during the Late Eocene and the Oligocene, has changed at the Oligocene–Miocene transition and became right lateral (Laubscher, 2001).

In the north, the southern North Sea basins continued to subside during this period. Seismic data reveals that minor fault activity has affected the Neogene sediments (Brun and Nalpas, 1996; Van Balen et

al., 2000), suggesting a continuous thermal subsidence. Nevertheless, the acceleration of the subsidence from the Pliocene could be explained by an accentuation of the thermal subsidence by a NW–SE in-plane force (Van Balen et al., 1998). Whatever the origin of this subsidence increase, geological and geophysical data clearly show that the tectonic activity related to the evolution of the WER stops in the northern end of the RVRS (Fig. 1). In the Channel area, inversion was maximum during Early Miocene but is still ongoing during the Quaternary (Ziegler, 1990).

Geological and geophysical data indicate that the present-day stress field in western Europe is characterized by a NW–SE to NNW–SSE maximum compressive stress (Müller et al., 1992; Plenefisch and Bonjer, 1997). Analysis of the earthquake focal mechanism data in the UGR and the RVRS shows that this maximum compressive stress induces left lateral displacement in the southern and central URG, whereas it causes NE–SW extension in the northern end of the URG and in the RVRS (Plenefisch and Bonjer, 1997).

In consequence, we interpret the general evolution of western Europe during the Miocene–Quaternary period as the result of the NW–SE collision between Europe and Africa (Fig. 16). In this model, the URG and the RVRS concentrate the main deformation. Due to the NW–SE compression, the URG is reactivated as a strike slip structure, which induced rifting in its northern ending and in the RVRS. This leads to the individualization of two crustal domains. Although the NE–SW relative motion of these crustal domains is assessable, the lack of precise and reliable geodetic data does not allow determination of the absolute motion of each domain. One can speculate that the Baltic shield, situated east of the northeastern domain, probably prevents the northeastern motion of this block. Consequently, the southwestern crustal domain was forced to migrate toward the southwest. The subsidence in the North Sea basins could result from the northward prolongation of a diffuse extension.

One fundamental feature is the change of the global deformation of the European lithosphere at the Oligocene–Miocene transition. Assuming that the Late Eocene–Oligocene extension was induced by the formation of a deep Alpine lithospheric root,
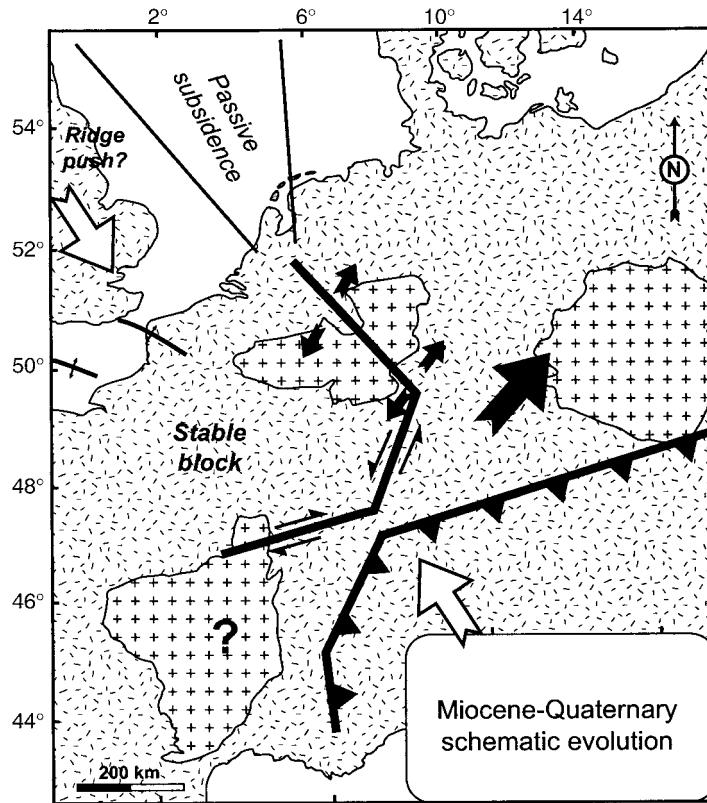
Fig. 16. Schematic evolution during the Neogene. The direction of extension could be explained by the NW–SE compression related to the Alpine collision. See text for explanation.

we propose that the Alpine chain was proned to a slab break-off at the Oligocene–Miocene transition. Such a slab break-off was already invoked by Von Blanckenburg and Davies (1995) to explain the development of the Tertiary magmatism in the central and eastern Alps between 42 and 25 Ma. However, they dated it at around 40 Ma. In the western Alps, geological data not show either magmatism or a radical change in the Alpine kinematics at this time. In contrast, the Oligocene–Miocene transition (25 Ma) corresponds to the beginning of thrusting of the external crystalline massifs and the reactivation of the Briançonnais front in normal faulting mode (Tricart et al., 2001). Then, we consider that the coeval change in the Alpine chain and western Europe could result from a slab detachment below the western Alps. This slab break-off at the Oligocene–Miocene transition could explain the stop of the Late Eocene–Oligocene extension and the

development of the NW–SE maximum compressional stress, which controls the European deformation since the beginning of the Miocene.

Appendix A

ROvD: Dienst der Rijksopsporing van Delfstoffen.

Number	Name	Date	Total depth (m)	
1	Werkendam-1 (WED-01)	1958	2275	Zijerveld et al. (1992)
2	Waalwijk-1 (WWK-01)	1987	3802	NITG-TNO (2001)
3	Oisterwijk-1 (OIW-01)	1967	2496	Zijerveld et al. (1992)
4	St-Michielsgestel-1 (SMG-01)	1969	3338	Zijerveld et al. (1992)
5	Heeswijk-1 (HSW-01)	1992	2544	Clyde Petroleum
6	Keldonk-1 (KDK-01)	1992	2330	Clyde Petroleum
7	Veldhoven-1 (VEH-01)	1967	2124	Zijerveld et al. (1992)
8	Asten-1 (AST-01)	1967	2664	Zijerveld et al. (1992)
9	Asten-2 (AST-02)	1992	1673	NITG-TNO (2001)
10	Nederweert-1 (NDW-01)	1965	2943	Zijerveld et al. (1992)
11	Molenbeersel-198	1988	1773	Demyttenaere and Laga (1988)
12	Oploo-16 (OPL-16)	1913	1150	Zijerveld et al. (1992)
13	America-11 (ACA-11)	1910	1201	Zijerveld et al. (1992)
14	Neer-71 (NER-71)	1953	1293	DSM Energie
15	Elmpt-77 (EPT-77)	1958	1215	DSM Energie
16	Melick-Herkenbosch-70 (MHB-70)	1955	524	NITG-TNO (2001)
17	Arcen-1 (ARC-01)	1987	888	Rijks Geologische Dienst
18	Beesel-72 (BEE-72)	1954	1234	DSM Energie
19	Belfeld-14 (BFD-74)	1911	1202	Zijerveld et al. (1992)
20	Broekzijde-1 (BKZ-01)	1989	2703	Clyde Petroleum
21	Cornelishof-4 (CNH-04)	1905	679	ROvD
22	Dongen-1 (DON-01)	1997	1542	Zijerveld et al. (1992)
23	Dorothea-1	1907	309	Krusch and Wunstorf (1907)

Appendix A (*continued*)

Number	Name	Date	Total depth (m)	
24	Emmerich-1	1962	1449	Elberskirch and Wolburg (1962)
25	Helden-75 (HDN-75)	1955	1353	NITG-TNO (2001)
26	Helenaveen-7 (HEL-07)	1907	1155	ROvD
27	Hilvarenbeek-1 (HVB-01)	1995	2621	Clyde Petroleum
28	Kerkwijk-1 (KWK-01)	1988	3281	NITG-TNO (2001)
29	Liessel-22 (LIE-22)	1915	1332	Zijerveld et al. (1992)
30	Loon op Zand-1 (LOZ-01)	1953	3062	Zijerveld et al. (1992)
31	Maasbommel-2 (MSB-02)	1966	1278	Zijerveld et al. (1992)
32	Maasniel-74 (MAN-74)	1955	1367	DSM Energie
33	Nijmegen-Valburg-1 (NVG-01)	1968	1277	Zijerveld et al. (1992)
34	Reuver-76 (RVR-76)	1956	1105	DSM Energie
35	Rijsbergen-1 (RSB-01)	1970	4645	NITG-TNO (2001)
36	Sanadome-1 (SNM-499)	1994	759	
37	Steelhoven-1 (STH-01)	1987	2798	NITG-TNO (2001)
38	Strijen-1 (STR-01)	1964	2779	American Overseas Petroluem
39	Vlodrop-1 (VDP-01)	1906	790	ROvD
40	Waspik-1 (WAP-01)	1959	2600	Zijerveld et al. (1992)
41	Almerk-1 (ALM-01)	1970	2370	Zijerveld et al. (1992)

References

Babuska, V., Plomerova, J., Granet, M., 1990. The deep lithosphere in the Alps: a model inferred from P residuals. Tectonophysics 176, 137–165

Barbarand, J., Carter, A., Pagel, M., 2002. Histoire thermotectonique mésocénozoïque du Massif Central—Conséquence sur la déformation de la lithosphère de l'Europe de l'Ouest. 19ème RST, Nantes, pp. 55–56.

Bergerat, F., 1985. Déformations cassantes et champs de contraintes tertiaires dans la plate-forme européenne. Thesis, P.M. Curie Univ. 315 pp.

Brun, J.P., Nalpas, T., 1996. Graben inversion in nature and experiments. Tectonics 15, 677–687.

Chlupac, I., Kodym, O., Suk, M., Holub, V., Elias, M., Cicha, I., Malkowsky, M., Tyracek, J., Mencik, E., Buday, T., 1984. Stratigraphic development of the units. In: Suk, M., et al., (Eds.), Geological History of the Territory of the Czech Socialist Republic. Geological survey, Prague, pp. 87–200.

Coulon, M., 1992. La distension oligocène dans le nord-est du bassin de Paris (perturbation des directions d'extension et distribution des stylolites). Bull. Soc. Géol. Fr. 163, 531–540.

de Lugt, I.R., van Wees, J.D., Wong, Th.E., 2003. The tectonic evolution of the southern Dutch North Sea during the Paleogene: a case study for basin inversion in pulses. Tectonophysics.

Demyttenaere, R., Laga, P., 1988. Breuken en isohypsenkaarten van het Belgische gedeelte van de Roerdal Slenk. Belgische Geologische Dienst Professional Paper, 1988/4, 234, 20 pp.

Duchêne, S., Blichert-Toft, J., Luais, B., Telouk, P., Lardeaux, J.M., Albarède, F., 1997. The Lu–Hf dating of garnets and the ages of the alpine high-pressure metamorphism. Nature 387, 586–589.

Elberskirch, W., Wolburg, J., 1962. Zur Tektonik des Karbons am linken Niederrhein im Profil der Bohrungen Wachtendonk 1-Emmerich 1. Fortschr. Geol. Rheinld. u. Westf. 6, 407–432.

Fleitout, L., 1984. Modélisation des contraintes tectoniques et des instabilités thermomécaniques dans la lithosphère. Thesis, Orsay University. 433 pp.

Geluk, M.C., Duin, E.J., Dusar, M., Rijkers, R.H, van den Berg, M.W., van Rooijen, P., 1994. Stratigraphy and tectonics of the Roer Valley Graben. Geol. Mijnb. 73, 129–141.

Gras, R., Geluk, M., 1999. Late Cretaceous–Early Tertiary sedimentation and tectonic inversion in the southern Netherlands. Geol. Mijnb. 78, 1–19.

Hippolyte, J.C., Angelier, J., Bergerat, F., Nury, D., Guieu, G., 1993. Tectonic–stratigraphic record of paleostress time changes in the Oligocene basins of the Provence, southern France. Tectonophysics 226, 15–35.

Houtgast, R.F., Van Balen, R.T., 2000. Neotectonics of the Roer Valley Rift System, the Netherlands. Global Planet. Change 27, 131–146.

Hugueney, M., Poidevin, J.L., Bodergat, A.M., Caron, J.B., Guerin, C., 1999. Des mammifères de l'Aquitanien inférieur à La Roche-Banche-Gergovie (Puy-de-Dôme, France), révélateurs de l'activité post-oligocène du rift en Limagne de Clermont. C. R. Acad. Sci. Paris 328, 847–852.

Illies, J.H., 1981. Mechanism of graben formation. Tectonophysics, 249–266.

Krusch, P., Wunstorf, W., 1907. Das Steinkohlengebiet nordöstlich der Roer nach den Ergebnisse der Tiefbohrungen und verglichen mit dem Cardiff-District. Glückauf 43, 425–436.

Lake, S.D., Karner, G.D., 1987. The structure and the evolution of the Wessex Basin, southern England: an example of inversion tectonics. Tectonophysics 137, 347–378.

Laubscher, H., 2001. Plate interactions at the southern end of the Rhine graben. Tectonophysics 343, 1–19.

Lefort, J.P., Agarwal, B.N.P., 1996. Gravity evidence for Alpine buckling of the crust beneath the Paris Basin. Tectonophysics 258, 1–14.

Le Griel, A., 1988. L'évolution géomorphologique du Massif Central français. Essai sur la genèse d'un relief. Thesis, Lyon II Univ. 569 pp.

Lickorish, W.H., Ford, M., Bürgisser, J., Cobbold, P.R., 2002. Arcuate thrust systems in sandbox experiments: a comparison to the external arcs of the Western Alps. Geol. Soc. Am. Bull. 114, 1089–1107.

Malkovsky, M., 1987. The Mesozoic and Tertiary basins of the Bohemian Massif and their evolution. Tectonophysics 137, 31–42.

Meier, L., Eisbacher, G.H., 1991. Crustal kinematics and deep structures of the northern Rhine Graben, Germany. Tectonics 10, 621–630.

Merle, O., Michon, L., 2001. The formation of the West European rift: a new model as exemplified by the Massif Central area. Bull. Soc. Géol. Fr. 172 (2), 213–221.

Merle, O., Michon, L., Camus, G., de Goër, A., 1998. L'extension oligocène sur la transversale septentrionale du rift du Massif Central. Bull. Soc. Géol. Fr. 169, 615–626.

Meyer, W., Albers, H.J., Berners, H.P., Gehlen, K., Glatthaar, D., Lohnertz, W., Pfeffer, K.H., Schnutgen, K., Wienecke, K., Zakosek, H., 1983. Pre-Quaternary uplift in the Central part of the Rhenish Shield. In: Fuchs, K., Von Gelhen, K., Malzer, H., Murawski, H., Semmel, A. (Eds.), Plateau Uplift. The Renish Shield—A Case History. Springer-Verlag, Berlin, pp. 39–46.

Michon, L., 2001. Dynamique de l'extension continentale—application au Rift Ouest Européen par l'étude de la province du Massif Central. Mém. Géosci. Rennes 99, 266 pp.

Michon, L., Merle, O., 2001. The evolution of the Massif Central rift: spatio-temporal distribution of the volcanism. Bull. Soc. Géol. Fr. 172, 201–211.

Monié, P., Philippot, P., 1989. Mise en évidence de l'âge Eocène moyen du métamorphisme de haute-pression dans la nappe ophiolitique du Monviso (Alpes occidentales) par la méthode ^{39}Ar–^{40}Ar. C. R. Acad. Sci. Paris 309, 245–251.

Müller, B., Zoback, M.L., Fuchs, K., Mastin, L., Gregersen, S., et al., 1992. Regional patterns of tectonics stress in Europe. J. Geophys. Res. 97, 11783–11803.

Murawski, H., Albers, H.J., Bender, P., Berners, H.P., Durr, St., Huckriede, R., Kauffmann, G., Kowalczyk, G., Meiburg, P., Muller, R., Ritzkowski, S., Schwab, K., Semmel, A., Stapf, K., Walter, R., Winter, K.P., Zankl, H., 1983. Regional tectonic setting and geological structure of the Rhenish Massif. In: Fuchs, K., von Gelhen, K., Malzer, H., Murawski, H., Semmel, A. (Eds.), Plateau Uplift. The Renish Shield—A Case History. Springer-Verlag, Berlin, pp. 9–38.

Nederlandse Aardolie Maatschappij BV, Rijks Geologische Dienst, 1980. Stratigraphic nomenclature of the Netherlands. Verh. K. Ned. Geol. Mijnbouwkd. Genoot. 32, 77 pp.

NITG-TNO, 2001. Geological Atlas of the Subsurface of the Netherlands: Explanation of map sheet XIII and XIV Breda-Valkenswaard and Oss-Roermond. NITG-TNO, Utrecht. 149 pp.

Oudmayer, B., De Jager, J., 1993. Fault reactivation and oblique-slip in the Southern North Sea. In: Parker, J.R. (Ed.), Petroleum Geology of Northwest Europe. Proceedings of the 4th Conference Geol. Soc., London, pp. 1281–1290.

Peterek, A., Rauche, H., Schroder, B., Franzke, H.-J., Bankwitz, P., Bankwitz, E., 1997. The late- and post-Variscan tectonic evolu-

tion of the Western Border fault zone of the Bohemian massif (WBZ). Geol. Rundsch. 86, 191–202.

Plenefisch, T., Bonjer, K.P., 1997. The stress field in the Rhine Graben area inferred from earthquake focal mechanisms and estimation of frictional parameters. Tectonophysics 275, 71–97.

Racero-Baena, A., Drake, J., 1996. Structural style and reservoir development in the West Netherlands oil province. In: Rondeel, H.E., Batjes, D.A.J., Nieuwenhuijs, W.H. (Eds.), Geology of Gas and Oil Under the Netherlands. Kluwer Academic Publishing, Dordrecht, pp. 211–227.

Rat, P., 1974. Le système Bourgogne–Morvan–Bresse (articulation entre le bassin parisien et le domaine péri-alpin). In: Debelmas, J. (Ed.), Géologie de la France; les chaînes plissées du cycle alpin et leur avant-pays. Doin, Paris, pp. 480–500.

Roure, F., Coletta, B., 1996. Cenozoic inversion structures in the foreland of the Pyrenees and Alps. In: Ziegler, P.A., Horvath, F. (Eds.), Peri-Tethys Memoir 2: Structure and Prospects of Alpine Basins and Forelands. Mém. Mus. Natn. Hist. Nat., vol. 170, pp. 173–209.

Schumacher, M.E., 2002. Upper Rhine Graben: role of preexisting structures during rift evolution. Tectonics 21, 6.1–6.17.

Sclater, J.G., Christie, P.A.F., 1980. Continental stretching: an explanation of post-mid-Cretaceous subsidence of the North Sea Basin. J. Geophys. Res. 85, 3711–3739.

Seranne, M., 1999. The Gulf of Lion continental margin (NW Mediterranean) revisited by IBS: an overview. In: Durand, B., Jolivet, L., Horvath, F., Seranne, M. (Eds.), The Mediterranean Basins: Tertiary Extension within the Alpine Orogen. Geol. Soc. Lond. Spec. Publ., vol. 156, pp. 15–36.

Sissingh, W., 1998. Comparative Tertiary stratigraphy of the Rhine Graben, Bresse Graben and Molasse Basin: correlation of Alpine foreland events. Tectonophysics 300, 249–284.

Spicakova, L., Ulicny, D., Koudelkova, G., 2000. Tectonosedimentary evolution of the Cheb basin (NW Bohemia, Czech Republic) between Late Oligocene and Pliocene: a preliminary note. Stud. Geophys. Geod. 44, 556–580.

Tapponnier, P., 1977. Evolution tectonique du système alpin en Mediterranée: poinçonnement et écrasement rigide-plastique. Bull. Soc. Géol. Fr. 19, 437–460.

Tilton, G.R., Schreyer, W., Schertl, H.P., 1991. Pb–Sr–Nd isotopic behavior of deeply subducted crustal rocks from the Dora Maira Massif, Western Alps, Italy: II. What is the age of the ultrahigh-pressure metamorphism? Contrib. Mineral. Petrol. 108, 22–33.

Tricart, P., Schwartz, S., Sue, C., Poupeau, G., Lardeaux, J.M., 2001. La dénudation tectonique de la zone ultradauphinoise et l'inversion du front briançonnais au sud-est du Pelvoux (Alpes occidentales): une dynamique miocène à actuelle. Bull. Soc. Géol. Fr. 172, 49–58.

Van Balen, R.T., Podladchikov, Y.Y., Cloetingh, S.A.P.L., 1998. A new multilayered model for intraplate stress-induced differential subsidence of faulted lithosphere, applied to rifted basins. Tectonics 17, 938–954.

Van Balen, R.T., Van Bergen, F., de Leeuw, C., Pagnier, H., Simmelink, H., Van Wees, J.D., Verweij, J.M., 2000. Modelling the hydrocarbon generation and migration in the West Netherlands Basin, the Netherlands. Geol. Mijnb., Neth. J. Geosci. 79, 29–44.

Van Balen, R.T., Verweij, J.M., Van Wees, J.D., Simmelink, H., Van Bergen, F., Pagnier, H., 2002. Deep subsurface temperatures in the Roer Valley Graben and the Peel Block, the Netherlands—new results. Neth. J. Geosci., Geol. Mijnb. 81, 19–26.

Van Hinte, J.E., 1978. Geohistory analysis—application of micropaleontology. Am. Assoc. Pet. Geol. Bull. 62, 201–222.

Verbeek, J.W., de Leeuw, C.S., Parker, N., Wong, Th.E., 2002. Characterisation and correlation of Tertiary seismostratigraphic units in the Roer Valley Graben. Geol. Mijnb., Neth. J. Geosci. 81, 159–166.

Villemin, T., Bergerat, F., 1987. L'évolution structurale du fosse rhenan au cours du Cénozoïque: un bilan de la déformation et des effets thermiques de l'extension. Bull. Soc. Géol. Fr. 3, 245–255.

Von Blanckenburg, F., Davies, J.H., 1995. Slab breakoff: a model for syncollisional magmatism and tectonics in the Alps. Tectonics 14, 120–131.

Winstanley, A.M., 1993. A review of the Triassic play in the Roer Valley Graben, SE onshore Netherlands. In: Parker, J.R. (Ed.), Petroleum Geology of Northwest Europe. Proceedings of the 4th Conference Geol. Soc., London, pp. 595–607.

Zagwijn, W.H., 1989. The Netherlands during the Tertiary and the Quaternary: a case history of coastal lowland evolution. Geol. Mijnb. 68, 107–120.

Ziegler, P.A., 1988. Evolution of the Artic North Atlantic and the western Tethys. Am. Assoc. Pet. Geol. Mem. 43, 198 pp.

Ziegler, P.A., 1990. Geological atlas of western and central Europe, 2nd ed. Shell Internationale Petroleum Mij., distributed by Geol. Soc., London, Publ. House, Bath. 238 pp., 56 encl.

Ziegler, P.A., 1992a. North Sea rift system. In: Ziegler, P.A. (Ed.), Geodynamics of Rifting, Volume I. Case History Studies on Rifts: Europe and Asia. Tectonophysics, vol. 208, pp. 55–75.

Ziegler, P.A., 1992b. European Cenozoic rift system. In: Ziegler, P.A. (Ed.), Geodynamics of Rifting, Volume I. Case History Studies on Rifts: Europe and Asia. Tectonophysics, vol. 208, pp. 91–111.

Ziegler, P.A., Roure, F., 1996. Architecture and petroleum systems of the Alpine orogen and associated basins. In: Ziegler, P.A., Horvath, F. (Eds.), Peri-Tethys Memoir 2: Structure and Prospects of Alpine Basins and Forelands. Mém. Mus. Natn. Hist. Nat., vol. 170, pp. 15–45.

Zijerveld, L., Stephenson, R., Cloetingh, S., Duin, E., Van den Berg, M.W., 1992. Subsidence analysis and modelling of the Roer Valley Graben (SE Netherland). Tectonophysics 208, 159–171.

Annexe 6 :

Michon, L., O. Merle (2000) Crustal structures of the Rhinegraben and the Massif Central grabens: an experimental approach. *Tectonics,* 19, 896-904*.*

Crustal structures of the Rhinegraben and the Massif Central grabens: An experimental approach

Laurent Michon and Olivier Merle

Laboratoire Magmas et Volcans, Clermont-Ferrand, France

Abstract Two of the most important segments of the west European Rift, the Rhinegraben and the Massif Central grabens, show in plan and in cross section a very different crustal structure. The Rhinegraben and the Massif Central grabens are roughly parallel and formed in the same time interval (i.e., Priabonian/Oligocene). The Rhinegraben in the north is a single half graben of ~35 km wide that resulted from the activity of a major detachment fault running from the surface to a MOHO discontinuity at depth. The Massif Central in the south is composed of two lateral half grabens, similar to the Rhinegraben, and a near-symmetric central graben. The opposing detachment faults of the two lateral half grabens reveal a striking mirror symmetry on either side of the symmetric central graben. Experiments have been conducted to explain mechanically this contrasted structural evolution in the same rift system. It is shown that this difference may be attributed to (1) the number of ruptures in the brittle part of the mantle lithosphere and (2) variations in the extension rate. A single rupture in the brittle mantle lithosphere results in either a single half graben or a pair of half and symmetric grabens in low and high extension rate experiments, respectively. Two ruptures in the brittle mantle lithosphere result in two half grabens in low rate experiments. The number of grabens is dependent upon the distance between the two ruptures in the brittle mantle lithosphere in high extension rate experiments and may vary from 2 to 4. Estimation of the extension rate in the Rhinegraben and the Massif Central matches experimental results and shows that the strength ratio between lower and brittle crust is the key parameter in determining the graben geometry.

1. Introduction

Understanding of the geometry of sedimentary basins associated with rifting processes in the continental lithosphere has made great progress over the past 10 years [e.g., *Allemand and Brun*, 1991; *Buck*, 1991; *Benes and Davy*, 1996; *Scholz and Contreras*, 1998]. Despite this progress, the process of graben initiation is still controversial. Because reflection seismic studies clearly show that some extensional structures are asymmetric at the graben scale as revealed for the Rhinegraben [*Brun et al.*, 1991], the Malawi rift [*Rosendhal et al.*, 1992], or the Basin and Range province [*Allimendinger et al.*, 1983], it is widely considered that the passive rifting may be induced by a lithospheric asymmetric simple shear [*Wernicke*, 1985; *Brun and*

Beslier, 1996]. However, several authors also propose that the initial stage of a passive margin evolution may be explained by a pure shear evolution at lithospheric scale [*Keen and Dehler*, 1993].

The aim of this paper is to determine, using scaled models, graben geometry during continental passive rifting. According to many authors [e.g., *Buck*, 1991; *Davy and Cobbold*, 1991; *Burg et al.*, 1994; *Allemand and Brun*, 1991], we assume that the continental lithosphere is characterized by a four-layer strength profile with two brittle high strength layers (the upper crust and the upper mantle lithosphere) and two ductile layers (the lower crust and the lower mantle lithosphere). As a result of such a lithospheric strength profile, it has been shown that crustal deformation is largely controlled by ruptures within the brittle mantle lithosphere [*Beslier*, 1991; *Brun and Beslier*, 1996].

In the present paper, we examine at crustal scale the graben geometry resulting from the failure of the brittle mantle lithosphere. As known from geomechanics, the strength of a viscous material is dependant on the strain rate, so that the rate of extension is supposed to be of paramount importance in the graben geometry. We study the influence of different parameters such as the variation of the strength ratio between the upper and the lower crust or the number of ruptures in the underlying mantle.

Experimental results explain mechanically why a single rupture in the brittle mantle may induce the formation of either a unique asymmetric graben or two parallel, symmetric and asymmetric, grabens. Our model also emphasizes the importance of the rate of extension upon the graben geometry in the crust. Finally, the experimental models may explain the differences depicted in the west European Rift between the Massif Central grabens and the Rhinegraben geometries.

2. Experimental Background

2.1. Scaling

Analogue modeling of crustal deformation is similar to nature if experimental models and natural systems are characterized by a similar distribution of stresses, densities, and rheologies [*Hubbert*, 1937]. The continental lithosphere with a normal thermal gradient is considered as a four-layer model for which the deformation is initiated from the failure of the brittle mantle [*Beslier*, 1991]. As a mantle lithospheric rupture occurs, the resulting crustal structure is highly dependent on the mechanical coupling between the brittle and ductile part of the crust. This brittle/ductile coupling can be estimated from the strength ratio between the upper and lower crust [*Allemand*, 1990; *Beslier*, 1991; *Benes and Davy*, 1996; *Brun*, 1999]. We use this strength

ratio to achieve similarities between nature and experiments. This ratio is a dimensionless number that must be of the same order of magnitude in model and nature.

$$\left(\frac{S_B}{S_D}\right)_{Model} = \left(\frac{S_B}{S_D}\right)_{Nature} . \tag{1}$$

The strength S_B of a brittle material corresponds to the deviatoric stress $\sigma_1-\sigma_3$ (where σ_1 and σ_3 are the maximum and minimum principal stresses, respectively), which increases linearly with depth h and fluctuates as a function of the density ρ, the angle of friction ϕ, the gravity acceleration g, and the cohesion τ_0 ((2)-(4)). It follows for a divergent tectonic regime

$$\sigma_1 = a + b\sigma_3 = \rho g h , \tag{2}$$

$$a = 2\tau_0 \sqrt{b} , \tag{3}$$

$$b = \frac{1+\sin\phi}{1-\sin\phi} . \tag{4}$$

In the upper crust the average density ρ_n is ~2700 kg m^{-3} (continental crust with an overall granitic composition), the cohesion is ~10^7 Pa, and the angle of friction is close to 30°. These natural values make it possible to determine the strength S_B of the brittle upper part of the crust. In experiments where cohesionless material is used the strength of the upper brittle part simplifies to

$$S_B = \sigma_1 - \sigma_3 = \frac{2}{3}\rho g h . \tag{5}$$

In the lower ductile layer the strength S_D is dependant on the viscosity μ and the strain rate ε, which may be calculated from the ratio between the extension rate V and the thickness of the ductile layer h_D.

$$S_D = \mu \frac{V}{h_D} . \tag{6}$$

Then, the strength ratio may be estimated both in nature and experiments. In experiments it simplifies to

$$\frac{S_B}{S_D} = \frac{\frac{2}{3}\rho g h}{\mu \varepsilon} . \tag{7}$$

In our experiments the brittle upper crust is made of sand, which is a cohesionless material [*Davison et al.*, 1993] with a density ρ_m of ~1400 kg m^{-3}. The length scale ratio is 10^{-6}, so that 1 cm in the model represents 10 km in nature. The angle of friction ϕ, being a dimensionless number, must be similar in nature and experiments (ϕ_{sand}=30° and ϕ_{nature}=30°). We use a silicone with a viscosity μ_m=3x10^4 Pa s to simulate a lower crust with a viscosity of ~ μ_n=10^{21} Pa s.

The experiments are an attempt to understand the mechanisms of crustal deformation in an overall slight extension of a few tens kilometers (10/30 km) within a time interval of ~10 million years. The strain rate in nature ranges from 10^{-15} to 10^{-16} s^{-1}. In order to achieve in experiments a strength ratio similar to that inferred in nature (a few tens to a few hundred) the extension rate in

experiments varies from 0.15 to 1.4 cm h^{-1}, which yields a strength ratio in experiments ranging from 4.5 to 130.

2.2. Apparatus

The experimental model is 50 cm long and 3 cm thick and is made of a brittle upper part and a ductile lower part. The brittle upper part is composed of alternating horizontal sand layers of different colors used as passive markers. The ductile lower part is a homogeneous pink silicone in most experiments. However, we have also used vertically and horizontally stratified silicone in order to determine the internal strain in the ductile level, following an experimental procedure already proposed and explained in detail by some authors [*Dixon*, 1974; *Merle*, 1982; *Brun and Merle*, 1985; *Allemand*, 1990]. The basal plate of the model simulates the boundary between the crust and the brittle mantle. As in the experiments of *Basile and Brun* [1999] the rupture within the brittle mantle, which is considered to govern crustal deformation, is achieved by a velocity discontinuity (VD) long the basal plate (Figure 1). In the end of the experiment the brittle material is wetted, and serial cross sections, perpendicular to the strike of the grabens, make it possible to analyze the geometry and the internal strain recorded in the model.

We have conducted two sets of experiments, which differ in the VD number. The first set was carried out with a single VD (one-velocity discontinuity model). The model is limited by a motionless wall on one side and by a mobile rim that is pulled out with the mean of a screw jack on the other side (Figure 2a). A plastic sheet underlying half of the model is attached to the mobile rim. The limit of the plastic sheet, which is underneath the silicone and parallel to the mobile rim, induces a VD in the middle central part of the model during motion. The second set of experiments was carried out with two VD (two-velocity
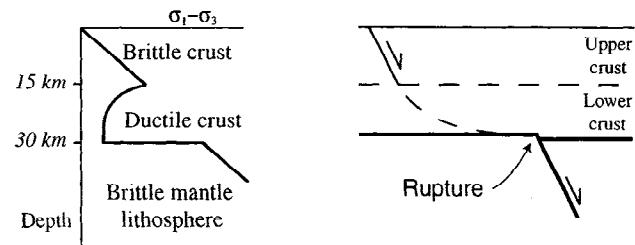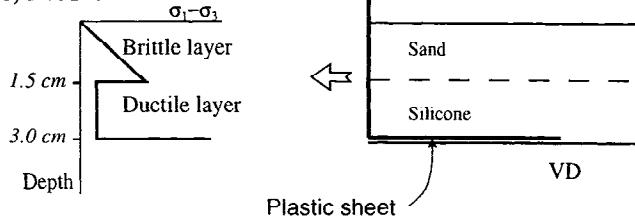

Figure 1. Strength profile in (a) nature and (b) experiments. The velocity discontinuity resulting from failure within the brittle mantle in nature is modeled in experiments by the rim of a mobile plastic sheet at the base of the model.
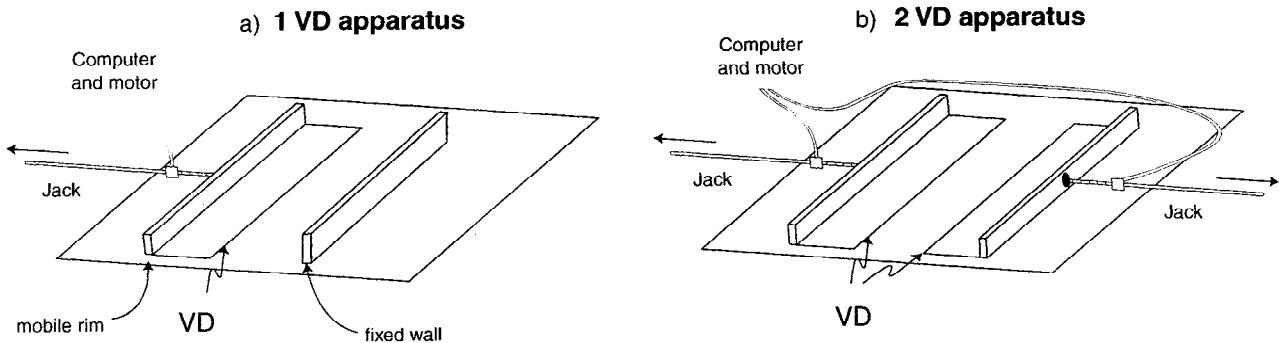
Figure 2. Experimental devices for (a) one-velocity discontinuity models and (b) two-velocity discontinuities models.

discontinuity model). The former motionless wall is replaced by a mobile rim to which is attached a second plastic sheet (Figure 2b). During each experiment the velocity of each mobile rim is achieved by a step by step motor controlled by a computer.

3. One-Velocity Discontinuity Model

The goal of these experiments is to study the geometry and the deformation mechanisms associated with the activity of a single VD. The strength ratio is dependent upon both the extension rate and the ratio of thickness between the brittle and the ductile part of the model. We have conducted several experiments with the same amount of extension and the same thickness ratio in order to determine the role of the extension rate on the graben geometry. Then, varying the velocity of the mobile wall makes the strength ratio to change from 4.5 to 130 and the role of the extension rate in the graben geometry needs to be determined.

3.1. Influence of the Strength Ratio

In experiments with a strength ratio <65-70 the extension initiates two linear and parallel grabens: a near-symmetric one located above the motionless part of the model and an


Figure 3. Two cross sections in one-velocity discontinuity experiments for (a) low strength ratio and (b) high strength ratio. The constant C_a is defined as the width of the symmetric graben, and C_b is defined as the final distance between the center of the symmetric graben and the master fault of the half graben.

asymmetric one located above the movable plastic sheet. The latter half graben presents a well-pronounced asymmetry with a major detachment fault facing the symmetric graben (Figure 3a). This overall geometry does not differ when varying the strength ratio from 4.5 to 65-70. Experiments with identical strength ratios allow one to define two constants C_a and C_b. The constant C_a is the width of the symmetric graben. For instance, C_a is ~2 cm for a strength ratio of ~25. The constant C_b is the distance between the center of the symmetric graben and the master detachment fault of the asymmetric graben. C_b is ~8 cm for a strength ratio of 25. However, the constant C_b slightly increases with time owing to the displacement of the half graben onto the movable plastic sheet. The constant C_b is also related to the strength ratio as it may increase (up to 1 cm) when increasing this ratio.

In experiments with a strength ratio >70 the extension generates a unique and asymmetric graben on the movable part (Figure 3b). On map view this half graben is linear and parallel to the rims of the model. In cross section the half graben is very similar to that observed in low strength ratio experiments, having the same width and the same orientation for the detachment fault. This result indicates that a high strength ratio prevents the formation of the symmetric companion graben observed in low strength ratio experiments.

3.2. Internal Strain in the Ductile Lower Part

In some experiments, along strike, half of the silicone is stratified vertically, whereas the second half is stratified horizontally. The width and the thickness of the vertical and horizontal layers are identical, so that a deformed grid is obtained by superposition of two cross sections in the horizontally and vertically stratified halves of the model after deformation (a complete description of this experimental procedure is given by Brun and Merle, [1985]). This allows one to fully define the strain pattern within the ductile lower part of the model during extension.

In experiments with a strength ratio equal to 24, cross sections reveal that the strain (1) can be slightly different along strike in the same experiment, (2) is due to major low-angle high-strain zones dipping ~25°-30°, and (3) is mainly localized between the two grabens (Figure 4). Cross sections allow two sets of nearly symmetric high-strain zones to be determined. First, two high-strain zones are arranged in a more or less pronounced mirror

a)

b)   Near symmetric shearing   5 cm   Asymmetric shearing

γ values
(10⁻²)
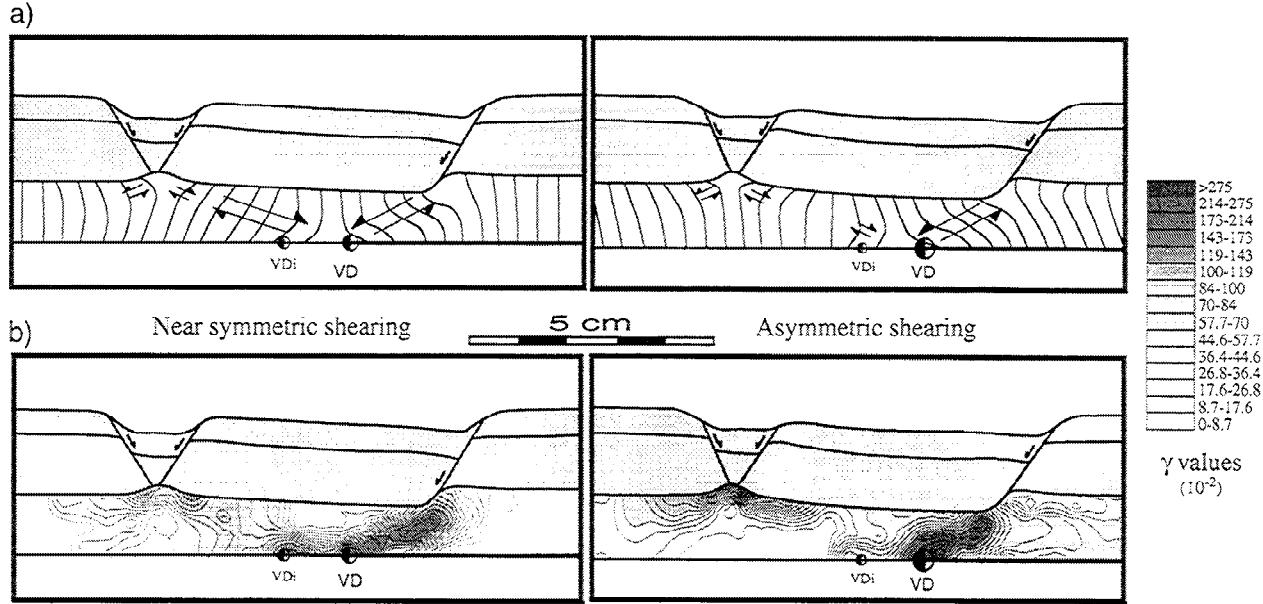
Figure 4. Cross sections in one-velocity discontinuity experiments showing the final shape of (a) initially vertical markers and (b) shear magnitudes in the lower ductile layer.

symmetry on both sides of the velocity discontinuity. The two high-strain zones intersect at depth between the initial (VD$_i$) and final position (VD) of the velocity discontinuity. The high-strain zone associated with the detachment fault of the half graben affects the entire thickness of the silicone layer in all experiments. Shear measurements γ reveal that the highest strain values are recorded along it (Figure 4b). It is also well worth noting that the brittle block in between the two grabens is slightly tilted according to the activity of the main detachment fault of the half graben. Second, two high-strain zones are localized below the symmetric graben on either side of its central axis and are restricted to the very upper part of the silicone layer.

This strain analysis shows that the prominent feature of the deformation in such an extensional process is the detachment fault of the half graben along which very high strain is recorded in the lower ductile part. We argue that extension with high strength ratio, which inhibits the formation of the symmetric graben, would be mainly characterized by a single major high strain-zone running from the bottom of the brittle fault in the sand to the velocity discontinuity at depth.

4. Two-Velocity Discontinuities Model

In experiments with a low strength ratio (<65-70) the overall geometry can be understood as a function of the initial distance between the two velocity discontinuities (Figure 5). As the initial distance between the two velocity discontinuities is superior to 6 cm (for a strength ratio equal to 18), each VD induces the formation of a pair of grabens in a way similar to that described for a low strength ratio in one-VD experiments (Figure 5a). Increasing the initial distance between the two VD makes the distance between the two pairs of graben (i.e., the central horst) increase.

In experiments with an initial distance equal to 5±1 cm, extension leads to the formation of three grabens only: two lateral half grabens and a central symmetric one (Figure 5b). The distance between this unique central graben and the two other lateral half grabens is identical to the distance between each pair
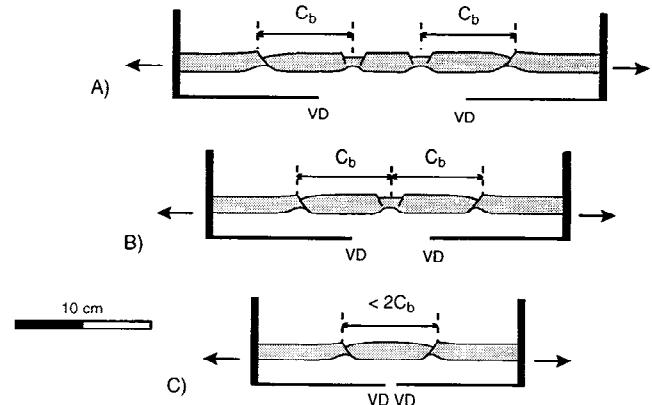
Figure 5. Schematic representation of extensional structures in two-velocity discontinuities and low strength ratio experiments. When the starting distance between the two VD is large, each VD initiates a pair of half graben/symmetric graben as in one-VD low strength ratio experiments (Figure 5a). A larger starting distance between the two VD merely increases the width of the central horst between the two pairs of grabens linked to each VD. When the starting distance between the two VD is reduced, a single symmetric graben is shared by the two half grabens as the distance between those two is not enough to create two symmetric grabens (Figure 5b). When the two VD are touching or are very close, the distance between the two border faults becomes too short for creating a symmetric graben, and the two half grabens are separated by a central horst (Figure 5c).
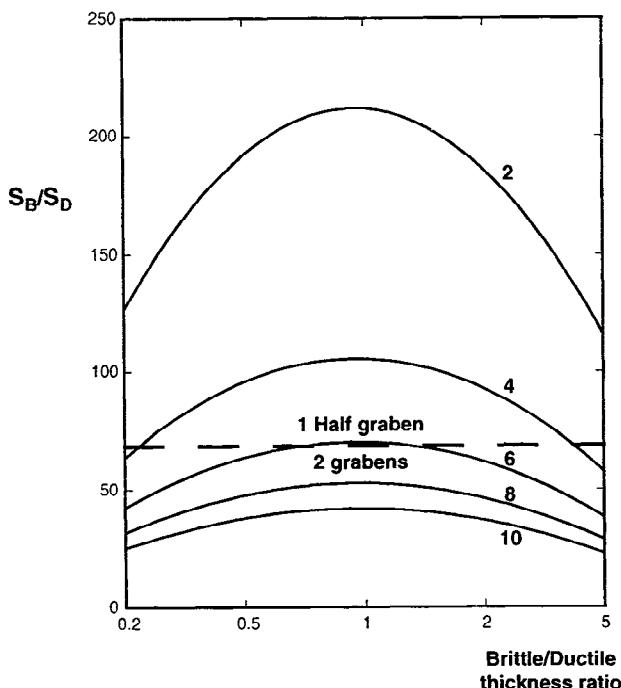
Figure 6. Strength ratio versus brittle/ductile thickness ratio for five different extension rates: 2, 4, 6, 8, and 10 10^{-11} m s^{-1} (see text for explanation).

of associated grabens (i.e., constant C_b) in previous experiments. We propose that the distance between the two half grabens being too small for two symmetric grabens to form, a single central graben develops and is shared by the two lateral half grabens.

Finally, with an initial distance inferior to 4 cm the system is restricted to the formation of the two lateral half grabens. The distance between the half grabens is smaller than the constant C_b, which probably prevents the formation of any symmetric graben in between (Figure 5c).

In experiments with a high strength ratio (>70) the extension always induces the formation of two half grabens, whatever the initial distance between the two velocity discontinuities. This result is consistent with high strength ratio one-VD experiments.

5. Discussion

It is interesting to analyze the influence of the thickness of the brittle upper part of the crust on the strength ratio. Computations show that the strength ratio reachs a maximum for a thickness ratio of 1, decreasing to zero as the thickness ratio tends both to zero and infinity (Figure 6). At high extension rate the thickness ratio has no effect on the number of grabens, and extension leads to the formation of two, symmetric and asymmetric, grabens. In contrast, at low extension rate a thickness ratio in the range from 0.2 to 5 may induce the formation of a single half graben (Figure 6).

In nature the thickness ratio may fluctuate from 0.5 to 2 according to the geothermal gradient within the crust at the time of the deformation. Considering these two end-members, Figure 7 shows that the strength ratio is more sensitive to changes in

extension rate than to variations in thickness ratio. No matter what the thickness ratio is, an extension rate higher or lower than $\sim 6 \times 10^{-11}$ m s^{-1} leads to the formation of a single half graben or of a pair of grabens, respectively (Figure 7). We conclude that the extension rate is the main parameter controlling the graben geometry in nature.

As the strength ratio is <65-70 (i.e., relatively high extension rate), the initial stage of the deformation in one-VD experiments is associated with the formation of two symmetric high-strain zones in the silicone layer. In the brittle layer these high-strain zones lead to the formation of two grabens. As the extension increases, the graben located on the mobile part becomes asymmetric, whereas the other remains symmetric. The shear zone related to the symmetric graben becomes less and less active whereas, high shear strain is recorded along the major shear zone related to the half graben. These results can be usefully compared with the experiments of *Brun and Beslier* [1996, Figure 4b] at lithospheric scale where the symmetric graben becomes progressively inactive with time and where the deformation is concentrated in the asymmetric one. The one-VD experiments with a strength ratio >65-70 (i.e., relatively low extension rate) show that the extension induces from the beginning a major high-strain zone, which leads to the formation of a single half graben in the brittle layer.

These experiments make it possible to assess in nature the role of the distance between the rupture zones in the brittle mantle with respect to the extension rate. In two-VD experiments with a strength ratio >65-70 (i.e., low extension rate) the extension always leads to the formation of two asymmetric grabens. This shows that the overall geometry at low extension rate is not controlled by the initial distance between the VD and that each rupture in the brittle mantle generates an half graben in the overlying crust. However, low strength ratio experiments (i.e., high extension rate) reveal that the geometry and the number of graben are controlled by the initial distance between the two VD (Figure 8).
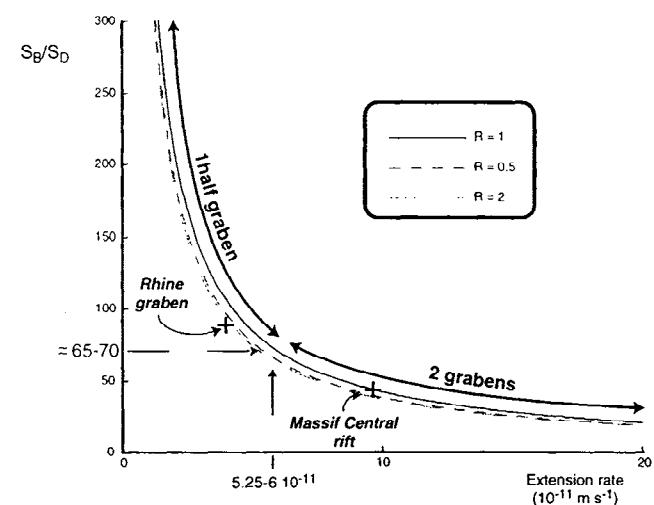

Figure 7. Strength ratio versus extension rate for three different brittle/ductile thickness ratios. The Rhinegraben plots in the single half graben field, whereas the Massif Central plots in the two grabens field.

		High extension rate	Low extension rate
1 VD		2 grabens	1 graben
2 VD	0<d<4	2 grabens	
	4<d<6	3 grabens	2 grabens
	d>6	4 grabens	

Figure 8. Table showing the number of grabens with respect to the number of velocity discontinuities and the extension rate. Here d (cm) is the initial distance between two velocity discontinuities.

According to the length ratio, an initial distance between the two mantle lithospheric ruptures >60 km, that is, for a distance between the two lateral detachment faults >160 km (2 C_b), should generate two pairs of grabens in nature, each symmetric/asymmetric pair being induced by the rupture in the underlying brittle mantle. The width of the two symmetric central grabens would be ~20 km. In contrast, as the initial distance between the two ruptures is <40 km, that is, where the distance between the two lateral detachment faults is <2 C_b, only two half grabens should form because the distance between them is not large enough for the symmetric graben to be initiated. Finally, between these two end-members a particular case may be defined

for which a central graben of 20 km width is shared by the two lateral half grabens. This geometry would occur where the two lithospheric ruptures are 50±10 km apart.

6. A Natural Example: The West European Rift

The west European Cenozoic rift is composed of three principal segments whose orientation is roughly parallel to the alpine front: the Eger graben in the east and the Rhinegraben and the Massif Central grabens in the west (Figure 9) [Ziegler, 1994]. Numerous seismic profiles [e.g., Morange et al., 1971; Bergerat et al., 1990; Brun et al., 1991; Zeyen et al., 1997] together with well-established geological data have unraveled the tectonic history and helped to visualize the crustal structure for the Rhinegraben and the Massif Central grabens.

6.1. Rhinegraben

The Rhinegraben is a 35-40 km wide and 300 km long linear structure which is NNE-SSW oriented and results from a near E-W extension. Geophysical data clearly show that the graben presents an asymmetry which is reversed from north to south. North to the Lalaye-Lubine-Baden-Baden Variscan fault the graben is bounded in the east by a west dipping major fault. South to the Variscan fault the main fault is east dipping, and the thickest sediment deposit is localized in the western part (Figure 10a). The Rhinegraben results from a lithospheric extension which started 40 myr ago. Between 40 and 30 Ma the evolution of the northern and southern parts was identical with a sedimentation at sea level [Sissingh, 1998] and similar subsidence rates [Villemin et al., 1986]. From the end of the Oligocene the evolution of the southern and northern parts differed. In the south
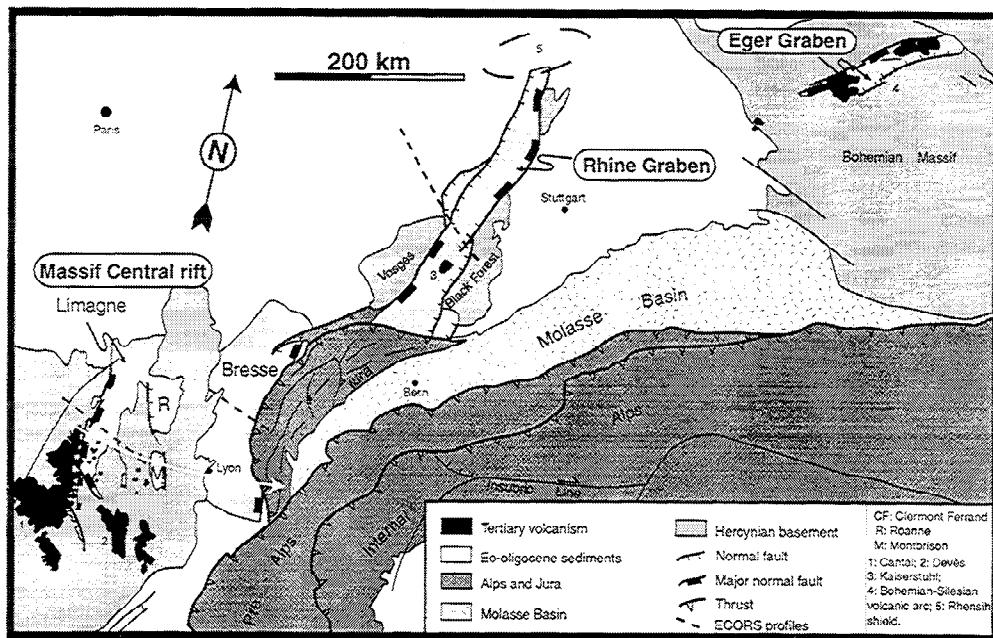

Figure 9. Geological map of the three main segments (Massif Central, Rhine, and Eger) of the west European Rift. Also shown is the location of the E-W cross section of the Massif Central (white arrow) and the three geophysical profiles including the ECORS profile in the Rhinegraben (dashed lines).
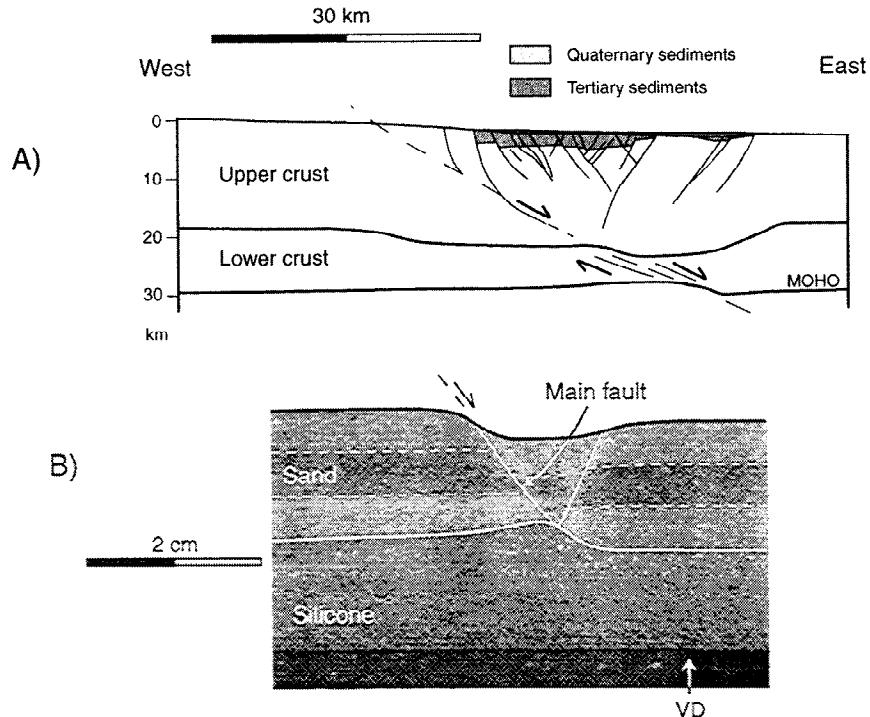
Figure 10. (a) The graben geometry of the southern part of the Rhinegraben as deduced from the ECORS profile shown on Figure 9 [modified after *Brun et al.*, 1992]. (b) Cross section in one-VD high strength ratio experiments. The half graben is bounded by a detachment fault from the surface to the velocity discontinuity at depth.

the subsidence drastically decreased, while it has continued to present in the northern part. The thickness of sediments and the crustal thinning is therefore larger in the northern than in the southern part. The sedimentation at sea level and the lack of volcanism during the rifting episode are considered as strong arguments to interpret the Rhinegraben in terms of passive rather than active rifting [e.g., *Park*, 1988; *Ruppel*, 1995].

The upper crustal stretching in the northern part deduced from the sedimentary fill is estimated between 5 and 7 km. Assuming a preservation of the volume of the crust, a total extension value of ~17 km can be estimated [*Brun et al.*, 1992]. This crustal stretching in the northern part results, on one hand, from the extension linked to the west European rift (between 40 and 30 Ma) and, on the other hand, from the Plio-Quaternary extension. This latter extensional episode is closely connected with the recent evolution of the Rhur and the southern North Sea graben [*Zijerveld et al.*, 1992; *Kooi et al.*, 1992]. In order to determine the stretching of the crust induced by the west European rift episode only, it is better to use the stretching value obtained in the southern part (12 km) [*Bois*, 1993].

The extension rate deduced for the 10 Myr Oligocene rifting episode in the southern part is close to 3.8×10^{-11} m s^{-1}. From seismic profiles the brittle/ductile thickness ratio is ~2 [*Brun et al.*, 1992]. Equations (2)-(6) allow one to calculate a strength ratio of ~88 for the southern Rhinegraben at that time. The strength ratio and the extension rate for the Rhinegraben are shown in the Figure 7. The corresponding point plots in the single half graben field.

As predicted by our experiments, the Rhinegraben geometry presents strong similarities with the half graben obtained in the high strength ratio one-VD experiments (Figure 10b). In nature and experiments the graben is bounded by a main detachment fault, and the maximum of subsidence is situated at the footstep of this fault. In experiments, many conjugate faults are created which migrate toward the graben center. In nature the first faults to be formed would be the external faults, whereas internal faults are late. We speculate that the east-dipping detachment fault remains active while many tilted blocs were formed eastward.

Experiments strongly suggest that each part of the Rhinegraben (southern and northern parts) results from a single rupture within the brittle mantle lithosphere. The Lalaye-Lubine-Baden-Baden fault is then interpreted as a transfer fault which linked the two ruptures in the brittle mantle.

6.2. The Massif Central Grabens

The Massif Central area, which is the most important segment of the west European Cenozoic rift, has been recently reinterpreted [*Merle et al.*, 1998]. The Eo-Oligocene graben structure is 180 km wide, composed of two lateral half grabens (the Limagne graben in the west and the Bresse graben in the east) and one near-symmetric, 20 km wide, central graben (the Roanne-Montbrison graben) (Figure 11a). The overall structure along an east-west cross section is bounded by the two opposing detachment faults of Limagne and Bresse lateral grabens and reveals a striking mirror symmetry on either side of the central part of the Roanne-Montbrison graben.
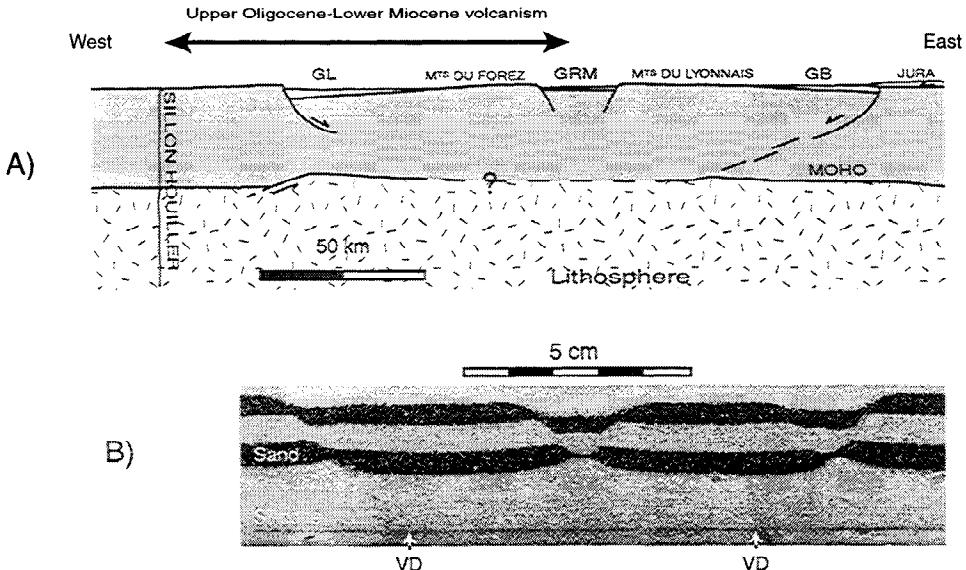
Figure 11. (a) The graben geometry of the Massif Central, which corresponds to a mirror symmetry on either side of an axis passing through the center of the central symmetric graben. The overall geometry results from upper Eocene/lower Oligocene extension. The necking of the crust revealed by seismic studies below the Limagne graben is thought to result from a late extensional stage in the upper Oligocene (see text). GL, Limagne graben; GRM, Roanne-Montbrison graben; GB, Bresse graben. (b) Cross section from a two-VD low strength ratio with an initial distance of ~5 cm between the two VD showing a similar overall symmetry. According to length scale ratio, the 20 km wide central graben in nature fits the 2 cm wide central graben in experiments.

The Massif Central grabens result from an east-west extension which lasted 10 Ma in the Oligocene time and during which each graben was filled by several hundred or thousand meters of sediments. During lower and middle Oligocene, marine incursions show that the sedimentation occurred at sea level in the Limagne and Bresse grabens [Giraud, 1902; Rat, 1984; Bodergat et al., 1999], while fluvio-lacustrian sedimentation only was recorded in the central graben of Roanne-Montbrison [Ech-Cherif El Kettani, 1996]. In the upper Oligocene this overall symmetry came to an halt. Persistence of marine incursions and sedimentation in the Limagne graben together with a lull in sediment deposits in the Roanne-Montbrison and Bresse grabens suggests that the extension became asymmetric at the scale of the whole system. During this period, crustal thinning only occurred in the western Limagne graben. This is clearly visible on geophysical profiles where crustal thinning reaches 25% in the Limagne graben whereas, it does not exceed 11% in other grabens.

We argue that the extensional process in the upper Oligocene differs from that recorded in the lower and middle Oligocene, during which the mirror symmetry of the grabens system were initiated. The more pronounced crustal and lithospheric thinning due to the upper Oligocene extension along the western part of the system is confirmed by the occurrence, from the end of the Oligocene and during lower Miocene, of a scattered volcanic phase mainly located within the Limagne graben and totally missing to the east of the Roanne-Montbrison graben (Figure 11a). As in the Rhinegraben the sedimentation at sea level, which lacks volcanic activity and was followed by a scattered volcanic

phase in the thinned area, may be interpreted in terms of passive rifting evolution [Merle et al., 1998].

The stretching value in the upper crust may be estimated from master fault geometries to be inferior to 10-15 km. As in the Rhinegraben this value is smaller than that deduced from geophysical data, which is close to 25-30 km. Again, this discrepancy can be explained by ductile flow in the lower crust during extension. Equations (2)-(4) and (6) allow an estimation of the strength ratio which ranges from 39 to 47. In contrast with the Rhinegraben, the corresponding point plots in the two grabens field on Figure 7. This strongly suggests that the whole geometry of the massif central grabens may be interpreted in terms of two-VD experiments.

Accordingly, the Massif Central grabens could result from two ruptures in the brittle mantle underlying the ductile crust. Low strength ratio would have induced the near-symmetric central graben, which is shared by the two lateral half grabens in a way similar to our experiments (Figure 5b). From the length ratio used in experiments it may be inferred that these two ruptures in the underlying brittle mantle are spaced by ~50 km (Figure 11b). Reactivation of former variscan faults could explain the distance between the two border faults (Bresse and Limagne detachment faults), which is slightly superior to that observed in experiments.

7. Conclusions

The main results of this experimental study may be summarized as follows.

1. As already proposed by some authors [e.g., Allemand, 1990;

Beslier, 1991; *Benes and Davy*, 1996), crustal-scale experiments show that the strength ratio is the key parameter which controls the geometry of the graben in rifting processes. In one-VD experiments a strength ratio value of ~65-70 (i.e., yield strength ratio) separates two deformation fields. Lower and higher strength ratio values induce either a pair of grabens or a single asymmetric graben, respectively. In two-VD experiments the extension leads to the formation of two asymmetric grabens as the strength ratio is higher than the yield strength ratio. For a strength ratio lower than the yield value the geometry and the number of grabens is a function of the initial distance between the two VD (Figure 5 and 8).

2. Variations of the thickness ratio between the brittle and ductile part of the crust have little influence on the strength ratio value, which is extremely sensitive to extension rate variations. The extension rate during extension is therefore a parameter of paramount importance in the understanding of the graben geometry.

3. Analogue modeling allows interpretation of the difference in the graben geometry observed in the Rhine and Massif Central areas. It may be inferred that the overall geometry results from (1) the number of ruptures within the brittle mantle lithosphere and (2) the difference in the extension rate. Two relatively close ruptures in the underlying brittle lithosphere as well as a high extension rate explain that three grabens formed in the Massif Central, whereas a unique rupture in the lithosphere and a low extension rate explain that a single half graben formed in the Rhine area.

References

Allemand, P., Approche expérimentale de la mécanique du rifting continental, *Mem. Doc. Geosci. Rennes*, 38, 175 p., 1990.

Allemand, P., and J.P. Brun, Width of continental rifts and rheological layering of the lithosphere, *Tectonophysics*, 188, 63-69, 1991.

Allimendinger, R., J.W. Sharp, D. Von Tish, D. Serpa, L. Brown, S. Kaufman, J. Oliver, and R.B. Smith, Cenozoic and Mesozoic structure of the eastern Basin and Range from COCORP seismic reflection data, *Geology*, 11, 532-536, 1983.

Basile, C., and J.P. Brun, Transtensional faulting patterns ranging from pull-apart basins to transform continental margins: An experimental investigation, *J. Struct. Geol.*, 21, 23-37, 1999.

Benes, V., and P. Davy, Modes of continental lithospheric extension: Experimental verification of strain localisation processes, *Tectonophysics*, 254, 69-87, 1996.

Bergerat, F., J.L. Mugnier, S. Guellec, C. Truffert, M. Cazes, B. Damotte, and F. Roure, Extensional tectonics and subsidence of the Bresse basin: An interpretation from ECORS data, *Mem. Soc. Geol. Fr.*, 156, 145-156, 1990.

Beslier, M.O., Formation des marges passives et remontée du manteau: Modélisation expérimentale et exemple de la marge de la Galice, *Mem. Doc. Geosci Rennes*, 45, 199p., 1991

Bodergat, A.M., D. Briot, M. Hugueney, J.L. Poidevin, L. Picot, F. Giraud, J.P. Berger, A Levy, and A Poignant, Incursions marines dans l'environnement lacustre du rift oligocène de Limagne (Massif Central, France): Apport des organismes halophiles et des isotopes du strontium: datations par les mammifères, *Bull Soc. Geol. Fr*, 170, 499-511, 1999.

Bois, C., Initiation and evolution of the Oligo-Miocene rift basins of Southwestern Europe: Contribution of deep seismic reflection profiling, *Tectonophysics*, 226, 227-252, 1993.

Brun, J.P., Narrow rifts versus wide rifts: Inferences for the mechanics of rifting from laboratory experiments, *Philos. Trans. R. Soc. London, Serv. A*, 357, 695-712, 1999.

Brun, J.P, and M.O. Beslier, Mantle exhumation at passive margin, *Earth Planet Sci. Lett.*, 142, 161-173, 1996.

Brun, J P., and O. Merle, Strain patterns in models of spreading-gliding nappes, *Tectonics*, 4, 7, 705-719, 1985.

Brun, J.P., F. Wenzel, and ECORS-DEKORP team, Crustal scale structure of the Southern Rhinegraben from ECORS-DEKORP seismic reflection data, *Geology*, 19, 758-762, 1991.

Brun, J.P., M.A. Gutscher, and DEKORP-ECORS teams, Deep crustal structure of the Rhine Graben from DEKORP-ECORS seismic reflection data: A summary, *Tectonophysics*, 208, 139-147,1992.

Buck, R., Modes of continental lithospheric extension, *J. Geophys. Res.*, 96, 20,161-20,178, 1991

Burg, J.P., P. Davy, and J. Martinod, Shortening of analogue models of the continental lithosphere: New hypothesis for the formation of the Tibetan Plateau, *Tectonics*, 13, 475-483, 1994.

Davison, I., M. Insley, M. Harper, P. Weston, D. Blundell, K. McClay, and A. Quallington, Physical modelling of overburden deformation around salt diapirs, *Tectonophysics*, 228, 255-274, 1993.

Davy, P., and P.R. Cobbold, P.R., Experiments on shortening of 4-layer continental lithosphere, *Tectonophysics*, 188, 1-25, 1991.

Dixon, J.M., A new method of determining finite strain in models of geological structures, *Tectonophysics*, 24, 99-114, 1974.

Ech-Cherif El Kettani, D., Géologie du fossé du Forez: Essai de synthèse et comparaison avec les autres bassins tertiaires du Massif Central français, *Ph.D. thesis, Univ. of St Etienne, St Etienne, France*, 1996.

Giraud, J., Etudes géologiques sur la Limagne (Auvergne), *Thèse d'Etat, Ed. Ch. Béranger, Paris*, 410p., 1902.

Hubbert, K.M., Theory of scale models as applied to the study of geologic structures, *Geol. Soc. Am. Bull.*, 48, 1459-1520, 1937.

Keen, C.E., and S.A. Dehler, Stretching and subsidence: Rifting of conjugate margins in the North Atlantic Region, *Tectonics*, 12, 1209-1229, 1993.

Kooi, H., M. Hettema, and S. Cloetingh, Lithospheric dynamics and the rapid Pliocene-Quaternary subsidence phase in the Southern North Sea Basin, *Tectonophysics*, 192, 245-259, 1991.

Merle, O., Cinématique et déformation de la nappe du Parpaillon, *Ph.D. thesis, Univ. of Rennes, Rennes, France*, 1982.

Merle, O., L. Michon, G. Camus, and A. Goër, L'extension oligocène sur la transversale septentrionale du rift du Massif central, *Bull. Soc. Geol. Fr.*, 169, 615-626, 1998.

Morange, A., F Heritier, and J. Villemin, Contribution de l'exploration pétrolière à la connaissance structurale et sédimentaire de la Limagne, dans le Massif Central, *Symposium J. Jung. Plein Air Service, Clermont Ferrand*, 295-308, 1971.

Park, R.G., Geological structures and moving plates, *Blackie & Son Ltd, Bishopbriggs, Glasgow*, 337p, 1988.

Rat, P., Une approche de l'environnement structural et morphologique du Pliocène et du Quaternaire bressan, *Géol. Fr.*, 3, 185-196, 1984.

Rosendhal, B.R., E. Kilembe, and K. Kaczmarick, Comparison of the Tanganyika, Malawi, Rukwa and Turkana Rift zones from analyses of seismic reflection data, *Tectonophysics*, 213, 235-256, 1992.

Ruppel, C., Extensional processes in continental lithosphere, *J Geophys Res*, 100, 24,187-24,215, 1995.

Scholz, C.H., and J.C. Contreras, Mechanics of continental rift architecture. *Geology*, 26, 967-970, 1998

Sissingh, W., Comparative Tertiary stratigraphy of the Rhine Graben, Bresse Graben and Molasse Basin: Correlation of Alpine foreland events, *Tectonophysics*, 300, 249-284, 1998.

Villemin, T., F. Alvarez, and J. Angelier, The Rhinegraben. Extension, subsidence and shoulder uplift, *Tectonophysics*, 128, 47-59, 1986.

Wernicke, B., Uniform-sense normal simple shear of the continental lithosphere, *Can. J. Earth Sci.*, 22, 108-125, 1985

Zeyen, H., O. Novak, M. Landes, C. Prodehl, L. Driard, and A. Him, Refraction-seismic investigations of the northern Massif Central (France), *Tectonophysics*, 275, 99-117, 1997.

Ziegler, P.A., Cenozoic rift system of western and central Europe: An overview, *Geol. Mijnbouw*, 73, 99-127, 1994.

Zijerveld, L., R. Stephenson, S Cloetingh, E. Duin, and M.W. Van Den Berg, Subsidence analysis and modelling of the Roer Valley Graben (SE Netherlands), *Tectonophysics*, 208, 159-171, 1992.

O. Merle and L. Michon, Laboratoire Magmas et Volcans, 5 rue Kessler, 63038 Clermont-Ferrand Cedex, France, (michon@opgc.univ-bpclermont.fr)

Annexe 7 :

Michon, L., O. Merle (2003) Mode of lithospheric extension: conceptual models from analogue modeling. *Tectonics*, 22, 4, 1028, doi:10.1029/2002TC001435.

Mode of lithospheric extension: Conceptual models from analogue modeling

Laurent Michon[1]

Netherlands Organization for Applied Scientific Research–Netherlands Institute of Applied Geoscience (TNO-NITG), Utrecht, Netherlands

Olivier Merle[2]

Laboratoire Magmas et Volcans, Université de Clermont, Clermont-Ferrand, France

[1] Comparison of analogue experiments at crustal and lithospheric scale provides essential information concerning the mode of deformation during lithospheric extension. This study shows that during extension, lithospheric deformation is controlled by the development of shear zones in the ductile parts. At lithospheric scale, the global deformation is initiated by the rupture of the brittle mantle lithosphere. This failure generates the formation of conjugate and opposite shear zones in the lower crust and the ductile mantle lithosphere. The analysis of the internal strain of the ductile layers suggests that the two opposite shear zones located below the asymmetric graben in the lower crust and the ductile mantle lithosphere prevail. Experiments show that from a similar initial stage, the relative predominance of these shear zones originates two different modes of deformation. If the crustal shear zone prevails, a major detachment-like structure crosscuts the whole lithosphere and controls its thinning. In this model named the simple shear mode, the resulting geometry shows that crustal and lithospheric thinning are laterally shifted. If the mantle shear zone predominates, the lithospheric thinning is induced by the coeval activity of the two main shear zones. This process called the necking mode leads to the vertical superposition of crustal and mantle lithospheric thinning. Applied to natural laboratories (West European rift, Red Sea rift and North Atlantic), this conceptual model allows a plausible explanation of the different geometries and evolutions described in these provinces. The North Atlantic and the Red Sea rift systems may result from a simple shear mode, whereas the necking mode may explain part of the evolution of the West European rift especially in the Massif Central and the Eger graben. *INDEX TERMS:* 8109 Tectonophysics: Continental tectonics—extensional (0905); 1744 History of Geophysics: Tectonophysics; 1645 Global Change: Solid Earth; 9335 Information Related to Geographic Region: Europe; *KEYWORDS:* lithospheric extension, analogue modeling, West European rift, Red Sea rift, passive margins. **Citation:** Michon, L., and O. Merle, Mode of lithospheric extension: Conceptual models from analogue modeling, *Tectonics*, *22*(4), 1028, doi:10.1029/2002TC001435, 2003.

1. Introduction

[2] The asymmetric feature of continental rifts has been clearly demonstrated during the past decades, whatever the origin of rifting (i.e., passive or active rifting) [e.g., *Mart and Hall*, 1984; *Bosworth*, 1985; *Brun et al.*, 1992; *Rosendahl et al.*, 1992]. Although a single passive margin presents an asymmetric geometry, conjugate and opposite margins like in the northern Atlantic (the Canadian and Iberian margins) mostly reveal a symmetric shape at the lithospheric scale [*Lister et al.*, 1991; *Brun and Beslier*, 1996]. Contrary to *McKenzie* [1978] and *Wernicke* [1981, 1985], who have respectively advocated pure shear and simple shear to interpret lithospheric deformations, *Cochran and Martinez* [1988], *Lister et al.* [1991] and *Kusznir and Ziegler* [1992] have assumed a combination of both simple and pure shear to explain these different geometries. According to these authors, crustal deformation may be controlled by low angle detachment faulting, and thinning of the mantle lithosphere may result from pure shear. Such models have been improved by *Beslier* [1991] and *Brun and Beslier* [1996] to explain the occurrence of shear zones in the mantle lithosphere [*Girardeau et al.*, 1988; *Vissers et al.*, 1995]. These authors have proposed that mantle lithospheric thinning could result from a necking of the lithosphere, generated by opposite and conjugate shear zones (Figure 5 of *Brun and Beslier* [1996]).

[3] In the present paper, we first summarize the main characteristics of several continental rifts and passive margins in order to show the different geometries resulting from extension. We have selected a number of structures which formed in different geodynamical contexts during the Mesozoic or the Cenozoic: the West European rift, the

---

[1]Also at Geologisches Institut, Universität Freiburg, Freiburg, Germany.
[2]Now at Laboratoire Magmas et Volcans, OPGC, Université Blaise Pascal, CNRS, Clermont-Ferrand, France.
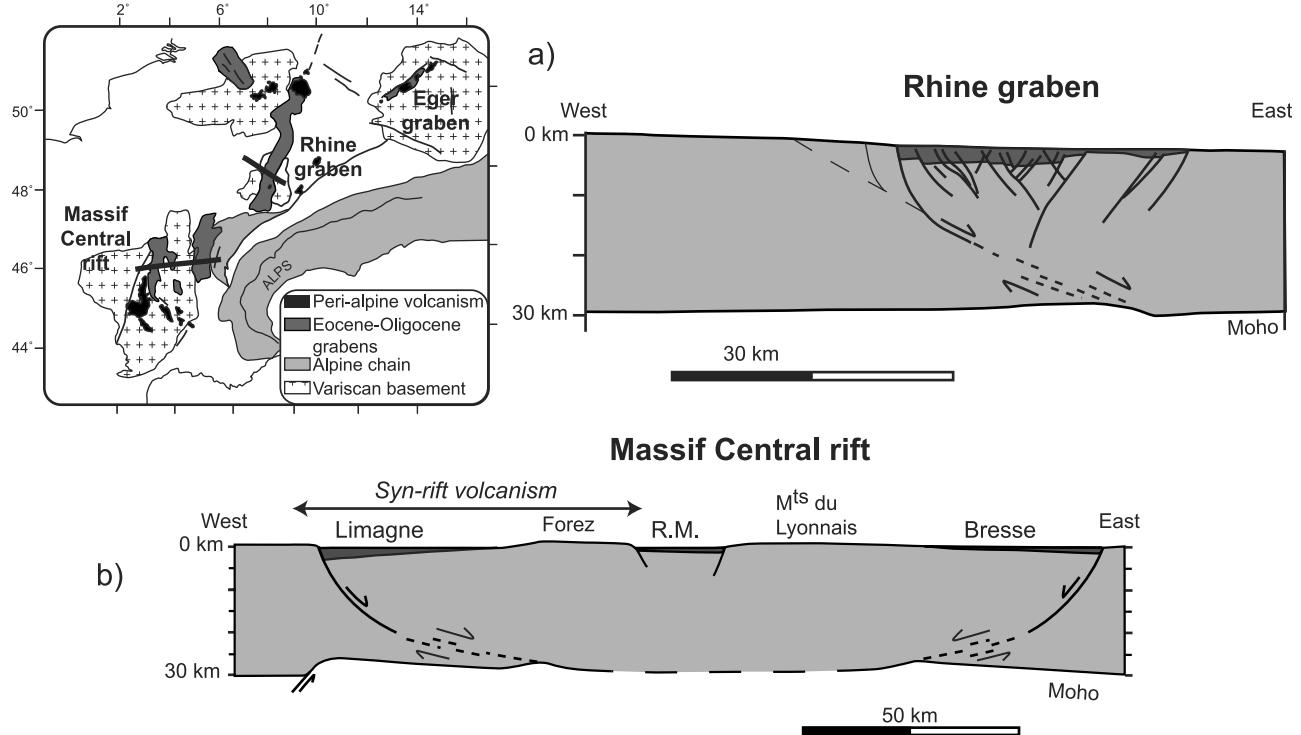
Figure 1. Synthetic geological map of the West European rift showing the Massif Central rift, the Rhine graben and the Eger graben. (a) Crustal cross section of the southern part of the Rhine graben showing the asymmetry of the graben (modified after *Brun et al.* [1992]). The master fault bounds the graben in the west and is probably connected to the Moho by a shear zone in the lower crust. (b) Crustal geometry of the Massif Central rift. The mirror symmetry revealed by the graben geometry and the Moho inflexions below the Forez and the Monts du Lyonnais results from symmetric extension between Priabonian and middle Oligocene. The development of the syn-rift volcanism in the western part of the rift and the Moho inflexion below the Limagne master fault are interpreted as the consequence of an asymmetric extension during upper Oligocene and lower Miocene.

North Atlantic passive margins and the Red Sea rift. According to the age of the continental lithosphere in each province, we assume that the vertical strength profile corresponds to a 4-layer model with two brittle high strength levels (the upper crust and the upper mantle lithosphere) and two ductile layers (the lower crust and the lower mantle lithosphere). In such a context, it has been suggested that the lithospheric deformation is initiated and controlled by failure of the brittle mantle lithosphere [*Brun and Beslier*, 1996].

[4] As the aim of this paper is to determine the process leading to continental rifts at lithospheric scale, we compare scaled analogue experiments at crustal scale [*Michon and Merle*, 2000] and lithospheric scale [*Brun and Beslier*, 1996]. In the 4-layer model, which represents the lithospheric strength profile, strain analysis of the ductile layers makes possible to define two main shear zones, which control the deformation and the thinning of the models after the boudinage of the brittle mantle lithosphere. This study shows that the simple shear mode and the necking of the lithosphere result from a similar initial evolution. Finally, we propose a model that can explain the various evolutions and geometries observed in the

West European rift, the North Atlantic passive margin and the Red Sea rift.

2. Natural Laboratories

2.1. West European Rift

[5] The West European rift is composed of three provinces extending from the Bohemian Massif in the east, through the Rhenish Province in the central part, to the Massif Central in the west (Figure 1). In all provinces, extension started contemporaneously 40 m.y. ago and led to the formation of a set of grabens and a syn-rift volcanic activity [*Michon*, 2001]. The global evolution with extension and sedimentation near sea level, closely followed in the Massif Central and the Eger graben (Bohemian Massif) by a volcanic activity, is interpreted in terms of passive rifting evolution [*Bois*, 1993; *Merle et al.*, 1998].

[6] In the Rhenish Province, the Rhine graben is a linear structure which results from W/WNW-E/ESE extension. Geophysical data clearly show that the Rhine graben is a single asymmetric graben of 35–40 km wide, which is associated with strong crustal thinning [*Brun et al.*, 1992].

In the north, the half graben is bounded in the east by a west dipping major fault. South to the Lalaye-Lubine-Baden-Baden Variscan fault, the asymmetry is reversed and the graben is limited in the west by an east dipping master fault (Figure 1a). The distribution of the depocenters close to these master faults reveals that the faults have controlled the subsidence [*Doebl and Olbrecht*, 1974; *Villemin et al.*, 1986]. From the Priabonian to the end of the middle Oligocene, a similar subsidence rate [*Villemin et al.*, 1986] and sedimentation at sea level [*Sissingh*, 1998] characterize the northern and southern parts suggesting that the amount of extension was identical at the graben scale. From the Late Oligocene, subsidence drastically decreased in the southern part whereas it was ongoing in the northern segment up to Middle Miocene. After an interruption of sedimentation during the Late Miocene, the northern Rhine graben was reactivated at the beginning of the Pliocene [*Sissingh*, 1998]. Subsidence was still active in the Pleistocene in the northern part and restarted in the southern part [*Schumacher*, 2002]. Whereas the Eocene-Oligocene rifting is clearly related to the extension of the West European rift, this latter extensional episode is closely associated with the recent evolution of the Roer Valley graben and the southern North Sea [*Kooi et al.*, 1991; *Zijerveld et al.*, 1992]. The twofold evolution of the northern part of the Rhine graben has resulted in a thicker pile of sediments and stronger crustal thinning than in the southern part. In the northern part of the Rhine graben, the stretching value deduced from the geometry of the faults in the upper crust is estimated to be in the range from 5 to 7 km. Assuming preservation of the volume of the crust, a total extension value of about 17 km can be deduced [*Brun et al.*, 1992]. In the southern part, the extension value estimated from preservation of the volume of the crust is about 12 km [*Bois*, 1993]. As it has been shown that the northern segment was affected by two distinct periods of extension, the extension value resulting from the West European rift episode only is probably about 12 km. Thus the extension rate deduced from the 10 m.y. Priabonian-Middle Oligocene rifting episode is close to 1.2 mm/yr.

[7] The Massif Central rift, which is the most important segment of the West European rift, has been recently reinterpreted [*Merle et al.*, 1998; *Michon*, 2001]. The Variscan basement is affected by a north-south 180 km wide rift composed by Eo-Oligocene grabens. Along an east-west cross section, the rift is characterized by two lateral and opposite half grabens (the Limagne graben in the west and the Bresse graben in the east) and a central and near-symmetric graben (the Roanne-Montbrison graben) (Figure 1b). Geophysical data show that the structure is bounded by the two opposite detachment faults of the Limagne and Bresse half grabens which might be connected at depth to the Moho discontinuity [*Michon*, 2001]. This overall geometry reveals a strikingly mirror symmetry on both sides of the central part of the Roanne-Montbrison graben (Figure 1b). The east-west cross section also shows asymmetrical features at the scale of the rift. The Moho inflexion below the Limagne half graben and the occurrence of a magmatic activity restricted in the western part of the rift correspond to geological characteristics which are hardly compatible with a purely symmetric evolution. The explanation can be found in the sedimentary record [*Merle et al.*, 1998]. Similar deposits in the Limagne and Bresse half grabens from the Late Eocene to the Early Oligocene together with sedimentation at sea level [*Giraud*, 1902; *Rat*, 1974; *Bodergat et al.*, 1999] suggest a symmetric extension during this period. However, in the Late Oligocene, persistence of marine incursions in the Limagne half graben and the lack of marine incursion and the lull in sediment deposits in the Bresse graben show that the overall symmetrical evolution came to a halt. During this period, crustal thinning occurred in the western Limagne graben. This is clearly established from geophysical profiles where crustal thinning reaches 25% in the Limagne graben whereas it does not exceed 13% in the Bresse graben. The asymmetric extension during the Late Oligocene is confirmed by the occurrence of a scattered magmatic activity in the Limagne half graben. Then, we interpret the mirror symmetry as resulting from the Late Eocene-Middle Oligocene symmetric extension whereas the Late Oligocene-Early Miocene evolution corresponds to an asymmetric extension located in the western part of the rift only. The stretching value deduced from master fault geometries in the upper crust is inferior to 10–15 km. However, as in the Rhine graben, this value is more than two times lower than the value estimated from geophysical data, which is close to 25–30 km [*Bois*, 1993]. Again, this discrepancy may be explained by ductile flow in the lower crust. The extension rate estimated for the Massif Central rift ranges from 2.5 to 3 mm/yr.

[8] In the Bohemian Massif, the evolution and the geometry of the Eger graben are still poorly constrained. This graben is 40–45 km wide, trending N60°E, and is bounded in the north by a main normal fault (the Krušné Hory fault), which gives to the whole structure a global asymmetry. The Priabonian age of the oldest sediments related to the extension [*Chlupac et al.*, 1984] indicates that the graben formation was coeval with the formation of the Massif Central rift and the Rhine graben. The thickness of the Late Oligocene-Middle Miocene sediments never exceeds 500–600 m and the depocenter are located close to the Krušné Hory fault suggesting (1) a small amount of extension and (2) a major role of this master fault in the graben evolution. From the Middle Oligocene (i.e., 10 m.y. ago after the onset of the extension) and up to the Middle Miocene, a syn-rift volcanic activity was located within the graben leading to the formation of large magmatic provinces [*Ulrych et al.*, 2000]. Despite the few amount of data, the formation of a single asymmetric graben and the development of a syn-rift volcanic phase within the extensional area correspond to geological information of primary importance, which can be help to determine the evolution and the deformation of the whole lithosphere.

2.2. North Atlantic Passive Margins

[9] The understanding of the North Atlantic passive margins has been largely improved by the discovery of a
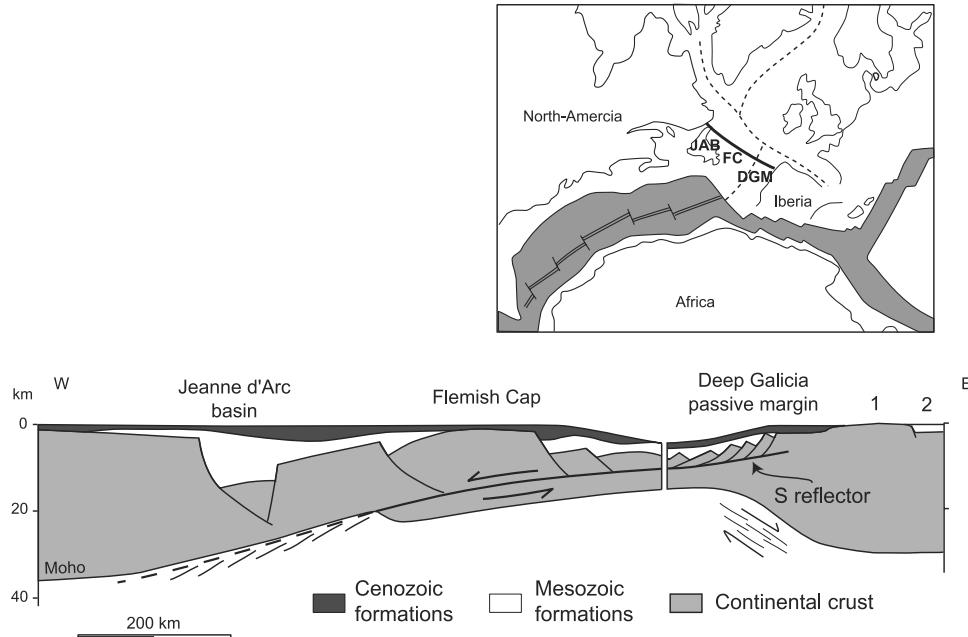
Figure 2. Reconstruction of the North Atlantic passive margin before oceanization (after *Tankard and Welsink* [1987]). In this cross section, only structures resulting from the main period of extension are represented (see text for explanation). 1: Galicia bank. 2: Interior Basin. JAB: Jeanne d'Arc Basin. FC: Flemish Cap. DGM: Deep Galicia Margin.

mantle ridge close to the ocean-continent transition zone in the Galicia passive margin [*Boillot et al.*, 1980]. At the latitude of Iberia, geophysical and tectonic studies have allowed to reconstruct the initial geometry of the rift before oceanization taking into account both Galicia and East Canadian margins (Figure 2) [*Tankard and Welsink*, 1987]. Seismic data show that the East Canadian margin is composed from west to east of a nearly symmetric graben (the Jeanne d'Arc basin) and a horst (the Flemish cap). The subsidence analysis of the Jeanne d'Arc basin reveals a main period of quick subsidence during the Late Barremian (around 120 Ma) [*Driscoll et al.*, 1995]. In the east, the Iberian margin can be divided in two different parts: the Interior Basins (Interior and Porto basins) and the Deep Galicia margin. The Interior Basins correspond to symmetric grabens of the proximal part of the margin which were active from the very beginning of the extension (i.e., Valanginian) [*Manatschal and Bernoulli*, 1999]. In contrast, the Deep Galicia margin is composed of eastward tilted blocks which yield a strongly asymmetric structure. The age of the syn-rift sediments (Hauterivian to Aptian) suggests that the extension has shifted from the Interior Basins to the Deep Galicia margin during rifting [*Manatschal and Bernoulli*, 1999]. Stretching values have been deduced for the whole period of rifting (300–350 km) [*Keen and Dehler*, 1993]. However, the multiphase extension in the North Atlantic leading to continental breakup as well as the previous extension in the Interior Basin [*Manatschal and Bernoulli*, 1999] make it difficult the estimation of the stretching value related to the main phase of rifting (Hauterivian to Albian).

[10] One of the main characteristics of the Galicia passive margin is the presence of a prominent seismic reflector, the so-called S reflector. In the Deep Galicia margin, the S reflector is located at the base of the tilted blocks and its dip evoluates from westward dipping in the east to a slightly eastward dipping close to the mantle ridge [*Boillot et al.*, 1980, 1988; *Mauffret and Montadert*, 1987]. In this area, the S reflector directly overlies the mantle ridge and seems to have merged into seafloor. Whereas the S reflector is mainly interpreted as a top-to-the-ocean low-angle detachment structure which was responsible for mantle exhumation during rifting [e.g., *Beslier et al.*, 1990; *Reston et al.*, 1996; *Manatschal and Bernoulli*, 1999], the origin and the age of a second opposite shear zone (top-to-the-continent) in the mantle peridotite is still a matter of controversy. *Boillot et al.* [1995] and *Brun and Beslier* [1996] have proposed to explain the mantle exhumation by the development of two nearly synchronous and opposite shear zones in both the lower crust and the mantle lithosphere leading to the necking of the lithosphere. According to this model, the S reflector and the mantle shear zone could correspond to the detachment structures in the lower crust and the mantle, respectively. However, using ^{40}Ar/^{39}Ar ages [*Féraud et al.*, 1988], *Manatschal and Bernoulli* [1999] have shown that the tectonic activity of the mantle shear zone is slightly older than the crustal one and have proposed that both mantle and crustal structures result from two different stages in continental extension. Whatever the exact chronology of these two detachment faults, the evolution of the syn-rift subsidence in both East Canadian and Galicia
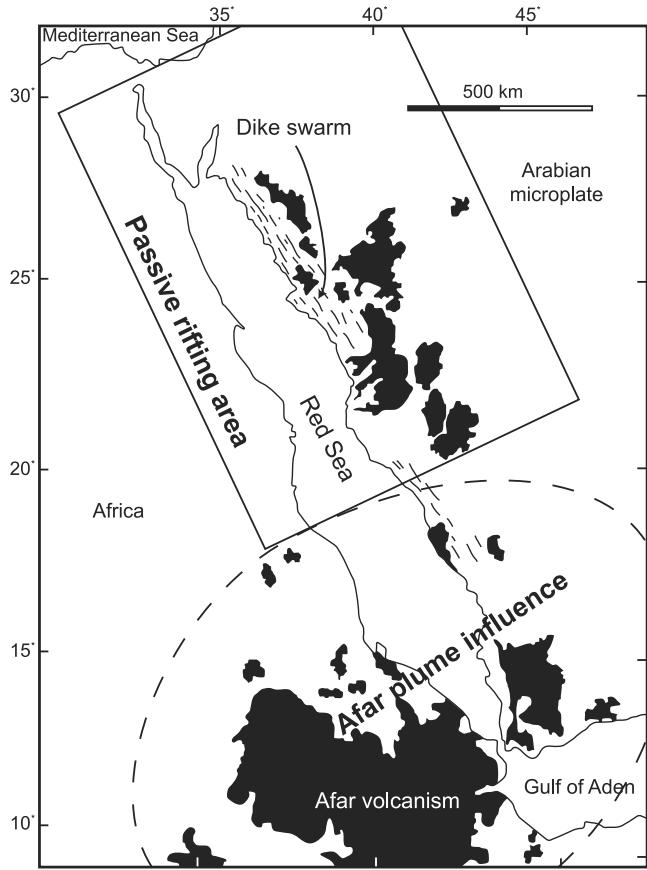
Figure 3. Geological map of the Red Sea area showing the distribution of the syn-rift volcanism on the Arabian microplate only.

opposite margins suggests that (1) maximal crustal thinning was superimposed on the two graben areas (Jeanne d'Arc basin and Deep Galicia margin) and that (2) mantle lithospheric thinning took place in the eastern part of the rift (i.e., east to the Flemish Cap) (Figure 12 of *Keen and Dehler* [1993]).

2.3. Red Sea Rift

[11] The Red Sea rift is a 1700 km length NNW-SSE oriented narrow rift which is located north to the Afar area (Figure 3). During the last decades, this rift was the subject of two main controversies. On one hand, the debate focuses on the origin of the extension (i.e., passive rifting versus active rifting) and the relation with the Afar plume [*Courtillot*, 1980; *Dixon et al.*, 1989; *Bohannon et al.*, 1989]. Recently, *Menzies et al.* [1997] have proposed that the extension in the northern Red Sea results from the northward propagation of the southern Red Sea, which is linked to the Afar plume. In their model, an active rifting origin is clearly advocated for the southern Red Sea, whereas the evolution of the northern segment can be interpreted in terms of passive rifting. On the other hand, assuming that the Red Sea rift results from a passive

rifting evolution, two opposite modes of extension have been proposed to explain the main geological and geophysical features of the area. *Wernicke* [1985] has referred to the development of a low-angle detachment structure (i.e., simple shear mode) to induce volcanism and uplift in the eastern border of the rift only (in the Saudi Arabian microplate). In contrast, *Buck et al.* [1988] have advocated a pure shear mode with an initial 110 km wide rifting area becoming narrower with time (20 km wide) to explain the present-day high and narrow heat flow in the central Red Sea. It is well worth noting that the simple shear mode is based on Eo-Miocene geological features, whereas present-day data are used to define the pure shear model. Consequently, these two modes of extension are deduced from different periods: the simple shear mode for an initial continental extension and the pure shear mode for a nearly oceanization stage.

[12] As the southern part of the Red Sea rift presents strong interactions with the Afar plume, we will summarize the main Oligo-Miocene geological features of the northern Red Sea in order to constrain the evolution of the rifting. Although the onset of the extension is not well established, *Bohanonn et al.* [1989] have suggested a normal faulting activity with sedimentation close to sea level from 23 to 29 Ma, with an increased extension rate around 25 Ma. During this period a first phase of volcanism started in the Arabian margin only. The age of the onset of magmatism is poorly constrained. K/Ar ages mainly obtained in the 1970s and 1980s suggest the occurrence of volcanism around 30–32 Ma (i.e., before extension) [*Brown et al.*, 1984]. However, several combined K/Ar and $^{40}Ar/^{39}Ar$ data have often shown strikingly differences between ages obtained with both methods suggesting that ages based on the K/Ar method must be handled with care [*Baker et al.*, 1996; *Rittmann and Lippolt*, 1998]. The oldest lava flows dated from the $^{40}Ar/^{39}Ar$ method in Saudi Arabia indicate an onset of the volcanic activity coeval with the beginning of the extension (27–28 Ma) [*Chazot et al.*, 1998]. After a lull of volcanism during several millions years, the Arabian margin was again affected by an intense magmatic phase coeval with a main period of continental rifting between 21–24 Ma [*Chazot et al.*, 1998]. This magmatism led to the formation of a 1000 km length dyke swarm parallel to the newly formed continental rift. Finally, from the Early Miocene (ca. 20 Ma), the Arabian margin was uplifted causing the present-day topographic asymmetry on either side of the Red Sea [*Bohannon et al.*, 1989]. According to many authors [e.g., *Wernicke*, 1985; *Bohannon et al.*, 1989], we consider that this general evolution of the period of continental rifting (i.e., rifting at sea level, volcanism and uplift) can be interpreted in terms of passive rifting. The overall geometry resulting from this Oligo-Miocene event reveals a strong asymmetry of the spatial distribution of magmatism and uplift restricted to the Arabian microplate. Likewise, this asymmetry can be readily seen in the seafloor topography of the Northern Red Sea (Figure 5 of *Cochran and Martinez* [1988]). The bathymetry decreases abruptly between the western shore
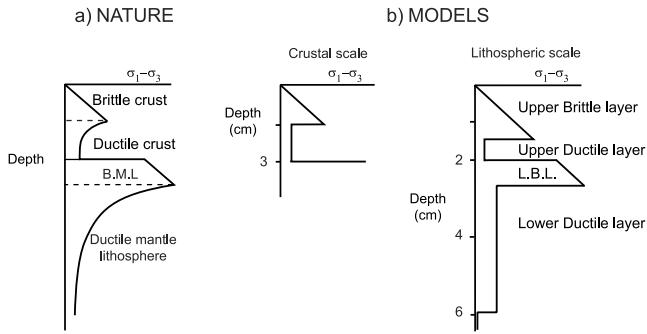
Figure 4. Strength profile (a) for a continental lithosphere with a normal thermal gradient and (b) in experiments. Sand is used to simulate the brittle parts of the lithosphere and silicone putty mimics the behavior of the lower crust and the ductile mantle lithosphere.

and the central axis of the Red Sea, whereas it gradually increases from the axial zone up to the eastern border. Contrary to the Oligo-Miocene asymmetric features, the present-day heat flow and seismicity distribution reveals a symmetric geometry [*Cochran and Martinez*, 1988; *Dixon et al.*, 1989], which could indicate a change in the rifting evolution.

[13] Although the extension rate of the northern Red Sea is fairly well estimated from the Late Miocene to the present-day (1cm/yr) [*Cochran and Martinez*, 1988], the stretching values and the extension rate are not known for the pre-Late Miocene period. Assuming that most of the extension has occurred in the past 12–14 Ma [*Le Pichon and Gaulier*, 1988], the extension rate may have been very slow during the initial period of rifting.

3. Analogue Experiments of Continental Extension

[14] In this part, we compare analogue experiments already published and carried out at crustal [*Michon and Merle*, 2000] and lithospheric scale [*Brun and Beslier*, 1996]. These

experiments resulting from independent studies, we first develop a common scaling approach defining several dimensionless numbers for the crustal and lithospheric experiments, in order to show that these experiments are properly scaled.

3.1. Experimental Background

[15] The analogue models can be compared to the natural systems if the distribution of stresses, densities and rheologies are similar in nature and experiments [*Hubbert*, 1937]. In the areas presented in the first sections of this paper, the lithosphere is assumed to have a normal thermal gradient before the rifting event. It is generally accepted [e.g., *Ranalli and Murphy*, 1987; *Buck*, 1991; *Davy and Cobbold*, 1991; *Fernandez and Ranalli*, 1997; *Burov and Poliakov*, 2001] that with such a thermal gradient (Moho-temperature less than 500°–600°C), the strength profile of the lithosphere before the rifting process is characterized from top to bottom by a brittle upper crust, a ductile lower crust, a brittle mantle lithosphere and a ductile mantle lithosphere (Figure 4a). The rheological structure of the lithosphere being highly dependent on the thermal gradient and the strain rate, this theoretical 4-layer strength profile can change during the thinning of the lithosphere with a shift of the brittle-ductile transition in the crust and the mantle lithosphere [*Davy and Cobbold*, 1991]. Experiments at lithospheric scale have been carried out with a 4-layer brittle-ductile model whereas experiments at crustal scale correspond to the upper part of the strength profile only (Figure 4b). In both experiments, the ductile and brittle behaviors of the lithosphere were simulated by silicone putty and sand layers, respectively. Although the behavior of the lithospheric ductile levels is characterized by a power law rheology, *Davy and Cobbold* [1991] have shown that the use of the silicone putty is a good approximation to simulate the lithospheric ductile parts.

[16] Numerical approaches show that the thermal regime of the lithosphere could play a major role on the mode of deformation during a rifting event [e.g., *Buck*, 1991; *Burov and Poliakov*, 2001]. The influence of the temperature

Table 1. Geometric and Mechanical Variables in Nature and Experiments at Crustal and Lithospheric Scale

Variable	Definition	Nature	Experiments		Dimensions
			Crustal Scale	Lithospheric Scale	
h_{UBL}	thickness of the upper crust (UBL)	$15-18 \times 10^3$	1.5×10^{-2}	$1.2-1.4 \times 10^{-2}$	m
h_{UDL}	thickness of the lower crust (UDL)	$12-15 \times 10^3$	1.5×10^{-2}	$0.5-0.6 \times 10^{-2}$	m
H_c	thickness of the crust (UBL + UDL)	$30-35 \times 10^3$	3×10^{-2}	$1.7-2 \times 10^{-2}$	m
H_{ML}	thickness of the mantle lithosphere (LBL + LDL)	$70-90 \times 10^3$	-	$2.3-2.8 \times 10^{-2}$	m
ρ_{UBL}	density of the upper crust (UBL)	2700	1400	1400	kg/m^3
ρ_{UDL}	density of the lower crust (UDL)	2800	1350	1100–1214	kg/m^3
ρ_{LBL}	density of the brittle mantle lithosphere (LBL)	3300	-	1400	kg/m^3
ρ_{LDL}	density of the ductile mantle lithosphere (LDL)	3300	-	1305	kg/m^3
Φ	angle of internal friction	30°	30°	30°	
μ	viscosity	1×10^{21}	3×10^4	$1.3-2.1 \times 10^4$	Pa.s
$\tau 0$	cohesion	2×10^6	1	1	Pa
ϵ	strain rate	5×10^{-15}	1.8×10^{-4}	$2.3 \times 10^{-4}-2.3 \times 10^{-3}$	s^{-1}
g	gravity acceleration	10	10	10	m/s^2

Table 2. Π Dimensionless Numbers in Nature and Experiments

Dimensionless Parameter	Definition	Nature	Experiments	
			Crustal Scale	Lithospheric Scale
Π_1	UBL/UDL thickness	$1-1.5$	1	$2.3-3$
Π_{1b}	crust/mantle lithosphere thickness	0.4	-	$0.6-0.85$
Π_2	angle of internal friction	30	30	30
Π_3	UBL/UDL density	0.96	1.04	$1.12-1.27$
Π_{3b}	LBL/LDL density	1	-	1.07
Π_4	gravitational/viscous stresses	81	37.5	$4-34.5$
Π_5	inertial/viscous stresses	3×10^{-24}	2.9×10^{-11}	$5.6 \times 10^{-9}-1.57 \times 10^{-11}$
Π_6	failure resistance/viscous stresses	31.75	15.16	$2.1-16.08$
Π_7	gravitational stress/cohesion	202.5	210	$168-196$

cannot be included directly in the analogue experiments. Nevertheless, in the experiments, a change of the thickness ratio between the brittle and ductile layers (i.e., thick upper crust and thin lower crust or thin upper crust and thick lower crust) is able to simulate different initial geotherms from an old and cold lithosphere up to a young and hot lithosphere. In addition, *Michon and Merle* [2000] have shown that the initial thermal regime of the lithosphere is a parameter that has a minor influence on the crustal deformation. Then, we consider that for the study of the first stage of a rifting process, analogue approach can be used to study the mode of deformation of the lithosphere.

[17] To guarantee similarity in nature and experiments, we define several variables related to the geometry and the properties of the materials (Table 1). The geometry of the different parts of the lithosphere is characterized by the thickness of the Upper Brittle Layer h_{UBL} (i.e., the upper crust in nature), the Upper Ductile Layer h_{UDL} (i.e., the lower crust), the whole crust H_C and the mantle lithosphere H_{ML}. Materials property variables are the density of the Upper Brittle Layer ρ_{UBL}, of the Upper Ductile Layer ρ_{UDL}, of the Lower Brittle Layer ρ_{LBL} and of the Lower Ductile Layer ρ_{LDL}. The viscosity μ of the ductile layer, and the internal angle of friction Φ and the cohesion τ_o of the brittle levels are also variables related to the materials properties. The relation between the deformation and the time corresponds to the strain rate ε. Finally, the only force is the gravity acceleration g.

[18] According to the Buckingham-Π theorem, there are 10 variables minus 3 dimensions equal to 7 independent dimensionless numbers (Table 2) that need to maintain the same value in nature and experiments. Of these, two dimensionless parameters correspond to the geometric ratios of the system:

$$\Pi_1 = \frac{h_{UBL}}{h_{UDL}}, \tag{1}$$

$$\Pi_{1b} = \frac{H_C}{H_{ML}}. \tag{2}$$

[19] In equation (1), h_{UBL} and h_{UDL} represent the thickness of the Upper Brittle Layer UBL (i.e., the brittle upper crust in nature) and the Upper Ductile Layer UDL of the system (i.e., the ductile lower crust), respectively. The second dimensionless parameter Π_{1b} is only used to scale the lithospheric experiments and corresponds to the thickness ratio between the crustal H_C and mantle lithospheric H_{ML} levels.

[20] The third dimensionless number can be defined as the frictional angle of the brittle material:

$$\Pi_2 = \Phi. \tag{3}$$

Two other dimensionless parameters must be related to the density ratio of the different layers.

$$\Pi_3 = \frac{\rho_{UBL}}{\rho_{UDL}}, \tag{4}$$

$$\Pi_{3b} = \frac{\rho_{LBL}}{\rho_{LDL}}. \tag{5}$$

[21] Π_3 defines the density ratio between the UBL and the UDL, whereas Π_{3b} allows to scale the density of the Lower Brittle Layers LBL and Lower Ductile Layers LDL in the experiments at lithospheric scale only.

[22] Knowing that gravity is balanced in the brittle materials by stresses that resist failure and in the ductile levels by inertial and viscous stresses, we define three other dimensionless parameters, which correspond to ratios of these stresses:

$$\Pi_4 = \frac{\rho g h_{UBL}}{\varepsilon \mu}, \tag{6}$$

$$\Pi_5 = \frac{\varepsilon \rho h_{UBL}^2}{\mu}, \tag{7}$$

$$\Pi_6 = \frac{2 \tan \Phi \rho g h_{UBL}}{3 \varepsilon \mu} + \tan \Phi. \tag{8}$$

[23] Equations (6), (7) and (8) represent respectively ratios between the gravitational stress and the viscous stress, the inertial stress and the viscous stress (i.e., the Reynolds

a-

b-
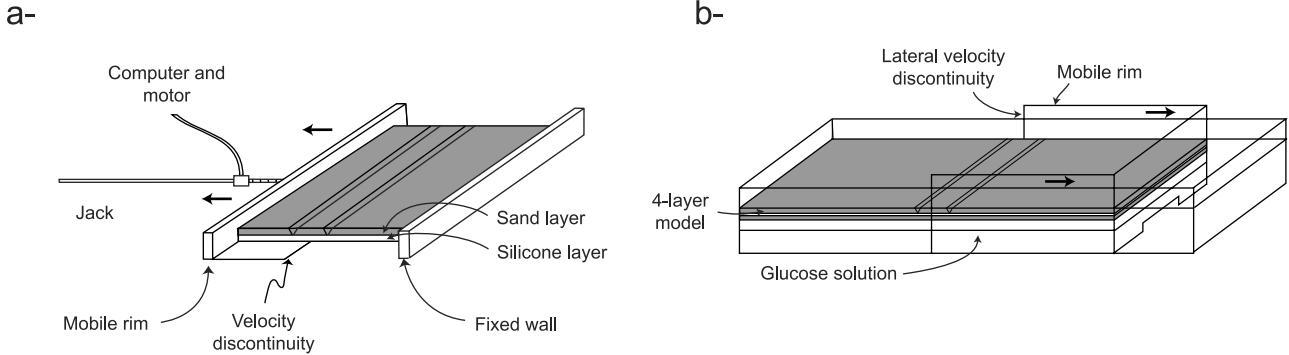
Figure 5. Experimental setup used in analogue experiments at (a) crustal and (b) lithospheric scale. Apparatus at lithospheric scale after *Brun and Beslier* [1996].

number) and the failure resistance stress and the viscous stress (see *Merle and Borgia* [1996] for details).

[24] Finally, the last dimensionless parameter corresponds to the ratio of gravitational stress to cohesion:

$$\prod_7 = \frac{\rho g h_{UBL}}{\tau_0} \qquad (9)$$

Results of equations (1), (1b), (3) and (3b) clearly show the similarity between nature and the experiments at both scales for the geometry and the density of the materials (Table 2). The angle of internal friction is the same for the sand and natural rocks (30°). Considering an average strain rate in nature (5×10^{-15} s^{-1}) and a viscosity of the lower crust of $\sim\mu = 10^{21}$ Pa s, Π_4 and Π_6 impose a strain rate in the experiments around 10^{-4}–10^{-3} s^{-1}. The very small value of Π_5 in nature (3.1×10^{-24}) shows that the inertial forces are negligible with respect to the viscous forces. In the experiments, such a low value cannot be reached even using materials with high viscosity and low density. Nevertheless, in experiments the low values of Π_5 (5.6×10^{-9}–1.57×10^{-11}) suggest that the inertial forces have also a minor importance with respect to the viscous forces. Thus this number may receive no further consideration. The last dimensionless parameter Π_7 is partly derived from the cohesion of the materials. The cohesion of intact and massive rock is considered to be $\sim10^7$ Pa [*Jaeger and Cook*, 1971]. However, it is widely accepted that the cohesion could decrease of 1 or 2 orders of magnitude for fractured rocks [e.g., *Merle et al.*, 2001]. In nature, the continental crust is generally affected by numerous faults resulting from different tectonic events (e.g. the Variscan continental crust in Europe). Then, it is reasonable to consider that the cohesion of the crust at a large scale is closer to 10^6 Pa than 10^7 Pa (Table 1). The resulting Π_7 is similar in nature and in experiments at crustal and lithospheric scale (Table 2).

[25] This scaling approach finally shows that (1) experiments carried out by independent studies [*Beslier*, 1991; *Brun*, 1999; *Michon and Merle*, 2000] can be compared and (2) the results and interpretation can be applied to natural laboratories.

[26] It has been proposed that the deformation in a lithosphere is initiated by failure in the brittle mantle lithosphere [*Allemand et al.*, 1989; *Brun and Beslier*, 1996]. In numerical modeling, such a failure is usually simulated by a preexisting weak zone in the lithosphere [e.g., *Huismans and Beaumont*, 2002]. In the analogue experiments, the rupture in the brittle mantle lithosphere was initiated by a velocity discontinuity (VD), which was forced by the border of a moving plastic sheet (Figure 5). As in the numerical approach, the VD concentrates the deformation and controls the development of the structures. At crustal scale, the VD was located at the base of the system (i.e., below the silicone layer corresponding to the lower crust), whereas it was situated on the vertical lateral boundaries of the apparatus in the experiments at lithospheric scale (Figure 5). Contrary to the analogue modeling at lithospheric scale, *Michon and Merle* [2000] have carried out experiments with one but also two VDs in order to determine the role of the number of ruptures upon crustal deformation. In experiments with one VD, the use of a vertically stratified silicone has allowed the analysis of the internal strain within the ductile layers and the determination of the highest strain zones (i.e., the shear zones).

3.2. Summary of Previous Studies

[27] Analogue experiments of continental rifting have been conducted during the last decade at crustal [*Michon and Merle*, 2000] and lithospheric scale [*Beslier*, 1991; *Brun and Beslier*, 1996; *Chemenda et al.*, 2002]. These studies have shown that major parameters control the mode of deformation and the strain during a rifting process: the extension rate and the development of shear zone in the mantle lithosphere and the crust. We summarize herein the main observations.

[28] Experiments with one VD and various extension rates show in both studies the occurrence of two deformation styles distinguished by the number of grabens. Low extension rate leads to the formation of a single half-graben on the movable part (Figure 6a). At both crustal and lithospheric scales, this asymmetric graben is bounded by a master fault in the brittle upper part, which is rooted along a slight silicone upwelling. In contrast, high extension rate

a) **Low extension rate**

b) **High extension rate**
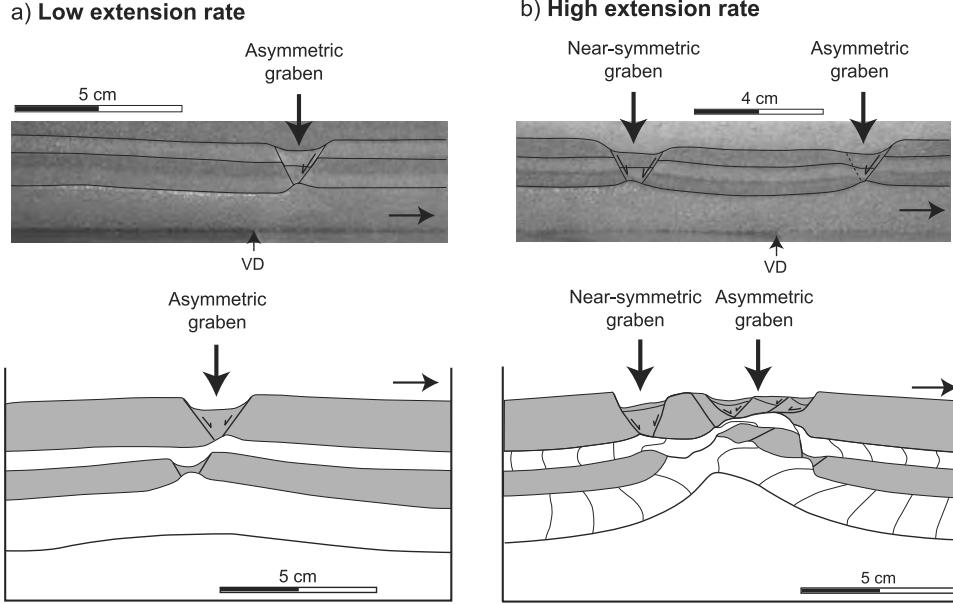
Figure 6. Comparison between experiments carried out at crustal and lithospheric scale. (a) At low extension rate the extension induces the formation of a single asymmetric graben on the movable part. (b) In contrast, a high extension rate leads to the creation of two grabens: a near-symmetric graben in the motionless part and an asymmetric graben in the movable part. Experiments at lithospheric scale after *Beslier* [1991].

generates simultaneously the formation of two parallel and linear grabens separated by a horst: a half graben on the movable part and a near-symmetric graben on the motionless part (Figure 6b). At lithospheric scale, it is worth noting that the maximum value of thinning of the analogue crustal layers is located in the central part of the asymmetric graben, whereas the analogue layers of the mantle lithosphere are mostly thinned below the border of the horst. The difference observed between the geometry of the near-symmetric and asymmetric grabens in crustal and lithospheric experiments is likely to result from the uplift of the UBL due the activity of the detachment fault and the resulting isostatic adjustment in lithospheric experiments. Whatever the extension rate, the deformation of the UBL seems to be directly linked at lithospheric scale to the rupture of the LBL or at crustal scale to the velocity discontinuity. These results indicate that a low extension rate prevents the formation of the symmetric companion graben observed in high extension rate experiments.

[29] Using a vertically stratified silicone, the internal strain of the ductile layers has also been studied at lithospheric scale in high extension rate experiments [*Brun and Beslier*, 1996]. According to these authors, extension induces the formation of two conjugate shear zones in each ductile part of the models (i.e., the LDL and the UDL), which control the thinning of the whole lithospheric model (see Figure 5 of *Brun and Beslier* [1996]). They have proposed that the mode of lithospheric extension corresponds to a necking of the lithosphere that can lead to mantle exhumation just before oceanization [*Brun and Beslier*, 1996]. It is interesting to note that *Chemenda et al.* [2002] have also determined the occurrence of litho-

spheric shear zones controlling the thinning of the models. Nevertheless, their experiments show that for an evoluate stage of extension only one lithospheric shear zone prevails mimicking the simple shear mode proposed by *Wernicke* [1981, 1985] (see Figure 5 of *Chemenda et al.* [2002]). Such a result is in disagreement with the necking model
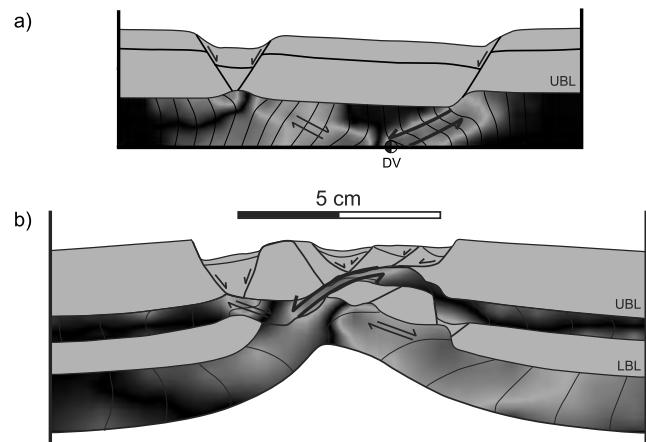
a)

b)

Figure 7. Internal strain of the silicone layers in high extension rate experiments deduced from the final geometry of the vertical markers in the silicone layers. Colors from light to dark blue indicate variations in strain intensity for the top-to-the-left shear zone whereas the yellow to red colors indicate strain intensity for the top-to-the-right shear zone (see text for explanation). See color version of this figure at back of this issue.
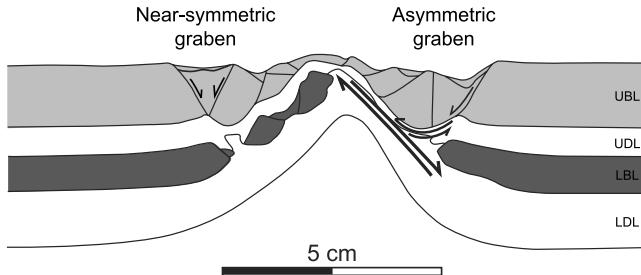
Figure 8. Cross section of an experiment at lithospheric scale characterized by a high extension rate and a nearly similar amount of extension (see text for explanation) (modified after *Brun and Beslier* [1996]).

proposed by *Brun and Beslier* [1996] where shear zone activity is coeval on both sides of the rift up to the formation of the ocean lithosphere.

3.3. New Results From the Comparison of Analogue Experiments at Crustal and Lithospheric Scale

[30] To solve the apparently different deformation at lithospheric scale, we compare the internal strain in the experiments at crustal and lithospheric scales.

[31] High extension rate experiments at crustal scale reveal that a VD always creates two conjugate shear zones in the ductile level, which are clearly related to the grabens in the UBL (see Figure 4 of *Michon and Merle* [2000]). Shear measurements also indicate that the top-to-the-left shear zone associated with the half graben always prevails with respect to the other one (Figure 7a). In contrast, the opposite shear zone, which is related to the near-symmetric graben is much less important and its activity decreases during extension.

[32] Using the same analytical approach in experiments at high extension rate, we have determined the internal strain of the silicone layers at lithospheric scale (Figure 7b). This clearly shows the occurrence of a continuous shear zone associated with the asymmetric graben which crosscuts the whole model down to the LDL. Such a shear zone is strikingly similar to the one observed in the experiments of *Chemenda et al.* [2002]. Very high shear strain is recorded in the UDL whereas strain is lower in the LDL. This major shear zone corresponds to a top-to-the-left low-angle detachment structure which controls the upwelling of the LBL. To this respect, it is interesting to note that the asymmetric shape of the glucose solution (i.e., the analogue asthenosphere) suggests that the detachment fault controls the thinning of the whole model. It is also possible to define two top-to-the-right shear zones that can be traced out in the UDL and the LDL (Figure 7a). Shear measurements deduced from the distortion of the initially vertical markers indicate that the highest shear strain along the shear zones are located below the asymmetric graben, that is in the UDL for the top-to the-left shear zone and in the LDL for the top-to-the-right shear zone. In a way similar to crustal scale experiments, the deformation concentrates along the major

detachment fault and the activity of the top-to-the-right shear zone in the UDL progressively decreases as it is suggested by the preservation of the initial geometry of the nearly symmetric graben.

[33] A second experiment at high extension rate (Figure 4a of *Brun and Beslier* [1996]) shows a different geometry at lithospheric scale. This model, conducted at an identical extension rate that the previous experiment (i.e., 5 cm/h), has been stopped at a slightly higher amount of extension (3.8 cm instead of 3.2 cm for the first experiment). The lack of vertically stratified silicone in the model does not allow the internal strain to be defined. Nevertheless, the geometry of the LBL with its uplift toward the nearly symmetric graben suggests that the deformation is controlled by the top-to-the-right shear zone located in the LDL (Figure 8). Crustal deformation is characterized by the development of a strongly asymmetric graben due to a top-to-the-left main shear zone in the UDL similar to the main shear zone observed in previous experiments. This top-to-the-left shear zone was passively deformed when the top-to-the-right shear zone became prominent (Figure 8). Thus, the total thinning of the model (i.e., mantle levels and crustal layers) is controlled by two conjugate and opposite main shear zones.

[34] In experiments at low extension rate, the internal strain of the silicone layers has not been studied in details. Nevertheless, the similar location and shape of the thinning of the silicone layer in crustal scale experiments also suggests the occurrence of two conjugate shear zones (Figure 9). We speculate that the top-to-the right shear zone in low rate experiments is not strong enough to induce the formation of a nearly symmetric graben in the UBL.

[35] All experiments suggest that a VD creates two opposite and conjugate shear zones in the ductile layers whatever the extension rate. This result is in agreement with purely brittle models in which a VD always leads to the
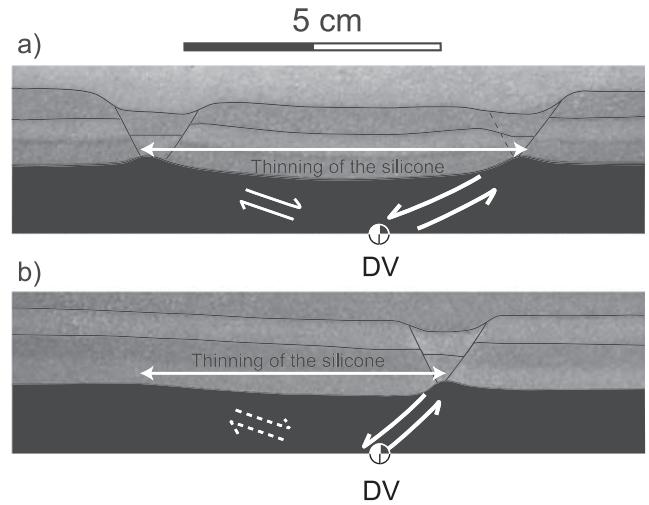

Figure 9. Comparison of the final geometry of the silicone layer in experiment at crustal scale with (a) high and (b) low extension rate. The similar shape of the thinning of the silicone layer suggests the occurrence of two conjugate shear zones in the experiments whatever the extension rate.
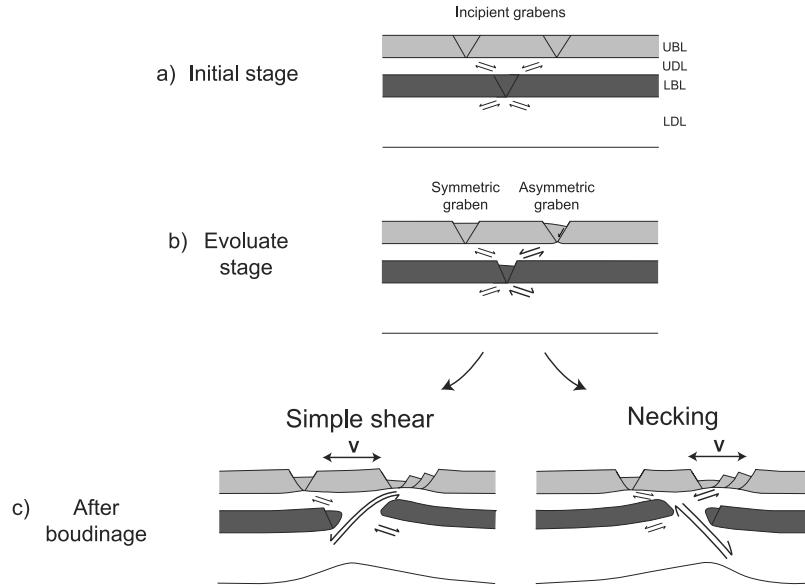
Figure 10. Synthetic evolution of the lithospheric deformation during continental rifting at high extension rates. During the initial stage of rifting, the extension induces (1) the development of conjugate shear zones in the ductile layers and (2) the formation of two incipient grabens. The evoluate stage is characterized by the predominance of two opposite shear zones located on the same vertical section. The crustal shear zone lead to the development of the asymmetric graben. When the brittle mantle lithosphere is broken out, the system can display two different mode of extension. In the necking model, the crustal shear zones control the crustal thinning and the mantle shear zone located below the asymmetric graben leads to the deformation of the mantle lithosphere. In the simple shear mode, the thinning and the deformation of the whole lithosphere is controlled by the shear zone associated with the asymmetric graben. V represents the potential location of the volcanism.

formation of two conjugate normal faults [e.g., *Faugère et al.*, 1986], and with the models of *Chemenda et al.* [2002] where the lithosphere is modeled by an elasto-plastic material. It also shows that the role of the top-to-the-right shear zone increases as a function of the extension rate.

[36] To sum up, analysis of the internal strain in the silicone layers shows (1) the development of two conjugate shear zones in each ductile level (i.e., the UDL and LDL) and (2) that the two shear zones located below the asymmetric graben predominate. Deformation of the mantle lithosphere levels in a final stage (i.e., after the boudinage of the LBL) is controlled by the shear zone located either in the UDL (Figure 7) or in the LDL (Figure 8).

4. Interpretation and Discussion

4.1. Modes of Lithospheric Extension During Continental Rifting

[37] Although analogue models at crustal and lithospheric scale have been carried out using different apparatus, the experimental results show striking similarities, proving that modeled deformation is indicative of a common tectonic process. As it has already been suggested [*Beslier*, 1991], we interpret the final geometry of crustal layers as resulting from the rupture of the brittle mantle.

[38] In high extension rate experiments, this rupture induces at the initial stage of extension a mirror symmetric deformation characterized by conjugate shear zones on both sides of the brittle mantle lithosphere (i.e., in the lower crust and the mantle ductile lithosphere) (Figure 10a). During this stage, the shear zones in the lower crust are responsible for the creation of two incipient grabens in the upper crust. This mode of extension mimics a pure shear deformation. With increasing amount of extension, this symmetric evolution stops. The activity of two shear zones is enhanced and they become prominent with respect to the two others. They are located on the same vertical section, one in the UDL and the other in the LDL (Figure 10b). The shear zone, which prevails in the UDL, induces the formation of an asymmetric graben (Figure 10b). In nature, this evolution is thought to originate the formation of an asymmetric graben (i.e. a half-graben) associated with a master normal fault in the upper brittle crust.

[39] Experiments at lithospheric scale show two different final geometries for a nearly similar amount of extension [*Brun and Beslier*, 1996]. These experiments reveal that during a later stage, the boudinage of the brittle mantle lithosphere leads to two contrasting evolutions resulting from the relative role of the main shear zones located in the lower crust and the ductile mantle lithosphere. If the UDL shear zone associated with the asymmetric graben prevails with respect to the mantle shear zone, boudinage of the brittle mantle lithosphere induces the formation of a master shear zone (i.e., a low-angle detachment structure), which crosscuts and controls the thinning of the whole lithosphere (Figure 10c left). In contrast, when the top-to-
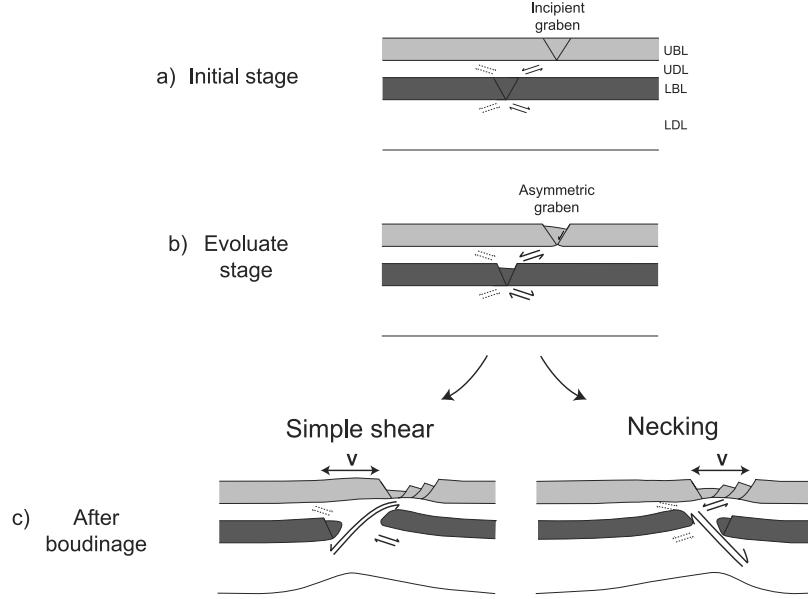
Figure 11. Synthetic evolution of the lithospheric deformation during continental rifting at low extension rates. During the initial stage of rifting, the extension induces (1) the development of conjugate shear zones in the ductile layers and (2) the formation of one incipient grabens. The evoluate stage is characterized by the predominance of two opposite shear zones located on the same vertical section. The crustal shear zone lead to the development of the asymmetric graben. When the brittle mantle lithosphere is broken out, the system can display two different mode of extension. In the necking model, the crustal shear zones control the crustal thinning and the mantle shear zone located below the asymmetric graben leads to the deformation of the mantle lithosphere. In the simple shear mode, the thinning and the deformation of the whole lithosphere is controlled by the shear zone associated with the asymmetric graben. V represents the potential location of the volcanism.

the-right shear zone located in the ductile mantle lithosphere is connected with the UDL shear zone associated with the nearly symmetric graben, the thinning of the lithosphere mainly results from the coeval activity of the two opposite and main shear zones (Figure 10c right). Thus, starting from a similar geometry before the boudinage of the brittle mantle lithosphere, extension can induce two different modes of extension: a simple shear mode which presents real similarities with the model proposed by *Wernicke* [1985], or a necking of the lithosphere as it has been described by *Brun and Beslier* [1996].

[40] In low extension rate experiments, it is assumed that during the initial stage, rupture of the brittle mantle lithosphere induces the formation of two conjugate shear zones in each ductile layer. However, experiments show that only one UDL shear zone is strong enough to initiate a graben in the upper crust. The resulting geometry defined by the set of shear zones corresponds to a mirror symmetry on both sides of the brittle mantle lithosphere (Figure 11a). As in the high extension rate evolution, subsequent deformation is controlled by the two main and opposite shear zones located in the ductile mantle lithosphere and the lower crust (Figure 11b). If the shear zone associated with the asymmetric graben prevails with respect to the mantle shear zone, a single low-angle detachment structure crosscuts the whole lithosphere when the brittle mantle lithosphere is broken out. The mode of extension then corresponds to a simple

shear mode and the maximum thinning of the crustal layers and the mantle lithospheric levels are not located on the same vertical line (Figure 11c left). If the shear zone of the ductile mantle lithosphere controls the deformation, the thinning of the different layers is vertically superposed, corresponding to the necking mode of extension (Figure 11c right).

[41] In experiments at lithospheric scale, the sand layer which represents the LBL is an isotope level without any previous fault and the difference of magnitude between the main shear zones can explain the different evolutions toward a simple shear or a necking mode. In nature, the previous history of a tectonic province can control the formation of structures at lithospheric scale. For example, an inherited structure in the brittle mantle lithosphere can be reactivated during continental extension and its geometry might favor the necking model or the simple shear mode.

[42] To sum up, the extension rate is a key parameter which controls the geometry of crustal deformation [*Michon and Merle*, 2000]. At low extension rate, extension induces the formation of a single asymmetric graben, whereas extension leads to the formation of two grabens at high extension rate. At lithospheric scale, deformation is mainly controlled by two opposite and main shear zones located below the asymmetric graben in the lower crust and the ductile mantle lithosphere. The thinning mode (i.e., simple shear or necking) is determined by the relative magnitude of

	Necking model	Simple shear mode
Low extension rate	*Eger graben*	*Red Sea rift* (Rhine graben)
High extension rate	*Massif Central Rift*	*North Atlantic passive margins*

Figure 12. Table showing the interpretation of the different provinces studied in this paper.

these two main shear zones, which may be due to the reactivation of inherited structures in the lithosphere. In both models, the thinning of the lithosphere may induce a volcanic activity by adiabatic decompression of the mantle. Volcanism should occur into the asymmetric graben with the necking mode and across the rift shoulder facing the master fault in the simple shear mode. These differences in the continental rift evolution can be considered as evidences which make possible to decipher the mode which has occurred in nature.

4.2. Application to Natural Examples

[43] In the first part of this paper, the review of the main geological features characterizing some continental rift has shown different evolutions which can exist in nature. We now apply our model to the natural laboratories in order to interpret their evolution.

4.2.1. Crustal Geometry

[44] At crustal scale, the Eger graben, the Red Sea rift and the Rhine graben correspond to single asymmetric grabens whereas major extensional structures created before oceanization in the North Atlantic passive margins (the Deep Galicia margin and the East Canadian margin) can be described as a pair of two companion grabens. We argue that these two types of basic structures result from a difference in the extension rate as already proposed by *Michon and Merle* [2000] for the Rhine graben and the Massif Central rift. This suggests that in the Eger graben and the Red Sea rift where the extension rate during the early stage of rifting is unknown, the extension rate was probably lower than in the North Atlantic passive margins (Figure 12). Using the relation between the strength ratio and the extension rate [*Michon and Merle*, 2000], an extension rate lower than 2 mm/yr can be proposed for the Eger graben and the first period of extension in the Red Sea rift. Likewise, an extension rate higher than 2 mm/yr may have induced the formation of the Deep Galicia margin and the Jeanne d'Arc basin.

[45] In the different areas (Eger graben, Red Sea rift and North Atlantic passive margins), the occurrence of one or two grabens also indicates that the crustal deformation was caused by a single rupture in the brittle mantle lithosphere. The Massif Central rift geometry could be explained by (1)

the occurrence of two simultaneous ruptures of the brittle mantle lithosphere initially spaced by around 50 km and (2) a high extension rate [*Michon and Merle*, 2000].

4.2.2. Mode of Extension

[46] In the Red Sea rift and the North Atlantic passive margins, geological data plead for a simple shear mode with the development of a main low-angle detachment structure. In the North Atlantic passive margins, such a mode of extension allows to explain (1) the predominance of the reflector S (the crustal shear zone) upon the mantle shear zone and (2) the lack of mantle lithospheric thinning below the Jeanne d'Arc basin as it has been shown by *Keen and Dehler* [1993]. Thus, the extension was mainly controlled by a single detachment structure connected with the Deep Galicia margin, which may have caused the exhumation of the lithospheric mantle before oceanization. In such a process, shifting of the extension from the Interior Basin toward the Deep Galicia margin suggests that the deformation narrows during lithospheric extension.

[47] Following *Wernicke* [1985], we consider that the asymmetric geological features resulting from the Late Oligocene-Early Miocene evolution in the Red Sea rift can be interpreted as the consequence of the activity of a single low-angle detachment structure. In contrast, the present-day data suggest that the mode of lithospheric extension which is interpreted as the result of a pure shear mode [*Buck et al.*, 1988] has changed. This indicates that the mode of extension during continental rifting probably evoluates toward a mode of extension where the pure shear deformation prevails during oceanization. At lithospheric scale, the nearly symmetric shape of opposite passive margins could therefore result from a change in the mode of extension after the onset of oceanization.

[48] Assuming that the magmatic activity appears above the zone of maximum lithospheric thinning, the occurrence of a syn-rift volcanic phase located within the graben areas in the Eger graben and the Massif Central rift cannot be explained by a simple shear mode for which the maximum of lithospheric thinning is located outside the graben. An alternative explanation is that the crust is affected by a single detachment structure, whereas the mantle lithosphere is thinned in pure shear mode (Figure 3d of *Lister et al.* [1991]). However, in this model, the mantle lithosphere is considered as purely ductile and the resulting strength profile does not correspond to the strength profile of a lithosphere with a normal thermal gradient [*Davy and Cobbold*, 1991]. In addition, experiments show that once the lithosphere is characterized by a brittle mantle layer, the rupture of this brittle part induces the development of shear zones in both the lower crust and the ductile mantle lithosphere. This is why we believe that the Eger graben and the Late Oligocene-Early Miocene evolution of the Massif Central rift result from lithospheric necking. In these provinces, necking of the lithosphere has induced a crustal thinning in the asymmetric graben and the development of a syn-rift volcanism into the graben. In the Eger graben, data at crustal scale suggest small stretching values, whereas the occurrence of the volcanic phase indicates a strong mantle lithospheric thinning. Such a paradox can be

explained by decoupling the crustal and mantle lithospheric deformations along the Moho mechanical discontinuity [*Fleitout*, 1984].

[49] Although the Rhine Graben likely results from a low extension rate [*Michon and Merle*, 2000], the mode of lithospheric extension cannot be surely constrained with available geological data as both lithospheric necking and simple shear mode can generate a single asymmetric graben. We can only speculate that the reflectors visible below the Moho and in the continuity of the major fault [*Brun et al.*, 1992] could represent a part of a continuous detachment-like structure, which crosscuts the whole lithosphere as in the simple shear mode.

[50] These conceptual models, based on analogue experiments, indicate that the extension rate and the mode of extension are the main parameters, which control the geometry of the continental rifts and passive margins. Recent numerical experiments suggest that rheological softening at lithospheric scale can also act on the symmetry of lithospheric extension, and has a complex interaction with the rate of extension [*Huismans and Beaumont*, 2002]. Also, even if our models can explain the main characteristics of several continental rifts, the role of the rheological distribution at lithospheric scale and sub-surface processes (i.e., erosion and syn-rift sedimentation) should be considered as potential parameters which can influence the geometry of deformation during continental rifting, as it has been proposed by *Burov and Cloetingh* [1997] and *Burov and Poliakov* [2001] for post-rift evolution.

5. Conclusions

[51] This study first shows that two independent sets of analogue experiments carried out at crustal [*Michon and Merle*, 2000] and lithospheric scale [*Beslier*, 1991; *Brun and Beslier*, 1996] can be compared if the models were initially properly scaled.

[52] As it has already been proposed [*Michon and Merle*, 2000], the extension rate plays a major role on the crustal deformation. Narrow rifts (single half-grabens) are formed with low extension rates whereas wider rift (two grabens) results from larger extension rate. According to *Michon and Merle* [2000], the development of more than two individual grabens (e.g., the Massif Central rift) results from several ruptures in the brittle mantle lithosphere.

[53] This study based on analogue experiments also shows an identical initial rifting stage characterized by two main shear zones, located below the asymmetric graben in the lower crust and the ductile mantle lithosphere. With increasing extension, these two main shear zones may produce a simple shear mode which shows similarities with the model proposed by *Wernicke* [1981, 1985], or a lithospheric necking as described by *Brun and Beslier* [1996]. These results allow an interpretation of the evolution of the Rhine graben, the Eger graben, the Massif Central rift, the Red Sea rift and the North Atlantic passive margins. In addition, these results could be applied to the North Sea rift where several mantle lithospheric shear zones have been identified by seismic studies [*Reston*, 1993].

[54] Finally, this study suggests an evolution of the mode of deformation during extension. The continental rifting is mainly characterized by a simple shear deformation that induces asymmetric structure in the crust. In contrast, pure shear deformation probably prevails during oceanization, explaining the global symmetry of conjugate passive margins superimposed to the asymmetry of the crustal deformation inherited from the continental rift stage.

References

Allemand, P., J.-P. Brun, P. Davy, and J. Van Den Driessche, Symetrie et asymetrie des rifts et mecanismes d'amincissement de la lithosphere, *Bull. Soc. Geol. Fr.*, *5*, 445–451, 1989.

Baker, J., L. Snee, and M. Menzies, A brief Oligocene period of flood volcanism in Yemen: Implications for the duration and rate of continental flood volcanism at the Afro-Arabian triple junction, *Earth Planet. Sci. Lett.*, *138*, 39–55, 1996.

Beslier, M. O., Formation des marges passives et remontée du manteau: Modélisation expérimentale et exemple de la marge de la Galice, *Mém. Géosci. Rennes*, *45*, 199 pp., 1991.

Beslier, M. O., J. Girardeau, and G. Boillot, Kinematics of peridotite emplacement during North Atlantic continental rifting, Galicia, northwestern Spain, *Tectonophysics*, *184*, 321–343, 1990.

Bodergat, A. M., D. Briot, M. Hugueney, J. L. Poidevin, L. Picot, F. Giraud, J. P. Berger, A. Levy, and A. Poignant, Incursions marines dans l'environnement lacustre du rift oligocène de Limagne (Massif central, France): Apport des organismes halophiles et des isotopes du strontium; datation par les mammifères, *Bull. Soc. Géol. Fr.*, *170*, 499–511, 1999.

Bohannon, R. G., C. W. Naeser, D. L. Schmidt, and A. Zimmermann, The timing of uplift, volcanism, and rifting peripheral to the Red Sea: A case for passive rifting?, *J. Geophys. Res.*, *94*, 1683–1701, 1989.

Boillot, G., S. Grimaud, A. Mauffret, D. Mougenot, J. Kornprobst, J. Mergoil-Daniel, and G. Torrent, Ocean-continent boundary off the Iberian margin: A serpentinite diapir west of the Galicia bank, *Earth Planet. Sci. Lett.*, *48*, 23–34, 1980.

Boillot, G., et al., *Proceedings of the Ocean Drilling Program: Scientific Results*, vol. 103, 858 pp., Ocean Drill. Program, College Station, Tex., 1988.

Boillot, G., M. O. Beslier, C. M. Krawczyk, D. Rappin, and T. J. Reston, The formation of passive margins: Constraints from the crustal structure and segmentation of the deep Galicia margin (Spain), in *The Tectonic, Sedimentation and Palaeoceanography of the North Atlantic Region*, edited by M. S. Stocker, G. B. Shimmlied, and A. W. Tudhope, *Geol. Soc. Spec. Publ.*, *90*, 71–91, 1995.

Bois, C., Initiation and evolution of the Oligo-Miocene rift basins of southwestern Europe: Contribution of deep seismic reflection profiling, *Tectonophysics*, *226*, 227–252, 1993.

Bosworth, W., Geometry of propagating continental rifts, *Nature*, *316*, 625–627, 1985.

Brown, G. F., D. L. Schmidt, and A. C. Huffman, Geology of the Arabian Peninsula shield area of western Saudi Arabia, *U.S. Geol. Surv. Open File Rep.*, *OF-84-0203*, 217 pp., 1984.

Brun, J. P., Narrow rifts versus wide rifts: Inferences for the mechanics of rifting from laboratory experiments, *Philos. Trans. R. Soc. London, Ser. A*, *357*, 695–712, 1999.

Brun, J. P., and M. O. Beslier, Mantle exhumation at passive margin, *Earth Planet. Sci. Lett.*, *142*, 161–173, 1996.

Brun, J. P., M. A. Gutscher, and DEKORP-ECORS Teams, Deep crustal structure of the Rhine Graben from DEKORP-ECORS seismic reflexion data: A summary, *Tectonophysics*, *208*, 139–147, 1992.

Buck, W. R., Modes of continental lithospheric extension, *J. Geophys. Res.*, *96*, 20,161–20,178, 1991.

Buck, W. R., F. Martinez, M. S. Steckler, and J. R. Cochran, Thermal consequences of lithospheric extension: Pure and simple, *Tectonics*, *7*, 213–234, 1988.

Burov, E., and S. Cloetingh, Erosion and rift dynamics: New thermomechanical aspects of post-rift evolution of extensional basins, *Earth Planet. Sci. Lett.*, *150*, 7–26, 1997.

Burov, E., and A. Poliakov, Erosion and rheology controls on synrift and postrift evolution: Verifying old and new ideas using a fully coupled numerical model, *J. Geophys. Res.*, *106*, 16,461–16,481, 2001.

Chazot, G., M. A. Menzies, and J. Baker, Pre-, syn- and post-rift volcanism on the south-western margin of the Arabian plate, in *Sedimentation and Tectonics of rift Basins*: *Red-Sea-Gulf of Aden*, edited by B. H. Purser and D. W. J. Bosence, pp. 50–55, Chapman and Hall, New York, 1998.

Chemenda, A., J. Deverchere, and E. Calais, Three-dimensional laboratory modelling of rifting: Application to the Baikal rift, Russia, *Tectonophysics*, *356*, 253–273, 2002.

Chlupac, I., O. Kodym, M. Suk, V. Holub, M. Elias, I. Cicha, M. Malkovsky, J. Tyracek, E. Mencyk, and T. Buday, Stratigraphic development of the units, in *Geological History of the Territory of the Czech Socialist Republic*, edited by M. Suk et al., pp. 87–200, Geol. Surv., Prague, 1984.

Cochran, J. R., and F. Martinez, Evidence from the northern Red Sea on the transition from continental to oceanic rifting, *Tectonophysics*, *153*, 25–53, 1988.

Courtillot, V. E., Opening of the Gulf of Aden and Afar by progressive tearing, *Phys. Earth Planet. Inter.*, *21*, 343–350, 1980.

Davy, P., and P. R. Cobbold, Experiments on shortening of a 4-layer model of the continental lithosphere, *Tectonophysics*, *188*, 1–25, 1991.

Dixon, T. H., E. R. Ivins, and B. J. Franhlin, Topographic and volcanic asymmetry around the Red Sea: Constraints on rift models, *Tectonics*, *8*, 1193–1216, 1989.

Doebl, F., and W. Olbrecht, An isobath map of the Tertiary base in the Rhine graben, in *Approaches to Taphrogenesis*: *Proceedings of an International rift Symposium Held in Karlsruhe*, edited by J. H. Illies and K. Fuchs, pp. 71–72, Schweizerbart, Stuttgart, Germany, 1974.

Driscoll, N. W., J. R. Hogg, N. Cristie-Blick, and G. Karner, Extensional tectonics in the Jeanne d'Arc Basin, offshore Newfoundland: Implications for the timing of the break-up between Grand Banks and Iberia, in *The Tectonic, Sedimentation and Palaeoceanography of the North Atlantic Region*, edited by M. S. Stocker, G. B. Shimmlied, and A. W. Tudhope, *Geol. Soc. Spec. Publ.*, *90*, 1–28, 1995.

Faugère, E., J. P. Brun, and J. van dan Driessche, Bassins asymétriques en extension pure et en décrochement: Modèles expérimentaux, *Bull. Cent. Rech. Explor. Prod. Elf Aquitaine*, *10*, 13–21, 1986.

Féraud, G., J. Girardeau, M. O. Beslier, and G. Boillot, Datation ³⁹Ar/⁴⁰Ar de la mise en place des peridotites bordant la marge de la Galice (Espagne), *C. R. Acad. Sci. Paris*, *307*, 49–55, 1988.

Fernandez, M., and G. Ranalli, The role of rheology in extensional basin formation modeling, *Tectonophysics*, *282*, 129–145, 1997.

Fleitout, L., Modélisation des contraintes tectoniques et des instabilités thermo-mécaniques dans la lithosphère, Thèse d'état, 433 pp., Univ. Orsay, France, 1984.

Girardeau, J., C. A. Evans, and M. O. Beslier, Structural analysis of plagioclase-bearing peridotites emplaced at the end of continental rifting: Hole 637A, ODP Leg 103 on Galicia margin, *Proc.*

Ocean Drill. Program Sci. Results, *103*, 209–223, 1988.

Giraud, J., Etudes géologiques sur la Limagne (Auvergne), Thèse d'état, 410 pp., Ed. Ch. Béranger, Paris, 1902.

Granet, M., S. Judenherc, and A. Souriau, Des images du système lithosphère-asthénosphère sous la France et leurs implications géodynamiques: L'apport de la tomographie télésismique et de l'anisotropie sismique, *Bull. Soc. Géol. Fr.*, *171*, 149–167, 2000.

Hubbert, K. M., Theory of scale models as applied to the study of geologic structures, *Geol. Soc. Am. Bull.*, *48*, 1459–1520, 1937.

Huismans, R. S., and C. Beaumont, Asymmetric lithospheric extension: The role of frictional plastic strain softening inferred from numerical experiments, *Geology*, *30*, 211–214, 2002.

Jaeger, J. C., and N. G. W. Cook, *Fundamental of Rock Mechanics*, 585 pp., Chapman and Hall, New York, 1971.

Keen, C. E., and S. A. Dehler, Stretching and subsidence: rifting of conjugate margins in the North Atlantic Region, *Tectonics*, *12*, 1209–1229, 1993.

Kooi, H., M. Hettema, and S. Cloetingh, Lithospheric dynamics and the rapid Pliocene-Quaternary subsidence phase in the Southern North Sea Basin, *Tectonophysics*, *192*, 245–259, 1991.

Kusznir, N. J., and P. A. Ziegler, The mechanics of continental extension and sedimentary basin formation: A simple-shear/pure-shear flexural cantilever model, *Tectonophysics*, *215*, 117–131, 1992.

Le Pichon, X., and J. M. Gaulier, The rotation of Arabia and the Levant Fault System, *Tectonophysics*, *153*, 271–294, 1988.

Lister, G. S., M. A. Etheridge, and P. A. Symonds, Detachment models for the formation of passive continental margins, *Tectonics*, *10*, 1038–1064, 1991.

Manatschal, G., and D. Bernoulli, Architecture and tectonics evolution of nonvolcanic margins: Present-day Galicia and ancient Adria, *Tectonics*, *18*, 1099–1119, 1999.

Mart, Y., and J. K. Hall, Structural trends in the northern Red Sea, *J. Geophys. Res.*, *89*, 11,352–11,354, 1984.

Mauffret, A., and L. Montadert, Rift tectonics on the passive continental margins off Galicia (Spain), *Mar. Pet. Geol.*, *4*, 49–70, 1987.

McKenzie, D., Some remarks on the development of sedimentary basins, *Earth Planet. Sci. Lett.*, *40*, 25–42, 1978.

Menzies, M., J. Baker, G. Chazot, and M. Al'Kadasi, Evolution of the Red sea volcanic margin, Western Yemen: Large igneous provinces, in *Continental, Oceanic, and Planetary Flood Volcanism, Geophys. Monogr. Ser.*, vol. 100, edited by J. Mahoney and M. Coffin, pp. 29–43, AGU, Washington, D. C., 1997.

Merle, O., and A. Borgia, Scaled experiments of volcanic spreading, *J. Geophys. Res.*, *101*, 13,805–13,817, 1996.

Merle, O., L. Michon, and G. Camus, L'extension oligocène sur la transversale septentrionale du rift du Massif Central, *Bull. Soc. Géol. Fr.*, *169*, 615–626, 1998.

Merle, O., N. Vidal, and B. Van Wyk de Vries, Experiments on vertical basement fault reactivation below volcanoes, *J. Geophys. Res.*, *106*, 2153–2162, 2001.

Michon, L., Dynamique de l'extension continentale-Application au rift Ouest-Européen par l'étude de

la province du Massif Central, *Mém. Géosci. Rennes*, *99*, 266 pp., 2001.

Michon, L., and O. Merle, Crustal structures of the Rhinegraben and the Massif Central grabens: An experimental approach, *Tectonics*, *19*, 896–904, 2000.

Ranalli, G., and D. C. Murphy, Rheological stratification of the lithosphere, *Tectonophysics*, *132*, 281–296, 1987.

Rat, P., Le système Bougogne-Morvan-Bresse (articulation entre le bassin parisien et le domaine péri-alpin), in *Géologie de la France*: *Les Chaînes Plissées du Cycle Alpin et Leur Avant-Pays*, edited by J. Debelmas, pp. 480–500, Doin, Paris, 1974.

Reston, T. J., Evidence for extensional shear zones in the mantle, offshore Britain, and their implications for the extension of the continental lithosphere, *Tectonics*, *12*, 492–506, 1993.

Reston, J. T., C. M. Krawczyk, and D. Klaeschen, The S reflector west of Galicia (Spain): Evidence from prestack depth migration for detachment faulting during continental breakup, *J. Geophys. Res.*, *101*, 8075–8091, 1996.

Rittmann, U., and H. J. Lippolt, Evidence for distortion of Tertiary K/Ar ages by excess argon-example given by three alkali olivine basalts from Northern Hesse, Germany, *Eur. J. Mineral.*, *10*, 95–110, 1998.

Rosendahl, B. R., E. Kilembe, and K. Kaczmarick, Comparison of Tanganyika, Malawi, Rukwa and Turkana rift zones from analyses of seismic reflection data, *Tectonophysics*, *213*, 235–256, 1992.

Schumacher, M., Upper Rhine Graben: Role of preexisting structures during rift evolution, *Tectonics*, *21*(1), 1006, doi:10.1029/2001TC900022, 2002.

Sissingh, W., Comparative Tertiary stratigraphy of the Rhine Graben, Bresse Graben and Molasse Basin: Correlation of Alpine foreland events, *Tectonophysics*, *300*, 249–284, 1998.

Tankard, A. J., and H. J. Welsink, Extensional tectonics and stratigraphy of Hiberia Oil Field, Grand Banks, Newfoundland, *AAPG Bull.*, *71*, 1210–1232, 1987.

Ulrych, J., V. Cajz, E. Pivec, J. K. Novak, C. Nekovarik, and K. Balogh, Cenozoic intraplate alkaline volcanism of western Bohemia, *Stud. Geoph. Geod.*, *44*, 346–351, 2000.

Villemin, T., F. Alvarez, and J. Angelier, The Rhinegraben: Extension subsidence and shoulder uplift, *Tectonophysics*, *128*, 47–59, 1986.

Vissers, R. L. M., M. R. Drury, E. H. Hogerduijn Strating, C. J. Spiers, and D. van der Wal, Mantle shear zones and their effect on lithosphere strength during continental breakup, *Tectonophysics*, *249*, 155–171, 1995.

Wernicke, B., Low-angle normal faults in the Basin and Range Province: Nappe tectonics in an extending orogen, *Nature*, *291*, 645–648, 1981.

Wernicke, B., Uniform-sense normal simple shear of the continental lithosphere, *Can. J. Earth Sci.*, *22*, 108–125, 1985.

Zijerveld, L., R. Stephenson, S. Cloetingh, E. Duin, and M. W. van den Berg, Subsidence analysis and modelling of the Roer Valley Graben (SE Netherland), *Tectonophysics*, *208*, 159–171, 1992.

———————

O. Merle, Laboratoire Magmas et Volcans, OPGC, Université Blaise Pascal, CNRS, F-63038 Clermont-Ferrand cedex, France.

L. Michon, Netherlands Organization for Applied Scientific Research–Netherlands Institute of Applied Geoscience (TNO-NITG), P.O. Box 80015, NL-3508 TA Utrecht, Netherlands. (l.michon@nitg.tno.nl)
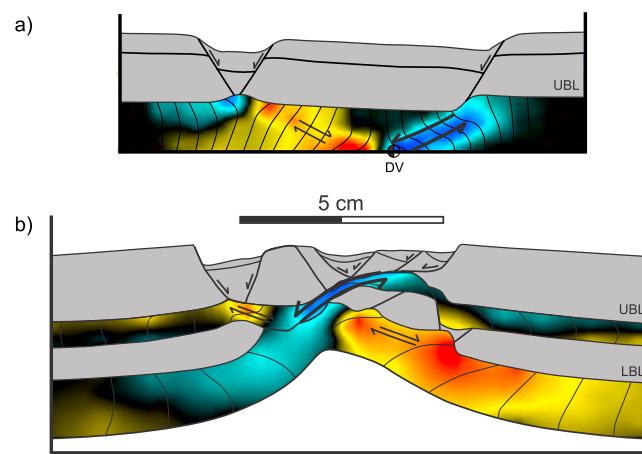
Figure 7. Internal strain of the silicone layers in high extension rate experiments deduced from the final geometry of the vertical markers in the silicone layers. Colors from light to dark blue indicate variations in strain intensity for the top-to-the-left shear zone whereas the yellow to red colors indicate strain intensity for the top-to-the-right shear zone (see text for explanation).

Annexe 8 :

Michon, L., D. Sokoutis (2005) Interaction between the structural inheritance and the stress field during graben and depocentre formation: new insights from an experimental approach. *Tectonophysics*, 409, 125-146.

Interaction between structural inheritance and extension direction during graben and depocentre formation: An experimental approach

Laurent Michon [a,*], Dimitrios Sokoutis [b]

[a] LSTUR, UMR 7154, Université de la Réunion, IPGP, BP7151, 97715 Saint Denis cedex 9, France
[b] Netherlands Centre for Integrated Solid Earth Science, Vrije Universiteit Amsterdam, De Boelelaan 1085, 1081 HV Amsterdam, the Netherlands

Abstract

Analysis of structural rift architecture shows that the graben formation is commonly controlled by the contemporaneous activity of two fault trends with an angular obliquity of approximately 40°. Inspection of the crustal basement and geophysical data reveals that these faults are parallel to inherited oblique crustal and lithospheric discrete fabrics, which are reactivated during the extension event. We conducted experiments at crustal scale to determine the role of the coeval reactivation of such oblique inherited fabrics in the graben and depocentre development. Experimentally the oblique inherited lithospheric faults were simulated by a basal discrete velocity discontinuity (VD) characterised by two different angles (α) with respect to the extension direction at the intersection of the VDs. Our models show that besides the extension direction which induces the formation of linear or independent en-echelon grabens, the intersection of the two oblique VD segments controls the location of the depocentre and concentrates subsidence. For different stretching direction values, the depocentre geometry varies from strongly asymmetric to symmetric when the stretching direction corresponds to the bisecting line of the two VD segments. Applied to the Upper Rhine graben (central segment of the West European rift), our models allow interpretation of the development of the Late Eocene–Oligocene depocentres at the intersection of two main oblique inherited structures, as the result of a constant NW–SE extension direction. Concerning the southern East African rift, the graben geometries and the evolution of the subsidence during the Mio-Pliocene period may be explained by the reactivation of two main Pan-African inherited shear zones with an E–W direction of extension.
© 2005 Elsevier B.V. All rights reserved.

Keywords: Analogue modelling; Extension; Depocentre; Rhinegraben; Tanganyika

1. Introduction

The major role of geological inheritance on graben formation has been recognised in many rifts for the past decades (e.g., Illies, 1981; Ring, 1994; Bonini et al., 1997; Schumacher, 2002). Graben faults are often superimposed on pre-existing crustal structures as in the Pan-African mountain belts of East Africa (McConnell, 1972; Ring, 1994; Lezzar et al., 2002), the Variscan main faults of the West European rift (Schumacher, 2002; Michon et al., 2003), and the Caledonian paleo-rifts and suture zones of the North Sea rift (Færseth et al., 1997; Rey et al., 1997). In the northern Lake Tanganyika rift, initial subsidence was controlled by reactivated Pan-African faults and the orientation of the two main fault trends which is parallel to the Pan-African belts (Lezzar et al., 2002) (Fig. 1a). In Cenozoic rifts of the French Massif

* Corresponding author. Tel.: +262 262 93 82 04.
  E-mail address: laurent.michon@univ-reunion.fr (L. Michon).
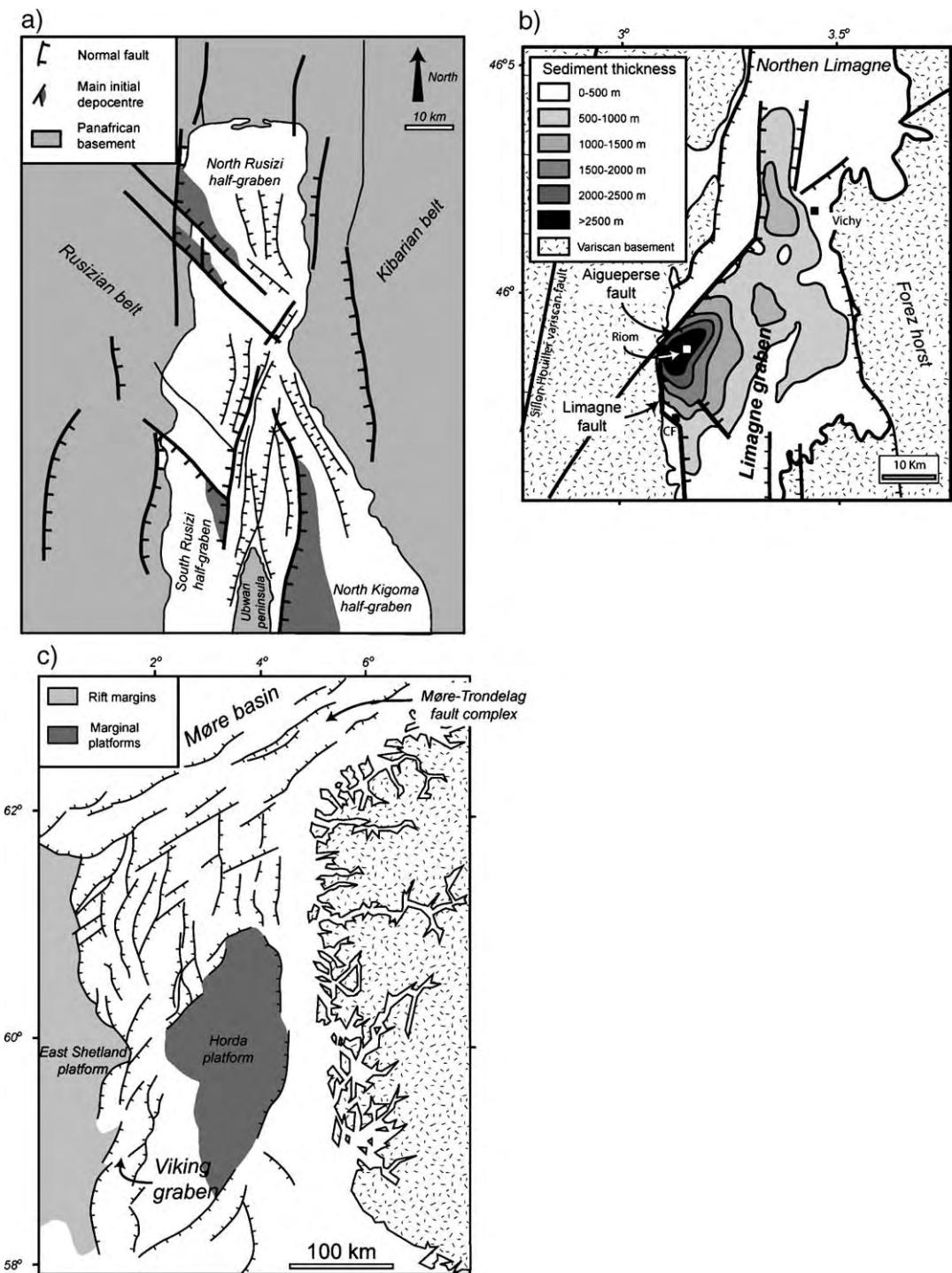
Fig. 1. (a) Simplified geological map of the northern segment of the Lake Tanganyika rift showing the location of the initial depocentres at the intersection of two main fault trends (after Lezzar et al., 2002). (b) Isopach map of the Late Eocene–Oligocene sediments in the Limagne graben (French segment of the West European rift). The maximum sedimentation appears at the intersection of the Aigueperse and Limagne faults (modified after Morange et al., 1971). (c) Structural map of the Viking graben and surrounding area showing the two main fault trends resulting from the reactivation of pre-existing faults (after Færseth et al., 1997).

Central (main segment of the West European rift), extension has reactivated the Variscan faults and the depocentre formed at the intersection of two main faults (Michon, 2001) (Fig. 1b). In the North Sea, the Caledonian inheritance played a major role on the development of the Viking graben and the Møre basin (Færseth et al., 1997) (Fig. 1c). In the Ethiopian rift, the occurrence of the two directions of faults was interpreted in terms of multistage rifting with two different extension directions (Bonini et al., 1997). However, the development of depocentres at the intersection of the two faults suggest, in many cases, a coeval fault history (Færseth et al., 1997; Lezzar et al., 2002; Schumacher, 2002; Michon et al., 2003).

Although these provinces were affected by distinct pre-extension histories with successive compression phases that developed several trends of crustal faults, they present a striking similarity, common to other rift systems: extension has reactivated only two main crustal fault trends with an angular difference of around 40° (Table 1). The geological origin of such an angle value is hard to explain. Indeed, the two 40° oblique trends do not correspond to the two fault orientations that affect the basement in the different areas. It also does not correspond to the theoretical value of around 60° between two conjugated fault trends formed during a compressive event. When successive deformation events occur the previously formed faults are reactivated as long as the stress field slightly differ from the previous ones. This reactivation prevents the formation of any new main fault in angle domains close to the

inherited fault. So, we consider that the 40° value corresponds to the minimum angle value between two main non-coeval fault zones.

The role of orthogonal and oblique extension has already been studied experimentally using brittle–ductile (Tron and Brun, 1991) or purely brittle models (McClay and White, 1995; McClay et al., 2002), and mainly linear discontinuities. The main result is that oblique extension leads to the formation of en-echelon grabens and intra-rift sub-basins, whereas linear grabens develop with orthogonal extension. Furthermore Bellahsen and Daniel (2005) recently show with brittle–ductile models that crustal pervasive and discrete fabrics, oblique to the stretching direction entails the development of grabens presenting two oblique directions. Although crustal inheritance plays a role in the graben geometry (Morley, 1999; Bellahsen and Daniel, 2005), it is widely accepted that lithospheric faults (i.e., discrete lithospheric structures) strongly control the development of structures in the crust (e.g., Davy and Cobbold, 1991; Brun and Beslier, 1996). As extension usually leads to reactivation of preexisting intersecting lithospheric fabrics, brittle–ductile experiments were carried out at crustal scale in which the intersecting lithospheric inheritance is simulated by a basal velocity discontinuity presenting two different orientations. Such a set up enables us to determine (1) the role of oblique lithospheric fabrics in the development of a graben and its related depocentres, (2) the effect of extension direction on the graben and depo-

Table 1
Obliquity of the main fault trends in several rift systems

Area	Main fault orientation	Angular difference	Reference
Northern Lake Tanganyika rift, EAR	Graben border fault (N0) and the "Rusizian" faults (N130-140)	45°	Lezzar et al., 2002
Ethiopian rift, EAR	Graben border faults (N10 and N45)	35°	Bonini et al., 1997
Upper Rhine graben, WER	Graben border fault (N20) and the LB transfer fault (N55)	35°	Schumacher, 2002
Limagne graben, WER	Graben border fault (N0) and the Aigueperse fault (N40)	40°	Michon, 2001
Roer Valley rift system, WER	Feldbiss (N150) and Veldhoven (N110) faults	40°	Michon et al., 2003
Gulf of Lion, NW Mediterranean rift	Nimes fault (N55) and N20 main orientation	35°	Seranne, 1999
Viking graben, North Sea	Graben border fault (N5) and N50 main orientation	45°	Færseth et al., 1997
Rio Grande rift, USA	The graben border fault (N0) and the Tijeras fault zone (N45)	45°	Baldridge et al., 1995
	Average angular difference	40°	

LBF: Lalaye–Lubine–Baden Baden transfer fault. EAR: East African Rift, WER: West European Rift.

centre geometry, and (3) the interaction between linear and en-echelon grabens.

2. Experimental background

2.1. Scaling

Small-scale crustal models are similar to natural system if the distribution of stresses, densities and rheologies are equivalent in nature and in experiments (Hubbert, 1937; Ramberg, 1981). It is widely accepted that a continental lithosphere with a normal thermal gradient is characterised by a 4-layer strength profile with two brittle layers (the upper crust and the brittle mantle lithosphere) and two ductile levels (the lower crust and the ductile mantle lithosphere) (e.g., Davy and Cobbold, 1991) (Fig. 2a). Analogue experiments suggest that during a rifting episode, the crustal deformation is initiated by a failure in the brittle mantle lithosphere (Allemand, 1990; Brun and Beslier, 1996). During the process of rifting crustal deformation is controlled by the coupling between the upper and lower crust (Allemand, 1990; Brun, 1999), and rate of extension (Michon and Merle, 2000). To take into account the role of this coupling, Michon and Merle (2000) have developed a scaling approach defining a strength ratio between the brittle (S_B) and ductile (S_D) layers. Similar scaling method is used in the present work to facilitate the comparison between our results and those obtained with a linear and continuous discontinuity at the base of the system (Michon and Merle, 2000).

The strength ratio being a dimensionless number, it must be of the same order of magnitude in model and nature (Eq. (1)):

$$\left(\frac{S_B}{S_D}\right)_{Model} = \left(\frac{S_B}{S_D}\right)_{Nature}. \tag{1}$$

In brittle materials, the strength S_B is defined as the differential stress $\sigma_1 - \sigma_3$; σ_1 and σ_3 corresponding to the maximum and minimum principal stresses, respectively. σ_1 can be expressed as a linear function of depth h_B (with gravity acceleration g and density ρ), or σ_3 (with a and b parameters depending of the angle of friction ϕ and the cohesion τ_0) (Eqs. (2)–(4))

$$\sigma_1 = a + b\sigma_3 = \rho g h_B, \tag{2}$$

where,

$$a = 2\tau_0 \sqrt{b}, \tag{3}$$

$$b = \frac{1 + \sin\phi}{1 - \sin\phi}, \tag{4}$$

In a rifting context with vertical σ_1, the strength of the brittle crust is then expressed as (Eq. (5))

$$S_B = \sigma_1 - \sigma_3 = \rho g h_B - \left(\frac{\rho g h_B - a}{b}\right). \tag{5}$$

In experiments where a cohesionless material is used, Eq. (5) simplifies to (Eq. (6)):

$$S_B = \sigma_1 - \sigma_3 = \frac{2}{3} \rho g h_B. \tag{6}$$

The strength S_D of the ductile layer depends on the viscosity μ of the material and the strain rate $\dot{\varepsilon}$, which corresponds to the ratio between the extension rate V and the thickness of the ductile layer h_D.

$$S_D = \mu\dot{\varepsilon} = \mu\frac{V}{h_D}. \tag{7}$$

In nature, the upper crust has an average density ρ of 2700 kg m^{-3}, a cohesion τ_0 of 10^7 Pa and a angle of friction ϕ between 30–32°. We used Fontainebleau dry quartz sand to simulate the upper crust (Fig. 2b). This material is a cohesionless material with a density ρ of 1600 kg m^{-3}, and an angle of friction ϕ around 30–35°. In the model, a silicone putty with a viscosity μ of 3×10^4 Pa s represented a lower crust with a viscosity of 10^{21} Pa s. Considering the strain rate in nature (10^{-15} s^{-1}), an extension rate of 2 cm h^{-1} has been


Fig. 2. Strength profile (a) for a continental lithosphere with a normal thermal gradient and (b) in experiments. Sand is used to simulate the brittle parts of the lithosphere while silicone putty mimics the behaviour of the lower crust and the ductile mantle lithosphere.

imposed in the experiments in order to obtain strength ratios of the same order of magnitude in nature and the models (56 and 13, respectively). As a consequence, the results of the experiments can be applied to natural systems. According to a geometrical scaling factor of 10^6 (length in nature/model), 1 cm in the model represents 10 km in nature. We conducted all the experiments with a large amount of extension (between 5 and 6 cm) to favour a better visualisation of the deformation. In nature such amounts of extension (50 to 60 km) correspond to extension values between those of continental rifts (e.g., 30 km in the French Massif Central grabens – Bois, 1993 – and 17 km in the Rhinegraben — Brun et al., 1992) and passive margins (e.g., several 100 km in the Galicia–Newfoundland passive margins — Manatschal et al., 2001).

2.2. Apparatus

Modelling was performed at the ISES Tectonic Laboratory of the Vrije Universiteit of Amsterdam

(The Netherlands). To simulate the reactivation of discrete lithospheric structures, we conducted brittle–ductile experiments composed of a basal layer of silicone and a brittle cover consisting of three horizontal stratified sand layers (Fig. 3a). The system lies on a basal plate, which simulates the boundary between the crust and the mantle lithosphere. As in the experiments of Basile and Brun (1999) and Michon and Merle (2000), the rupture within the brittle mantle, which is considered to govern crustal deformation, was achieved by a velocity discontinuity (VD). The VD corresponds to the limit of a plastic sheet, which is attached to the mobile wall and located underneath the silicone layer. In all experiments, the VD is characterised by two oblique orientations differing by 40° (Fig. 3b).

As many authors (Tron and Brun, 1991; McClay and White, 1995; Clifton and Schlische, 2001; McClay et al., 2002), we used the angle α between the VD and the extension direction to define the experiments and to allow comparison of our results with those obtained in
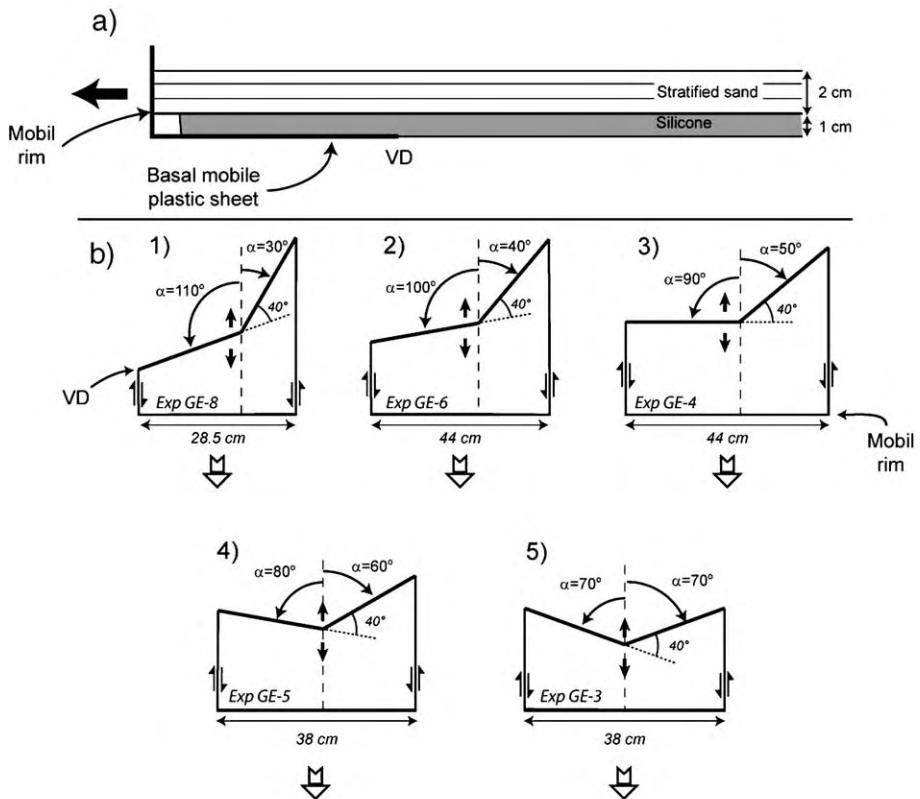

Fig. 3. (a) Model cross-section before extension. The deformation is initiated by the limit of the basal plastic sheet, which induces a velocity discontinuity (VD) during extension. (b) Plan view geometry of the basal plastic sheet on which the silicone layer is emplaced. See text for the definition of α. The arrows indicate the extension direction. The strike-slip motion associated with the lateral edges of the plastic sheet is also reported.

previous works. However, in each experiment α was measured from the intersection of the two VD segments allowing distinction between the VD segments characterized by identical absolute α-values (i.e., 70° and 110°, and 80° and 100°) (Fig. 3b). An α-value difference between the two VD segments (α-VAD) was also defined to discuss the role of the geometry of the VD segment intersection in the location of the subsidence. The experiments were carried out with five distinct geometries in which two α-values were applied simultaneously (Fig. 3b). The motion of the basal plastic sheet led extension along the VD segments and strike-slip motion along the plastic sheet lateral borders. During the experimental run, the main grabens were infilled with sand to simulate sedimentation. Surface photographs were taken at regular intervals to analyse the initiation and propagation of the deformation. At the end of each experiment, the sand is soaked in water, and serial cross-sections were made parallel to the extension direction. For experiment 5, we reconstructed the 3D geometry of the model with GOCAD®, in order to visualise the deformation and to understand its relationship to the strain within the silicone layer.

3. Results

3.1. Evolution of the deformation

3.1.1. Initial stages of deformation

In all experiments, the first increments of extension (i.e.,~1 cm) is characterised by the development of 2 cm wide parallel grabens located on each side of the VD (Fig. 4). Of these two structures, the graben located above the mobile basal plate is separated from the second graben by a 4.0–4.5 cm wide horst. Fig. 4 shows that this general deformation changes in each experiment. In experiments with an α-value difference (αVAD) between the two VD segments equal or greater than 40° (Fig. 4a, b, c), grabens and faults form simultaneously along the VD, which presents the greatest α-value (i.e., 90°, 100° and 110°). In these models, the geometry of the graben located on the mobile part varies from an en-echelon graben with α=110° (Fig. 4a), to a purely linear structure with α=90° and 100° (Fig. 4b, c). These variations in graben geometry situated on the mobile part, slightly contrast with the geometry of the graben located on the fixed part, which is always linear. For a αVAD of less than 40° (Fig. 4d, e), the initial fault pattern is different during the first stages of deformation being restricted to the central part of the model, around the intersection of the two VD directions. With coeval α-values (i.e., α=70°

and α-VAD=0°), the grabens are centred above the intersection of the two oblique VDs (Fig. 4e), while they are slightly shifted along the VD with highest α-value when α differs (Fig. 4d).

3.1.2. Propagation of the deformation

Fig. 5 shows the evolution of the deformation with increasing amount of extension for three different models. Surface views reveal that the incipient faults which developed during the first increment of extension (1) propagate laterally along the VD segments characterised by the highest α-values (i.e., 80°, 90° and 100°) and (2) control the formation of two parallel and linear main grabens. Then, when extension exceeds 2 cm, en-echelon grabens start to develop along the oblique VD segments (i.e., α-values ranging from 40° to 60°). The geometry of these grabens varies as a function of α: increase of the graben number and obliquity with low α-values (Fig. 5b). Experiments show that the en-echelon grabens are linked by accommodation zones rather than transfer zones as suggested by the lack of strike-slip fault between each graben (Fig. 5).

Note that the formation of the en-echelon grabens is associated with strike-slip deformation along the model lateral borders. The simultaneous development of the grabens and the strike-slip zones, and the lack of deformation between these two structures (Fig. 5) suggests that the strike-slip motion along the lateral borders do not induce the formation of the grabens but accommodates the extension on the borders.

3.1.3. Final stage deformation

In the domains with nearly orthogonal extension (i.e., α-value ranging from 80° to 110°) (Fig. 6A, B, C and D), the two main grabens are linear and bounded by parallel to sub-parallel faults. In the domains characterized by α=70°, the geometry of the grabens is linear at the rift scale with en-echelon intra-rift sub-grabens (Fig. 6E). With strong oblique extension (α between 30° and 60°), the formation of en-echelon grabens is limited by border faults, which are roughly parallel to the extension direction (Fig. 6A, B, C and D). Considering the system of grabens located on the fixed plate, it is interesting to note that the distance between each en-echelon grabens and their obliquity increases for low α-values. This suggests that with oblique extension the fault have a limited lateral prolongation and the deformation is accommodated by the creation of new grabens. In contrast, with orthogonal extension, lateral fault prolongation is favoured and the size of the graben
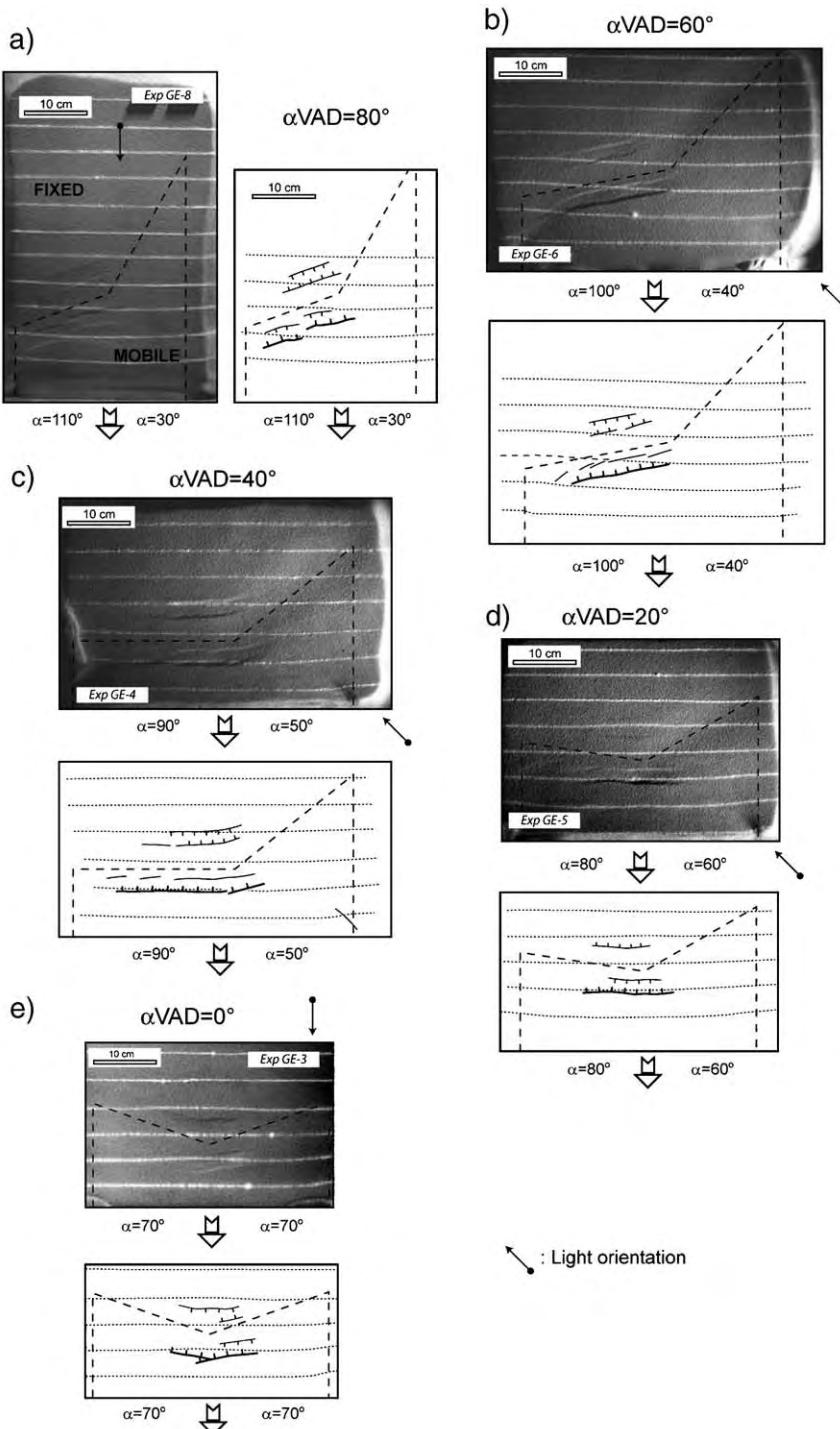
Fig. 4. Overhead views of the initial stage of surface deformation after ~1 cm of extension. (a) $\alpha = 30°$ and $110°$. (b) $\alpha = 40°$ and $100°$. (c) $\alpha = 50°$ and $90°$. (d) $\alpha = 60°$ and $80°$. (e) $\alpha = 70°$. The dashed lines on the pictures represent the location of the basal plastic sheet.

increases laterally. The development of en-echelon grabens with high oblique extension ($\alpha = 30°$ to $50°$) is in agreement with the deformation style observed by Tron and Brun (1991) with a single VD orientation and a strong oblique extension ($\alpha = 45°$ and $30°$), where the main border faults and
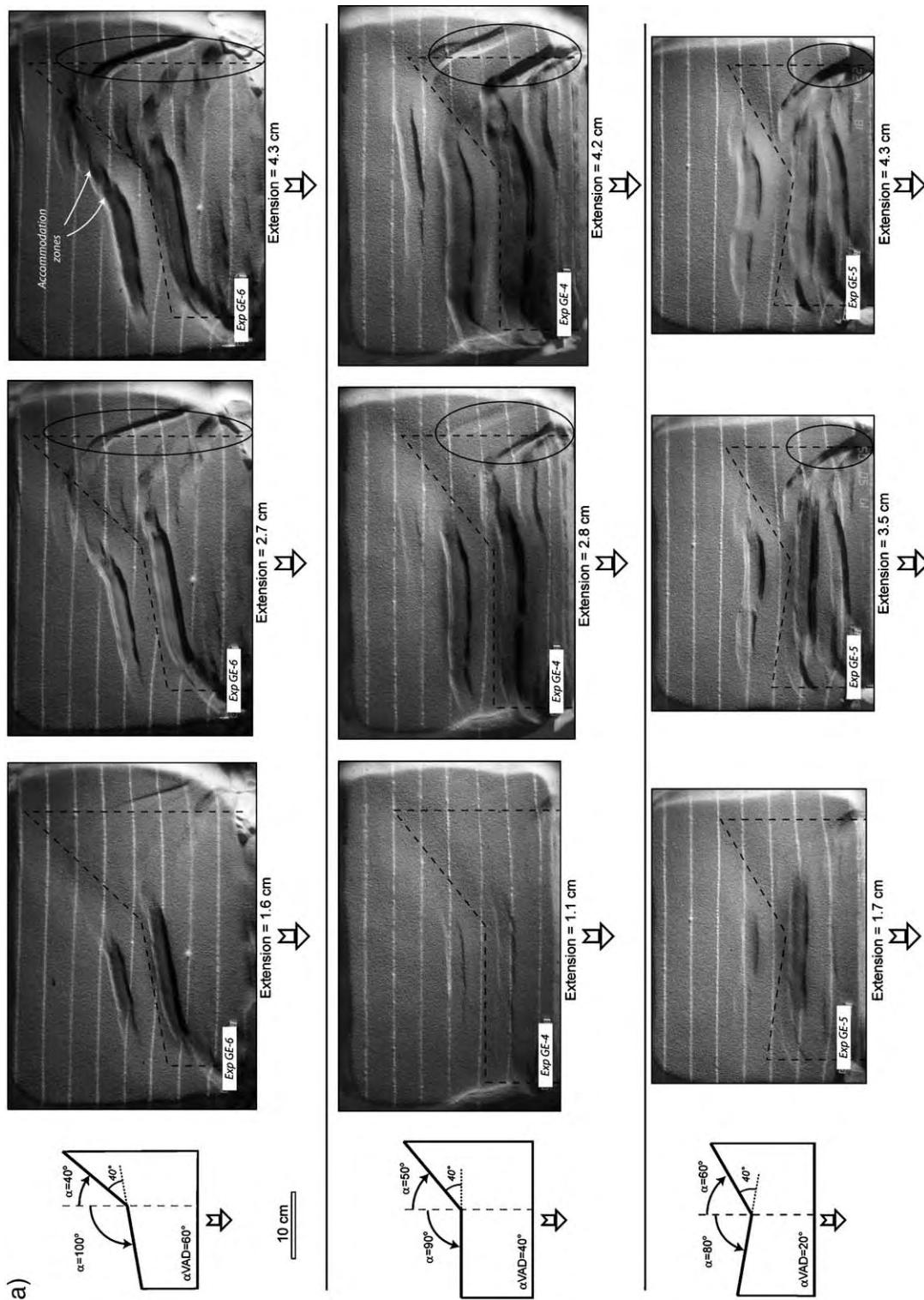
Fig. 5. (a) Overhead views for successive increments of extension with three different settings. Areas affected by the lateral edge effect are indicated by ellipses. See text for discussion on the role of the edge effect on the graben deformation. (b) Successive views illustrating the development of the grabens related to the VDs (grey) and to border effects.
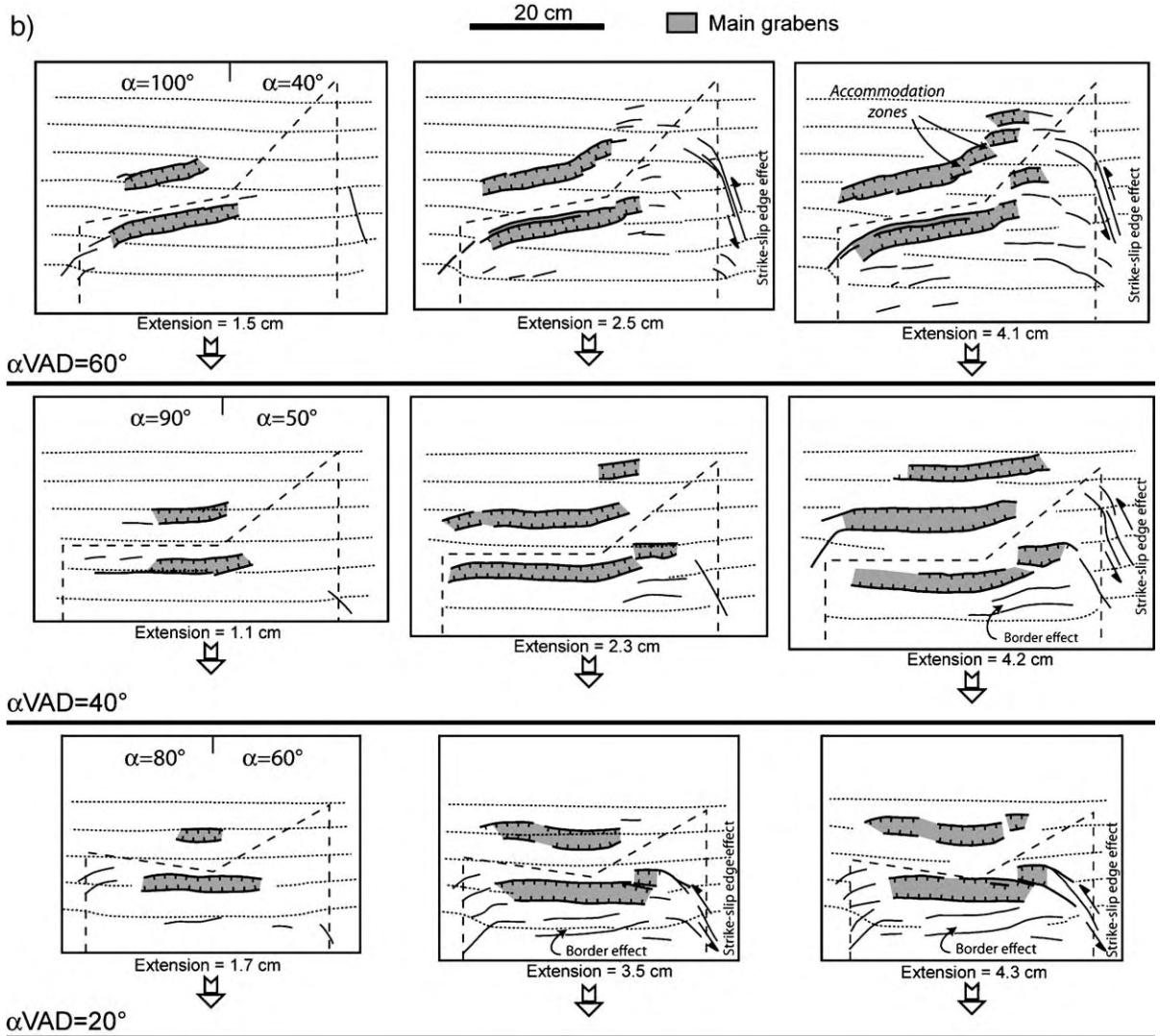
Fig. 5 (*continued*).

the intra-rift grabens are nearly perpendicular to the direction of extension. In contrast, it differs from the deformation obtained by McClay et al. (2002) in purely brittle models in which the graben border faults always remains parallel to the VD and the intra-rift basins are perpendicular to the extension direction.

3.2. Characteristics of the subsidence

3.2.1. Cross-section deformation analysis

In cross-section, the deformation varies as a function of α (Fig. 7). With high α-values ($70° < \alpha < 90°$), the system geometry is characterized by an asymmetric graben above the movable plastic sheet and a symmetric graben on the fixed part. The half-graben presents a pseudo-roll-over geometry, indicating a flattening of the graben master fault with depth mimicking a kinked planar or a nearly listric detachment. Due to the asymmetric thinning of the silicone, the initial horst located between the two main grabens evolves as a tilted and homogeneous block. Although the surface deformation reveals the development of several other faults and grabens during the experiments, the concentration of the subsidence remains into the two main grabens (Fig. 8a) and the strongest thinning of the silicone layer
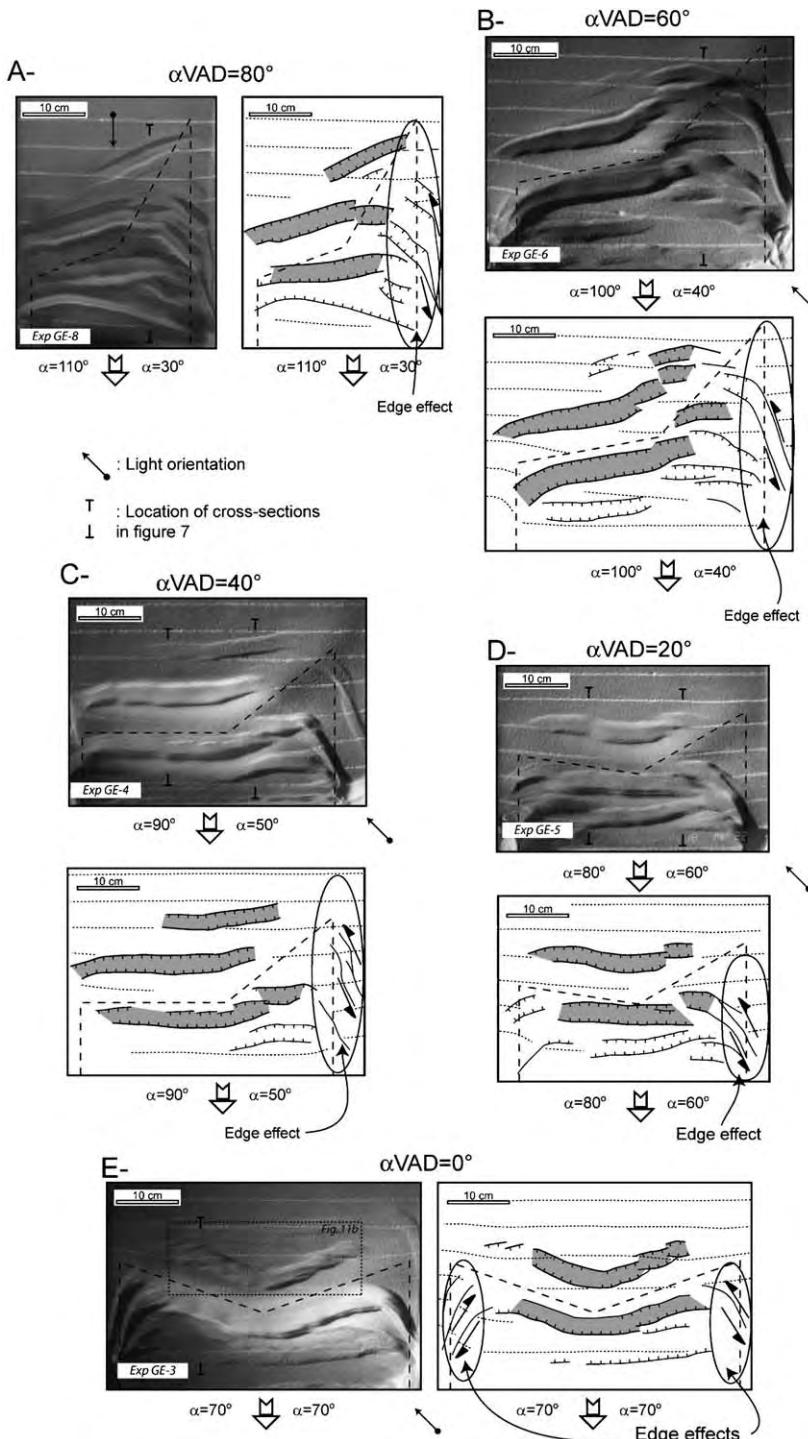
Fig. 6. Overhead views of the final stage deformation. (A) α=110° and 30°. (B) α=100° and 40°. (C) α=90° and 50°. (D) α=80° and 60°. (E) α=70°. The dashed lines on the pictures represent the location of the basal plastic sheet. Thick lines designate the faults controlling the main graben formation (grey).

between the two grabens (Fig. 8b), confirms that a basal VD induced the development of two main grabens at high extension rates (i.e., >1.4 cm/h) (Michon and

Merle, 2000). The faults of minor importance might result from edge effects and/or secondary flow of the silicone layer during the VD displacement. Michon and
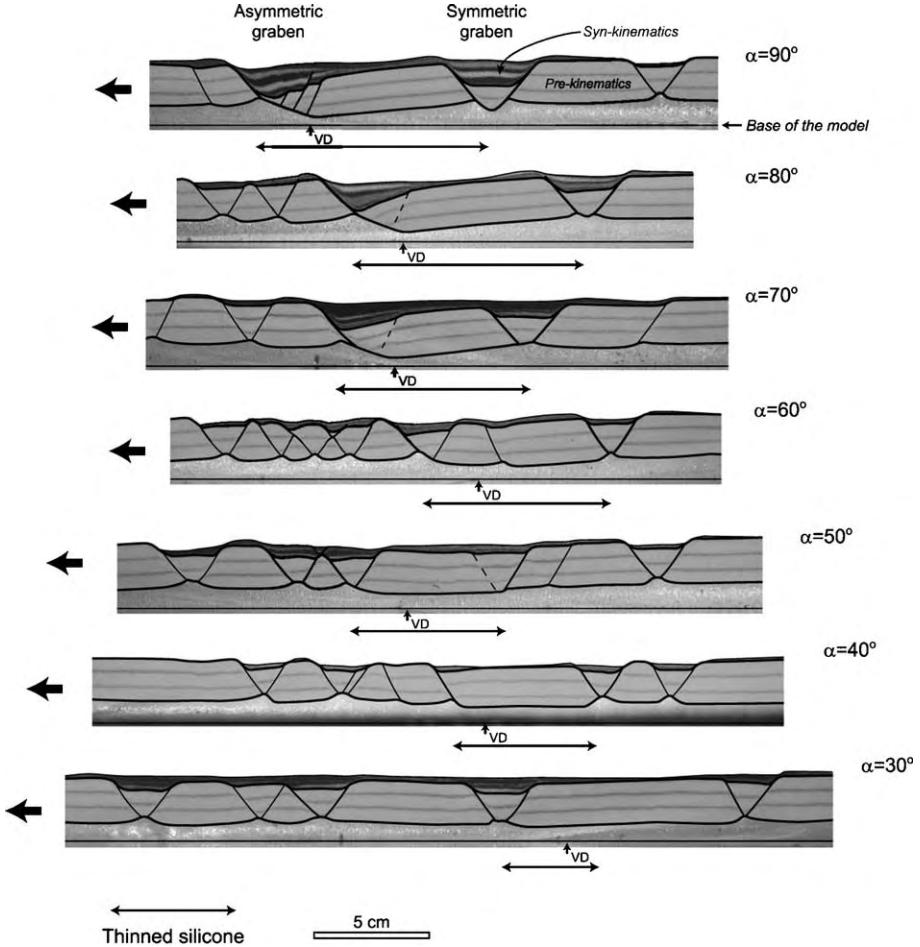
Fig. 7. Cross-sections in the models for different α-values showing the development of two main grabens when α<60° and several grabens with α>70°. With high α-values the progressive decrease of the area affected by the silicone thinning (with a similar amount of extension) suggests an increase of the strike slip component in the silicone layer. See cross-section location on Fig. 6.

Merle (2000) also shown that with low extension rate, only the asymmetric graben located on the movable part remains.

In the present study, our analysis of the subsidence in the asymmetric graben is therefore relevant as it is the only graben that always develops whatever the extension rate.

With α-values lower than 70°, the overall system geometry changes. The predominance of the two main grabens disappears and the deformation is distributed across the whole model (Fig. 7). Although the structures related to the VD are poorly visible in the brittle part of the model, cross-sections illustrate that the thinning of the silicone layer associated with the VD remains. We explain the decrease of the thinned silicone width for low α-values by a progressive predominance of the strike-slip component into the silicone layer when high oblique extension is applied.

3.2.2. Location and geometry of the depocentres

Analysis of the maximum amount of subsidence in each cross-section allows definition of the shape and the location of the depocentres. For low and high α-values, the amount of subsidence is determined in the main graben associated with the thinning of the silicone layer (i.e., the asymmetric graben for high α-values). Fig. 9 shows that the characteristics of the depocentres depend on the direction of extension with respect to fabrics. When the αVAD between the two VDs is greater than 40° (Fig. 9a), the subsidence is almost homogeneous along each segment and is maximum in the graben related to the VD with the highest α-value (α=100°). In contrast, when the αVAD is lower than 40°, the subsidence is maximum above the intersection of the two VDs, inducing the development of a depocentre (Fig. 9b, c and d). For decreasing αVAD (from 40° to 0°), subsidence values become progressively
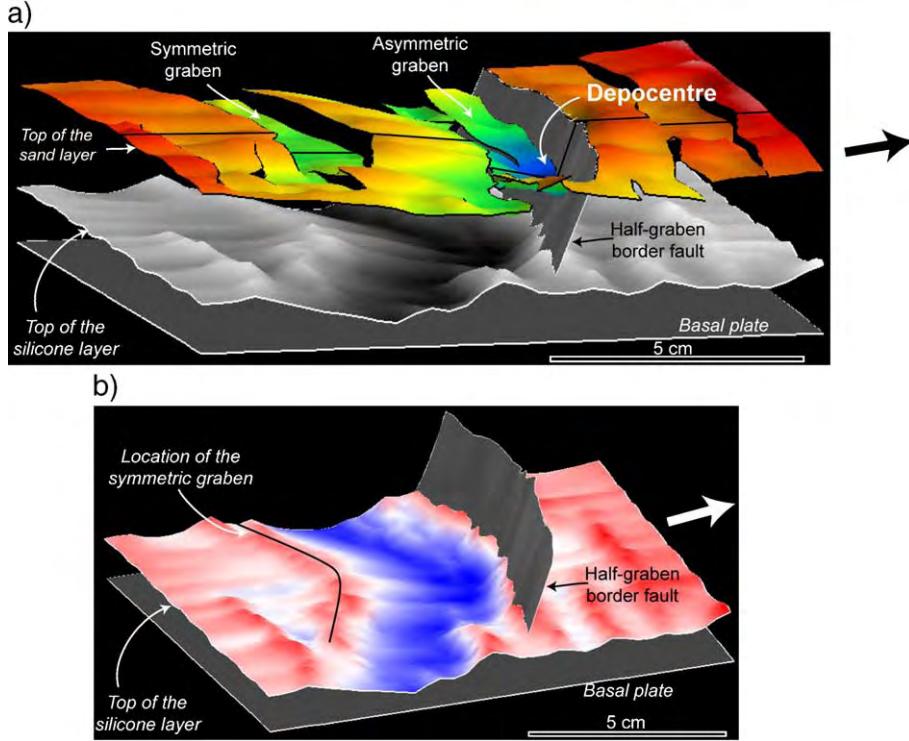
Fig. 8. 3D reconstruction of the experiment with $\alpha = 70°$ (Fig. 6E). (a) 3D geometry of the model showing the location of both the depocentre and the silicone thinning. For the top of the sand layer, red to blue colours are used to show the increasing amount of subsidence. The black line indicates the location of the intersection between the two orientations. The black arrow shows the direction of extension. (b) Thinning of the silicone layer. Red, white and blue colours correspond to low, medium and high amount of thinning, respectively. The grey plane represents the fault plane of the major fault linked to the half-graben. The white arrow indicates the direction of extension.

symmetric and centred above the VD intersection, creating a crescent shape depocentre for $\alpha VAD = 0°$.

Fig. 9 also illustrates the thinning of the silicone layer for each cross-section. The comparison of the subsidence and the thinning of the silicone values for different αVAD provide information, which are noteworthy. When αVAD equals $60°$ (Fig. 9a), both subsidence and thinning of the silicone layer are nearly constant along each VD segment (around 75–80% for $\alpha = 100°$ and 25–35% for $\alpha = 40°$). The constant thinning of the silicone layer along the VD segments remains when $\alpha VAD = 40°$ (Fig. 9b), whereas the subsidence is concentrated above the intersection of the two VDs. Finally, when αVAD is lower than $40°$ (Fig. 9c and d), the thinning of the silicone layer is slightly greater at the intersection of the two VD segments than along them (i.e., around 15–20% of additional thinning), and the amount of subsidence significantly changes between the intersection and the VD segments (i.e., 40 to 50% higher subsidence in the central part of the depocentre than in its borders). These different observations suggests that the development of the depocentre is not only

controlled by the thinning of the silicone, but also by the location of the intersection of the two VD segments when αVAD is lower or equals to $40°$. This interpretation is confirmed by the location of the initial deformation and subsidence (Fig. 4). Finally, our study reveals that the depocentres are not prone to migration with increasing amount of extension. Therefore, the displacement of the depocentre location most likely results from a change of the extension rate and/or the direction of extension.

4. Discussion

Oblique rifting was already studied during the last decade using different type of extension (symmetric vs. asymmetric), different experimental apparatuses, different rheological stratifications and a linear VD s.l. (i.e., mobile or fixed edge of a basal plate, or rubber sheet) (Tron and Brun, 1991; McClay and White, 1995; Clifton et al., 2000; McClay et al., 2002).

We carried out analogue experiments with asymmetric extension to analyse (1) the role of oblique extension and (2) the effect of the coeval activity of two
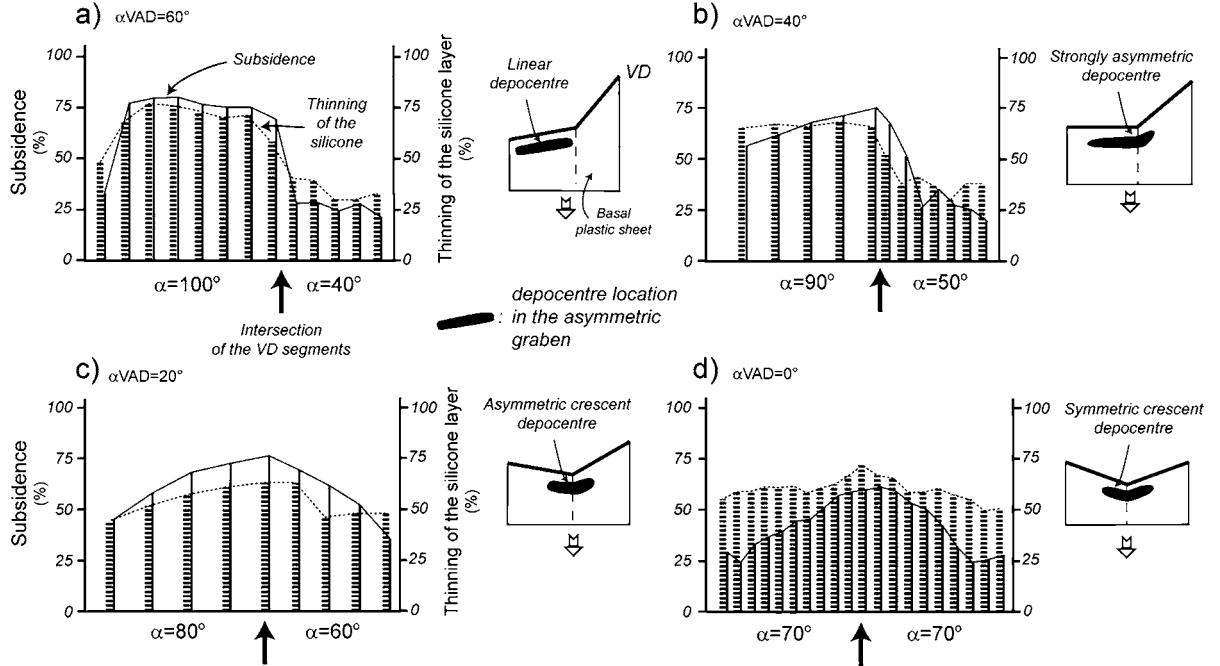
Fig. 9. Subsidence (thin lines) and thinning of the silicone layer (thick dashed lines) measured in percent of the initial thickness (i.e., 1 cm for the silicone layer and 2 cm for the sand layer) on cross-sections form experiments with α = 40° and 100° (a), α = 50° and 90° (b), α = 60° and 80° (c), and α = 70° (d). For each experiment, small cartoons illustrate the location of the depocentre with respect to the basal plastic sheet.

oblique inherited lithospheric faults in the graben and depocentre formation.

4.1. Comparison of the experimental procedures

We first focus our discussion on the effect of the type of extension (i.e., symmetric vs. asymmetric) and the different experimental procedures in the deformation of purely brittle and brittle–ductile models in order to estimate the a priori difference of deformation related to both the apparatus and the type of extension.

4.1.1. Experiments with brittle materials only

Two main procedures are usually used to simulate rifting processes in the upper crust. Extension is induced by either the limit of a basal plastic sheet lying on a fixed platform (e.g., Faugère et al., 1986), or by a central basal rubber sheet (BRS) linked to one or two movable parts (McClay and White, 1995; McClay et al., 2002). The first procedure with a discrete VD allows simulation of discrete crustal fabric while in the second procedure the BRS mimics a basal detachment (McClay and White, 1995).

With asymmetric orthogonal extension (i.e., moving only one part), a discrete mobile or fixed VD entails the formation of an asymmetric graben with a permanent master fault and several conjugate normal

faults (Faugère et al., 1986; Allemand and Brun, 1991) (Fig. 10a). With a symmetric orthogonal extension imposed by two discrete VDs, the deformation pattern depends on the initial distance between the VDs. If the initial distance is large enough to prevent any interaction between the half-grabens related to each VD, two opposite half-grabens form, bounding a central horst above the fixed central part. This global geometry (i.e., two lateral half-grabens and a central horst) is nearly similar to the one obtained with a 10 cm wide BRS where two asymmetric grabens separated by a central horst are created (McClay et al., 2002) (Fig. 10b). The development of an asymmetric graben above each limit of the BRS suggests that the latter(s) correspond to two discrete VDs.

Experiments with oblique extension show that whatever the approach is (i.e., BSR or discrete VD above a fixed basal plate), extension always entails the formation of linear rift, parallel to the VD (Higgins and Harris, 1997; McClay et al., 2002) (Fig. 11a). The main difference is that in the BRS approach the model central part, which lies above the BRS is affected by several normal faults roughly perpendicular to the extension direction while no deformation occurs above the fixed central part with the discrete VD approach. Thus, in experiments with brittle material and a BRS, the rift orientation is imposed by the VD
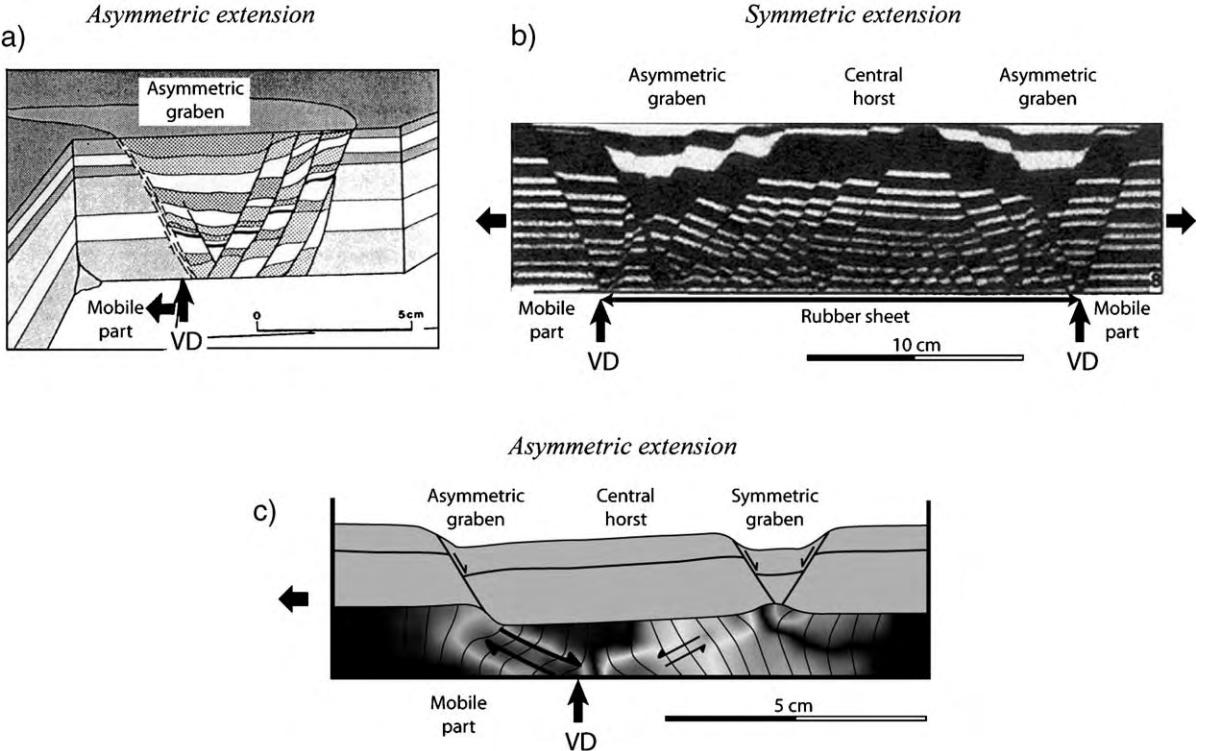
Fig. 10. Comparison of the structures obtained with different experimental procedures and orthogonal extension. (a) Experiment with brittle material only and a discrete mobile VD (after Faugère et al., 1986). (b) Experiment with brittle material only and a basal rubber sheet (after McClay et al., 2002). (c) Brittle ductile experiment with a discrete mobile VD (after Michon and Merle, 2003). See text for discussion.

orientation and only the intra-rift fault and intra-graben orientation depend on the extension direction. The use of a BRS subsequently allows a partial decoupling between the deformation controlled by the VDs (i.e., parallel to the VDs) and the deformation related to the stretching of the rubber sheet (i.e., perpendicular to extension).

4.1.2. Experiments with brittle–ductile materials

Instead of using a BRS to allow a decoupling in the model, several studies performed experiments with a basal silicone layer and simulated rifting processes at crustal scale (e.g., Allemand and Brun, 1991; Tron and Brun, 1991; Bonini et al., 1997; Michon and Merle, 2000). Michon and Merle (2000) have shown that asymmetric orthogonal extension due to a basal discrete VD leads to the development of one or two grabens, depending on the extension rate. With symmetric orthogonal extension (i.e., 2 discrete VDs), the overall geometry depends on both the extension rate and the initial distance between the VDs. The 2, 3 or 4 grabens that are prone to form are connected to the VDs by shear zones within the ductile layer (Fig. 10c). Thus, in a way similar to models with brittle materials, symmet-

ric extension induces a multiplication of the structures and subsequently complexifies the rift geometry.

Experiments with oblique extension clearly demonstrate that the silicone layer allows a decoupling of the deformation between the VDs and the upper brittle layer (Tron and Brun, 1991; Bonini et al., 1997; Higgins and Harris, 1997). Our models with two oblique basal VDs suggest that this decoupling is partial as the rift system shape mimics the geometry of the VD (Fig. 6).

Comparison of an experiment performed by McClay and White (1995) with $\alpha = 60°$, with the geometry of the symmetric graben developed in our model with $\alpha = 70°$ reveals striking similarities in terms of fault orientation and depocentre location (Fig. 11). Despite the use of different experimental procedures in both models, (1) the depocentre and sub-graben formation is caused by intra-rift normal faults with an orientation sub-orthogonal to the stretching direction, and (2) the depocentres are laterally shifted and linked by accommodation zones, which form topographic highs. The similarity between the structures obtained by McClay and White (1995) and in the present work is kept for high α-values ($\geq 60°$) and stops for low α-values
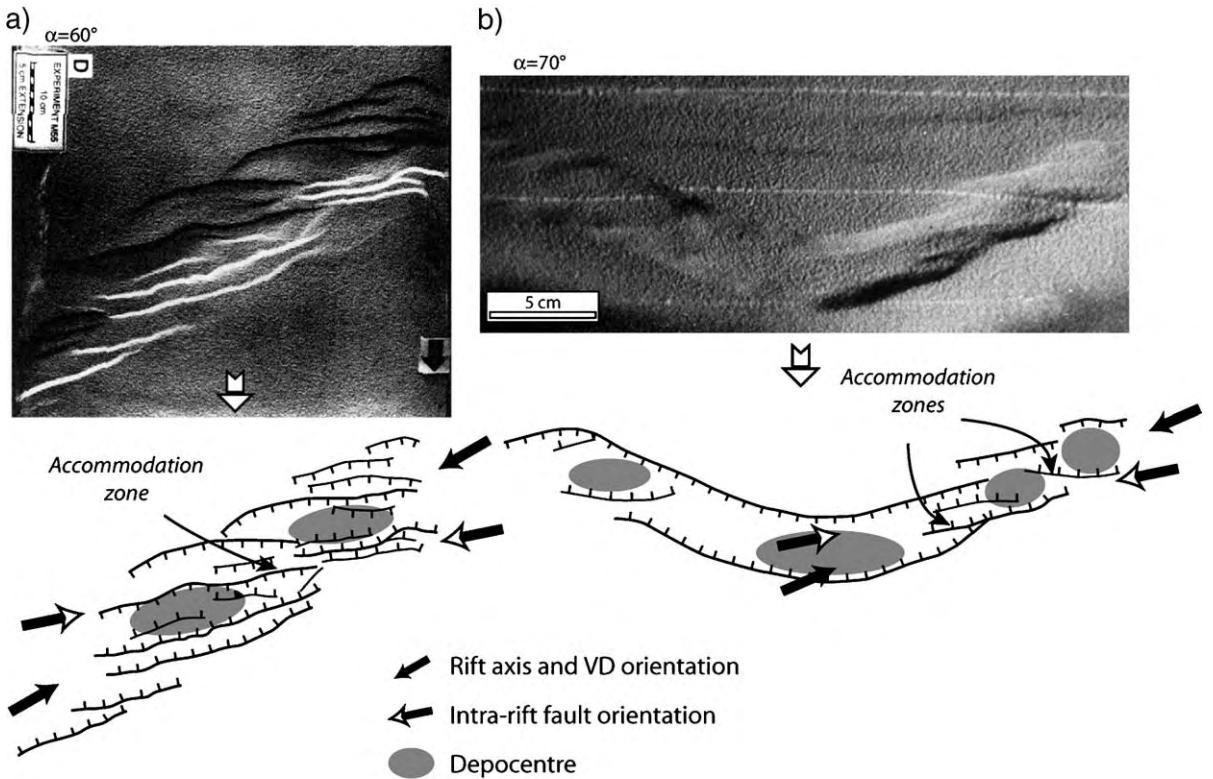
Fig. 11. Comparison of fault pattern in experiments carried out with (a) a linear basal rubber sheet, a brittle material and α=60° (after McClay and White, 1995), and (b) coeval oblique VDs (α=70°), brittle–ductile materials. See text for explanation.

(<60°). Indeed, in experiment with a BRS and α=45°, the overall structure remains linear with intra-rift en-echelon sub-basins (see Fig. 6 in McClay et al., 2002), whereas independent en-echelon grabens are formed in our models (Fig. 6). This geometry difference (i.e., presence or absence of faults parallel to the VDs) suggests that the decoupling is more important in the brittle–ductile experiments than with a BRS and brittle materials only.

Finally, one could ask whether asymmetric or symmetric extension best simulates rifting processes. Experiments with brittle materials and a BRS were performed with both asymmetric extension (i.e., one moving wall) (McClay and White, 1995) and symmetric extension (i.e., two moving walls) (McClay et al., 2002). Similarly, crustal or lithospheric scale brittle–ductile experiments were conducted with asymmetric (e.g., Brun and Beslier, 1996) and symmetric extension (Michon and Merle, 2000). Sandbox experiments with a linear BRS show similar deformation patterns with asymmetric or symmetric extension (McClay and White, 1995; McClay et al., 2002), suggesting that the extension mode does not correspond to the key parameter that controls the graben geometry. In brit-

tle–ductile experiments at crustal or lithospheric scale, asymmetric extension is achieved with one VD (e.g., Brun and Beslier, 1996; Michon and Merle, 2000), while symmetric extension is performed by two VDs (e.g., Michon and Merle). It is widely accepted that the VD simulates the rupture of the brittle mantle lithosphere (Brun and Beslier, 1996). Subsequently, asymmetric or symmetric extensions are not used to determine the effect of the extension mode in the graben formation but are simply used to understand the role of the brittle mantle lithosphere rupture number in the rift system geometry. It consequently follows that symmetric and asymmetric extension does not have the same signification in the sandbox experiments with a BRS and in brittle–ductile experiments. Symmetric and asymmetric extension is complementary extension modes allowing to understand better the complexity of rift systems.

4.2. Model deformation

It is widely accepted that the formation of a depocentre results from differential displacements along the graben or sub-basin border faults. The location of the

depocentres in experiments with a linear VD reveals that this maximum amount of vertical displacement is achieved along the newly formed faults (i.e., sub-orthogonal to the stretching direction) (McClay and White, 1995). In a first approximation order, this result is confirmed by our experiment with two coeval oblique VDs, where depocentres are located in the VD domain characterised by the most orthogonal extension direction (Fig. 9a, c and d). However, it is noteworthy that in experiment with $\alpha = 90°$ and $50°$ (Fig. 9b), the depocentre developed above the two VD segment intersection, while orthogonal extension is achieved uniformly along the VD segment with $\alpha = 90°$. Furthermore, the different deformation pattern obtained along segments with the same angle to the extension direction (i.e., $80°$ and $100°$ are of the same obliquity with respect to the extension direction) (Fig. 9a and c) indicates that besides the extension direction the intersection of the two VD segments is a key parameter, which plays a role in the development of depocentres. Finally, the more parallel to the stretching direction the bisecting line of the two VD segments is, the more symmetric the depocentres are prone to develop. Applied to nature, these results first suggest that when two oblique lithospheric faults are reactivated they concentrate the deformation (i.e., the subsidence) at their intersection. At crustal scale, Bellahsen and Daniel (2005) have recently shown a similar control of the intersection of oblique inherited and new crustal faults in the depocentre development. Then, the structural inheritance may act at both crustal and lithospheric scale, controlling the rift system geometry and inducing heterogeneous subsidence within the graben. Additionally the depocentre geometry and location are highly sensitive to the extension direction. These geological features can be used in nature for establishing the extension direction.

Experiments with coeval sub-orthogonal and oblique stretching directions show that grabens appear first in the domain with the highest α-value and are secondly formed in en-echelon pattern along the oblique VD segments (Fig. 5). This timing of deformation is explained by a partitioning of the total displacement in strike-slip and normal components along the oblique VDs, while only normal component exists in orthogonal extension. In consequence, for a uniform amount of displacement in the model or in nature, the rupture due to normal stress (i.e., leading to the development of pure normal faults) is reached first in the domain characterised by orthogonal extension and secondly along the oblique VD segments or the oblique lithospheric faults.

5. Application to natural examples

5.1. The Upper Rhine graben (West European rift)

The Upper Rhine graben (URG) is a 300 km long linear Cenozoic structure, which corresponds to the central segment of the West European rift (Fig. 12a). The graben subsidence started during the Late Eocene (Priabonian) and is still active during the Quaternary. Recent models proposed several extension directions to explain the URG formation and geometry. Early models argued that the graben development resulted from an E–W extension due to the N–S collision between Eurasian and African plates (Tapponnier, 1977). A second interpretation, based on microtectonic studies stated that the graben formation was characterised by successive changes of the paleo-stress since the Late Eocene (e.g., Bergerat, 1987). This model was recently supported by a comparison between the paleo-stress results and the geometry of the URG depocentres (Schumacher, 2002). According to these authors the graben formation could result from 4 successive paleo-stresses (i.e., Priabonian N–S compression, Rupelian E–W extension, Chattian SW–NE compression and Miocene–Quaternary SE–NW compression), which originated from plate reorganisation during the Eurasia–Africa collision. Based on a three-dimensional kinematic restoration, Behrmann et al. (2003) proposed a two-fold evolution of the graben with a N80 Late Eocene–Oligocene early extension, followed by a N60 Miocene–Quaternary oblique extension. This model agreed the NE–SW oblique rifting interpretation already proposed by Chorowicz and Deffontaines (1993).

Structurally, the URG is characterized by two main orientations referred as Permo-Carboniferous and Rhenish trends, which are inherited from the Variscan to Late Variscan evolution (Schumacher, 2002). The main Permo-Carboniferous structure is the Lalaye–Lubine–Baden–Baden fault (LBF) bounding the Saxothuringian and Moldanubian Variscan lithospheric domains (Wickert and Eisbacher, 1988). This WSW–ENE trending fault crosscuts the graben in its central part and forms a topographic high separating two zones of subsidence (Fig. 12). The structure is interpreted as a transfer fault for the Late Eocene–Oligocene period as it separates two half-grabens of opposite polarity (Brun et al., 1992). In the North, the graben is bounded in the east by a west dipping major fault. South to the Variscan fault, the fault is east dipping and the thickest sediment deposit is localized in the Western part. The second Variscan orientation (i.e., Rhenish trend) is parallel to the Cenozoic graben and is recognized in
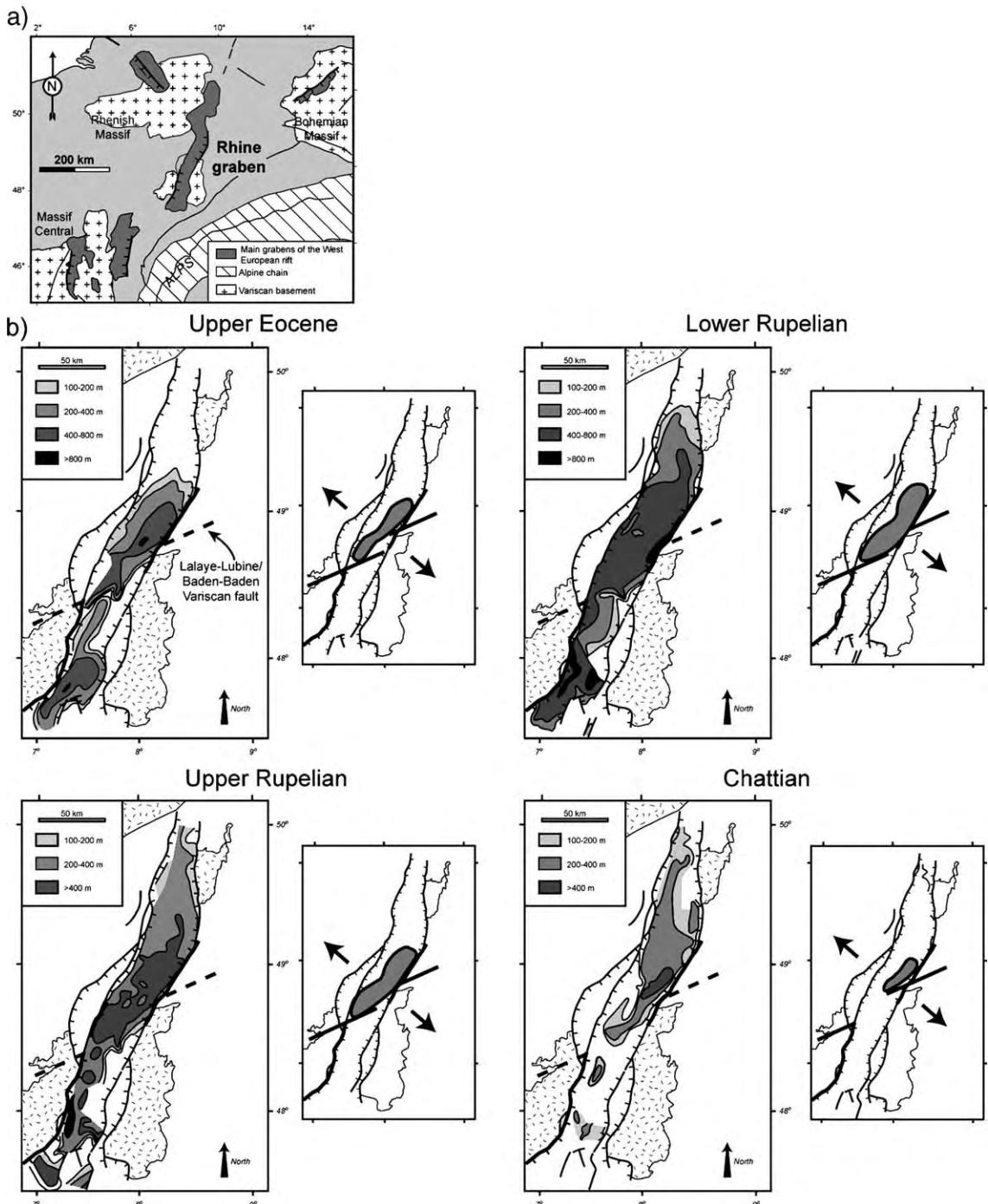
Fig. 12. Geological map of the West European Rift. The Upper Rhine graben corresponds to the central segment of this Cenozoic rift system. (b) Isopach maps of the Upper Eocene, Lower Rupelian, Upper Rupelian and Chattian sedimentation (after Schumacher, 2002). The small cartoons indicate the general shape of the depocentres and our interpretative stress field inferred from this geometry (constant NW–SE direction of extension).

outcrops in the Variscan massifs (Vosges, Black Forest and Odenwald) and with geophysical methods into the graben (Edel and Fluck, 1989). This Rhenish trend was

reactivated during the Late Eocene–Oligocene extension and has controlled the orientation of the graben borders faults. Recent tomographic data show that these

faults affect the whole lithosphere (Lopes Cardozo and Granet, 2003).

We use in the following section our experimental results to determine the paleo-stress fields, which affected the URG during the Late-Eocene–Oligocene evolution. Experiments show that the development of a depocentre is highly sensitive to a contemporaneous activity of oblique faults and to the extension direction. Isopach maps were published for four periods between the Late Eocene and the Oligocene (Schumacher, 2002) (Fig. 12b). As the Oligocene sedimentation was partly eroded during the Miocene to present-day uplift south to the LBF (Villemin et al., 1986), we focus our analysis in the northern part of the graben. In this segment, each period is characterized by the development of a main depocentre which is always bounded in the south and the east by the LBF and the eastern main border fault, respectively (Fig. 12b). This suggests first a continuous coeval activity of these two main structures, which have controlled the formation of the depocentres. Although the depocentre geometry has slightly changed between the Late Eocene to Oligocene, one can note that it is nearly symmetric from the intersection of the two main faults. According to our models, the development of a nearly symmetric depocentre at the intersection of two oblique orientations occurs for extension directions corresponding to the bisecting line of the two directions. In consequence, we interpret the development of the Late Eocene–Oligocene depocentres and the URG formation as resulting from a constant NW–SE extension direction. Variations of the extension rate and a slight rotation of the extension direction ($<10°$) may explain the depocentre geometry differences.

As proposed by several authors (Meier and Eisbacher, 1991; Schumacher, 2002; Michon et al., 2003), we interpret the Early Miocene migration of the Late Eocene–Oligocene depocentre towards the northern part of the URG as the result of a change in the stress field at the Oligocene–Miocene transition. The superposition of the Miocene and Quaternary depocentres suggests a constant NE–SW stress field since the beginning of the Miocene.

This two-fold evolution of the URG with a Late Eocene–Oligocene NW–SE extension followed by a NE–SW Miocene–Quaternary extension is similar to the one observed in the Roer Valley rift system (i.e., the northern continuity of the URG) (Michon et al., 2003). According to these authors, the URG development and the global evolution of the European platform may result from the formation of the Alpine mountain chain since the latest Cretaceous.

5.2. Southern East African rift (Tanganyika, Rukwa and Malawi rifts)

The southern East African rift (SEAR) corresponds to the southern part of the western branch of the East African rift. It is composed from north to south of the Tanganyika, Rukwa and Malawi rifts (Fig. 13). At a regional scale, the Tanganyika rift is characterised by two different orientations. North of the Rukwa shear zone, the graben trends N–S whereas it presents a N150 direction south of this Precambrian shear zone. The Rukwa rift is a N130–140 half-graben parallel to the Rukwa shear zone. The southernmost main expression of the SEAR (i.e., the Malawi rift) is a N–S trending structure limited in the north by the Rukwa shear zone. In the SEAR, the first sediments related to the extension deposited 12 My ago in the central part of the incipient Tanganyika rift (Lezzar et al., 2002). Subsidence then propagated diachronously toward the northern (7–8 Ma) and southern (2 Ma) halves of the graben (Rosendahl et al., 1992; Lezzar et al., 2002). In the Malawi rift, the first syn-rift sediments have an age estimated at 8.6 Ma (Ring and Betzler, 1995). Sedimentation started first in the northern half of the Malawi rift and propagated toward the south with ongoing extension (Rosendahl et al., 1992).

Seismic profiles reveal that the two main grabens (i.e., the Malawi and Tanganyika rifts) are asymmetric grabens characterised by a succession of opposing half-grabens (Rosendahl et al., 1992). The Rukwa graben is a half-graben, which overlies Permo-Triassic and Mesozoic basin structures. In contrast to the Malawi and Tanganyika rifts, seismic data show a lack of alternating half-graben in the Rukwa rift (Rosendahl et al., 1992) which may result from a strong control of the Precambrian to Mesozoic structures on the development of this graben during the Cenozoic. Such an influence of pre-existing structures on the graben geometry in the SEAR has been suggested by many authors (e.g., Ring, 1994; Bonini et al., 1997; Lezzar et al., 2002).

At a regional scale, the province is characterised by (1) two Precambrian cratonic areas (the Tanzanian and Zambian blocks) separated by the N130–140 Rukwa shear zone and (2) several orogenic belts resulting from Kibaran and Panafrican orogenies. West of the Tanzanian craton (i.e., in the northern Tanganyika Lake area), the dominant foliation in the Precambrian basement trends N–S while it turns to N130–140 in the Tanganyika Lake central part. This foliation direction, which is associated with the Ubendian belt, is connected toward the southeast to the Rukwa shear zone. South of the Tanzanian craton, the pre-Cenozoic basement
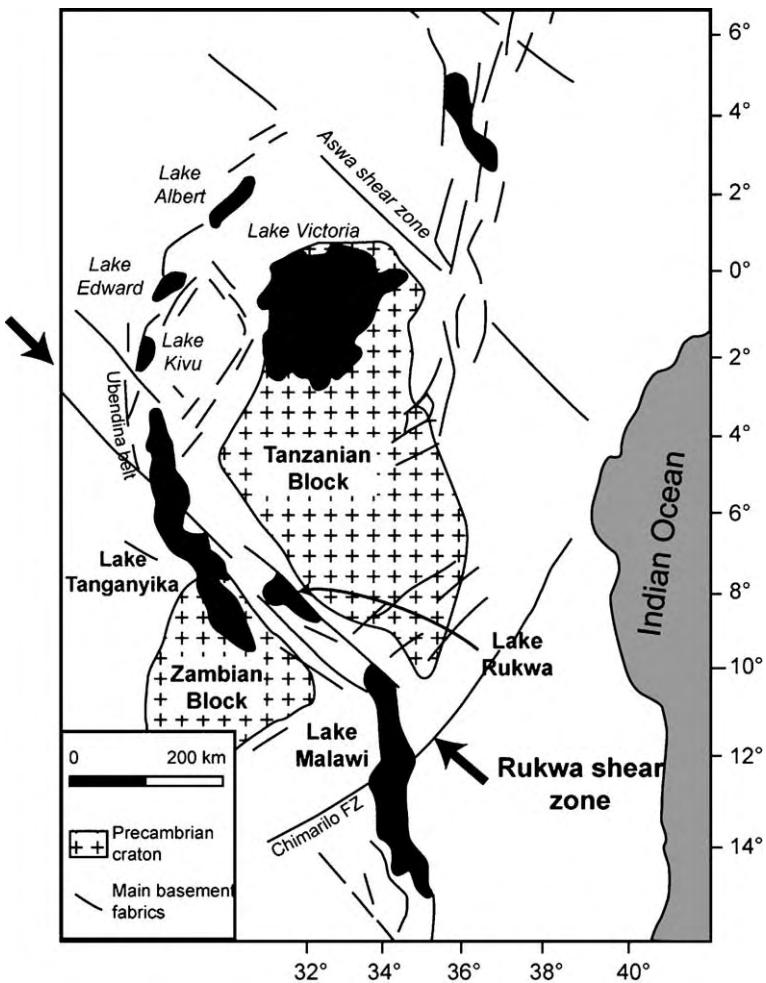
Fig. 13. Geological map of the South East African rift (SEAR) showing the graben location and the Precambrian and Panafrican structural inheritance.

presents two mains orientations (i.e., SE–NW and SW–NE) in relation with the Ubendian belt, and the Chimaliro shear zone and NE–SW Karoo grabens, respectively (Ring, 1994). It is noteworthy that each rift is parallel to a pre-existing structure except the southern branch of the Tanganyika rift which is the only rift segment that affects a cratonic province (i.e., the Zambian block) south of the Rukwa shear zone.

During the last decades, several extension directions were proposed to explain the formation and the geometry of the East African rift. Based on the overall geometry of the graben, selected earthquake focal mechanism solutions and the potential existence of large NW–SE transfer zones, Chorowicz and Mukonk (1980) and Rosendahl et al. (1992) argued that the rift system results from an oblique NW–SE extension. In opposition, some studies suggested an E–W extension for the same period (Morley, 1988; Ebinger, 1989).

These interpretations are supported by reconstructions of plate kinematics indicating a roughly E–W extension direction (Jestin et al., 1994). Microstructural analysis in the Malawi rift reveals a multi-stage extensional history with an initial ENE/E–WSW/W rifting direction between 8.6 and 0.55 Ma and a ESE/SE–WNW/NW extension since 0.55 Ma (Ring, 1994). Based on basin analysis in the northern Tanganyika rift a similar two-fold evolution was proposed by Lezzar et al. (2002) with a E–W extension between 12 and 3.5 Ma followed by a second NW–SE extension (1.1–0.4 Ma).

In the light of our experimental results which allow determination of the extension direction from the subsidence location and evolution, we consider that the regional geometry of the SEAR and the location of the incipient subsidence during the Miocene resulted from an initial E–W extension. First as shown above, the Tanganyika rift is characterised by two oblique orienta-

tions, which intersect in the rift central part. The beginning of the subsidence at the intersection of two structural trends (N–S and SE–NW) and its propagation in the northern branch can be compared to the deformation pattern observed in experiment with $\alpha = 90°$ and $50°$ (Fig. 14).

Second, the location and style of deformation suggest that the Rukwa shear zones and the segment of the Ubendian orogenic belt which is located below the northern branch of the Tanganyika rift were contemporaneously reactivated at a lithospheric scale during extension. The location of the southern Lake Tanganyika rift, south of the main structural trend intersection and into the "strong" Zambian cratonic area may explain its delayed and less intense deformation. As shown in Fig. 14b, the reactivation of oblique lithospheric structures leads to the formation of en-echelon grabens above the mobile part of the model. Comparison of these experimental results and integration of the natural pre-existing structures in the southern end of the SEAR may explain the formation and the orientation of the Malawi rift (Fig.

14). The different location of the en-echelon graben in nature (i.e., Malawi rift) and in the model may result from the strong role of the Rukwa shear zone, which has induced a transfer of deformation east of the Zambian cratonic area. In addition, the deformation (i.e., narrow subsidence) recorded in the Rukwa rift while no oblique graben is formed in our isotropic models may result from the control of the Rukwa shear zone at crustal and lithospheric scale. Finally, the lack of secondary grabens (visible above the motionless part of our models) parallel to the Tanganyika and Malawi rifts likely results from a low extension rate.

The present interpretation may explain the large-scale geometry of the SEAR with a E–W direction of extension and the reactivation of two main lithospheric structures (i.e., the NE–SW Rukwa shear zone and the N–S trending Ubendian orogenic belt in the northern part of the Lake Tanganyika rift). This Mio-Pliocene evolution is not in disagreement with a recent NW–SE extension direction deduced from microstructural (Ring, 1994) and basin (Lezzar et al., 2002) analyses.
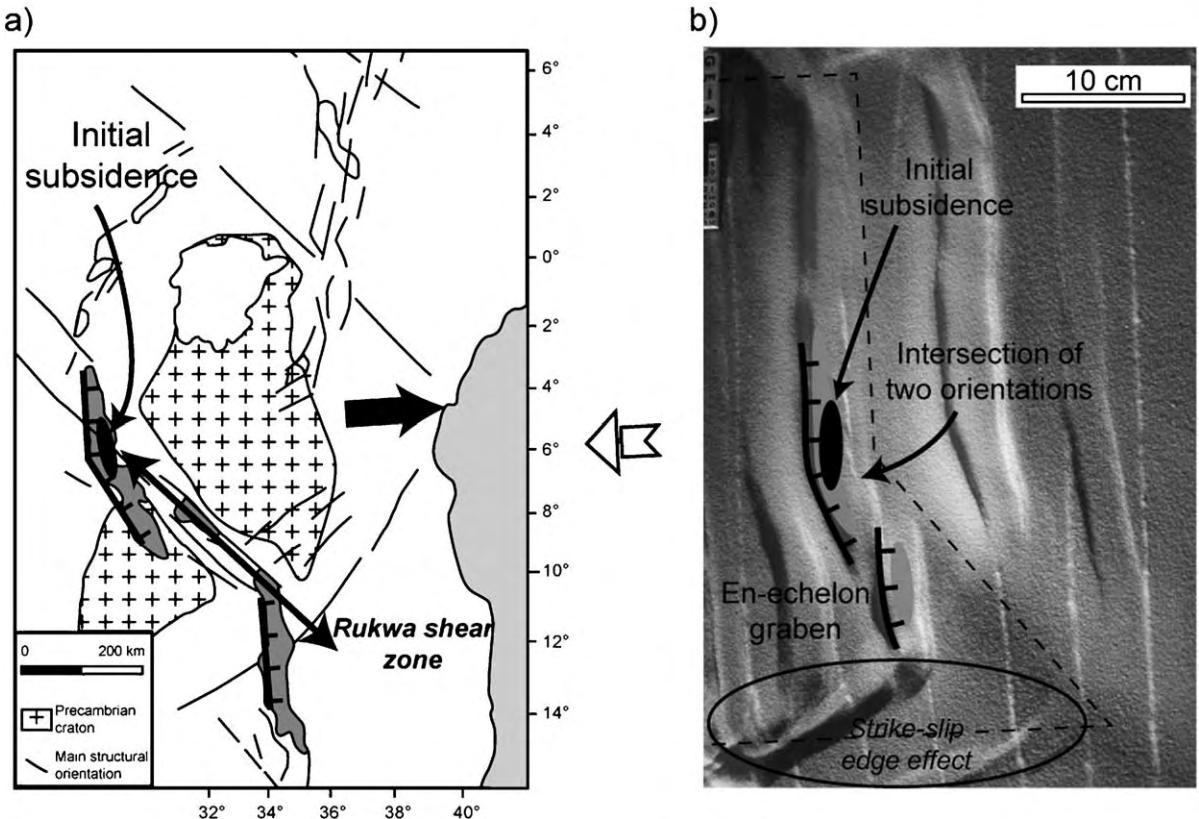

Fig. 14. Comparison of the deformation in the SEAR (a) and in experiment with $\alpha = 50°$ and $90°$ (b). Note (1) the location of the initial subsidence and (2) the roughly similar graben shape (grey) in nature and in the model. The difference in the location of the en-echelon graben between the model and the SEAR may result from a transfer of the deformation east of the Zambian Block favoured by the Rukwa shear zone.

6. Conclusions

Analysis of natural graben geometries and fault patterns reveals the nearly systematic occurrence of two fault orientations with an angular obliquity of around 40° during extension. These faults are parallel or sub-parallel to pre-existing crustal and lithospheric fabrics. We carried out experiments to simulate the reactivation of coeval oblique lithospheric faults in the graben and depocentre development. Comparison of our results with those obtained with different experimental procedures shows differences and similarities which highlight the limits of each experimental approach. Nevertheless, common results are observed. In previous works (Tron and Brun, 1991; McClay and White, 1995; McClay et al., 2002), the depocentre formation is controlled by faults which present the most orthogonal orientation with respect to the stretching direction. Our experiments with two oblique VD segments, which simulate the reactivation of two inherited lithospheric faults complete these results and allow to better understand the role of the inheritance in the graben formation. When two oblique lithospheric fabrics are contemporaneously reactivated, the models suggest that the intersection of the two lithospheric faults controls the location of the depocentres, its geometry (i.e., symmetric or asymmetric) depending on the stretching direction. Then, analysis of the natural depocentre geometry allows determination of the direction of extension during syn-rift sedimentation.

Application to the Upper Rhine Graben suggests that this segment of the West European rift was affected by a constant NW–SE extension direction between the Late Eocene and the Late Oligocene. In the Southern East African Rift the global geometry and the distribution of the subsidence may result from the coeval reactivation of the Rukwa shear zone and the Ubendian segment of the Pan-African orogenic belt located in the northern part of the Lake Tanganyika rift. The location of the initial subsidence suggests an E–W extension direction which has induced the progressive formation of the Late Tanganyika rift, Rukwa rift and Lake Malawi rift.

Acknowledgments

References

Allemand, P., 1990. Approche expérimentale de la mécanique du rifting continental. Mém. Doc. Géosci. Rennes 38 175 pp.

Allemand, P., Brun, J.P., 1991. Width of continental rifts and rheological layering of the lithosphere. Tectonophysics 188, 63–69.

Baldridge, W.S., Keller, G.R., Haak, V., Wendlandt, E., Jiracek, G.R., Olsen, K.H., 1995. The Rio Grande rift. In: Olsen, K.H. (Ed.), Continental Rifts: Evolution, Structure, Tectonics, Development in Geotectonics, vol. 25. Elsevier, Amsterdam.

Basile, C., Brun, J.P., 1999. Transtensional faulting patterns ranging from pull-apart basins to transform continental margins: an experimental investigation. J. Struct. Geol. 21, 23–37.

Behrmann, J.H., Hermann, O., Horstmann, M., Tanner, D.C., Bertrand, G., 2003. Anatomy and kinematics of oblique continental rifting revealed: a three-dimensional case study of the southeast Upper Rhine graben (Germany). Bull. Am. Assoc. Pet. Geol. 87, 1–17.

Bellahsen, N., Daniel, J.-M., 2005. Fault reactivation control on normal fault growth: an experimental study. J. Struct. Geol. 27, 769–780.

Bergerat, F., 1987. Stress fields in the European platform at the time of Africa–Eurasia collision. Tectonics 6, 99–132.

Bois,, 1993. Initiation and evolution of the Oligo-Miocene rift basins of southwestern Europe: contribution of deep seismic reflection profiling. Tectonophysics 226, 227–252.

Bonini, M., Souriot, T., Boccaletti, M., Brun, J.P., 1997. Successive orthogonal and oblique extension episodes in a rift zone: laboratory experiments with application to the Ethiopian Rift. Tectonics 16, 347–362.

Brun, J.P., 1999. Narrow rifts versus wide rifts: inferences for the mechanics of rifting from laboratory experiments. Philos. Trans. R. Soc. Lond. Ser. A: Math. Phys. Sci. 357, 695–712.

Brun, J.P., Beslier, M.O., 1996. Mantle exhumation at passive margin. Earth Planet. Sci. Lett. 142, 161–173.

Brun, J.P., Gutscher, M.A.DEKORP-ECORS team, 1992. Deep crustal structure of the Rhine graben from DEKORP-ECORS seismic reflexion data: a summary. Tectonophysics 208, 139–147.

Chorowicz, J., Deffontaines, B., 1993. Transfer faults and pull-apart model in the Rhine graben from analysis of multi-source data. J. Geophys. Res. 98, 14.339–14.351.

Chorowicz, J., Mukonk, N.B., 1980. Linéament anciens, zones transformantes récentes et géotectonique des fossés de l'Est Africain, d'après la télédétection et la microtectonique, Museum Royal de l'Afrique centrale, Département de Géologie et Minéralogie, Tervuren. Rapp. Ann., 143–167.

Clifton, A.E., Schlische, R.W., 2001. Nucleation, growth, and linkage of faults in oblique rift zones: results from experimental clay models and implications for maximum fault size. Geology 29, 455–458.

Clifton, A.E., Schlische, R.W., Withjack, M.O., Ackermann, R.V., 2000. Influence of rift obliquity on fault population systematics: results of experimental clay models. J. Struct. Geol. 22, 1491–1509.

Davy, Ph., Cobbold, P.R., 1991. Experiments on shortening of 4-layer continental lithosphere. Tectonophysics 188, 1–25.

Ebinger, C.J., 1989. Tectonic development of the western branch of the East African Rift System. Geol. Soc. Amer. Bull. 101, 885–903.

Edel, J.B., Fluck, P., 1989. The Upper Rhenish shield basement (Vosges, Upper Rhinegraben, Schwarzwald) main structural features deduced from magmatic, gravimetric and geological data. Tectonophysics 169, 303–316.

Færseth, R.B., Knudsen, B.E., Liljedahl, T., Midbøe, P.S, Søderstrøm, B., 1997. Oblique rifting and sequential faulting in the Jurassic development of the northern North Sea. J. Struct. Geol. 19, 1285–1302.

Faugère, E., Brun, J.P., Van Den Driessche, J., 1986. Bassins asymétriques en extension pure et en décrochement: modèles expérimentaux. Bull. Cent. Rech. Explor. Prod. Elf-Aquitaine 10, 13–21.

Higgins, R.I., Harris, L.B., 1997. The effect of cover composition on extensional faulting above re-activated basement faults: result from analogue modelling. J. Struct. Geol. 19, 89–98.

Hubbert, K.M., 1937. Theory of scale models as applied to the study of geologic structures. Geol. Soc. Amer. Bull. 48, 1459–1520.

Illies, J.H., 1981. Mechanism of graben formation. Tectonophysics 73, 249–266.

Jestin, F., Huchon, P., Gaulier, M., 1994. The Somalia plate and the East African Rift System: present-day kinematics. Geophys. J. Int. 116, 637–654.

Lezzar, K.E., Tiercelin, J.J., Le Turdu, C., Cohen, A.S., Reynolds, D.J., Le Gall, B., Scholz, C.A., 2002. Control of normal fault interaction on the distribution of major Neogene sedimentary depocenters, Lake Tanganyika, Eat African rift. Bull. Am. Assoc. Pet. Geol. 86, 1027–1059.

Lopes Cardozo, G., Granet, M., 2003. Teleseismic investigations in the Southern Upper Rhine Graben. Geophys. Res. Abstr. 5 (EAE03-A-01967).

Manatschal, G., Froitzheim, N., Rubenach, M., Turrin, B.D., 2001. The role of detachment faulting in the formation of an ocean-continent transition: insights from the Iberia Abyssal Plain. In: Wilson, R.C.L., Whitmarsh, R.B., Taylor, B., Froitzheim, N. (Eds.), Non-Volcanic Rifting of Continental Margins: a Comparison of Evidence from Land and Sea, Geol. Soc. London Spec. Public, vol. 187, pp. 405–428.

McClay, K.R., White, M.J., 1995. Analogue modelling of orthogonal and oblique rifting. Mar. Pet. Geol. 12, 137–151.

McClay, K.R., Dooley, T., Whitehouse, P., Mills, M., 2002. 4-D evolution of rift systems: insights from scaled physical models. Am. Assoc. Pet. Geol. 86, 935–959.

McConnell, R.B., 1972. Geological development of the rift system of eastern Africa. Geol. Soc. Amer. Bull. 83, 2549–2572.

Meier, L., Eisbacher, G.H., 1991. Crustal kinematics and deep structures of the northern Rhine Graben, Germany. Tectonics 10, 621–630.

Michon, L., 2001. Dynamique de l'extension continentale-application au rift ouest-européen par l'étude de la province du Massif Central. Mém. Geosci. 99 263 pp.

Michon, L., Merle, O., 2000. Crustal structures of the Rhinegraben and the Massif Central grabens: an experimental approach. Tectonics 19, 896–904.

Michon, L., Merle, O., 2003. Mode of lithospheric extension: conceptual models from analogue modelling. Tectonics 22, 1028, doi:10.1029/2002TC001435.

Michon, L., Van Balen, R.T., Merle, O., Pagnier, H., 2003. The Cenozoic evolution of the Roer Valley rift system integrated at a European scale. Tectonophysics 367, 101–126.

Morange, A., Heritier, F., Villemin, J., 1971. Contribution de l'exploration pétrolière à la connaissance structurale et sédimenatire de la Limagne, dans le Massif Central. Symposium J. Jung, Plein Air Service, Clermont-Ferrand, pp. 295-308.

Morley, C.K., 1988. Variable extension in Lake Tanganyika. Tectonics 7, 785–802.

Morley, C.K., 1999. How successful are analogue models in addressing the influence of pre-existing fabrics on rift structures. J. Struct. Geol. 21, 1267–1274.

Ramberg, H., 1981. Gravity, Deformation and the Earth's Crust. Academic Press, London. 452 pp.

Rey, P., Burg, J.P., Casey, M., 1997. The Scandinavian Caledonides and their relationship to the Variscan belt. In: Burg, J.P., Ford, M. (Eds.), Orogeny Through Time, Spec. Publ. Geol. Soc. London, vol. 121, pp. 179–200.

Ring, U., 1994. The influence of preexisting structure on the evolution of the Cenozoic Malawi rift (East African rift system). Tectonics 13, 313–326.

Ring, U., Betzler, C., 1995. Geology of the Malawi Rift: kinematic and tectonosedimentary background to the Chiwondo Beds, northern Malawi. J. Hum. Evol. 28, 7–21.

Rosendahl, B.R., Kilembe, E., Kaczmarick, K., 1992. Comparison of the Tanganyika, Malawi, Rukwa and Turkana Rift zones from analyses of seismic reflection data. Tectonophysics 213, 235–256.

Schumacher, M.E., 2002. Upper Rhine Graben: role of preexisting structures during rift evolution. Tectonics 21, 6.1–6.17.

Seranne, M., 1999. The Gulf of Lion continental margin (NW Mediterranean) revisited by IBS: an overview. In: Durand, B., Jolivet, L., Horvath, F., Seranne, M. (Eds.), The Mediterranean Basins: Tertiary Extension within the Alpine Orogen, Spec. Publ. Geol. Soc. London, vol. 156, pp. 15–36.

Tapponnier, P., 1977. Evolution tectonique du système alpin en Méditerranée: poinçonnement et écrasement rigide-plastique. Bull. Soc. Géol. Fr. 19, 437–460.

Tron, V., Brun, J.P., 1991. Experiments on oblique rifting in brittle–ductile systems. Tectonophysics 188, 71–84.

Villemin, T., Alvarez, F., Angelier, J., 1986. The Rhinegraben : extension, subsidence and shoulder uplift. Tectonophysics 128, 47–59.

Wickert, F., Eisbacher, G.H., 1988. Two-sided Variscan thrust tectonics in the Vosges Mountains, north-eastern France. Geodin. Acta 2, 101–120.

Annexe 9 :

Michon, L., V. Cayol, L. Letourneur, A. Peltier, N. Villeneuve, T. Staudacher (2009). Edifice growth, deformation and rift zone development in basaltic setting: insights from Piton de la Fournaise shield volcano (Réunion Island), *in press to J. Volcanol. Geotherm. Res.*

Edifice growth, deformation and rift zone development in basaltic setting: insigths from Piton de la Fournaise shield volcano (Réunion Island)

Laurent Michon[1], Valérie Cayol[2], Ludovic Letourneur[3], Aline Peltier[4], Nicolas Villeneuve[5], Thomas Staudacher[6]

[1] Laboratoire GéoSciences Réunion, Université de la Réunion, Institut de Physique du Globe de Paris, CNRS, UMR 7154 – Géologie des Systèmes Volcaniques, 15 avenue René Cassin, 97715 Saint Denis, France.

[2] Laboratoire Magmas et Volcans, UMR 6524, CNRS-IRD-Université Blaise Pascal, 5 rue Kessler, 63038 Clermont-Ferrand, France.

[3] Department of Structural Geology and Geodynamics, Geoscience Centre, University of Göttingen, Goldschmidtstrasse 3, D-37077 Göttingen, Germany.

[4] Institut de Physique du Globe de Paris, CNRS, UMR 7154 – Géologie des Systèmes Volcaniques, 4 place Jussieu, 75252 Paris cedex 05.

[5] Institut de Recherche pour le Développement, US 140, BP172, 97492 Sainte-Clotilde cedex, France.

[6] Observatoire Volcanologique du Piton de la Fournaise (OVPF), Institut de Physique du Globe de Paris, CNRS, UMR 7154 – Géologie des Systèmes Volcaniques, 97418 La Plaine des Cafres, France.

Abstract

The overall morphology of basaltic volcanoes mainly depends on their eruptive activity (effusive vs. explosive), the geometry of the rift zones and the characteristics of both endogenous and exogenous growth processes. The origin of the steep geometry of the central cone of Piton de la Fournaise volcano, which is unusual for a basaltic effusive volcano, and its deformation are examined with a combination of a detailed morphological analysis, field observations, GPS data from the Piton de la Fournaise Volcano Observatory and numerical models. The new caldera walls formed during the April 2007 summit collapse reveal that the steep cone is composed of a pyroclastic core, inherited from an earlier explosive phase, overlapped by a pile of thin lava flows. This suggests that exogenous processes played a major role in the building of the steep central cone. Magma injections into the cone, which mainly occur along the N25-30 and N120 rift zones, lead to an asymmetric outward inflation concentrated in the cone's eastern half. This endogenous growth progressively tilts the southeast and east flanks of the cone, and induces the development of a dense network of flank fractures. Finally, it is proposed that intrusions along the N120 rift zone are encouraged by stresses induced by magma injections along the N25-30 rift zone.

Keywords: Piton de la Fournaise, morphology, volcano fractures, numerical modelling, growth process, rift zone.

1- Introduction

Basaltic shield volcanoes grow by the combined effect of endogenous and exogenous processes (e.g., Annen et al., 2001). Endogenous growth is mainly related to dyke intrusions, which preferentially propagate along the existing rift zones. The volcano shape consequently depends on the intensity of their activity and may vary from elongated, e.g., Karthala in Grande Comore, and Mona Loa and Kilauea in Hawaii, to sub-circular, e.g., volcanoes of Western Galapagos. Exogenous growth results from the accumulation of lava flows and pyroclastic cones (Naumann and Geist, 2000; Rowland and Garbeil, 2000). Long lava flows tend to flatten the volcano morphology, whereas short and thick ones may encourage the development of steep edifices (Naumann and Geist, 2000; Annen et al., 2001).

At Piton de la Fournaise, Réunion Island, however, the magmatic activity led to the development of a steep central cone in the Enclos caldera despite the predominance of fissure eruptions that feed fluid basaltic lava flows. Moreover the cone is almost circular whereas most of the eruptions develop along the N25-30 and N120 rift zones (Fig 1; Michon et al., 2007a). To answer these paradoxes, Annen et al.

(2001) proposed, using numerical models, that the geometry of the cone was resulting from a predominant endogenous growth with only 30% of the edifice volume directly related to short lava flows. Although the models roughly fit the current cone's geometry, the input and natural data partly disagree. First, the simulated dykes (mean thickness of 3m) are not as thick in nature as in the models. Indeed, recent works showed that the mean dyke thickness related to the post-1997 eruptions was around 0.5-0.7 m (Fukushima, 2005; Peltier et al., 2007). Second, the model of Annen et al. (2001) simulates 10000 dyke intrusions, 7% of them leading to an eruption. Such an intrusion/eruption ratio is the opposite of that observed since 1972, 81 eruptions (92%) and 7 intrusions (8%). Models with more realistic parameters show that the central cone should be much flatter (Annen et al., 2001).

This paper aims at understanding the origin of the atypical geometry of the central cone of Piton de la Fournaise. It examines the morphology and inner structure of the cone. It also considers the role of the magmatic and volcano-tectonic structures in both the growth and the deformation of the cone, by combining field data and GPS data, as well as numerical models of rift dyke intrusions. Such a multi-

disciplinary approach highlights the existing links between the deformation observed in the field, the displacement measured by GPS, and the recurrent intrusions of the dykes along preferential paths. The origin of the central cone and its deformation are interpreted in the light of both endogenous and exogenous growths.

2- Morphology and inner structure of the central cone

Piton de la Fournaise is the active volcano of Réunion Island (Fig 1). The eruptive centre is located in the upper part of a large U-shaped caldera, the Enclos-Grand Brûlé structure, where most of the eruptions have occurred in the past 4.5 ka (Bachèlery, 1981). The concentration of activity in the upper part of the caldera led to the construction of a 400 m high cone. Magma intrusions, which originate from a magma chamber located at about sea level below the cone (Peltier et al., 2007), are concentrated along two N25-30 and N120 rift zones (Fig 1; Michon et al., 2007a). Outside the Enclos caldera, magma intrusions may continue along the NE and SE rift zones. The present day cone summit shows two collapse structures: Bory crater in the West, which is currently inactive, and Dolomieu in the East, which experienced a caldera collapse during the large April 2007 eruption (Fig 1; Michon et al., 2007b). Before this collapse, the elongated shape of the pre-existing Dolomieu was the result of the coalescence of several pit craters (Lénat and Bachèlery, 1990; Carter et al., 2007). As a whole, Bory and Dolomieu confer a global E-W elongation to the summit of the central cone.
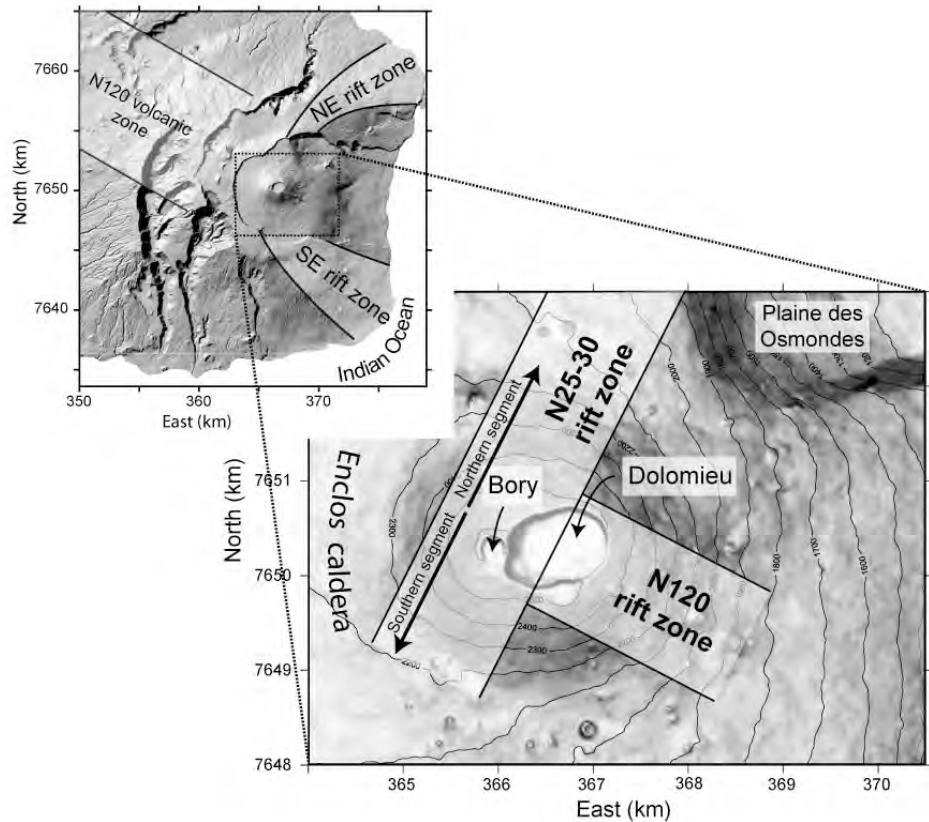

Figure 1: 25 m step Digital Elevation Model of Piton de la Fournaise. The edifice is characterised by two NE and SE rift zones outside the Enclos caldera. In the Enclos caldera, the recent eruptions are concentrated along two N25-30 and N120 rift zones (Michon et al., 2007a). The central cone is cut by two summit collapse structures, Bory and Dolomieu. Coordinates in UTM WGS84 (zone 40S).

The use of a 25 m step digital elevation model (DEM) provided by the Institut Géographique National allows a precise description of the limits of the cone, the distribution of the slopes and the structure of the summit zone. The cone's lower limit corresponds to an almost continuous sharp break-in-slope that separates the caldera floor and the steep flanks of the cone (Fig 2). The local outlined discontinuities are due to the Puy Mi-Côte parasitic cone in the North, and the N120 topographic ridge in the SE, which is formed by the alignment of large pyroclastic cones along the N120 rift zone. These two structures disregarded, the base of the cone presents a sub-circular shape with a radius of about 1.6 km (Fig 2a). The flanks of the cone present steep slopes, which contrast with the classical view of a basaltic effusive edifice. The western part of the cone, i.e., west of a N15 trending line centred on Dolomieu, is characterised by relatively homogeneous slopes ranging between 15° and 25°. East of the N15 boundary, the cone shows steeper slopes (25-30°), which locally reach 35°. Although the N120

topographic ridge gives to the southeast flank a complex slope distribution, the low-pass filtered DEM strikingly shows that the steep slopes of the cone's eastern half are not circumferentially distributed, but present two linear trends in the N150 and N55 directions (Fig 2b). It is noteworthy that the N55 trend is aligned with a 500 m wide and 700 m long zone characterised by a network of parallel lineaments (Fig 2c). Field observations and aerial photographs reveal that the lineaments correspond neither to the limit of lava flows, nor to eruptive fissures. Therefore, it is likely that the lineaments coincide to the surface trace of a fault zone, the activity of which may be related to the dynamics of the magmatic system. Finally, the summit morphology of the cone is characterised by present collapse structures, Bory and Dolomieu, surrounded by relatively flat areas which were interpreted as fully filled pit craters (Fig 2b; Bachèlery, 1981; Lénat and Bachèlery, 1990). Past and present collapse structures are restricted to a slightly elongated zone, the centre of which is nearly superimposed to that of the 3.2 km-across circle marking the base of the cone (Fig 2b).
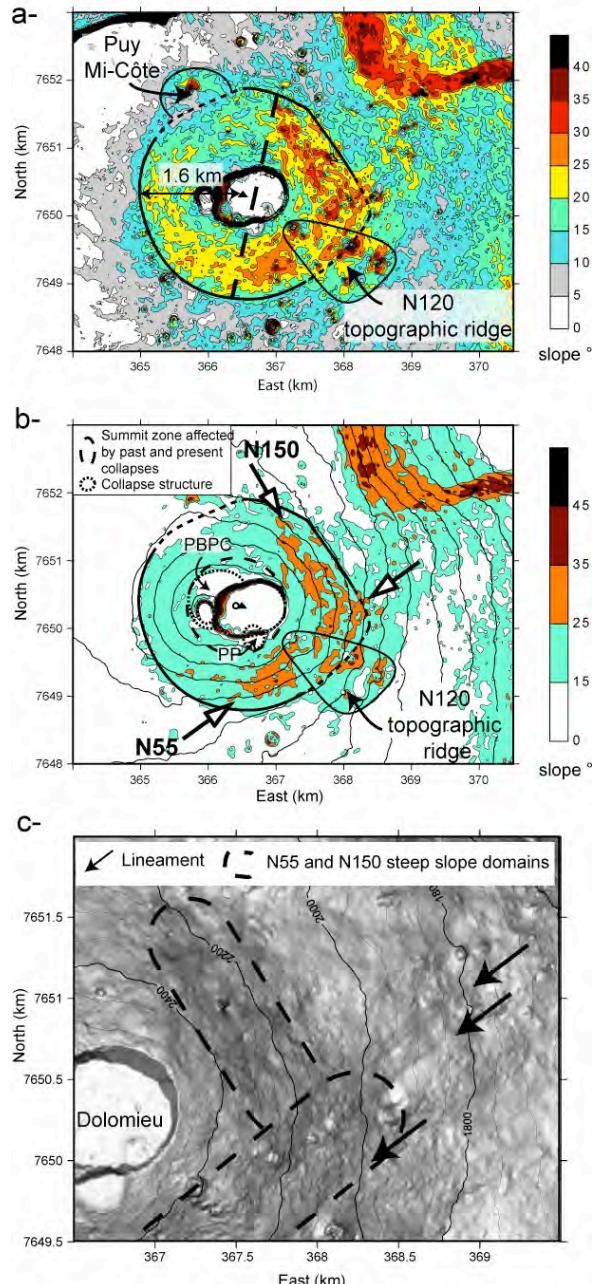

Figure 2: a- Slope map of the central cone calculated from the 25 m step DEM. The cone, which is sub-circular with a radius of 1.6 km, is coalescent to a parasitic cone in the north and a N120 topographic ridge in the NE, formed by several pyroclastic cones. The western and eastern parts of the cone present different slope values. b- Slope map of the calculated from a low-pass filtered DEM in order to determine the main characteristics of the morphology. The very steep slopes of the cone's eastern half are distributed in two linear steep slope zones trending in the N55 and N150 directions. PP: Petit Plateau; PBPC: Pre Bory pit crater. c- Shaded relief representation of a 7 m step DEM calculated by stereophotogrammetry from a set of aerial photographs performed in 1989. This high resolution DEM highlights clear, parallel lineaments in the northeastern continuity of the N55 steep slope zone. Coordinates in UTM WGS84 (zone 40S).

The April 2007 caldera, which deeply cut the central cone, formed new scarps that reveal its internal structure (Fig 3). The northern and southern caldera walls exhibit three main structural features. 1- The northwestern part of the cone built up above a pre-Bory pit crater, the existence of which was already hypothesised by Lénat and Bachèlery (1990) from the occurrence of gentle slopes north of Bory (Figs 2b and 3a). The limits of this collapse structure are underlined in the caldera wall by a strong lithological contrast characterised by thick lava units, and the succession of thin lava flows and scoria layers, inside and outside the pit respectively. 2- The volcanic units cut by the pre-Bory pit crater are sub-horizontal and parallel to the present day surface, suggesting that the current geometry of the cone is inherited from a stage predating the development of the pre-Bory pit crater. This evolution disagrees with the historical reports of the 18th and 19th centuries in which the cone is considered to be symmetric and centred on the Bory pit crater until 1760, and becoming asymmetric when the activity shifted to the east flank of the cone in 1766 (Bory de Saint-Vincent, 1804). 3- The caldera walls reveal a relatively constant lithological pile with a succession of scoria and scoria-rich units underneath a pile of thin lava flows (Fig 3). The scoria materials suggest a period of predominantly explosive activity, which probably led to the construction of a large pyroclastic cone.
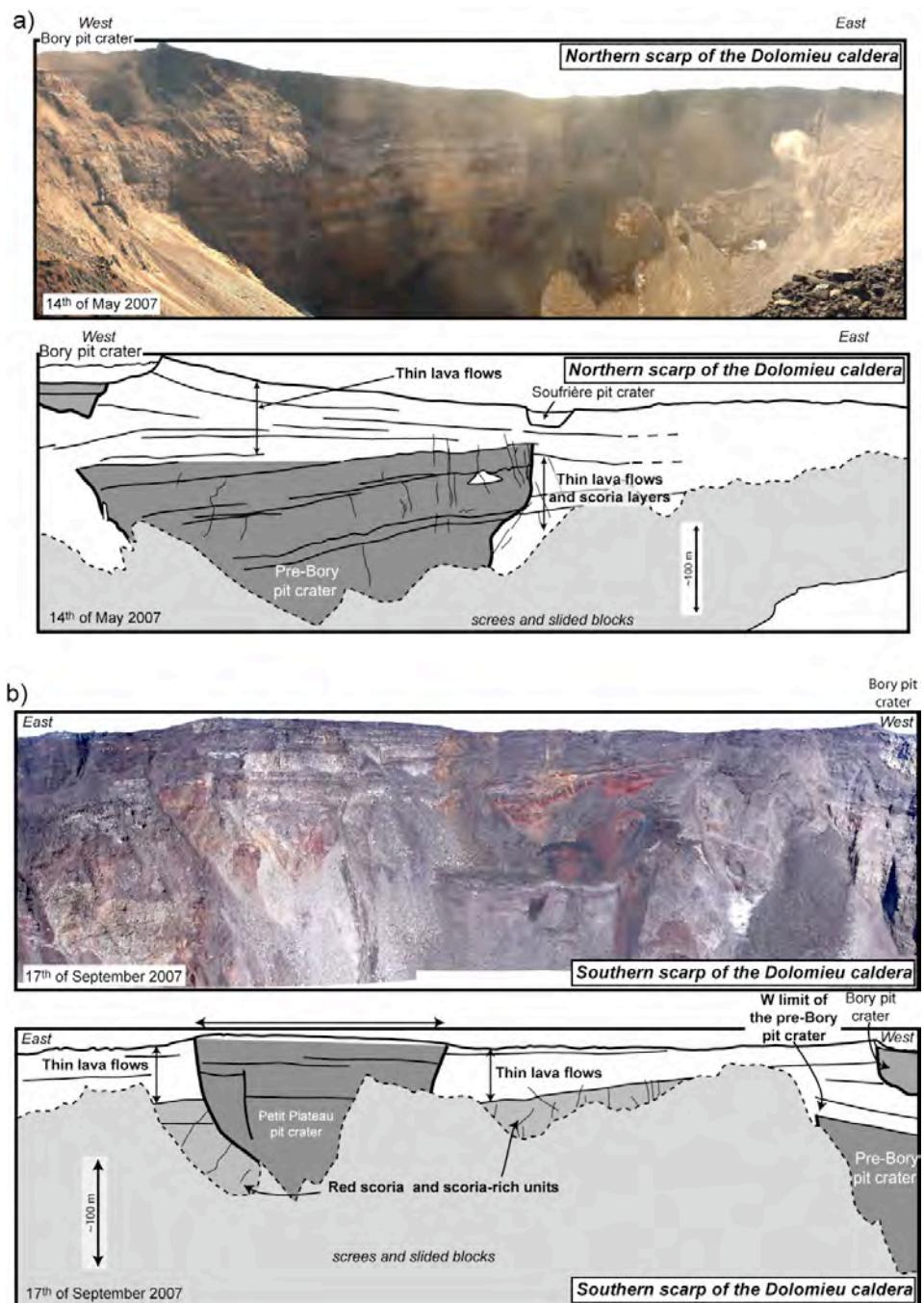

Figure 3: Panoramas and interpretations of the northern (a) and southern (b) scarps of the April 2007 caldera (photo b: Frederic Massin).

3- Fractures of the central cone

During the last decades, several works have addressed the origin of the tectonic structures of the central cone (Bachèlery, 1981; Bachèlery et al., 1983; Lénat and Bachèlery, 1990; Carter et al., 2007). The different analyses, which were essentially or strictly restricted to the summit of the central cone, revealed the coexistence of concentric and radial volcano-tectonic structures, consisting mainly of extensional fractures and eruptive fissures, respectively. The concentric fractures are restricted within the first tens of meters from the rim of Dolomieu and Bory. Their formation is interpreted as related to the current and paleo pit crater development, and the dynamics of the superficial magma chamber. Only one fracture network which trends obliquely to the northeast rim of Dolomieu, is linked to another process, i.e., the slumping of the eastern flank (Carter et al., 2007). The volcano-tectonic structures described on the flanks of the central cone correspond to eruptive fissures, which usually present a radial strike and open en échelon during dyke injection. This distribution locally changes in the east flank where the eruptive fissures mimic conjugate systems (Carter et al., 2007). The en échelon distribution on the northern and southern flanks of the central cone was initially interpreted as indicative of co-intrusive left-lateral and right-lateral displacements in the respective flanks, causing the eastward motion of the eastern flank of Piton de la Fournaise (Bachèlery et al., 1983). However, Michon et al (2007a) recently showed that the en échelon pattern most likely resulted from a reorientation of the magma intrusion close to the surface due to the rotation of the main principle stress σ_1 from vertical to downslope, rather than a shear deformation during dyke intrusion.

Since the last structural work at the cone scale in 1990, Piton de la Fournaise underwent 27 eruptions and 3 intrusions, each of them leading to deformation of the summit zone. A new structural analysis was realised on the central cone and the adjacent Enclos floor in order to determine if tectonic structures developed and accommodated the deformation measured from GPS and interferometry (Briole et al., 1998; Sigmundsson et al., 1999; Froger et al., 2004; Fukushima et al., 2005). Our field observations reveal a wide range of fractures affecting the eruptive system. In a way similar to Carter et al. (2007), the present work only considers the fractures cutting at least two adjacent geological units. Fractures restricted to single lava flows or cones, and related to their own dynamics, such as the syn-cooling

subsidence or collapse, were disregarded. According to the fracture geometry, size and relationship with the geological formations, three different types of volcano-tectonic structures were distinguished, among which the two first correspond to the radial and concentric fractures already described by Bachèlery et al. (1983) and Carter et al. (2007).

1- Eruptive fissures mainly open perpendicular to the slope (Fig 4a). Their mean length inferred from 68 post-1997 eruptive fissures is 180 m. Only few eruptive fissures are oblique to the slope. Their length is significantly higher (i.e., 2.5 to 11 times longer) than that of the downslope eruptive fissures. They are located in the SSE and east flanks of the cone, where they strike N20-25 and N65 respectively. In the east flank, the recent N65 trending eruptive fissure of the August 2004 eruption is connected to the southeastern corner of Dolomieu. Aerial photographs of 1936 reveal that older eruptive fissures developed at the same location with a similar geometry. The geometric association of the N65 eruptive fissures with the radial ones forms the conjugate-like systems described by Carter et al. (2007). Occurrence of long and oblique eruptive fissures in the flanks suggests that besides the sub-surface downslope σ_1, which controls the orientation of most of the eruptive fissures (Michon et al., 2007a), local stress fields or structures may influence the magma migration through the east flank. The local structural control is corroborated by the development of N80 and N50 eruptive fissures close to the southern rim of Dolomieu and northwest of Bory, respectively. Indeed, their orientation is parallel to the southern fault of Dolomieu and at the limit of the pre-Bory pit-crater.

2- Concentric fractures consist in tens to hundreds of metres long extensional fractures either parallel to the scarps of Bory and Dolomieu (Fig 5a), or at the limit of paleo pit craters. Fracture width evolves from few centimetres to 1-2 m close to the limits of the pit-crater. The maximum fracture density is observed in Bory, southwest and north of Dolomieu and at the limit of Petit Plateau. Carter et al. (2007) recently proposed that these concentric fractures result from annular extension related to pit-crater collapses. Analysis of the fractures before and after the April 2007 caldera reveals that most of the fractures form during the collapse events and are reactivated by radial extension stresses during the filling of the collapse structure (Michon et al., 2009, this issue).
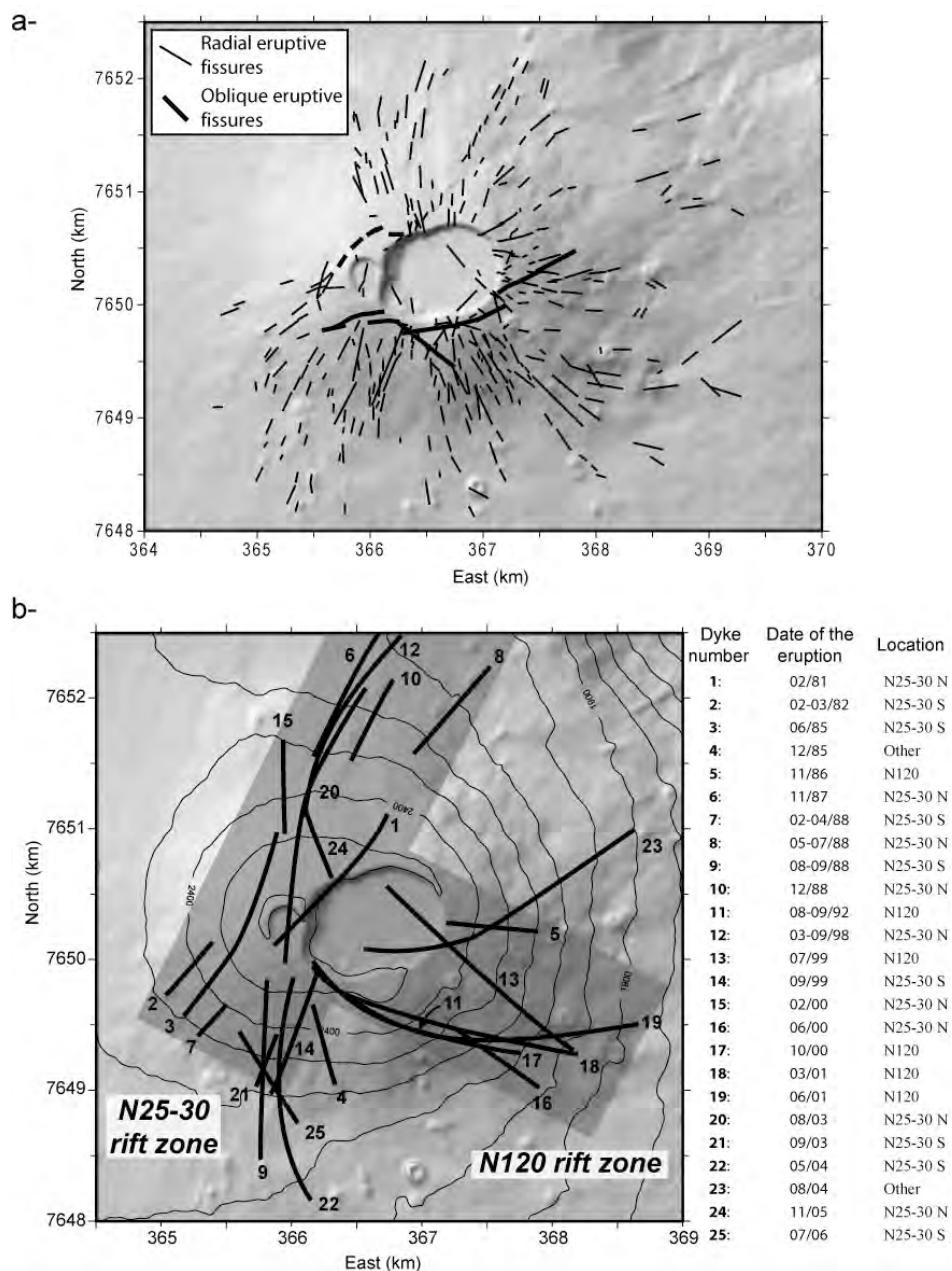
Figure 4: a- Distribution of the eruptive fissures. b- List and location of the dykes associated to proximal eruptions since 1981. Coordinates in UTM WGS84 (zone 40S).

a-

b-

N150 trending
parallel fractures

N150 trending
single fracture
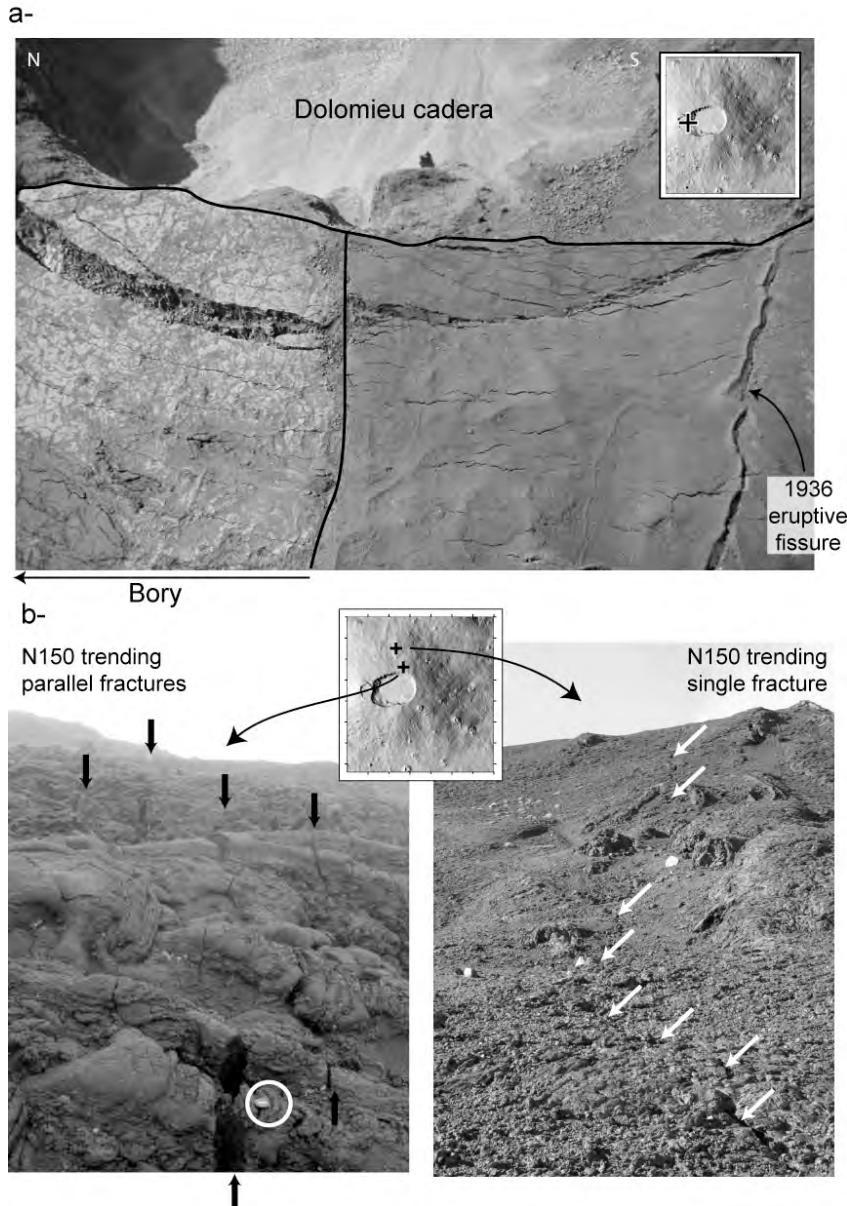
Figure 5: a- Picture of the concentric fractures associated to the collapse structures. b- Pictures of the flank fractures that affect the eastern half of the central cone. Here, the N150 deformation zone.

3- The third type of fracture corresponds to linear structures that usually affect several geological units, i.e., lava flows or pyroclastic cones. They differ from concentric fractures either by the distance to the collapse structures or by their obliquity with respect to the concentric faults. Here they are named flank fractures even though some of them are located close to the summit or in the Enclos caldera floor. Two distinct geometries were observed in the field. They correspond to (i) several tens of meters long single linear structures or (ii) 10-50 m wide tectonic corridors in which parallel fractures are concentrated (Fig 5b). Whatever their geometry, all the fractures are extensive structures showing a slight lateral component in few cases. Systematic mapping of fractures on both the central cone and the proximal part of the Enclos caldera floor shows a strongly heterogeneous spatial distribution (Fig 6a). Most of the fractures are located in the eastern half of the

central cone. They are characterised by three main orientations trending in the N20-30, N55-65 and N150-160 directions. It is remarkable that each trend presents a specific spatial distribution (Fig 6b). All N20-30 trending fractures are situated east of the N25-30 rift zone. The N55-65 fracture network is concentrated along a main axis, which corresponds to the locus of the clear northeast trending lineaments northeast of the N55 steep slope zone (Fig 2c). The continuity of the fractures affecting the old lava units in the August 2004 pahoehoe lava flow, and the decreasing opening of the fractures as a function of the age of the lava flow, suggest a continuous deformation process. Finally, N150-160 fractures are mainly located in the northeastern part of the summit (Fig 6b). These fractures are concentrated between the eastern rim of Dolomieu and the top of the N150 trending steep slope zone in the northeastern flank. Most of the deformation is restricted to two parallel

tectonic corridors of around 450 and 640 m long in which fractures indicate an almost exclusive extension. Only a small part of these deformation zones corresponds to the N150 *R'* shear network described by Carter et al (2007). Contrary to these authors, we believe that the shear indicators and the lava tube offsets, which suggest minor opposite lateral displacements, result from small differential movements between the lava blocks during a general extension rather than a succession of opposite senses of shear.
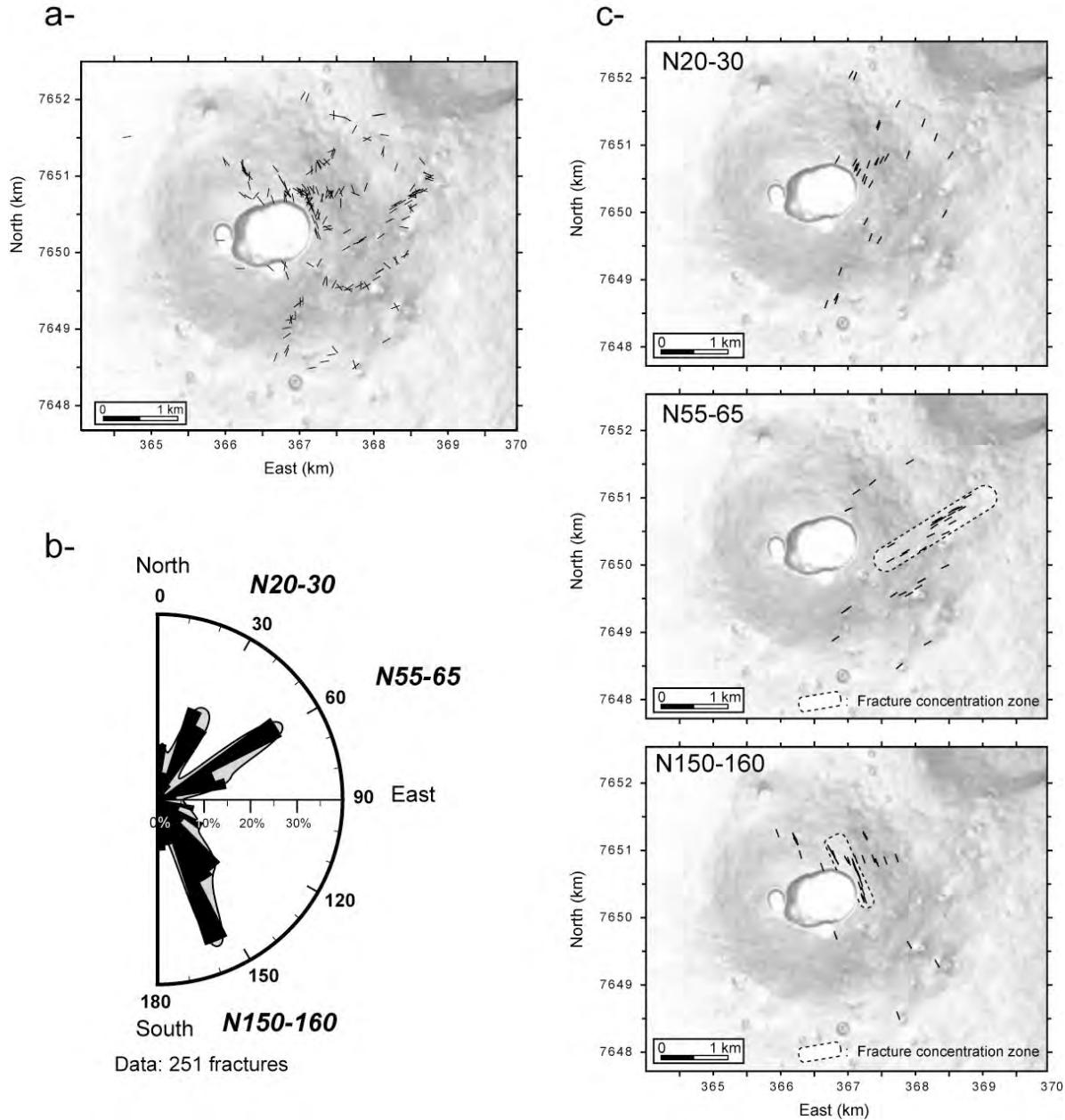

Figure 6: a- Spatial distribution of the flank fractures. b- Rose diagram illustrating the three main fracture trends: N20-30, N55-65 and N150-160. c- Spatial distribution of the three main fracture trends. Coordinates in UTM WGS84 (zone 40S).

4- Co-intrusive deformation

4.1- Types of eruptions and the related magmatic paths

Activity of Piton de la Fournaise is characterised by fissure eruptions fed by a magma reservoir located at about sea level (Nercessian et al., 1996; Peltier et al., 2007). Considering the location of the eruption site, three types of eruptions can be distinguished (Peltier et al., 2008). 1- Summit eruptions that start and remain in Dolomieu. 2- Proximal eruptions, which may start in the summit but progress to the flanks of the central cone and usually propagate downslope to the Enclos caldera floor. 3- Distal eruptions that develop away from the central cone, starting in the Enclos caldera floor. Numerical models suggest that the elevation of the first eruptive fissure, which opens during an eruption corresponds to the maximum elevation reached by the feeding dyke (Fukushima, 2005; Peltier et al., 2007). Then, only the

dykes related to summit and proximal eruptions (68% of the total eruptions) intrude into the central cone. We determined the dyke orientations related to the 25 proximal eruptions from the distribution of the related eruptive fissures for the period between 1981 and 2007 (Fig 4b). Note that summit eruptions were disregarded since their dyke orientation cannot be accurately determined. Our compilation shows that 92% of the proximal dykes follow the N25-30 and N120 rift zones described by Michon et al (2007a). 74% of them occur along the N25-30 axis with the same number of dyking events to the North and the South, and 26% of the eruptions developed on the SE flank along the N120 rift zone (Fig 4b).

4.2- Co-intrusive displacements inferred from GPS

At Piton de la Fournaise, dyke intrusions usually lead to an asymmetric deformation of the volcano characterised by a concentration of displacements east of the dykes (Lénat et al., 1989; Sigmundsson et al., 1999 ; Froger et al., 2004 ; Fukushima et al., 2005). GPS measurements carried out in 1981 and 1995 indicate that the eastern part of the cone summit experienced a 1.5-2 m eastward displacement during this period, whereas the western half remained stable (Briole et al., 1998). A denser GPS network composed of about 80 stainless steel benchmarks cemented around the crater, on the flanks and at the base of the summit cone was installed by the Piton de la Fournaise Volcano Observatory in order to better constrain co-intrusive deformation of the edifice. Since 2002, this network was repeatedly measured after each eruption. The location of each benchmark was determined with respect to a reference receiver situated north of the Enclos caldera. Sampling-rate of both receivers was of 1 s and benchmark locations were recorded during a 7-min stop on each.

As demonstrated above, between 1981 and 2007, dykes intruding the central cone followed the N120 rift zone, and the northern and southern segments of the N25-30 rift zone, in roughly the same proportion. Between April 2003 and November 2003, 3 eruptions and 1 intrusion occurred at the summit and along each rift zone, making the co-intrusive deformation of this period representative of the general behaviour during summit and proximal eruptions. GPS data clearly show the deformation decoupling between the eastern and western parts of the cone (Fig 7a). West of a N-S decoupling axis located between Bory and Dolomieu, displacements are small at the summit (<22 cm) and negligible at the base of the cone and in the Enclos (Table 1). East of the axis, displacements rotate from a north-eastward to a south-eastward motion from north to south, showing an average eastward motion of the eastern half of the central cone. Total displacement values of the summit are three times larger than in the West. GPS data reveal that vertical displacements are restricted to the cone,

reaching a maximum at the summit. In contrast, both the cone and the proximal part of the Enclos caldera floor experience significant outward horizontal displacements. Finally, it is interesting to note that the northern and western flanks present a steady decrease of displacement values, whereas the south-east and east flanks are characterised by a step wise decrease, correlated with variations of the topography. For the E flank, the GPS data located in the steepest part (data points 1a to 4a in Table 1a and Fig 7a) indicate a slight decrease of vertical displacements, i.e., between 39.5 and 34.2 cm, whereas they sharply decrease from 24.2 to 3.3 cm over the same distance in the Enclos floor (data points 5a to 7a).

As a consequence, the recurrent dyke intrusions up to the summit and along the intra-cone segments of the N25-30 and N120 rift zones lead to heterogeneous growth of the central cone. Between April and November 2003, the cone underwent a very slight steepening of the western flank ($\approx 4 \ 10^{-3\circ}$/yr), and a significant inflation of the eastern part, leading to a steepening of the south and east flanks ($\approx 1.5 \ 10^{-2\circ}$/yr). Moreover, GPS data suggest that each N55 and N150 trending steep slope zone undergoes a homogeneous deformation. This overall deformation pattern inferred for the period between April 2003 – November 2003 fully agrees with the slope change determined by Fukushima (2005) between March 1998 and June 2000, during which 5 eruptions occurred along the S and N segments of the N25-30 rift zone and along the N120 rift zone. The striking similarities between the two different periods suggest a relatively constant mode of deformation of the cone when summit and proximal eruptions occur.

Most of the deformation determined for the period between March 2002 and January 2006 is similar to that of April to November 2003 in terms of (i) decoupling between the western and eastern parts and (ii) and progressive decrease of displacement amplitudes from the top to the base of the cone in the north, south-west and west flanks (Fig 7b). It only differs in one point, which is the regular increase of total displacement values from 146.5 to 180.4 cm between the eastern part of the summit and the Enclos floor (Table 1b). Contrary to the periods between March 1998 and June 2000 and between April 2003 and November 2003, during which only summit and proximal eruptions occurred, the period between March 2002 and January 2006 was characterised by summit, proximal and also 3 distal eruptions in the Plaine des Osmondes (see Fig 1 for location). The displacement pattern related to one of these eruptions, in January 2004, suggests that the progressive increase of displacements when going east of the summit is induced by distal intrusions toward the Plaine des Osmondes (Fig 7c and Table 1c). Moreover, GPS data related to the January 2004 distal eruption indicate the existence of different

displacement domains separated by the N55 deformation zone described above. The N55 fracture zone limits a differential uplift, which is twice as high west of the fracture zone as east.

In summary, our data clearly show two different co-intrusive modes of deformation. The cumulated deformation related to summit and proximal intrusions is centred on the summit craters and is mostly restricted to the central cone. In contrast, the distal intrusions led to a widespread deformation, the limits of which cannot be determined with the current GPS network.
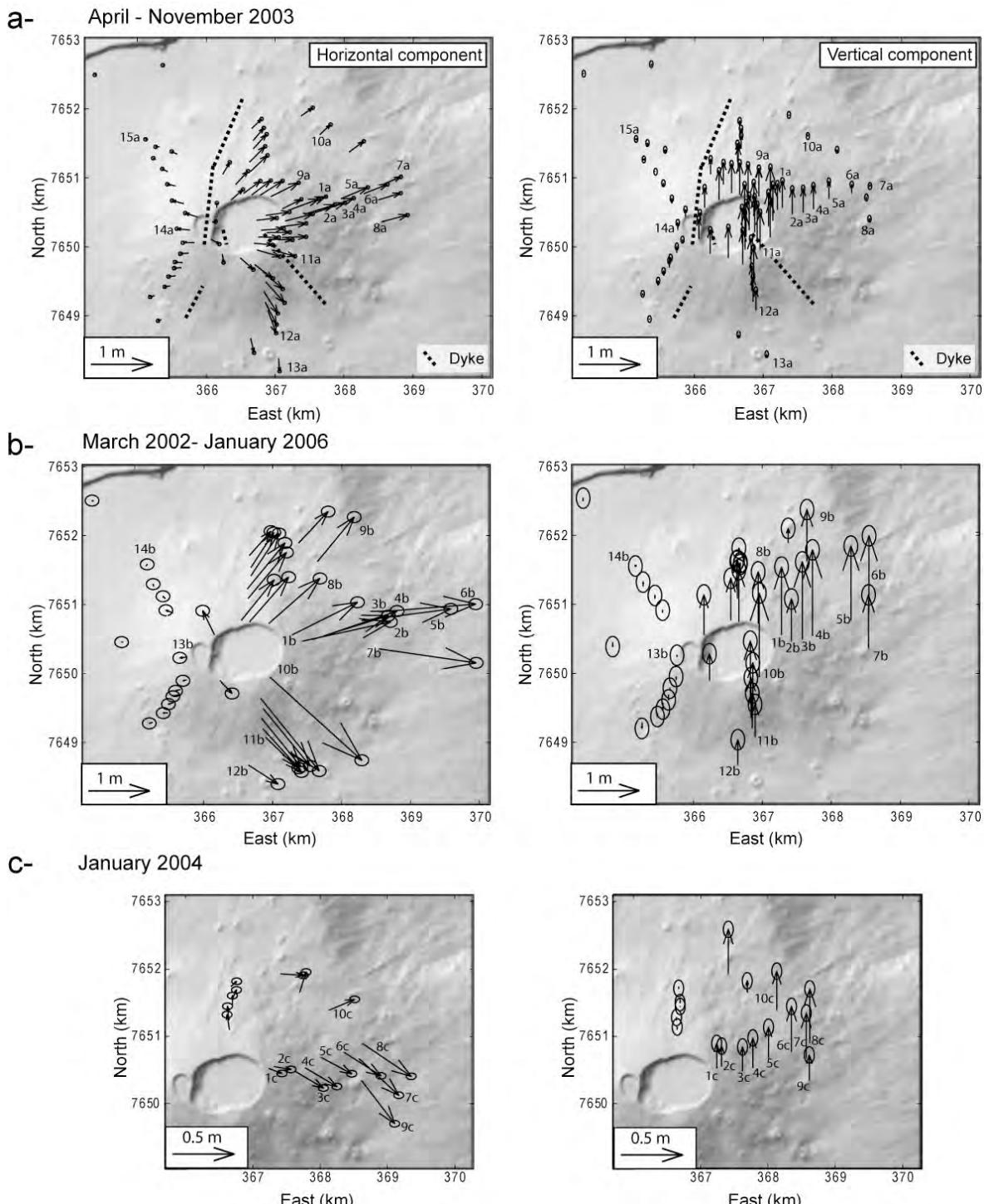

Figure 7: Horizontal (left) and vertical (right) co-intrusive displacements recorded by GPS. a- Between April and November 2003. The dashed lines indicate the location of the dykes. b- Between March 2002 and January 2006. c- During the January 2004 eruption. Coordinates in UTM WGS84 (zone 40S).

a- April 2003 - November 2003

	Data point	Horizontal (cm)	Vertical (cm)	Total (cm)
East profile — E. Flank	1a	49.2	39.5	**63.1**
	2a	46.8	36.8	**59.5**
	3a	45.7	34.9	**57.5**
	4a	44.7	34.2	**56.3**
Enclos	5a	42.8	25.4	**49.8**
	6a	37.5	13.2	**39.8**
	7a	34.0	(3.3)	**34.2**
	8a	39.8	(4.4)	**40**
NE p.	9a	45.5	41.3	**60.4**
	10a	21.5	(-2.3)	**21.6**
South p.	11a	34.8	54.7	**64.8**
	12a	35.2	29.7	**46.1**
	13a	19.1	5.5	**19.9**
NW p.	14a	19.1	10.6	**21.8**
	15a	3.9	(-0.1)	**3.9**

b- March 2002 - January 2006

	Data point	Horizontal (cm)	Vertical (cm)	Total (cm)
East — E. Flank	1b	107.4	99.6	**146.5**
	2b	133.1	62.0	**146.8**
	3b	116.4	113.9	**162.9**
	4b	114.9	126.8	**171.1**
Enclos	5b	132.5	109.5	**171.9**
	6b	141.7	111.6	**180.4**
	7b	144.2	79.3	**164.6**
NE	8b	100.4	75.9	**125.9**
	9b	84.7	76.4	**114.1**
South	10b	182.2	123.0	**219.8**
	11b	73.1	48.4	**87.7**
	12b	51.9	37.1	**63.8**
NW	13b	11.5	(2.7)	**11.8**
	14b	(3.1)	(0.1)	**3.1**

c- 01-2004 eruption

	Data point	Horizontal (cm)	Vertical (cm)	Total (cm)
Flank — E.	1c	10.2	18.3	**21**
	2c	12.6	14.9	**19.5**
	3c	24.2	17.6	**29.9**
	4c	26.8	21.8	**34.5**
Enclos	5c	25.5	21.9	**33.6**
	6c	32.2	33.4	**46.4**
	7c	39.8	33.0	**51.7**
	8c	43.2	39.6	**58.6**
	9c	39.6	18.7	**43.8** ← N55 fracture zone
	10c	20.2	28.6	**35**

(3.3): data smaller than the instrumental error

Table 1: Displacements measured by GPS for periods between April and November 2003 (a), March 2002 and January 2006 (b) and caused by the magma migration linked to the January 2004 distal eruption (c). See figure 8 for the location of the data points.

4.3- Modelling of co-intrusive deformations

We use a three-dimensional boundary element method (Cayol and Cornet, 1997) to investigate (1) the injection-related endogenous growth of the central cone, (2) the interaction between dyke injections and fractures, and (3) stress changes due to dyke injection along the northern and southern segments of the N25-30 rift zone. Models consider an elastic medium. Young's modulus is 5 GPa and Poisson ration is 0.25 (Cayol and Cornet, 1998). For the modelling, a mesh of the topography is constructed from a Digital Elevation Model of the volcano (Fig 8). This mesh is dense close to the deformation sources and coarse further away. In order to limit errors caused by the finite extension of the ground surface mesh, its extension is chosen to be 5 times the source dimensions.
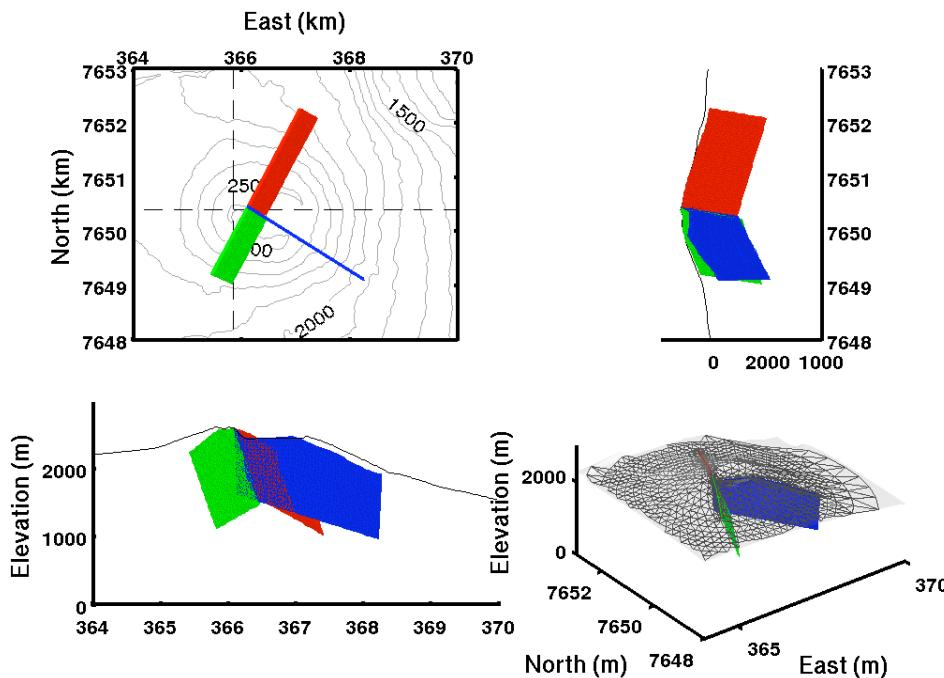

Figure 8: Map view, E-W and N-S cross sections, and perspective view of the Boundary Element Model computed to test the influence of repeated dyke injections into the N120 and N25-30 rift zones. All dykes are 1000 m high. The N120 dyke is represented by a blue mesh. It is vertical and 2.5 km long. The northern segment is represented by a red mesh. It dips 70° to the East and is 2.3 km long. The southern segment is represented by a green mesh. It dips 70° to the East and is 1.2 km long. The perspective view only shows a portion of the surface of the topography mesh, which extends five times further than shown.

Three rift zone dykes were modelled, two along the N25-30 rift zone, to the North and to the South of the summit cone, and one along the N120 rift zone, east of the summit cone. Length of the dykes, heights and dips (Fig 8) are typical of intrusions in rift zones (Sigmundsson et al, 1999; Froger et al, 2004; Fukushima et al, 2005; Peltier et al., 2007, 2008). The overpressure of the dykes is assumed to be 3 MPa, leading an average dyke opening of 2.3 m at the surface. As Piton de la Fournaise eruptions typically correspond to average dyke openings of 30 cm at the surface, these models are representative of more than 20 successive dyke intrusions, a number similar to the amount of intrusions that occurred between 1998 and 2007. Models show that dyke intrusions trigger an asymmetric deformation of the central cone (Fig 9a). Flanks steepen east of the N25-30 rift zone of around 0.05° and do not significantly change in the cone's western half. Only the summit part located north of Dolomieu and Dolomieu itself flatten. It is worth noting that the N150-160 fracture zone, which shows predominant extensional deformation, is located at the transition between domains showing contrasting deformation, i.e. increasing and decreasing slopes (Fig 9b).
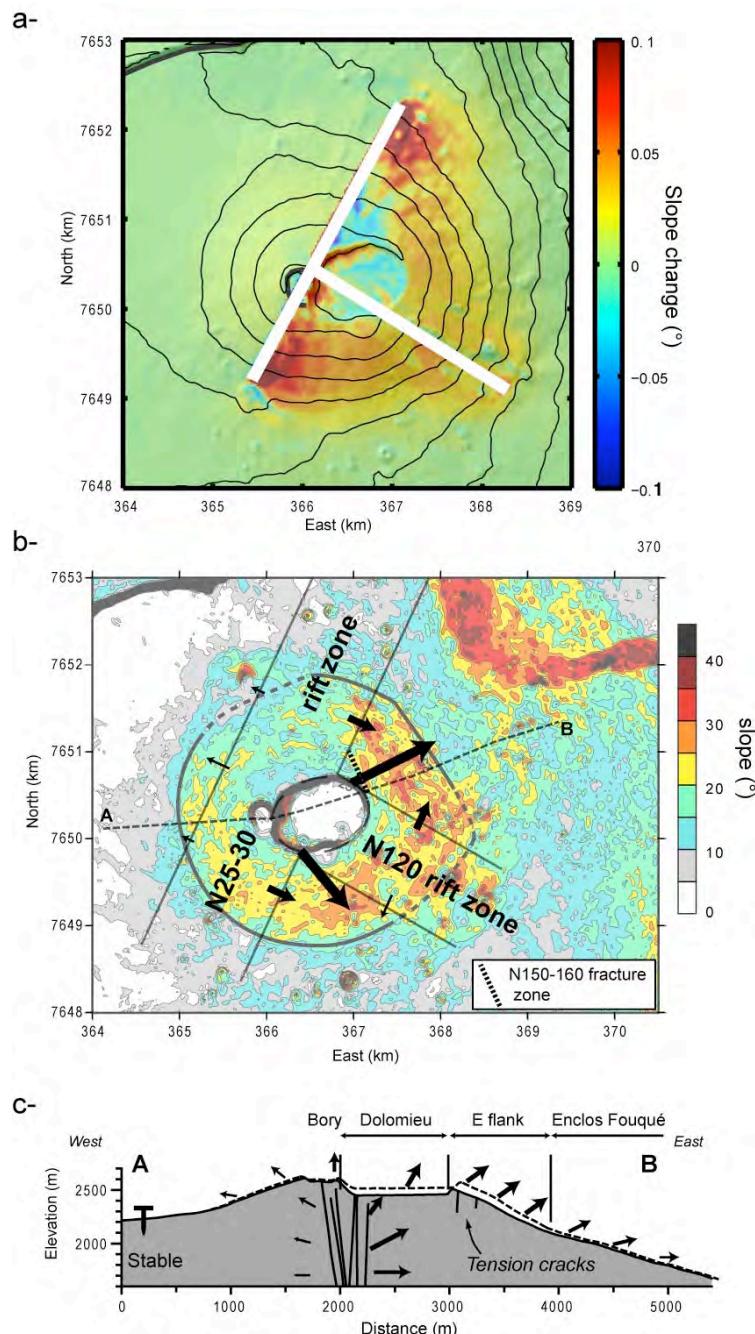

Figure 9: a- Modelled slope changes due to repeated dyke intrusions into the N25-30 and N120 rift zones (see Fig 8 for the dyke intrusion geometries). Dyke surface traces are represented with a white thick solid line. Thin lines represent elevation contours at 100m intervals. b- Slope map suggesting the effect of dyke intrusions in the development of the eastern and south-eastern steep flanks. c- E-W cross section presenting the outward inflation of the cone's eastern half.

We computed changes of Coulomb stresses on N55 vertical faults in order to investigate the influence of intrusions in the N25-30 and N120 rift zones on the N55 fractures network. Changes of Coulomb stress (ΔS) depend on normal and shear stress changes at given fault plane orientations for a given slip directions. They are defined by $\Delta S=\Delta\tau-\mu'\Delta\sigma$ (King et al., 1994), where $\Delta\tau$ is the shear stress change on a given failure plane (positive in the direction of fault slip), $\Delta\sigma$ is the change in normal stress on the plane (positive in compression) and μ', the apparent coefficient of friction, includes the effect of pore pressure changes. Here, we set $\mu'=0.4$, corresponding to laboratory values and small fluid pressure. Positive values of Coulomb stress changes bring faults closer to failure whereas negative values inhibit failure. We considered Coulomb stress changes induced by single dyke intrusion in each segment of the rift zones and by combined intrusions (Fig 10). Dyke injections in the northern segment of the N25-30 rift zone promote right-lateral fault slip in the area of the N55-65 fractures, whereas injections in the southern segment of the N25-30 rift zone and in the N120 rift zone encourage left-lateral slip in the N55-65 fracture zone. Combinations of injections in the northern and southern segments of the N25-30 rift zone as well as in the N120 rift zone favour right lateral slip of N55 faults located one km East of Dolomieu crater.
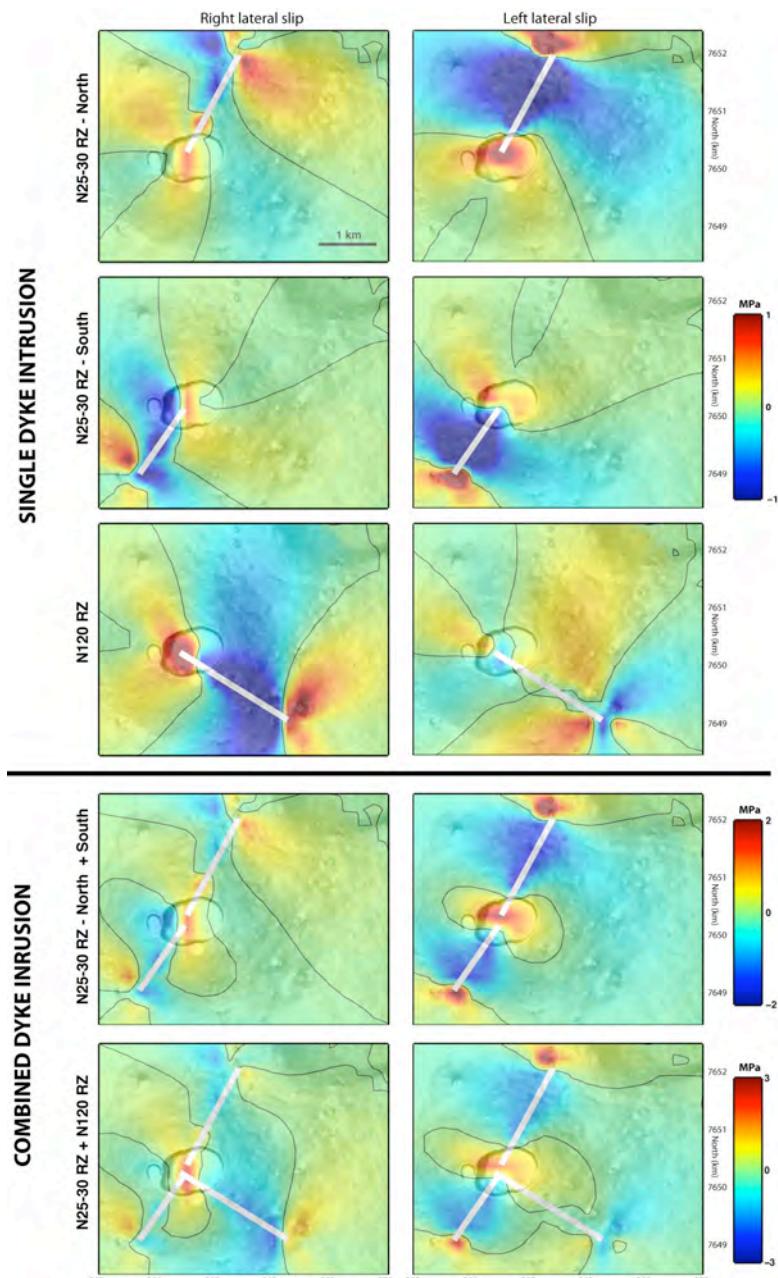

Figure 10: Coulomb stress changes (Mpa) at a 1500 m elevation induced on N55 vertical faults by intrusions in the N25-30 and N120 rift zones (see Fig 8 for the dyke intrusion geometries). Stress changes for right-lateral (left column) and left lateral (right column) slip are compared. Surface traces of the intruded dykes are shown as bold white lines. Null Coulomb stress changes are indicated by a light black line.

Coulomb stress changes on optimally oriented vertical planes were also calculated to determine whether a N55 fault zone could result from repeated rift zone intrusions. Following Cayol and Cornet (1998), we assumed a roughly isotropic regional stress in the horizontal plane. Models reveal that one kilometre east of Dolomieu the direction of the optimally oriented planes is consistent with the observed N55-65 lineaments (Fig 11). It suggests that failure can be reached along N55-65 trending faults. However, the moderate Coulomb stress changes in the area of the N55-65 fracture zone suggest that stresses related to repeated dyke injections are probably not important enough to create faults.

## Coulomb stress shange on optimaly oriented vertical planes
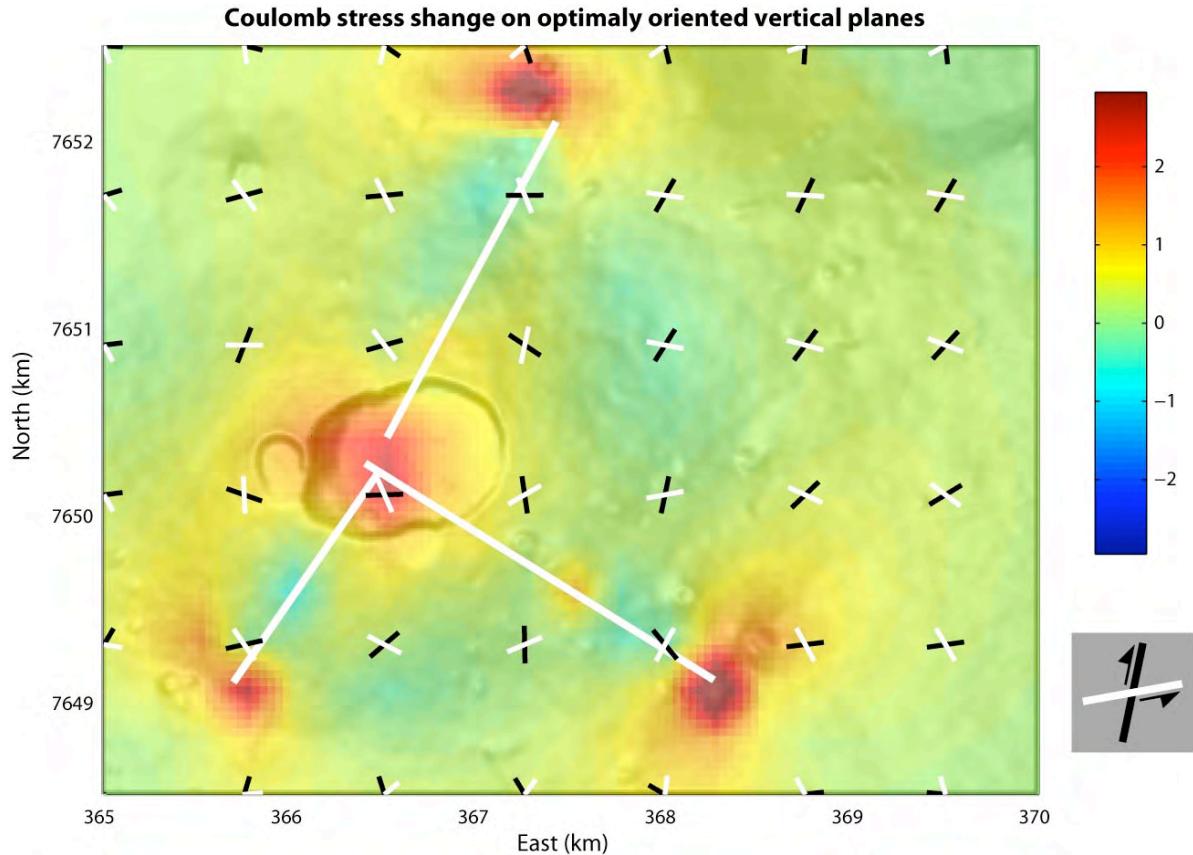
Figure 11: Coulomb stresses changes (MPa) at a 1500 m elevation on optimally oriented vertical faults induced by repeated dyke intrusions in the N25-30 and N120 rift zones (see Fig 8 for dyke intrusion geometries). Surface traces of the intruded dykes are shown as bold white lines. The directions of optimal slip planes are indicated in black and white, where the black and white colours indicate opposite slip sense.

Finally, computations were carried out to unravel principal stress variations due to repeated injections in the northern and southern segments of the N25-30 rift zone. Dyke propagation is controlled by the distribution of the total stress σ^t, which corresponds to $\sigma^t = \Delta\sigma + \sigma^f$, where $\Delta\sigma$ is the stress change due to magma injections and σ^f is the pre-existing regional stress. The pre-existing regional stress being quantitatively unassessable, we solely determined the stress variations caused by dyke intrusions. Figure 12a reveals that minimum principal stresses changes, $\Delta\sigma_3$, are subvertical and parallel to the rift zone, while intermediate principal stresses changes, $\Delta\sigma_2$, are subhorizontal and parallel to the rift dyke (Fig 12a). Letourneur et al. (2008) showed that the maximum principal stress σ^f_1 of the regional stress is vertical. Consequently, the total minimum principal stress σ^t_3 is probably horizontal and parallel to the N25-30 rift zone. As dykes intrude perpendicular to the total minimum principal stress, σ^t_3, the stress field induced by N25-30 rift injections promotes N120 dyke injections (Fig 12b).
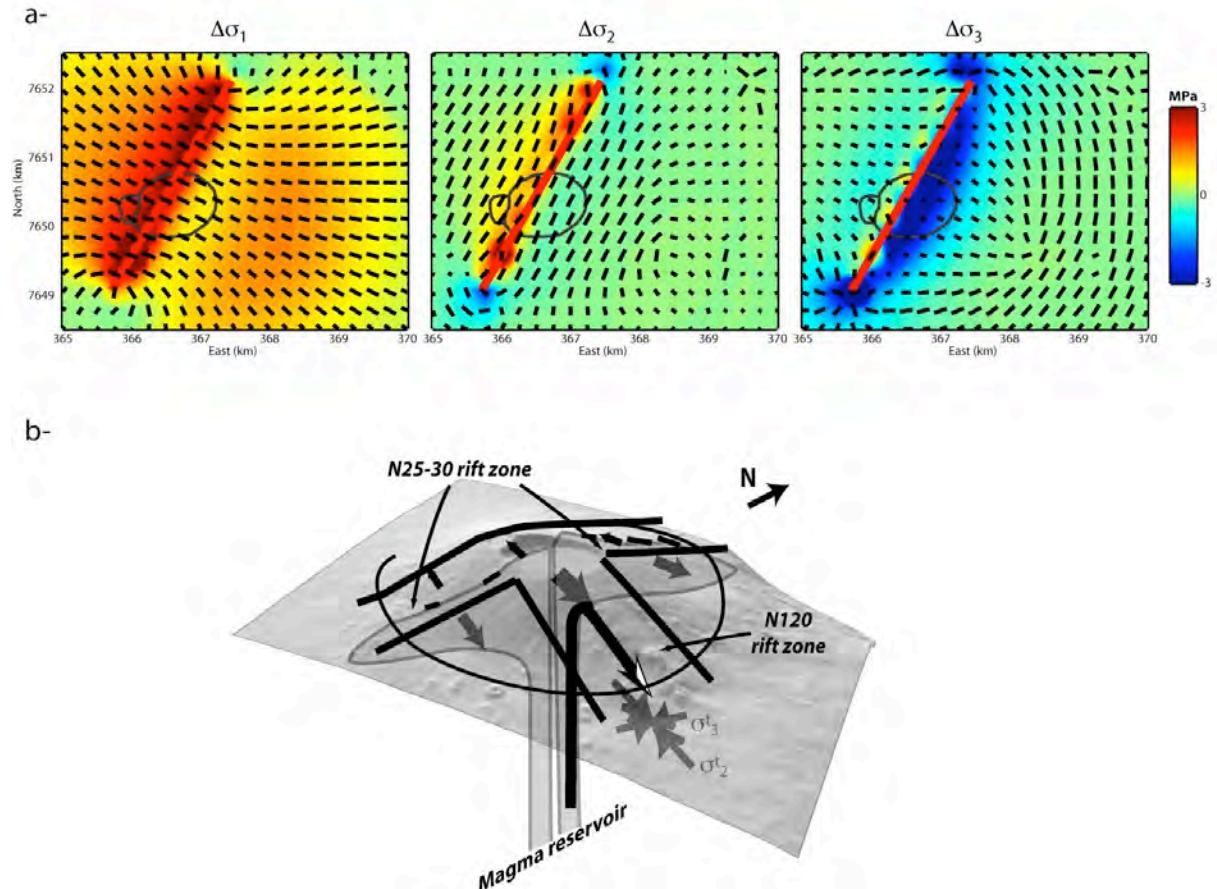
Figure 12: a- Principal stress changes $\Delta\sigma$ corresponding to repeated magma injections in the northern and southern segments of the N25-30 rift zone (see Fig 8 for dyke intrusion geometries). $\Delta\sigma_1$, $\Delta\sigma_2$ and $\Delta\sigma_3$ correspond to the maximum, intermediate and minimum principal stress changes, respectively. b- Interpretative sketch of the short, narrow N120 rift zone as resulting from the stress accumulation induced by recurrent intrusion along the N25-30 rift zone.

5- Discussion

5.1- Origin of the steep central cone

The central cone of Piton de la Fournaise presents abnormally steep flanks for a basaltic volcano characterised by fissure eruptions and fluid lava flows. Annen et al. (2001) proposed that this morphology mainly results from predominant endogenous processes with recurrent thick and short intrusions originating from a small and shallow magma chamber, i.e., 200 m in diameter and located 500 m below the summit. Besides the disagreement between the input and natural data concerning the intrusion vs. eruption ratio (see the description in section 1), the existence of a small shallow magma chamber is questionable. Indeed, the present deformation and seismic data suggest that the feeding dykes originate from a relatively deep magma chamber located at about sea level (Fukushima et al., 2005; Peltier et al., 2007, 2008). Furthermore, a small magma reservoir cannot explain the development of collapse structures such as the pre-Bory pit crater or the recent Dolomieu caldera, which are much larger than the hypothesized shallow magma chamber. Hence, we consider that the geometry of the central cone of Piton de la Fournaise does not result from the predominant endogenous processes described by Annen et al (2001).

The April 2007 caldera collapse, which was coeval to the largest historical eruption deeply cut the central cone (Michon et al., 2007b, Urai et al., 2007). Observations of the caldera walls reveal that the cone predating the pre-Bory pit crater was essentially made of red scoria. It was subsequently covered by several tens of metres of thin lava flows. We propose that the scoria formations are evidences of the occurrence of a hidden strombolian pyroclastic cone below the upper thin lava flows. Strombolian cinder cones are usually characterised by slopes between 25° to 30°, corresponding to the repose angle of the material (Porter, 1972; Wood, 1980). At Piton de la Fournaise, the east and southeast flanks of the central cone present such slope values. However, our GPS data, which clearly show progressive slope tilting during the recurrent intra-cone intrusions, suggest that part of the present slope values result from deformation processes. In the cone's western half, where the intrusion-related deformation is limited, slope values are 10° less than that of a classical cinder cone. Consequently, we interpret the present cone's geometry as resulting from a twofold evolution: a first period during which a cinder cone built up in the Enclos caldera floor, and a second period of

predominant effusive activity overlapping and smoothing the initial cone geometry. A similar scenario was proposed to explain the steep morphology of Nyiragongo (Democratic Republic of Congo), where an initial explosive phase built up a steep cone and a lava lake activity with periodic overflowing veneered over the pyroclastic core (McDonald, 1972; Demant et al., 1994).

5.2- Tectonic structures, co-intrusive deformation and rift zones

Since 1981, all the structural analyses and geodetic measurements have shown that the eastern part of the central cone of Piton de la Fournaise was affected by an eastward motion (Bachèlery, 1981; Bachèlery et al., 1983; Delorme et al., 1989; Lénat et al., 1989; Zlotnicki et al., 1990; Briole et al., 1998; Sigmundsson et al., 1999; Froger et al., 2004; Fukushima et al., 2005; Carter et al., 2007; Peltier et al., 2007; Tinard, 2007). It has been first proposed that the entire eastern flank was involved in the deformation process (e.g., Bachèlery, 1981; Lénat et al., 1989). The NE and SE rift zones were then considered as sinistral and dextral shear zones accommodating the lateral displacements of the volcano flank. However, recent GPS and radar interferometry data do not confirm such a general process and reveal that the deformation is directly related to dyke intrusions and concentrated around the central cone (Sigmundsson et al., 1999; Froger et al., 2004; Fukushima et al., 2005; Peltier et al., 2007). If the deformation pattern is well constrained with these types of data, little is known about the effect of recurrent intrusions in the development, or interaction with tectonic structures. Using field data collected around the summit collapse structures, i.e., the break-in-slope in the upper eastern flank, the fractures in the northern part of the N150-160 fracture zone and the conjugate-like geometry of the eruptive fissures, Carter et al. (2007) proposed an additional deformation process. According to these authors, the east flank of the central cone undergoes a progressive slump above a low strength layer, which is favoured by the recurrent intrusions along the N10 and N170 rift zones. We disagree with this model for the following reasons: 1- the fractures used to interpret the northern limit of the slump as a dextral shear zone do indicate a predominant extension, and correspond to a small part of a much longer extension structure, i.e., the N150-160 fracture zone; 2- the conjugate-like geometry of eruptive fissures results from two sets of eruptive fissures that are the common radial fissures and the long N55 trending fissures which develop in the east flank only; 3- the eastern base of the cone lacks any thrust fault or concentric compressional structures which would result from the slump; 4- The summit collapses disregarded, the deformation of the cone can be exclusively due to the dyke intrusions (Froger

et al., 2004; Fukushima et al., 2005) and to a minor pre-eruptive inflation centred on the cone (Peltier et al., 2007, 2008).

This brief review reveals a lack of any global model in which both field observations and GPS or radar interferometry data are integrated. In the following, we propose to combine our multi-disciplinary data in order to determine (i) the origin of the different tectonic structures (except for the summit collapses and the concentric fractures that are clearly linked to the magma withdrawal; Hirn et al., 1991; Longpré et al., 2007; Michon et al., 2007b; Michon et al., 2009, this issue), (ii) the role of the recurrent dyke intrusions in the morphology of the central cone and (iii) the origin of the N25-30 and N120 rift zones and their consequences in the cone's evolution.

Our structural analysis of the central cone allows identification of two sets of tectonic structures. First, the different spatial distributions of flank fractures, eruptive fissures and dykes, especially in the western part of the cone (Figs 4 and 6a), confirm that the development of the flank fractures does not correspond to the dyke-induced proximal deformation. In contrast, the superposition of the areas affected by these fractures and the co-intrusive deformation (Figs 6a, 7a and 9a) suggests that the flank fractures are linked to the outward inflating tilting of the eastern part of the cone. Hence, we propose that the flank fractures, which are essentially characterised by extension, correspond to relatively shallow (maximum depth of few hundreds of metres) tension cracks that accommodate the endogenous growth during summit and proximal injections. The N20-30 trending fractures may result from the recurrent intrusions along the N25-30 rift zone whereas the N150-160 fractures may originate from the combined effect of intrusions along the N120 rift zone and the northern segment of the N25-30 rift zone (Fig 9b and 9c).

The N55 fracture zone represents the second set of fractures. It is underlined by (i) long, oblique eruptive fissures in the east flank of the cone (Fig 4), (ii) a dense fracture network (Fig 6c), (iii) striking lineaments on the DEM (Fig 2c), and (iv) linear very steep slopes in the SE flank (Fig 2b). As a whole, it corresponds to a 3 km-long structure, which is parallel to a larger tectonic structure that accommodated the collapse of the southern part of the Enclos caldera (Michon and Saint-Ange, 2008). Given the characteristics of the N55 fracture zone and the occurrence of volcano-tectonic events along or close to the lineaments (Sapin et al., 1996), we interpret it as a fault zone. The direction of the eruptive fissures in the eastern flank suggests that the fault zone controls the magma intrusion in the eastern part of the cone. Numerical models show that the N55-65 fault zone may be punctually reactivated by stresses related to dyke intrusions along the rift

zones. They also indicate that the development of the fault zone does probably not result from intrusion-related stresses. Hence, we propose that the N55-65 fault zone is a tectonic structure inherited from the collapse of the Enclos Fouqué caldera, which is reactivated by the present day dynamics of the magmatic system.

Our numerical models and GPS data indicate that the recurrent intrusions along the rift zones induce a heterogeneous deformation of the cone with (i) a significant inflation of the eastern part of the summit, (ii) the steepening of the southeast and east flanks, and (iii) very slight tilting of the western part (Fig 9a). The superposition of the tilted zones and the N55 and N150 very steep slope zones strongly suggests that the slope value difference of about 5-10° between the east and southeast flanks, and the west and north flanks results from the endogenous growth associated with intra-cone intrusions along the N25-30 and N120 rift zones (Fig 9). Hence, if most of the present morphology of the central cone results from an exogenous growth, the specific morphology of the cone's eastern part is clearly due to endogenous processes.

The absence of any elongation along the N25-30 rift zone despite the substantial concentration of the intrusions along this structure contrasts with the morphologies of Hawaiian volcanoes and Karthala. Annen et al. (2001) showed that the geometry of the volcanoes was sensitive to the dyke length/source depth ratio. Volcanoes with ratios lower than 1 present an elongation perpendicular to the rift zones, whereas the elongation is parallel to the rift zones for ratios greater than 1. For ratios close to one, the edifice remains circular despite the presence of radial rift zones. At Piton de la Fournaise, the mean dyke length along the northern and southern segments of the N25-30 rift zone and the source depth are of the same range (about 2000 m). Then, the development of short dykes along the N25-30 and N120 rift zones may explain the sub-circular geometry of the central cone.

The N25-30 and N120 rift zones were determined from the orientation and location of the dykes intruded since 1981. Michon et al. (2007a) proposed that the N25-30 rift zone, on which the cone built up, results from recurrent magma intrusions along a large, 10 km-long structure in the Enclos caldera floor. The origin of the N120 rift zone is less constrained. It could be related to the regional N120 trending volcanic zone between Piton des Neiges and Piton de la Fournaise, the development of which has been interpreted as to be controlled by N120 crustal faults (Fig 1; Chevallier and Vatin-Pérignon, 1982; Michel and Zlotnicki, 1998; Michon et al., 2007a). However, the lack of any N120 trending intrusions in the Enclos caldera, west of the N25-30 rift zone, and the contrasted geometries between the narrow rift zone east of the cone and the wide volcanic zone between Piton de la Fournaise and Piton des Neiges suggest a different origin of both structures. Our numerical modelling reveals that recurrent intrusions along the northern and southern segments of the N25-30 rift zone encourage intrusions in the N120 direction (Fig 12a). Hence, we explain both the existence of the N120 rift zone East of the N25-30 rift zone and the lack of N120 trending dykes West of it, as a consequence of the general eastward dip of the N25-30 dykes (Fig 12b). Such a geometry, which has been deduced from several sets of deformation data (Sigmundsson et al, 1999; Froger et al, 2004; Fukushima et al, 2005; Peltier et al., 2007, 2008), induces asymmetric deformations associated with much larger stress changes East of the N25-30 rift zone than West. The small length of the N120 rift zone may originate from a rapid decrease of the stress increase due to the N25-30 intrusions away from the plumbing system. This rift system, which has been determined from the summit and proximal intrusions is not fully connected with the NE and SE rift zones outside the Enclos caldera. Indeed, recent geophysical data (Brenguier et al., 2007) suggest that the NE and SE rift zones along which the distal eruptions occur are related to tectonic structures that are located below the magma chamber that feeds the summit and proximal eruptions.

6- Conclusion

Our work corresponds to the first analysis of the central cone of Piton de la Fournaise, which combines structural and GPS data, and numerical modelling. The main results can be summarised as follows:

- Similarly to Nyiragongo (Demant et al., 1994), the central cone is formed by a pyroclastic core overlapped by few tens of metres of lava flows. The general steep geometry of the cone does consequently not result from endogenous processes but from an initial phase during which a pyroclastic cone formed.
- The cone undergoes a contrasted co-intrusive deformation during summit and proximal eruptions along two N25-30 and N120 rift zones. Most of the co-intrusive displacements are concentrated in its eastern half where they induce a progressive outward inflation and the tilting of the eastern and southeastern flanks. A dense network of flank fractures, which differs from the eruptive fissures and the concentric fractures linked to the summit collapses, accommodate the progressive endogenous growth.
- The dynamics of the plumbing system also reactivates a N55 fault zone, which mainly controls magma intrusions in the eastern flank and decouples the deformation of the Enclos caldera floor during the north-eastward distal eruptions.

- The N25-30 rift zone is related to a large, 10 km-long fracture zone, whereas the short, narrow N120 rift zone results from a N120 trending stress accumulation west of the N25-30 rift zone, which guides magma intrusions.

References

Annen, C., J.-F. Lénat, A. Provost, 2001. The long-term growth of volcanic edifices: numerical modelling of the role of dyke intrusion and lava-flow emplacement, J. Volcanol. Geotherm. Res., 105, 263-289.

Bachèlery, P., 1981. Le Piton de la Fournaise (Ile de la Réunion). Etude volcanologique, structurale et pétrologique. PhD thesis, Univ. Clermont-Ferrand II, 215pp.

Bachèlery, P., L. Chevallier, J.-P. Gratier, 1983. Caractères structuraux des eruptions historiques du Piton de la Fournaise (Ile de la Réunion), C. R. Acad. Sc. Paris, 296, 1345-1350.

Bory de Saint-Vicent, J.B.G.M., 1804. Voyage dans les quatre principales îles des Mers d'Afrique, Paris, XIII, 3 vol. in 8.

Brenguier, F., N. M. Shapiro, M. Campillo, A. Nercessian, V. Ferrazzini, 2007. 3-D surface wave tomography of the Piton de la Fournaise volcano using seismic noise correlations, Geophys. Res. Lett., 34, L02305, doi:10.1029/2006GL028586.

Briole, P., P. Bachèlery, B. Mc Guire, J. Moss, J.-C. Ruegg, Ph. Sabourault, 1998. Deformation at Piton de la Fournaise: Evolution of the monitoring techniques and knowledge acquired in the last five years. In: R. Casal, M. Fytikas, G. Sigvaldasson, G. Vougioukalakis (eds) Volcanic risk – the European laboratory volcanoes, European commission, EUR 18161 EN, pp. 467-474.

Carter, A., B. van Wyk de Vries, K. Kelfoun, P. Bachèlery, P. Briole, 2007. Pits, rifts and slumps: the summit structure of Piton de la Fournaise, Bull. Volcanol., 69, 741-756. DOI 10.1007/s00445-006-0103-4.

Cayol, V., F.H. Cornet, 1997. 3D mixed boundary elements for elastostatic deformation field analysis, Int. J. Rock Mech. Min. Sci., 34, 275-287.

Cayol, V., F. H. Cornet, 1998. Three-dimensional modeling of the 1983–1984 eruption at Piton de la Fournaise volcano, Réunion Island, J. Geophys. Res., 103, 18,025–18,037.

Chevalier, L., N. Vatin-Perignon, 1982. Volcano-structural evolution of Piton des Neiges, Reunion Island, Indian Ocean, Bull. Volcanol., 45, 285-298.

Delorme, H., P. Bachèlery, P. A. Blum, J. L. Cheminée, J. F. Delarue, J. C. Delmond, A. Hirn, J. C. Lepine, P. M. Vincent, J. Zlotnicki, 1989. March 1986 eruptive episodes at Piton de la Fournaise volcano (Reunion Island), J. Volcanol. Geotherm. Res., 36, 199-208.

Demant, A., P. Lestrade, R.L. Lubala, A.B. Kampuzu, J. Durieux, 1994. Volcanological and petrological evolution of Nyiragongo volcano, Virunga volcanic field, Zaire, Bull. Volcanol., 56, 47-61.

Froger, J.-L., Y. Fukushima, P. Briole, Th. Staudacher, Th. Souriot, N. Villeneuve, 2004. The deformation field of the August 2003 eruption at Piton de la Fournaise, Reunion Island, mapped by ASAR interferometry, Geophys. Res. Lett., 31, L14601, doi:10.1029/2004GL020479.

Fukushima, Y., 2005. Transferts de magma au volcan du Piton de la Fournaise determinés par la modélisation 3D des données d'interférométrie radar entre 1998 et 2000, PhD thesis, Université Clermont-Ferrand II, 149pp. http://tel.archives-ouvertes.fr/tel-00011582.

Fukushima, Y., V. Cayol, P. Durand, 2005. Finding realistic dike models from interferometric synthetic aperture radar data: The February 2000 eruption at Piton de la Fournaise, J. Geophys. Res., 110, B03206, doi: 10.1029/2004JB003268.

Hirn, A., J.-C. Lépine, M. Sapin, H. Delorme, 1991. Episodes of pit-crater collapse documented by seismology at Piton de la Fournaise, J. Volcanol. Geotherm. Res., 47, 89-104.

King, G.C.P., R.S. Stein, J. Lin, 1994. Static stress changes and the triggering of earthquake, Bull. Seism. Soc. Am., 84, 935-953.

Lénat, J.-F., P. Bachèlery, A. Bonneville, A. Hirn, 1989. The beginning of the 1985-1987 eruptive cycle at Piton de la Fournaise (La Réunion); New insights in the magmatic and volcano-tectonic systems, J. Volcanol. Geotherm. Res., 36, 209-232.

Lénat, J.-F., P. Bachèlery, 1990. Structure and dynamics of the central zone of Piton de la Fournaise volcano. In: J.-F. Lénat (eds) Le volcanisme de la Réunion, Monographie. Cent. De Rech. Volcanol., Clermont-Ferrand, pp. 257-296.

Letourneur, L., A. Peltier, Th. Staudacher, A. Gudmundsson, 2008. The effects of rock heterogeneities on dyke paths and asymmetric ground deformation: The example of Piton de la Fournaise (Réunion Island), J. Volcanol. Geotherm. Res., 173, 289-302.

Longpré, M.A. , Th. Staudacher, J. Stix, 2007. The November 2002 eruption at Piton de la Fournaise volcano, La Réunion Island: ground deformation, seismicity, and pit crater collapse, Bull. Volcanol., 69, 511-525.

McDonald, G., 1972. Volcanoes, Prentice-hall, inc., Englewood cliffs, New Jersey, 510p.

Michel, S., J. Zlotnicki, 1998. Self-potential and magnetic surveying of La Fournaise volcano (Réunion Island: Correlations with faulting, fluid circulation, and eruption. J. Geophys. Res., 103, 17845-17857.

Michon, L., F. Saint-Ange, 2008. The morphology of Piton de la Fournaise basaltic shield volcano (La Réunion island): characterization and implication in the volcano evolution, J. Geophys. Res., 113, B03203, doi:10.1029/2005JB004118.

Michon, L., F. Saint-Ange, P. Bachèlery, N. Villeneuve, Th. Staudacher, 2007a. Role of the structural inheritance of the oceanic lithosphere in the magmato-tectonic evolution of Piton de la Fournaise volcano (La Réunion Island). J. Geophys., 112, B04205, doi:10.1029/2006JB004598.

Michon, L., Th. Staudacher, V. Ferrazzini, P. Bachèlery, J. Marti, 2007b. April 2007 collapse of Piton de la Fournaise: a new documented example of caldera formation, Geophys. Res. Lett., 34, L21301, doi:10.1029/2007GL031248.

Michon, L., N. Villeneuve, Th. Catry, O. Merle, How summit calderas collapse on basaltic volcanoes: new insights from the April 2007 caldera collapse of Piton de la Fournaise, J. Volcanol. Geotherm. Res., this issue.

Naumann, T., D. Geist, 2000. Physical volcanology and structural development of Cerro Azul Volcano, Isabela Island, Galapagos: implications for the development of Galapagos-type shield volcanoes. Bull. Volcanol., 61, 497-514.

Nercessian, A., A. Hirn, J.-C. Lépine, M. Sapin, 1996. Internal structure of Piton de la Fournaise volcano from seismic wave propagation and earthquake distribution, J. Volcanol. Geotherm. Res., 70, 123-143.

Peltier, A., V. Ferrazzini, Th. Staudacher, P. Bachèlery, 2005. Imaging the dynamics of dyke propagation prior the 2000-2003 flank eruptions at Piton de la Fournaise, Réunion island., Geophys. Res. Lett., 32, L22302,10.1029/2005GL023720.

Peltier, A., Th. Staudacher, P. Bachèlery, 2007. Constraints on magma transfers and structures involved in the 2003 activity at Piton de La Fournaise from displacement data, J. Geophys. Res., 112, B03207, doi: 10.1029/2006JB004379.

Peltier, A., V. Famin, P. Bachèlery, V. Cayol, Y. Fukushima, Th., Staudacher, 2008. Cyclic magma storages and transfers at Piton de La Fournaise volcano (La Réunion Island) inferred from deformation and geochemical data, Earth. Planet. Sci. Lett., 270, 180-188, doi:10.1016/j.epsl.2008.02.042.

Porter, S.C., 1972. Distribution, morphology and size frequency of cinder cones on Mauna Kea volcano, Hawaii, Geol. Soc. Am. Bull., 83, 3607-3612.

Rowland, S.K., H. Garbeil, 2000. Slopes of oceanic basalt volcanoes, in: P.J. Mouginis-Mark, J.A. Crisp, J.H. Fink (eds) Remote sensing of active volcanism, AGU Monograph, 116, pp.223-247.

Sapin, M., A. Hirn, J.-C. Lépine, A. Nercessian, 1996. Stress, failure and fluid flow deduced from earthquakes accompanying eruptions at Piton de la Fournaise volcano, J. Volcanol. Geotherm. Res., 70, 145-167.

Sigmundsson, F., Ph. Durand, D. Massonnet, 1999. Opening of an eruptive fissure and seaward displacement at Piton de la Fournaise volcano measured by RADARSAT satellite radar interferometry, Geophys. Res. Lett., 26, 533-536.

Tinard P., 2007. Caractérisation et modélisation des déplacements du sol associés à l'activité volcanique du Piton de la Fournaise, île de La Réunion, à partir de données interférométriques. Août 2003 – Avril 2007, Ph.D. Thesis, Univ. Blaise Pascal, 334p. http://tel.archives-ouvertes.fr/action/open_file.php?url=http://tel.archives-ouvertes.fr/docs/00/27/15/39/PDF/PhD_Tinard.pdf&docid=271539

Urai, M., N. Geshi, T. Staudacher, 2007. Size and volume evaluation of the caldera collapse on Piton de la Fournaise volcano during the April 2007 eruption using ASTER stereo imagery, Geophys. Res. Lett., 34, L22318, doi:10.1029/2007GL031551.

Wood, C.A., 1980. Morphometric evolution of cinder cones, J. Volcanol. Geotherm. Res., 7, 387-413.

Zlotnicki, J., J.C. Ruegg, P. Bachèlery, P.A. Blum, 1990. Eruptive mechanisms on Piton de la Fournaise volcano associed with the December 4, 1983, and January 18, 1984, eruptions from ground deformation monitoring and photogrammetric surveys. J. Volcanol. Geothem. Res., 40, 197 – 217.

Annexe 10 :

Michon L., Villeneuve N., Catry Th, Merle O., How summit calderas collapse on basaltic volcanoes: new insights from the April 2007 caldera collapse of Piton de la Fournaise volcano, *In press to J. Volcanol. Geotherm. Res.*
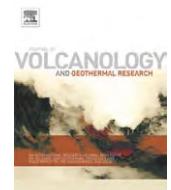
How summit calderas collapse on basaltic volcanoes: New insights from the April 2007 caldera collapse of Piton de la Fournaise volcano

Laurent Michon [a,*], Nicolas Villeneuve [b], Thibault Catry [a,c], Olivier Merle [a,d]

[a] Laboratoire GéoSciences Réunion, Université de la Réunion, Institut de Physique du Globe de Paris, CNRS, UMR 7154 — Géologie des Systèmes Volcaniques,
15 avenue René Cassin, 97715 Saint Denis, France
[b] Institut de Recherche pour le Développement, US 140, BP172, 97492 Sainte-Clotilde cedex, France
[c] Dipartimento di Scienze della Terra e Geologico Ambientali, University of Bologna, Piazza di Porta S. Donato 1, 40127, Bologna, Italy
[d] Laboratoire Magmas et Volcans, UMR 6524 CNRS-IRD-Université Blaise Pascal, 5 rue Kessler 63 038 Clermont-Ferrand, France

ARTICLE INFO

ABSTRACT

In April 2007, Piton de la Fournaise volcano experienced a caldera collapse during its largest historical eruption. We present here a structural analysis both of the caldera and the surrounding area, and precise GPS data recorded with a dense GPS network specifically dedicated to the analysis of deformation related to the summit collapse structures. Despite a collapse of more than 300 m in the central zone, the geometry of the new caldera is similar in map view to that of the pre-existing collapsed structure, which was formed from the coalescence of several pit craters. The caldera shows an asymmetric inner geometry with sub-vertical walls in the NW quadrant and steep scarps composed of inward tilted blocks in the southern half. The presence of preserved polished surfaces on the lower part of the sub-vertical scarp indicates that it corresponds to the caldera north-western ring fault. The April 2007 caldera collapse led to the development and the reactivation of concentric fractures on the caldera rim, mostly along the southern limit of the caldera. GPS data show that fractures result from radial extensional stresses that are restricted within the first tens of meters of the caldera edge. GPS data also reveal that the caldera collapse was coeval with a centripetal deflation, whose magnitude is largest along the southern half of the caldera. The displacements recorded by GPS result from both a general deflation, due to magma withdrawal from Piton de la Fournaise's summit magma chamber, and additional local effects related to the caldera collapse. Comparison of the caldera collapses at Piton de la Fournaise, Miyakejima and Fernandina reveals striking similarities, with cyclic seismic signals accompanying small-scale deflation–inflation cycles. This strongly suggests a common mode of collapse. Hence, we propose a unifying model of caldera collapse in basaltic setting, in which the inward deflation due to magma withdrawal from the magma chamber prevents the collapse of the caldera roof until the gravitational stress acting on the rock column above the magma chamber exceeds the shear strength along pre-existing ring faults. The downward displacement stops when the pressure increase into the magma chamber is able to again sustain the rock column. The succession of (1) inward deflation that prevents the collapse, (2) collapse due to gravitational stress and (3) stopping of the downward motion is repeated many times. The frequency of the cycles is influenced by the rate of magma withdrawal and by the amount of intrusion of magma along the ring faults.

1. Introduction

Basaltic volcanoes present summit calderas, whose formation is related in most cases to lateral magma migration from a shallow magma reservoir (e.g. MacDonald, 1965). Observations of basaltic calderas worldwide, and the few recorded collapse events, show common structural characteristics and collapse mechanisms, which can be summarised as follows. First, caldera collapses are contemporaneous with a periodic seismicity underlined by either a very-long-period seismic signal (Miyakejima in 2000, Kumagai et al., 2001) or large earthquakes, i.e. between M_s 4.4 and 5.5 (Fernandina in 1968, Simkin and Howard, 1970; Filson et al., 1973). Despite differences in the type of seismic signal, their periodicity has been interpreted in the same way, i.e. an intermittent collapse of the rock column into the magma chamber (Simkin and Howard, 1970; Filson et al., 1973; Kumagai et al., 2001). Questions remain on the source of the periodicity which is interpreted as being controlled either by the constant magma outflow (Kumagai et al., 2001), by an irregular geometry of the bottom of the collapsing rock column (Filson et al., 1973) or by regular stress built up along the caldera fault, which is sporadically relieved by movement along the ring fault (Simkin and

* Corresponding author. Tel.: +33 262 262 93 82 04; fax: +33 262 262 93 82 66.
E-mail address: laurent.michon@univ-reunion.fr (L. Michon).
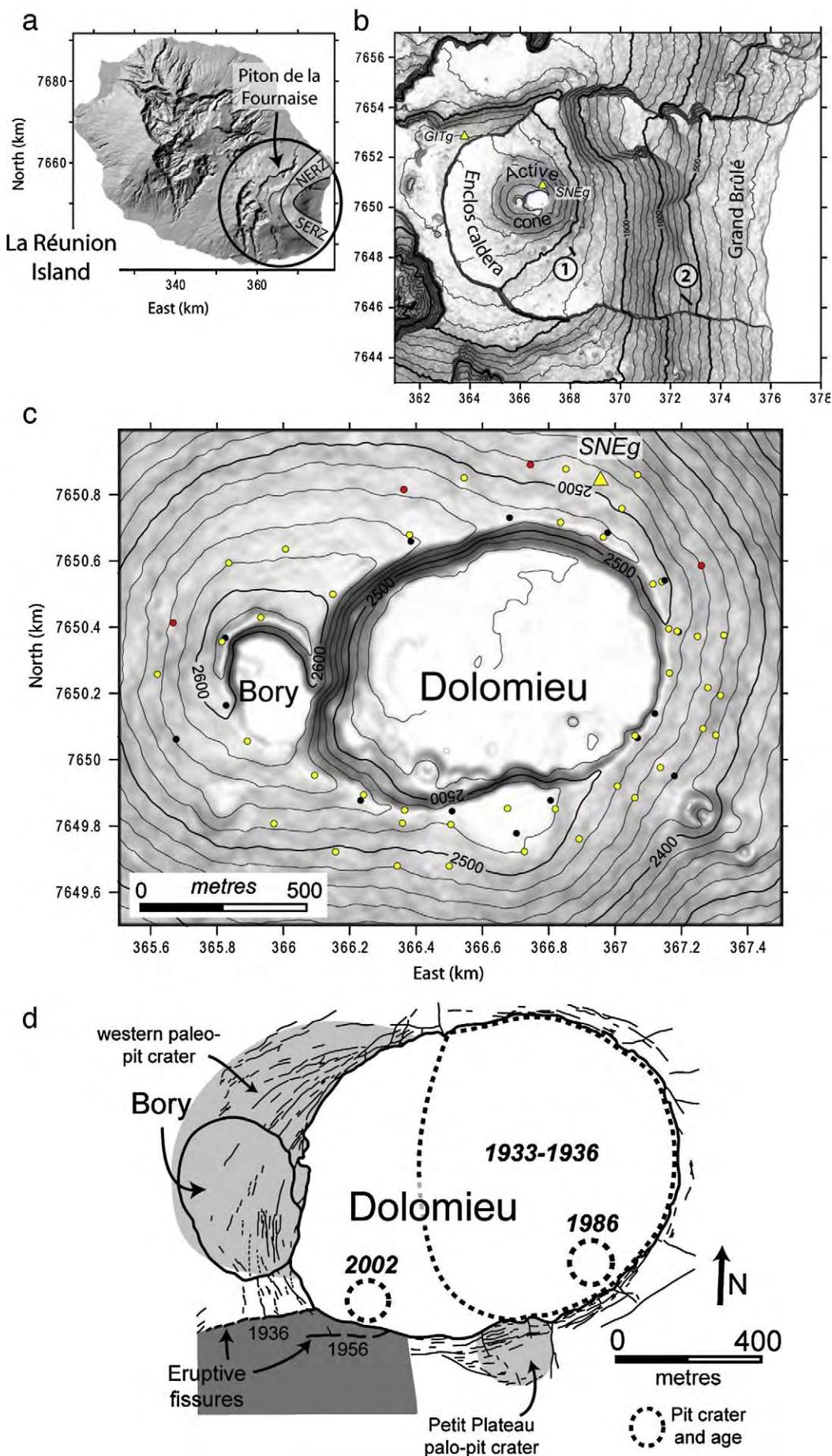
Howard, 1970). Second, analyses of the surface deformation have long-revealed that collapses are coeval with centripetal deflation of the edifice (Wilson, 1935; Ryan et al., 1983). Both deformations, i.e. the collapse and the inward subsidence, result from pressure decrease within the magma chamber and/or the plumbing system (Mogi, 1958; Walsh and Decker, 1971; Ito and Yoshioka, 2002). Third, collapse calderas often show peripheral concentric extensional fractures hundreds of metres from the edge of their caldera rim (Simkin and Howard, 1970; Lénat and Bachèlery, 1990; Troll et al., 2002; Acocella, 2006; Carter et al., 2007). The various authors describe an increase of extension and vertical displacements close to the caldera rim, but their interpretations differ. The changes in rim geometry are thought to result from superficial processes postdating the caldera formation (Acocella, 2006), from extensional stresses related to the centripetal subsidence (Branney, 1995), or from inflation–deflation cycles (Lénat and Bachèlery, 1990).

In April 2007, Piton de la Fournaise volcano experienced a caldera collapse during its largest historical eruption (Michon et al., 2007). We present here the summit deformation accompanying this event. We integrate a detailed analysis of both concentric fractures and intra-caldera structures and faults, with high precision GPS data from a dense network implemented surrounding the caldera. Our study benefited from an initial field and GPS campaign carried out in March 2007, a few days before the onset of the eruption and collapse. The GPS network has been reoccupied twice, in May and November 2007, in order to determine the syn-collapse and post-collapse displacements, respectively. This paper aims at determining the relationship between the concentric fractures and the collapse. It also attempts to better understand the collapse mechanism and its relation to eruption dynamics. Finally, it addresses the role of pre-existing structures in the development of a new caldera.

2. Geological setting

Piton de la Fournaise volcano is one of the world's most active volcanoes (Lénat and Bachèlery, 1987). At the edifice scale, it is characterised by two NE and SE rift zones and an E–W U-shaped caldera formed around 4.5 ka ago (Bachèlery, 1981; Fig. 1a and b). The volcanic activity is concentrated in the upper part of the U-shaped structure, the Enclos caldera, where the accumulation of volcanic products has built up a steep central cone (Michon et al., this issue). Prior to April 2007, the summit of the active cone was cut by two collapse structures: Bory in the west, which is currently inactive, and Dolomieu in the east, the location of the caldera collapse during the large April 2007 eruption (Fig. 1c). Before this collapse, the elongated shape of the pre-existing Dolomieu was the result of the coalescence of several pit craters (Lénat and Bachèlery, 1990; Carter et al., 2007). The largest of these events occurred between 1933 and 1936, during which the eastern half of Dolomieu experienced a 150 m-deep collapse (Fig. 1d; Lacroix, 1939; Bachèlery, 1981). Until 1953, the western part of Dolomieu also suffered recurrent collapses that were accompanied by progressive subsidence of the crater floor. From 1953 the lava accumulated during the frequent summit eruptions and progressively filled the collapse structure, whose outer contour remained unchanged until March 2007, despite the small pit crater collapse in 1986 (Hirn et al., 1991) and a brutal but minor subsidence in 2002 (Fig. 1d; Longpré et al., 2007). It is noteworthy that the August 2006–January 2007 summit eruption created a lava pile of 20–30 m on the Dolomieu floor, filling the crater and overtopping the eastern caldera wall (Michon et al., 2007).

In 1990, a detailed structural analysis of the summit of the active cone revealed a complex network of concentric extensional fractures concentrated around Dolomieu only (Fig. 1d; Lénat and Bachèlery, 1990). It also highlighted the asymmetric distribution of the concentric fractures around the east and west parts of Dolomieu. The eastern rim of Dolomieu was characterised by a few fractures restricted to a 50–80 m wide zone. In contrast, concentric fractures were scattered within a 200–300 m wide zone around the western half of Dolomieu. The northern limit of this fracture network coincides with a topographic break-in-slope that corresponds to the hidden boundary of a paleo-pit crater (Lénat and Bachèlery, 1990; Michon et al., this issue). South of Dolomieu, the Petit Plateau paleo-pit crater, formed around 1911 (Bachèlery, 1981), consists of an independent system of concentric fractures that delimitates the hidden collapsed structure. The age of the overall fracture system is hard to determine. However, the lack of any significant fractures south of the western fracture zones, where the lava emitted by the 1936 and 1956 eruptive fissures covers the surface (Fig. 1d), suggests that fractures in the west predate these eruptions. In the east, the similar distribution of both the limits of the 1933–1936 pit crater and the peripheral concentric fractures supports a temporal relationship between the main collapse event and the development of extension fractures close to the rim. Since 1990, the only significant change in the concentric fracture system was observed during the August 2006–January 2007 eruption, during which fractures close to the rim in the south-eastern part of Dolomieu opened of a few tens of centimetres to a few metres. These fractures accommodated the progressive inward tilting of rock panels torn apart from the rim of the collapse structure.

The April 2007 caldera collapse of Piton de la Fournaise occurred during the largest historical eruption, starting on 30th March and ended the 1st May 2007. Although the detailed evolution of the eruption has already been presented (Michon et al., 2007; Staudacher et al., this issue), we summarise below the main characteristics that allow us to interpret the origin and dynamics of the caldera collapse. On 30th March, a first eruptive fissure opened south-east of the central cone at about 1900 m above sea level (Fig. 1b). After less than 10 h, the magma emission ceased, whereas the summit seismicity remained at a very high level. The magma emission started anew on 2nd April when an eruptive fissure opened at about 600 m asl, 7 km away from the summit (Fig. 1b). The rate at which magma was discharged, which was already large, increased during 5th April contemporaneously with a summit centripetal deflation. The first summit collapse occurred on 5th April at 20:48, contemporary to a magnitude 3.2 volcano-tectonic event (Michon et al., 2007). It was immediately followed by a sudden centrifugal uplift of the caldera rim (Michon et al., 2007; Staudacher et al., this issue). The collapse also had a striking impact at the eruption site where the seismic signal increased by around 50%. Then, both the seismic signal and the summit displacements began to occur in cycles characterised by an inward deflation accompanied by an increase of the seismic signal, ending with a sharp outward uplift contemporaneous with sudden decrease of the seismicity. The cycle frequency gradually increased from 2 h to 30 min (Michon et al., 2007; Staudacher et al., this issue). A total of 38 collapse events were distinguished between 5th April, 20:48, and 7th April, 00:40. First observations of the new caldera, in the afternoon of 6th April, revealed that the 16 first collapses triggered the development of most of the summit collapse caldera (Michon et al., 2007). Disregarding continued spalling of material from the caldera wall, the final geometry of the caldera was attained on 10th April. The eruption continued at a low level until the 1st May 2007.

Fig. 1. a — Location of Piton de la Fournaise volcano on La Réunion Island. b — Location of the eruptive centre within the Enclos caldera. Eruptive fissures opened on March 30th and April 2nd are located by 1 and 2, respectively. SNEg and GITg correspond to the reference receivers of the summit GPS network. c — Distribution of the benchmarks around the summit collapsed structures of Dolomieu and Bory. Benchmarks measured in March and May 2007 (yellow), in May and November (black) and for both periods (red). d — Fracture network around the summit collapsed structures (after Lénat and Bachèlery, 1990).

3. Summit deformation related to the April 2007 eruption

3.1. Structural analysis

On 6th April, the first observations indicated that the collapse was elongated along an E–W axis and concentrated in the northern part of Dolomieu (see Fig. 4b in Michon et al., 2007). It was bounded by 200–300 m-high subvertical scarps in the east, west and north, and by subsiding terraces in the south. Two annular plateaus corresponding to the pre-existing floor of Dolomieu remained in the E and SW (see Fig. 4 in Michon et al., 2007).

At the end of the collapse, on 10th April, the new caldera had a maximum depth of 320–340 m (Michon et al., 2007; Urai et al., 2007)

at the location of the initial collapsed structure. The deepest part of the caldera is covered by scree resulting from the frequent rock slides from the caldera walls (Fig. 2a). Two different topographic expressions of the collapse are distinguished. The southern, eastern and north-eastern walls have average slopes of 40–50°, whereas the north-western wall is sub-vertical (70–80°). The distribution of these two distinct geometries coincides with the structure differences observed on 6th April. The north-western caldera flank already existed on 6th April, by which time it was bounding the northern collapse structure. The preservation of polished surfaces, found only on the lower half of this scarp (Fig. 2b), suggests that the north-western caldera wall corresponds to an inward-dipping ring fault. In contrast, the geometry of the southern, eastern and north-eastern flanks post-dates 6th April.
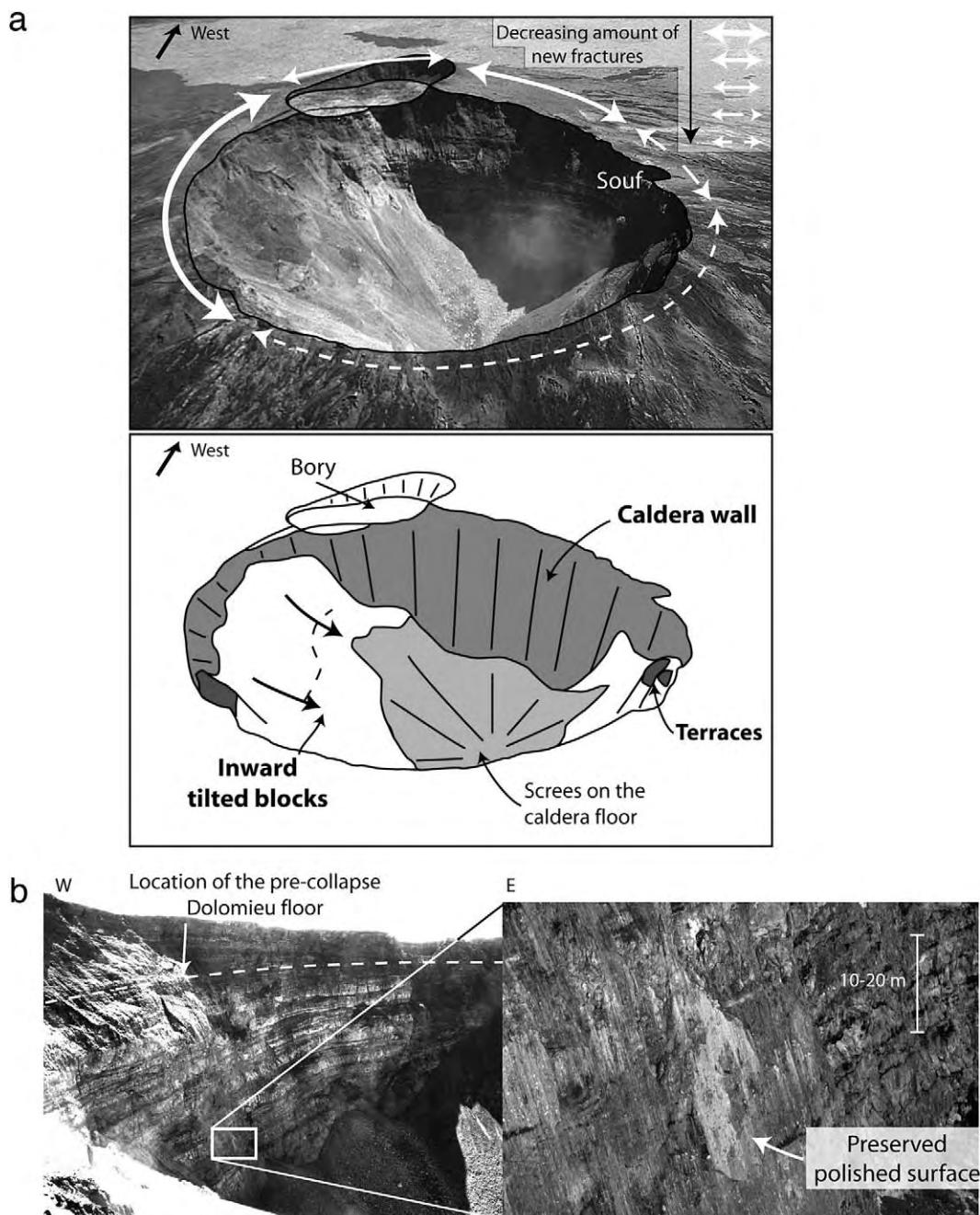

Fig. 2. a — The April 2007 caldera. The maximum depth is located in the northern half of the caldera. Note the differences between the northern and southern caldera flanks. New concentric fractures are represented by arrows. Fractures opened essentially south of the caldera. Souf: Soufrière pit crater. b — View of the north-western caldera wall. Several polished surfaces were preserved few days after the caldera collapse until destruction of this scarp by landslide in May 2007.
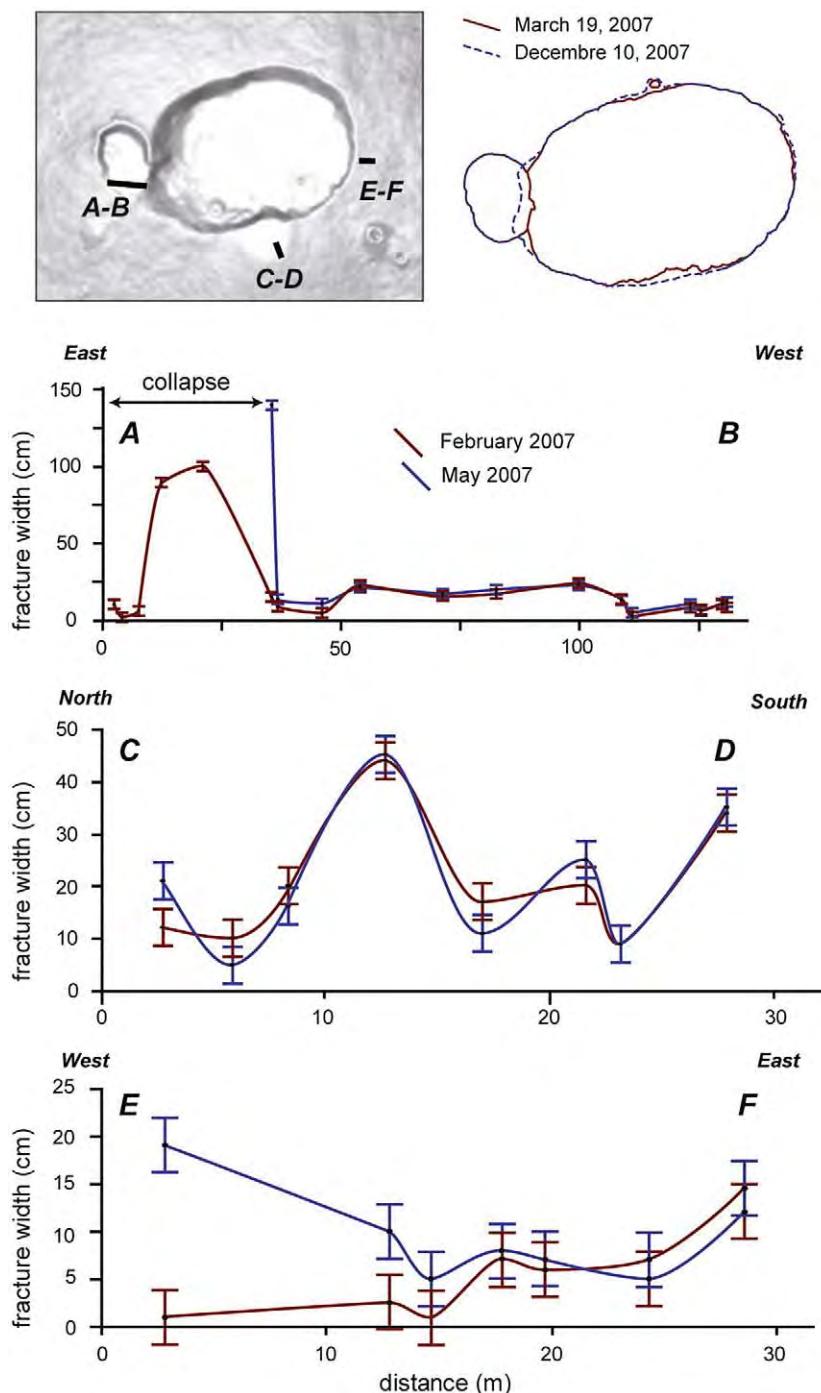
Fig. 3. Contours of the summit structures before and after the caldera collapse. Fracture width along three radial profiles measured in February and May 2007.

This likely results from the inward subsidence of the southern and eastern plateaus similar to that observed during the caldera formation at Miyakejima (Geshi et al., 2002).

In map view, Dolomieu was a 1–1.1 km-long and 0.76–0.80 km-wide elongated structure before the April 2007 eruption (Fig. 3). The April 2007 caldera collapse constitutes the largest collapse event ever observed at Piton de la Fournaise. However, despite a collapse of several hundreds of metres, the contour of the new caldera did not significantly change. The new caldera widened only a few tens of metres in the north, west and south parts, mostly a few days after the caldera collapse (Fig. 3). The similar geometry of the pre-existing collapse structure and the new caldera, and the lateral growth of the initial collapse up to the pre-existing Dolomieu boundary can be compared to the map view evolution of the caldera collapse at Miyakejima, where the initial caldera grew laterally up to approximately the limit of the pre-existing 2.5 ka-old Hatchodaira caldera (Geshi et al., 2002).

We also showed in Section 2 that, prior to 2007, the rim of Dolomieu was affected by asymmetrically distributed concentric fractures (Fig. 1). Three radial profiles were implemented in February 2007 around Dolomieu, at different distances from the caldera edge, in order to determine the potential reactivation of these fractures during collapse events (Fig. 3). The effect of the April 2007 caldera collapse has been evaluated by a reiteration of the profiles in May 2007. Fig. 3, which shows the fracture width before and after the collapse, illustrates the influence of the April 2007 caldera collapse in the

fracture system. It clearly shows that the collapse reactivated only the closest fractures to the caldera edge, and had no impact away from the edge. The concentration of the deformation is corroborated by the development of a narrow fracture system within the first tens of metres from the caldera edge, the density of which varies laterally. The new concentric fractures are densely distributed around the southern part of the caldera, whereas they are nearly non-existent in the east (Fig. 2a).

3.2. GPS data

Since 2001, the deformation of Piton de la Fournaise related to dyke intrusion has been regularly monitored by the GPS network of the Piton de la Fournaise Volcano Observatory (OVPF/IPGP; Peltier, 2007). This network, which is composed of about 80 stainless steel benchmarks cemented around the crater, on the flanks and at the base of the summit cone, accurately measures large scale deformation of the Piton de la Fournaise edifice, but is inadequate to evaluate in detail the summit deformation linked to collapse events. Hence, we implemented a new GPS network in November 2005, specifically dedicated to the structural analysis in a narrow zone around Bory and Dolomieu.

3.2.1. Methodology

The new GPS network is composed of 62 benchmarks (geodetic nails fixed into massive lava) installed along 24 radial profiles, and of two permanent receivers of the OVPF/IPGP located at the summit and outside the Enclos caldera (Fig. 1b and c). The position of each point of the network was measured before the eruption (in March 2007), and twice after the eruption (in May and November 2007). This allows the determination of the deformation related to the April 2007 caldera collapse and the residual subsidence following this event. Measurements were performed in differential mode with dual-frequencies receivers (2 Ashtech Zextrem and 2 Trimble NetRS). The SNEg summit receiver of the permanent GPS network of OVPF/IPGP (Fig. 1) was used as reference. Its position was systematically calculated with respect to a stable permanent receiver (GITg) located outside the Enclos caldera. The location of SNEg was precisely measured in static mode during 6 h with a 1 s sampling rate. In a way similar to measurements at Merapi volcano (Beauducel et al., 2006), measurements of the benchmarks were performed with a small base line (<1.5 km), a 1 s sampling rate and station on the benchmarks of 3 min. During each GPS campaign, several benchmarks were measured twice with a time interval of several hours in order to take into account not only the instrumental RMS values, but also the handling error. Thus, the average horizontal
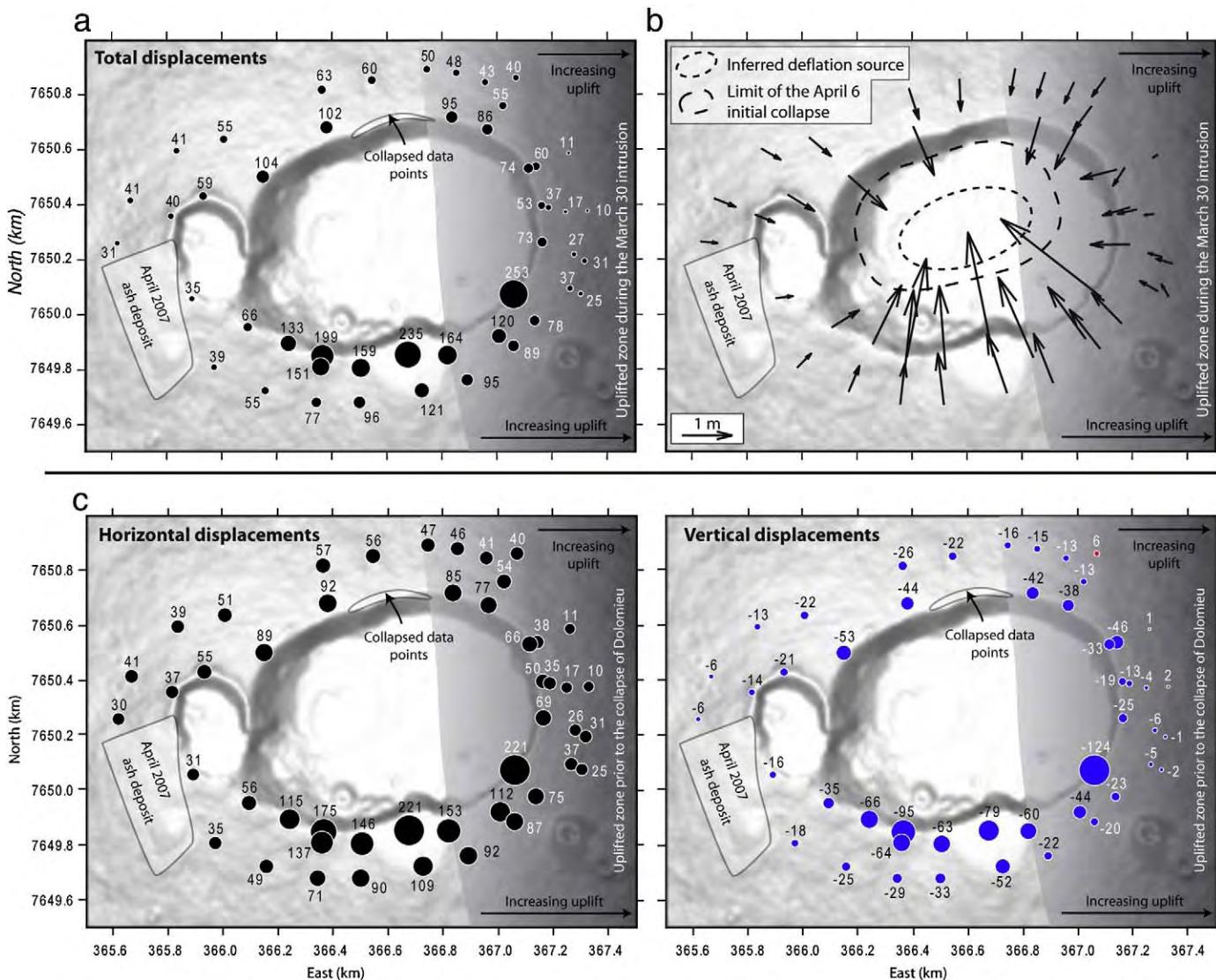

Fig. 4. Displacements between March and May 2007. a — Total displacements (in cm). b — Displacement vectors for horizontal components. c — Horizontal and vertical components (in cm).
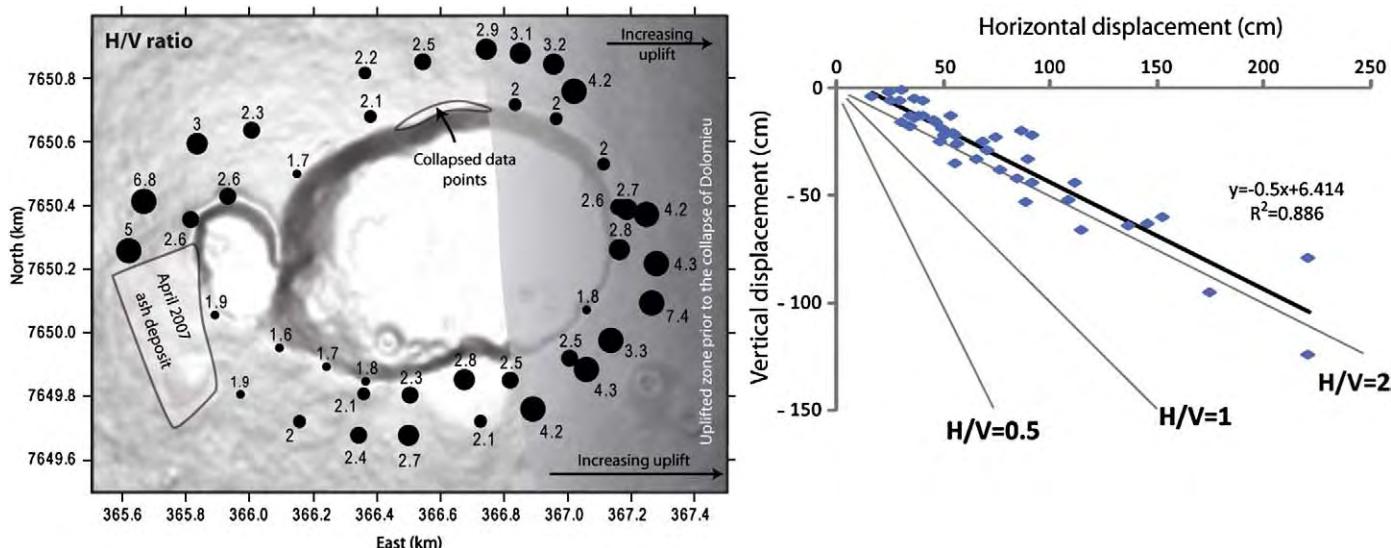
Fig. 5. Horizontal/vertical ratio for the period between March and May 2007. The *H/V* ratios are linearly organised suggesting a predominant common source of deformation.

precision calculated for each benchmark is of 1.1 cm and the vertical average precision is of 0.8 cm.

3.2.2. Displacements between March and May 2007

Between March and May 2007, the summit of Piton de la Fournaise experienced a progressive pre-eruptive outward inflation, additional uplift related to a dyke intrusion, and the caldera collapse. The permanent GPS network of the OVPF/IPGP clearly shows that the initial outward deformation was of minor importance with respect to the eastward dyke intrusion and much less than that measured during the caldera collapse (Peltier et al., this issue). Hence, most of the displacements inferred from our GPS campaigns in March and May 2007 result from the collapse event. Only the easternmost benchmarks are significantly influenced by the 30th March intrusion.

Our GPS data clearly show the large centripetal deformation related both to magma chamber deflation and the collapse event (Fig. 4b). When excluding the easternmost data points, which were also affected by the 30th March dyke intrusion that led to the opening of eruptive fissures SE of the cone (Fig. 1b), the displacement values range between 31 and 253 cm (Fig. 4a). It is likely that the latter value, which strongly differs from the surrounding ones, results from the displacement of an isolated block. The largest surface displacements are located on the southern caldera rim, where values higher than 130 cm are reached close to the caldera wall. Our data also exhibit a sharp decrease of the displacements (−38 to −61%) in the first two hundred metres from the northern and southern caldera edge. Such differences, which suggest the occurrence of extensional stresses on the proximal caldera rim, can be correlated with the location of the new concentric fractures, i.e. in a narrow zone around the western half of the caldera (Fig. 2a). Additional information can be found in the direction of the displacement vectors, which indicate the approximate location of the deflation source (Walsh and Decker, 1971). Here, the overall displacements suggest a deflation source elongated along a N75 axis that corresponds to the direction of elongation of the pre-existing Dolomieu and of the 6th April initial collapse (Fig. 2a).

The comparison of the horizontal and vertical components of displacement provides further information that can be used to better constrain the geometry of the deflation source (Dieterich and Decker, 1975). GPS data show that the summit deflation led mostly to horizontal displacements (Figs. 4c and 5). For every benchmark, the ratio between horizontal and vertical displacements, the *H/V* ratio, is always higher than 1 (Fig. 5). It shows a remarkably linear distribution with an average value around 2, confirming that most of the

benchmark displacements measured between March and May result from a similar, and likely a single origin, i.e. the syn-collapse deflation. The GPS network of the OVPF/IPGP also recorded predominant horizontal displacements at the base of the cone (Peltier et al., this issue). Despite lateral variations between the western and eastern parts, along each transect, the closer to the caldera edge, the lower the *H/V* ratios (Fig. 5). Then, with the exception of the caldera walls, which suffered mostly vertical displacements, the central cone of Piton de la Fournaise experienced a predominant centripetal "horizontal collapse".

3.2.3. Displacements between May and November 2007

The GPS network has been reoccupied in November 2007 in order to identify post-collapse subsidence. Data show that during the 6 month-long period, the caldera rim continued to slightly subside (Fig. 6). According to Staudacher et al. (this issue), 95% of the post-collapse deformation occurred during the first 3 months and the remaining 5% during July to November 2007. The distribution of the displacements for the period between May and November 2007 differs from that of the period between March and May 2007. The direction of the displacement vectors and the distribution of the largest displacements around the western half of the collapse caldera, could suggest a deflation source located below the western half of the caldera (Fig. 6). However, it cannot be excluded that the difference in the deformation pattern results from local deformation. It is noteworthy that the latest caldera wall destabilisations only occurred along the western scarps, where the inward displacements were still significant. Contrary to the *H/V* ratios for the period between March and May 2007, which show important lateral variations, the *H/V* ratios for the period between May and November 2007 present a homogeneous spatial distribution with values lower close to the caldera edge than at the distal extremity of the transects (Fig. 6c). This suggests an identical deformation style all around the caldera, which is independent of the amount of deformation. In consequence, our GPS data provides information both on the source and the mode of deformation.

4. Discussion

4.1. Origin of the concentric fractures around basaltic calderas

Concentric fractures consist of extensional structures that are commonly observed around calderas. For example, at Erta 'Ale, (1)
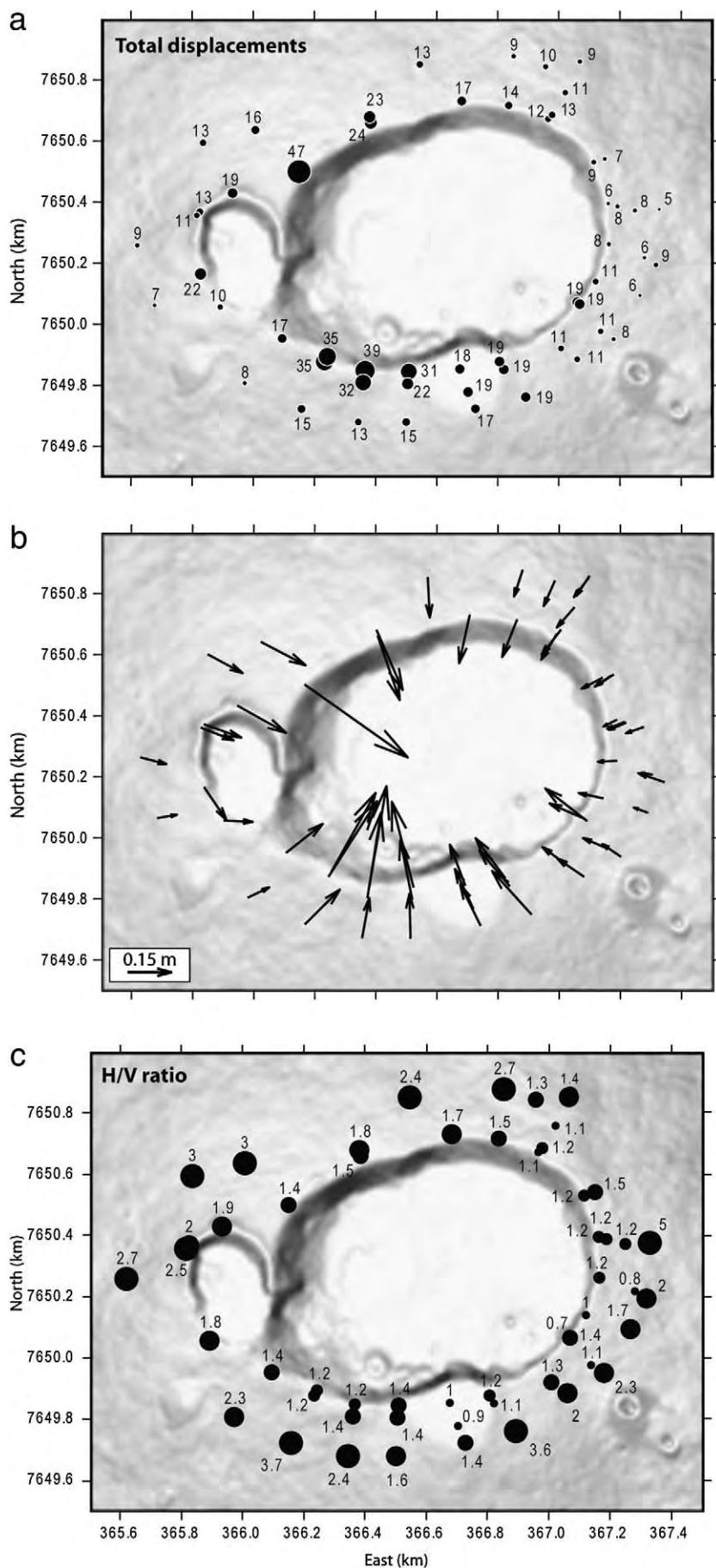
they are found within 20–60 m of the caldera rim, (2) their distance from the rim increases with the height of the caldera scarps, and (3) their opening width tends to increase when they are nearer to the rim (Acocella, 2006). Their development is consequently interpreted in terms of gravitational destabilisation of the caldera walls after the collapse (Acocella, 2006). At Fernandina, a similar fracture network has been observed around the caldera after the 1968 collapse (Simkin and Howard, 1970). Fractures are present on the rim 500 m from the edge and their density and size increase approaching the edge. Contrary to Erta 'Ale, the fracture network is interpreted as resulting from the collapse event (Simkin and Howard, 1971). These different interpretations of similar fracture networks raise the question of the multiple origins of the concentric fractures. Considering the concentric fracture network of Piton de la Fournaise, we propose several mechanisms that lead to the development or reactivation of concentric fractures.

1- The analysis of the fracture network before and after the April 2007 caldera collapse of Piton de la Fournaise reveals that concentric fractures do form on the caldera rim during collapse events. At Piton de la Fournaise, they are restricted to a few tens of metres of the caldera edge. A combination of GPS and structural data indicates that their formation is related to extensional stresses, which affected the proximal part of the caldera rim. They developed essentially south of the caldera where the sub-vertical part of the walls is of a few tens of metres (Fig. 2). The lack of correlation between the fracture density and the height of the caldera walls suggests that most of the extensional stresses do not result from local gravitational effects. This process can however not be entirely ruled out, specifically for the nearest fractures of the caldera edge. In consequence, we propose that most of the new concentric fractures result from extensional stresses that affect the proximal part of the caldera rim during the inward tilt of the caldera floor during successive collapses of the rock column. Such a mechanism is supported by the spatial correlation between the densest fracture zone and the tilted blocks around and into the southern half of the caldera. The development of the new fracture network was coeval with the reactivation of the pre-existing concentric fractures, which were the closer to the edge (Fig. 3).

2- Concentric fractures form at the limit of paleo-collapsed structures such as Petit Plateau and the western paleo-pit crater (Fig. 1d). The concentric fractures around these paleo-collapsed structures could result from a progressive subsidence due to compaction of the formations that filled the depression. However, 90–95% of the filling is composed of massive lava bodies that can hardly be compacted and the upper lava unit, which flowed outside the crater, is also affected by the concentric fractures. We propose that the whole paleo-collapsed structures may slightly subside during later collapses, triggering the development of circumferential extensional fractures above their hidden limits. Such a mechanism is suggested by our GPS data, which show for the period between March and May 2007 vertical displacements of the benchmarks located above the Petit Plateau paleo-pit crater between 20 and 40% greater than those outside the structure.

3- Finally, concentric fractures are reactivated during the progressive filling of the caldera. This process has been clearly observed during the August 2006–January 2007 summit eruption, during which concentric fractures progressively opened while lava accumulated within Dolomieu. It is likely that the extensional stresses that favour the fracture reactivation in a narrow zone around the caldera result from the increased weight of lava accumulated in the collapsed structure.

In summary, our observations of the concentric fractures between August 2006 and November 2007 allowed us to distinguish three mechanisms of fracture formation and reactivation. Contrary to Acocella (2006), we doubt that gravitational instabilities of the caldera wall explain the development of an entire concentric fracture network. The similarities between the fracture networks around the April 2007 caldera of Piton de la Fournaise and the caldera of Erta 'Ale rather suggest that the concentric fractures at Erta 'Ale may result from extension stresses related to the caldera collapse and maybe to the progressive filling of the caldera.

4.2. Origin and dynamics of caldera collapse

The geometry of caldera ring faults and the conditions required to promote a caldera collapse have been intensively studied during the last decades (e.g. Marti et al., 1994; Gudmundsson, 1998; Acocella et al., 2000; Roche et al., 2000, 2001; Roche and Druitt, 2001; Walter and Troll, 2001; Folch and Marti, 2004; Acocella, 2007). However, very few dealt with the dynamics of the collapse, i.e. continuous collapse or pulsating collapse, although the related magma deposits (Rosi et al., 1996; Reubi and Nicholls, 2004) and monitoring data (Filson et al., 1973; Kumagai et al., 2001) show contrasting behaviours. We compare, in what follows, the deformation and seismic data monitored during the caldera collapses of Fernandina, 1968, Miyakejima, 2000 and Piton de la Fournaise, 2007, in order to (1) stress the similarities between each event and consequently (2) determine a unifying mechanism that explains the different dynamics of caldera collapse.

Deformation data at Miyakejima and Piton de la Fournaise show that the caldera collapses have been preceded by an inward deflation of the edifice (Ukawa et al., 2000; Michon et al., 2007; Staudacher et al., this issue). The seismicity, which was characterised by frequent volcano-tectonic (VT) events before the onset of the subsidence, drastically changed once Miyakejima and Piton de la Fournaise started to deflate. The VT events disappeared and a low-frequency seismic signal progressively increased (Ukawa et al., 2000; Michon et al., 2007). The initial deflation phase ended by a sudden outward uplift of the edifice coeval with a magnitude 3.2 VT event at Piton de la Fournaise and a very-long-period event at Miyakejima (Kumagai et al., 2001; Michon et al., 2007). Afterwards, the edifices experienced identical deformation patterns with a succession of cycles characterised by a progressive deflation immediately followed by a sudden uplift (Fig. 7a). The deformation cycles were contemporaneous with a pulsating seismic signal (Kumagai et al., 2001; Michon et al., 2007). At Piton de la Fournaise, every cycle was characterised by a progressive amplification of the seismic signal, which then suddenly decreased to a low level (Fig. 7b). The periodicity of the cycles gradually increased from 2 h to 30 min. Among the 38 cycles, only the two earliest ones were ended by large volcano-tectonic events (Michon et al., 2007). At Miyakejima, the seismicity evolved during each deformation cycles from an increasing swarm-like activity of low-frequency earthquakes coeval with the progressive deflation, up to very-long-period seismic events during the outward uplift (Ukawa et al., 2000; Kumagai et al., 2001). The cyclic distribution of the seismicity at Piton de la Fournaise and Miyakejima shows striking similarities with the seismicity monitored by a regional seismic network mostly distributed in North and South America during the 1968 caldera collapse of Fernandina. Indeed, the caldera formation was coeval with the occurrence of 30 earthquakes, the magnitude of which exceeded 4.5 (Fig. 7b; Filson et al., 1973). Each main event was preceded by an increase of the seismicity and followed by an almost aseismic period. This distribution consequently suggests the existence of seismic cycles

---

Fig. 6. Displacements measured for the period between May and November 2007. a — Total displacements (in cm). b — Displacement vectors for horizontal components. c — Horizontal/vertical ratio.
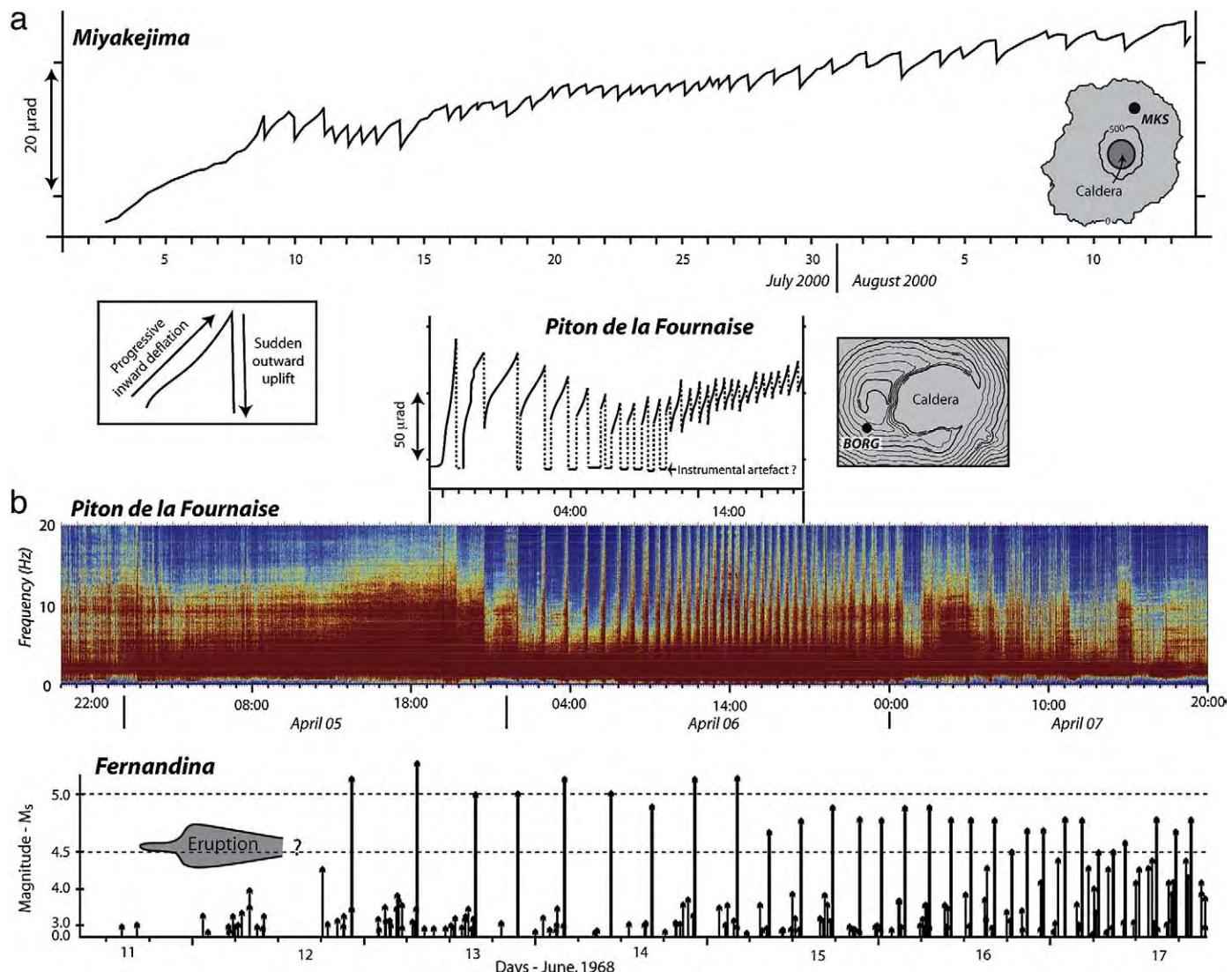
Fig. 7. a — Deformation recorded by radial tiltmeters at Miyakejima (Ukawa et al., 2000) and Piton de la Fournaise (Staudacher et al., this issue) during the caldera collapses. Here, the increase and decrease of angle (in microradian) indicate summit deflation and inflation, respectively. b — Seismicity during the collapse of Piton de la Fournaise (Michon et al., 2007) and Fernandina (Filson et al., 1973). See text for discussion.

whose duration progressively decreased from 6 h to 2 h. Note that the largest earthquakes, $M_s > 5$, appeared during the first seismic cycles (Fig. 7b). Despite differences in the type of seismic signal (VT or very-long-period events) that may originate from the geometry of the ring faults and the type of seismic networks, this overview of both the seismicity and the deformation recorded at Fernandina, Miyakejima and Piton de la Fournaise strongly suggests that each caldera collapse occurred in a similar way.

It has already been proposed that the main earthquakes at Fernandina, the very-long-period events at Miyakejima and the sharp decreases of the seismic signal at Piton de la Fournaise originate from the incremental collapse of the rock column into the magma chamber (Simkin and Howard, 1970; Filson et al., 1973; Kumagai et al., 2001; Michon et al., 2007). Although the periodicity is an obvious common feature, its origin has been interpreted in different ways for each volcano. The periodic very-long-period events and collapses at Miyakejima have been considered as to be caused by the constant magma outflow, which episodically sucked the rock column into the magma reservoir (Kumagai et al., 2001). At Fernandina, the irregular geometry of the bottom of the collapsing rock column (Filson et al., 1973) and the regular stress built up along the caldera fault, which is

sporadically relieved by movement along the ring fault (Simkin and Howard, 1970), are two different mechanisms that have been proposed to explain the step by step collapse.

Combining the different characteristics of the caldera collapses at Fernandina, Miyakejima and Piton de la Fournaise, we put forward a unifying mechanism of basaltic caldera formation. We focus our discussion on calderas related to magma withdrawal from a magma chamber during eruptions or intrusions. Calderas formed by the deformation of the hydrothermal system (e.g. Merle and Lénat, 2003; Merle et al., 2006) are consequently not addressed in this paper.

First of all, the deformation of the summit of basaltic volcanoes is intimately linked to large lateral eruptions or magma intrusions (MacDonald, 1965). Natural examples of Piton de la Fournaise and Miyakejima reveal that calderas may develop over times of days to weeks during or after the magma withdrawal (Geshi et al., 2002; Wright and Sakai, 2004; Michon et al., 2007). The pressure decrease into the magma chamber caused by the magma withdrawal entails, above all, the centripetal subsidence of the edifice (Fig. 8b). The continuous inward deflation progressively changes the stress within the edifice. Despite the pressure decrease within the magma chamber, the centripetal deflation prevents the downward motion of the rock
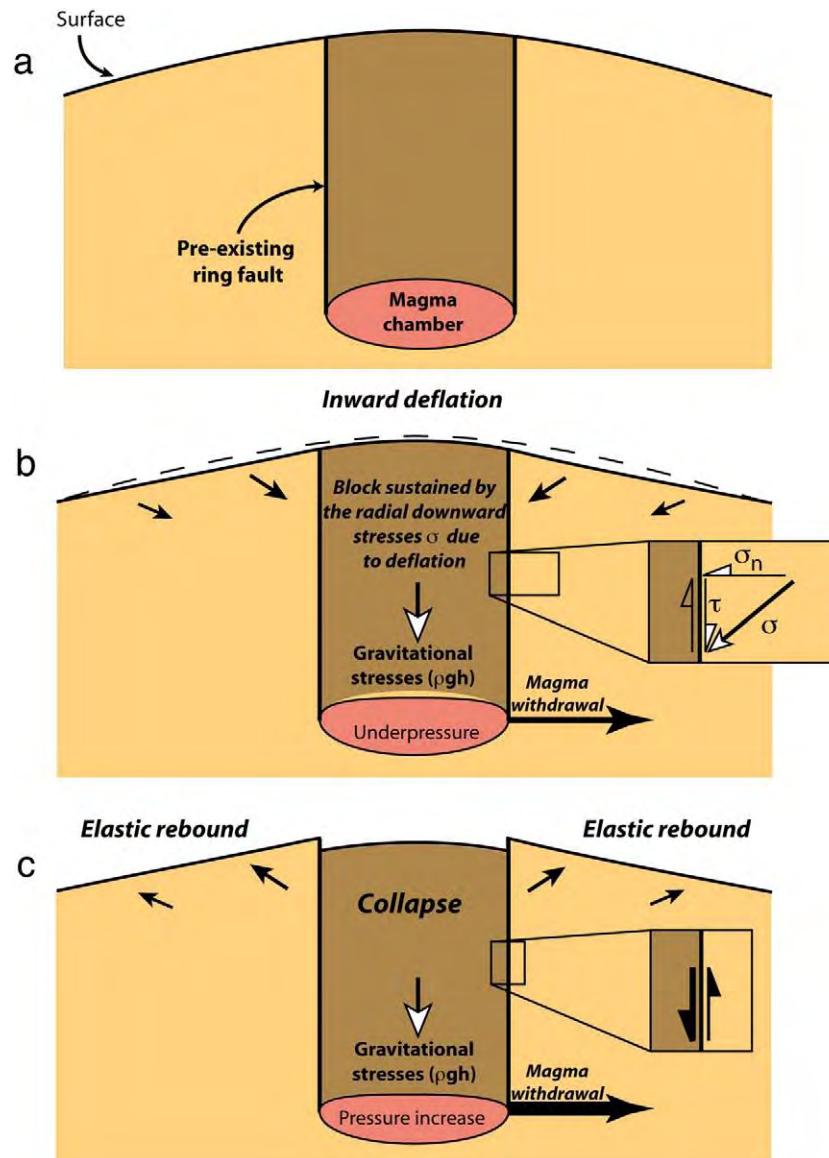
Fig. 8. Schematic representation of the mechanics of caldera collapse in basaltic setting. a — Initial stage. Long-lived volcanoes commonly present pre-existing ring faults resulting from previous caldera collapse. b — Inward deflation related to magma withdrawal from the magma chamber. Despite gravitational stresses acting on the rock column above the magma chamber, the column is sustained by additional normal and shear stresses applied on the ring fault and the remaining pressure within the magma chamber. The stress σ resulting from deflation acting on the fault is decomposed into a normal σ_n and a shear τ component. ρ, h and g correspond to the density and the height of the rock column, and gravitational acceleration, respectively. Black and white arrows represent displacement vectors and stresses, respectively. c — Collapse of the rock column when the gravitational stresses exceed the shear strength along the ring faults. The collapse of the column triggers an elastic rebound of the edifice by stress release. It may also induce an increase of the magma outflow as revealed by the step by step increase of the emission rate at the surface after the first collapses during the April 2007 eruption of Piton de la Fournaise (Michon et al., 2007). Each cycle is subsequently characterised by the succession of step b (inward deflation) and c (collapse and outward uplift).

column due to gravitational stress by increasing both the shear stress τ opposite to the collapse and the shear strength along the pre-existing ring faults, which are common on long-lived volcanoes (Fig. 8b). The collapse of the rock column occurs when the difference between the gravitational stress and the pressure within the magma chamber is sufficient so that the shear strength of the ring faults is exceeded (Fig. 8c). Then, the downward displacement stops when the pressure increase into the magma chamber sustains the rock column anew.

We showed above that every collapse at Piton de la Fournaise and Miyakejima were coeval with outward uplift of the caldera rim. Such displacements were interpreted for Miyakejima as resulting from the expansion of the magma chamber when the rock column intrudes it (Kumagai et al., 2001). Although this hypothesis cannot be ruled out, we prefer the following alternative explanation. The immediate, short outward deformation of the caldera rim after the collapse corresponds

to the elastic response of the edifice, when the downward stress is sporadically released during the motion of the rock column. The ongoing subsidence, which directly results from the magma withdrawal, promotes a new stress increase along the ring fault and prevents the collapse of the rock column. The collapse occurs anew when the shear strength is overcome by the gravitational stress exerted on the rock column. Each cycle is consequently characterised by the succession of (1) a deflation phase which inhibits the downward displacement of the rock column, and (2) a sudden collapse when the gravitational stress exceeds the shear strength along the faults. The duration between two collapses may be influenced by the injection of magmatic fluids along the ring faults. In such a case, their shear resistance declines (Anderson, 1951; Hubbert and Rubbey, 1959) and the time span between two collapses could therefore decrease like at Fernandina and Piton de la Fournaise for a constant or increasing magma withdrawal, and increase if the

rate of magma outflow decreases. Recently Wright and Sakai (2004) proposed that calderas develop only following high rates of magma withdrawal. Following Druitt and Sparks (1984), Martí et al. (2000), Roche and Druitt (2001), Geyer et al. (2006), we think that the amount of magma withdrawal is the critical parameter that initiates caldera formation. To this respect, one can note that the February and December 2005 lateral eruptions of Piton de la Fournaise, which shows similarities with the April 2007 eruption in terms of location of the eruption site and nature of magma, but a volume of magma one order of magnitude less important ($15–20 \cdot 10^6$ m^3 in 2005 and about $130 \cdot 10^6$ m^3 in April 2007; Staudacher et al., this issue), triggered a slight summit subsidence only (Peltier, 2007). Besides the volume of withdrawn magma, the occurrence of a caldera collapse is likely influenced by the strength of the edifice, the occurrence and geometry of pre-existing ring faults, the depth and size of the magma chamber (e.g. Acocella, 2007).

At Piton de la Fournaise, the step by step increase of both the tremor and the emission rate at the eruption site, after the first collapses, indicates that the rock column directly affected the magma chamber by increasing the pressure into the magma reservoir (Michon et al., 2007). Each collapse was accompanied by an ash plume composed of lithics solely above the summit (Staudacher et al., this issue). The simultaneity between deep and surface processes suggests a continuum of deformation from the roof of the magma chamber up to the surface. The collapse of such a piston-like rock column may explain the predominance of the horizontal component at both the base of the cone and the summit, where H/V values are around 2 for the period between March and April 2007. According to Dieterich and Decker (1975), such a displacement pattern is better explained by a vertically elongate axisymmetric source of deformation. This deflation source could correspond to the piston-like rock column that progressively moved downward. Hence, we propose that the predominantly horizontal centripetal deformation of the edifice results from the vertical motion of the piston-like column that allowed the "horizontal collapse" of the edifice.

This synthesis on the three best known basaltic calderas suggests that when the magma withdrawal-related inward subsidence is sufficiently advanced, the rock column between the magma chamber and the surface, intermittently collapses. We propose that the

pulsating dynamics were resulting from a competition between deflation, which prevents the collapse, and gravity exerted on the block, which makes it possible despite deflation. It is noteworthy that pulsating eruption dynamics have also been proposed for several silicic calderas (Rosi et al., 1996, 1999; Troll et al., 2000; Reubi and Nicholls, 2004). This dynamic was mostly interpreted in terms of piecemeal caldera collapses. We assume that the collapse mechanism determined for basaltic calderas can be applied to silicic eruptions. The type of collapse, i.e., intermittent or continuous, would be then influenced by the emission rate. In summary, the volume and the rate of magma withdrawal would control the collapse initiation and dynamics, respectively.

4.3. Geometry of the collapse at Piton de la Fournaise

Carter et al. (2007) recently proposed that the magma chamber associated with the recurrent collapses of Dolomieu, before the April 2007 eruption, was located at around 1000 m below the surface, i.e. 1500 m asl. However, inversions of deformation data, GPS and interferometry, related to the eruptions of Piton de la Fournaise strongly suggest that dykes originate from a magma reservoir lying between 0 and 800 m asl (Fukushima et al., 2005; Peltier et al., 2007). Assuming that magma withdrawal from this magma chamber triggered the April 2007 caldera collapse, the aspect ratio of the caldera system, which corresponds to the depth versus width of the magma reservoir (Roche et al., 2000), is about 2. Analogue models indicate that for high aspect ratios multiple reverse faults break up the roof into large pieces and subsidence occurs as a series of nested cones (Roche et al., 2000, 2001). However, at Piton de la Fournaise, as at Miyakejima where the aspect ratio is also high (Geshi et al., 2002), the pulsating dynamics of the collapse rather suggests that the collapsed rock column behaved as a coherent block (Kumagai et al., 2001). We propose that the geometry differences between models and nature are mainly due to the presence of pre-existing ring faults in nature, whereas models are composed of isotropic materials.

On 6th April, 2007, the first observations of the caldera at Piton de la Fournaise indicated the occurrence of a first elongated collapse structure bounded by sub-vertical scarps (Michon et al., 2007). The presence of preserved polished surfaces on the scarps (Fig. 2b)
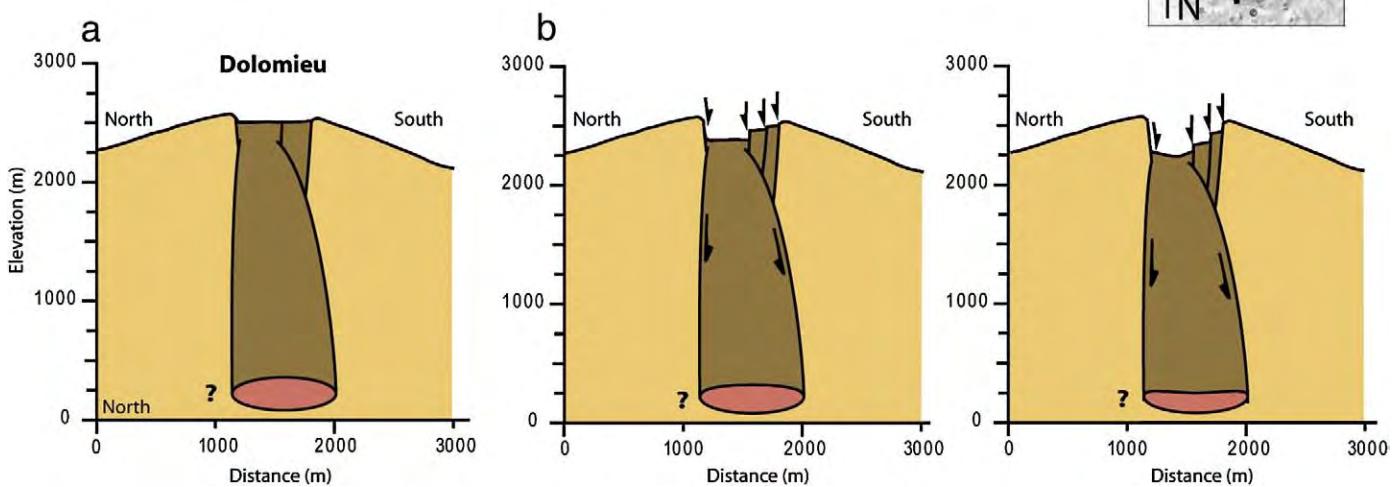
Fig. 9. Evolution of the caldera collapse during the April 2007 eruption inferred from the surface deformation. a — Initial stage. b — On April 6. c — After the collapse. The geometry and depth of the magma chamber is still poorly constrained.

suggests that the subsidence was controlled by inward steep normal faults in sub-surface (Fig. 9b). Considering the usual development of steep outward reverse faults in analogue models (e.g., Marti et al., 1994), we propose that the base of these inward faults is connected to outward dipping reverse faults, which are vertical at depth. The remaining southern and eastern plateaus subsequently collapsed on 7th April (see Fig. 4 in Michon et al., 2007). Their inward collapse can be usefully compared to the tilting blocks, which develop on analogue models between the central collapse and the outer normal ring faults (Roche et al., 2000, 2001; Acocella, 2007). Hence, the pre-existing southern and eastern boundaries of Dolomieu were probably reactivated in normal faulting mode (Fig. 9c). The inward deformation related to the tilt of the southern plateau probably affected the southern rim of the caldera as suggested by the occurrence of maximal inward displacements along its southern limit for the period between March and May 2007. Thus, the spatial correlation between the densest fracture zone, the maximal displacements of the caldera rim and the inward tilt of the southern plateau into the caldera suggests that the displacements recorded by GPS result from both a general deflation due to the magma withdrawal from the magma chamber and local effects due to the caldera collapse. Besides the clear control of pre-existing structures in the April 2007 collapse, the similar geometry of Dolomieu before and after the collapse suggests that the source of the collapse, i.e. the magma chamber, did not significantly change during the last hundred years.

5. Conclusion

We implemented in November 2005 a new GPS network around the summit collapsed structure of Piton de la Fournaise in order to determine the deformation related to collapse events. The present work clearly shows that the network allowed a precise determination of the summit deformation during and after the April 2007 caldera collapse. Moreover, combining GPS data and a structural analysis, we highlight the relationship between the inward displacements, the development of concentric fractures and the dynamics of collapse.

The paper also presents several sources leading to the formation of concentric fractures. Concentric fractures, which are restricted to the first tens of meters of the caldera edge result from extension stresses that are related to (1) the inward tilt of the caldera floor during the successive collapses of the rock column, (2) the reactivation of hidden limits of paleo-collapsed structures and (3) the progressive replenishment of the caldera by lava flows, the load causing a local downsag.

The seismicity and deformation data for the caldera collapses at Fernandina, 1968, Miyakejima, 2000, and Piton de la Fournaise, 2007, suggest a similar pulsating collapse mechanism. Taking into account the stress evolution into the edifice, we propose a unifying model of caldera collapse in basaltic setting that explains the cyclic deformation. The pulsating dynamics result from a competition between deflation, which prevents the collapse, and gravity exerted on the rock column above the magma chamber, which makes it possible despite deflation.

Finally, the structure of the new caldera of Piton de la Fournaise and its evolution during the collapse is explained by the collapse of a coherent block limited by vertical to outward dipping faults at depth and sub-surface normal faults. The similar contours of Dolomieu before the collapse and of the new caldera, remarkably shows the control of the pre-existing structures in the April 2007 caldera collapse.

References

Acocella, V., 2006. Regional and local tectonics at Erta Ale caldera, Afar (Ethiopia). J. Struct. Geol. 28, 1808–1820.

Acocella, V., 2007. Understanding caldera structure and development: an overview of analogue models compared to natural calderas. Earth-Sci. Rev. 85, 125–160.

Acocella, V., Cifelli, F., Funiciello, R., 2000. Analogue models of collapse calderas and resurgent domes. J. Volcanol. Geotherm. Res. 104, 81–96.

Anderson, E.M., 1951. The dynamics of faulting. Trans. Edinb. Geol. Soc. 8, 387–402.

Bachèlery, P., 1981. Le Piton de la Fournaise (Ile de la Réunion). Etude volcanologique, structurale et pétrologique. PhD thesis, Univ. Clermont-Ferrand II, 215pp.

Beauducel, F., Agung Nandaka, M., Cornet, F.H., Diament, M., 2006. Mechanical discontinuities monitoring at Merapi volcano using kinematic GPS. J. Volcanol. Geotherm. Res. 150, 300–312.

Branney, J.M., 1995. Downsag and extension at calderas: new perspectives on collapse geometries from ice-melt, mining, and volcanic subsidence. Bull. Volcanol. 57, 303–318.

Carter, A., van Wyk de Vries, B., Kelfoun, K., Bachèlery, P., Briole, P., 2007. Pits, rifts and slumps: the summit structure of Piton de la Fournaise. Bull. Volcanol. 69, 741–756. doi:10.1007/s00445-006-0103-4.

Dieterich, J.H., Decker, R.W., 1975. Finite element modeling of surface deformation associated with volcanism. J. Geophys. Res. 80, 4094–4102.

Druitt, T.H., Sparks, R.S.J., 1984. On the formation of calderas during ignimbrite eruptions. Nature 310, 679–681.

Filson, J., Simkin, T., Leu, L.-K., 1973. Seimicity of a caldera collapse: Galapagos Islands 1968. J. Geophys. Res. 78, 8591–8622.

Folch, A., Marti, J., 2004. Geometrical and mechanical constraints on the formation of ring-fault calderas. Earth Planet. Sci. Lett. 221, 215–225.

Fukushima, Y., Cayol, V., Durand, P., 2005. Finding realistic dike models from interferometric synthetic aperture radar data: the February 2000 eruption at Piton de la Fournaise. J. Geophys. Res. 110, B03206. doi:10.1029/2004JB003268.

Geshi, N., Shimano, T., Chiba, T., Nakada, S., 2002. Caldera collapse during the 2000 eruption of Miyakejima Volcano, Japan. Bull. Volcanol. 64, 55–68.

Geyer, A., Folch, A., Marti, J., 2006. Relationship between caldera collapse and magma chamber withdrawal: an experimental approach. J. Volcanol. Geotherm. Res. 157, 375–386.

Gudmundsson, A., 1998. Formation and development of normal-fault calderas and the initiation of large explosive eruptions. Bull. Volcanol. 60, 160–170.

Hirn, A., Lépine, J.-C., Sapin, M., Delorme, H., 1991. Episodes of pit-crater collapse documented by seismology at Piton de la Fournaise. J. Volcanol. Geotherm. Res. 47, 89–104.

Hubbert, M.K., Rubbey, W.W., 1959. Role of fluid pressure in mechanics of overthrust faulting. Bull. Geol. Soc. Am. 70, 115–166.

Ito, T., Yoshioka, S., 2002. A dike intrusion model in and around Miyakejima, Niijima and Kozushima in 2000. Tectonophysics 359, 171–187.

Kumagai, H., Ohminato, T., Nakano, M., Ooi, M., Kubo, A., Inoue, H., Oikawa, J., 2001. Very-long-period seismic signals and the caldera formation at Miyake Island, Japan. Science 293, 687–690.

Lacroix, A., 1939. Les transformations récentes du sommet du volcan actif (Piton de la Fournaise) de l'Ile de la Réunion. Bull. Volcanologique, serie II tome V, pp. 3–18.

Lénat, J.-F., Bachèlery, P., 1987. Dynamics of magma transfer at Piton de la Fournaise volcano (Réunion Island, Indian Ocean). In: Chi-Yu, Scarpa (Eds.), Modeling of Volcanic Processes. Friedr. Vieweg and Sohn, Brauschweig/Wiesbaden, pp. 57–72.

Lénat, J.-F., Bachèlery, P., 1990. Structure and dynamics of the central zone of Piton de la Fournaise volcano. In: Lénat, J.-F. (Ed.), Le volcanisme de la Réunion, Monographie. Cent. De Rech. Volcanol., Clermont-Ferrand, pp. 257–296.

Longpré, M.-A., Staudacher, Th., Stix, J., 2007. The November 2002 eruption at Piton de la Fournaise volcano, La Réunion Island: ground deformation, seismicity, and pit crater collapse. Bull. Volcanol. 69, 511–525. doi:10.1007/s00445-006-0087-0.

MacDonald, G.A., 1965. Hawaiian calderas. Pac. Sci. 19, 320–334.

Marti, J., Ablay, G.J., Redshaw, L.T., Sparks, R.S.J., 1994. Experimental studies of collapse calderas. J. Geol. Soc. (Lond.) 151, 919–929. doi:10.1144/gsjgs.151.6.0919.

Martí, J., Folch, A., Macedonio, G., Neri, A., 2000. Pressure evolution during caldera-forming eruptions. Earth Planet. Sci. Lett. 175, 275–287.

Merle, O., Lénat, J.-F., 2003. Hybrid collapse mechanism at Piton de la Fournaise volcano, Reunion Island, Indian Ocean. J. Geophys. Res. 108, 2166. doi:10.1029/2002JB002014.

Merle, O., Barde-Cabusson, S., Maury, R.C., Legendre, C., Guille, G., Blais, S., 2006. Volcano core collapse triggered by regional faulting. J. Volcanol. Geotherm. Res. 158, 269–280.

Michon, L., Staudacher, Th., Ferrazzini, V., Bachèlery, P., Marti, J., 2007. April 2007 collapse of Piton de la Fournaise: a new example of caldera formation. Geophys. Res. Lett. 34, L21301. doi:10.1029/2007GL031248.

Michon, L., Letourneur, L., Peltier, A., Villeneuve, N., Staudacher, Th., 2008-this issue. Morphology, structure and deformation of the steep central cone of Piton de la Fournaise shield volcano (Réunion Island, Indian Ocean), J. Volcanol. Geotherm. Res. doi:10.1016/j.jvolgeores.2008.11.002.

Mogi, K., 1958. Relations of the eruptions of various volcanoes and the deformations of the ground surfaces around them. Bull. Earthq. Res. Inst. Univ. Tokyo 36, 99–134.

Peltier, A., 2007. Suivi, modélisation et évolution des processus d'injections magmatiques au Piton de La Fournaise (Réunion), à partir d'une analyse croisée des données de déformation, géochimiques et structurales. PhD Thesis, Univ. Réunion, 282p. http://tel.archivesouvertes.fr/index.php?halsid=gljus7suihg3og6qn3850l6jn5&view_this_doc=tel-00167895&version=1.

Peltier, A., Staudacher, Th., Bachèlery, P., 2007. Constraints on magma transfers and structures involved in the 2003 activity at Piton de La Fournaise from displacement data. J. Geophys. Res. 112, B03207. doi:10.1029/2006JB004379.

Peltier, A., Staudacher, Th., Bachèlery, P., Cayol, V., 2008-this issue. Evolution of the deformation source related to the 2007 collapse at Piton de La Fournaise volcano. J. Volcanol. Geotherm. Res. doi:10.1016/j.jvolgeores.2008.09.009.

Ryan, M.P., Blevins, J.Y.K., Okamura, A.T., Koyanagi, R.Y., 1983. Magma reservoir subsidence mechanics: theoretical summary and application to Kilauea Volcano, Hawaii. J. Geophys. Res. 88, 4147–4181.

Reubi, O., Nicholls, I.A., 2004. Variability in eruptive dynamics associated with caldera collapse: an example from two successive eruptions at Batur volcanic field, Bali, Indonesia. Bull. Volcanol. 66, 134–148. doi:10.1007/s00445-003-0298-6.

Roche, O., Druitt, T.H., 2001. Onset of caldera collapse during ignimbrite eruptions. Earth Planet. Sci. Lett. 191, 191–202.

Roche, O., Druitt, T.H., Merle, O., 2000. Experimental study of caldera formation. J. Geophys. Res. 105, 395–416.

Roche, O., Van Wyk de Vries, B., Druitt, T.H., 2001. Sub-surface structures and collapse mechanisms of summit pit craters. J. Volcanol. Geotherm. Res. 105, 1–18.

Rosi, M., Vezzoli, L., Aleotti, P., De Censi, M., 1996. Interaction between caldera collapse and eruptive dynamics during the Campanian Ignimbrite eruption, Phlegraean Fields, Italy. Bull. Volcanol. 57, 541–554.

Rosi, M., Vezzoli, L., Castelmenzano, A., Grieco, G., 1999. Plinian pumice fall deposit of the Campanian Ignimbrite eruption (Phlegraean Fields, Italy). J. Volcanol. Geotherm. Res. 91, 179–198.

Simkin, T., Howard, K.A., 1970. Caldera collapse in Galapagos Islands, 1968. Science 169, 429–437.

Staudacher, Th., Ferrazzini, V., Peltier, A., Kowalski, Ph., Boissier, P., Catherine, Ph., Lauret, F., Massin, F., 2008-this issue. The April 2007 eruption and the Dolomieu crater collapse, two major events at Piton de la Fournaise (La Réunion Island, Indian Ocean). J. Volcanol. Geotherm. Res. doi:10.1016/j.jvolgeores.2008.11.005.

Troll, V.R., Emeleus, C.H., Donaldson, C.H., 2000. Caldera formation in the Rum Central Igneous Complex, Scotland. Bull. Volcanol. 62, 301–317. doi:10.1007/s004450000099.

Troll, V.R., Walter, T.R., Schmincke, H.-U., 2002. Cyclic caldera collapse: piston or piecemeal subsidence? Field and experimental evidence. Geology 30, 135–138.

Ukawa, M., Fujita, E., Yamamoto, E., Okada, Y., Kikuchi, M., 2000. The 2000 Miyakejima eruption: crustal deformation and earthquakes observed by the NIED Miyakejima observation network. Earth Planets Space 52, xix–xxvi.

Urai, M., Geshi, N., Staudacher, Th., 2007. Size and volume evaluation of the caldera collapse on Piton de la Fournaise volcano during the April 2007 eruption using ASTER stereo imagery. Geophys. Res. Lett. L22318. doi:10.1029/2007GL031551.

Walsh, J.B., Decker, R.W., 1971. Surface deformation associated with volcanism. J. Geophys. Res. 76, 3291–3302.

Walter, T.R., Troll, V.R., 2001. Formation of caldera periphery faults: an experimental study. Bull. Volcanol. 63, 191–203.

Wilson, R.M., 1935. Ground surface movement at Kilauea Volcano, Hawaii. Univ. Hawaii Res. Publ. 10 (56p.).

Wright, T.L., Sakai, S., 2004. Interpretation of the Miyakejima 2000 eruption and dike emplacement using time animations of earthquakes. Bull. Earthq. Res. Inst., Univ. Tokyo 79, 1–16.

Annexe 11 :

Michon, L., T. Staudacher, V. Ferrazzini, P. Bachèlery, J. Marti (2007), April 2007 collapse of Piton de la Fournaise: A new example of caldera formation, Geophys. Res. Lett., 34, L21301, doi:10.1029/2007GL031248.

April 2007 collapse of Piton de la Fournaise: A new example of caldera formation

Laurent Michon,[1] Thomas Staudacher,[2] Valérie Ferrazzini,[2] Patrick Bachèlery,[1] and Joan Marti[3]

[1] Collapse calderas are frequent in the evolution of volcanic systems, but very few have formed during historical times. Piton de la Fournaise is one of the world's most active basaltic shield volcanoes. The caldera collapse, which occurred during the April 2007 lateral eruption is one of the few large documented collapse events on this volcano. It helps to understand the mode and origin of caldera collapses in basaltic volcanoes. Field observations, GPS and seismic data show that the collapse occurred at an early stage of the eruption. The cyclic seismic signal suggests a step by step collapse that directly influenced the lateral eruption rate. Likely, the caldera results from the combined effect of (i) the progressive collapse of the plumbing system above the magma chamber since 2000, and (ii) the large amount of magma withdrawal during the early stage of the eruption by both a significant intrusion within the edifice and an important emission rate. **Citation:** Michon, L., T. Staudacher, V. Ferrazzini, P. Bachelery, and J. Marti (2007), April 2007 collapse of Piton de la Fournaise: A new example of caldera formation, *Geophys. Res. Lett.*, *34*, L21301, doi:10.1029/2007GL031248.

1. Introduction

[2] Caldera collapse structures are common on basaltic to silicic volcanoes [e.g., *Cole et al.*, 2005]. In basaltic setting, they are defined either as pit crater or caldera. Pit craters, which correspond to small structures, tens to hundreds of meters across, may have several origins. They form along the rift zones by stopping over an underlying large-aperture rift zone fracture [*Okubo and Martel*, 1998], and at the volcano's summit by magma withdrawal in shallow reservoirs [*Hirn et al.*, 1991; *Rymer et al.*, 1998; *Longpré et al.*, 2007]. Basaltic calderas are kilometric structures usually formed during large lateral eruptions or intrusions, which affect the main magma chamber [*MacDonald*, 1965; *MacPhie et al.*, 1990; *Kumagai et al.*, 2001; *Kaneko et al.*, 2005]. Two of the most recent caldera collapses on basaltic or intermediate volcanoes occurred in 1968 in Fernandina Island, Western Galapagos [*Simkin and Howard*, 1970], and in 2000 at Miyakejima volcano [*Geshi et al.*, 2002]. In both cases, caldera collapse was interpreted as the result of large lateral magma intrusions within the edifice or the underlying crust.

[3] At Piton de la Fournaise (PdF), the volcano's summit zone experienced several coalescent pit craters during the last centuries [*Carter et al.*, 2007]. The April 2007 eruption led to the largest collapse of the summit zone and the most recent example in basaltic setting. It developed contemporaneously to one of the largest historical lateral eruptions on Reunion, suggesting a very close link between magma withdrawal and the summit collapse. This study summarizes the April 2007 eruption in order to explain the origin, the timing and the effects of the collapse. It brings new constrains on (1) the relationship between magma withdrawal and the collapse and (2) the timing of the collapse regarding recent recurrent eruptions.

2. Geological Setting of Piton de la Fournaise

2.1. General View

[4] PdF is the active volcano of La Réunion Island (Figure 1). The eruptive centre is located in a large 8 km across caldera, the Enclos Fouqué, where most of the eruptions occur since 4.5 ky [*Bachèlery*, 1981]. The present day summit shows two collapsed structures named the "Bory crater", which is currently inactive, and the "Dolomieu crater", which is the locus of numerous summit eruptions. *Carter et al.* [2007] recently showed that the pre-2007 elongated geometry of Dolomieu results from recurrent pit crater collapses.

[5] The activity of PdF is characterized by fissure eruptions fed by a magma reservoir located at about sea level [*Fukushima et al.*, 2005; *Peltier et al.*, 2007]. Considering the location of the eruption site, three types of eruptions can be distinguished. 1- Summit eruptions start and remain in Dolomieu. 2- Proximal eruptions, which may start in the summit but progress to the flanks of the central cone and usually propagate downslope to the Enclos caldera floor. 3- Distal eruptions develop away from the central cone, starting in the Enclos caldera floor. During the last century, the distal eruptions were in some cases associated with the development of summit collapses [*Bachèlery*, 1981; *Carter et al.*, 2007]. Among them, the most voluminous eruption of 1931 with 130 Mm^3 was related to a large collapse corresponding to the eastern half of Dolomieu [*Lacroix*, 1938, Figure 1]. The lack of any continuous observation and monitoring during the largest events does not allow the determination of the precise relationship between these eruptions and the associated summit collapses.

[1]Laboratoire GéoSciences Réunion, Institut de Physique du Globe de Paris, Université de La Réunion, CNRS, UMR 7154-Géologie des Systèmes Volcaniques, La Réunion, France.

[2]Observatoire Volcanologique du Piton de la Fournaise, Institut de Physique du Globe de Paris, CNRS, UMR 7154-Géologie des Systèmes Volcaniques, La Réunion, France.

[3]Institute of Earth Sciences "Jaume Almera," Consejo Superior de Investigaciones Científicas, Barcelona, Spain.
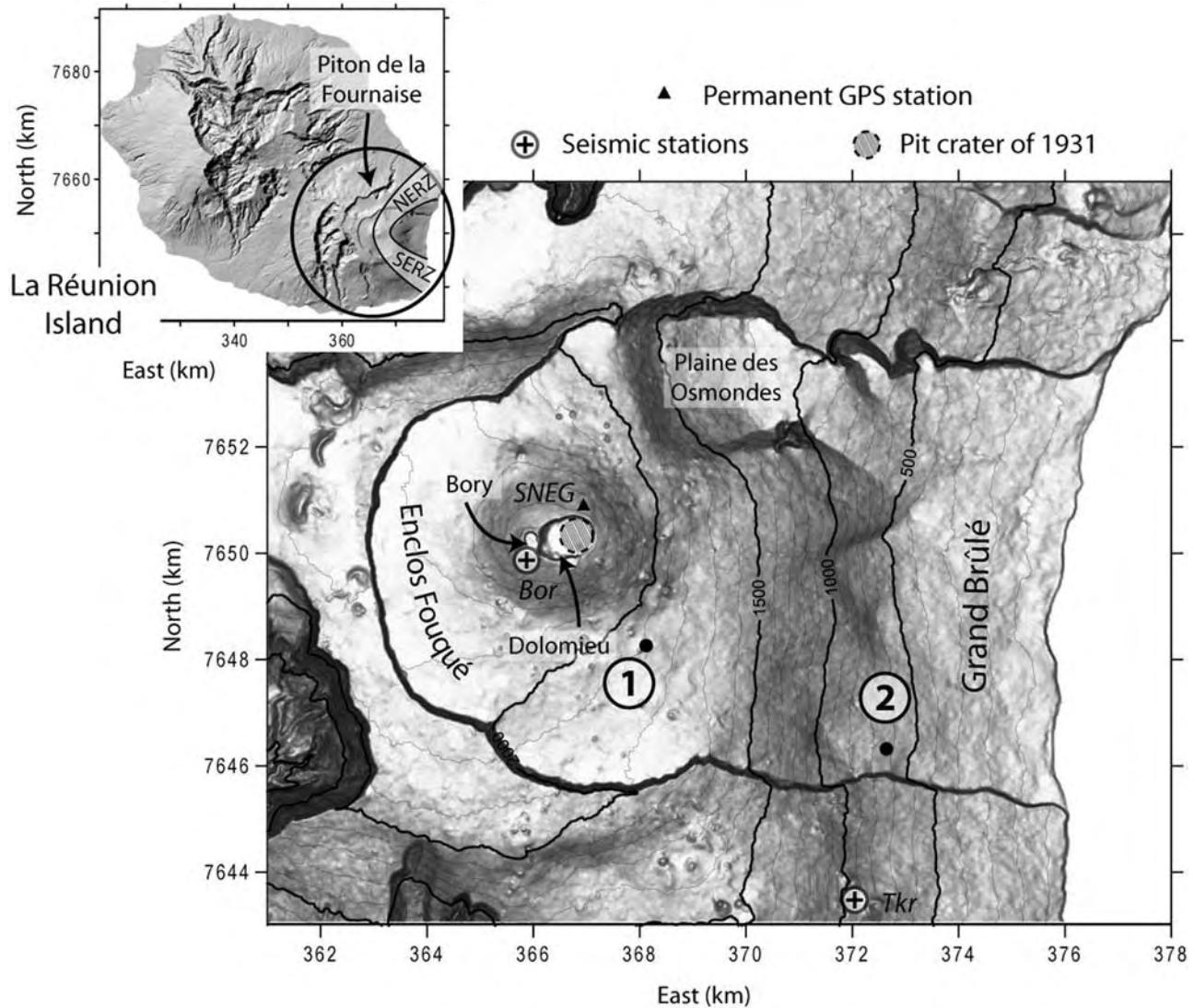
Figure 1. Location of Piton de la Fournaise volcano. The central cone is cut by two collapsed craters, Bory and Dolomieu. 1 and 2 represent the location of eruptive fissures during the first and second eruptive phases, respectively. Bor and Tkr correspond to the seismic stations used in Figure 3. NERZ and SERZ: NE and SE rift zones.

2.2. Summary of the March 1998–February 2007 Evolution

[6] Since 1998, PdF has been characterized by an intense eruptive activity with 2–4 eruptions per year. Most of the eruptions correspond to summit and proximal events. Some of them, the summit eruptions, contributed to the progressive filling of Dolomieu by the accumulation of pahoehoe lava flows. Total filling of Dolomieu was attained with the August 2006–January 2007 summit eruption during which a pile of 20–30 m of lava flows accumulated on the crater floor. Five distal eruptions occurred during the 1998–2007 period. They were mainly concentrated in the Plaine des Osmondes depression, along the NE rift zones (Figure 1).

[7] Before 2000, the eruptions of PdF were showing a similar evolution with a progressive disappearance of the tremor [*Battaglia et al.*, 2005]. Volcano-tectonic (VT) events seldom occurred during the eruptive phases (Figure 2). The eruption evolution progressively changed with an increase of both tremor amplitude and seismicity before a rapid end of the eruption [*Longpré et al.*, 2007]. Since 2000, the seismicity was especially abundant during voluminous eruptions, most of them being distal. During the November 2002 eruption, the seismicity intensified 5 days before the end of the eruption and continued at shallower levels before the collapse of a small pit crater on December 23 in Dolomieu [*Longpré et al.*, 2007]. Such a surface phenomena did not occur during the other distal eruptions despite a strong increase of the VT seismicity in both frequency and magnitude below the summit. However, the coeval intensification of the emission rate and the VT events
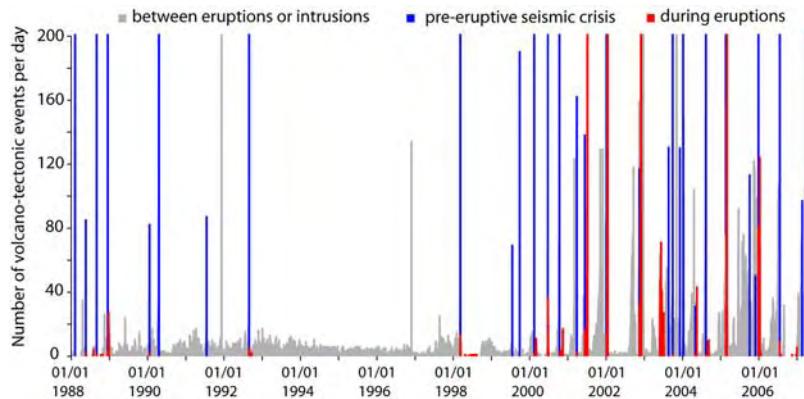
Figure 2. Volcano-tectonic seismicity between 1988 and March 2007. Note the onset of the co-eruptive seismicity since 2000.

suggests that the overlying rock column beneath Dolomieu experienced recurrent destabilizations.

3. April 2007 Eruption

3.1. Development of the Eruption

[8] On February 26 the seismic activity began below the summit zone. It progressively increased and reached the value of more than 100 daily events on March 28 to 30. A seismic crisis started on March 30 at 16:25 UTM and the magma emission begun at 18:50 from an eruptive fissure located at 1900 m asl SE of the central cone (Figure 1). The tremor ceased on March 31 at 05:15, after a first eruptive phase of less than 10 hours during which only a small volume of magma was emitted. The summit seismicity continued until the April 2 new eruptive phase in the Grand Brûlé at ~600 m above sea level and 7 km away from the summit (Figures 1 and 3). The eruption site was characterized by ~50 m high continuous lava fountains feeding voluminous lava flows. After a classical period of decreasing activity, the number of VT events gradually increased from April 3 (period 1 in Figure 3). On April 5, the VT events disappeared while both a general low frequency seismic signal and the tremor intensified (period 2 in Figure 3). The permanent GPS located ~200 m north of the northwestern rim (see Figure 1 for location) started to show an inward displacement of the summit zone at ~12:00 (Figure 3e), which was coeval with the increase of the seismic signal at the eruption site. The activity changed at 20:48 after a M_d 3.2 earthquake occurred below the summit crater (C_1 in Figures 3c and 3e). This event was contemporaneous with a sudden outward displacement of ~15 cm of the GPS station (Figure 3e). An increase of the seismic signal of ~50% was recorded at Tkr seismic station after the large earthquake. Then, the seismic signal was organized in cycles, the frequency of which gradually increased from one cycle every two hours to one cycle every 30 minutes (period 3 in Figure 3b). The seismic cycles were coeval with a step-by-step increase of the tremor until April 06 08:00 (Figure 3d). GPS data indicate that each cycle was characterized by progressive inward displacements and ended by a sharp outward motion. April 6 corresponds to a paroxysmal phase during which 200 m high lava fountains were observed in the Grand Brûlé. The first observations of the summit zone made the afternoon of the 6th revealed that the intensification of both the seismicity and the tremor was coeval with a collapse of Dolomieu (Figure 4b). The tremor progressively went down to its initial level, i.e., before the paroxysmal phase, whereas the cyclic seismic signal remained until the 7th of April 01:00. The eruption continued until the 1st of May with a fluctuating tremor. The total volume of magma emitted during the eruption is hard to assess since a large amount of lava flowed down to the sea where it formed a large platform. However, given the topography and the bathymetry before the event, a volume of $\sim100-140 \times 10^6$ m^3 has been inferred. This makes this eruption one of the most voluminous of PdF during the XXth and XXIth centuries.

3.2. Collapsed Structure

[9] Prior to the April 2007 eruption the summit zone of the central cone was occupied by a main collapsed structure, the Dolomieu crater. Historical reports reveal that it results from the coalescence of several pit craters aligned in the E-W direction [*Lénat and Bachèlery*, 1990; *Carter et al.*, 2007]. Before April 2007, the $\sim74 \times 10^4$ m^2 structure (800 m wide and 1100 m long), was completely filled in by lava flows (Figure 4a).

[10] The April 2007 eruption led to the largest historical collapse of PdF, i.e., since 1760. Although the previous coalescent collapse structures were interpreted as pit craters [*Carter et al.*, 2007], we propose that the new structure, which is at least twice larger than the previous collapses is most akin to calderas. Indeed, the collaspe that is of the size of small calderas [*Geshi et al.*, 2002] directly influenced the magma chamber dynamics. The caldera was first recognized in the afternoon of April 6, about 16 hours after the beginning of the seismic cycles. Observations revealed that the collapse affected first the northern part of the pre-existing Dolomieu (Figure 4b). The new structure was elongated along an E-W direction and bounded by sub-vertical scarps in the E, N and W. Its geometry was about 200–300 m deep, ~1 km long and ~600 m wide. Two annular plateaus corresponding to the pre-existing floor of Dolomieu were remaining in the E and the S. On April 10 the caldera was enlarged to about the size of the pre-existing Dolomieu structure (i.e., 800 m wide and 1100 m long; Figure 4c), and deepened to ~330 m. Only few perched terraces remained from the collapse eastern plateau.
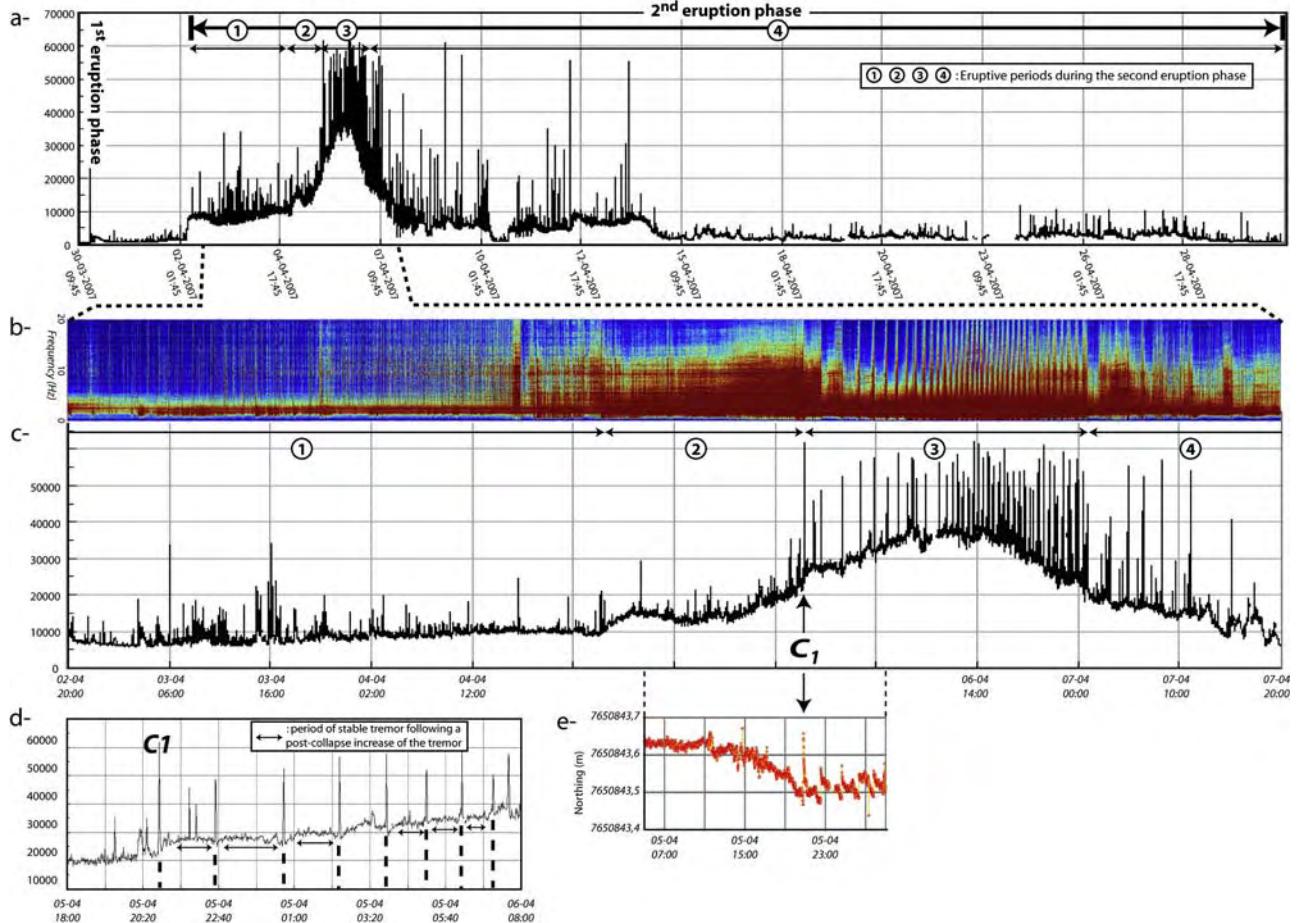
Figure 3. a) Eruptive signal recorded by the Takamaka seismic station. The peaks mark the VT events below the summit crater. b) Spectrogram of the seismicity recorded at the Bory seismic station for the pre-collapse and collapse periods. Red color between 0 and 5 Hz corresponds to the volcanic tremor. Red color between 5 and 15 Hz is interpreted as the vibration of the edifice during the stress accumulation. The short signals between 0 and 20 Hz indicate the VT events. c) Seismic signal recorded at Takamaka for the same period. C_1 is the initial collapse. d) Zoom of the seismic signal recorded at Takamaka illustrating the step-by-step increase of the tremor. e) N-S displacements recorded by the SNEG summit permanent GPS station (see Figure 1 for location).

[11] The geometry of the collapsed caldera did not significantly change after April 10. The size of the caldera increased by a few tens of meters with the lateral collapses of the western and north-western scarps along pre-existing concentric fractures already described by *Lénat and Bachèlery* [1990] and *Carter et al.* [2007]. The total area of the April 2007 caldera (82×10^4 m^2) is roughly similar to that of the pre-existing Dolomieu (74×10^4 m^2). This might be due to the fact that the collapse was mainly controlled by pre-existing concentric faults and/or that the magma chamber, the size and the location of which were recently determined from inversion of GPS data (diameters of 1.4 and 1 km in the E-W and N-S directions, and 0.3 km a.s.l. [*Peltier et al.*, 2007]) did not change since the XXth century. A maximum caldera depth of ~320–340 m was determined from triangulation, leading to a final volume of the caldera of 100–120 $\times$ 10^6 m^3. These values are confirmed by ASTER stereo images (M. Urai et al., Depression volume at Piton de la Fournaise volcano estimated by ASTER stereo imaging function, submitted to *Geophysical Research Letters,* 2007).

Note that ~80% of this volume results from the early stage of the collapse, before the first observations on April 6.

4. Discussion and Conclusion

[12] The collapse of PdF is one of the few examples showing the direct impact of a caldera formation on the dynamics of the eruptive system. The collapse started three days after the onset of the second eruptive phase of the April 2007 eruption. Most of the deformation happened between April 5 and 6, and continued until April 10. During this time span, the seismic signal progressively increased. Summit GPS data reveal that the first collapse occurred on April 5 at 20:48, triggering a large VT event (C_1 in Figure 3). It happened after a 7 hours long period of inward deflation coeval with a progressive increase of the effusion rate at the eruption site, i.e., ~7 km away from the summit zone. The first collapse marks a change in the eruption dynamics. Figures 3c and 3d show that the increase of the seismic signal changed from continuous to step by step. The close temporal link between the following seismic cycles and the
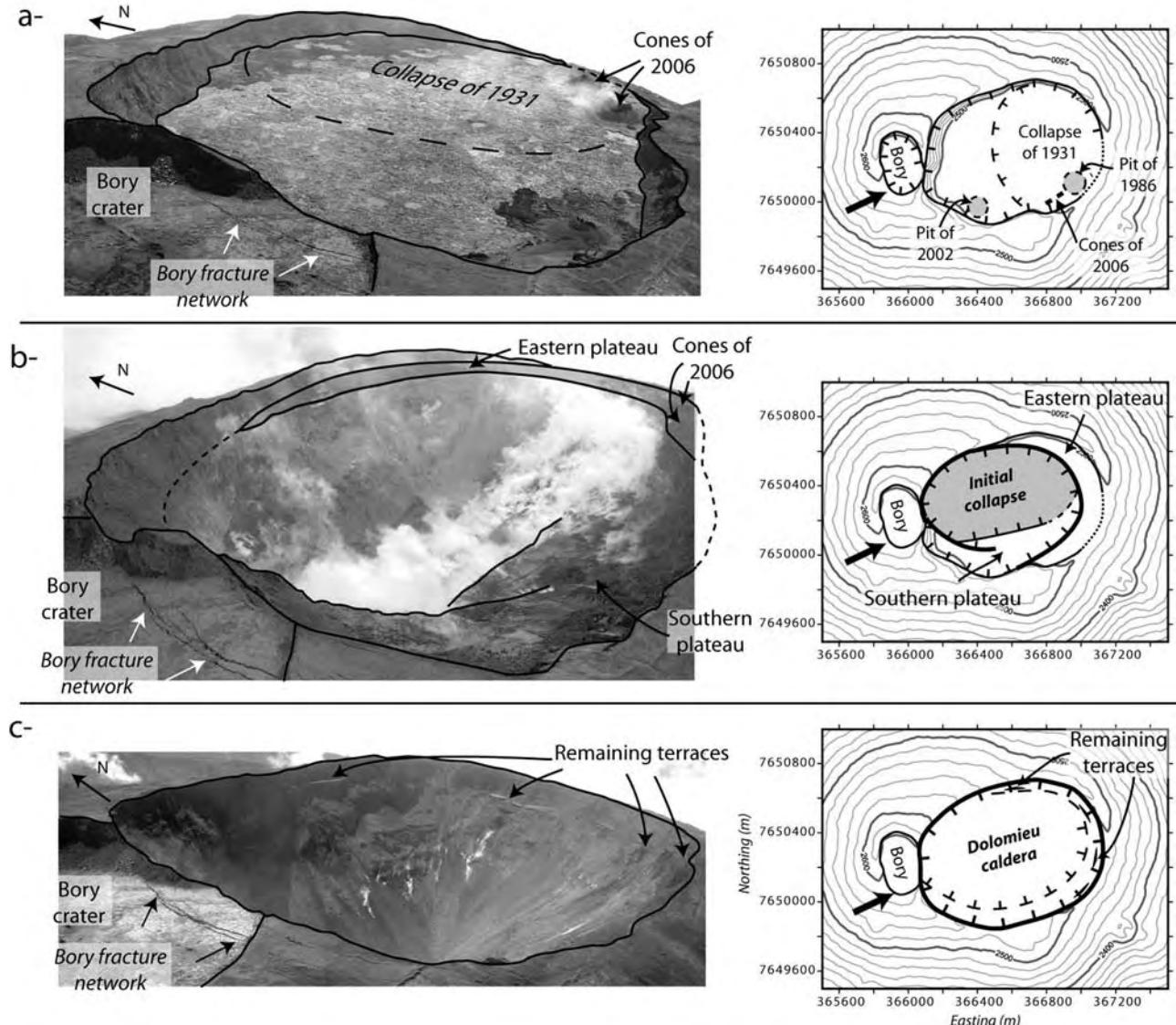
Figure 4. The Dolomieu crater on 31 October 2006 (a), on April 6 in the afternoon (b) and on April 10 (c). The Bory fracture network studied by *Carter et al.* [2007] in indicated for relocation.

step by step tremor intensification until 08:00 on April 6 strongly suggests a cogenetic origin. We propose that the slow increase of the seismic signal during each cycle corresponds to a stress build up in the overlying rock column beneath Dolomieu, which results from the progressive inward deflation of the summit zone. GPS and seismic data indicate that the sudden peak of each cycle denotes the collapse of the rock column. Likely, the GPS sudden outward displacements coeval with the collapses result from the collapse-related stress relaxation. We interpret the step by step increase of the seismic signal after the collapses as a consequence of the incremental overpressure in the magma reservoir. The decrease of the seismic signal amplification from April 6 08:00, after each seismic cycle, suggests that the effect of the collapses on the magma chamber vanished with time. Our data on the April 2007 collapse of Dolomieu confirm that this caldera collapse does not result from a single event but from the rapid succession of collapse events as already shown for Miyakejima [*Kumagai et al.*, 2001].

They also suggest that each cycle corresponds to a progressive stress accumulation due to the inward deflation followed by a rapid stress relaxation during the collapse.

[13] *Geshi et al.* [2002] showed that the caldera of Miyakejima formed progressively after the magma lateral intrusion. A similar scenario is proposed by *Simkin and Howard* [1970] to explain the caldera collapse at Fernandina. At PdF, the collapse occurred shortly after the beginning of the eruption when less than 30×10^6 m^3 of lava had been emitted. The volume difference of $60-70 \times 10^6$ m^3 between the collapse and the emitted magma when the collapse occurred may have several origins. 1- The beginning of the eruption was coeval to a large magma intrusion within the edifice leading to identical volumes of magma withdrawal and collapse. Usually the propagation of such intrusions triggers a clear seismic swarm [*Battaglia et al.*, 2005; *Aloisi et al.*, 2006]. At PdF, the seismic network recorded subtle northeastward and southeastward dike propagation few tens of minutes before the first eruption phase,

on March 30. However, its geometry can be hardly estimated with the deformation network of the OVPF, which is concentrated on and in the vicinity of the central cone. Hence, an intrusion likely occurred before the April 2007 eruption but its direct implication in the caldera collapse is hard to determine. 2- The collapse of the summit zone of PdF does not result from the April 2007 eruption only but is the consequence of the successive eruptions. We showed above that the final evolution of the distal and voluminous proximal eruptions changed since 2000 with the occurrence of an intense seismicity between the magma chamber and the summit during and after the last days or hours of eruptions (Figure 2). The abundance of the VT events, which indicates a deep deformation, was always coeval with an increase of both the tremor and the emission rates. However, it was never correlated with a surface deformation. The small pit crater formed in December 2002 after the November 2002 eruption is the only evidence of a subsurface deformation [*Longpré et al.*, 2007]. We propose that the co-eruptive final seismicity is related to a progressive collapse and weakening of the zone located above the magma chamber. In consequence, the caldera collapse at PdF could correspond to the surface deformation of a process which was initiated at depth several years ago.

[14] Therefore, we propose that the April 2007 caldera results from the combine effect of (1) an early intrusion, which substantially decrease the pressure in the magma reservoir during the first phase of the April 2007 eruption and (2) a progressive weakening of the rock column above the magma chamber since 2000.

References

Aloisi, M., A. Bonaccorso, and S. Gamboni (2006), Imaging composite dike propagation (Etna, 2002 case), *J. Geophys. Res.*, *111*, B06404, doi:10.1029/2005JB003908.

Bachèlery, P. (1981), Le Piton de la Fournaise (Ile de la Réunion). Etude volcanologique, structural et pétrologique, Ph.D. thesis, Univ. Clermont Ferrand II, Clermont Ferrand, France.

Battaglia, J., V. Ferrazzini, T. Staudacher, K. Aki, and J.-L. Cheminée (2005), Pre-eruptive migration of earthquakes at the Piton de la Fournaise volcano (Réunion Island), *Geophys. J. Int.*, *161*, 549–558.

Carter, A., B. van Wyk de Vries, K. Kelfoun, P. Bachèlery, and P. Briole (2007), Pits, rifts and slumps: the summit structure of Piton de la Fournaise, *Bull. Volcanol.*, *69*, 741–756, doi:10.1007/s00445-006-0103-4.

Cole, J. W., D. M. Milner, and K. D. Spinks (2005), Calderas and caldera structures: A review, *Earth Sci. Rev.*, *69*, 1–26.

Fukushima, Y., V. Cayol, and P. Durand (2005), Finding realistic dike models from interferometric synthetic aperture radar data: The February 2000 eruption at Piton de la Fournaise, *J. Geophys. Res.*, *110*, B03206, doi:10.1029/2004JB003268.

Geshi, N., T. Shimano, T. Chiba, and S. Nakada (2002), Caldera collapse during the 2000 eruption of Miyakejima Volcano, Japan, *Bull. Volcanol.*, *64*, 55–68.

Hirn, A., J.-C. Lépine, M. Sapin, and H. Delorme (1991), Episodes of pit-crater collapse documented by seismology at Piton de la Fournaise, *J. Volcanol. Geotherm. Res.*, *47*, 89–104.

Kaneko, T., A. Yasuda, T. Shimano, S. Nakada, T. Fujii, T. Kanazawa, A. Nishizawa, and Y. Matsumoto (2005), Submarine flank eruption preceding caldera subsidence during the 2000 eruption of Miyakejima Volcano, Japan, *Bull. Volcanol.*, *67*, 243–253, doi:10.1007/s00445-004-0407-1.

Kumagai, H., T. Ohminato, M. Nakano, M. Ooi, A. Kubo, H. Inoue, and J. Oikawa (2001), Very-long-period seismic signals and the caldera formation at Miyake Island, Japan, *Science*, *293*, 687–690.

Lacroix, A., (1938), *Le Volcan Actif de l'Ile de la Réunion (Supplément) et Celui de la Grande Comores*, 57 pp., Gauthier-Villars Ed., Paris.

Lénat, J.-F., and P. Bachèlery (1990), Structure and dynamics of the central zone of Piton de la Fournaise volcano, in *Le Volcanisme de la Réunion*, *Monogr. Cent. De Rech. Volcanol.*, edited by J-F Lénat, pp. 257–296, Cent. De Rech. Volcanol., Clermont-Ferrand, France.

Longpré, M.-A., T. Staudacher, and J. Stix (2007), The November 2002 eruption at Piton de la Fournaise volcano, La Réunion Island: Ground deformation, seismicity, and pit crater collapse, *Bull. Volcanol.*, *69*, 511–525, doi:10.1007/s00445-006-0087-0.

MacDonald, G. A. (1965), Hawaiian calderas, *Pacific Sci*, *19*, 320–334.

MacPhie, J., G. P. L. Walker, and R. L. Christiansen (1990), Phreatomagmatic and phreatic fall and surge deposits from explosions at Kilauea volcano, Hawaii, 1790 a.d.: Keanakakoi Ash Member, *Bull. Volcanol.*, *52*, 334–354.

Okubo, C. H., and S. J. Martel (1998), Pit crater formation on Kilauea volcano, Hawaii, *J. Volcanol. Geotherm. Res.*, *86*, 1–18.

Peltier, A., T. Staudacher, and P. Bachèlery (2007), Constraints on magma transfers and structures involved in the 2003 activity at Piton de La Fournaise from displacement data, *J. Geophys. Res.*, *112*, B03207, doi:10.1029/2006JB004379.

Rymer, H., B. van Wyk de Vries, J. Stix, and G. Williams-Jones (1998), Pit crater structure and processes governing the persistent activity at Masaya volcano Nicaragua, *Bull. Volcanol.*, *59*, 345–355.

Simkin, T., and K. A. Howard (1970), Caldera collapse in Galapagos Islands, 1968, *Science*, *169*, 429–437.

———————————

P. Bachèlery and L. Michon, Laboratoire GéoSciences Réunion, Institut de Physique du Globe de Paris, Université de La Réunion, CNRS, UMR 7154-Géologie des Systèmes Volcaniques, 15 avenue Rene Cassin, BP 7151, F-97751 Saint Denis cedex 9, La Réunion, France.

V. Ferrazzini and T. Staudacher, Observatoire Volcanologique du Piton de la Fournaise, Institut de Physique du Globe de Paris, CNRS, UMR 7154-Géologie des Systèmes Volcaniques, F-97418, La Plaine des Cafres, La Réunion, France.

J. Marti, Institute of Earth Sciences "Jaume Almera," Consejo Superior de Investigaciones Científicas, Lluis Sole Sabaris s/n, E-08028 Barcelona, Spain.

Annexe 12 :

Michon, L., F. Saint-Ange, (2008), The morphology of Piton de la Fournaise basaltic shield volcano (La Réunion island): characterization and implication in the volcano evolution, J. Geophys. Res., 113, B03203, doi:10.1029/2005JB004118.

Morphology of Piton de la Fournaise basaltic shield volcano (La Réunion Island): Characterization and implication in the volcano evolution

Laurent Michon[1] and Francky Saint-Ange[1]

[1]   The topography of Piton de la Fournaise volcano (PdF) differs from the classic view of basaltic shield volcanoes as it is characterized by (1) several steep slope zones on its flanks and (2) a large U-shaped caldera, the Enclos-Grand Brûlé structure (EGBS). Most of these structures were previously interpreted as the scars of lateral landslides, the deposits of which cover the submarine flanks of PdF. We carried out a detailed analysis of the morphology of PdF, which reveals that the steep slope zones form two independent, circumferential structures that continue into the caldera. The development of circumferential steep slopes on volcano flanks may have several origins: constructive, destructive, and deformation processes. We interpret those processes acting on PdF as caused by the spreading of the volcanic edifice above a weak hydrothermal core, leading to outward displacements and a summit extensive stress field. The continuity of the steep slope on both sides of the EGBS escarpments suggests that this structure was not caused by a 4.5 ka old giant landslide as it is usually proposed but is due to a mainly vertical collapse. The recent debris avalanche deposits east of the island indicate that this event likely destabilized part of the submarine flank. We propose that the collapse of the Grand Brûlé, the lower half of the EGBS, was due to the downward drag related to the dense intrusive complex of the Alizés volcano, which is located 1 km below the Grand Brûlé. The collapse of the Enclos is interpreted as the consequence of the deformation of the hydrothermal system of the pre-Enclos volcano. Although the continuity of the geological and morphological structures between the Enclos and the Grand Brûlé suggests a narrow link between these two collapse events, their chronology and relationship are still uncertain. Finally, we hypothesize that the persistence of the NE and SE rift zones during the last 150 ka, despite the large changes of the topography related to the recurrent flank destabilizations, is linked to a deep sources, which can be either underlying crustal faults or the continuous downward subsidence of the Alizés intrusive complex.

Citation: Michon, L., and F. Saint-Ange (2008), Morphology of Piton de la Fournaise basaltic shield volcano (La Réunion Island): Characterization and implication in the volcano evolution, *J. Geophys. Res.*, *113*, B03203, doi:10.1029/2005JB004118.

1.   Introduction

[2]   The morphology of volcanoes results from construction, destruction and deformation processes that interact during their evolution [e.g., *Moore*, 1964; *Moore and Mark*, 1992; *Rowland and Garbeil*, 2000; *Merle and Borgia*, 1996; *Cecchi et al.*, 2005]. Hence the analysis of the morphology allows the identification of structures the development of which is related to internal processes and/or a specific eruption history [e.g., *Tort and Finizola*, 2005]. At Piton de la Fournaise, one of the world's most active shield volcanoes [e.g., *Lénat and Bachèlery*, 1987], the succession of construction and dismantling phases (i.e., erosion and landslide) led to the development of a complex morphology [e.g., *Bachèlery*, 1981; *Rowland and Garbeil*, 2000]. One of the most striking features is the E-W elongated horseshoe-shaped collapse structure in which the currently active cone developed (Figure 1). The structure is composed, from west to east, by the Enclos depression, the Grandes Pentes, and the Grand Brûlé and is bounded by 100- to 200-m-high escarpments, the Bois Blanc, Bellecombe and Tremblet escarpments in the north, west and south, respectively. The formation of the Enclos-Grand Brûlé structure (EGBS) is one the greatest scientific controversies on PdF. One interpretation is that the Enclos depression results from a polyphase caldera collapse whereas the Grand Brûlé exhibits the scars of lateral landslides with the Grandes Pentes as their headwall [*Bachèlery*, 1981] (Figure 2a). Another interpretation is that the entire EGBS results from a giant landslide that was also partly responsible for the debris

---

[1]Laboratoire GéoSciences Réunion, Institut de Physique du Globe de Paris, Université de la Réunion, CNRS, UMR 7154, Géologie des Systèmes Volcaniques, Saint Denis, France.
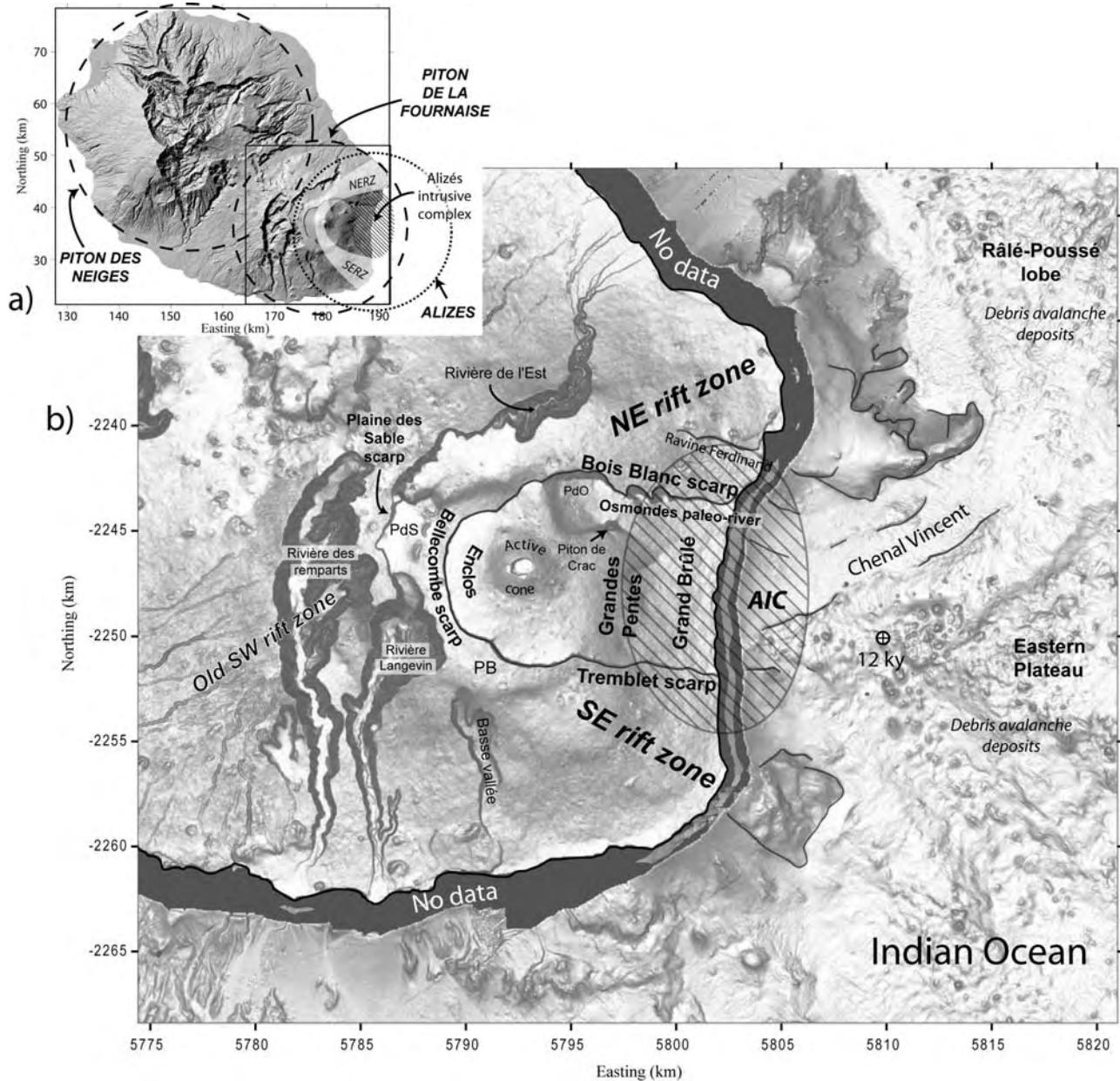
Figure 1. (a) Shaded relief image (illumination from the NW) presenting Piton de la Fournaise in the setting of La Réunion (NERZ, northeast rift zone; SERZ, southeast rift zone). Coordinates in Gauss Laborde Réunion. (b) Digital terrain model of the subaerial and submarine parts of Piton de la Fournaise showing the structures discussed in the text (i.e., scarps, valleys, rift zones, debris avalanche deposits). The dating at 12 ka of a sample dredged on the proximal submarine flank is also reported [*Labazuy*, 1996]. AIC, Alizés intrusive complex; PB, Planèze du Baril; PdO, Plaine des Osmondes; PdS, Plaine des Sables. Coordinates are in Mercator.

avalanche deposits on the submarine flanks [*Duffield et al.*, 1982; *Gillot et al.*, 1994; *Labazuy*, 1996] (Figure 2b). A third interpretation was recently proposed by *Merle and Lénat* [2003], who take into account the role of both hydrothermal systems and deep décollement levels in the volcano's deformation. In their model, a lateral movement (the Grand Brûlé) triggered a vertical collapse in the summit area (the Enclos depression; Figure 2c). Several additional large-scale structures may be related to the same mechanism, resulting in 100-m-high escarpments and steep slope zones

outside the structures mentioned above [e.g., *Bachèlery*, 1981; *Oehler et al.*, 2004].

[3] The present study aims at describing in detail the morphology of PdF and at understanding the origin of the main structures, i.e., the steep slope zones on the volcano flanks and the EGBS. We use different digital elevation models (with 25- and 50-m resolution) to determine the detailed and first-order morphologies of the edifice. Integration of the available geological and geophysical data, and of the different published conceptual models, allows us
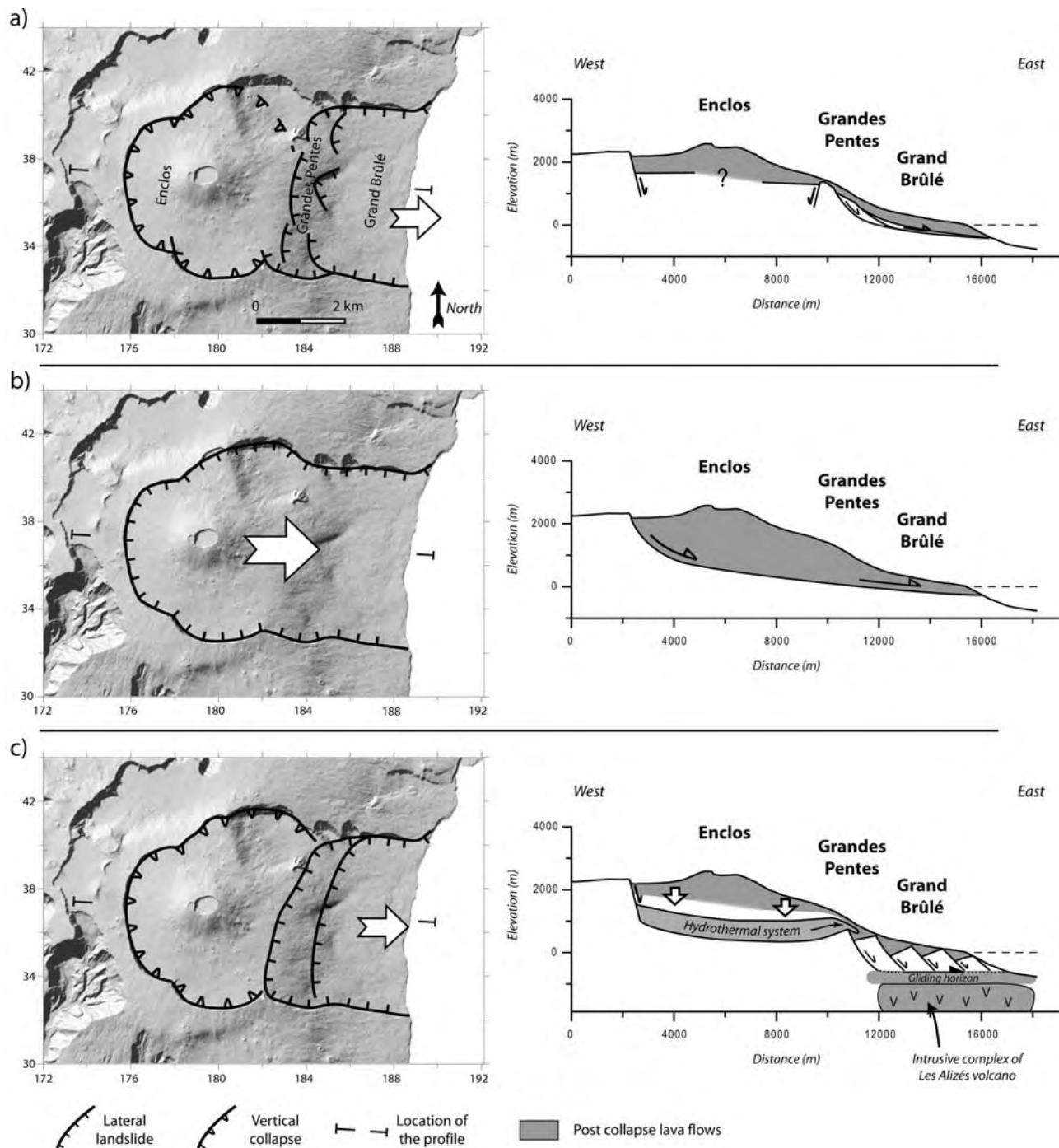
Figure 2. Schematic views and cross sections of the three different models previously proposed to explain the formation of the large Enclos-Grand Brûlé structure (EGBS). (a) A polyphase caldera collapse and the Grand Brûlé is the scar of one or several lateral landslides, the Grandes Pentes being the headwall of these slides [after *Bachèlery*, 1981]. (b) The entire structure is the scar of a single, landslide [after *Labazuy*, 1996; *Oehler et al.*, 2004]. (c) A slide of the Grand Brûlé due to a deep décollement induced a collapse of the Enclos caldera [after *Merle and Lénat*, 2003]. Coordinates are in Gauss Laborde Réunion (km).

to constrain their spatiotemporal relationship and their potential origin. Finally, we present a chronology for the last 150 ka of PdF in which we consider the potential role of the rift zones and the intraedifice density contrasts in the volcano evolution.

2. Evolution of Piton de la Fournaise in the Geological Setting of La Réunion Island

[4] Measured from the seafloor, La Réunion Island is a 7-km-high oceanic shield volcano with a diameter of 220–240 km. Considering the historical magma production rate and the oldest dated subaerial basalts (2.1 Ma [*MacDougall*, 1971]), an age of around 5 Ma was estimated since the beginning of the edifice growth [*Gillot et al.*, 1994]. The initial magmatic evolution was characterized by the development of two adjacent volcanoes (the Piton des Neiges and Alizés), which encountered recurrent flank destabilizations [*Lénat et al.*, 2001; *Bachèlery et al.*, 2003; *Oehler et al.*, 2004]. The Alizés volcano is now completely dismantled and the only evidence of its past existence is the large intrusion complex discovered by drilling below the Grand Brûlé (Figure 1) [*Rançon et al.*, 1989], the old submarine remnants [*Labazuy*, 1996] and the pre-Brunhes reverse magnetic anomalies, which were determined as magmatic formations older than those of Piton de la Fournaise [*Lénat et al.*, 2001]. The destabilization of the Alizés volcano led to the development of the Eastern Plateau, which corresponds to a submarine relief composed of several hundreds of km^3 of debris avalanche deposits [*Labazuy*, 1991; *Oehler*, 2005, available at http://tel.archivesouvertes.fr/tel-00010498/en/]. Around 530 ka ago, Piton de la Fournaise appeared west of the center of Alizés, which had stopped its activity. Between 530 and 12 ka (the date of Piton des Neiges' last eruption [*Deniel et al.*, 1992]), Piton des Neiges and Piton de la Fournaise showed contemporaneous activity. Finally, for the last 12 ka, eruptions are restricted to Piton de la Fournaise.

[5] Geochronological [*Gillot and Nativel*, 1989] and geological data [*Mairine and Bachèlery*, 1997] indicate that PdF results from two main building phases, 0.53–0.29 Ma and 0.15 Ma to present-day, separated by a period during which erosion prevailed. The first construction period led to the formation of the "ancient" PdF, which was likely centered on the present-day Plaine des Sables [*Bachèlery and Mairine*, 1990]. The distribution of dike swarms in the Rivière des Remparts indicates that at least one rift zone developed during this first phase (i.e., the SW rift zone [*Mairine and Bachèlery*, 1997]). Debris flow units in the eastern scarp of the Rivière des Remparts and western scarp of the Rivière Langevin intercalated with 0.22 Ma old lava flows indicate that the "ancient" Fournaise suffered intense erosion, which induced the incision of the paleo-Rivière des Remparts [*Bachèlery and Mairine*, 1990]. This valley was progressively filled in until the collapse of the Morne Langevin caldera 0.15 Ma ago. This event led to an eastward shift of the volcanic center. As a result, the geometry of the feeding zone changed: two NE and SE rift zones developed from the volcanic center [*Bachèlery*, 1981] (Figure 1). Part of the debris avalanche deposits covering the Eastern Plateau and forming the Ralé Poussé lobe are interpreted as related to this large collapse [*Oehler*, 2005]. During the last 0.15 Ma, the "recent" PdF

was affected by at least two caldera collapses whose origins are still controversial.

[6] 1. The Plaine des Sables caldera resulted from several collapse events starting 60 ka ago [*Bachèlery and Mairine*, 1990]. Several datings of the debris avalanche deposits (between 110 and 45 ka) dredged on the Eastern Plateau show that these events were associated with large flank landslides, the deposits of which spread over the proximal part of the submarine plateau and the Râlé Poussé (Figure 1b) [*Labazuy*, 1996].

[7] 2. The Enclos caldera formed around 4.5 ka ago [*Bachèlery and Mairine*, 1990]. Pyroclastic deposits around the Enclos indicate that the collapse was simultaneous to a large explosive eruption [*Abchir et al.*, 1998]. However, as for other basaltic calderas [e.g., *MacDonald*, 1972; *Munro and Rowland*, 1996], the volume of the deposit (around 0.5–1 km^3 [*Abchir et al.*, 1998]) is 1 order of magnitude lower than that of the Enclos caldera. The summit part of the Râlé Poussé debris avalanche lobe, which age is uncertain is considered as to be related to the slide of the Grand Brûlé [*Labazuy*, 1996; *Oehler*, 2005].

[8] During the "recent" Fournaise evolution (post-0.15 Ma), intense erosion led to the formation of deep valleys (Rivière des Remparts, Rivière Langevin, Rivière Basse Vallée, and Rivière de l'Est; Figure 1). An additional erosional structure was discovered on the eastern flank of PdF. Geophysical data and a drill hole in the northern part of the Grand Brûlé revealed the presence of the Osmondes paleoriver [*Courteaud*, 1996], where more than 170 m of alluvial formations were encountered below 60 m of recent lava flows. The relationship and the chronology between this valley and the Grand Brûlé are poorly understood.

3. Analysis of the Piton de la Fournaise Morphology

[9] Piton de la Fournaise is characterized by three main morphological features: (1) The flanks, which are continuous from the summit to the sea in the north, east and south, whereas the western flank is buttressed by Piton des Neiges, (2) two visible calderas, the Plaine des Sables and the EGBS, bounded by 100-m-high escarpments, and (3) very deeply incised valleys (the Rivière des Remparts, Rivière Langevin, Rivière de l'Est, and Rivière Basse Vallée), which dissect the western part of the edifice. We focus our analysis on the two first morphological structures.

3.1. Characterization of the Flanks of PdF

[10] Our analysis of the morphology of PdF is mainly based on the study of a 25-m step digital elevation model (DEM) developed by Institut Géographique National (IGN). This DEM was calculated by stereophotogrammetry from a set of aerial photographs taken in 1997. Stereotriangulation and 967 ground control points were used to control the accuracy of the model (vertical error of ±4.5 m at 2σ [*Villeneuve*, 2000]). The DEM being calculated from aerial photographs, its accuracy slightly decreases in densely vegetated areas (i.e., the flanks of the edifice) and increases around the Enclos depression. As a consequence, minor topographic structures are disregarded.

[11] The flanks of PdF are characterized by different slope domains from the coast to the summit [*Rowland*
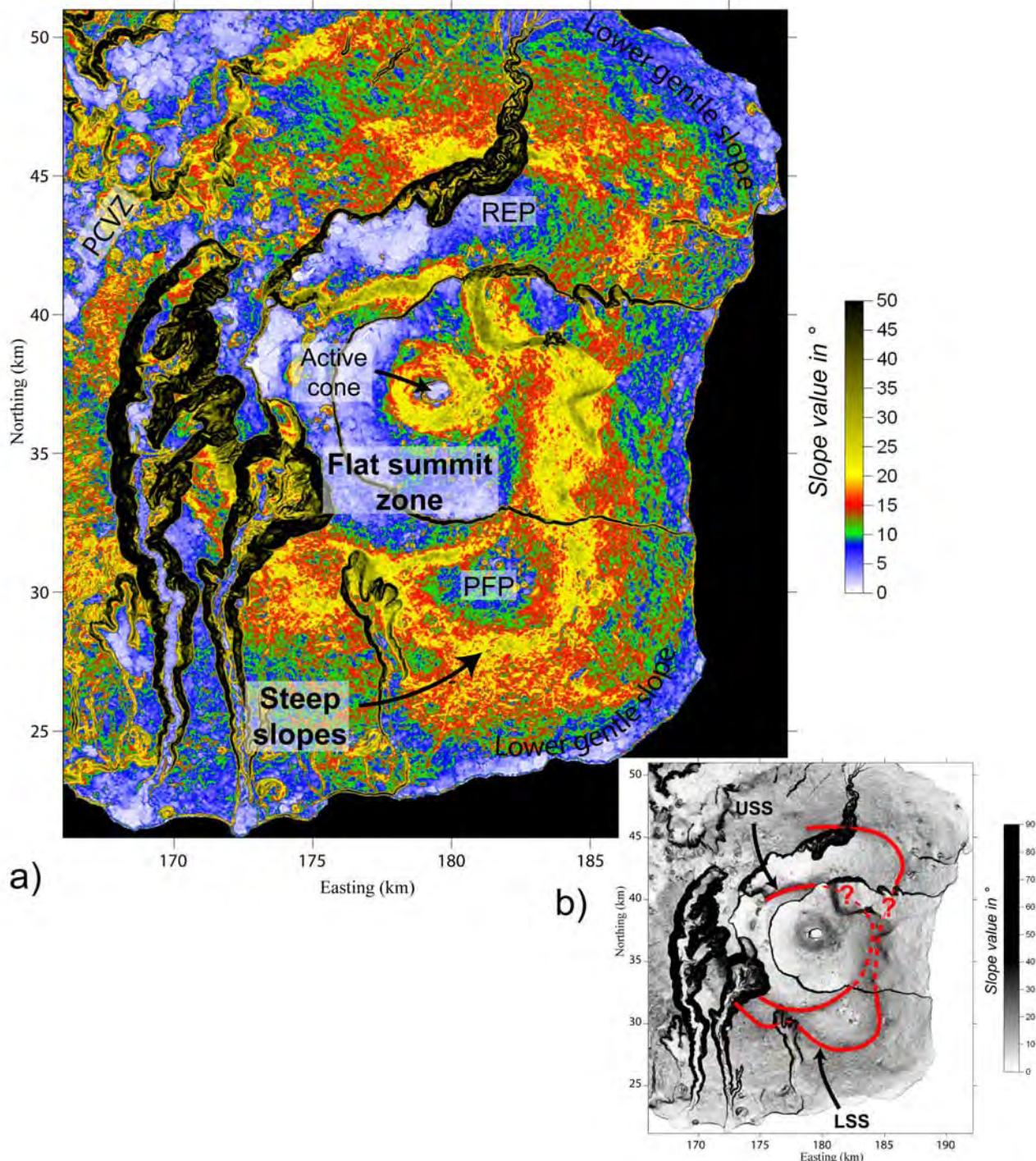
Figure 3. (a) Slope map of PdF showing the variable slopes on the volcano flanks. PFP, Piton de Fourche Plateau; REP, Rivière de l'Est Plateau; PCVZ, Plaine des Cafres Volcanic Zone. (b) Gray scale slope image with location of the upper and lower steep slope zones highlighted in red (USS and LSS) characterized by slope values ranging between 20° and 30°. Coordinates are in Gauss Laborde Réunion.

and Garbeil, 2000] (Figure 3a). At low elevations, the slope value range between 8° and 15°, corresponding to typical values of basaltic oceanic volcanoes [*Mark and Moore*, 1987; *Hürlimann et al.*, 2004]. At higher elevations, the topography of the southern, eastern and northern flanks is characterized by steep slope zones ranging between 20° and

35° (Figures 3 and 4), while the summit shows slopes between 2° and 8°, if the escarpments and the active cone are disregarded. Such a slope distribution is strikingly similar to what is observed on Volcán Fernandina, Wolf, and Cerro Azul in the western Galapagos archipelago [*Rowland*, 1996; *Rowland and Garbeil*, 2000]. In contrast,
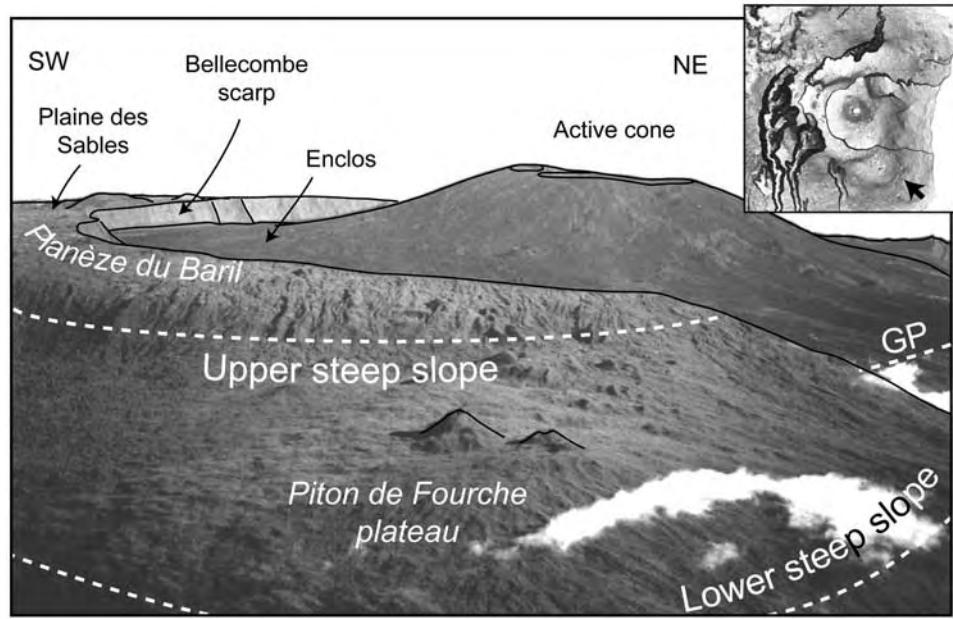
Figure 4. Northwestward view of the PdF summit. The USS separates two areas of low slope values (i.e., the Piton de Fourche Plateau below and the Planèze du Baril above). GP, Grandes Pentes. The black arrow in the insert indicates the location and the viewing direction.

this slope distribution is not observed on the western flank of PdF where the edifice is buttressed by Piton des Neiges.

[12] Radial topographic profiles allow a better characterization of the flank geometry (Figure 5). On the southern and eastern flanks, single linear profiles were produced from digital elevation models, but a composite profile was required for the northern flank in order to avoid complications of Rivière de l'Est and Plaine des Osmondes (Figure 5a). Topographic profiles, except for profile 3 (the east flank), reveal a seaward tilted stair-like topography with two steep slope zones separated by inclined plateaus such as the Piton de Fourche and the Rivière de l'Est (Figure 5a). Each steep slope zone corresponds to one step between flank segments that are characterized by constant slope values. The elevation changes across the upper steep slope (USS) and lower steep slope (LSS) are similar with 160, 230, and 210 m for the upper slope and 240, 285, and 220 m for the lower slope, respectively. Moreover, for each profile, the elevation change across the USS is always smaller than that across the LSS. In the SW, SE and north flanks, the USS and LSS are located at a nearly constant elevation at around 2000 m for the USS and 1000–1200 m for the LSS (Figure 5b). The resulting morphology is characterized by a geometry resembling an "overturned soup plate." Combining the slope map and topographic profiles suggests that the USS and LSS form two independent morphological structures on the southern and northern flanks of PdF. Concerning profile 3 on the east flank, only one steep slope zone is observed. This exception raises the problem of the relationship between the steep slope zones outside the EGBS and in the Grandes Pentes. The Grandes Pentes could correspond either to an independent structure whose development is related to the formation of the EGBS [e.g., *Bachèlery*, 1981; *Merle and Lénat*, 2003], or to the continuity of the upper and lower steep slope zone, which would

merge in the east flank. Whatever the relationship between the Grandes Pentes and the USS and LSS, two morphological structures can be determined in the south, SE, NE, and north flanks (Figure 3b). The upper morphological structure is subcircular, whereas the lower structure presents two lobes at the location of the NE and SE rift zones. Along the NE rift zone, the lower structure presents relatively low slope values, which could be due to burial by lava flows such as during the 1977 eruption.

3.2. Analysis of the Enclos-Grand Brûlé Structure

[13] The EGBS is the most recent large-scale structure of Piton de la Fournaise. From east to west, it is composed of the Enclos depression, the Grandes Pentes and the Grand Brûlé (Figure 6). Secondary structures correspond to the Plaine des Osmondes and Piton de Crac. The Plaine des Osmondes is interpreted as the most recent collapse structure of the Enclos [*Bachèlery*, 1981]. The similar geometry (dip and thickness of the lava flows), the petrology of the lava flows of Piton de Crac and Bois Blanc scarp, and the orientation of the only dike observed on Piton de Crac toward the active summit cone suggests that Piton de Crac is a remnant part of PdF isolated by collapse events and erosion [*Bachèlery*, 1981].

[14] For our analysis of the EGBS, we consider three different zones that help reinterpreting the evolution and the formation of the overall collapse structure.

3.2.1. Enclos

[15] The floor topography of the Enclos reveals a series of relatively flat plateaus at different elevations: 2050–2200, 1750–1900, and 1900–2000 m for the western, southern, and northern plateau, respectively, which are separated by steeper slope zones (Figure 7a). The transition between the western and southern plateaus consists of a N65° trending steep slope zone, which is associated with a subtle kilome-
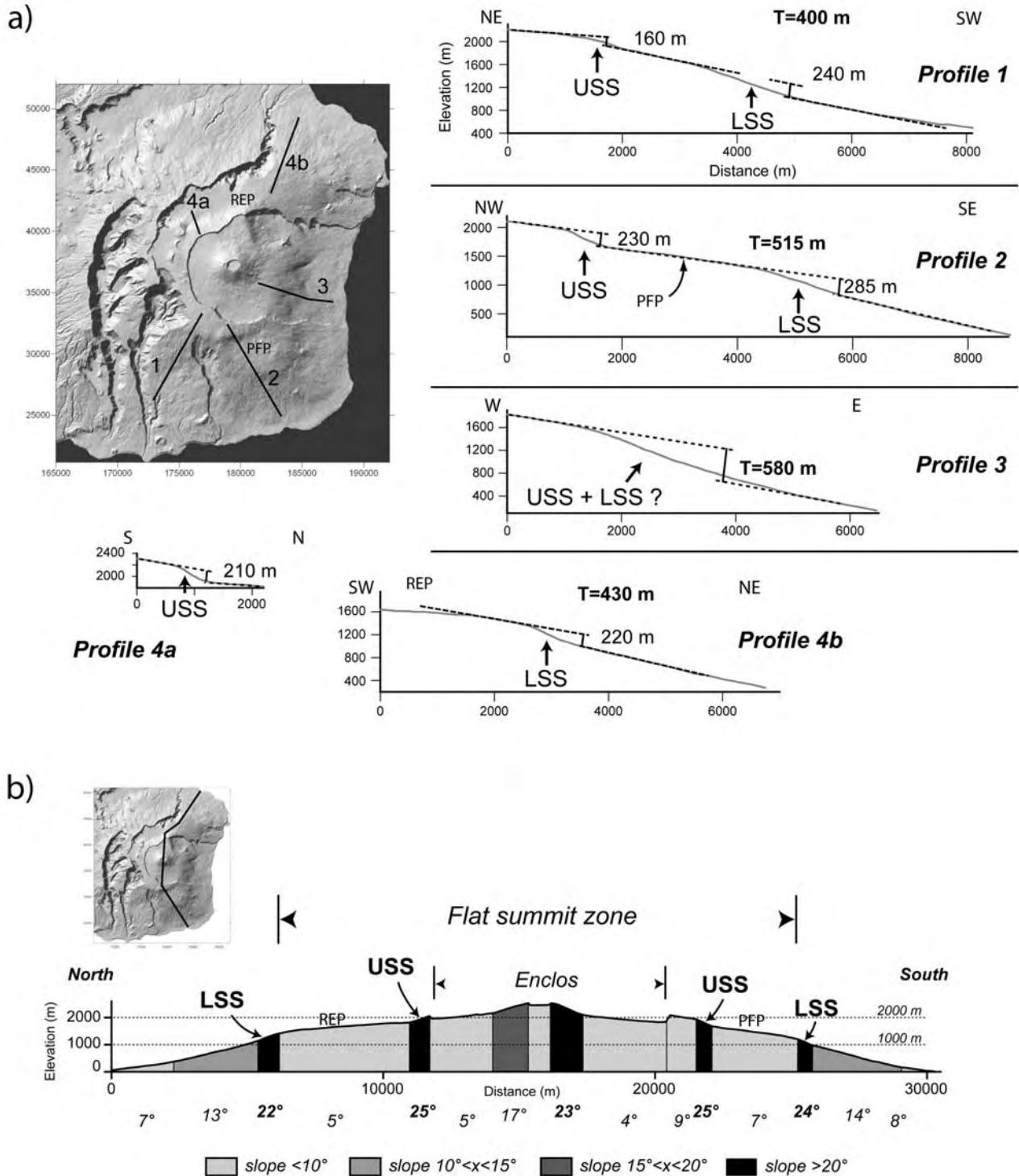
Figure 5. (a) Radial topographic profiles showing the succession of steep slopes and domains of gentle slopes. Elevation changes between each domain of gentle slopes are determined. No vertical exaggeration. T corresponds to the total elevation difference for each profile. USS, upper steep slope; LSS, lower steep slope; REP, Rivière de l'Est Plateau; PFP, Piton de Fourche Plateau. (b) North-south topographic profile illustrating the shield morphology of PdF and its variable slope domains. Note the nearly identical elevation of both the LSS and USS on the north and south flanks.

ter-long lineament, located at the slope change (Figure 7b). It appears that this lineament is restricted to the EGBS, i.e., it cannot be traced south of the Enclos scarp, and continues northeast toward the Grandes Pentes (Figure 7c). In a

volcanic setting, a lineament can have several origins: the margin of a lava flow, the trace of a lava channel or lava tube, a spatter rampart, a fluvial gully or a fault. In the present case, the orientation of the lineament, oblique to the
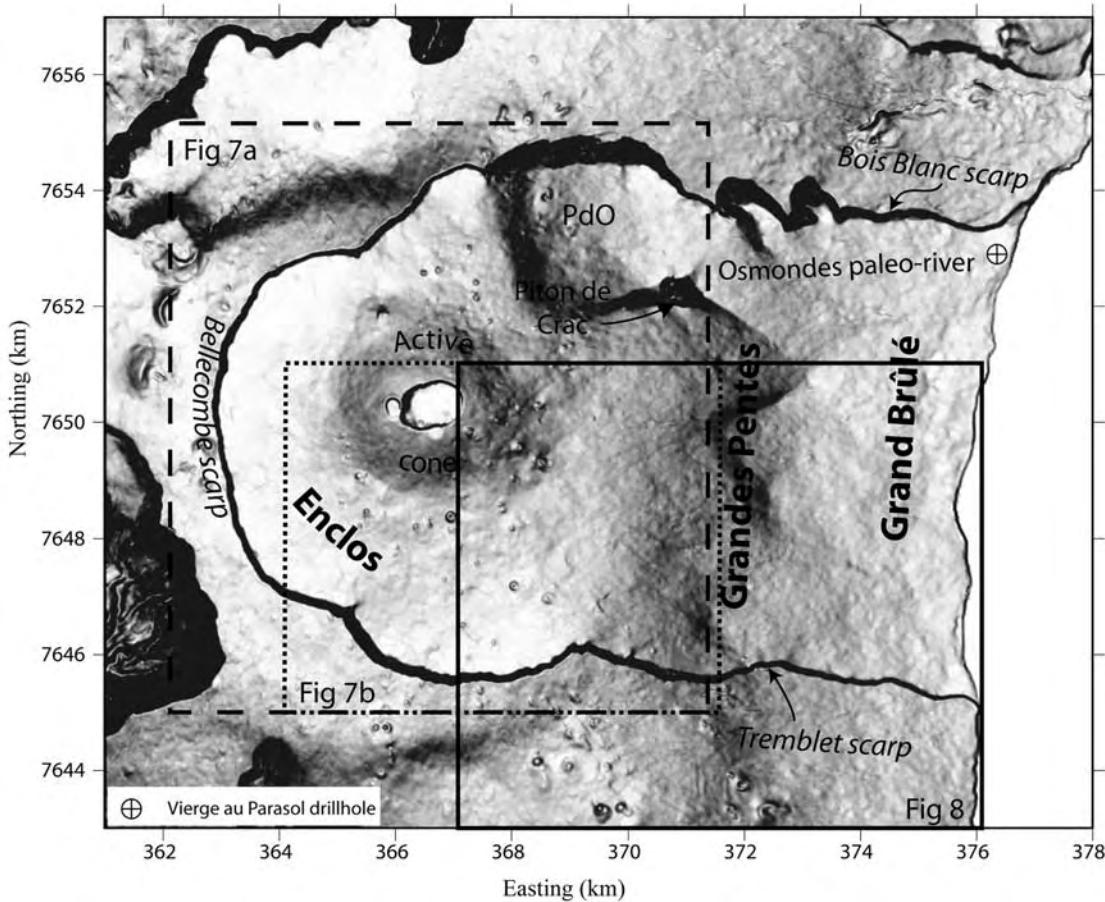
Figure 6. Gray scale slope map representing the structures of the EGBS. Figures 7a, 7b, and 8 are located. Coordinates are in UTM WGS84.

general slope, and its length are difficult to explain as lava structures or river patterns. Field observations reveal that long and linear extensive fractures cut several units of lava flows of different ages at the upper break-in-slope, which corresponds to the location of the lineament (Figure 7b). The older the lava flows, the wider the fractures. The development of such a fracture network is in agreement with a continuous process of deformation. Moreover, this part of the Enclos is characterized by recurrent tectonic earthquakes confined to the region south of the lineament [*Lénat et al.*, 1989; *Sapin et al.*, 1996] (Figure 7a). We suggest that the alignment of the extensive fractures, the lineament and the seismicity results from the activity of a normal fault (Figure 7b). We also propose that the 100-m-high offset of the Enclos floor results from tectonic activity along this large fault during or after the EGBS formation.

3.2.2. Tremblet Scarp

[16] Analysis of the morphology of PdF reveals the existence of steep slope zones both inside and outside the EGBS. The possible link between these morphological structures across the Tremblet scarp in the south and across the Bois Blanc scarp in the north is still unclear even though the different steep slope zones are characterized by identical slope values. The detailed analysis of the slope distribution on both sides of the Tremblet scarp provides new constrains

on the relationship between the morphological structures outside and inside the EGBS.

[17] The lowest part of the Grandes Pentes is characterized by a V-shaped structure (VSS), which was commonly interpreted as the trace of a small-scale landslide that has occurred after the Grand Brûlé landslide [e.g., *Bachèlery*, 1981] (Figures 7c and 8). This structure is limited by two NE and SE linear steep slope zones where slope values exceed 30° (Figure 8). The slope map suggests that another SE trending steep slope zone seems to be continuous south of the Tremblet scarp (Figure 8b). However, the irregularity of the topography does not allow establishing firmly this continuity outside the EGBS. We calculated a 50-m low-pass-filtered DEM from the original 25-m step DEM (Figure 8c) in order to smooth the rough topography and to keep the first-order morphology. Three different slope domains can be distinguished from this DEM: domain A with an average slope of 10°, domain B with 14° and domain C exceeding 18°. Geometrically, these areas are continuous on both sides of the Tremblet scarp. Domain A is at low elevation. Inside the EGBS, it corresponds to the upper part of the Grand Brûlé. South of the Tremblet scarp, domain A is situated between the seacoast and domain B. The lowest part of the Grand Brûlé, which is characterized by gentle slopes between 4° and 8° corresponds to the coastal plain formed by the overlap of multiple lava deltas
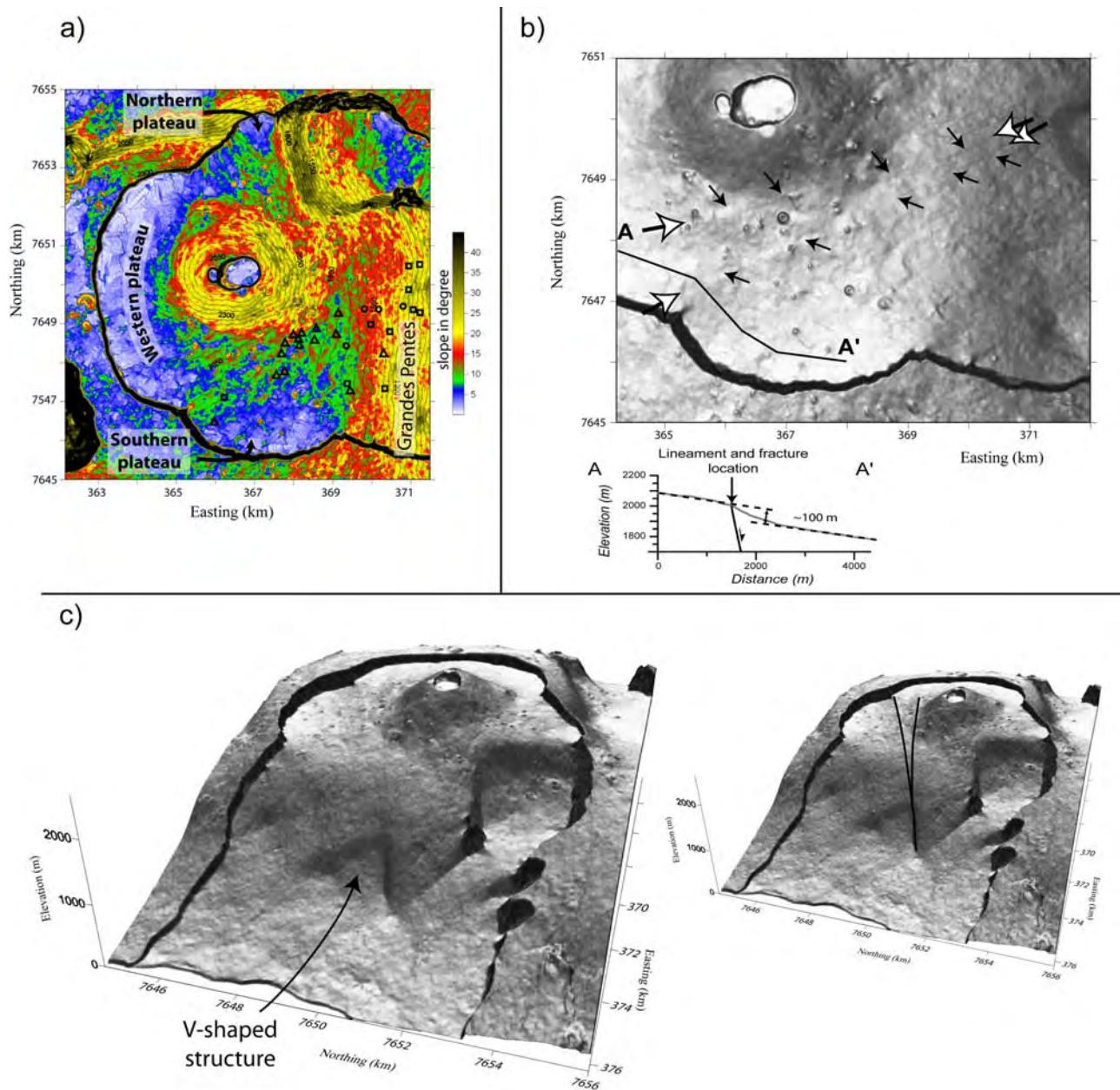
Figure 7. (a) Slope map of the Enclos showing the presence of three different plateaus east of the Grandes Pentes and the Plaine des Osmondes. (b) A main N65° and kilometer-long lineament is observed between the western and southern plateaus. Topographic profile A-A′ reveals that the lineament and the fractures are located at the slope change. The distribution of the nonmagmatic earthquakes in the lineament vicinity strongly supports a fault origin for the lineament (circles, post-1997 events, data of the Piton de la Fournaise Volcano Observatory; squares, July 1985 events [after *Lénat et al.*, 1989]; triangles, 1985–1988 events [after *Sapin et al.*, 1996]). (c) Three-dimensional representation of the EGBS slope map with the inferred N65° faults. Coordinates are in UTM WGS84.

[see *Rowland and Garbeil*, 2000] after the collapse of the EGBS. Domain B is restricted to a small area, which overlaps the Tremblet scarp. Part of its upper limit coincides with the margin of the SE trending steep slope located south of the VSS. Laterally, domain B stops in the north, whereas it continues southward between domains A and C. Note that Piton Takamaka increases the slope of this domain (Figure 8c). Domain C is characterized by the steepest

slopes and corresponds to the Grandes Pentes in the EGBS divided in two branches south of the Tremblet scarp (i.e., the LSS and USS). It is noteworthy that the lowest part of the Grandes Pentes and LSS present the same morphological features that form the steep SE trending slopes.

[18]   The clear continuity of the slope domains across the scarp into the EGBS suggests a continuity of the USS and LSS in the EGBS where they coalesce in a main steep slope

(the Grandes Pentes). Furthermore, the two morphological structures related to the USS and LSS are continuous in the north, east and south flanks of PdF. The classic interpretation in which the Grandes Pentes are restricted to the EGBS and are due to its formation [e.g., *Duffield et al.*, 1982; *Gillot et al.*, 1994; *Labazuy*, 1996; *Merle and Lénat*, 2003; *Oehler et al.*, 2004] is therefore in disagreement with the present data. Finally, the continuity of the steep slopes
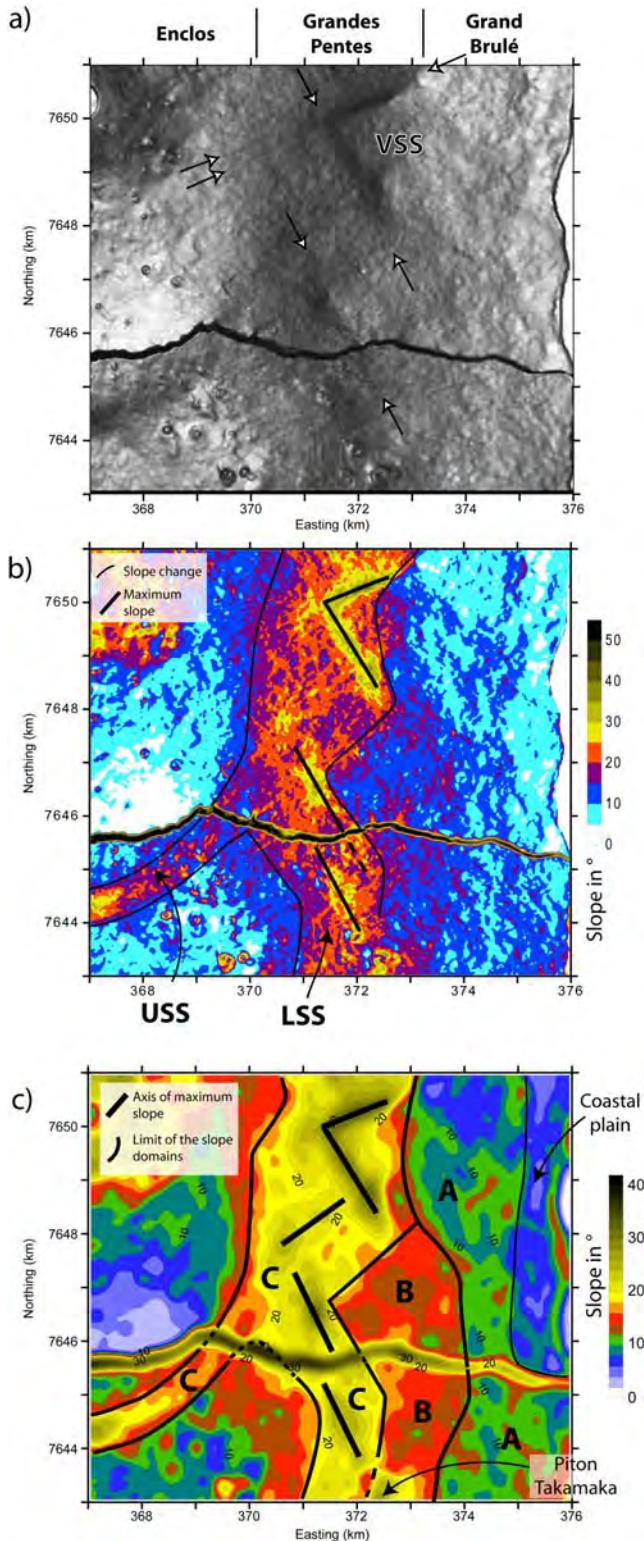
across the Tremblet scarp raises the questions of the chronology between the EGBS formation and the development of the USS and LSS, and of the direction of motion (vertical versus lateral), along the Tremblet scarp.

3.2.3. Bois Blanc Scarp

[19] The Bois Blanc scarp is usually considered to be the limit of the Grand Brûlé landslide, which is considered to have occurred 4.5–10 ka ago [*Bachèlery*, 1981; *Duffield et al.*, 1982; *Labazuy*, 1996; *Merle and Lénat*, 2003]. We have shown above that more than 170 m of alluvial formations, the Osmondes paleovalley, occur at the foot of the Bois Blanc scarp [*Courteaud*, 1996]. This suggests that the Osmondes paleovalley was deeply incised, below the present sea level, after the Grand Brûlé slide and was subsequently filled by fluvial deposits. Was the development of such a deep paleovalley possible after the Grand Brûlé slide?

[20] P. Mairine's unpublished data (2004) from drill holes in most of the main rivers of La Réunion Island reveal that the bottom of these valleys is always located 100–120 m below sea level. It is widely assumed that the incision depth is directly related to the elevation of the base level, which is considered to be the sea level in an island setting [e.g., *Schumm*, 1993]. Incision and sedimentation develop above and below the base level, respectively. The occurrence of alluvial sediments below sea level, at the foot of the Bois Blanc scarp clearly indicates that the Osmondes paleovalley was incised during a period of low sea level and was subsequently filled in. In the Indian Ocean, the last significant sea level low (-120 ± 5 m) occurred 17–18 ka ago during the last glacial period [*Camoin et al.*, 2004]. It was followed by a rapid sea level rise until 8–9 ka ago, when the sea level reached an elevation of 10 m below the present sea level. This evolution, which is common to the other oceans [e.g., *Hanebuth et al.*, 2000], implies that the incision of the Osmondes paleovalley cannot postdate 17–18 ka.

[21] The identical morphology (i.e., slope value of 55° to 60° and escarpment heights of 100 to 200 m) of the Tremblet and Bellecombe scarps, which bound the Grand Brûlé and Enclos structures, respectively, suggests a nearly similar age for the scarp formation [*Merle and Lénat*, 2003]. For comparison, the Plaine des Sables scarps which have been altered by erosion for about 60–45 ka, present slope values of 45°. Hence we argue that, the incision of the Osmondes paleoriver predates the formation of the Grand Brûlé, and the Bois Blanc scarp does correspond to the northern margin of the Osmondes paleovalley, rather than to the limit of a landslide. The northern limit of the Grand

Figure 8. (a) Gray scale slope map illustrating the morphology of the Grandes Pentes. Several subtle lineaments limited by arrows are observed into the EGBS. Two of them bound a V-shaped structure (VSS) which is classically interpreted as to be the trace of a secondary landslide. (b) Slope map showing the maximum slope axes and the slope changes. (c) Slope map of a 50-m resolution filtered DEM illustrating the longer-wavelength morphology. The slope domains A, B, and C are continuous on both sides of the Tremblet scarp. The coastal plain of the Grand Brûlé likely results from the accumulation of lava deltas. Coordinates are in UTM WGS84.

Figure 9. Construction processes able to develop steep slopes in basalt shield volcanoes.

Brûlé is subsequently located south of the Osmondes paleovalley axis and the Piton de Crac is a remnant part of the southern flank of the paleovalley.

4. Discussion

[22] Our study of the morphology of Piton de la Fournaise reveals the existence of two subcircumferential steep slope zones on the volcano's north, NE, SE, and south flanks, which are locally incised by deep valleys and, which are continuous on the east flank, into the Enclos-Grand Brûlé structure. In the following, we show the main implications of this geometric relationship that led to the recent evolution of Piton de la Fournaise and the development of the EGBS.

4.1. Steep Slope-Forming Processes

[23] Basaltic shield volcanoes are commonly characterized by a relatively flat summit zone and gentle oceanward slopes. This classic shape results from the superposition of thin low-viscosity lava flows the run out distances of which vary from few hundreds of meters to several kilometers. However, steep slopes are also observed on basaltic volcanoes [e.g., *Rowland and Garbeil*, 2000] and several processes can explain their development.

[24] Steep slopes may result from the concentration of eruptive vents and pyroclastic cones in the summit area, leading to a differential vertical growth between the summit and the volcano flanks (Figure 9) [*Rowland and Garbeil*, 2000]. The differential vertical growth may also originate from the development of small-size lava flows related to concentric summit vents [*Naumann and Geist*, 2000]. These two constructional processes lead to the formation of steep convex-outward slopes like at Cerro Azul, Wolf and Fernandina volcanoes, western Galapagos [*Rowland and Garbeil*, 2000; *Naumann and Geist*, 2000]. Endogenous growth through recurrent dike intrusion [e.g., *Annen et al.*, 2001], the growth of cryptodomes [*Donnadieu and Merle*, 2001] and an overpressurized magmatic chamber [*Cullen et al.*, 1987] are possible processes, which induce the formation of steep slopes on the summit or the flanks of the volcano. For dike intrusions, the resulting slope geometry ranges from elongated slopes along-strike of a rift zone to an isotropic slope distribution restricted to the summit [*Rowland and Garbeil*, 2000; *Annen et al.*, 2001]. The growth of a cryptodome leads to an asymmetric deformation and the development of concave- and convex-outward steep slopes [*Donnadieu and Merle*, 2001].

[25] Destruction processes such as erosion and landslides can also form steep slopes (Figure 10). Erosion is responsible for valleys the development of which can be controlled
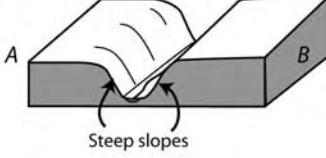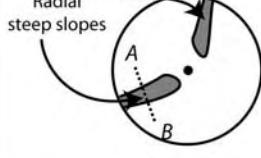
Figure 10. Destruction processes able to develop steep slopes in basalt shield volcanoes.

by preexisting faults or structural limits such as caldera walls [*Stearns and MacDonald*, 1946; *Bachèlery*, 1981]. Small-size and large-scale landslides also produce steep slopes on the volcano flanks presenting a concave-ocean-ward geometry [*Moore*, 1964; *Bachèlery*, 1981; *Oehler et al.*, 2004].

[26] Deformation processes have a strong influence on the volcano morphology (Figure 11). An edifice may deform above a basal layer composed of low-strength sediments, ultramafic cumulates or intrusive complexes [e.g., *Borgia et al.*, 1990; *Borgia*, 1994]. Circumferential thrust-fault-related

steep slopes develop at the base of the edifice and normal faults accommodate the spreading motion [*Merle and Borgia*, 1996]. The lack of any deformation within the pelagic sediments below the submarine flanks and of any distal anticline, even several tens of kilometers away from the volcano suggests that this process did not occur at La Réunion [*Michon et al.*, 2007]. A hydrothermally altered interior of a volcano may also act as a décollement level. As shown by *Cecchi et al.* [2005], the sagging of the volcano's summit part results in the upward lateral extrusion of the altered interior. The resulting morphology presents circum-
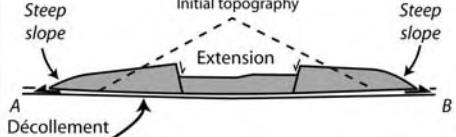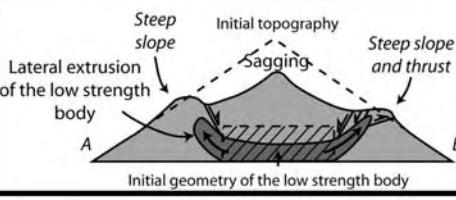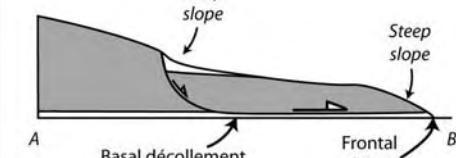

Figure 11. Deformation processes able to develop steep slopes in basalt shield volcanoes.

ferential steep slopes that are locally associated with thrust faults (Figure 11). Finally, slumping units above a local décollement level are bounded upward by normal faults, which also form steep slopes on the volcano flanks [*Stearns and Clark*, 1930; *Moore and Krivoy*, 1964; *Merle and Lénat*, 2003]. Steep slopes related to thrust faults present a convex-outward shape whereas concave-outward steep slopes are attributed to normal faults.

[27] In summary, circumferential steep slopes like those observed at PdF can only result from either construction processes or spreading processes, and not through erosion.

4.2. Caldera-Forming Processes

[28] Several mechanisms may lead to the development of circular to elliptical, and horseshoe-shaped calderas. Their geometry and size depend on the mechanisms encountered. On volcanoes other than basaltic shields, the development of large calderas is attributed to the collapse of the chamber roof during large explosive eruptions [e.g., *Lipman*, 1997; *Roche et al.*, 2000]. In that context, the size of the caldera is dependent on the volume of the erupted magma. On basaltic shield volcanoes, large calderas with diameters ranging from 5 to 20 km may also develop [*MacDonald*, 1965; *Bachèlery*, 1981; *Munro and Rowland*, 1996]. However, they usually lack of significant related pyroclastic deposits suggesting nonexplosive or minor explosive mechanisms to explain their development [e.g., *MacDonald*, 1972; *Munro and Rowland*, 1996]. In Hawaii, the caldera of Kilauea is interpreted as resulting from either the coalescence of several pit craters [*MacDonald*, 1965], a main collapse related to the lateral magma withdrawal during the large lateral eruption of 1790 [*MacPhie et al.*, 1990] or from the load of a cumulate complex at the base of the magma chamber [*Walker*, 1988]. In the western Galapagos, the combined effect of magma withdrawal and the load of cumulative bodies is considered to be responsible for the development of the large and deep calderas [*Munro and Rowland*, 1996]. Recently, *Cecchi et al.* [2005] showed that the deformation of the hydrothermal system, which is obviously larger that the magmatic reservoir may lead to the collapse of large calderas. It is important to note that whatever the model, the collapse of the volcano's summit is related to the active magmatic system.

[29] Horseshoe-shaped calderas are relatively common on island volcanoes like Fogo, El Hierro, Tenerife, and La Réunion islands. Their geometry is characterized by a flat summit zone and a large depression bounded by regular scarps that link the summit depression to the sea coast. The frequent occurrence of debris avalanche deposits on the submarine flanks suggests that their formation is due to destabilizations and subsequent landslides. Several models have been proposed to explain their origin. They can result from a single large landslide that affects both the volcano flank and the summit [*Duffield et al.*, 1982; *Labazuy*, 1996; *Cantagrel et al.*, 1999; *Day et al.*, 1999]. *Hürlimann et al.* [1999] proposed that the collapse of the summit was able to destabilize the volcano flank, leading to flank landslide. *Merle and Lénat* [2003] recently showed with analog models that the slide of a volcano flank may trigger a lateral flow in the hydrothermal system, which leads to the development of a large caldera in the summit area. They

applied this model to PdF in order to explain the development of the EGBS.

4.3. Origin of the Steep Slopes and the EGBS

[30] One of the main observations made in the present study is the apparent continuity of the different slope domains across the Tremblet scarp into the EGBS without any visible lateral offset (Figure 7). Such a continuity suggests that the steep slopes and the EGBS are independent structures. We have used the geometry of both structures and their intersection to determine their temporal relationship and origin.

4.3.1. Age and Origin of the LSS and USS

[31] We put forward two hypotheses to explain the continuity of the slope domains on both sides of the Tremblet scarp:

[32] Hypothesis 1 is that the development of the LSS and USS post-dates the formation of the EGBS the lower part of which (i.e., the Grand Brûlé) has previously been considered as the trace of a landslide. Assuming that the EGBS formed 4.5 to 10 ka ago, the steep slopes developed quite rapidly. We showed that circumferential steep slopes result from two different processes: differential growth (construction process) or spreading (deformation process).

[33] Differential growth is highly unlikely for the following reasons. (1) In contrast to the volcanoes of western Galapagos, no concentric eruptive vents are found above the USS and LSS. (2) There is no concentration of pyroclastic cones in the two areas delimited by the steep slopes. (3) The length of lava flows is not constant and varies from hundreds of meters to several kilometers, making the lava flow accumulation hypothesis unrealistic. (4) Finally, 97% of the post-EGBS volcanic activity has been restricted to the Enclos. The total elevation changes along each topographic profile (T value in Figure 5a), which would reveal the differential growth should not be similar outside and inside the EGBS.

[34] Spreading is the second process capable of the development of circumferential steep slopes. If the elevation changes related to the LSS and USS are related to deformation, the total deformation is a combination of outward lateral and upward displacements. Considering the upward motion only, which corresponds to the elevation change measured for each profile, minimum displacement rates of 2 to 4 cm/a and 2.5 to 5 cm/a are calculated for the USS and LSS and are inferred for a deformation starting at 10 and 5 ka, respectively. These values are similar to the total deformation rates measured for the very active spreading at Kilauea where large earthquakes occurred [*Delaney et al.*, 1998]. At PdF the lack of seismicity in the vicinity of the steep slopes is in disagreement with a very active deformation. Moreover, geodetic data acquired outside the EGBS in the flat summit zone do not show any displacement [*Briole et al.*, 1998]. Consequently, the development of the LSS and USS due to spreading does not agree with the available data.

[35] Hypothesis 2 is that the development of the LSS and USS predates the formation of the EGBS and does not result from a large deeply rooted landslide. It seems unrealistic that a superficial landslide occurred on a décollement level presenting a topography characterized by similar slope domains than outside the EGBS. The exact motion along

the lateral scarps and subsequently of the Grand Brûlé cannot be determined precisely. However, only a predominantly vertical collapse is possible. Hence the formation of the EGBS results from a vertical to subvertical collapse rather than a giant landslide. Such a motion could explain the lack of clear continuity between subaerial and submarine structures [*Oehler*, 2005] (Figure 1b) in contrast to what is observed at large landslide deposits [e.g., *Le Friant et al.*, 2004; *Tibaldi*, 2001]. The preservation of the slope domains inside the EGBS would be explained by a low amount of overlapping lava flows in the Grandes Pentes and the Grand Brûlé since the collapse. Such a hypothesis is supported by the map of the historical lava flows, which shows that most of the lava flows are restricted to the upper part of the EGBS (i.e., the Enclos) and only few flows occur in the Grande Pentes [*Stieltjes et al.*, 1986].

[36] As for hypothesis 1, construction and deformation processes might form circumferential steep slopes. We showed above that construction processes like those proposed by *Naumann and Geist* [2000] and *Rowland and Garbeil* [2000] cannot be applied to PdF. The eruptive vents are not concentrically distributed above the LSS and USS, and the lava flow length strongly varies.

[37] In contrast, spreading may have occurred. The pre-EGBS edifice built up after the Plaine des Sables collapse about 60–45 ka ago. According to this potential onset of deformation, and given the elevation changes, expected deformation rates are of few millimeters per year. Volcanoes might spread under gravity if a low-strength body/layer exists at the base of the edifice, and if the load of the edifice acting on the low-strength material is high enough. Two different modes of spreading lead to the development of circumferential steep slopes. On the one hand, the spreading can be related to the deformation of a basal low-strength layer [e.g., *Merle and Borgia*, 1996; *Oehler et al.*, 2005]. In such a case, the steep slopes are located at the base of the edifice and radial normal faults develop. On the other hand, the spreading is induced by an internal low-strength layer or body [e.g., *Cecchi et al.*, 2005]. The resulting steep slopes are on the volcano flanks and normal faults are circumferential. At PdF, the exact topography of the pre-EGBS volcano cannot be firmly determined. Nevertheless, the morphology and the slope adjacent to the Enclos depression, which are preserved from the pre-EGBS period, and the shape of the active cone, allows estimating a pre-EGBS collapse topography of around 3000 m located at the place of the present active cone. The location of the circumferential LSS and USS on the volcano flanks supports the presence of an internal low-strength body rather than a basal décollement. In conclusion, we propose that the LSS and USS do result from neither construction processes nor a basal spreading, but from the deformation of the weak internal part of the volcano under gravity (Figure 12).

[38] The nature and geometry of the weak core are unknown. According to geoelectrical data acquired in the Enclos, the Plaines de Sables, and the Planèze du Baril [*Benderitter*, 1990; *Courteaud*, 1996; *Lénat et al.*, 2000], PdF is characterized by a deep widespread low-resistivity body which could correspond to the top of the hydrothermal system of the pre- EGBS volcano. The lack of hot springs [*Coudray et al.*, 1990] in the adjacent deep valleys and fumaroles would suggest that this hydrothermal system is

no longer active. Nevertheless, these characteristics are not conclusive against the active hydrothermal system as despite a current intense volcanic activity and a large hydrothermal system [*Lénat et al.*, 2000], PdF presents only very few fumaroles restricted to the summit pit crater and no hot springs at all. It is subsequently hard to determine whether spreading is still active, but we suggest that the deformation stopped when the Enclos collapsed 4.5 ka ago. Indeed, the summit of the volcano, which was acting on the hydrothermal body was dismantled. The lack of steep slope on the west part of PdF could suggest that the remnant part of the "ancient" Fournaise blocked the deformation in the west.

[39] Contrary to the experiments of *Cecchi et al.* [2005] in which only one circumferential steep slope zone is described, two steep slope zones developed at PdF. Such a vertical complexity in the steep slope geometry also occurs on other volcanoes where several bulges are visible (e.g., Etna, Arenal [*Cecchi et al.*, 2005]). This can be explained by the complexity of the hydrothermal system compared to the simplified models. For instance, intra-edifice preexisting discontinuities might induce a deformation partitioning and subsequently several steep slope levels. Laterally the steep slope geometry can also be influenced by the rift zones along which recurrent magma intrusions decrease the strength of the rocks by hydrothermal alteration. Such a lateral variation could explain the NE and SE lobes of the LSS along the NE and SE rift zones, respectively. This indicates that the current rift zones have been inherited from the pre-Enclos volcano.

4.3.2. Origin of the EGBS

[40] Usually, vertical collapses are restricted to the area of the magmatic system (i.e., summit and rift zones). At PdF, besides the summit zone, the eastern flank also suffered a vertical collapse. Given the geomorphological and geological continuity between the Enclos and the Grand Brûlé (identical scarps slope and continuous faults in the EGBS), we propose that the collapse of the Enclos was associated to that of the Grand Brûlé. Although large lateral eruptions already caused the development of summit calderas on basaltic and andesitic volcanoes [e.g., *MacPhie et al.*, 1990; *Kaneko et al.*, 2005], the collapse of the Grand Brûlé, several kilometers away from any active magmatic system, is unlikely related to magmatic withdrawal. The vertical collapse of the EGBS might also be triggered by a deeply rooted slump in which the displacements in the upper part (close to the upper normal fault) can be predominantly vertical whereas they evolve to lateral away from the fault (above the low dipping décollement). Assuming a maximum depth of the décollement at the top of the oceanic crust (6 km below sea level (bsl) [*de Voogd et al.*, 1999]) and the Bellecombe scarp as the trace of the upper normal fault, the vertical motion would be restricted to the few first kilometers only, i.e., west of the Grandes Pentes, and not extended to the overall EGBS.

[41] We showed that the Grand Brûlé was located above the large intrusive complex of the Alizés volcano, the age of which is considered as to be older than 0.78 Ma [*Lénat et al.*, 2001]. This complex was drilled between 950 and 2850 m bsl, end of the drilling. It is composed of gabbros in the 1400 upper meters and dunites and wehrlite dunites below [*Rançon et al.*, 1989]. Gravimetric data suggest that the complex continues down to at least 4 km bsl
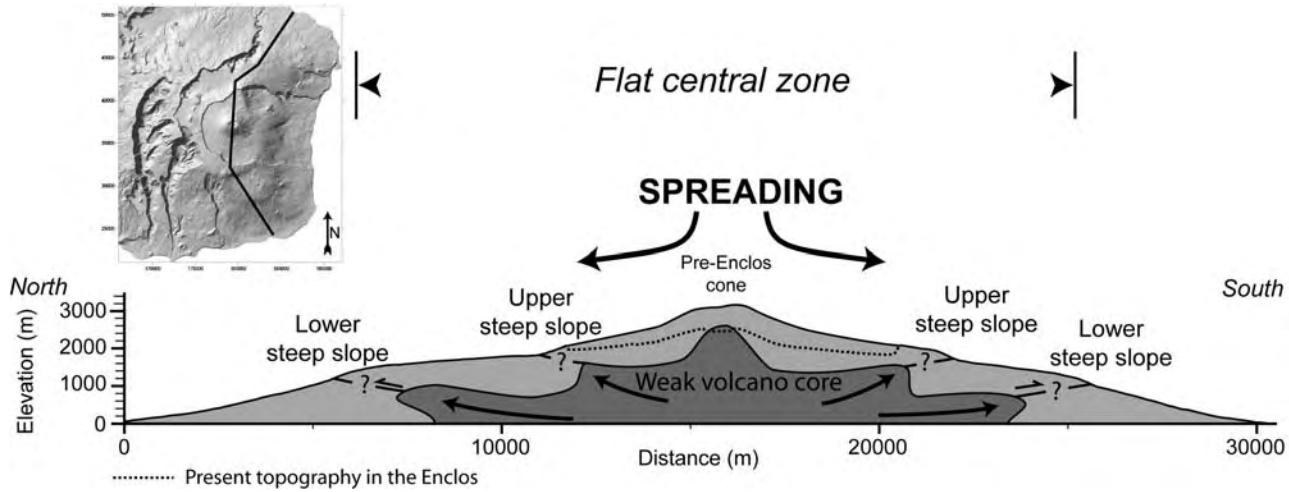
Figure 12. N-S cross section of PdF illustrating the potential origin of the upper and lower circumferential steep slopes by the spreading of the edifice above a weak hydrothermal core.

[*Malengreau et al.*, 1999]. Such a body may have two different implications in the evolution of PdF:

[42]   1. It has been shown that olivine cumulates at high temperature (>1100°C) may deform as ice [*Clague and Denlinger*, 1994]. The Alizés cumulative complex could have deformed under gravitational forces and subsequently induced the vertical collapse of the Grand Brûlé. However, as the drilling project aimed at determining the geothermal potential of the intrusive complex, it has been shown that the present temperature of the complex was far from hot (142°C at 3003.5 m below the surface [*Rançon et al.*, 1989]). Even if the 4.5 ka ago temperature cannot be firmly determined, analysis of secondary minerals within the gabbro and dunite reveals a progressive cooling of the complex from late magmatic biotite crystallization at 600–900°C to serpentine crystallization at 350°C maximum [*Lerebour et al.*, 1989]. Hence it is strongly unlikely that the olivine cumulates of the Alizés intrusive complex deformed in the recent times and triggered the collapse of the Grand Brûlé 4.5 ka ago.

[43]   2. *Walker* [1988] proposed that dense bodies, such as cumulates are able to trigger a downward drag and the collapse of the summit. Such a mechanism has been proposed as a source of subsidence to explain the development of the large calderas of the volcanoes of western Galapagos [*Munro and Rowland*, 1996]. Considering the presence of the large intrusive complex of the Alizés volcano, we hypothesize that the vertical collapse of the Grand Brûlé would correspond to a discrete event (i.e., collapse of 100–150 m of a 7-km-wide area) simultaneously to the long-term downward motion of this dense body. This model differs from *Walker* [1988] as the dense body is related to an ancient volcano (i.e., the Alizés) rather than an active volcano. The occurrence of the vertical collapse of the Grand Brûlé potentially destabilized the adjacent submarine flank and initiated debris avalanches which deposits could correspond to the youngest unit described by *Oehler* [2005].

[44]   The Enclos caldera was interpreted in different ways: (1) an independent structure resulting from successive syneruptive collapses [*Bachèlery*, 1981]; (2) the upper part

of the scar of a large flank landslide [*Duffield et al.*, 1982; *Labazuy*, 1991; *Gillot et al.*, 1994]; and (3) a summit deformation initiated by the slide of the Grand Brûlé [*Merle and Lénat*, 2003]. Although the occurrence of pyroclastic deposits around the Enclos indicates that the collapse was simultaneous to an explosive eruption [*Abchir et al.*, 1998], the volume of the deposit (around 0.5–1 km³ [*Abchir et al.*, 1998]) is 1 order of magnitude lower than that of the Enclos caldera. This volume difference and the lack of any evidence of large submarine eruption suggest that the collapse of the Enclos does not result from the emptying of the magmatic reservoir. It has been recently proposed that the collapse of the Enclos has been caused by the lateral flow of the large summit hydrothermal system [*Merle and Lénat*, 2003]. This model, which can explain the collapse of a large structure without the same erupted volume faces one main problem. According to *Merle and Lénat* [2003], the deformation of the hydrothermal system was made possible by the lateral slide of the Grand Brûlé only, which headwall corresponds to the Grandes Pentes. Our data strongly suggest that this slide did not occur 4.5 ka ago and that the Grandes Pentes (domain C in Figure 8) are not restricted to the EGBS. Hence the deformation as the authors proposed cannot be applied to PdF. However, we follow *Merle and Lénat* [2003] on two points: (1) the deformation of the Grand Brûlé and the Enclos are linked and (2) the Enclos may result from the deformation of the summit hydrothermal system.

[45]   Taking into account our results, we propose two distinct evolutions in which a first collapse initiated the second one. On the one hand, the collapse of the EGBS was initiated by the vertical collapse of the Grand Brûlé, due to the continuous downward drag of the Alizés intrusive complex. This event allowed the deformation of the hydrothermal system of the pre-Enclos volcano and subsequently the collapse of the summit zone. On the other hand, the collapse of the Enclos results from the deformation of the summit hydrothermal system under gravity, which also led to the development of the LSS and USS. This hypothesis is supported by analog models, which show that the spreading of a volcano related to a weak internal core entails the

coeval development of circumferential steep slopes on the volcano flanks and the vertical collapse of the summit zone [*Cecchi et al.*, 2005]. We propose that this event may have destabilized part of the eastern flank of PdF, which was continuously affected by a downward drag. The relationship between summit collapse and flank deformation has already been suggested for Tenerife [*Marti et al.*, 1997; *Hürlimann et al.*, 1999]. However, contrary to what geological data show for PdF, the summit collapse triggered a flank landslide at Tenerife.

4.4. Evolution of PdF During the Last 150 ka

[46] Considering the geological data and the interpretations presented above, we propose the following chronology for the last 150 ka of PdF. This date corresponds to the collapse of the Morne Langevin caldera [*Bachèlery and Mairine*, 1990]. According to *Oehler* [2005], this event corresponds to the first and most voluminous eastward destabilization of PdF, which spread over the Eastern Plateau. Afterward, the "recent" PdF (<150 ka) built up at a location west of the present active cone [*Bachèlery and Mairine*, 1990]. This edifice the shape and evolution of which are unknown suffered recurrent collapses between 60 and 45 ka, forming the Plaine des Sables calderas. Although the origin of the upper part of this caldera is still uncertain (vertical [*Bachèlery and Mairine*, 1990] versus lateral [*Duffield et al.*, 1982; *Gillot et al.*, 1994; *Oehler et al.*, 2004]), the debris avalanche deposits on the submarine Eastern Plateau indicate that the collapses were coeval to at least one major landslide [*Labazuy*, 1996; *Oehler*, 2005]. It is noteworthy that the northern limit of the landslide scar (the Ravine Ferdinand [*Merle and Lénat*, 2003]) is the only well-observed structure which is really continue in both the subaerial and submarine domains (Figure 1b).

[47] The pre-Enclos edifice built up at a location close to the present active cone. This volcano progressively spread above its weak hydrothermal core. The geometry of this low-strength body was likely controlled by preexisting structures such as the décollement level of previous slides, the magma chambers and the intrusion complexes. Two circumferential steep slopes (i.e., the LSS and USS) result from this deformation (Figure 13a). At the same time, the volcano was incised by deep valleys, among which is the Osmondes paleovalley in the east flank. The presence of the Osmondes paleovalley in the northern part of the EGBS, whose minimum age is of 18–19 ka clearly indicates that PdF did not subsequently suffered the slide of the Grand Brûlé as it was usually proposed. Around 4.5 ka ago, both the summit and east flank were cut by a vertical collapse that led to the development of the west and south parts of the EGBS; the present northern limit of EGBS consisting of the Osmondes paleovalley's northern flank (Figure 13b). This collapse event likely destabilized part of the coastal zone and the eastern submarine flank. The related debris avalanche covered the proximal Eastern Plateau as revealed by the age of a dredged sample (12 ka [*Labazuy*, 1996]) (Figure 1b) and flowed through the Chenal Vincent down to the Rålé Poussé [*Labazuy*, 1996; *Oehler*, 2005]. The coastal and submarine origin of the debris avalanche could explain the absence of clear continuity between the subaerial and submarine domains. Similar or larger submarine destabilizations occurred during the recent evolution of PdF. How-

ever, their importance was underestimated until recently. According to *Oehler* [2005], their deposits cover around half of the surface of the submarine flanks.

[48] The lack of lava flows intercalated in the alluvial sediments of the Osmondes paleoriver could suggest the existence of a relief between the eruption zone and the valley. This barrier disappeared when the Plaine des Osmondes collapsed (Figure 13c). Even though the age of this event is unknown, a vertical mode of deformation can be reasonably inferred. Indeed, the width of the lowest part of the Plaine des Osmondes (i.e., between the Piton de Crac and the Bois Blanc scarp) is more than twice lower than at its maximum width. Such a geometry disagrees with the classic landslide scar. After the collapse of the Plaine des Osmondes, the lava flowed through the Osmondes paleo-valley and completely counterbalanced the erosion process that developed since tens of thousands of years ago.

[49] One of the most striking features of this 150 ka lasting evolution is the persistence of the NE and SE rift zones, despite the recurrent collapses and landslides, and the eastward migration of the eruptive center. This contrasts with the general observations made on other volcanoes, where flank destabilizations or large changes of the topography induce a reorganization of the rift zones [*Tibaldi*, 2003; *Walter and Troll*, 2003; *Acocella and Tibaldi*, 2005]. The persistence of both rift zones, which contributed to form the NE and SE submarine plateaus (Figure 1), suggests that their location and development are controlled by deep sources. *Walter et al.* [2006] proposed that the NE and SE rift zones results from the intermittent eastward spreading of PdF. However, the undeformed marine sedimentation east of the island [*de Voogd et al.*, 1999] and the lack of anticline structures in the bathymetry [*Oehler et al.*, 2005] suggest that PdF did not experience such a deformation.

[50] In what follows we put forward two different features, which could have played a key role in the development of the stable rift zones:

[51] 1. It has been recently shown that the main structures of La Réunion volcanoes are parallel to the oceanic lithospheric structures, suggesting a control of the crustal discontinuities in the tectonomagmatic evolution [*Michon et al.*, 2007]. The persistence of both rift zones could then result from a control of the crustal structures.

[52] 2. The lower part of the NE and SE rift zones, the submarine parts included, are located north and south of the Alizés intrusive complex, respectively. Assuming that a continuous downward drag related to a dense body entails a diffuse extension in its vicinity, we hypothesize that the dike lateral migration in the NE and SE flanks of PdF was controlled by this stress field. In a certain way, this model presents similarities with that of *Walter et al.* [2005] in which the gravity-driven flank movement leads to a radial adjacent extension controlling the magma lateral migration and the development of two concentric curved rift zones. Whatever the model, the rarity of the eruptions along the rift zone lower parts, i.e., outside the Enclos caldera (only 3% of the eruptions since the 18th century [*Villeneuve*, 2000]) and their fan-shaped geometry suggest the existence of a diffuse stress field, which does not efficiently favor the magma lateral migration on the flanks. Despite the slight lateral propagation of the magma intrusions along the rift zones, the combined effect of the summit frequent intrusion
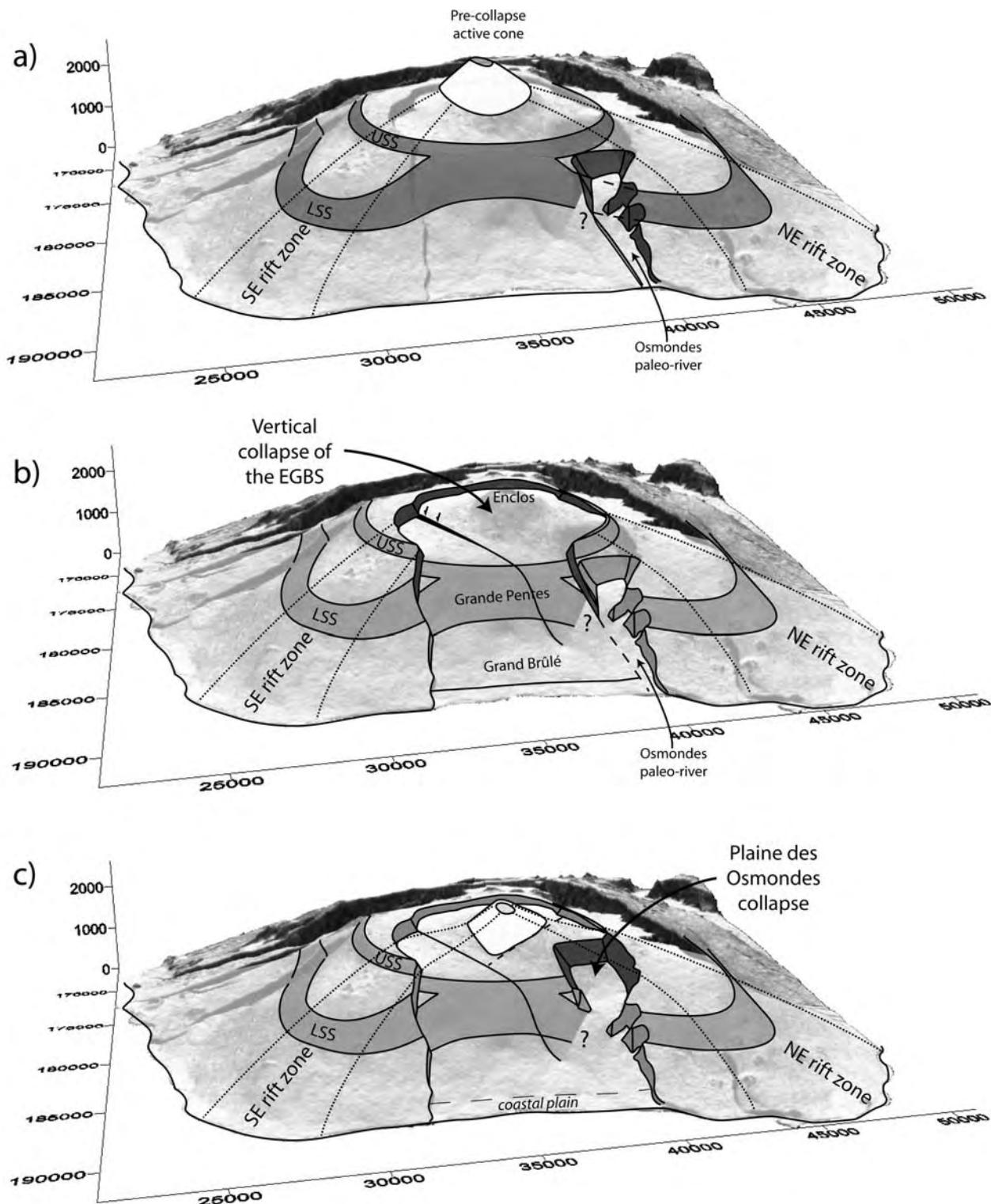
Figure 13. Chronology of the geological events that marked the last 60 ka of PdF. (a) After the collapse of the Plaine des Sables caldera, two circumferential steep slopes developed on the north, east, and south flanks. Simultaneously, the Osmondes paleovalley incised the east flank. (b) Around 4.5 ka ago, the EGBS collapsed vertically. The Osmondes paleovalley was likely separated from the magmatic system by a barrier as no lava flow is intercalated in the alluvial sediments drilled in the lower part of the valley. (c) The collapse of the Plaine de Osmondes, which occurred after 4.5 ka, allowed the lava to flow through the Osmondes paleovalley.

and the very likely existence of a décollement level within the edifice (the top of the Alizés volcano) potentially favored the large eastward destabilizations, which occurred between 45 and 60 ka.

5. Conclusions

[53] Our study of PdF aimed at the understanding of the present-day edifice morphology, which recorded the most recent geological events. The analysis was focused on the steep slope zones located on the volcano flanks and the Enclos-Grand Brûlé structure, which cut the upper part and eastern flank of the edifice. We took into account the different available geological data and tested them against the potential processes, which may form both structures. We presented new results allowing a reappraisal of the recent evolution of Piton de la Fournaise.

[54] 1. The steep slope zones were previously interpreted as slide headwalls and/or caldera margins [e.g., *Bachèlery*, 1981; *Oehler et al.*, 2004]. However, their distribution and morphological characteristics suggest that they form two independent circumferential structures (the USS and LSS), which coalesce in the east flank. Their development is interpreted as resulting from the spreading of the pre-Enclos volcano above a weak hydrothermal core.

[55] 2. The Enclos-Grand Brûlé structure (a U-shaped structure) is formed by the Enclos depression, the Grandes Pentes, and the Grand Brûlé. Although the Enclos origin was a matter of great debate during the last decades (vertical versus lateral collapse), there had been a general agreement on a sliding origin of the Grand Brûlé [*Bachèlery*, 1981; *Duffield et al.*, 1982; *Gillot et al.*, 1994; *Labazuy*, 1996; *Merle and Lénat*, 2003; *Oehler et al.*, 2004]. However, our analysis of the continuity of different slope domains inside and outside the EGBS suggests that the Grand Brûlé results from a mainly vertical collapse instead of a giant landslide. The entire EGBS subsequently underwent a vertical collapse ~4.5 ka ago. Among different potential sources for the collapse of the Grand Brûlé, we prefer the continuous downward drag induced by the dense intrusive complex of the Alizés volcano. Following *Merle and Lénat* [2003], we propose that the collapse of the Enclos was caused by the deformation of the hydrothermal system of the pre-Enclos volcano. Despite the clear continuity between the Enclos and the Grand Brûlé, which suggests a close relationship in the development of both structures, their chronology and exact links remain poorly understood.

References

Abchir, M. A., S. M. Semet, G. Boudon, P. Ildefonse, P. Bachèlery, and R. Clocchiati (1998), Huge hydrothermal explosive activity on Piton de la Fournaise, Réunion Island: The Bellecombe ash member, 2700 BC, in *Volcanic Risk—The European Laboratory Volcanoes*, *Publ. EUR 18161 EN*, edited by R. Casal et al., pp. 447–455, Eur. Comm., Brussels.

Acocella, V., and A. Tibaldi (2005), Dike propagation driven by volcano collapse: A general model tested at Stromboli, Italy, *Geophys. Res. Lett.*, *32*, L08308, doi:10.1029/2004GL022248.

Annen, C., J.-F. Lénat, and A. Provost (2001), The long-term growth of volcanic edifices: Numerical modelling of the role of dyke intrusion and lava-flow emplacement, *J. Volcanol. Geotherm. Res.*, *105*, 263–289.

Bachèlery, P. (1981), Le Piton de la Fournaise (Ile de la Réunion). Etude volcanologique, structurale et pétrologique, Ph.D. thesis, 215 pp., Univ. Clermont-Ferrand II, Clermont-Ferrand, France.

Bachèlery, P. and P. Mairine (1990), Evolution volcano-structurale du Piton de la Fournaise depuis 0.53 Ma, in *Le Volcanisme de la Réunion, Monographie*, edited by J.-F. Lénat, pp. 213–242, Cent. de Rech. Volcanol., Clermont-Ferrand, France.

Bachèlery, P., B. Robineau, M. Courteaud, and C. Savin (2003), Avalanches de débris sur le flanc occidental du volcan-bouclier Piton des Neiges (Réunion), *Bull. Soc. Geol. Fr.*, *174*, 125–140.

Benderitter, Y. (1990), Etudes géoélectriques et électromagnétiques à la Réunion, in *Le Volcanisme de la Réunion, Monographie*, edited by J.-F. Lénat, pp. 29–42, Cent. de Rech. Volcanol., Clermont-Ferrand, France.

Borgia, A. (1994), Dynamic basis of volcanic spreading, *J. Geophys. Res.*, *99*, 17,791–17,804.

Borgia, A., J. Burr, W. Montero, L. D. Morales, and G. E. Alvarado (1990), Fault propagation folds induced by gravitational failure and slumping of the Central Costa Rica Volcanic Range: Implications for large terrestrial and Martian volcanic edifices, *J. Geophys. Res.*, *95*, 14,357–14,382.

Briole, P., P. Bachèlery, B. McGuire, J. Moss., J. C. Ruegg, and P. Sabourault (1998), Deformation at Piton de la Fournaise: Evolution of the monitoring techniques and knowledge acquired in the last five years, in *Volcanic Risk—The European Laboratory Volcanoes*, *Publ. EUR 18161 EN*, edited by R. Casal et al., pp. 467–474, Eur. Comm., Brussels.

Camoin, G. F., L. F. Montaggioni, and C. J. R. Braithwite (2004), Late glacial to post glacial sea levels in the western Indian Ocean, *Mar. Geol.*, *206*, 119–146.

Cantagrel, J. M., N. O. Arnaud, E. Ancochea, J. M. Fúster, and M. J. Huertas (1999), Repeated debris avalanches on Tenerife and genesis of Las Cañadas caldera wall (Canary Islands), *Geology*, *27*, 739–742.

Cecchi, E., B. van Wyk de Vries, and J. M. Lavest (2005), Flank spreading and collapse of weak-cored volcanoes, *Bull. Volcanol.*, *67*, 72–91, doi:10.1007/s00445-004-0369-3.

Clague, D. A., and R. P. Denlinger (1994), Role of olivine cumulates in destabilizing the flanks of Hawaiian volcanoes, *Bull. Volcanol.*, *56*, 425–434, doi:10.1007/s004450050052.

Coudray, J., P. Mairine, E. Nicolini, and J. M. Clerc (1990), Approches hydrogéologique, in *Volcanic Risk—The European Laboratory Volcanoes*, *Publ. EUR 18161 EN*, edited by R. Casal et al., pp. 307–355, Eur. Comm., Brussels.

Courteaud, M. (1996), Etude des structures géologiques et hydrogéologiques du Massif de la Fournaise par la méthode audiomagnétotellurique, Ph.D. thesis, 212 pp., Univ. Réunion, Saint Denis, France.

Cullen, A., A. R. MacBirney, and R. D. Rodgers (1987), Structural controls on the morphology of Galapagos shields, *J. Volcanol. Geotherm. Res.*, *34*, 143–151.

Day, S. J., S. I. N. Heleno da Silva, and J. F. B. D. Fonseca (1999), A past giant lateral collapse and present-day flank instability of Fogo, Cape Verde Islands, *J. Volcanol. Geotherm. Res.*, *94*, 191–218.

Delaney, P. T., R. P. Denlinger, M. Lisowski, A. Miklius, P. G. Okubo, A. T. Okamura, and M. K. Sako (1998), Volcanic spreading at Kilauea, 1976–1996, *J. Geophys. Res.*, *103*, 18,003–18,023.

Deniel, C., G. Kieffer, and J. Lecointre (1992), New ^{230}Th and ^{238}U and ^{14}C age determinations from Piton des Neiges volcano, Reunion. A revised chronology for the differentiated series, *J. Volcanol. Geotherm. Res.*, *51*, 253–267.

de Voogd, B., S. Pou Palomé, A. Hirn, P. Charvis, J. Gallart, D. Rousset, J. Dañobeitia, and H. Perroud (1999), Vertical movements and material transport during hotspot activity: seismic reflection profiling offshore La Réunion, *J. Geophys. Res.*, *104*, 2855–2874.

Donnadieu, F., and O. Merle (2001), Geometrical constraints of the 1980 Mount St. Helens intrusion from analogue models, *Geophys. Res. Lett.*, *28*, 639–642.

Duffield, W. A., L. Stieltjes, and J. Varet (1982), Huge landslide blocks in the growth of Piton de la Fournaise, La Réunion, and Kilauea Volcano, Hawaii, *J. Volcanol. Geotherm. Res.*, *12*, 147–160.

Gillot, P.-Y., and P. E. Nativel (1989), Eruptive history of the Piton de la Fournaise Volcano, Reunion Island, Indian Ocean, *J. Volcanol. Geotherm. Res.*, *36*, 53–65.

Gillot, P.-Y., J.-C. Lefèvre, and P. E. Nativel (1994), Model for the structural evolution of the volcanoes of Réunion island, *Earth Planet. Sci. Lett.*, *122*, 291–302.

Hanebuth, T., K. Statteger, and P. M. Grootes (2000), Rapid flooding of the Sunda Shelf: A late glacial sea level record, *Science*, *288*, 1033–1035.

Hürlimann, M., E. Turon, and J. Marti (1999), Large landslides triggered by caldera collapse events in Tenerife, Canary Islands, *Phys. Chem. Earth A*, *24*, 921–924.

Hürlimann, M., J. Marti, and A. Ledesma (2004), Morphological and geological aspects related to large slope failures on oceanic islands: The huge La Orotava landslides on Tenerife, Canary Islands, *Geomorphology*, 62, 143–158.

Kaneko, T., A. Yasuda, T. Shimano, S. Nakada, T. Fujii, T. Kanazawa, A. Nishizawa, and Y. Matsumoto (2005), Submarine flank eruption preceding caldera subsidence during the 2000 eruption of Miyakejima Volcano, Japan, *Bull. Volcanol.*, 67, 243–253, doi:10.1007/s00445-004-0407-1.

Labazuy, P. (1991), Instabilités au cours de l'évolution d'un édifice volcanique en domaine océanique: Le Piton de la Fournaise (ıcirc;le de la Réunion), Ph.D. thesis, 252 pp., Univ. Clermont Ferrand II, Clermont Ferrand, France.

Labazuy, P. (1996), Recurrent landslides events on the submarine flank of Piton de la Fournaise volcano (Réunion Island), in *Volcano Instability on the Earth and Other Planets*, edited by W. J. McGuire, A. P. Jones, and J. Neuberg, *Geol. Soc. Spec. Publ.*, 110, 293–305.

Le Friant, A., C. L. Harford, C. Deplus, G. Boudon, R. S. J. Sparks, R. A. Herd, and J. C. Komorowski (2004), Geomorphological evolution of Montserrat (West Indies): Importance of flank collapse and erosional processes, *J. Geol. Soc.*, 161, 147–160.

Lénat, J.-F. and P. Bachèlery (1987), Dynamics of magma transfer at Piton de la Fournaise volcano (Réunion Island, Indian Ocean), in *Modeling of Volcanic Processes*, edited by C.-Y. King and R. Scarpa, pp. 57–72, F. Vieweg, Brauschweig, Germany.

Lénat, J.-F., P. Bachèlery, A. Bonneville, and A. Hirn (1989), The beginning of the 1985–1987 eruptive cycle at Piton de la Fournaise (la Réunion): New insights in the magmatic and volcano-tectonic systems, *J. Volcanol. Geotherm. Res.*, 36, 209–232.

Lénat, J.-F., D. Fitterman, D. B. Jackson, and P. Labazuy (2000), Geoelectrical structure of the central zone of Piton de la Fournaise volcano (Réunion), *Bull. Volcanol.*, 62, 75–89.

Lénat, J.-F., B. Gibert-Malengreau, and A. Galdéano (2001), A new model for the evolution of the volcanic island of Réunion (Indian Ocean), *J. Geophys. Res.*, 106, 8646–8663.

Lerebour, P., J.-P. Rançon, and T. Augé (1989), The Grand Brûlé exploration drilling: New data on the deep framework of the Piton de la Fournaise volcano. part 2: Secondary minerals, *J. Volcanol. Geotherm. Res.*, 36, 129–137.

Lipman, P. W. (1997), Subsidence of ash-flow calderas: Relation to caldera size and magma chamber geometry, *Bull. Volcanol.*, 59, 198–218.

MacDonald, G. A. (1965), Hawaiian calderas, *Pac. Sci.*, 19, 320–334.

MacDonald, G. A. (1972), *Volcanoes*, 510 pp., Prentice-Hall, Englewood Cliffs, N. J.

MacDougall, I. (1971), The geochronology and evolution of the young island of Réunion, Indian Ocean, *Geochim. Cosmochim. Acta*, 35, 261–270.

MacPhie, J., G. P. L. Walker, and R. L. Christiansen (1990), Phreatomagmatic and phreatic fall and surge deposits from explosions at Kilauea volcano, Hawaii, 1790 A.D.: Keanakakoi Ash Member, *Bull. Volcanol.*, 52, 334–354.

Mairine, Ph., and P. Bachèlery (1997), Un grand épisode érosionnel dans l'histoire ancienne du Piton de la Fournaise (ıcirc;le de la Réunion), *C. R. Acad. Sci.*, 325, 243–249.

Malengreau, B., J.-F. Lénat, and J.-L. Froger (1999), Structure of the Reunion Island (Indian Ocean) inferred from the interpretation of gravity anomalies, *J. Volcanol. Geotherm. Res.*, 88, 131–146.

Mark, R. K., and J. Moore (1987), Slopes of the Hawaiian ridge, *U.S. Geol. Surv. Prof. Pap.*, 1350, 101–107.

Marti, J., M. Hürlimann, G. J. Ablay, and A. Gudmundsson (1997), Vertical and lateral collapses on Tenerife (Canary Islands) and other volcanic ocean islands, *Geology*, 25, 879–882.

Merle, O., and A. Borgia (1996), Scaled experiments of volcanic spreading, *J. Geophys. Res.*, 101, 13,805–13,817.

Merle, O., and J. Lénat (2003), Hybrid collapse mechanism at Piton de la Fournaise volcano, Reunion Island, Indian Ocean, *J. Geophys. Res.*, 108(B3), 2166, doi:10.1029/2002JB002014.

Michon, L., F. Saint-Ange, P. Bachelery, N. Villeneuve, and T. Staudacher (2007), Role of the structural inheritance of the oceanic lithosphere in the magmato-tectonic evolution of Piton de la Fournaise volcano (La Réunion Island), *J. Geophys. Res.*, 112, B04205, doi:10.1029/2006JB004598.

Moore, J. G. (1964), Giant submarine landslides on the Hawaiian ridge, *U.S. Geol. Surv. Prof. Pap.*, 501-D, 95–98.

Moore, J. G., and H. L. Krivoy (1964), The 1962 flank eruption of Kilauea volcano and structure of the east rift zone, *J. Geophys. Res.*, 69, 2033–2045.

Moore, J. G., and M. K. Mark (1992), Morphology of the Island of Hawaii, *GSA Today*, 2, 257–262.

Munro, D. C., and S. K. Rowland (1996), Caldera morphology in the western Galapagos and implications for volcano eruptive behavior and mechanisms of caldera formation, *J. Volcanol. Geotherm. Res.*, 72, 85–100.

Naumann, T., and D. Geist (2000), Physical volcanology and structural development of Cerro Azul Volcano, Isabela Island, Galapagos: Implications for the development of Galapagos-type shield volcanoes, *Bull. Volcanol.*, 61, 497–514.

Oehler, J.-F. (2005), Les déstabilisations de flanc des volcans de l'Ile de La Réunion (Océan Indien): Mise en évidence, implications et origins, Ph.D. thesis, 422 pp., Univ. Clermont Ferrand II, Clermont Ferrand, France.

Oehler, J.-F., P. Labazuy, and J.-F. Lénat (2004), Recurrence of major flank landslides during the last 2–Ma-history of Reunion Island, *Bull. Volcanol.*, 66, 585–598, doi:10.1007/s00445-004-0341-2.

Oehler, J. F., B. Van Wyk de Vries, and P. Labazuy (2005), Landslides and spreading of oceanic hot-spot and arc shield volcanoes and low strength layers (LSLs): An analogue modelling approach, *J. Volcanol. Geotherm. Res.*, 144, 169–189.

Rançon, J.-P., P. Lerebour, and T. Augé (1989), The Grand Brûlé exploration drilling: New data on the deep framework of the Piton de la Fournaise volcano. part 1: Lithostratigraphic units and volcanostructural implications, *J. Volcanol. Geotherm. Res.*, 36, 113–127.

Roche, O., T. H. Druitt, and O. Merle (2000), Experimental study of caldera formation, *J. Geophys. Res.*, 105, 395–416.

Rowland, S. K. (1996), Slopes, lava flow volumes, and vent distributions on Volcán Fernandina, Galapagos Islands, *J. Geophys. Res.*, 101, 27,657–27,672.

Rowland, S. K., and H. Garbeil (2000), Slopes of oceanic basalt volcanoes, in *Remote Sensing of Active Volcanism*, Geophys. Monogr. Ser., vol. 116, edited by P. J. Mouginis-Mark, J. A. Crisp, and J. H. Fink, pp. 223–247, AGU, Washington, D. C.

Sapin, M., A. Hirn, J.-C. Lépine, and A. Nercessian (1996), Stress, failure and fluid flow deduced from earthquakes accompanying eruptions at Piton de la Fournaise volcano, *J. Volcanol. Geotherm. Res.*, 70, 145–167.

Schumm, S. A. (1993), River response to baselevel change: Implications for sequence stratigraphy, *J. Geol.*, 101, 279–294.

Stearns, H. T., and W. O. Clark (1930), Geology and water resources of the Kau District, Hawaii, *U.S. Geol. Surv. Water Supply Pap.*, 616, 194 pp.

Stearns, H. T., and G. A. MacDonald (1946), Geology and ground-water resources of the Island of Hawaii, *Bull. 9*, 363 pp., Hawaii Div. of Hydogr., Honolulu.

Stieltjes, L., P. Bachèlery, A. Bacquet, A. de Villèle, M. Kasser, J.-F. Lénat, and P. Moutou (1986), Carte des coulées historiques du volcan de la Fournaise (Ile de la Réunion, Océan Indien), 43 pp., BRGM, Orléans, France.

Tibaldi, A. (2001), Multiple sector collapses at Stromboli volcano, Italy: How they work, *Bull. Volcanol.*, 63, 112–125.

Tibaldi, A. (2003), Influence of cone morphology ion dykes, Stromboli, Italy, *J. Volcanol. Geotherm. Res.*, 126, 79–95.

Tort, A., and A. Finizola (2005), Structural survey of Misti volcanic cone (southern Peru) combining elliptical Fourier function analysis of the volcano morphology and self-potential measurements, *J. Volcanol. Geotherm. Res.*, 141, 283–297.

Villeneuve, N. (2000), Apports multi-sources à une meilleure compréhension de la mise en place des coulées de lave et des risques associés au Piton de la Fournaise: Géomorphologie quantitative en terrain volcanique, Ph.D. thesis, 378 pp., Inst. de Phys. du Globe de Paris, Paris.

Walker, G. P. L. (1988), Three Hawaiian calderas: An origin through loading by shallow intrusions, *J. Geophys. Res.*, 93, 14,773–14,784.

Walter, T. R., and V. R. Troll (2003), Experiments on rift zone evolution in unstable volcanic edifices, *J. Volcanol. Geotherm. Res.*, 127, 107–120.

Walter, T. R., V. R. Troll, B. Cailleau, A. Belousov, H.-U. Schmincke, F. Amelung, and P. v. d. Bogaard (2005), Rift zone reorganization through flank instability in ocean island volcanoes: An example from Tenerife, Canary Islands, *Bull. Volcanol.*, 67, 281–291, doi:10.1007/s00445-004-0352-z.

Walter, T. R., A. Klügel, and S. Münn (2006), Gravitational spreading and formation of new rift zones on overlapping volcanoes, *Terra Nova*, 18, 26–33.

———————————

L. Michon and F. Saint-Ange, Laboratoire GéoSciences Réunion, Université de la Réunion, BP 7151, F-97715 Saint Denis cedex 9, France. (laurent.michon@univ-reunion.fr)

Annexe 13 :

Michon, L., F. Saint-Ange, P. Bachèlery, N. Villeneuve, T. Staudacher (2007). Role of the structural inheritance of the oceanic lithosphere in the magmato-tectonic evolution of Piton de la Fournaise volcano (La Réunion Island), J. Geophys. Res., 112, B04205, doi:10.1029/2006JB004598.

Role of the structural inheritance of the oceanic lithosphere in the magmato-tectonic evolution of Piton de la Fournaise volcano (La Réunion Island)

Laurent Michon,[1] Francky Saint-Ange,[1] Patrick Bachelery,[1] Nicolas Villeneuve,[2] and Thomas Staudacher[3]

[1] La Réunion Island is located east of Madagascar, on the eastern rim of the tectonically inactive Mascarene Basin. This island is composed of three shield volcanoes of which only Piton de la Fournaise is currently active. Although the magmatic activity is restricted to Piton de la Fournaise, a scattered seismicity occurs on the whole 200 km wide volcanic edifice and in the underlying oceanic crust. We carried out a multiscale analysis to understand (1) the origin of the seismicity in the geodynamic context and (2) the role of the oceanic lithosphere in the deformation of Piton de la Fournaise and La Réunion Island. Analysis of the magmatic system suggests that the magma ascent is controlled by large N25–30 and N125–130 fracture zones located below the Enclos depression. We also show that the orientation difference between the eruptive fissures and the related dykes result from a rotation of the main principal stress σ_1 from vertical to downslope through the surface. Combining a Digital Elevation Model (DEM) analysis, field observations and the geophysical data reveals that the volcano is affected by large fault zones. The fault distribution indicates the predominance of a main N70–80 trend. Magnetic data show the same N80 orientation characterizing the remnant part of the Alizés volcano. Such parallel alignment suggests a control exerted by the underlying Alizés volcano on Piton de la Fournaise. Furthermore, the alignment between the crustal orientations and the structures determined on the island suggests a control of the crustal structures in La Réunion's volcano-tectonic activity. Contrary to several volcanic islands such as Hawaii and Tenerife, La Réunion volcanoes lie on an upbending crust. Then, we interpret the reactivation of the crustal faults as resulting from a crustal uplift related to the thermal erosion of the base of the lithosphere and/or to strong underplating. The upward deformation may prevent the spreading of the volcanoes, as no evidence of such a mechanism is observed in the bathymetry and the seismic data around the island.

1. Introduction

[2] The building of an oceanic island is mainly induced by the development of a mantle plume at depth and its upwelling below the oceanic lithosphere [*Morgan*, 1971]. The volcanic activity resulting from the ascent of this mantle anomaly is frequently radially distributed around a volcanic center and concentrated in volcanic rift zones [e.g., *Walker*, 1999]. As documented for the Hawaiian volcanoes [*MacDonald and Abbott*, 1970] and the Society and Austral Islands [*Binard et al.*, 1991], the orientation of these rift zones is superimposed to main crustal orientations as transform zones and/or paleoridges. Active faulting is frequently associated with the volcanism. Fault analysis reveals that (1) normal faulting always prevails whatever the geodynamic context is and (2) faults and dyke swarms (i.e., rift zones) are parallel [*MacDonald and Abbott*, 1970; *Marinoni and Gudmundsson*, 2000]. As mentioned by *Binard et al.* [1991], such an alignment between tectonics and volcanism, and the rift zones and the crustal structures, respectively, suggests a control of the oceanic lithosphere on the deformation of shield volcanoes and on the location of the magmatism.

[3] La Réunion Island is located east of Madagascar and is related to the mantle plume that generated the Deccan

[1]Laboratoire des Sciences de la Terre de l'Université de la Réunion (LSTUR), Institut de Physique du Globe de Paris, CNRS, Saint Denis, France.
[2]CREGUR, Université de la Réunion, Saint Denis, France.
[3]Observatoire volcanologique du Piton de la Fournaise (OVPF), Institut de Physique du Globe de Paris, CNRS, La Plaine des Cafres, France.

Traps at the Cretaceous-Tertiary boundary [*Courtillot et al.*, 1986; *O'Neill et al.*, 2003]. The island built up on an oceanic lithosphere characterized by N30–40 transform zones, predominant N120–130 trending magnetic anomalies [e.g., *Fretzdorff et al.*, 1998], and local N80 magnetic anomalies east of La Réunion (Figure 1a) [*Lénat et al.*, 2001]. The N120–130 orientation also corresponds to the overall elongation of the island, which results from the emplacement of three volcanoes along this axis (the Alizés, Piton des Neiges, and Piton de la Fournaise volcanoes; Figure 1b [*Lénat et al.*, 2001]). Contrary to Hawaiian volcanoes no active faults were identified at Piton des Neiges and Piton de la Fournaise, suggesting no or undetectable tectonic activity. However, the seismic monitoring carried out by the Piton de la Fournaise Volcano Observatory recorded numerous earthquakes originating in the crust below the island and its vicinity (Figure 2). More distant (∼100 km) earthquakes, which cannot be precisely located with the current seismic network, occur below the submarine flanks of the edifice. Although the occurrence of earthquakes indicates an active tectonic regime, its origin and consequences in the development of the volcano are poorly understood.

[4] Using a multiscale and multidisciplinary analysis, we aim at studying the tectonic activity of La Réunion, integrating it at a lithospheric scale, and understanding the origin of the deformation, taking into account the regional geodynamics and the role of the mantle plume. We focus our work on four different scales: (1) the active magmatic system of PdF, (2) the overall edifice of PdF, (3) the island and the proximal submarine flanks, and (4) the oceanic crust in the island's vicinity. The magmatic system is studied through the analysis of the eruptive fissure and dyke distribution in the Enclos caldera. The tectonic structures of PdF are inferred from a combination of surface deformation derived from a 25 m resolution digital elevation model (DEM), available geophysical data such as seismic, self-potential, magnetic, and audiomagnetotelluric data, field observations, and aerial photographs. As the dense tropical vegetation makes most of the volcanic flanks inaccessible, the field observations are focused on the deep valleys which incise the volcano's western part. Structures of the southern and northern flanks are studied with the DEM and the available geophysical data. At the island scale, a 100 m resolution DEM, gravimetric and magnetic data and sonar images are used to determine the first order subaerial and submarine structures. Finally, the magnetic crustal structures and the oceanic floor topography are integrated in our study to extend the analysis from a kilometer scale to a several hundred kilometers scale.

2. Geological Setting

[5] La Réunion Island is the subaerial part of a 7 km high oceanic shield volcano with a diameter of 220–240 km. Considering the historical magma production rate and the oldest dated subaerial basalts (∼2 Ma [*MacDougall*, 1971]), an age of around 5 Ma was estimated for the beginning of the edifice growth [*Gillot et al.*, 1994]. The initial evolution was characterized by the development of two adjacent volcanoes (Piton des Neiges and Alizés volcanoes), which encountered

recurrent flank destabilizations [*Lénat et al.*, 2001; *Bachèlery et al.*, 2003; *Oehler et al.*, 2004]. Around 530 ka ago, Piton de la Fournaise appeared west of the Alizés volcano which stopped its activity. Between 530 ka and 12 ka (date of the last eruption of Piton des Neiges (PdN) [*Deniel et al.*, 1992]) PdN and PdF showed contemporaneous activity. Finally, since 12 ka, eruptions are restricted to PdF.

[6] This multiphase evolution made the structure of the overall edifice of La Réunion very complex. The Alizés volcano is now completely dismantled and the only evidence of its past existence is (1) a large intrusion complex identified by drilling below the Grand Brûlé (Figure 3) [*Rançon et al.*, 1989], (2) the remnant old submarine relieves [*Labazuy*, 1996], and (3) the pre-Brunhes reverse magnetic anomalies which characterize magmatic formations older than those of Piton de la Fournaise [*Lénat et al.*, 2001].

[7] Piton des Neiges results from a more than 2 m.y. long activity during which construction and dismantling phases alternated. The oldest parts correspond to La Montagne, the Dimitile, and Takamaka massifs (Figure 3). The other volcano flanks consists on piles of differenciated lava flows which date from the volcano's late activity, some 350 ka ago. Large explosive eruptions occurred during this period [*Fretzdorff et al.*, 2000]. The volcano's central part exhibits three major depressions: the cirques of Cilaos, Mafate, and Salazie, which originate from an intense erosion controlled by structural limits such as large landslides [*Oehler et al.*, 2004]. In the depressions, most of the outcropping formations are intensively weathered rocks and debris avalanche deposits, intruded by a large number of dykes [*Chevallier*, 1979; *Maillot*, 1999].

[8] Piton de la Fournaise is the active volcano of La Réunion Island. Geochronological and geological data allow defining two main phases of construction, separated by a main collapse event: the "ancient Fournaise" (530–150 ka) and the "recent Fournaise" (150 ka to present day) [*Gillot and Nativel*, 1989; *Bachèlery and Mairine*, 1990; *Gillot et al.*, 1990]. This large landslide led to an eastward shift of the volcano center from the present-day location of the Plaine des Sables to the current position of the active volcano. During the last 0.15 Ma, the "recent Fournaise" was affected by at least two caldera collapses whose exact origin is still under debate [*Bachèlery*, 1981; *Duffield et al.*, 1982; *Gillot et al.*, 1994; *Labazuy*, 1996; *Merle and Lénat*, 2003]. The resulting structures are the Plaine des Sables and the large U-shaped structure composed of the Enclos depression and the Grand Brûlé (Figure 3). Since the formation of the Enclos depression 4.5 ky ago, the volcanic activity is mainly restricted to the caldera. Only few eruptions occurred along the NE and SE rift zones, in the Plaine des Sables and in the Rivière des Remparts [*Bachèlery*, 1981].

[9] Intense erosion incised the edifice leading to the formation of deep valleys (Rivière des Remparts, Rivière Langevin, Rivière Basse Vallée, and Rivière de l'Est (Figure 3). An additional erosional structure was discovered on the eastern flank of PdF. Geophysical data (audiomagnetotelluric and time domain electromagnetic) and cores with fluvial sediments from a drill hole in the northern part

a)

b)
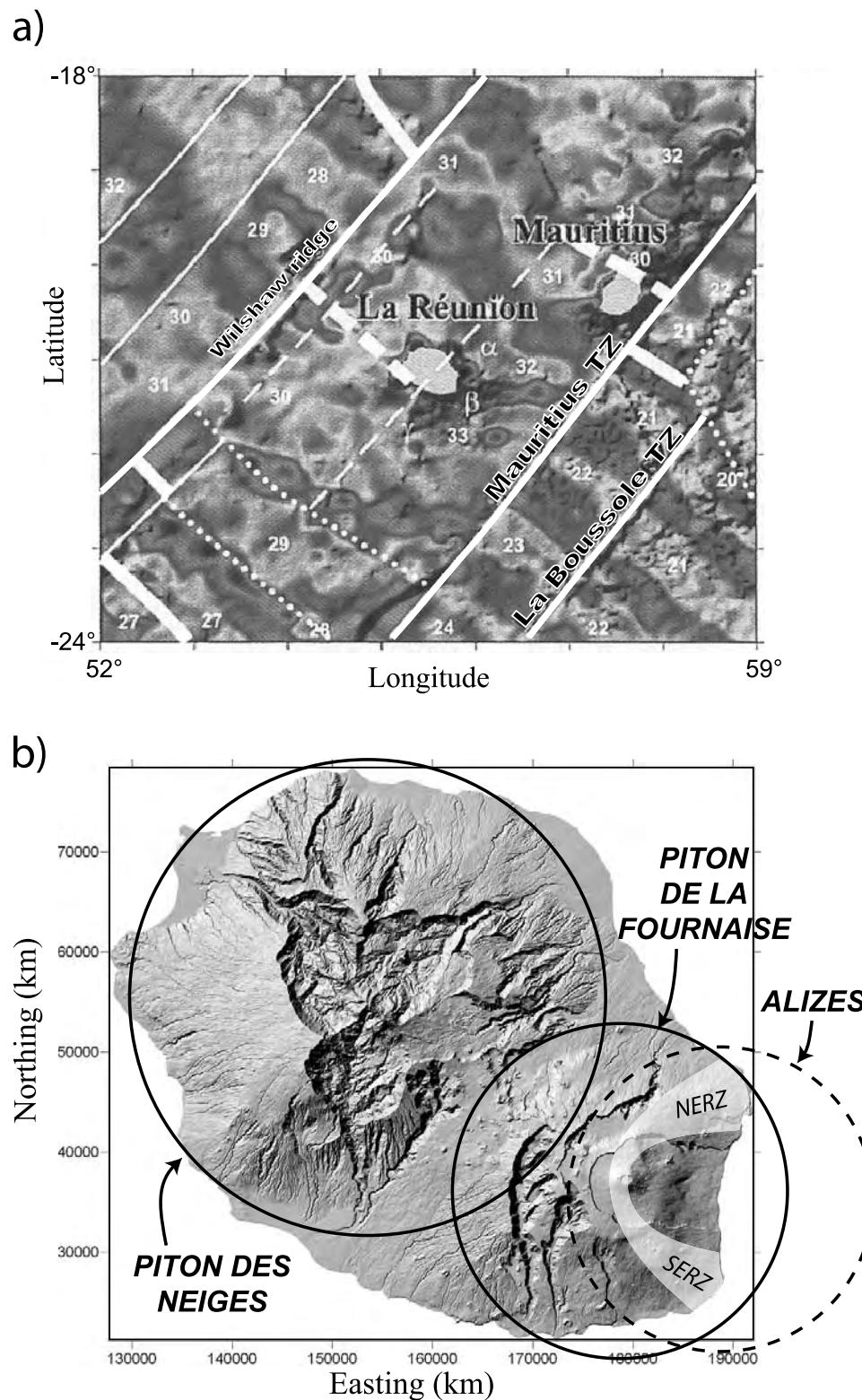
Figure 1. a) Map of the crustal magnetic anomalies in the vicinity of La Réunion and Mauritius Islands. Transform zones trend N30–40 while the magnetic anomalies present a N120–130 orientation. After *Lénat et al.* [2001]. (b) Location of the three basaltic volcanoes that constructed La Réunion Island. SERZ: Southeast rift zone; NERZ: Northeast rift zone.
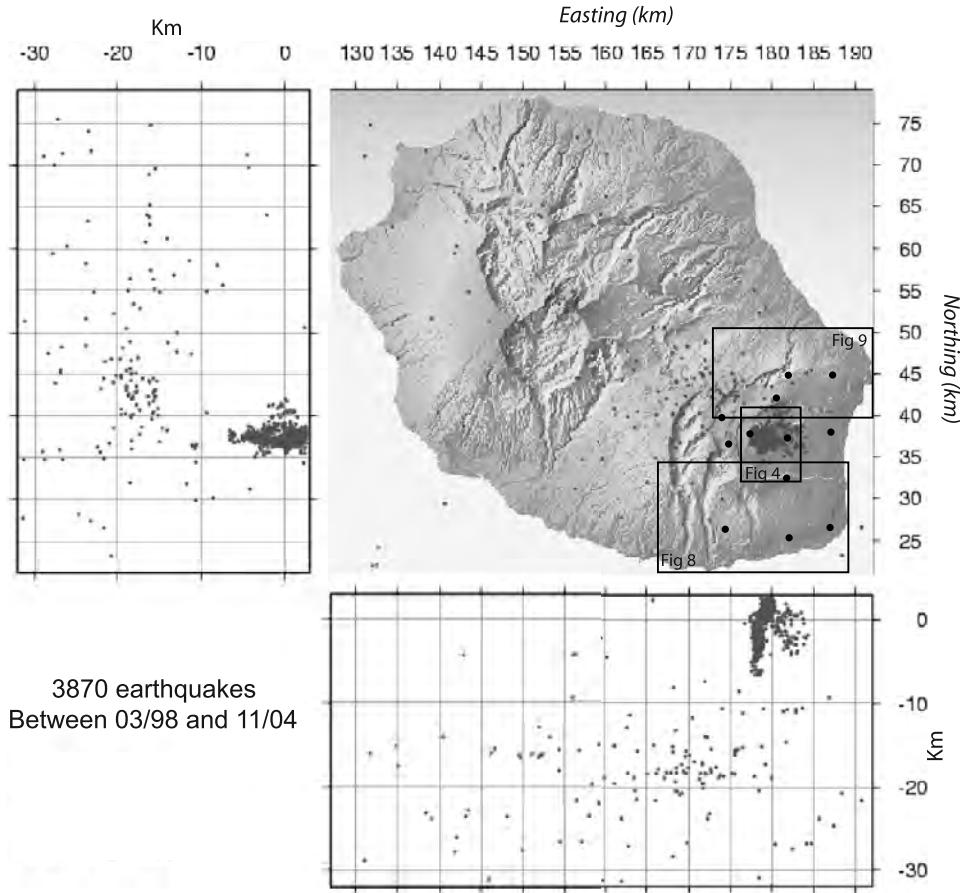
Figure 2. Map of the post-1997 seismicity occurring on La Réunion Island. Location of Figures 4, 8, and 9 is indicated by rectangles. Black dots represent the seismic stations of the Piton de la Fournaise Volcano Observatory.

of the Grand Brûlé reveal the presence of the Osmondes paleoriver [*Courteaud*, 1996].

3. Multiscale Structures of the Piton de la Fournaise

3.1. Structure of the Magmatic System

[10] During the eruptions of PdF, magma ascent mainly leads to the formation of eruptive fissures in the Enclos and on the flanks of the central cone. Most of the eruptions induce the development of en échelon eruptive fissures, which are commonly interpreted as the result of lateral shear during the dyke intrusion [e.g., *Bachèlery et al.*, 1983; *Lénat et al.*, 1989; *Zlotnicki et al.*, 1990]. According to these studies the northern and southern rift zones are characterized by left lateral and right lateral deformation, respectively, which would contribute to the eastward destabilization of the volcano flank. Although this general view is well established, we believe that it raises several questions. Are the eruptive fissures adequate to determine the rift zone orientation? Is the en échelon geometry an evidence of lateral shear along the rift zones?

3.1.1. Eruptive Fissures and Feeder-Dyke Orientation

[11] The visible pre-2003 eruptive fissures are predominantly oriented along three main directions (N10–20, N70–80, and N170), which are in agreement with the three trends determined by *Bachèlery* [1981] (Figure 4). The N10–20 and N170 trends are interpreted as the upper part of the NE and SE rift zones, named the N10 and N170 rift zones, respectively [*Bachèlery*, 1981], and were inferred from the eruptive fissure distribution [*Bachèlery*, 1981]. A detailed inspection of the recent en échelon eruptive fissures clearly shows that both orientations can develop during a single event (e.g., the March 1998 eruption, August 2003) and that N170 eruptive fissures also form in the northern flank, which is commonly described as the "site of the N10 rift zone" (Figure 5). Figure 5 reveals en échelon fissures which are parallel or subparallel to the slope. This distribution of the recent fissures is common to most of the visible pre-2003 eruptive fissures (Figure 4). Only a few are linear and oblique to the slope (e.g., the August 2004 eruption). Their constant orientation and location east of the Dolomieu crater could indicate a control of local subsurface structures in the fissure development.

[12] As for Stromboli [*Tibaldi*, 2003] and Etna [*MacGuire and Pullen*, 1989], it has been recently shown for the March 1998 [*Battaglia and Bachèlery*, 2003], February 2000, June 2000, and August 2003 eruptions [*Peltier et al.*, 2005] that the orientation of the en échelon eruptive fissures do not represent the orientation of the magmatic dyke at depth. Moreover, numerical models show that the en échelon pattern results from the intrusion of linear dykes at
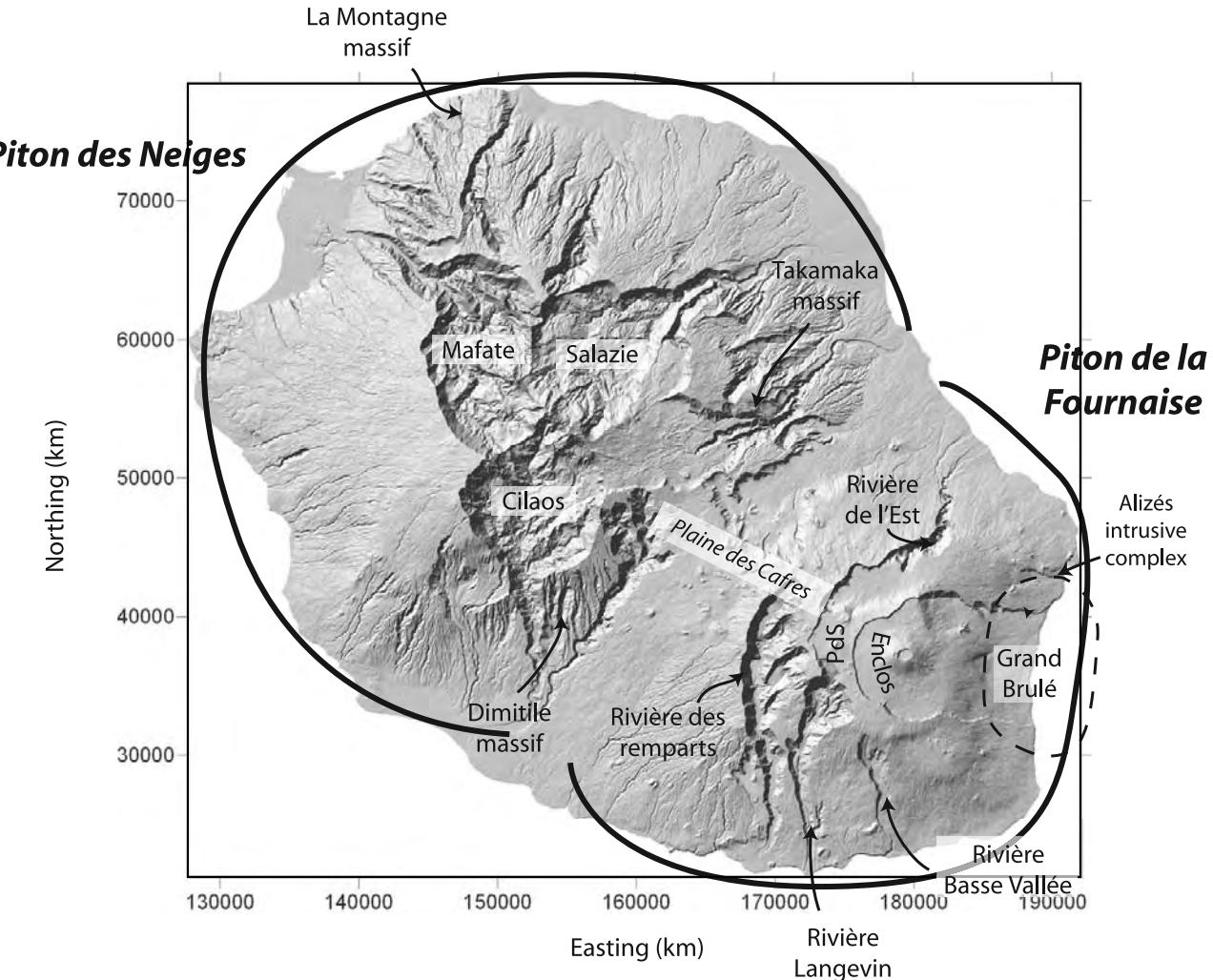
Figure 3. Overview of the main geological structures of La Réunion Island discussed in the text. PdS: Plaine des Sables.

depth [*Cayol and Cornet*, 1998; *Battaglia and Bachèlery*, 2003; *Fukushima et al.*, 2005; *Peltier et al.*, 2005]. Considering these results, we compared the orientation of 17 dykes for the 1998–2004 period with the distribution of the 63 eruptive fissures formed during the same time span (Figure 6a). It appears that the fissure and dyke orientations differ from each other.

3.1.2. Dyke, Fissure, and Stress Field

[13] As dykes and eruptive fissures are strongly sensitive to the stress distribution (σ_3 and σ_1, the least and main principal stress component, respectively), the difference in the orientation between dykes and fissures suggests distinct stress field orientations at depth and near the surface. In a homogeneous volcanic cone, σ_3 is perpendicular to the slope and σ_1 varies from a vertical orientation at depth to a downslope one in subsurface [*van Wyk de Vries and Matela*, 1998]. Note that the magnitude of the downslope σ_1 increases through the surface [*Borgia*, 1994]. In such an ideal cone, eruptive fissures and dykes, which correspond to tension cracks are radially distributed [*Pollard*, 1987]. However, in nature additional effects such as magma overpressure, contrasted rheological layering, volcano insta-

bilities, faulting activity and structural inheritance lead to a strongly anisotropic stress field, which may influence the dyke intrusion along preferential orientations [*Chadwick and Dieterich*, 1995; *Tibaldi*, 1996, 2003; *Walker*, 1999; *Marinoni and Gudmundsson*, 2000; *Walter and Troll*, 2003; *Gudmundsson*, 2006].

[14] At PdF the radial to subradial distribution of the eruptive fissures and the deformation field observed through interferometry and only showing deformation perpendicular to the dyke [*Sigmundsson et al.*, 1999; *Froger et al.*, 2004; *Fukushima et al.*, 2005] suggest that the fissure orientation is controlled by downslope σ_1 rather than by the lateral shear during the dyke intrusion. According to the numerical models simulating the coeruptive deformation observed in interferometry [*Fukushima et al.*, 2005], the transition depth at which the dykes transform into eruptive fissures, that is the depth at which σ_1 rotates from vertical to downslope, evolves from ~200 m below the top of the cone to ~100 m below the base of the cone. Such variation agrees with the distribution of the downslope σ_1 which affects a greater vertical section close to the top of a cone than at its base [*van Wyk de Vries and Matela*, 1998].
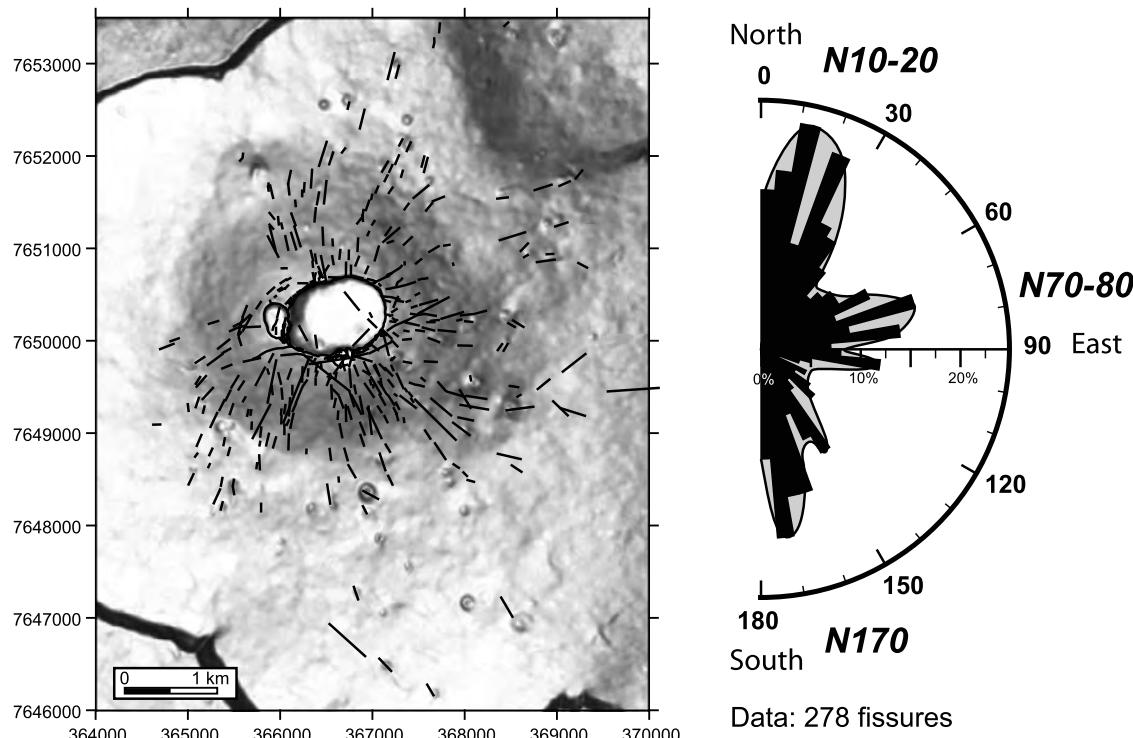
Figure 4. Distribution of the pre-2003 eruptive fissures visible in the summit part of Piton de la Fournaise. Eruptive fissures trend in three main directions: N10–20, N70–80, and N170. Coordinates in meters (WGS 84).

3.1.3. Rift Zone Orientation

[15] In contrast to the fissure distribution, the dyke distribution for post-1997 eruptions is far from radial. More than 70% of the eruptions are concentrated in two zones (i.e., the N25–30 and N125–130 intrusion trends) suggesting that the dyke emplacement is controlled at depth (Figure 6a). These two trends strikingly coincide with the two positive self-potential (SP) anomalies, determined in 1992–1993 by *Michel and Zlotnicki* [1998], during the 1993–1997 gap of activity, and 5 years before the beginning of the post-1997 eruptive cycle. Positive SP anomalies up to 1000 mV indicate upward fluid flow which originates from permanent preferential fluid migration along a fracture zone or from a recent dyke intrusion. Figure 6b shows that some small-scale anomalies (few hundred of meters) are correlated with the eruptive fissures of 1987 and 1988 in the northern part of the N25–30 intrusion trend. However, it also reveals that these anomalies are of small-scale compared to the 1–2 km wide N30 and N125 SP anomalies. This suggests that the large N30 and N125 SP anomalies cannot be explained by the recent dyke-induced fluid circulation only. Therefore following *Michel and Zlotnicki* [1998], we believe that the large SP anomalies are caused by the upward fluid migration along fracture zones [*Michel and Zlotnicki*, 1998]. Moreover, (1) the superposition of the N25–30 and N125–130 intrusion trends, inferred from the post-1997 dyke distribution and the N30 and N125 SP anomalies, and (2) the recurrence of most of the eruptions (during the 1981–1992 period and since 1998) along the preferential magmatic paths, suggest that the magma ascent in the Enclos is controlled by a large, 10 km-long, N25–30

trending fracture zone and a secondary fracture trending N125–130.

[16] *Lénat and Bachèlery* [1990] and *Fukushima* [2005] proposed that the overpressure due to each dyke intrusion along one rift zone temporally prevents another intrusion along the same rift zone. This would subsequently explain the alternation of the eruptions along the northern and southern segments of the N25–30 rift zone and the N125–130 rift zone. However, the succession of three eruptions between October 2000 and June 2001 along the same N125–130 rift zone partly contradicts this model. Indeed, although each dyke increased the overpressure (i.e., the stress perpendicular to the intrusion), the next magma intrusion followed the N125–130 fracture zone. Such a recurrence along the N125–130 rift zone reveals the control of the fracture zone in the magma migration. At PdF, the guiding role of the N25–30 and N125–130 fracture zones is explained by the quasi-isostatic stress state [*Cayol and Cornet*, 1998] and a likely weaker Young's modulus within the fracture zone than in the surrounding parts [*Gudmundsson*, 2002; *Peltier et al.*, 2005].

[17] In summary, we cannot confirm the existence of the N10 and N170 rift zones as previously described. We agree that one main magmatic path controls the magma intrusion north of the cone. However, a unique N170 rift zone disagrees with the present data for the southern part. The fan shape geometry of the SE and NE rift zones outside the Enclos (Figure 1b) suggests that magmatic intrusions are not as controlled as in the Enclos. This indicates that once the magma reaches the limit of the Enclos caldera, its
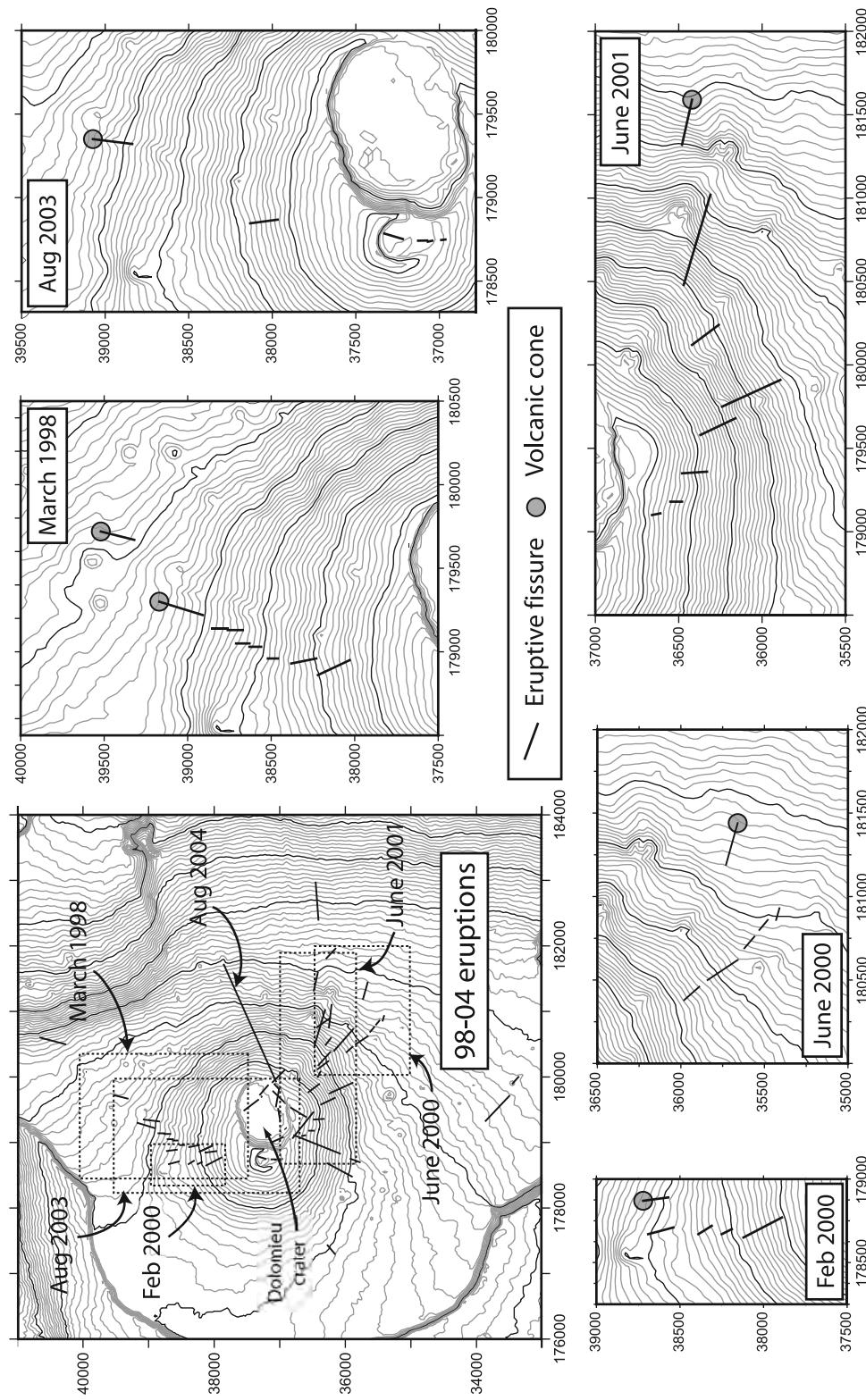
Figure 5. Distribution of the 1998−2004 eruptive fissures. En échelon patterns develop for most of the eruption: March 1998, February 2000, June 2000, June 2001, August 2003. Coordinates in meters (Gauss Laborde−Réunion).
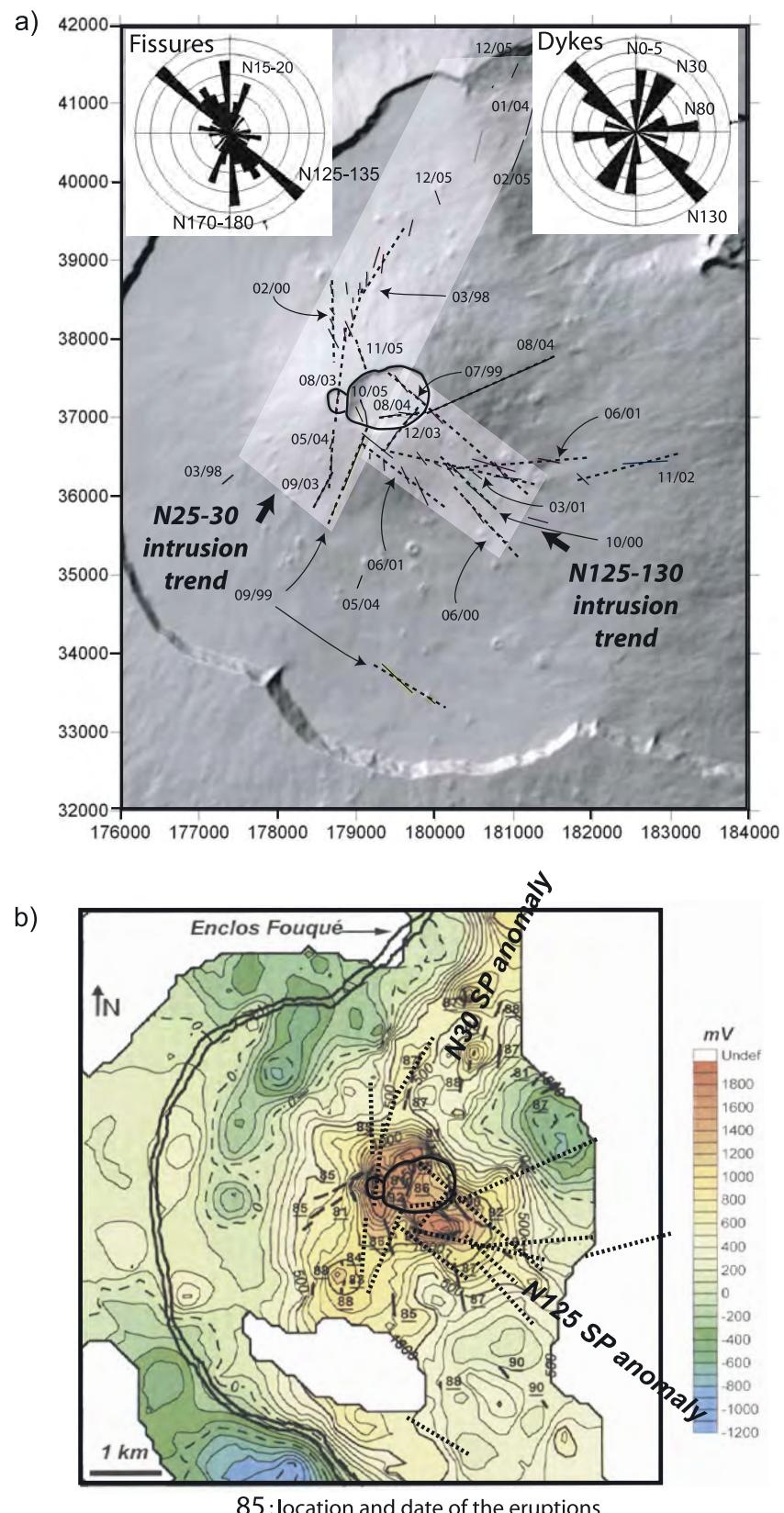
Figure 6. (a) Post-1997 eruptive fissures and the related dykes (dotted lines). The dyke distribution highlights two main N25–30 and N125–130 intrusion trends. Coordinates in meters (Gauss Laborde–Réunion). (b) Distribution of the post-1997 dykes (dotted lines) with respect to the Self-Potential anomalies measured by *Michel and Zlotnicki* [1998].

propagation is controlled by the stress field of the shallow edifice rather than by deep, narrow fracture zones.

3.2. Edifice Structures

3.2.1. Field Observations

[18] As the flanks of PdF are covered by either a dense vegetation or recent lava flows, we carried out a structural analysis in the deep valleys where geological units outcrop at the base of the scarps. We focused our analysis in the Rivière des Remparts and Rivière Langevin where the formations of the "ancient" and current Fournaise outcrop in 1000 m high scarps. Although dense vegetation covers most of the scarps, combination of structural and aerial photograph analysis allows determination of several main faults (Figure 7a). A large N05 trending, 15 km long fault zone is observed in the Rivière des Remparts inducing at different locations intense brecciation of the lava flows. In the southern half of the Rivière des Remparts, the fault zone controls the valley orientation and dyke emplacement (site 1 in Figure 7b). Further to the north (i.e., in the Mahavel and Bras Caron valleys), the fault zone, which is inaccessible but visible in aerial photographs is composed of several segments that induced a left-lateral offset of another subperpendicular fault (i.e., the N95 normal fault visible in the Rivière Langevin; Figure 7a). At site 1, geological formations do not show any vertical offset, suggesting a strike-slip motion along the fault plane. Although this outcrop is of small size the strike-slip motion is in agreement with the observation obtained further north by an aerial photograph.

[19] The second main fault presents a N40 orientation and is continued up in the scarp. The fault plane is characterized by constant subhorizontal slickenside, which indicates a right lateral movement with a slightly normal component (site 2 in Figure 7b). The fault plane outcrop is punctual and its lateral continuity cannot be determined directly. Nevertheless, it is interesting to note that the fault is in the western continuity of the Mahavel valley. Recent analogue models show that incisions of such deep valleys in volcanic settings result in structurally controlled erosion [Fèvre et al., 2004]. This indicates that erosion, which led to the valley formation, was favored by the presence of the N40 trending fault. A third main fault is located in both the Rivière des Remparts and Rivière Langevin. In the Rivière Langevin this N95 trending fault affects both the tabular lava flows of the "ancient" Fournaise and the inclined lava flows of the recent Fournaise (60–70 ky) (site 3 in Figure 7b). The fault activity which is younger than 60 ky induced a vertical offset of around 100 m. This N95 fault being slightly disturbed by the N05 fault, a maximum age of 60 ky can be attributed to the last activity of the N05 trending fault.

[20] Thus field observations demonstrate that large faults developed during the Piton de la Fournaise evolution. However, it remains to be shown whether the faults are related to the PdF's own evolution or to the regional stress field.

3.2.2. DEM Analysis

[21] The flanks of Piton de la Fournaise are covered by tropical vegetation which prevents any field observation. To fill this gap, we combine the analysis of a 25 m DEM with the available geophysical data to extend the struc-tural analysis to the whole flanks of PdF. In the southern flank, an audiomagnetotelluric (AMT) survey revealed the occurrence of two N65 and N145–150 trending preferential orientations of the subsurface basement, which are interpreted as large structural discontinuities (Figure 8) [Courteaud et al., 1996]. The slope map shows the presence of numerous lineaments, which can have different origins. To prevent any integration of human-made structures and boundaries of geological formations such as lava flows and the river patterns, we compared the lineaments with geological and topographic maps. We consider only kilometer-scale and well-developed lineaments. Once rivers and the margins of the geological formations are excluded, the DEM shows two predominant lineament trends: a large N80 lineament on both sides of the Basse Vallée River and N155 lineaments parallel to the Basse Vallée River (Figure 8). The lack of geophysical data at the lineament location does not allow the study of their origin. Moreover, the extremely dense vegetation makes direct observation of the structures in the scarp of Basse Vallée absolutely impossible. It has been proposed that the basement structures in the lower part of the southern flank most likely correspond to faults [Courteaud et al., 1996]. The alignment of these faults with the lineament trends inferred from the DEM analysis (N65–80 and N145–155) suggests a tectonic origin of the lineaments. Further studies are required to constrain better the exact origin of these structures.

[22] In the northern flank of PdF, two different slope domains can be determined from the slope orientation map (Figure 9a). Domains 1 and 2 are characterized by regular eastward and north-north-eastward slopes, respectively. In a homogeneous setting, rivers flow downslope. One striking exception is the Ravine Bellevue in domain 2, which flows in a N70–75 orientation that is strongly oblique to the slope. The development of straight and abnormally oriented rivers is usually due to a structural control [e.g., Twidale, 2004]. The pattern and orientation of Ravine Bellevue suggest that its formation was controlled by a N70–75 trending structure. This interpretation is supported by two sets of geophysical data. First, two-dimensional magnetic profiles carried out in the lower part of the flank reveals strong reverse magnetic anomalies below the Piton Balmann and 500 m south of the Piton Bellevue (Figure 9b) [Michel and Zlotnicki, 1998]. Reverse magnetized structures predate the Bruhnes period (normal magnetization since 0.78 My) and are consequently older than the formation of PdF. It is likely that these structures correspond to a remnant part of the Alizés volcano [Michel and Zlotnicki, 1998], which shows in this area a N75 orientation. The second set of data is located in the upper part of the Rivière de l'Est where 19 seismic events were recorded from 1985 to the end of 1988 (Figure 9b) [Nercessian et al., 1996]. These events, which occurred outside the present-day magmatic zone between 6 km b.s.l. and the surface, are disconnected from any recognized faults. Nevertheless, the earthquake distribution along a N70–75 main axis suggests the occurrence of a deep and active N70–75 fault. Hence the combination of the geophysical data and DEM analysis suggests that the northern flank of PdF is affected by a N70–75 fault zone, the

development of which was likely controlled by structures that also influenced the evolution of the Alizés volcano.

[23] The DEM analysis allowed us to extend the structural analysis to the PdF southern and northern flanks. Our work suggests the predominance of large N65–80 trending fault zones outside the Enclos-Grand Brûlé structure and secondary N145–155 faults. It is worth noting that the fault orientation differs from the field observations. This differ-
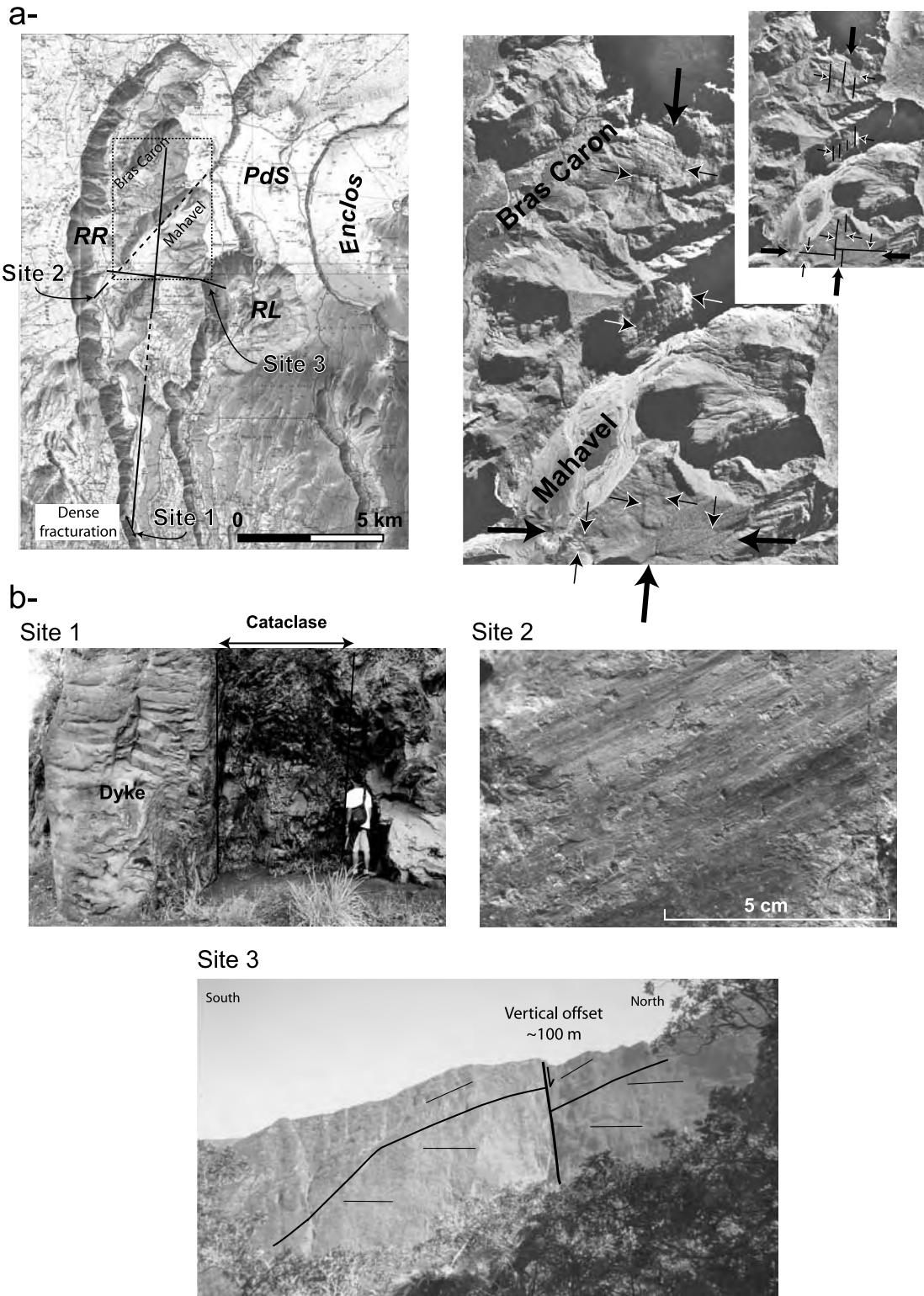

Figure 7

ence could indicate that the structural control of the Alizés volcano is predominant in the eastern half of PdF.

4. Island and Crustal Orientations

4.1. Island Structures

[24] La Réunion Island presents a N120–130 trending elongated shape which corresponds to the alignment of the Piton de la Fournaise, the Plaine des Cafres volcanic zone, and the Piton des Neiges (Figure 10a). In the past decades several structural analyses and geophysical studies were carried out to determine the first order structures of La Réunion Island [e.g., *Malengreau et al.*, 1999; *Lénat et al.*, 2001]. Gravimetric data show two main orientations (N40 and N120–130), which correspond to the orientations of deep gravity anomalies located below PdN and the PdN-PdF alignment, respectively [*Malengreau et al.*, 1999]. Two additional large and old structures (i.e., prior to the formation of PdF) were determined on the island's submarine flanks from a sea-level magnetic survey: a N35 reverse anomaly that corresponds to the continuity of a rift zone of PdN, and a N80 reverse anomaly east of PdF which is interpreted as a remnant of the Alizés volcano (Figure 10b) [*Lénat et al.*, 2001].

[25] Geological and structural analyses carried out in the three central depressions of PdN (i.e., Salazie, Mafate, and Cilaos) and on its outcropping flanks reveal the complexity of PdN and the difficulties to study it. An initial work suggested a polyphase evolution, the development of four paleorift zones presenting a star-like distribution (N10, N45, N120, and N160; Figure 10a) and the formation of three main fault trends (N30, N70, and N120) [*Chevallier*, 1979]. Additional studies confirmed the occurrence of radial intrusion and fracture trends with slight differences of 5–10° in orientation which corresponds to the expected error related to the measure of old structures in scarps [*Robert*, 1980; *Haurie*, 1987; *Rocher*, 1988]. If the recent investigations confirm the fracture orientations, observations in the central depressions combined with geophysical data partly disagree with the rift zone distribution as it was initially proposed. For instance, in the Cilaos depression where a N10 rift zone should have existed in the eastern part of the depression [*Chevallier*, 1979], *Maillot* [1999] highlighted two main N30 and N55 intrusion trends in the western margin of the depression and did not observe any N10 trending dyke. It is important to note that most of the geological formations outcropping in the depressions correspond to debris avalanche deposits [*Bret et al.*, 2003; *Oehler*, 2005; *Arnaud*, 2005]. It is likely that a significant part of the dykes measured in previous studies consists of displaced intrusions. Moreover, the only well-developed rift zone in the S flank, the N35 Etang Salé rift zone, which

presents cone alignment, a topographic ridge in bathymetry and a strong magnetic anomaly, was not considered previously (Figure 10a). This rift zone is connected to the summit of PdN by the N30 intrusions which turn to N55 close to the summit. Hence the occurrence of the N10 rift zone in the southern part of Piton des Neiges is highly questionable. It is hard to evaluate with the available data the other rift zones (i.e., N45, N120, and N160). Nevertheless, the N40 orientation of the apex of the gravimetric anomaly of PdN suggests a magmatic system which could explain the development of the N45 rift zone on the NE flank of PdN. It subsequently follows a ~N40 structural alignment between the N35 Etang Salé rift zone and the N45 rift zone on the SW and NE flanks of PdN, respectively. The dykes related to the N120 rift zone are mainly observed in the western part of La Montagne Massif, the Mafate depression and east of PdN. This intrusion direction also corresponds to (1) the overall orientation of the Plaine des Cafres volcanic zone which was interpreted as controlled by crustal structures [e.g., *Chevallier*, 1979; *Michel and Zlotnicki*, 1998] and (2) the gravimetric anomaly which links the PdF and PdN [*Malengreau et al.*, 1999]. The N120 orientation is consequently a strong structural orientation that influenced the dyke intrusion. Finally, the N160 rift zone was determined in the eastern part of La Montagne massif and in the Rivière Saint-Denis where a dense dyke network outcrops (Figure 3). Contrary to the N35, N45, and N120 rift zones, the N160 rift zone is not correlated with gravimetric or magnetic data. This could suggest that this intrusion path is of minor importance or is structurally shallower than the three other rift zones. In summary, three main rift zones are recognized at PdN: the N35 rift zone on the S flank, the N45 rift zone on the NE flank, and the N120 which affects both the WNW and ESE flanks.

[26] Different bathymetric campaigns revealed the presence of huge amount of mass deposits on the submarine flanks of La Réunion Island [*Lénat et al.*, 1990; *Labazuy*, 1996; *Bachèlery et al.*, 2003; *Oehler et al.*, 2004]. The Digital Terrain Model shows that the debris avalanche deposits are incised by deep channels which are connected to active or ancient rivers (Figure 11a). Additional erosion structures are interpreted as secondary submarine slides [*Oehler*, 2005]. The lack of geophysical data and the precision of the DTM which strongly varies around the island make a determination of active faults very hard. Nevertheless, one can note that some of the deep channels that incise the debris avalanche deposits or some straight escarpments are locally strikingly linear and oblique to the slope. We propose that the alignment of the subaerial fault zones inferred in the present study with straight lineaments on the submarine flank indicates a fault origin of part of the lineaments visible on the DTM. To this respect, the N05

Figure 7. (a) Location of the three main fault zones visible in the Rivière des Remparts and Rivière Langevin. The black lines do not correspond to the exact fault trace but to the overall fault zone location. Aerial photographs showing the trace of the N05 and N95 faults. The small arrows highlight the visible traces in the valley flanks. (b) At site 1 the N05 fault induced a brecciation of the lava flows of the "ancient" Fournaise and was subsequently followed by a basaltic dyke of the present-day Fournaise. At site 2 outcrops the N40 strike-slip fault, which is aligned with the Bras de Mahavel, suggesting that the valley formation was probably controlled by the fault orientation. Site 3 allows determination of a 100 m offset caused by the N95 fault. Note the angular unconformity between the planar lava flows located in the lower part of the rampart and the upper lava flows, which filled the paleovalley 60 ky ago (photo: Jean-Lambert Join).

a)

b)
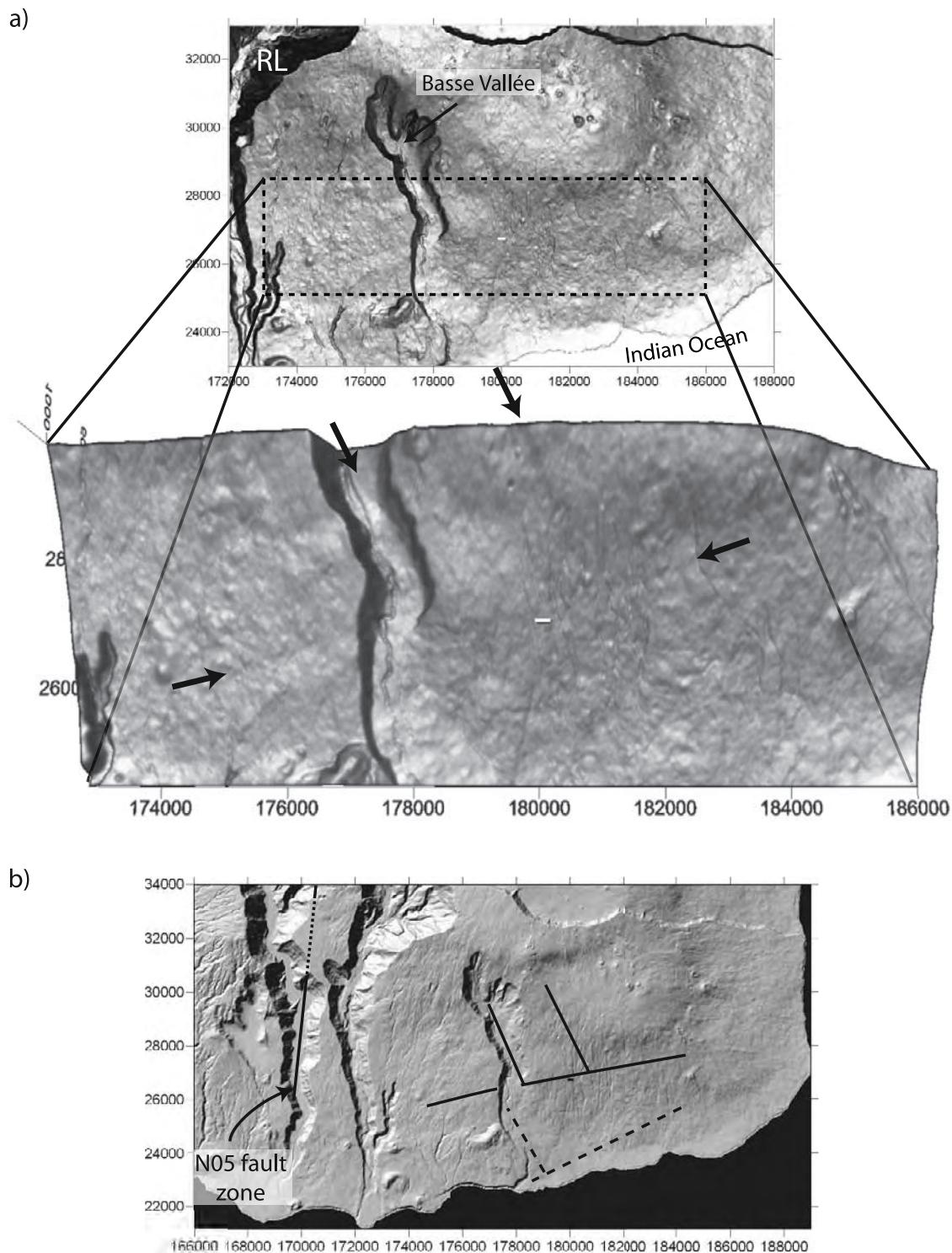
Figure 8. (a) Greyscale slope map representation of the southern flank of PdF. Arrows highlight the main lineaments. RL: Rivière Langevin. (b) Distribution of the main tectonic structures that affect the volcano flank. Dotted lines represent the faults inferred from audiomagnetotellurics method [*Courteaud et al.*, 1996]. The N05 fault zone observed in the Rivière des Remparts is added. Coordinates in meters (Gauss Laborde−Réunion).

trending fault zone observed in the Rivière des Remparts is aligned with the N05 lineament visible in the submarine topography (Figure 11a). Considering the length of this lineament and its continuation on the island, a total length of 45−50 km can be inferred for the fault zone. The northern margin of the Eastern Plateau corresponds to a N75 linear scarp, which is aligned with the N70−75 fault zone that affects the PdF northern flank and the N80 reverse magne-
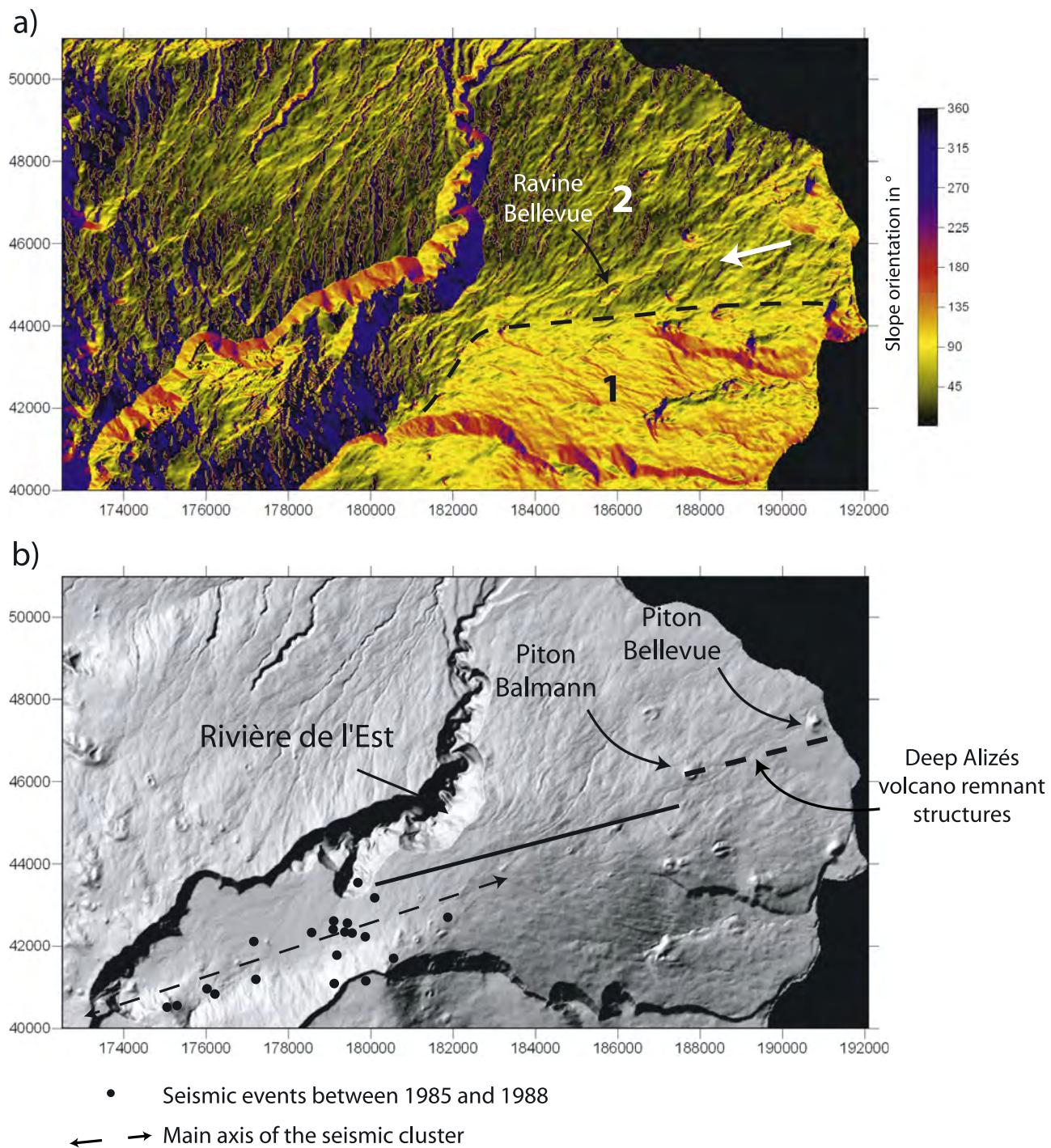
Figure 9. (a) Slope orientation map of the northern flank of PdF. 1 and 2 correspond to two different slope domains. The white arrow highlights the N70–75 trending kilometer-long lineament of the Ravine Bellevue. (b) Shaded relief representation (artificial illumination from the NW) of the northern flank of PdF. The thick dotted line indicates the location of a strong reverse magnetised body [*Michel and Zlotnicki*, 1998]. Black dots represent the earthquakes recorded between 1985 and the end of 1988 [*Nercessian et al.*, 1996]. Note that the earthquakes are distributed along a main N70–75 axis, which is parallel to the Ravine Bellevue lineament and the deep reverse magnetised body. Coordinates in meters (Gauss Laborde–Réunion).

a)

b)
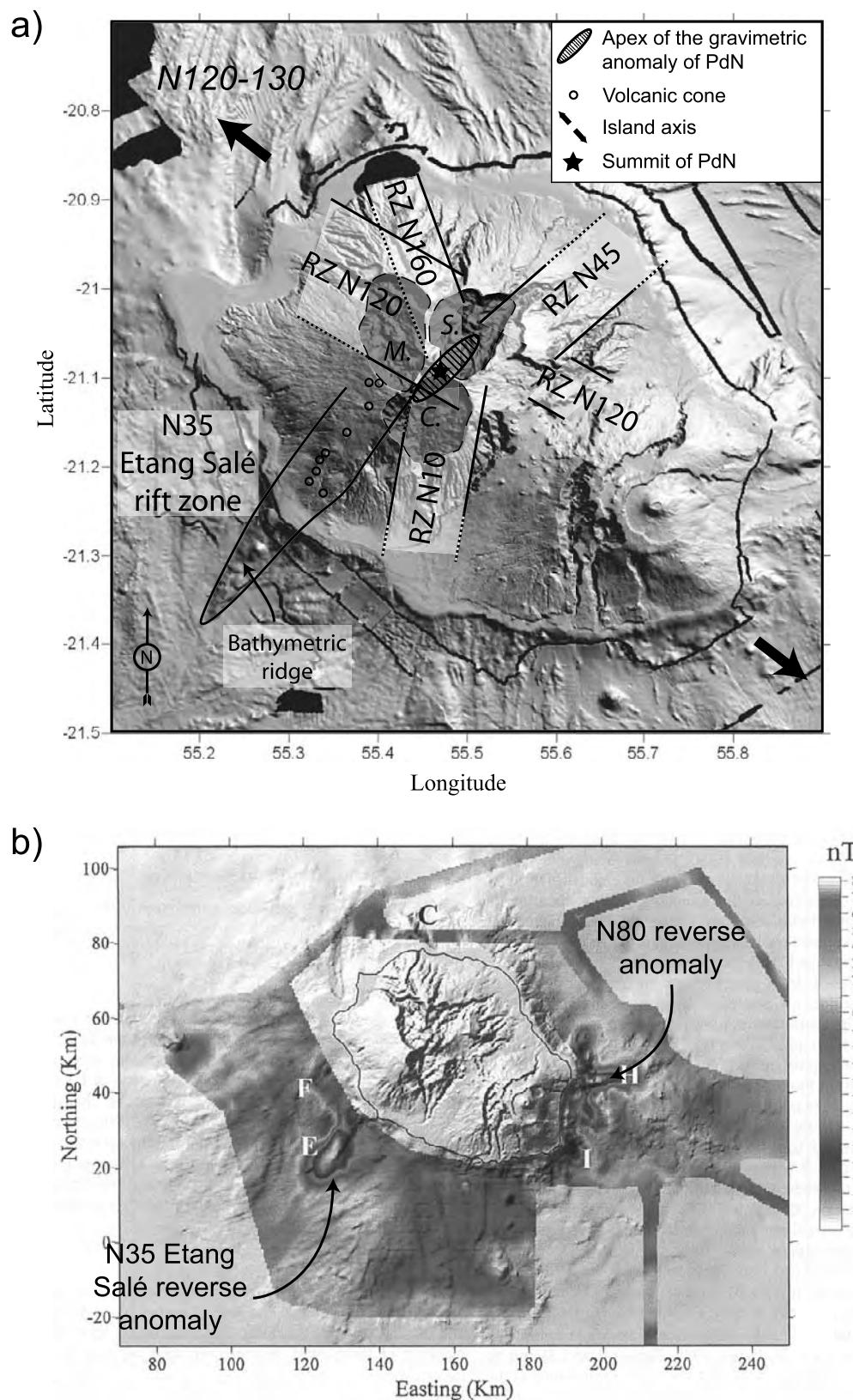
Figure 10

tized anomaly. Such an alignment between the structures could be explained by the occurrence of a large N70–N80 fault in the eastern part of the edifice. Finally, the southern submarine flank of PdF is characterised by a N150 lineament for which sonar images show that it does not consist of either a geological limit or an incised channel (Figure 11b). It is noteworthy that the N145–150 direction also corresponds to clear lineaments and geophysical structures (inferred from time domain electromagnetic and audiomagnetotelluric methods) in the southern subaerial flank of PdF (Figure 8). Thus we show that the different faults observed in the subaerial part of PdF coincide with those on a larger scale.

4.2. Oceanic Crust Orientations

[27] Recent aeromagnetic, sea level magnetic, seismic surveys, and bathymetric data allowed the determination of the structures of oceanic crust in the surrounding areas of La Réunion and Mauritius Islands [*Dyment*, 1991; *de Voogd et al.*, 1999; *Lénat et al.*, 2001]. Around the islands, the lithosphere shows N30–40 transform zones and N120–130 trending magnetic anomalies (Figure 1a). The N120–130 crustal orientation is also present below the island as suggested by the global alignment of the magmatic massifs of La Réunion, and the elongated seamount located on the western submarine flank (Figure 11a). This general pattern with two main crustal orientations changes between La Réunion Island and the Mauritius transform zone where magnetic anomalies trend in the N80 direction. The presence of this crustal orientation below the eastern part of the volcanic edifice has been revealed by seismic data, which show the occurrence of a N80 trending basement high below the Eastern Plateau [*de Voogd et al.*, 1999]. Bathymetric data [*Smith and Sandwell*, 1997; *Fretzdorff et al.*, 1998] indicate that south of the island the crust is characterized by N55–60 trending topographic ridges and elongated seamounts, which continue below the eastern part of the island (Figure 12a).

5. Discussion and Conclusions
5.1. Scale Integration

[28] Our study aimed at the characteristics of tectonic and volcanic structures at different scales allowing comparison of large and small-scale structures (i.e., oceanic crust, submarine and island structures, volcano faults, and eruptive fissures).

[29] We showed that each structural level is characterized by several structural orientations. It is hard to discriminate for a given structural level alone whether the different structures are related to large-scale processes or to local effects due to the intraedifice stress field or volcano evolution. However, the combination of several scales allows distinction of these origins. Indeed, structures induced by local effects such as the intraedifice deformation, the

landslide-induced stress field, or magmatic overpressure are restricted to the edifice, whereas large-scale deformation may influence the development of multiscale structures. To this respect, the data show the recurrence of several structural trends from the crustal scale to the small-scale magmatic system of PdF (i.e., N30–40, N70–80, and N120–130; Figure 12b). The N30–40 and N120–130 trends correspond to (1) preferential directions of magmatic intrusion at both PdF and PdN, (2) the elongation of dense intrusive complexes in PdN and between PdF and PdN [*Malengreau et al.*, 1999], (3) two of the main fault trends of PdN [*Chevallier*, 1979], and (4) the regional orientations of the transform zone and spreading center. Even though the N70 faults are observed in PdN [*Chevallier*, 1979], the N70–80 structural direction is mainly restricted to PdF and between PdF and the Mauritius transform zone. This structural orientation is represented by (1) surface and subsurface structures in the N and S flanks of PdF (Figures 8 and 9), (2) a strong reverse anomaly below the E submarine flank (Figure 10b) [*Lénat et al.*, 2001], (3) an elongated basement high [*de Voogd et al.*, 1999], and (4) the local crustal fabrics revealed by magnetic anomalies (Figure 1). We interpret the parallelism between the magmatic, the island scale, and crustal structures as resulting from a structural control played by the oceanic crust in the past and present construction of La Réunion's volcanoes.

[30] Other structures such as the N05 fault zone south of PdF or the N160 rift zone of PdN, which are spatially isolated and not observed at different structural levels may formed as the consequence of independent geological processes. Local geological events such as flank destabilization are able to control the development of volcanic rift zones [e.g., *Tibaldi*, 2003; *Walter and Troll*, 2003]. The deformation of a volcano above a décollement level [e.g., *Merle and Borgia*, 1996] is an additional feature to decouple the structural influence of both the oceanic crust and the volcanic edifice. In consequence, we consider that the secondary structural directions in La Réunion's volcanoes may result from intraedifice processes rather than a regional stress-field.

5.2. Origin of the Large-Scale Deformation
5.2.1. General Context

[31] La Réunion Island is located east of Madagascar and on the southeastern rim of the Mascarene Basin. Magnetic anomalies indicate that this basin results from oceanic extension between the Campanian (Late Cretaceous; anomaly 34) and the Early Paleocene (anomaly 27 [e.g., *Dyment*, 1991]). This extension was accommodated by large transform zones such as the Wilshaw Ridge and the Mauritius Transform Zone (Figure 1a). Between these two transform zones, the age and the structure of the crustal domain on which La Réunion Island is built are poorly constrained.

Figure 10. (a) Digital Terrain Model (DTM) of the sub-aerial part and proximal sub-marine flanks of La Réunion Island. The island presents a N125-130 elongation. According to *Chevallier* [1979], the magmatic intrusions of Piton des Neiges were restricted to four rift zones (N10, N45, N120, and N160). Note that the well-developed Etang-Salé rift zone, which forms a submarine ridge and is characterized by a cone alignment, was not considered by *Chevallier* [1979]. (b) Sea-level magnetic map showing the N35 reverse magnetized anomaly of the Etang-Salé rift zone. The N80 reverse magnetized anomaly east of the Piton de la Fournaise is interpreted as a remnant part of the Alizés volcano (after *Lénat et al.* [2001]).

Dyment [1991] proposed that the island is located at the intersection of a small-scale transform zone and a paleo-ridge. Whatever the exact structure, the age of the oceanic spreading in the Mascarene Basin suggests that the trans-form zones are tectonically inactive since 60 m.y. Conse-quently, the recent, active deformation determined in the present study and the seismicity on an island scale are
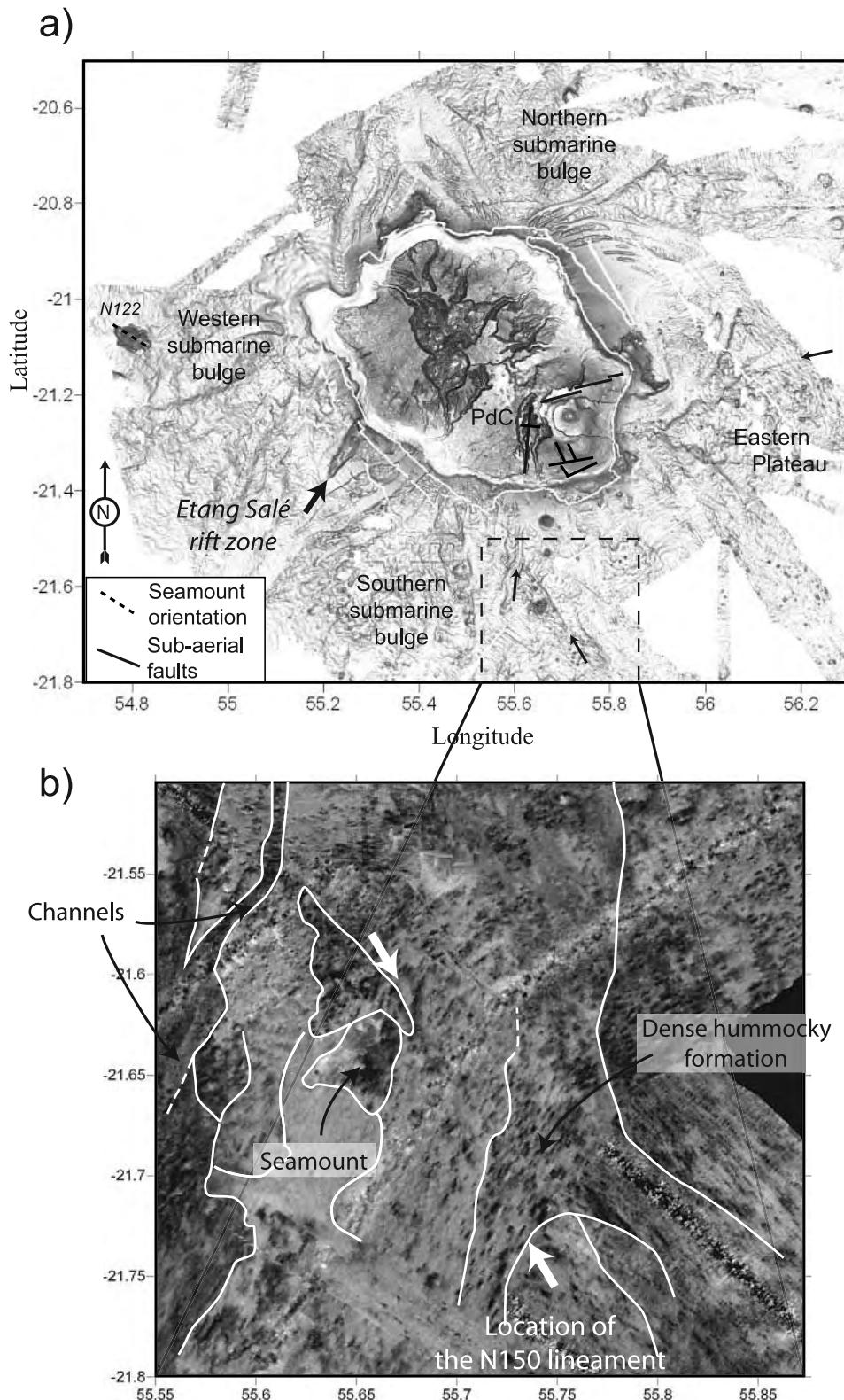

Figure 11

hardly explainable by the present-day activity of the pale-oridge and the transform zones.

5.2.2. Effect of the Mantle Plume and the Magmatic Underplating

[32] Geophysical campaigns in the past decades have allowed the determination of the crustal topography around and below the main volcanic islands [*Watts et al.*, 1985; *Binard et al.*, 1991; *Watts et al.*, 1997; *de Voogd et al.*, 1999; *Ali et al.*, 2003]. Large lithospheric flexures have been determined below the Hawaiian chain [*Watts et al.*, 1985] and the Tenerife Island [*Watts et al.*, 1997]. In the island's vicinity, the lithospheric flexure led to the formation of large angular unconformities between prevolcanic and syn/post-volcanic formations [e.g., *Watts et al.*, 1997, Figure 2]. In the Cape Verde Islands, angular unconformities reveal a past crustal flexure during the Miocene, which has been subsequently balanced by a general uplift [*Ali et al.*, 2003]. In contrast to these evolutions, reflection seismic data in La Réunion Island show a lack of angular unconformity, firmly establishing the lack of significant vertical downward movement and flexure [*de Voogd et al.*, 1999]. Furthermore, the base of the edifice that is the top of the preexisting oceanic plate is roughly domed and is characterised by several N55–60 and N80 topographic highs and lows.

[33] The amount of lithospheric flexure is controlled by three main parameters: (1) the size of the volcanic edifice (i.e., the surface load), (2) the elastic thickness of the lithosphere (T_e) which depends on the effective flexural rigidity (D_e) [*Burov and Diament*, 1995], and (3) the sub-surface upward loads induced by underplated materials and lithospheric thinning [*Watts et al.*, 1980; *Ali et al.*, 2003]. As the height of La Réunion, Cape Verde, Hawaii, and Tenerife islands are of the same order of magnitude, the downward load due to the volcano weight are roughly similar and it cannot explain alone the differences observed in the crust geometry. One could consider that the lack of lithospheric flexure in La Réunion Island could be caused by different T_e values in La Réunion Island, Hawaii, Cape Verde, and Tenerife. However, T_e values of the oceanic lithosphere are nearly similar in La Réunion (28 km [*Bonneville*, 1990]), Cape Verde (29 km [*Ali et al.*, 2003]), Tenerife (26 km [*Watts et al.*, 1997]), and Hawaii (30–35 km [*Wessel and Keating*, 1994]). Even if the T_e values may present uncertainties due to the complexity of determining the effective flexural rigidity for a oceanic lithosphere (A. Gudmundsson, personal communication, 2006), the "normal" value of lithosphere elastic thickness in La Réunion Island cannot explain the lack of flexure and moreover the slight doming of the edifice basement. Two different processes may produce upward forces and subsequent doming: (1) a thermal erosion of the base of the lithosphere caused by the mantle anomaly and (2) magmatic underplating. The amount of thermally eroded lithosphere and the related uplift depend on the time that a lithosphere stays above a hot anomaly. Large isostatic disequilibrium will be favored in slow plate motion settings and almost nonexistent in fast moving plates (Figure 13). It has been proposed that the displacement of La Réunion Island relative to the hot spot, for the time of known volcanic activity (2.1 My [*MacDougall*, 1971]), was less than 40 km [*Charvis et al.*, 1999]. In such a context, an efficient lithospheric thinning was possible. Furthermore, geophysical data reveal that a large amount of underplated material exists below the southwestern part of La Réunion edifice [*Charvis et al.*, 1999], supporting the underplating hypothesis as an additional cause of the doming.

[34] Hence we interpret the slight crustal doming below La Réunion Island as resulting from a combination of lithospheric thinning due to thermal erosion and magmatic underplating.

5.3. Consequences in the Evolution of La Réunion Volcanoes

[35] The development of a dome-like geometry of the oceanic basement and the occurrence of 500 to 1500 m of pelagic sediments [*de Voogd et al.*, 1999] below the volcanic edifice potentially had strong influences in the evolution of the volcanoes on La Reunion.

[36] The dome-like geometry suggests that the oceanic crust underwent an uplift during the development of the edifice. In a continental setting, the uplift of the lithosphere induces the reactivation of preexisting crustal structures (inherited faults and/or metamorphic fabrics) which subsequently control the location of the volcanism and the geometry of the extension structures [e.g., *Le Gall et al.*, 2004]. In a similar way, we interpret the uplift of the oceanic lithosphere at La Réunion as the motor of the reactivation of the preexisting crustal faults. Such a reactivation can explain the parallelism between the crustal structures and most of the structures observed on the volcanoes. It is obviously wrong to consider that each fault or rift zone observed at the surface is directly linked to reactivated crustal faults. Several additional factors potentially triggered the development of tectonic and magmatic structures. The huge amount of mass deposits on the submarine flanks of the edifice [e.g., *Labazuy*, 1996; *Oehler et al.*, 2004] and in the subaerial part [*Bachèlery et al.*, 2003; *Bret et al.*, 2003] suggests that large flank destabilizations occurred during the evolution of the volcano. The occurrence of large landslides may have produced a rift zone reorientation [e.g., *Walter and Troll*, 2003] and an isostatic deformation [*Smith and Wessel*, 2000]. The deformation of a volcano above low strength layers [*Borgia*, 1994; *Merle and Borgia*, 1996; *Oehler et al.*, 2005] can also develop independent stress fields that lead to the formation of numerous faults. Although a large-scale spreading could have theoretically occurred at La Réunion Island (presence of potential décollement layer at the base of

Figure 11. (a) DTM of the bathymetry showing the distribution of the mass deposits which are mainly concentrated in four bulges (the western, southern, and northern bulges and the Eastern Plateau [*Oehler et al.*, 2004]). The main faults of PdF inferred in this study are represented by black lines. Small arrows indicate the N80, and N05 lineaments visible in the submarine flanks which are aligned with subaerial structures. The N150 lineament is parallel to the structures observed on the southern flank of PdF. Rectangle in dashed line represents the location of Figure 10b. (b) Sonar image of the southern submarine flank of PdF showing the location of the N150 lineament (white arrows) and the distinct geological formations. Note that the lineament does not correspond to either the limit of geological formations or to an incised channel.

	N30-40 trend	N55-60 trend	N70-80 trend	N120-130 trend
Piton de la Fournaise	N25-30 *(rift zone)*	N55-65 *(structural liniation)*	N75-80 *(structural liniation)*	N125-130 *(rift zone)*
Island structures	N30-40 *(faults, rift zones and intrusive complex at PdN)*		N70-80 *(faults at PdN, crustal highs, remnant of the Alizés volcano)*	N120-130 *(faults, rift zones and intrusive complex at PdN, seamount, island elongation)*
Crustal structures	N30-40 *(transform zones)*	N55-60 *(volcanic ridges)*	N80 *(crustal structure E of La Réunion)*	N120-130 *(regional crustal structure)*

Figure 12. (a) Distribution of the main structures of PdF, PdN, La Réunion edifice and the oceanic crust. Yellow, red and green lines correspond to the N30–40, N120–130, and N70–80 structural trends, respectively. (b) Summary of the main trends observed at different scales: Piton de la Fournaise, island, and crust.
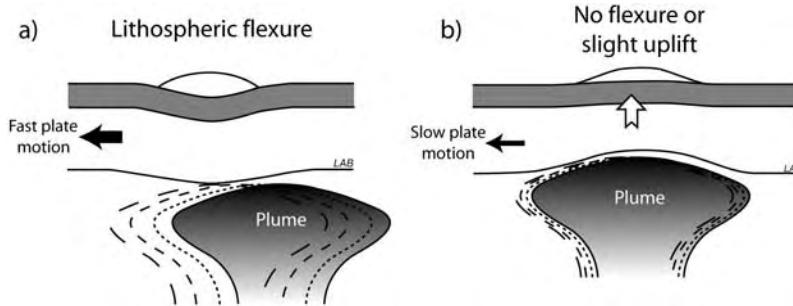
Figure 13. (a) The impact of a plume emplacement below a fast moving plate. The fast plate movement above the mantle anomaly does not allow significant thermal erosion of the base of the lithosphere below the volcanic island. The volcano load subsequently leads to a lithospheric flexure as in Hawaii. Dotted shapes represent the mantle anomaly location at different times. (b) Efficient thermal erosion of a slow moving lithosphere. The thermal erosion induces an isostatic disequilibrium and an uplift of the lithosphere, which at least balances the load of the volcanic edifice. This evolution may partly explain the lack of lithospheric flexure below La Réunion Island.

the edifice), its existence is still unclear. The pelagic sediments below the submarine flanks are undeformed and no expected distal anticline and thrust are observed in reflection seismic data on the SW and NE flank, even several tens of kilometers away from the volcano [*de Voogd et al.*, 1999]. Additional to the large-scale spreading, *Oehler et al.* [2005] proposed that small-scale low strength layers (e.g., deltas and hyaloclastites layers) have induced the edifice deformation and flank landslides.

[37] We therefore propose that the deformation of La Réunion Island and the development of the magmatic rift zones result from the superposition of a general stress field, which is induced by the uplift of the oceanic crust, and local stress fields related to the dynamics and settings of each of the volcanoes.

[38] The volcanoes of La Réunion experienced recurrent flank destabilizations [*Oehler*, 2005]. Recent field observations [*Bachèlery et al.*, 2003; *Bret et al.*, 2003] and analogue experiments [*Merle and Lénat*, 2003; *Oehler et al.*, 2005] suggest that the landslides of La Réunion are due and/or favored by the occurrence of low strength levels in the edifice. Most of these low strength layers correspond to hydrothermally altered materials which mainly develop in the vicinity of the intrusive complex of PdN, PdF, and the Alizés volcano. We propose that the presence of in situ décollement composed of hydrothermally altered and weakened materials is probably not the only cause of a landslide. Indeed, analogue models show that the reactivation in normal faulting mode of crustal preexisting faults below a volcanic edifice leads to the development of normal and reverse faults in the volcano, which can result in gravity instabilities such as flank landslides [*Vidal and Merle*, 2000]. The stability of the edifice decreases when oblique basement faults are simultaneously reactivated and landslides occur after vertical basement displacements of ~150–300 m. Such large amplitudes of vertical displacement are currently not observed in the subaerial part of La Réunion. However, as the faults correspond to the lateral borders of the landslides, the initial offsets related to the reactivation of the basement fault would have not been preserved in the upper part of the edifice. Moreover, the analogue experiment of *Vidal and Merle* [2000] was carried

out with brittle materials only. It has been widely demonstrated that the occurrence of low strength materials in volcanoes is a crucial parameter in the deformation and the destabilization of the edifice [e.g., *Siebert*, 1984; *Day*, 1996; *Cecchi et al.*, 2005] We hypothesize that the deformation related to the reactivation of the basement fault would be enhanced by the presence of hydrothermally weakened material in the edifice. Part of the widespread landslides in La Réunion Island would consequently result from the combination of basement fault reactivation and the occurrence of hydrothermally altered materials.

References

Ali, M. Y., A. B. Watts, and I. Hill (2003), A seismic reflection profile study of lithospheric flexure in the vicinity of the Cape Verde Islands, *J. Geophys. Res.*, *108*(B5), 2239, doi:10.1029/2002JB002155.

Arnaud, N. (2005), Les processus de démantèlement des volcans; le cas d'un volcan bouclier en milieu océanique: Le Piton des Neiges (Ile de la Réunion), Ph.D. thesis, 407 pp., Univ. la Réunion, Saint-Denis Messag, France.

Bachèlery, P. (1981), Le Piton de la Fournaise (Ile de la Réunion): Etude volcanologique, structurale et pétrologique, Ph.D. thesis, Univ. é Clermont-Ferrand II, Clermont-Ferrand, France.

Bachèlery, P., and P. Mairine (1990), Evolution volcano-structurale du Piton de la Fournaise depuis 0,53 Ma, in *Le Volcanisme de la Réunion*, edited by J.-F. Lénat, pp. 213–242, Cent. de Rech. Volcanol., Clermont-Ferrand, France.

Bachèlery, P., L. Chevalier, and J.-F. Gratier (1983), Caractères structuraux des éruptions historiques du Piton de la Fournaise, *C. R. Acad. Sci.*, *296*, 1345–1350.

Bachèlery, P., B. Robineau, M. Courteaud, and C. Savin (2003), Avalanches de débris sur le flanc occidental du volcan-bouclier Piton des Neiges (Réunion), *Bull. Soc. Geol. Fr.*, *174*, 125–140.

Battaglia, J., and P. Bachèlery (2003), Dynamic dyke propagation deduced from tilt variations preceding the March 9, 1998, eruption of Piton de la Fournaise volcano, *J. Volcanol. Geotherm. Res.*, *120*, 289–310.

Binard, N., R. Hékinian, J. L. Cheminée, R. C. Searle, and P. Stoffers (1991), Morphological and structural studies of the Society and

Austral hotspot regions in the South Pacific, *Tectonophysics*, *186*, 293–312.

Bonneville, A. (1990), Structure de la lithosphere, in *Le Volcanisme de la Réunion*, edited by J-.F. Lénat, pp. 1–18., Cent. de Rech. Volcanol., Clermont-Ferrand, France.

Borgia, A. (1994), Dynamic basis of volcanic spreading, *J. Geophys. Res.*, *99*, 17,791–17,804.

Bret, L., Y. Fèvre, J.-L. Join, B. Robineau, and P. Bachèlery (2003), Deposits related to degradation processes on Piton des Neiges volcano (Réunion Island): Overview and geological hazard, *J. Volcanol. Geotherm. Res.*, *123*, 25–41.

Burov, E. B., and M. Diament (1995), The effective elastic thickness (T_e) of continental lithosphere: What does it really mean?, *J. Geophys. Res.*, *100*, 3905–3927.

Cayol, V., and F. H. Cornet (1998), Three-dimensional modeling of the 1983–1984 eruption at Piton de la Fournaise volcano, Réunion Island, *J. Geophys. Res.*, *103*, 18,025–18,037.

Cecchi, E., B. van Wyk de Vries, and J. M. Lavest (2005), Flank spreading and collapse of weak-cored volcanoes, *Bull. Volcanol.*, *67*, 72–91.

Chadwick, W. W., Jr., and J. H. Dieterich (1995), Mechanical modeling of circumferential and radial dike intrusion on Galapagos volcanoes, *J. Volcanol. Geotherm. Res.*, *66*, 37–52.

Charvis, P., A. Laesanpura, J. Gallart, A. Hirn, J.-C. Lépine, B. de Voogd, T. A. Minshull, Y. Hello, and B. Pontoise (1999), Spatial distribution of hotspot material added to the lithosphere under la Réunion, from wide-angle seismic data, *J. Geophys. Res.*, *104*, 2875–2893.

Chevallier, L. (1979), Structures et évolution du volcan Piton des Neiges, île de la Réunion: Leurs relations avec les structures du Bassin des Mascareignes, Océan Indien occidental, 187 pp., Ph.D. thesis, Grenoble Univ., Grenoble, France.

Courteaud, M. (1996), Etude des structures géologiques et hydrogéologiques du Massif de la Fournaise par la méthode audiomagnétotellurique, Ph.D. thesis, 212 pp., Univ. la Réunion, Saint-Denis Messag, France.

Courteaud, M., M. Ritz, M. Descloitres, B. Robineau, and J. Coudray (1996), Cartographie AMT du biseau salé sur le flanc sud du Piton de la Fournaise (Ile de la Réunion), *C. R. Acad. Sci.*, *322*, 93–100.

Courtillot, V., D. Besse, D. Vandamme, R. Montigny, J. J. Jaegger, and H. Capetta (1986), Deccan flood basalts at the Cretaceous/Tertiary boundary?, *Earth Planet. Sci. Lett.*, *80*, 361–374.

Day, S. (1996), Hydrothermal pore fluid pressure and the stability of porous, permeable volcano, in *Volcano Instability on the Earth and Other Planets*, edited by W. J. McGuire, A. P. Jones, and J. Neuberg, *Geol. Soc. Spec. Publ.*, *110*, 77–93.

Deniel, C., G. Kieffer, and J. Lecointre (1992), New ^{230}Th and ^{238}U and ^{14}C age determinations from Piton des Neiges volcano, Reunion: A revised chronology for the differenciated series, *J. Volcanol. Geotherm. Res.*, *51*, 253–267.

de Voogd, B., S. Pou Palomé, A. Hirn, P. Charvis, J. Gallart, D. Rousset, J. Dañobeitia, and H. Perroud (1999), Vertical movements and material transport during hotspot activity: Seismic reflection profiling offshore la Réunion, *J. Geophys. Res.*, *104*, 2855–2874.

Duffield, W. A., L. Stieltjes, and J. Varet (1982), Huge landslide blocks in the growth of Piton de la Fournaise, la Réunion, and Kilauea volcano, Hawaii, *J. Volcanol. Geotherm. Res.*, *12*, 147–160.

Dyment, J. (1991), Structure et évolution de la lithosphère océanique dans l'océan Indien: Apports des anomalies magnétiques, Ph.D. thesis, 374 pp., Univ. Strasbourg, Strasbourg, France.

Fèvre, Y., F. Saint-Ange, S. Bonnet, A. Crave, and B. Robineau (2004), Role of groundwater flow in oceanic volcanoes evolution: Experimental modelling and application to la Reunion Island, paper presented at IAVCEI General Assembly 2004, Int. Assoc. of Volcanol. and Chem. of the Earth's Inter., Pucon, Chile.

Fretzdorff, S., P. Stoffers, C. W. Devey, and M. Munschy (1998), Structure and morphology of submarine volcanism in the hotspot region around Réunion Island, western Indian Ocean, *Mar. Geol.*, *148*, 39–53.

Fretzdorff, S., M. Paterne, P. Stoffers, and E. Ivanova (2000), Explosive activity of the Reunion Island volcanoes through the past 260,000 years as recorded in deep-sea sediments, *Bull. Volcanol.*, *62*, 266–277.

Froger, J.-L., Y. Fukushima, P. Briole, T. Staudacher, T. Souriot, and N. Villeneuve (2004), The deformation field of the August 2003 eruption at Piton de la Fournaise, Reunion Island, mapped by ASAR interferometry, *Geophys. Res. Lett.*, *31*, L14601, doi:10.1029/2004GL020479.

Fukushima, Y. (2005), Transferts de magma au volcan du Piton de la Fournaise determinés par la modélisation 3D des données d'interférométrie radar entre 1998 et 2000, Ph.D. thesis, 149 pp., Univ. é Clermont-Ferrand II, Clermont-Ferrand, France.

Fukushima, Y., V. Cayol, and P. Durand (2005), Finding realistic dike models from interferometric synthetic aperture radar data: The February 2000 eruption at Piton de la Fournaise, *J. Geophys. Res.*, *110*, B03206, doi:10.1029/2004JB003268.

Gillot, P.-Y., and P. Nativel (1989), Eruptive history of the Piton de la Fournaise volcano, Reunion Island, Indian Ocean, *J. Volcanol. Geotherm. Res.*, *36*, 53–65.

Gillot, P.-Y., P. Nativel, and M. Condomines (1990), Géochronologie du Piton de la Fournaise, in *Le Volcanisme de la Réunion*, edited by J-.F. Lénat, Cent. de Rech. Volcanol., pp. 243–255, Clermont-Ferrand, France.

Gillot, P.-Y., J.-C. Lefèvre, and P. E. Nativel (1994), Model for the structural evolution of the volcanoes of Reunion Island, *Earth Planet. Sci. Lett.*, *122*, 291–302.

Gudmundsson, A. (2002), Emplacement and arrest of dykes in central volcanoes, *J. Volcanol. Geotherm. Res.*, *255*, 279–298.

Gudmundsson, A. (2006), How local stresses control magma-chamber ruptures, dyke injections, and eruptions in composite volcanoes, *Earth Sci. Rev.*, *79*, 1–31, doi:10.1016/j.earscirev.2006.06.006.

Haurie, J.-L. (1987), Géodynamique des cirques de la Réunion: Implications géotechniques et stabilité des versants, Ph.D. thesis, 284 pp., Univ. Grenoble, Grenoble, France.

Labazuy, P. (1996), Recurrent landslides events on the submarine flank of Piton de la Fournaise volcano (Réunion Island), in *Volcano Instability on the Earth and Other Planets*, edited by W. J. McGuire, A. P. Jones, and J. Neuberg, *Geol. Soc. Spec. Publ.*, *110*, 293–305.

Le Gall, B., L. Gernigon, J. Rolet, C. Ebinger, R. Gloaguen, O. Nilsen, H. Dypvik, B. Deffontaines, and A. Mruma (2004), Neogene-Holocene rift propagation in central Tanzania: Morphostructural and aeromagnetic evidence from the Kilombero area, *Geol. Soc. Am. Bull.*, *116*, 490–510.

Lénat, J.-F.. and P. Bachèlery (1990), Structure and dynamics of the central zone of Piton de la Fournaise volcano, in *Le Volcanisme de la Réunion, Monogr. Cent. De Rech. Volcanol.*, edited by J-.F. Lénat, pp. 257–296, Cent. De Rech. Volcanol., Clermont-Ferrand, France.

Lénat, J.-F., P. Bachèlery, A. Bonneville, and A. Hirn (1989), The beginning of the 1985–1987 eruptive cycle at Piton de la Fournaise (la Réunion): New insights in the magmatic and volcano-tectonic systems, *J. Volcanol. Geotherm. Res.*, *36*, 209–232.

Lénat, J.-F., P. Bachèlery, A. Bonneville, A. Galdéano, P. Labazuy, D. Rousset, and P. Vincent (1990), Structure and morphology of the submarine flank of an active basaltic volcano: Piton de la Fournaise (Réunion Island, Indian Ocean), *Oceanol. Acta*, *10*, 211–223.

Lénat, J.-F., B. Gibert-Malengreau, and A. Galdéano (2001), A new model for the evolution of the volcanic island of Réunion (Indian Ocean), *J. Geophys. Res.*, *106*, 8646–8663.

MacDonald, G. A., and A. T. Abbott (1970), *Volcanoes in the Sea: The Geology of Hawaii*, 441 pp., Univ. Press of Hawaii, Honolulu.

MacDougall, I. (1971), The geochronology and evolution of the young island of Réunion, Indian Ocean, *Geochim. Cosmochim. Acta*, *35*, 261–270.

MacGuire, W. J., and A. D. Pullen (1989), Location and orientation of eruptive fissures and feeder-dykes at Mount Etna: Influence of gravitational and regional tectonic stress regimes, *J. Volcanol. Geotherm. Res.*, *38*, 325–344.

Maillot, E. (1999), Les systèmes intrusifs des volcans boucliers océaniques: Ile de la Réunion (Océan Indien): Approche structurale et experimentale, Ph.D. thesis, 289 pp., Univ. la Réunion, Saint-Denis Messag, France.

Malengreau, B., J.-F. Lénat, and J.-L. Froger (1999), Structure of the Réunion Island (Indian Ocean) inferred from the interpretation of gravity anomalies, *J. Volcanol. Geotherm. Res.*, *88*, 131–146.

Marinoni, L. B., and A. Gudmundsson (2000), Dykes, faults and palaeostresses in the Teno and Anaga massifs of Tenerife (Canary Islands), *J. Volcanol. Geotherm. Res.*, *103*, 83–103.

Merle, O., and A. Borgia (1996), Scaled experiments of volcanic spreading, *J. Geophys. Res.*, *101*, 13,805–13,817.

Merle, O., and J. Lénat (2003), Hybrid collapse mechanism at Piton de la Fournaise volcano, Reunion Island, Indian Ocean, *J. Geophys. Res.*, *108*(B3), 2166, doi:10.1029/2002JB002014.

Michel, S., and J. Zlotnicki (1998), Self-potential and magnetic surveying of la Fournaise volcano (Réunion Island): Correlations with faulting, fluid circulation, and eruption, *J. Geophys. Res.*, *103*, 17,845–17,857.

Morgan, W. J. (1971), Convection plumes in the lower mantle, *Nature*, *230*, 42–43.

Nercessian, A., A. Hirn, J.-C. Lépine, and M. Sapin (1996), Internal structure of the Piton de la Fournaise volcano from seismic wave propagation and earthquake distribution, *J. Volcanol. Geotherm. Res.*, *70*, 123–143.

Oehler, J.-F. (2005), Les déstabilisations de flanc des volcans de l'Ile de la Réunion (Océan Indien): Mise en évidence, implications et origines, Ph.D. thesis, 422 pp., Univ. é Clermont-Ferrand II, Clermont-Ferrand, France.

Oehler, J.-F., P. Labazuy, and J.-F. Lénat (2004), Recurrence of major flank landslides during the last 2 Ma-history of Réunion Island, *Bull. Volcanol.*, *66*, 585–598.

Oehler, J.-F., B. Van Wyk de Vries, and P. Labazuy (2005), Landslides and spreading of oceanic hot-spot and arc shield volcanoes and Low Strength Layers (LSLs): An analogue modelling approach, *J. Volcanol. Geotherm. Res.*, *144*, 169–189.

O'Neill, C., D. Müller, and B. Steinberger (2003), Geodynamic implications of moving Indian Ocean hotspots, *Earth Planet. Sci. Lett.*, *215*, 151–168.

Peltier, A., V. Ferrazzini, T. Staudacher, and P. Bachèlery (2005), Imaging the dynamics of dyke propagation prior the 2000–2003 flank eruptions at Piton de la Fournaise, Réunion Island, *Geophys. Res. Lett.*, *32*, L22302, doi:10.1029/2005GL023720.

Pollard, D. D. (1987), Elementary fracture mechanics applied to the structural interpretation of dykes, in *Mafic Dyke Swarms*, edited by H. C. Halls and W.F. Fahrig, *Geol. Assoc. Can. Spec. Pap.*, *34*, 5–24.

Rançon, J.-P., P. Lerebour, and T. Augé (1989), The Grand Brulé exploration drilling: New data on the deep framework of the Piton de la Fournaise volcano. part 1: Lithostratigraphic units and volcanostructural implicationsm, *J. Volcanol. Geotherm. Res.*, *36*, 113–127.

Robert, D. (1980), Inventaire et analyse systématiques des différents ensembles d'intrusions volcaniques (dykes et sills) de l'île de la Réunion, *Rap. BRGM 80 SGN 532 GTH/80 REU 17,* 71 pp., Bur. de Rech. Geol. et Min., Orléans, France.

Rocher, P. (1988), Contexte volcanique et structural de l'hydrothermalisme recent dans le massif du Piton des Neiges, île de la Réunion: Etude détaillée du cirque de Salazie, Ph.D. thesis, 443 pp., Univ Paris-Sud, Paris.

Siebert, L. (1984), Large volcanic debris avalanches: Characteristics of source areas, deposits, and associated eruptions, *J. Volcanol. Geotherm. Res.*, *22*, 163–197.

Sigmundsson, F., P. Durand, and D. Massonnet (1999), Opening of an eruptive fissure and seaward displacement at Piton de la Fournaise volcano measured by RADARSAT satellite radar interferometry, *Geophys. Res. Lett.*, *26*, 533–536.

Smith, J. R., and P. Wessel (2000), Isostatic consequences of giant landslides on the Hawaiian Ridge, *Pure Appl. Geophys.*, *157*, 114–1097.

Smith, W. H. F., and D. T. Sandwell (1997), Global sea floor topography from satellite altimetry and ship depth soundings, *Science*, *277*, 1956–1963.

Tibaldi, A. (1996), Mutual influence of diking and collapses at Stromboli volcano, Aeolian Arc, Italy, in *Volcano Instability on the Earth and Other Planets*, edited by W. J. McGuire, A. P. Jones, and J. Neuberg, *Geol. Soc. Spec. Publ.*, *110*, 55–63.

Tibaldi, A. (2003), Influence of cone morphology on dykes, Stromboli, Italy, *J. Volcanol. Geotherm. Res.*, *126*, 79–95.

Twidale, C. R. (2004), River patterns and their meaning, *Earth Sci. Rev.*, *67*, 159–218.

van Wyk de Vries, B., and R. Matela (1998), Styles of volcano-induced deformation: Numerical models of substratum flexure, spreading and extrusion, *J. Volcanol. Geotherm. Res.*, *81*, 1–18.

Vidal, N., and O. Merle (2000), Reactivation of basement faults beneath volcanoes: A new model of flank collapse, *J. Volcanol. Geotherm. Res.*, *99*, 9–26.

Walker, G. P. L. (1999), Volcanic rift zones and their intrusion swarms, *J. Volcanol. Geotherm. Res.*, *94*, 21–34.

Walter, T. R., and V. R. Troll (2003), Experiments on rift zone evolution in unstable volcanic edifice, *J. Volcanol. Geotherm. Res.*, *127*, 107–120.

Watts, A. B., J. H. Bodine, and M. S. Steckler (1980), Observations of flexure and the state of stress in the oceanic lithosphere, *J. Geophys. Res.*, *85*, 6369–6376.

Watts, A. B., U. S. ten Brink, P. Buhl, and T. M. Brocher (1985), A multi-channel seismic study of lithospheric flexure across the Hawaiian-Emperor seamount chain, *Nature*, *315*, 105–111.

Watts, A. B., C. Pierce, J. Collier, R. Dalwood, J. P. Canales, and T. J. Henstock (1997), A seismic study of lithospheric flexure in the vicinity of Tenerife, Canary Islands, *Earth Planet. Sci. Lett.*, *146*, 431–447.

Wessel, P., and B. Keating (1994), Temporal variations of flexural deformation in Hawaii, *J. Geophys. Res.*, *99*, 2747–2756.

Zlotnicki, J., J.-C. Ruegg, P. Bachèlery, and P. A. Blum (1990), Eruptive mechanism on Piton de la Fournaise volcano associated with the December 4, 1983 and January 18, 1984 eruptions from ground deformation monitoring and photogrammetric surveys, *J. Volcanol. Geotherm. Res.*, *40*, 197–217.

————————
P. Bachelery, L. Michon, and F. Saint-Ange, Laboratoire des Sciences de la Terre de l'Université de la Réunion (LSTUR), Institut de Physique du Globe de Paris, CNRS, UMR 7154, BP7151, 15 rue René Cassin, F-97715 Saint Denis messag 9, France. (laurent.michon@univ-reunion.fr)

T. Staudacher, Observatoire volcanologique du Piton de la Fournaise (OVPF), Institut de Physique du Globe de Paris, CNRS, UMR 7154, F-97418 La Plaine des Cafres, France.

N. Villeneuve, CREGUR, Université de la Réunion, 15 rue René Cassin, F-97715 Saint Denis messag 9, France.